Effects of Blast Loading on Reinforced Concrete Facade Systems

by

Indunil Rajith Kumara Galhena, GALHENA APPUHAMILAGE

Thesis submitted in fulfilment of the requirements of the degree of Doctor of Philosophy

March, 2015

College of Engineering and Science

Victoria University

ABSTRACT

Facade systems are an integral part of modern day construction, especially with reinforced concrete structures. These facade systems are typically designed to withstand the effects of normal service loads and severe weather conditions. However, these elements are rarely designed to withstand the effects of an external explosion, which is considered as a rising threat to structural safety with the recent escalation of terrorist activities. In addition, these facade systems will act as the first layer of defence against an external explosion limiting the damage to the main structure.

The aim of this research is to study the effects of blast loading on reinforced concrete facade systems. More specifically, the behaviour of reinforced concrete facade panels with flexible support conditions will be investigated. The overall aim was pursued by evaluating and utilising experimental studies relevant to this research to undertake 3-D finite element modelling using LS-DYNA and 1-D analytical modelling using a theoretical development. The validated numerical and analytical models were then utilised in a comprehensive parametric study.

The 3-D finite element model was developed using the LS-DYNA finite element model. Eight different material model combinations for concrete and reinforcing steel were considered for the initial model development along with a mesh sensitivity analysis. The developed finite element model was calibrated using selected experimental results where the material model combination with least error percentage was selected for further validation. The developed model was validated for standard connection and idealized support types with varying concrete strengths and typical reinforcements with yield strengths around 600 MPa. Three scaled distances (0.518 m/kg$^{1/3}$, 0.591 m/kg$^{1/3}$ and 1.19 m/kg$^{1/3}$) of explosive loading were examined. Also, strengths and drawbacks of using the 3-D finite element modelling of reinforced concrete facade systems subjected to explosive loading were discussed.

The 1-D analytical solution was developed using the Timoshenko Beam Theory (TBT), as an alternative to the 3-D finite element tool. The analytical solution was constructed using different constitutive relationships to predict the flexural, diagonal shear and direct shear behaviour including the strain rate effects. This tool was developed with the capability of generating the pressure-time relationships for known charge weight-

standoff combinations, in addition to the user defined pressure-time relationships. The developed analytical solution was programed to a computer application using FORTRAN, where it was verified with experimental results. Accuracy levels beyond 80% were achieved with the 1-D solution, which is similar to the accuracy levels achieved with the 3-D finite element model.

A comprehensive parametric study was conducted on reinforced concrete facade systems using the developed 1-D analytical solution and the 3-D finite element model. Comparison of the chosen dowel and angle cleat connections revealed that angle cleat connections are significantly better at transferring the effects of explosive loading safely with limited deflections and stresses. The effects of flexible fixing assemblies were evaluated in terms of cleat thickness and bolt diameters. It was identified that the use of bolt diameters between 16-25 mm and cleat thicknesses between 16-24 mm would result in the most effective force transfer mechanisms. Openings in facade panels were examined with size, location and reinforcement configuration. Although the introduction of openings were found to alter the structural behaviour, redistribution of the curtailed reinforcement around the opening was enough to maintain the maximum deflection to that of the panels without openings. In addition, performance of architectural facade panels with built-in curvatures was assessed. The introduction of curvatures were found to be effective in minimizing the maximum deflection although which comes with the cost of elevated compressive stresses within the concrete section.

Finally, conclusions were presented on sizing the structural components, fixing assemblies, opening sizes and locations of facade systems based on the outcomes of the parametric study. These can be used to design reinforced concrete facade systems with improved safety under the effects of explosive loading.

DECLARATION

I, Indunil Rajith Kumara Galhena, Galhena Appuhamilage, declare that the PhD thesis entitled “Effects of Blast Loading on Reinforced Concrete Facade Systems” is no more than 100,000 words in length, including quotes and exclusive of tables, figures, appendices, bibliography, references and footnotes. This thesis contains no material that has been submitted previously, in whole or in part, for the award of any other academic degree or diploma. Except where otherwise indicated, this thesis is my own work

Signature: …… Date: ……

ACKNOWLEDGEMENT

Reading for a PhD degree would be a remarkable lifetime opportunity that anyone can ever be dreamed of. There were many helping hands behind this achievement. In that context, I make this opportunity to convey my sincere gratitude to all who contributed in various ways to complete my candidature at the Victoria University.

First and foremost, I would like to express my heartfelt gratitude to my supervisor, Professor Sam Fragomeni for his excellent guidance, encouragement, commitment, kindness and patience extended throughout this period. The guidance and commitment given by him in order to complete my study was extraordinary.

I am particularly grateful for my external Supervisor, Dr. Tuan Ngo, University of Melbourne for his valuable suggestions, comments, criticisms and commitment given upon this research. His expertise in this field has been very useful to direct this research in the precise direction.

Next, I would like to express my very great appreciation to my former associate supervisor Dr. Nirdosha Gamage, RMIT University for accepting my PhD application and also for her excellent supervision and understanding. Apart from her academic supervision, her kind guidance during initial stage of the study was really useful for me to settle in the new life in Australia.

My heartfelt gratitude goes to Victoria University for accepting my application and providing me financial assistance by a research scholarship to conduct my research. Similarly, I would like to offer my special thanks to Professor Chris Perera, Dean, research and Dr. Srikanth Venkatesan, Senior lecturer, Victoria University for the assistance and guidance provided in difficult times.

I would also like to extend my gratitude to all the technical team in Victorian Partnership for Advanced Computing (V-PAC) for providing the analysis solutions/software licences for LS-DYNA and PGI visual FORTRAN in V-PAC servers. Likewise, I am grateful to LEAP Australia (Pvt) Ltd and Dr. Danh Tran, Victoria University, for arranging LS-DYNA and ANSYS training programs.

I owe to my loving parents, for their dedication and commitment given to make my education effective and fruitful. I extend my deep gratitude to my loving mother, for sacrificing her all dreams on behalf of me and supporting me all the way through as a single parent.

Finally, I am indebted to my beloved wife, Samanthi for her understanding and encouraging me for almost 5 years of life in Australia. I also appreciate her valuable comments and suggestions given for my research and for helping me with proof reading this thesis.

Last but not least, I am grateful to all the staff members and colleagues of Victoria University, Melbourne for their assistance given during various stages of my study.

TABLE OF CONTENTS

Appendix B

Appendix C

Appendix D

LIST OF FIGURES

LIST OF TABLES

LIST OF SYMBOLS

A_c : Area of concrete/ Concrete core area

A_d : Area of diagonal reinforcement bars for direct shear restrain

A_s : Shear area of the bolts/ Area of tensile reinforcement

$A_s{}'$: Area of compressive reinforcement

A_t : Tensile area of the bolts

C : Damping coefficient for single degree of freedom system

C_L : Highest velocity of the disturbance propagation

d : Effctive depth of tensile reinforcement

d' : Effctive depth of compressive reinforcement

d_c : Effective depth between compressive and tensile reinforcement

E : Initial tangent modulus

E_1^c : Secant modulus of concrete in direction-1, considering Hsu/Zhu ratios

$\bar{E}_1^c$: Secant modulus of concrete in direction-1, neglecting Hsu/Zhu ratios

E_2^c : Secant modulus of concrete in direction-2, considering Hsu/Zhu ratios

$\bar{E}_2^c$: Secant modulus of concrete in direction-2, neglecting Hsu/Zhu ratios

E_l^s : Secant modulus of steel in direction –*l*, considering Hsu/Zhu ratios

$\bar{E}_l^s$: Secant modulus of steel in direction –*l*, neglecting Hsu/Zhu ratios

E_c : Elastic modulus of concrete

E_s : Elastic modulus of steel

E_t^s : Secant modulus of steel in direction –*t*, considering Hsu/Zhu ratios

$\bar{E}_t^s$: Secant modulus of steel in direction –*t*, neglecting Hsu/Zhu ratios

f_c' : Compressive strength of concrete

$(f_c')_c$: Compressive strength measured from a standard cylinder test

$(f_c')_{cu}$: Compressive strength measured from a standard cube test

f_{ck}' : Characteristic compressive strength of concrete

f_{cm}' : Mean compressive strength of the sample

f'_{cc} : Compressive strength of confined concrete

f_{cr} : Cracking tensile strength of concrete

f_{dy} : Dynamic yield strength (reinforcement)

f_{du} : Dynamic ultimate strength (reinforcement)

f'_{dc} : Dynamic compressive strength (concrete)

f_l : Smeared (average) steel stress in longitudinal direction (*l*-axis)

f_{ly} : Yield stress of longitudinal bare steel bars

f_n : Smeared (average) tensile steel stress at first yield

f_r : Modulus of rupture/ Flexural tensile strength of concrete

f_{res} : Residual stress of confined concrete

f'_{res} : Residual stress of unconfined concrete

f_{st} : Splitting tensile strength of concrete

f_u, f_{su} : Ultimate tensile strength of reinforcing steel

f_t : Smeared (average) steel stress in transverse direction (*t*-axis)

f_{ty} : Yield stress of transverse bare steel bars

f_y, f_{sy} : Yield strength of reinforcing steel

f'_y : Yield stress of bare steel bars

f_{yh} : Yield strength of hoop reinforcement

G : Shear modulus of bolting material

G^c_{21} : Shear modulus of concrete in 2-1 coordinates of applied stresses

G_f : Fracture energy

G_{f0} : Base fracture energy

h'' : Width of concrete core

I_1 : First invariant of volumetric stress tensor

I_{so} : Peak incident impulse

I_r : Peak reflected impulse

J_2, J_3 : Second and third invariants of deviatoric stress tensor

K : Stiffness coefficient for single degree of freedom system/ bulk modulus of concrete/ Cofinement coefficient

K_a : Axial stiffness of the bolting material

K_b : Flexural (translational) stiffness of the angle section.

k_d : Internal scalar multiplier

K_r : Rotational stiffness (linear) of support/Fixing assembly

K_s : Shear stiffness of the bolt

K_t : Translational stiffness (linear) of support/Fixing assembly

K_z : Translational stiffness

L : Length/ Span length of the beam/ Initial length of the bolt shear plane

l : Direction of longitudinal steel bars

L_b : Length of the bolt shank up to the fastener (nut)

M : Lumped mass for single degree of freedom system/ Bending moment

M_a : Applied bending moment at a given node

M_b : Resisting moment at support/Fixing assembly

$(M)_y$: Yielding moment (corresponding to initial cracking)

M_u : Ultimate moment capacity

N_u : Axial force applied at the same section of shear design

P : Pressure exerted by the elemet

P_{atm} : Atmospheric (ambient) pressure

P_r : Reflected overpressure

P_r^+ : Peak reflected overpressure

P_{so}/P_{so}^+: Peak incident overpressure (positive)/Incident overpressure

P_{so}^- : Peak incident overpressure (negative)

Q : Dynamic pressure/ Shear force

q : Uniformly distributed load transverse to the beam

Q_a : Applied shear force at a given node

Q_b : Resisting Shear force at support/Fixing assembly

R : Distance from charge centre to target/Standoff distance/ Strength reduction factor for residual strength of concrete

r : Spall radius

r_T : Tensile membrane capacity

s : Spacing of hoop reinforcement along the length of the member

s_h : Spacing of shear reinforcement (hoop spacing)

S_s : Spacing of stirrups parallel to main reinforcement

r : Spall radius

t : Direction of transverse steel bars/ Time

t_a : Arrival time

t_d^+ : Positive phase duration

t_d^- : Negative phase duration

t_r : Idealized Positive Phase duration

U : Shock front velocity

v_u : Ultimate shear stress

v_c : Shear strength of unrerinforced concrete

v_d : Direct shear capacity

W : Charge weight

w : Transverse displacement

W_{adj} : Shape adjusted charge weight

W_b : Ttransverse deflection of support/Fixing assembly

x : Ratio of strain at maximum stress between confined and unconfined concrete

Z : Scaled distance

Z_m : Softening slope for confined concrete

Z'_m : Softening slope for unconfined concrete

α : Angle between diagonal and longitudinal reinforcement

a_0 : Impulse constant

α_2 : Angle of applied principal compressive stress (2-axis) with respect to longitudinal steel bars (*l*-axis)

α_a : Angle of incidence (incidence angle)

β : Angle of bending rotation

β_b : Angle of bending rotation of support/Fixing assembly

γ_{21} : Smeared (average) shear strain in 2-1 coordinate of applied stresses

γ_{21}^c : Smeared (average) shear stress of concrete in 2-1 coordinates

γ_{lt} : Smeared (average) shear strain in *l*-*t* coordinate of steel bars

δ : Deflection

$\Delta\lambda$: The modified plastic strain increment

ε_0 : Strain at maximum stress in concrete/ Concrete cylinder strain at peak strength

ε_1 : Smeared (average) strain in 1-direction considering Hsu/Zhu ratios or bi-axial strain in 1-direction

ε_2 : Smeared (average) strain in 2-direction considering Hsu/Zhu ratios or bi-axial strain in 2-direction

ε_c : Compressive strain/ Strain at maximum stress for unconfined concrete

ε_{cc} : Strain at maximum stress for confined concrete

ε_{cr} : Cracking tensile strain of concrete

ε_{cu} : Failure strain of concrete

ε_{ij}^p : Plastic strain

ε_l : Smeared (average) strain in l -direction considering Hsu/Zhu ratios or bi-axial strain in l -direction

ε_n : Smeared (average) strain of steel bars at first yield neglecting Hsu/Zhu ratios or uniaxial strain in l -direction

ε_{sf} : Smeared (average) tensile strain of steel bars that yields first

ε_t : Smeared (average) strain in t -direction considering Hsu/Zhu ratios or bi-axial strain in t-direction

ε_{su} : The failure strain of reinforcement

ε_u : Ultimate strain of reinforcing steel

ε_v : Volumetric strain

$\varepsilon_{v,yield}$: Volumetric strain corresponding to yield surface

ε_y : Yield strain of reinforcing steel

$\dot{\varepsilon}_s$: Quasi-static strain rate

$\dot{\varepsilon}^*$: Effective total strain rate (strain rate / quasi-static threshold rate)

$\dot{\varepsilon}_{ij}^p$: Plastic strain rate

$\bar{\varepsilon}_1$: Smeared (average) strain in 1-direction neglecting Hsu/Zhu ratios or uniaxial strain in 1-direction

$\bar{\varepsilon}_2$: Smeared (average) strain in 2-direction neglecting Hsu/Zhu ratios or uniaxial strain in 2-direction

$\bar{\varepsilon}^p$: Effective plastic strain

$\bar{\varepsilon}_l$: Smeared (average) strain in l -direction neglecting Hsu/Zhu ratios or uniaxial strain in l –direction

$\bar{\varepsilon}_n$: Smeared (average) strain in steel bars neglecting Hsu/Zhu ratios; becomes or when applied to the longitudinal and transverse steel, respectively

$\bar{\varepsilon}_t$: Smeared (average) strain in t -direction neglecting Hsu/Zhu ratios or uniaxial strain in t -direction

η : Parameter defined as $(\rho_t f_{ty} - \sigma_t)/(\rho_l f_{ly} - \sigma_l)$ / Yield scale factor ($0 \leq \eta \leq 1$)

η' : η or its reciprocal, whichever is less than unity; $\eta' \geq 0.2$

θ/θ_m : Support rotation

λ : Material parameter for strain rate enhancement of reinforcement/ Modified effective strain/ Function of lode angle (θ)

λ_m : Maximum modified effective strain (corresponds to limit stress surface)

ξ : Softening coefficient of concrete in compression when peak stress-softened coefficient is equal to strain-softened coefficient

ρ : Density/ Tensile reinforcement ratio

ρ_l : Steel ratio in longitudinal direction

ρ_m : Mass density

ρ_t : Steel ratio in transverse direction

ρ_s : Volumetric ratio of hoop reinforcement

ρ_{sh} : Volumetric ratio of hoop reinforcement

σ : Standard deviation of the sample

σ_1^c : Smeared (average) tensile stress of concrete in 1-direction

σ_2^c : Smeared (average) tensile stress of concrete in 2-direction

σ_l : Applied normal stress in *l*-direction of steel bars

σ_t : Applied normal stress in *t*-direction of steel bars

$\sigma_{xx}, \sigma_{yy}, \sigma_{zz}$: Principle stresses in a Cartesian coordinate system

τ_m : Maximum shear capacity of a given cross-section

τ_e : Shear strain corresponding to elastic limit

υ : Poisson's ratio

υ_{12} : Hsu/Zhu ratio (ratio of resulting tensile strain to source compressive strain)

υ_{21} : Hsu/Zhu ratio (ratio of resulting compressive strain to source tensile strain)

φ : Curvature of the section/ Lode angle

ϕ_{max} : Maximum curvature

$(\phi)_y$: Curvature corresponding to yielding of the section

ψ : Spall parameter / Ratio of tensile meridian radius to compression meridian

ω : Natural frequency of vibration

$\Re(J_3)$: Rubin reduction factor

LIST OF ABBREVIATIONS

ACI : American Concrete Institute

ALE : Arbitrary Lagrangian Eularian

ANFO : Ammonium-nitrate-fuel-oil

BGU : Ben-Gurion University

CDM : Concrete Damage Model

CFD : Computational Fluid Dynamics

CFRP : Carbon Fibre Reinforcing Polymer

CFT : Compression Field Theory

COV : Coefficient of variance

CSCM : Continuous Surface Cap Model

CSM : Computational Structural Mechanics

DEM : Discrete Element Modelling

DIF : Dynamic increase factor

EBBT : Euler – Bernoulli Beam Theory

EFG : Element-free Galerkin

EOS : Equation of State

FA-STM : Fixed Angle Softened Truss Model

FE : Finite element

FEM : Finite Element Model

FEMA : Federal Emergency Management Agency

FRC : Fibre Reinforced Concrete

FRP : Fibre Reinforced Polymer

GFRP : Glass Fibre Reinforcing Polymer

HSC : High Strength Concrete

JC : Johnson Cook

MDOF : Multy Degree of Freedom

MSM : Modified Scott Model

NSC : Normal Strength Concrete

PCI : Precast/Prestress Concrete Institute

PETN : Penta-erythritol-tetra-nitrate

PK : Plastic Kinematic

RAM : Random Access Memory

RA-STM : Rotating Angle Softened Truss Model

RC : Reinforced Concrete

RE : Relative effectiveness

RPC : Reactive Powder Concrete

SDCM : Strain-Rate Dependent Concrete Model

SDOF : Single Degree of Freedom

SFRC : Steel Fibre Reinforced Concrete

SJC : Simplified Johnson Cook

SMM : Softened Membrane Model

TBT : Timoshenko Beam Theory

TNT : Tri nitro-toluene

UFC : Unified Facilities Criteria

USDoD : United States Department of Defence

WCM : Winfrith Concrete Model

CHAPTER 1

INTRODUCTION

1.1. Background

The United States Department of States' (USDOS) Country report on terrorism (2010) stated that more than 11,000 terrorism-related attacks were reported in 2010 alone resulting in 13,000 fatalities and another 30,000 injured. The report further illustrates that among the 11,000 attacks, 13% involved explosions, targeting civilian or commercial structures. Terrorist related incidents such as in London (in 2005), Madrid (in 2004), Istanbul (in 2003), Bali (in 2002), and New York (in 2001) (Buchan and Chen, 2007) have illustrated the performance related problems of structures subjected to intense dynamic loading. Apart from terrorist attacks targeted towards civil, commercial or military buildings, accidental explosions such as in storage facilities have further shown a similar vulnerability of structures against the intense dynamic loading.

Concrete has been used as a construction material for more than 100 years and is still one of the most preferable construction material in all forms of construction from domestic units to skyscrapers. Although concrete is used primarily as a construction material for structural elements, it is also used more frequently in architectural applications such as facade systems in recent years. These facade systems are generally designed to withstand normal service loads such as wind load, self-weight and loads induced by severe weather conditions such as cyclones. Although facade systems are the first layer of defence against a terrorist bombing, these are rarely being designed to withstand even a small scale explosion.

Reinforced concrete facade panels can be considered similar to structural concrete panels, except for differences in connection mechanisms. Failure of reinforced concrete cladding panels subjected to explosive loading can be of two types, failure of the panel itself or failure of connection mechanisms. A failure in the panel itself tends to be local while failure of fixing assemblies can result in a more catastrophic failure as it can cause dislodgement of the entire facade system. More alarmingly, post blast surveys on past events (Corley et al. 1996, Hayes Jr et al. 2005, Pham, 2010) have shown that connections in reinforced concrete facade systems are the most vulnerable to explosive

events. Furthermore, failure of facade systems can result in more casualties due to the fragmentation effects from extreme pressure release.

The history of quantitative research on blast loading of reinforced concrete panels date back to early 1960s' (United States Army Corps of Engineers, 2008) where many of the studies were conducted by the United States Department of Defence (USDOD). However, these studies were primarily focussed on strengthening military facilities which are not always applicable to commercial and civilian structures. Furthermore, most of these were experimental studies which did not have the required instrumentation and technology to adequately capture loading effects, as well as structural and material behaviour at that time. The problem has been partially addressed in recent years, through experimental and numerical studies of reinforced concrete structural elements subjected to explosive loading. However, non-structural elements such as facade panels have been ignored along with the dynamic behaviour of connection mechanisms and fixing assemblies, where overly simplified support conditions have been used in limited studies.

Reinforced concrete facade systems with flexible support condition have been effectively used as a passive method of energy dissipation in earthquake and wind resistant applications (Pinelli et al. 1993, Hayes Jr et al. 2005, Azad et al. 2012, Samali et al. 2014). These studies have highlighted the importance of facade panel-fixing assembly interaction and the importance of proper fixing assemblies. Furthermore, limited studies on facade panels subjected to explosive loading suggested that the effects of flexible fixing assemblies are more significant in short duration dynamic loading (i.e. explosive loading) than the low-frequency dynamic loading (i.e. earthquake loading). However, detailed studies have not been conducted on the performance of reinforced concrete facade panels with flexible fixing assemblies, subjected to explosive loading. In addition, available design guidelines (United States Army Corps of Engineers, 2008) do not consider the effects of flexible fixing assemblies. Hence it is essential to study the behaviour and response of reinforced concrete facade panels with flexible fixing assemblies, when subjected to explosive loading.

1.2. Problem statement

Facade systems are an integral part of modern day construction, especially with reinforced concrete structures. These facades work as an envelope system providing

cover to the main structure and occupants. However, these systems are generally designed to withstand the effects of normal service loads and severe weather conditions. On rare occasions, these facade systems are designed to withstand the effects of earthquake loads and also utilised as a passive method of earthquake energy dissipation. These facade systems have rarely been designed to withstand the effects of explosive loading, although terrorist-borne explosives are considered as a rising threat to structural safety. In addition, none of the major design codes, including UFC 3-340 (United States Army Corps of Engineers, 2008), provide guidelines for blast resistant design of facade systems.

Several experimental studies have been conducted on the behaviour of reinforced concrete facade systems subjected to explosive loading (Pan and Watson, 1996, Pan and Watson, 1998, Pan et al. 2001, Starr and Krauthammer, 2005, Pham et al. 2008, Pham, 2010). However, only a limited number of studies have considered the interaction between RC panel and the fixing assemblies (Pan and Watson, 1996, Pham et al. 2008, Pham, 2010). Even these limited studies have observed promising results showing reduced forces in fixing assemblies and reduced maximum deflections. However, only a limited number of connection configurations were considered for these studies.

In the case of reinforced concrete cladding panels, the stiffness ratio between panel and fixing assembly was found to play a major role in determining the response of the panel system. Several analytical and numerical studies conducted on RC cladding panels with flexible support conditions observed improved panel resistance with reduced deflections (Pham et al. 2008, Pham, 2010, Pan and Watson, 1998). However, allowing too much flexibility in fixing assemblies found to be catastrophic as a failure in fixing assemblies.

Considering the cost of an experimental study, it is common to study the problems of explosive loading on structures using alternative methods. 3-D finite element modelling is considered as an effective tool for analysing reinforced concrete structures under explosive loading (Wang et al. 2008, Zhou et al. 2008, Musselman, 2007, Pantelides et al. 2012, Vasudevan, 2013). However, these 3-D finite element programs require large setting up time and computational resources, in addition to the large data requirements in the case of problems in the dynamic domain. Hence, a considerable user experience is essential in the successful modelling of explosive related problems.

Alternative to 3-D finite element programs, analytical solutions based on the single degree of freedom systems (SDOF) and multi-degree of freedom systems (MDOF) are used. However, use of SDOF systems has the inherent disadvantage of the establishment of the fundamental mode of vibration, typically known as bending mode. Although it is capable of accurately predicting the response for explosive loading, it requires a long list of approximations (Krauthammer et al. 1986, El-Dakhakhni et al. 2009, Hussein, 2010). On the other hand, the multi-degree of freedom systems (MDOF) can predict the response more accurately. Several researchers (Krauthammer et al. 1993a, Krauthammer et al. 1993b, Pham, 2010) used MDOF systems with one-way spanning RC elements. However, there are improvements that can be made in MDOF systems, which could be used to analyse the reinforced concrete panel systems.

1.3. Significance of the study

As discussed earlier, a limited number of studies have been conducted on reinforced concrete facade systems subjected to explosive loading. However, these studies suggested the importance of the interaction between concrete facade panels and fixing assemblies during an explosive event. This study will try to quantify the interaction between the panel and fixing assemblies, and provide guidelines for sizing the panel and fixing assemblies. Since none of the major design codes, including UFC 3-340, do not provide guidelines for the design of facade panels and fixing assemblies, these proposals can be used to design reinforced concrete facade systems and fixing assemblies for optimum explosive loading protection.

1.4. Scope and Objective

The aim of this research is to study the effects of blast loading on reinforced concrete facade systems. More specifically, the behaviour of reinforced concrete facade panels with flexible support conditions will be investigated. The overall aim will be pursued through,

i. Conducting a comprehensive literature review to identify the experimental studies relevant to this research and utilising them in numerical and analytical model development.

ii. Development of a comprehensive 3D numerical model of a facade system with its assemblies using LS-DYNA finite element package with calibration, verification and validation using relevant experimental results.

iii. Development of a 1D analytical solution using FORTRAN with calibration, verification and validation using relevant experimental results.

iv. Investigation on the behaviour of different facade systems and assemblies through various parametric studies using the validated 3D finite element model and 1D analytical solution.

1.5. Research outline

This research study consists of four major sections, as highlighted in the scope of the research. A detailed literature review, including evaluation of experimental and numerical studies, is conducted with the aim of selecting applicable experimental results for numerical and analytical model validation. In addition, stress-strain relationships, strain rate enhancement factors, constitutive relationships and material models applicable to dynamic domain were critically evaluated and selected during the literature review for the development of the 1-D analytical model and 3-D numerical model. Figure 1.1illustrates the outline of this research.

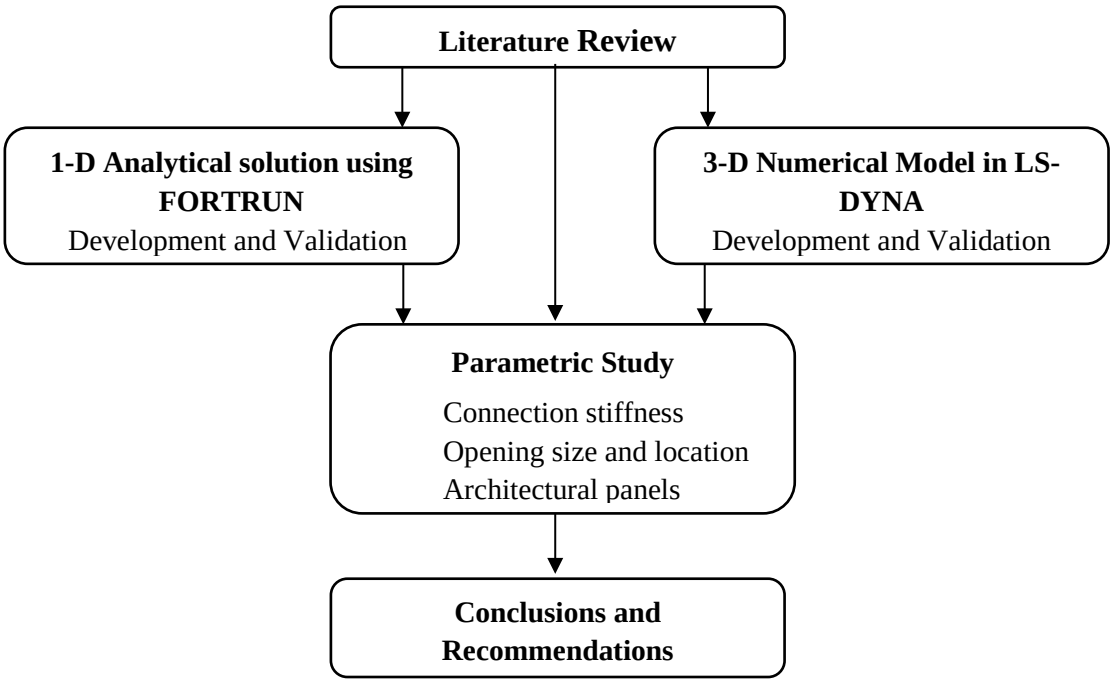

Figure 1.1: Research Outline

The 3-D numerical model was developed using LS-DYNA finite element module. The development is based on the carefully selected constitutive relationships and material model combinations and validated using the selected experimental results. Eight different material model combinations were considered for the numerical model development in addition to the mesh sensitivity analysis for the model development. The developed model was validated using two independent experimental studies among the handful of quantitative experimental details available.

The 1-D analytical solution was developed as an alternative to the 3-D finite element model to improve the efficiency of the analysis, by minimising the setting up time and computational requirements. This analytical solution is developed using the Timoshenko beam theory (TBT) and carefully selected constitutive relationships. The developed solution was programmed to a computer application using the FORTRAN programming language and validated using the selected experimental results. Finally, results from the LS-DYNA, 3-D numerical model and the 1-D analytical approach are comprehensively compared.

A parametric study is conducted using the validated LS-DYNA, 3-D finite element model and the 1-D analytical solution. Different connection configurations of two common connection types are evaluated for the panel and fixing assembly performance. In addition, the parametric study is utilised to include facade panels with openings and architectural facade panels with curvatures. Openings of different sizes, locations and reinforcing (stiffening) combinations were considered for panels with the openings and curvatures in longitudinal and transverse directions were considered for the architectural panels.

1.6. Thesis layout

This thesis contains 8 chapters, and a short summary of work presented in each chapter is outlined below.

Chapter 1:

Chapter one provides an introduction to the problem, objectives and research outline of this study.

Chapter 2:

A detailed literature review is presented on the prediction of blast loading parameters and structural response/failure mechanisms of reinforced concrete structures subjected to blast loading.

Chapter 3:

A detailed review of quasi-static and dynamic properties of concrete and reinforcing steel is presented in Chapter 3, along with constitutive relationships for material modelling in 3-D finite element programs. In addition, concrete and steel reinforcement material models (in LS-DYNA) were reviewed.

Chapter 4:

An Overview of recent experimental and numerical studies on reinforced concrete panel systems is presented in Chapter 4. A review of UFC 3-340 design guidelines for reinforced concrete panels is also included.

Chapter 5:

The development and validation of the 3-D finite element model using LS-DYNA finite element package is described in here. In addition, experimental details selected for the model validation are described at the beginning of the chapter.

Chapter 6:

The development and validation of the 1-D analytical solution is described in Chapter 6. In addition, the validation results are compared with the LS-DYNA validation results from Chapter 5.

Chapter 7:

The parametric study conducted on reinforced concrete facade systems is described in this chapter. The use of different fixing assemblies, effect of opening configuration and architectural panels with built-in curvatures is discussed.

Chapter 8:

Major conclusions drawn from the development and validation of the two analysis models and parametric study are presented in Chapter 8.

CHAPTER 2

BLAST LOADING AND STRUCTURAL RESPONSE

2.1. Introduction

Estimation of loading and predicting the response of a structure is one of the key responsibilities of a structural engineer. Loading conditions experienced by a structure during its lifespan can be roughly divided into two major categories, static and dynamic loading. Static loading is considered the everyday loading experienced by the structure, including the dead and imposed loads. Estimation and prediction of structural response against the static loads is straightforward, even with different combinations of loads. However, predicting dynamic loading as well as the dynamic response of a structure is not as easy.

Dynamic loading on a structure can be developed from different sources such as human activities and movements, wind, earthquake, high-speed impacts and explosions (blast). Most of these loading conditions are covered by modern design (loading) codes (European Committee for Standardisations, 2006, American Society of Civil Engineers, 2002, Standards Australia, 2011). However, all the major design codes have given limited attention to explosive loading, partly due to the scarcity and extreme nature of the loading. The United States Army Corps of Engineers have published series of comprehensive design guidelines (United States Army Corps of Engineers, 1986, United States Army Corps of Engineers, 1990, United States Army Corps of Engineers, 2008) for the construction of military and storage facilities focusing on explosions.

Explosive events mainly originate from terrorist attacks targeting civilian or commercial structures. However, accidental events such as explosions in storage facilities or gas explosions also occur from time to time. The severe nature of loading results in catastrophic failures of structural elements and ultimately loss of life either from direct or indirect effects of the explosion. Hence, it is essential to estimate and predict the effects of explosions and provide designs to protect structures against the potential explosive events.

A detailed review of explosive loading and structural response is presented in this chapter. Different explosive types and their specific properties, comparison methods of different explosives and prediction of blast pressure and impulse parameters are discussed in terms of high explosives. These prediction methods are also compared against the available code guidelines on blast pressure prediction. Finally, structural response to blast loading and associated failure mechanisms is assessed.

2.2. Explosion and blast phenomenon

An explosion is defined as a rapid (violent) release of energy in a short duration of time. Explosions can be of three different types, namely physical, nuclear or chemical depending on the origin and the type of energy release. Physical explosions are associated with a sudden change in physical properties of the material as the mechanism of energy release. Catastrophic failure of a cylinder or a pressure vessel is considered a prime example of a physical explosion, generating a blast wave and a field of debris. Volcanic eruptions, as well as the rapid mixing of two liquids in different temperatures, are also considered physical explosions (Ngo et al. 2007a). Physical explosions are considered the weakest form of explosions even though they can generate blast waves and high-velocity debris.

Explosions generated using the redistribution of subatomic particles are considered as nuclear explosions. Basically, there are two types of nuclear reactions, named as “fission” and “fusion”. Fission is the splitting of heavy atoms, and Fusion is the joining of small, lightweight atoms that were used for nuclear explosions. The magnitude of energy released from a nuclear explosion is several orders of magnitude higher than the energy released from a physical explosion (Smith and Hetherington, 1994). Therefore, a small nuclear explosion can be much more devastating than an industrial level physical explosion. Creating a nuclear explosion requires highly skilled personnel and technology hence, it is quite rare for these to be used to target civilian and commercial structures.

Chemical explosions are based on the energy released from the rapid oxidation of fuel elements in materials. However, not all chemical explosives are capable of generating an explosion as in the case of low explosives. Explosive materials that have decomposition speed less than the speed of sound are defined as low explosives. Low explosives burn rapidly in deflagration producing fire, smoke, heat and noise in contrast

to detonation in high explosives. For the context of this study, high explosive detonation and associated structural response is the prime focus as low explosives rarely produce enough pressure-impulse combination to damage structural elements.

High explosives are normally found in condensed liquid or solid form and are inert at room temperature. However, when stimulated, high explosives produce gasses under pressure up to 30,000 MPa and temperatures in the range of 3000 – 4000 ^{0}C (Ngo et al. 2007a). The released gases expand violently forcing the volume it occupies and forms a thin layer of compressed air which is known as the blast wave or shock front. Most of the energy released during the explosion is condensed within this layer of compressed air and travel at supersonic speeds (shock front velocity), away from the explosion source. After a short duration, pressure behind the shock front falls below the ambient pressure, creating a partial vacuum behind the shock front. This partial vacuum is responsible for high suction winds that carry the debris from long distances away from the explosion source (Ngo et al. 2007a). Finally, the pressure will return to ambient pressure.

2.2.1. High explosive classification

High explosives can be broadly classified as primary, secondary and tertiary, based on the sensitivity to ignition. Primary explosives can be detonated using simple ignition from a spark, flame, impact or even friction. Mercury fulminate, lead azide and Nitrogen tri-iodide are good examples of primary explosives. These are generally used as percussion caps and blasting caps in detonation devices for secondary explosives (Ngo et al. 2007a).

Secondary explosives are more inert than the primary explosives and require substantially higher energy than friction or flame. Therefore, a small amount of primary explosives is used to detonate the secondary explosives. These explosives are used in a variety of applications as they are comparatively safer to handle and store than primary explosives. Tri-Nitro-Toluene (TNT) and Research-Department-Explosive (RDX) are considered as secondary explosives.

Tertiary explosives also known as blasting agents are the most inert type of explosives, which may not even be detonated using primary explosives. In comparison to primary and secondary types, tertiary explosives are much easier and safer to handle as well as

economical. Typical applications are in large-scale mining and construction. Tertiary explosives have also been used in terrorist attacks in the form of nitrate fertilizers. Ammonium-Nitrate-Fuel-Oil (ANFO) is a well-known tertiary explosive (Ngo et al. 2007a).

2.2.2. Air blast loading

The detonation of explosive materials releases heat, noise and kinetic energy in the form of a blast wave (shock front). The blast wave propagates through the air away from the source. Figure 2.1 illustrates the instantaneous pressure (P_s) and shock front velocity (U) at a particular time after the detonation.

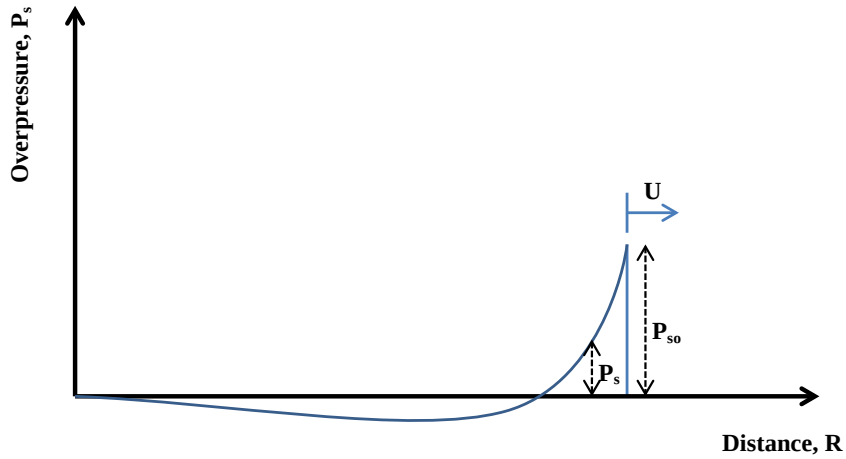

Figure 2.1: Incident overpressure variation (P_s) with the distance from the charge centre (R) at a given time (Source: Pham, 2010)

Pressure behind the shock front is defined as the ***incident overpressure (P_s)***, which could be positive or negative depending on the distance from the shock front. The maximum value of incident overpressure occurs just behind the shock front which is known as the peak incident overpressure (P_{so}). For a given explosive event, the value of peak incident overpressure reduces with the distance from the charge centre, as shown in Figure 2.2. The incident overpressure and dynamic pressure time histories for a given explosive event for a specific location is shown in Figure 2.3. The ***dynamic pressure (Q)*** is defined as the specific kinetic energy of the blast wave. Figures 2.2 and 2.3 indicate that the value of peak overpressure (P_{so}) not only depends on the distance from

the charge centre to the location of the measuring point (R), but also on the type and weight (W) of the explosive charge and its vertical distance to the ground.

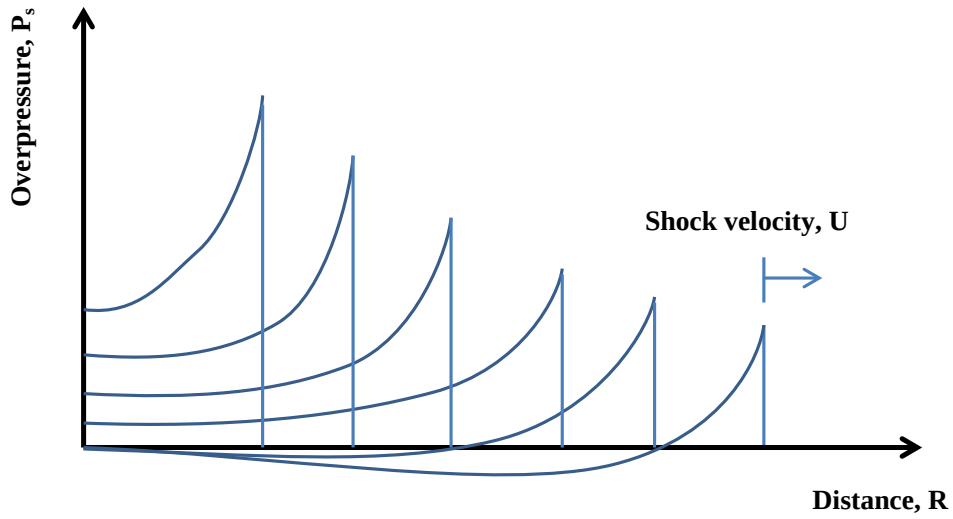

Figure 2.2: Incident overpressure (P_s) variation with the distance (R) from the charge centre (Source: Ngo et al. 2007a)

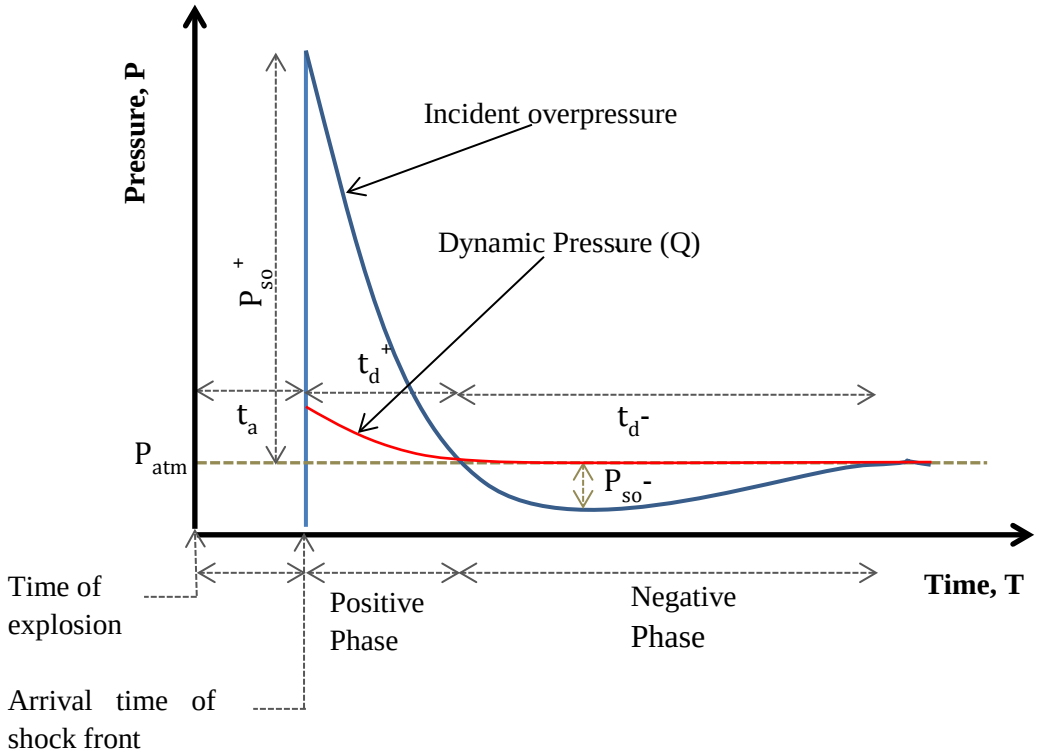

Figure 2.3: Pressure time history for a selected point along a blast wave path (Source: Anderson et al. 1985)

In Figure 2.3, arrival time, t_a, is the time taken for the shock front to arrive after the detonation. This parameter depends on the distance from the explosive load and the target, type and mass of the explosive material and the speed of sound.

Arrival of the shock front is captured by a sudden increase in pressure, where the increment occurs in very short duration (rise time, where time taken for pressure to rise from P_{atm}, ambient pressure, to P_{so}^{+}). This rise time can be neglected due to the very small duration. This increment in pressure is equal to the positive peak incident pressure (P_{so}^{+}) for the selected location. Once the shock front passes through the point of observation, pressure is decayed to ambient pressure and further creating a partial vacuum. The time duration pressure remaining above the ambient pressure is called the positive phase duration (t_d^{+}), which depends on the value of peak positive incident pressure (P_{so}^{+}). All these pressure time parameters are shown in Figure 2.3.

The time duration pressure remaining below the ambient pressure is known as the negative phase duration (t_d^{-}), which is usually longer than the positive phase duration. The maximum value of negative incident pressure is known as peak negative incident pressure (P_{so}^{-}) which is significantly lower than the peak positive incident pressure. Once the peak negative incident pressure is reached, then pressure remains below the ambient value until it reaches the ambient pressure again.

Along with the shock front, a high-velocity wind blowing in the direction of the shock front is also created with the explosive detonation. This high-velocity wind exists immediately behind the shock front and creates drag forces exactly as in normal wind loading, which is measured as the dynamic pressure (Q). The value of this dynamic pressure is significantly less than the peak incident overpressure although the positive phase duration of dynamic pressure is slightly longer than the positive phase duration of incident overpressure. There is a negative phase of the dynamic pressure, which is significantly close to zero and is ignored.

The total energy of a blast wave at a specific time is defined as the incident impulse. This time dependent parameter is determined by integrating the incident overpressure time history curve. The peak value of incident impulse is known as the peak incident impulse (I_{so}) which depends on the value of peak incident overpressure (P_{so}) and positive phase duration (t_d^{+}). A typical incident impulse time history is shown in Figure 2.4.

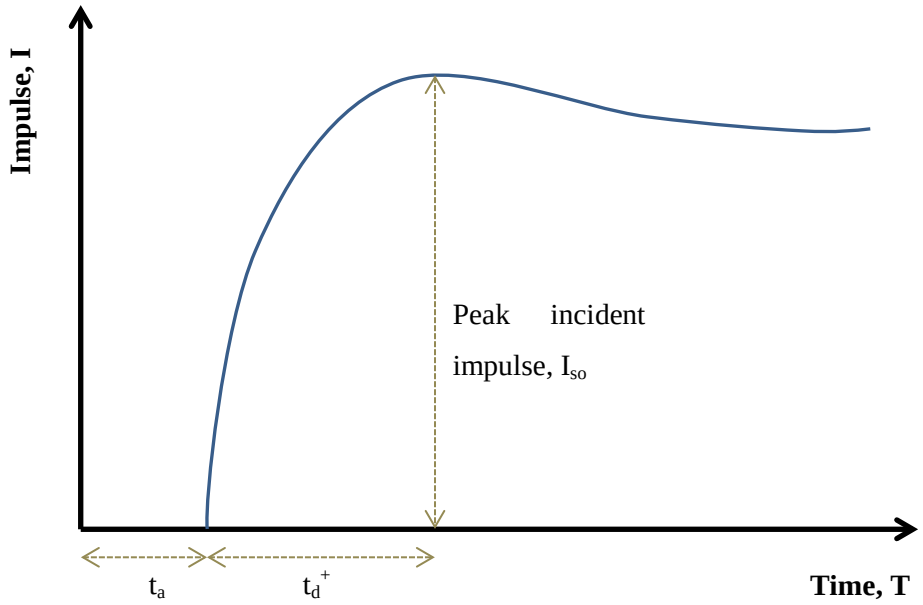

Figure 2.4: Impulse time history for a selected point along a blast wave path

2.2.3. Blast structure interaction

Once the blast wave is generated by the detonation of an explosive, it propagates away from the source at supersonic speeds, until it meets obstacles. When the blast wave encounters an object in its path, then reflection, refraction and diffraction occurs similar to a sound wave travelling through an air medium.

The occurrence of reflection, diffraction or refraction depends on the physical and geometrical properties of the obstruction. When the blast wave strikes perpendicular to the object, reflection occurs with increased pressure, density and temperature. The maximum increase of these parameters is observed when the obstruction has infinite dimensions perpendicular to the blast wave travel direction. These increases in physical parameters are directly due to the interaction of the original wave and the reflected wave. The overpressure measured after the reflection is known as the ***reflected overpressure (P_r)***, which is several times higher than the incident overpressure.

When the blast wave encounters a finite object in its path, diffraction may occur at the edges of the obstruction. In particular when a 3-dimensional object is exposed to blast waves, diffraction may reduce the effects of blast pressure on the side walls as shown in Figure 2.5. The front of the rectangular structure will encounter the maximum blast pressure while side walls and back wall will encounter much lower incident pressure.

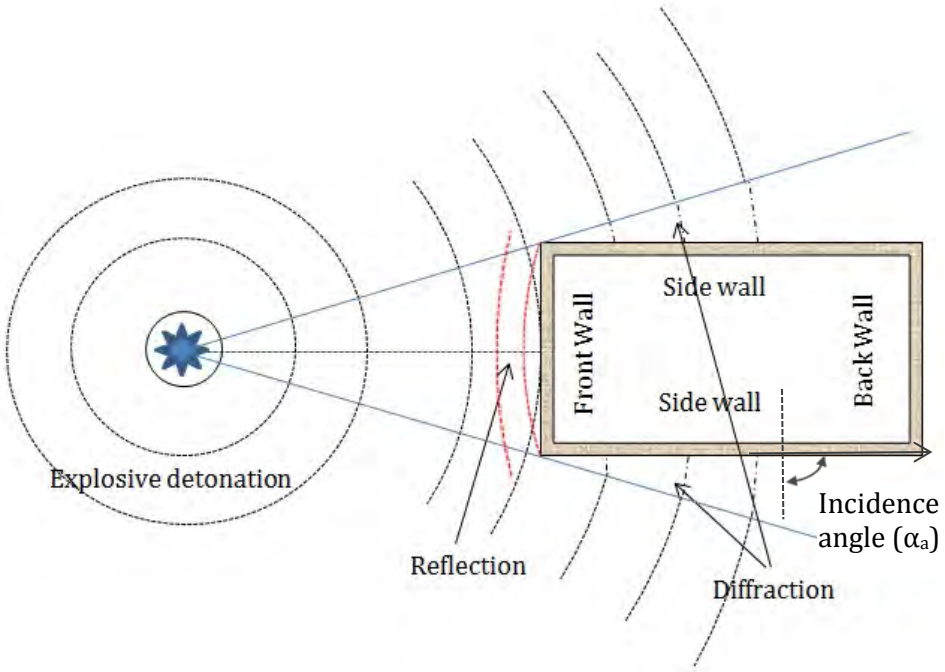

Figure 2.5: Interaction of blast wave with an object with finite dimensions (Ngo et al. 2007a)

The magnification factor for the peak reflected pressure (Peak reflected pressure (P_r) / Peak positive incident pressure (P_{so}^+)) depends on the rigidity of the obstacle and incidence angle (α_a). The incident angle is defined as the angle between the blast wave propagation direction and the normal of the facing element of obstruction. When the obstruction is rigid and perpendicular to the blast wave, ($\alpha_a=0^o$) (i.e. Front wall, Figure 2.5) maximum magnification will occur and when the obstruction is parallel to blast wave ($\alpha_a=90^o$) (i.e. Side walls, Figure 2.5) magnification will be equal to unity.

Reflection of blast waves can be classed either normal or Mach reflections (Anderson, 2001) depending on the incidence angle. Mach reflection is a supersonic shockwave effect observed when the shock wave propagates over a solid edge, which involves the formation of a triple point reflection. It has been found that Mach reflections can occur only in the case of incident angle greater than 40^o and when the incident angle is less than 40^o, normal reflection will occur (Baker, 1973, cited in Ben-Dor, 2007).

The blast winds generated by the dynamic pressure also interact with the obstructions in its path in the same way as normal winds on structures, resulting in drag pressures. Drag pressures on a surface of an object depend on the dynamic pressure and the drag

coefficient for that specific surface. Typical drag coefficients used for a rectangular structure are shown in Figure 2.6.

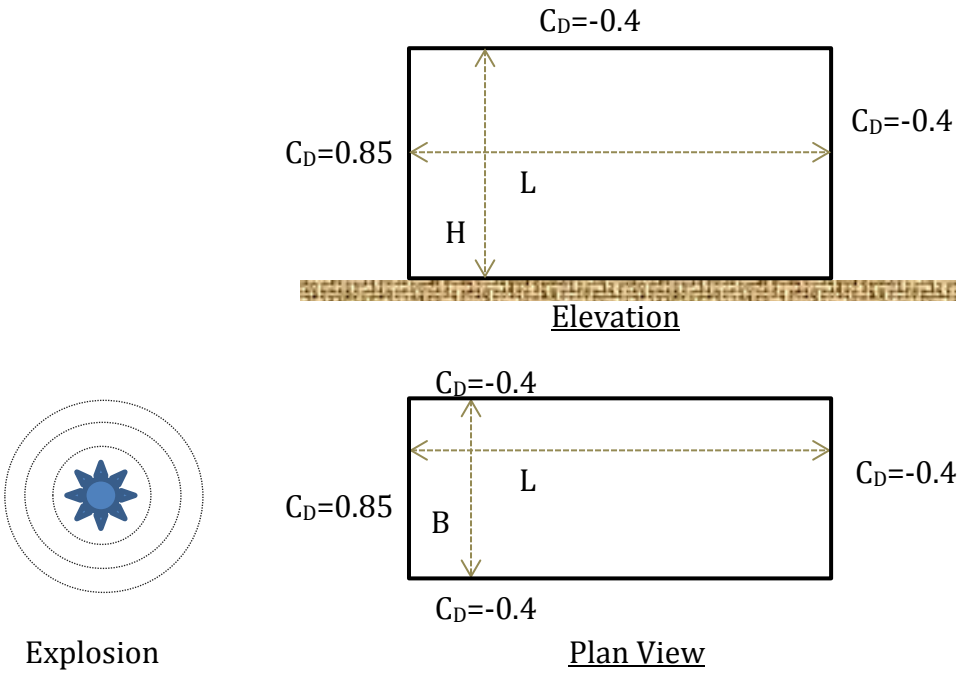

Figure 2.6: Drag coefficients for a rectangular building subjected to explosive loading (Source: Pham, 2010)

2.2.4. Blast wave scaling

A comparison of different explosive events for blast wave/shock front parameters is required when different types of explosives and different charge weight/standoff distance combinations are used. In order to compare different charge weight/standoff distances, the cube-root scaling law was introduced and for the comparison of different explosive types, the TNT equivalence was proposed.

2.2.4.1. Scaled distance and cube-root scaling law

The Hopkinson-Cranz scaling law, known as cube-root scaling law (Hopkinson, 1915, Cited in Ohashi et al. 2001), compare the different explosive events with different explosive charges and standoff distances. As quoted by Smith and Hetherington (1994) similar blast waves are produced at identical scaled distances (Z) when two explosive charges of similar geometry and of the same explosive, but of different weights, are detonated in the same atmosphere. The scaling parameter, Z, is defined as the scaled distance, using the cube-root scaling law as shown in Equation 2.1.

$$Z = {}^{R}/_{W^{1/3}} \quad (2.1)$$

Where;

R = Distance between explosive charge and target (Standoff distance) (m)

W = Mass of explosive (kg)

2.2.4.2. TNT equivalence

In order to compare the blast wave parameters generated by different explosive materials, a non-dimensional parameter is defined. TNT equivalence factor is based on the specific energy of the explosive material. TNT itself has a specific energy of 4520 kJ/kg (Smith and Hetherington, 1994) and a ratio of specific energy of the explosive material to specific energy of TNT is defined as the TNT equivalency factor. TNT equivalency factors and specific energies for several explosives materials are shown in Table 2.1.

Table 2.1: TNT equivalent factors and specific energies for several explosive materials (Source: United States Army Corps of Engineers, 1986)

Explosive	Specific Energy Q_X (kJ/kg)	TNT equivalency (Q_X/Q_{TNT})
Amatol 80/20	2650	0.586
Composition B (60/40)	5190	1.148
RDX (Cyclonite)	5360	1.185
HMX	5680	1.256
Lead Azide	1540	0.340
Mercury Fulminate	1790	0.395
Nitroglycerine (Liquid)	6700	1.481
PETN	5800	1.282
Pentolite 50/50	5110	1.129
Tetryl	4520	1.000
TNT	4520	1.000
Blasting Gelatin	4520	1.000
Nitroglycerine Dynamite	2710	0.600

2.3. Prediction of blast wave parameters using theoretical and empirical methods

The earliest record of blast pressure related discovery dated back to 1870 when Rankine and Hugoniet (Rankine, 1870, cited in Smith and Hetherington, 1994) described the normal shocks in ideal gases. However, it wasn't until Brode (1955), who painted the complete picture with the prediction of spherical blast waves using scaled distance. A list of blast pressure estimation studies conducted is given in Table 2.2, considering both theoretical and empirical formulations.

Table 2.2: Summary of studies on blast pressure estimation

Researcher	Year	Type of Blast	Method
Von Neumann and Bethe	(1947)	Spherical free air	Theoretical
Brode	(1955)	Spherical free air	Theoretical
Newmark and Hansen	(1961)	Hemispherical	Empirical
Henrych and Major	(1979)	Spherical free air	Semi-empirical
Kingery and Bulmash	(1984)	Spherical free air and hemispherical	Empirical
Mills	(1987)	Hemispherical	Empirical

A summary of blast pressure estimation predictions proposed by these researchers are discussed in the following sections.

2.3.1. Peak incident overpressure (positive)

Brode (1955) was the first to introduce the range based solution for incident overpressure. The peak incident overpressures for near field (P_{so} >10 bar) and medium to far field (0.1 bar < P_{so} < 10 bar) were presented in two different equations using the scaled distance approach (Equation 2.2).

$$P_{so} = {}^{6.7}/_{Z^3} + 1\ (bar), (P_{so} > 10)$$

$$P_{so} = {}^{0.975}/_{Z} + {}^{1.455}/_{Z^2} + {}^{5.85}/_{Z^3} - 0.019\ (bar), (0.1 < P_{so} < 10) \quad (2.2)$$

Where;

Z = Scaled Distance (m/kg$^{1/3}$)

P_{so} = Peak incident overpressure (bar)

Henrych and Major (1979) proposed similar equations for incident overpressure with combined numerical and experimental results. These equations were also based on the scaled distances (Equation 2.3).

$$P_{so} = {14.072}/{Z} + {5.540}/{Z^2} - {0.357}/{Z^3} + {0.00625}/{Z^4}\ (bar) \quad (0.05 \le Z \le 0.3)$$

$$P_{so} = {6.194}/{Z} - {0.326}/{Z^2} + {2.132}/{Z^3}\ (bar) \quad (0.3 \le Z \le 1.0) \qquad (2.3)$$

$$P_{so} = {0.662}/{Z} + {4.05}/{Z^2} + {3.288}/{Z^3}\ (bar) \quad (1.0 \le Z \le 10)$$

Blast detonations adjacent to ground level or infinite rigid objects are known as hemispherical surface blasts. When a detonation occurs close to ground level, a generated blast wave will interact with the ground prior to its propagation, which results in amplification of wave parameters. Newmark and Hansen (1961) proposed a simplified equation for peak overpressure generated from a hemispherical surface blast as shown in Equation 2.4. This equation is valid for all scaled distance ranges.

$$P_{so} = 6784\left({W}/{R^3}\right) + 93\left({W}/{R^3}\right)^{1/2} \quad (bar) \qquad (2.4)$$

Where;

W = Charge weight (Metric Tons)

R = Standoff Distance (m)

Mills (1987) also proposed a similar solution for peak overpressure resulting from hemispherical surface blasts using the experimental results (Equation 2.5).

$$P_{so} = {1772}/{Z^3} - {114}/{Z^2} + {108}/{Z}\,(bar) \qquad (2.5)$$

Kingery and Bulmash (1984) blast pressure predictions are the most widely used predictions to date. Original Kingery-Bulmash equations (Kingery, 1966) were later re-examined and presented as simplified airblast calculations as in Equation 2.6 (Swisdak, 1994). These simplified Kingery-Bulmash equations determine all pressure related parameters for both spherical free air blasts and hemispherical surface bursts. The

equations were applicable to a scaled distance (Z) range of 0.06 m/kg$^{1/3}$ to 40 m/kg$^{1/3}$ (Pham, 2010).

$$P_{so} = 10^{Y}$$

$$Y = 1.94225 - 1.69589K - 0.15415K^2 + 0.51460K^3 + 0.9885K^4 - 0.29391K^5 - 0.02681K^6 + 0.10909K^7 + 0.00162K^8 - 0.02146K^9 + 0.00014K^{10} + 0.00167K^{11} \quad (2.6)$$

$$K = -0.75645 + 1.35034T$$

$$T = \log(Z)$$

Where;

P_{so} = Peak incident overpressure (psi)

Z = Scaled Distance (ft/lb$^{1/3}$)

Modifications (Swisdak, 1994) allowed the scaled distance (Z) to be extended to 198.5 m/kg$^{1/3}$. However, the lower limit of scaled distance applicable for the equation was increased to 0.2 m/kg$^{1/3}$ up from the original value of 0.067 m/kg$^{1/3}$. Instead of a single equation for the whole range of scaled distance, separate parameters were introduced for three different ranges. The simplified equations by Swisdak (1994) are available in both imperial and metric units and are given as,

$$P_{so} = EXP(7.2106 - 2.1069(\ln(Z)) - 0.3229(\ln(Z))^2 + 0.1117(\ln(Z))^3 + 0.0685(\ln(Z))^4) \quad (0.2 < Z < 2.9)$$

$$P_{so} = EXP(7.5938 - 3.0523(\ln(Z)) + 0.40977(\ln(Z))^2 + 0.0261(\ln(Z))^3 - 0.01267(\ln(Z))^4) \quad (2.9 < Z < 23.8)$$

$$P_{so} = EXP\big(6.0536 - 1.4066(\ln(Z))\big) \quad (23.8 < Z < 198.5) \quad (2.7)$$

Where;

P_{so} = Peak incident overpressure (kPa)

Z = Scaled distance (m/kg$^{1/3}$)

Figure 2.7 illustrates a comparison by Smith and Hetherington (1994) of incident overpressure predictions of Brode (1955), Henrych and Major (1979) and prediction based on the experimental results of Kingery and Bulmash (1984). Similar predictions

were observed for intermediate and large scaled distances (far field/far range) ($Z \geq 1$ m/kg$^{1/3}$). In the case of small scaled distances (near field/close range), predictions were scattered, especially with Brode's predictions. The authors argued that this was due to the complexity of the blast wave formation close to the explosives.

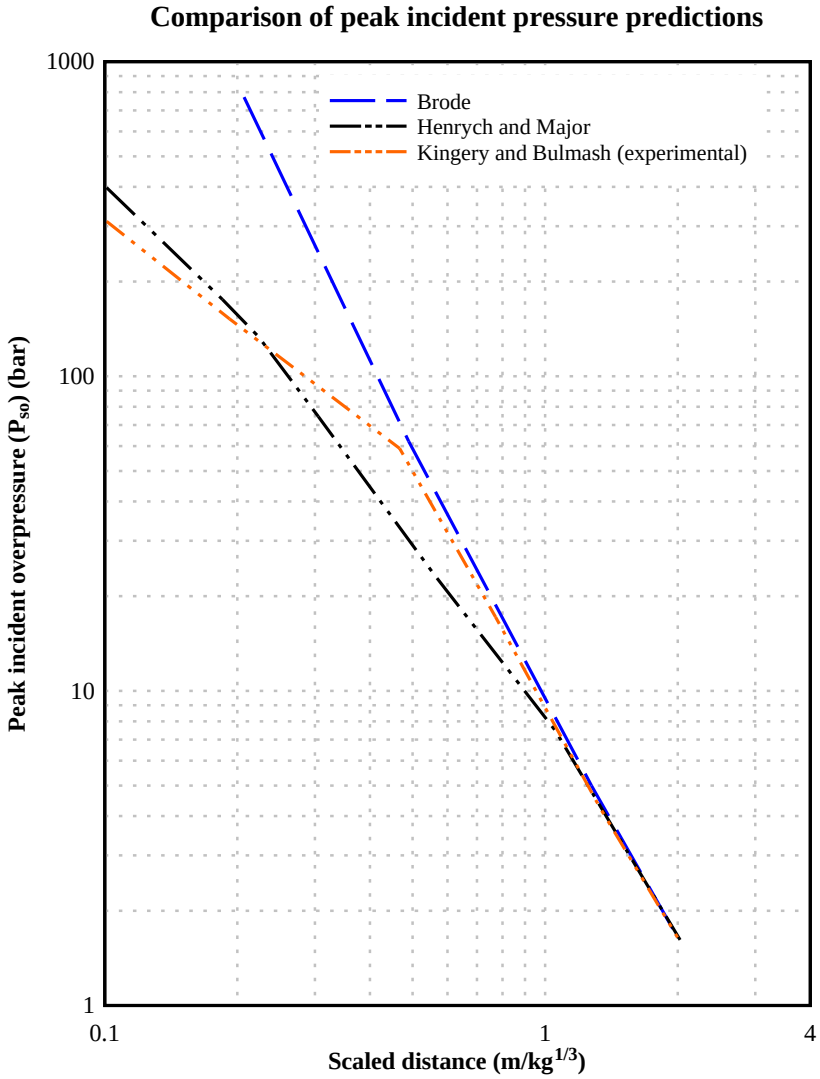

Figure 2.7: Comparison of peak incident overpressure predictions with experimental results (Source: Smith and Hetherington, 1994)

Instead of using the equations, charts provided in UFC 3-340 (United States Army Corps of Engineers, 2008) can be used to estimate the peak incident overpressure. These charts are based on the Kingery and Bulmash equations (Kingery and Bulmash, 1984). In case of scaled distances beyond 40 m/kg$^{1/3}$ is required, simplified (extended) Kingery and Bulmash (Swisdak, 1994) can be used for the estimation. As for this study,

simplified Kingery and Bulmash (Swisdak, 1994) equations were used as these were available for an extended range of scaled distances with comparable accuracy.

2.3.2. Peak reflected overpressure (P_r) (positive)

Peak reflected overpressure is defined as the overpressure measured on the surface of an obstacle in the path of a blast wave. The value of peak reflected overpressure (P_r) depends on the peak incident overpressure (P_{so}) and reflection coefficient (C_r). The reflection coefficient is in direct correlation with the angle of incidence (α_a). A 90^o incidence angle results in the minimum reflection coefficient of unity (side on overpressure or peak incident overpressure), and the maximum reflection coefficient will result with a 0^o angle of incidence. Since the peak reflected pressure also depends on the peak incident pressure, the value of maximum reflection coefficient has a range instead of a single value. Smith and Hetherington (1994) derived an equation for peak reflected pressure based on the Rankine-Hugoniet (1870) relationship, which predicts the reflection coefficient to be between two (2) and eight (8). However, Peak reflected pressure charts in Unified Facilities Criteria (United States Army Corps of Engineers, 2008) states a maximum value of twelve (12) based on the experimental evidence of Kingery and Bulmash (1984). This discrepancy is considered to be due to ideal gas approximations in the older Rankine-Hugoniet relationship. On this basis, the Kingery and Bulmash relationships are considered applicable for the scope of this thesis.

Kingery and Bulmash (1984) proposed equations for peak reflected pressure which were similar to the equations proposed for peak incident pressure. The simplified equations (Swisdak, 1994) for peak reflected pressure is presented in Equation 2.8. Alternatively, Figures 2.8 and 2.9, which are extracts of UFC 3-340, can be used for the same purpose.

$$P_r = EXP(9.006 - 2.6893(\ln(Z)) - 0.6295(\ln(Z))^2 + 0.1011(\ln(Z))^3 + 0.29255(\ln(Z))^4 + 0.13505(\ln(Z))^5 + 0.019736(\ln(Z))^6) \qquad (0.06 < Z < 2.0)$$

$$P_r = EXP(8.8396 - 1.733(\ln(Z)) - 2.64(\ln(Z))^2 + 2.293(\ln(Z))^3 - 0.08232(\ln(Z))^4 + 0.14247(\ln(Z))^5 - 0.0099(\ln(Z))^6) \qquad (2.0 < Z < 40.0) \qquad (2.8)$$

Where;

P_r = Peak incident overpressure (kPa)

Z = Scaled distance ($m/kg^{1/3}$)

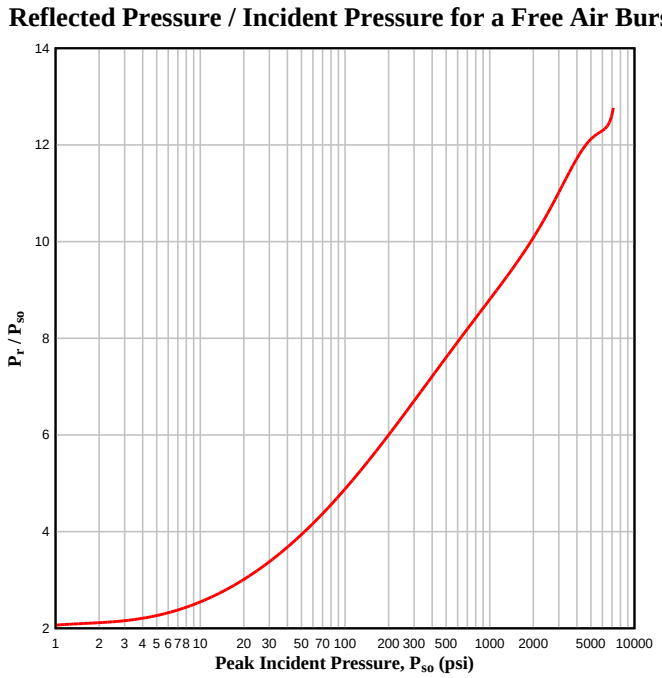

Figure 2.8: Variation of reflection coefficient with the peak incident pressure (Source: United States Army Corps of Engineers, 2008)

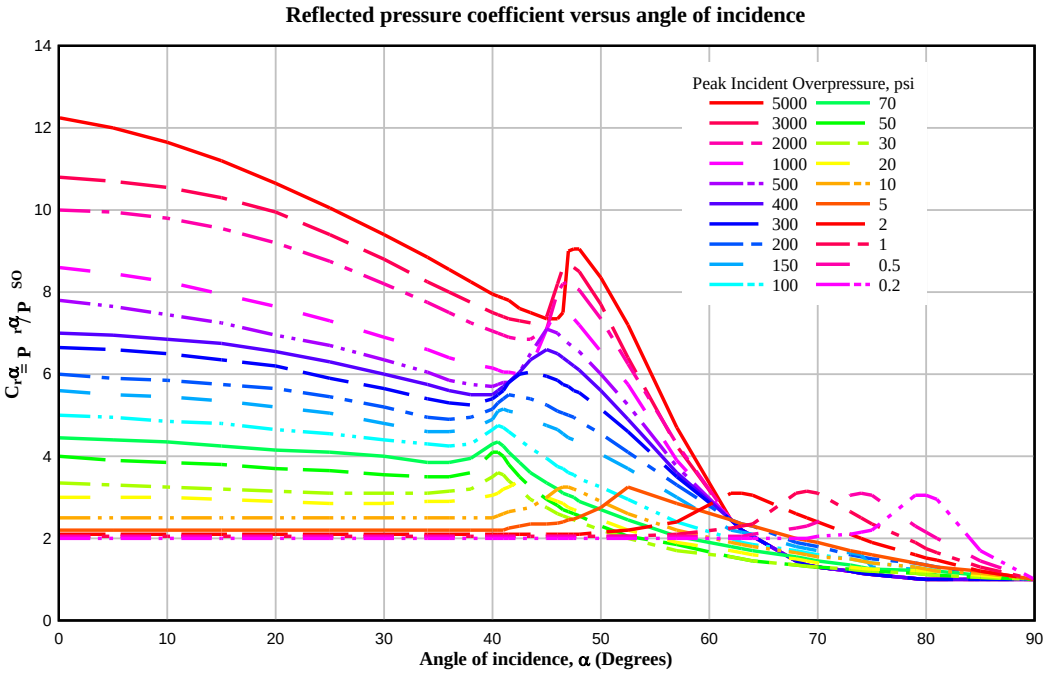

Figure 2.9: Variation of reflection coefficient with the angle of incidence (Source: United States Army Corps of Engineers, 2008)

2.3.3. Peak incident overpressure (negative) (P_{so}^-)

Peak negative overpressure (P_{so}^-) is not considered as a major parameter in comparison to peak positive overpressure (P_{so}) in the case of structural safety. However, large negative pressures can attract debris which could trigger further damage to already weakened structures. Brode (1955) was the first to predict the peak negative overpressure as shown in Equation 2.9. However, the equation can only be used with scaled distances higher than 1.6 ($Z \geq 1.6$ m/kg$^{1/3}$).

$$P_{so}^- = -{}^{0.35}/_{Z} \ \ (bar) \tag{2.9}$$

Instead of Brode's equations, charts provided in the Unified Facilities Criteria (UFC 3-340) (United States Army Corps of Engineers, 2008) or simplified Kingery-Bulmash equations (Swisdak, 1994) can be used to predict the peak negative overpressure.

2.3.4. Incident (I_{so}) and reflected (I_r) impulse

As mentioned previously, Impulse is a measure of momentum change in a system usually calculated using the integration of pressure time history curves. Integration of incident pressure time history yields incident impulse (I_{so}) while integrating reflected pressure time history yields reflected impulse (I_r). The most convenient method for predicting the incident impulse is to use the UFC 3-340 charts based on the scaled distance (Z). Although there are other methods available, the simplified Kingery and Bulmash equations (Swisdak, 1994) are more convenient to use, which are shown in Equation 2.10.

$$I_{so} or\ I_r = W^{1/3} EXP(A + B(\ln(Z)) + C(\ln(Z))^2 + D(\ln(Z))^3 + E(\ln(Z))^4) \tag{2.10}$$

Where;

Incident Impulse (kPa.ms)					
Range (Z) (m/kg$^{(1/3)}$)	A	B	C	D	E
0.20-0.96	5.522	1.117	0.600	-0.292	-0.087
0.96-2.38	5.465	-0.308	-1.464	1.362	-0.432
2.38-33.7	5.2749	-0.4677	-0.2499	-0.0588	-0.00554
33.7-158.7	5.9825	-1.062	0	0	0
Reflected Impulse (kPa.ms)					
0.06-40.0	6.7853	-1.3466	0.101	-0.01123	0

2.3.5. Arrival time (t_a), positive (t_d^+) and negative (t_d^-) phase duration

Arrival time (t_a), positive (t_d^+) and negative (t_d^-) phase durations depend on the scaled distance (Z). The Unified Facilities Criteria (United States Army Corps of Engineers, 2008) provide charts for evaluation of these parameters. Alternatively, the simplified Kingery Bulmash equations (Swisdak, 1994) can be used with metric units (instead of UFC 3-340 charts in imperial units), as given in Equation 2.11.

$$t_a \text{ or } t_d = W^{1/3} EXP(A + B(\ln(Z)) + C(\ln(Z))^2 + D(\ln(Z))^3 + E(\ln(Z))^4 + F(\ln(Z))^5) \quad (2.11)$$

Where;

Time of Arrival (ms)						
Range (Z) (m/kg$^{(1/3)}$)	A	B	C	D	E	F
0.06-1.50	-0.7604	1.8058	0.1257	-0.0437	-0.0310	-0.00669
1.50-40.0	-0.7137	1.5732	0.5561	-0.4213	0.1054	-0.00929
Positive Phase Duration (ms)						
0.20-1.02	0.5426	3.2299	-1.5931	-5.9667	-4.0815	-0.9149
1.02-2.80	0.5440	2.7082	-9.7354	14.3425	-9.7791	2.8535
2.80-40.0	-2.4608	7.1639	-5.6215	2.2711	-0.44994	0.03486

2.3.6. Shock front velocity, Dynamic pressure and Wavelength

Kingery and Bulmash (1984) derived the equations for other blast wave parameters including shock front velocity, dynamic pressure and wavelength. Since these are not the primary parameters defining the response of a structure subjected to blast loading, limited attention has been given to the evaluation and prediction. However, if these parameters were required for any kind of design of a structure or just the evaluation of parameters, UFC 3-340 (United States Army Corps of Engineers, 2008) provides charts for the evaluation of these parameters.

Two different charts with different scaled distances are provided for positive phase and negative phase parameters as shown in Figures 2.10 and 2.11 respectively. The values obtained from these charts are for a one pound of equivalent TNT charges. Therefore, values should be moderated by multiplying the cube root of charge weight ($W^{1/3}$) for

different weights, where charge weight is in Pounds. Remennikov (2002) converted the positive parameter chart to metric units, which looks identical to Figure 2.10, except for the unit system.

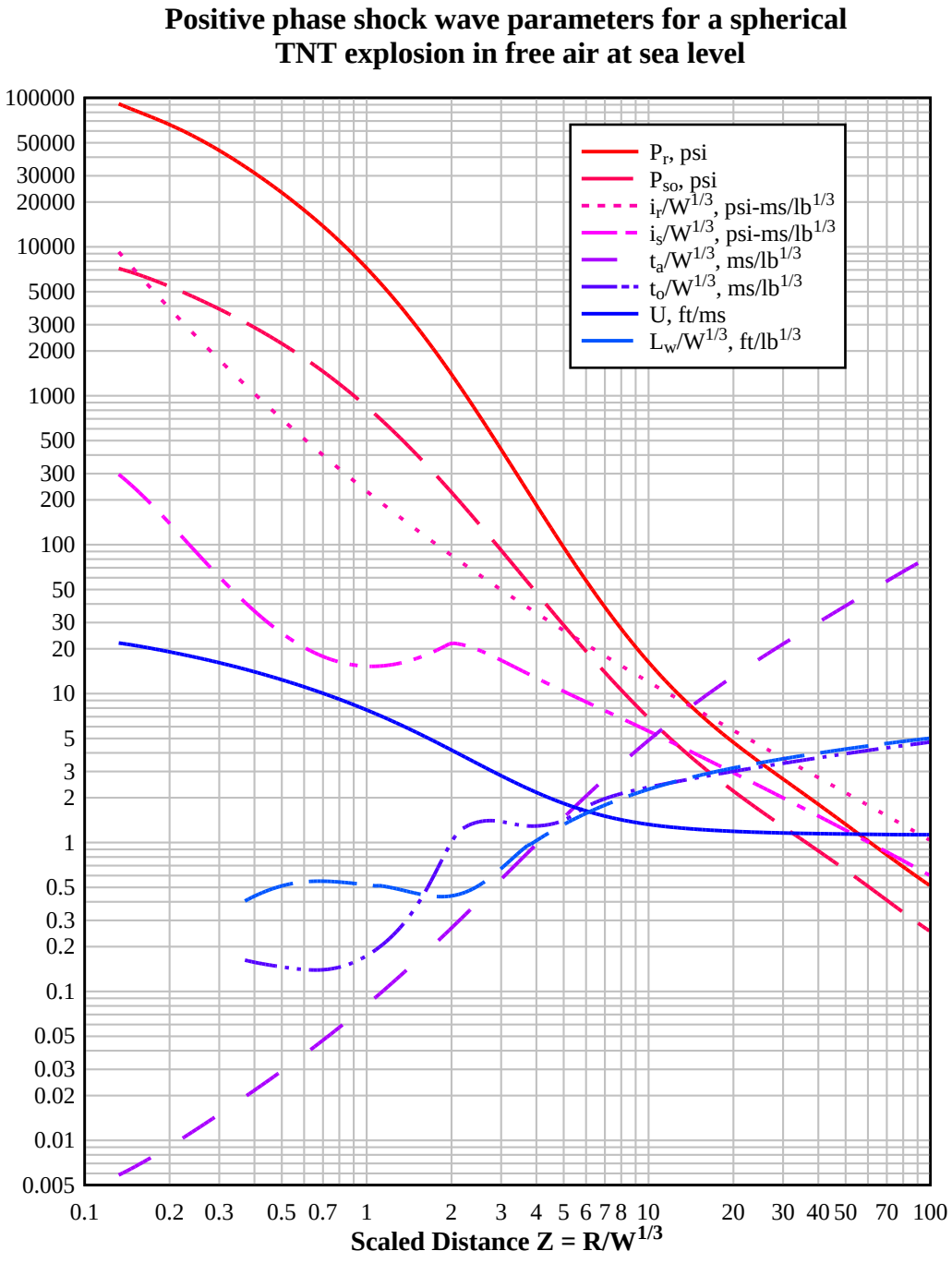

Figure 2.10: Positive phase parameters for spherical free air blast (Source: United States Army Corps of Engineers, 2008)

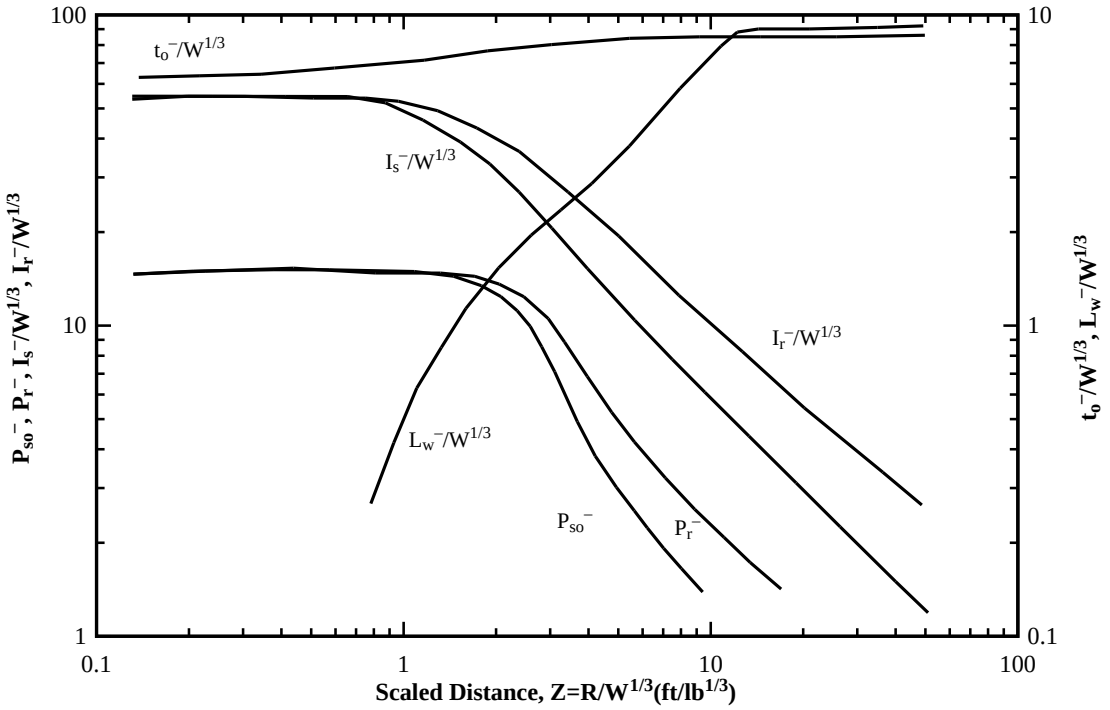

Figure 2.11: Negative phase parameters for spherical free airblast (Source: United States Army Corps of Engineers, 2008)

2.3.7. Blast wave propagation and time dependent overpressure

Time-dependent pressure (incident or reflected) is one of the most important parameters in the dynamic analysis of structures. A typical pressure–time relationship of a high explosive detonation has the shape shown in Figure 2.3. The pressure profile of a blast wave is often described as an exponential decay function, such as the Friedlander equation (Cited in Kinney and Graham, 1985) given in Equation 2.12. The same equation can be used to calculate the pressure profile for reflected pressure using the value of P_r instead of P_{so}.

$$P_s(t) = P_{so} e^{-bt/t_d} \left(1 - t/t_d\right) \tag{2.12}$$

Where;

T = Time elapsed since the arrival time

b = Waveform parameter

The waveform parameter (b) depends primarily on the scaled distance. Smith and Hetherington (1994) derived the values of the waveform parameter based on the scaled distance graphs found in the literature. (Baker et al. 1983). Typical blast waveform

parameters taken from Smith and Hetherington (1994) for different scaled distances are shown in Table 2.3.

Table 2.3: Blast waveform parameters for different scaled distances (Source: Smith and Hetherington, 1994)

Scaled Distance, Z ($m/kg^{1/3}$)	Waveform parameter, b
0.4	8.50
0.6	8.60
0.8	10.0
1.0	9.00
1.5	3.50
2.0	1.90
5.0	0.65
10.0	0.20
20.0	0.12
50.0	0.24
100.0	0.50

However for simple applications, approximate methods are used assuming linear decay in the form of a triangular pressure pulse. A more conservative approach is to match the positive phase durations without changing the value of overpressure, which results in increased impulse (See line 1 in Figure 2.12). The second option is to match the impulse and reduce the positive phase duration accordingly (See line 2 in Figure 2.12). The parameter t_r can be calculated using the Equation 2.13 given below. Both these options are extensively used in the blast-resistant design.

$$t_r = {}^{2I_r}/_{P_r} \tag{2.13}$$

Where;

t_r = Idealized Positive Phase duration

I_r = Incident or reflected impulse, whichever applicable

P_r = Incident or reflected pressure, whichever applicable

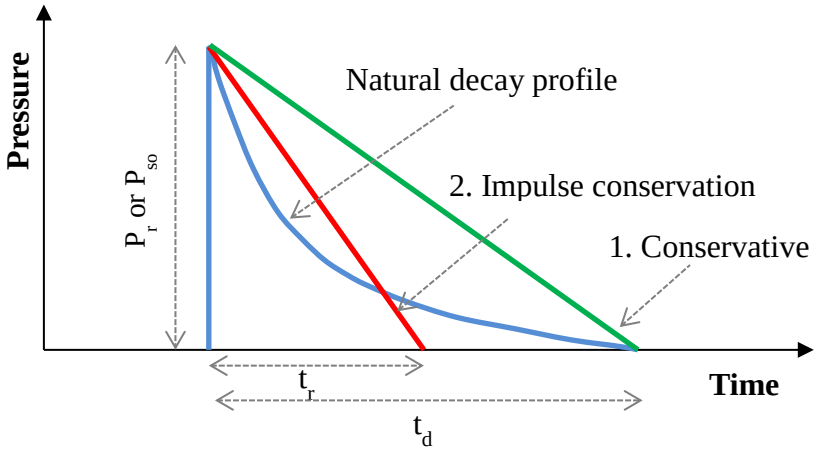

Figure 2.12: Idealisation of pressure time history

For the scope of this thesis, the natural decay function proposed by Friedlander equation (Equation 2.12) (Cited in Kinney and Graham, 1985) was used, as it does not use any approximations.

2.4. Prediction of blast wave parameters using computational techniques

Computational techniques are considered as very effective research and design tools due to lower cost and reduced health and occupational hazards. In addition, recent developments in computer technology have led to improved accuracy of these computational methods resulting in improved predictions.

Computational methods in explosive loading and response can be broadly split into two categories; a) prediction of blast pressure parameters, and b) prediction of structural response to an explosive event. Computational programs that are only capable of predicting blast pressure parameters utilise either empirical relationships derived using the available experimental results or first principles using computational fluid dynamics.

Computational programs developed using first principles can be further categorised as coupled and uncoupled analysis programs. The difference between these two computational programs is the availability of an additional module to predict the structural response in coupled analysis programs. Sevin et.al. (1995), Ngo (2007a) and Pham (2010) all have compiled lists of computational programs that were used for the evaluation of blast pressure and response of structural elements to blast loading. Table 2.6 provides an updated list of computational programs for blast wave parameter estimation.

Table 2.4: Computer programs used for the predictions of blast loading and response (Source: Sevin et al. 1995, Ngo et al. 2007a, and Pham, 2010)

Name	Capabilities	Type	Author/Vendor	Reference
CONWEP	Blast Prediction	Empirical	United States Army Waterways Experiment Station	(Hyde, 1991)
BLASTX	Blast Prediction	Semi Empirical	Science Applications International Corporation	(Britt and Lumsden, 1994)
RCBLAST	Blast Prediction	Semi Empirical	Eric Jacques	(Jacques et al. 2012)
CTH	Blast Prediction	First Principles	Sandia National Laboratories	(McGlaun et al. 1990)
FEFLO	Blast Prediction	First Principles	Science Applications International Corporation	(Baum et al. 1995)
FOIL	Blast Prediction	First Principles	Applied Research Associates/ Waterways Experiment Station	(Windham et al. 1993)
HULL	Blast Prediction	First Principles	Orlando Technology, Inc	(Gunger, 1992)
SHARC	Blast Prediction	First Principles	Applied Research Associates, Inc	(Hikida et al. 1988)
AIR3D	Blast Prediction	First Principles	Royal Military College of Science, canfield University	(Rose, 2003)
DYNA3D	Structural Response	First Principles	Lawrence Livermore National Laboratory	(Hallquist, 1993)

Table 2.4 (contd.)

EPSA-II	Structural Response	First Principles	Weidlinger Associates	(Atkatsh et al. 1994)
ALEGRA	Coupled Analysis	First Principles	Sandia National Laboratories	(Budge and Peery, 1993)
ALE3D	Coupled Analysis	First Principles	Lawrence Livermore National Laboratory	(Nichols, 2007)
FUSE	Coupled Analysis	First Principles	Weidlinger Associates	(Sandler and Rubin, 1990)
DYTRAN	Coupled Analysis	First Principles	MSC software corporation	(Ding and Buijk, 2005)
MAZe	Coupled Analysis	First Principles	TRT Corporation	(Schlamp et al. 1995)
LS-DYNA	Coupled Analysis	First Principles	Livermore Software Technology corporation	(LSTC, 2013)
AUTODYN	Coupled Analysis	First Principles	Century Dynamics/ANSYS, Inc	(ANSYS Inc, 2013)
ABAQUS	Coupled Analysis	First Principles	Dassault Systems	(ABAQUS, 2013)

2.4.1. Uncoupled computational programs

Computational programs that can only predict the blast wave parameters irrespective of the flexibility of the obstructing structure are known as uncoupled computational programs. Empirical, semi-empirical or first principle-based methods are used to predict the blast wave parameters for these programs. All blast wave interactions were defined assuming that all objects in the blast wave path are rigid and do not deform during the application of the loading. Hence, uncoupled programs generally over-predict the blast wave parameters, particularly pressure and impulse. However, these programs require less computational power compared to the coupled analysis programs.

CONWEP (Hyde, 1991), BLASTX (Britt and Lumsden, 1994) and Air3D (Rose, 2003) are well known uncoupled analysis programs. CONWEP uses the Kingery and Bulmash (1984) empirical equations to predict the blast wave parameters while Air3D is based on the first principle computational fluid dynamics (CFD) formulation. BLASTX is based on the combination of empirical equations and first principles to predict the blast wave parameters. Air3D was extensively used in predicting the blast wave parameters in complex infrastructure and geometries (Remennikov and Rose, 2005, Smith and Rose, 2006). Figure 2.13 illustrates a blast wave propagation study conducted on a 2D city geometry using Air3D (Remennikov and Rose, 2005).

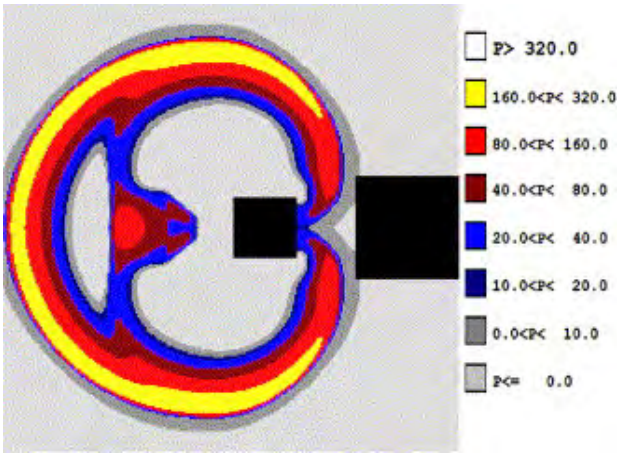

Figure 2.13: Air3D visualisation of pressure contours for an explosive detonation (Source: Remennikov and Rose, 2005)

2.4.2. Coupled computational programs

A coupled computational program is a combination of Computational Fluid Dynamics (CFD) module and Computational Structural Mechanics (CSM) module working in tandem. The CFD module predicts the blast wave parameters and the CSM module predicts the response of a structure to the blast wave usually with explicit time integration. Unlike in uncoupled analysis, the combined analysis process allows the structures to deform and even predicts the failure, resulting in more accurate blast wave parameters. LS-DYNA, ABAQUS and AUTODYN are typical examples of coupled analysis programs. All three finite element programs possess in-built blast wave generation options using first principles. LS-DYNA is also capable of predicting the blast wave parameters using the inbuilt empirical relationship, which is based on the Kingery and Bulmash (1984) equations.

There are three main types of coupled analysis based on the CSM module used for the structural response, namely Lagrangian, Eulerian or Arbitrary Lagrangian Eulerian (ALE). Among the three methods, the Lagrangian analysis is the most widely used method for structural analysis, especially when the deformations are small. In this method, the material is defined by a mesh which also moves with the material. Hence, the mesh deformation is identical to the material deformation. However in the case of large deformations, large mesh distortions are observed with smaller than usual time steps and increased computational times.

Material flowing through a spatially fixed mesh is the basis for the Eulerian method of analysis. Since the mesh is spatially fixed, a surrounding domain needs to be defined in order to use the Eulerian method, requiring more computational power. One other disadvantage of this method is that material deformations take the shape of the mesh and finer meshing is required to attain accurate results.

A more advanced ALE method consists of two separate mesh systems for the material and the background. Since this is a combination of both Lagrangian and Eulerian methods, inherent disadvantages of both systems are eliminated by the other system. The moving background mesh reduces the mesh distortion hence, making ALE one of the best methods to analyse large deformation problems such as the response of structures subjected to blast loading. LS-DYNA is one of the computational programs that implements the ALE method successfully for the dynamic analysis of structures.

Two other CSM modules are available with some computational programs, namely the Smooth Particle Hydrodynamics (SPH) (Gingold and Monaghan, 1977) and Element-free Galerkin (EFG) method (Belytschko et al. 1994). The main advantage of both these modules is that smooth meshing isn't required to obtain respectable results. Although SPH has been used successfully for explosive response modelling (Swegle and Attaway, 1995, Prochazka et al. 2008, Liu et al. 2003, Miyoshi, 2008), it hasn't been included in commercial packages until recently. The EFG method is mainly used in energy and heat flow simulations.

2.5. Response of structures subjected to blast loading

When a structure is subjected to any kind of load, the typical response of the structure is to deform and accumulate resistance against the applied load. Hence, the response of the structure depends on the type, magnitude, duration of loading and the natural period of the structure. In the case of explosive loading, positive phase duration (t_d) (see Figure 2.3) and the natural circular frequency of vibration (ω) typically determine the type of response of the structure. Mays and Smith (1995) predict three different types of responses expected from structures subjected to blast loading based on the product of natural frequency (ω) and positive phase duration (t_d) of the blast load as given in Equation 2.14.

$$\begin{aligned} &Impulsive: && \omega t_d \leq 0.4 && \left[\propto \frac{t_d}{T}\right] \\ &Quasi\ Static: && \omega t_d \geq 40 && \left[\propto \frac{t_d}{T}\right] \\ &Dynamic: && 0.4 < \omega t_d < 40 && \left[\propto \frac{t_d}{T} \approx 1\right] \end{aligned} \tag{2.14}$$

Where;

T = Natural period of vibration of the target structure

As discussed earlier in the chapter, a significant explosive event will generate blast pressure parameters which are either in the dynamic range or impulsive range of the targeted structure. The quasistatic range will be applicable only in the case of structures with extremely short natural periods of vibration (T) targeted with small explosive charges.

2.5.1. Comparison of dynamic and static response of structures

Structural response to blast loading is considerably different to the response of quasi-static loading. The amount of energy transferred to the targeted structure from a blast wave is much greater than its usual quasi-static capacity. A study on dynamic performance of glass panels subjected to impact loading (Lumantarna et al. 2006) showed that dynamic capacity is several times higher than the equivalent static capacity. The higher capacity and different response of the structure during dynamic and impulsive loading cases were due to four main reasons;

- Enhancements of material properties due to higher rate of loading
- Inertia effects which are ignored during static analysis
- Higher modes of vibration instead of basic first mode of vibration
- Interaction of the structure and its support conditions (fixing assemblies)

These are discussed in more detail in the sections that follow.

2.5.1.1. Enhancements of material properties due to higher rates of loading

In general, material properties are tested under equivalent static conditions where the load is applied at a very slow rate. Specific to concrete, compressive strength testing is carried out at a loading rate of 20 MPa/minute with a 10% variation (Standards Australia, 2014). However, blast loads can result in loading rates well above the equivalent static loading rates. Therefore, it is essential to consider the variation of strength parameters of materials for elevated loading rates.

Properties relating to dynamic enhancements are different for each material and even different rate enhancement properties are available for the same material. More significant variations are observed with strength parameters such as compressive and tensile strengths. The general term used for the enhancement in properties due to higher loading rate is defined as ***strain rate enhancement***.

The strain rate enhancement is usually defined in terms of the ***dynamic increase factor*** (DIF) which is the ratio of dynamic strength to equivalent static strength. In this study, concrete and steel will be the material considered and there is a long list of researchers who have studied rate enhancements of concrete and reinforcing steel. The CEB-FIP model code for concrete (Comite Euro-International du Beton, 1990) proposed

equations for dynamic increase factors for both tension and compression based on previous experimental results. A latter re-examination of earlier test results (Malvar and Crawford, 1998, Malvar and Ross, 1998) have yielded different dynamic increase factors for concrete in tension. In 2007, Ngo (2007b) extended the dynamic increase factor equations to be used with the high strength concrete. Similar studies (Malvar, 1998) were conducted for reinforcing steel as well and equations for dynamic increase factors were introduced.

Dynamic increase factors in the order of three (3) in compression and ten (10) in tension have been recorded for concrete, which can make a significant difference to the structural response prediction of concrete structures subjected to explosive loading. More detailed evaluation of DIF is presented in Chapter 3 for both concrete and reinforcing steel.

2.5.1.2. Inertia effects

When any load is applied, the structure will accelerate from its initial position to develop resistance against the applied loading. While the resistance grows with increased deflection, the difference between applied load and the resistance is reduced and the structure will decelerate. Ultimately the structure will come to rest when the developed resistance is matched with the applied load. However in order for this to happen, the applied load should remain constant for the entire duration of time until the structure reaches the maximum deflection emulating quasi-static response.

In the case of dynamic or impulsive loading, the structure will accelerate during the initial phase of the loading as usual. However, different from quasi-static loading, when the resistance required is eventually developed, loading has already changed to a different value. Hence, the required resistance is different to what is actually required and will result in acceleration in the other direction, depending on the magnitude of the external load at that specific time. This phenomenon is quite critical in the impulsive loading regime where applied load can vanish before the structure reaches its resistance to initial loading. This initial acceleration phenomenon is well explained with D'Alambert's principle (Goldstein et al. 2001). The force applied to accelerate the structure from its original position is called the D'Alambert's force and acts in a direction opposite to the direction of acceleration of the structure. The magnitude of this force depends on the acceleration itself and the deformation of the structure. As a

result, the deformation of the structure is not caused by the entire applied load, but only from part of it and the response of the structure is different to an equivalent static load.

2.5.1.3. Higher modes of vibration

When a structure is subjected to quasi-static loading, the structure will deform in the fundamental mode of vibration. However with loading in the dynamic and impulsive domain, structures will deform with higher modes of vibration. In general, higher modes of vibrations will always dissipate more energy than the fundamental mode of vibration resulting in different bending and shear responses from the structure. However, extremely higher frequencies of vibrations will not have a considerable effect on the shear and bending response of the structure.

2.5.1.4. Interaction of structure and support conditions/fixing assemblies

In the case of static loading, forces transferred to the supports/fixing assemblies will not depend on the stiffness of the panel, as loading remains constant until the required resistance is developed. The proportion of the loading transferred to the fixing assemblies and the applied load is equal to unity for static loading. In the case of dynamic loading, the same proportion will vary depending on the stiffness of the panel and stiffness of the support/fixing assembly. Several researchers (Pan and Watson, 1996, Pan and Watson, 1998, Pan et al. 2001, Starr and Krauthammer, 2005) have agreed that the stiffness of a panel plays a significant role in forces being transferred to the fixing assemblies, but all of the studies were of qualitative basis. However, a recent study on reinforced concrete cladding panels (Pham, 2010) shows that 25 to 50 percent of total peak forces were reduced with flexible fixing assemblies. Reduced forces transferring through the fixing assemblies will alter the response of the panel and response will mainly depend on panel stiffness and duration of the loading. Hence, careful planning and design of fixing assemblies could be used as a passive method of energy dissipation when structures are subjected to short duration dynamic loading.

2.5.2. Methods of predicting the structural response to blast loading

The response of structures against explosive loading is significantly different from quasi-static loading. Complexities in loading combined with rate enhancements, dynamic and inertia effects with higher modes of vibration makes it extremely difficult to predict the response of structural elements subjected to explosive loading accurately.

However, with reasonable assumptions, researchers have developed methodologies to adequately predict the response of structures against the effects of explosive loading.

The methods available for predicting the structural response to blast loading can be categorised as empirical, semi-empirical or numerical (Hussein, 2010). Empirical methods are proposed based on previous experimental studies. Although these predictions are applicable for selected range of parameters, accuracy of these methods diminish rapidly when the parameters fall outside the specified range. These methods can predict the far range response of a structure, but not validated for complex close range explosions (Hussein, 2010).

Semi-empirical methods are based on the combination of simplified physical phenomena and experimental studies. The important parameters are identified and simplified equations are proposed eliminating the minor parameters. Once established, equations are validated against a series of experimental case studies for adjustments. Generally, these semi-empirical methods tend to predict the structural response better than the empirical methods.

Numerical methods are mathematical models based on the basic laws of physics. The conservation of mass, energy and momentum are the basic principles along with constitutive relationships to describe the stress-strain behaviour of the materials. Although numerical models are the best option to date to predict the structural response to explosive loading, accuracy depends on the constitutive relationships used for the material models. Usually, these numerical models are based on the finite element or the finite difference techniques, which also require finer meshing and high computational demand.

All these methods, including simplified methods like single degree of freedom (SDOF), multi-degree of freedom (MDOF) and code-based method, and the basics of numerical models will be discussed in the following sections.

2.5.2.1. Single degree of freedom (SDOF) method

The single degree of freedom method involves simplifying the structure to a single lumped mass (M), single damping coefficient (C) and single stiffness coefficient (K). However in most cases, the damping coefficient is also ignored in order to simplify the conditions. Simplified diagrams for SDOF models with and without damping are shown

in Figures 2.14(a) and 2.14(b) respectively. The typical pressure profile (Parabolic using Friedlander equation) generated by an explosion is also simplified to a triangular pressure pulse as described in section 2.3.7 (Figure 2.12). A thorough description and the derivation process can be found in Mays and Smith (1995).

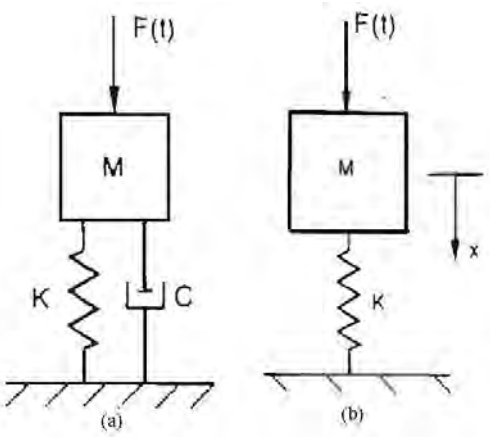

Figure 2.14: (a): Equivalent SDOF model with damping and (b): Equivalent SDOF model with without damping (Source: Pham, 2010)

For a simplified triangular blast load, without considering the effects of damping, the following equations define the response of the structure.

$$M\ddot{x} + C\dot{x} + Kx = F\left(1 - {}^{t}/_{t_d}\right)(t < t_d)$$

$$M\ddot{x} + C\dot{x} + Kx = 0(t \geq t_d) \tag{2.15}$$

Where;

x = Displacement

$\dot{x} = \frac{dx}{dt}$ = Velocity

$\ddot{x} = \frac{d\dot{x}}{dt}$ = Acceleration

The solution for displacement and velocity for the positive phase duration can be given as,

$$x(t) = \left({}^{F}/_{K}\right)(1 - \cos\omega t) + \left({}^{F}/_{Kt_d}\right)\left(\sin\omega t/_{\omega} - t\right) \tag{2.16}$$

$$\dot{x}(t) = \left({}^{F}/_{K}\right)\left[\omega\sin\omega t + \left({}^{1}/_{t_d}\right)(\cos\omega t - 1)\right] \tag{2.17}$$

Where;

ω = Natural frequency of vibration defined as $\sqrt{{}^{K}/_{M}}$

As indicated by the Equations 2.16 and 2.17, deflection and velocity of the structure depends on the natural frequency of vibration (ω) of the structure. Using the natural frequency of vibration and the positive phase duration of loading, structural response can be categorised for quasi-static, dynamic or impulsive regimes as indicated in Equation 2.14.

These equations can be used with elastic, single degree of freedom (E-SDOF) systems as well as plastic single degree of freedom systems (P-SDOF). The more preferred method is to use the elastic system rather than a plastic system for dynamic analysis since it involves lesser complexities. However, when structural elements are subjected to explosive loading, elements tend to undergo large inelastic deformation. Therefore, a closer evaluation of SDOF systems with plasticity is considered better than the elastic system.

Material plasticity could be of three forms, elastic-plastic hardening, elastic-perfectly plastic and elastic-plastic softening. For all three categories, the initial elastic deformation is followed by a plastic deformation after yielding of material. Elastic-plastic hardening materials increase in strength after yielding until failure, while elastic-plastic softening materials decrease in strength after yielding. Elastic-perfectly plastic materials remain unchanged in terms of strength yielding. General resistance deflection functions that can be observed for the three plasticity material types from SDOF analysis are presented in Figure 2.15.

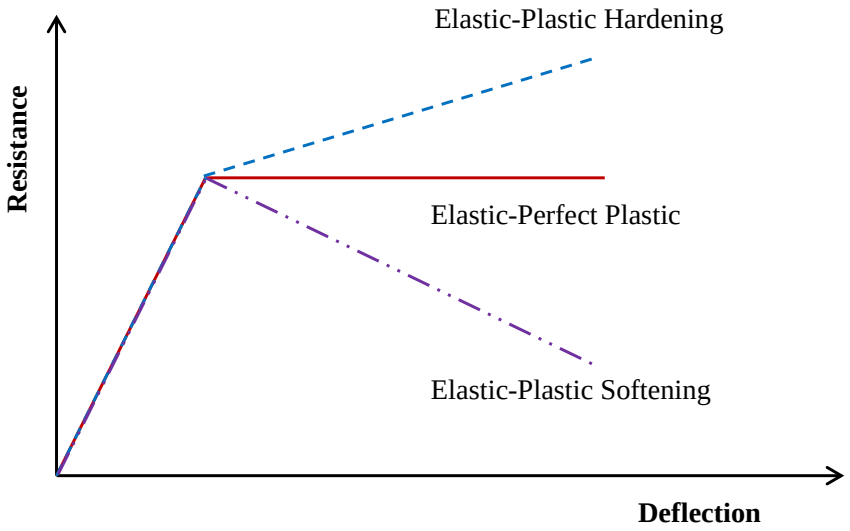

Figure 2.15: Resistance deflection functions for SDOF systems with elastic-plastic materials

2.5.2.2. Multi-degree of freedom (MDOF) method

Although a single degree of freedom (SDOF) is capable of predicting the time-dependent deflection and velocity of a structure subjected to explosive loading, by no means is it the perfect solution. The major disadvantage of SDOF systems is that local effects cannot be evaluated, hence, local failure models are ignored. The solution is to introduce multi-degrees of freedom, where the number of degrees of freedom dictates the possible modes of vibrations in the structure. However, the introduction of a higher number of nodes will make manual calculations more complex. In order to cater for the complexities in analysis, computers are introduced in the form of finite element or finite difference methods with explicit time integration.

2.5.2.3. Use of code methods and design guidelines

The Unified Facilities Criteria (United States Army Corps of Engineers, 2008) and its predecessors have provided guidance and chart options to predict the response of structures subjected to explosive loading. Elastic and elasto-plastic single degree of freedom systems as well as simplified triangular to complex sinusoidal loading functions with rise time have been considered and separate non-dimensional parameter charts were presented for maximum deflection and time to reach maximum deflection. A typical chart used for the evaluation of dynamic response using an SDOF system for a triangular load is presented in Figure 2.16.

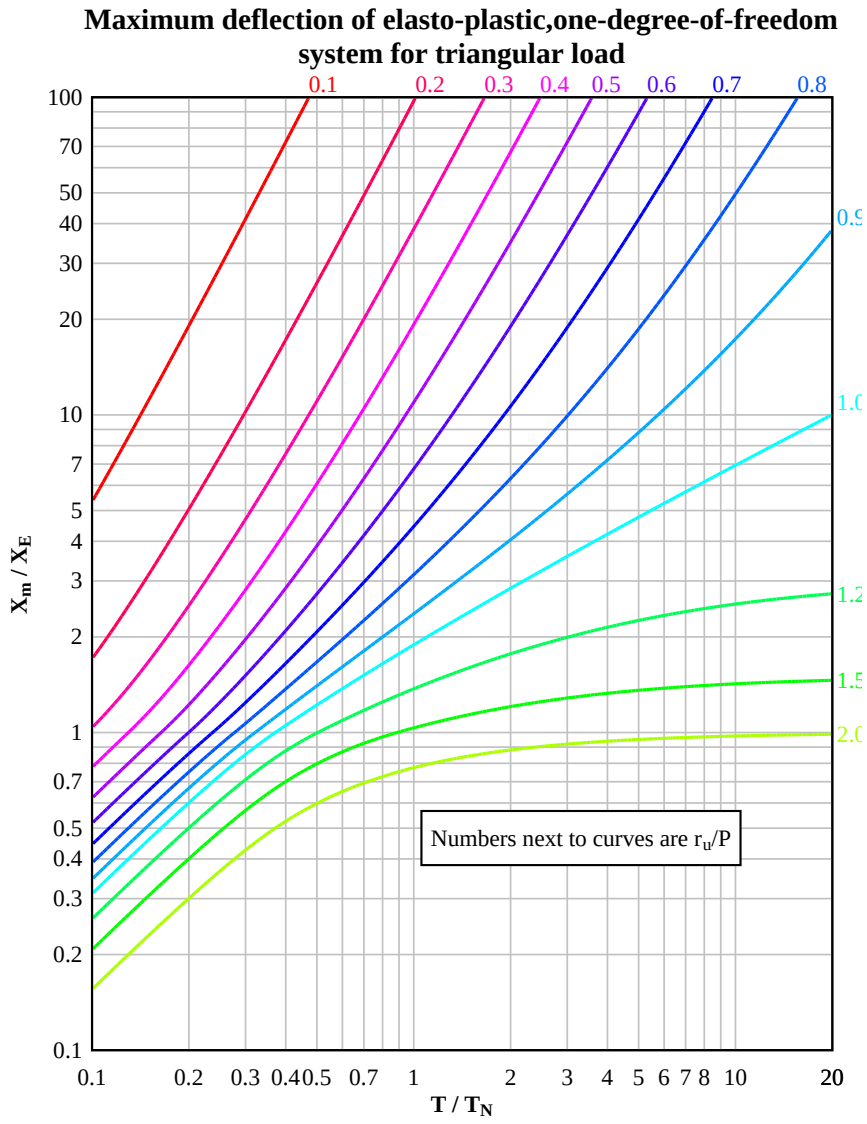

Figure 2.16: Charts for evaluating structural parameters to simplified blast loads using SDOF method (Source: United States Army Corps of Engineers, 2008)

2.5.2.4. Pressure impulse diagrams

In each of the response domains, quasi-static, dynamic and impulsive, the behaviour of the structure is different. A specific value for a selected damage parameter (i.e. deflection of a selected point or a location of the structure) can be calculated for different values of pressure and impulse combinations. When a specific value of damage parameter is plotted against different pressure-impulse combinations, it is defined as a pressure-impulse diagram. Although these diagrams are not capable of predicting the time-dependent damage parameters of the selected structure, they can predict a black and white picture of whether the structure can withstand the applied

load-impulse combination without failure. Since designers and engineers are specifically interested in the final stages of the structure rather than the intermediate response, pressure (load) impulse diagrams can be effectively used as a preliminary evaluation tool for pre-defined load impulse combinations.

Although these are known as pressure impulse diagrams and derived using pressure and impulse combinations, they are expressed in the form of a non-dimensional coordinate system through mathematical coordinate transformations. A typical pressure impulse diagram is shown in Figure 2.17 with the three different response regimes and two different loading profiles.

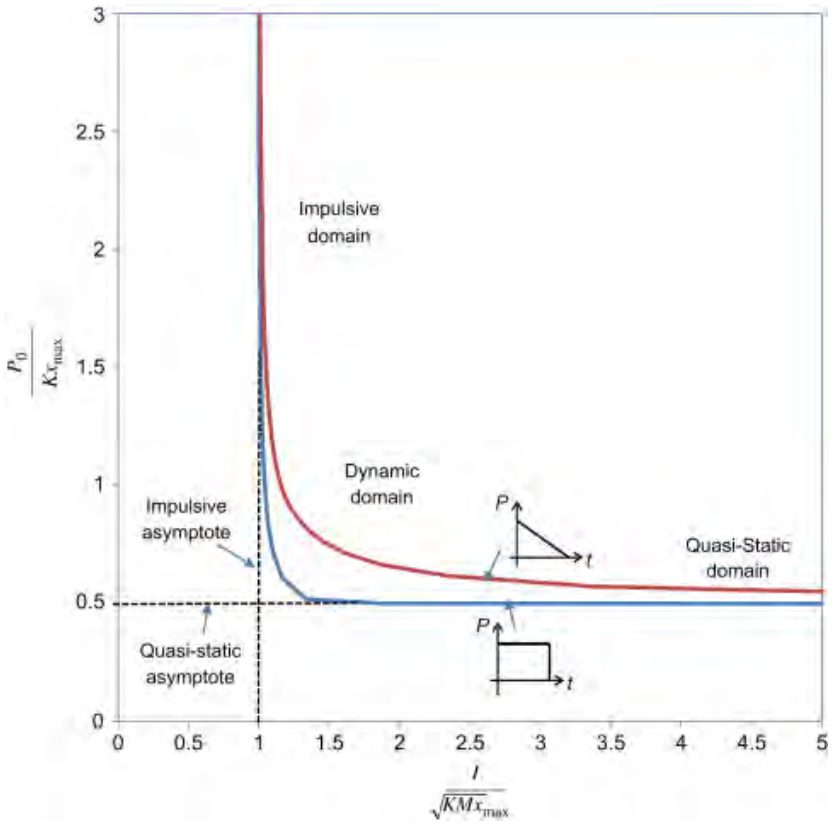

Figure 2.17: Typical pressure impulse diagram (Source: Krauthammer et al. 2008)

2.5.2.5. Physics based numerical methods

As discussed earlier, coupled analysis programs that can predict blast wave parameters can be used to predict the structural response to blast loading. The computational structural mechanics (CSM) module predicts the response of the structure based on the applied loads through the computational fluid dynamics module (CFD) or explosive

loading applied through any other method. A reliable constitutive relationship for the material model is also required in order to predict the structural response.

Unlike in SDOF, MDOF or code based methods, numerical methods can provide more detailed results including stress, strain, strain rates and system energy, etc. Furthermore, modern finite element programs are capable of visualising the failure patterns and real life behaviour of the structures. All these advantages in numerical models come with a cost of higher computational power and more skilled personnel power to build, run and interpret the results.

2.6. Summary

A brief summary of blast loading and structural response was presented in this chapter. The discussion was specifically focused on high explosive detonation (Chemical explosives) and prediction of blast wave parameters along with different scaling laws. Interaction of blast waves and response of structures subjected to blast waves was also discussed without specifically discussing the failure modes, which will be discussed in the second part of the literature review (in Chapter 3).

As for the loading prediction, the simplified Kingery and Bulmash equations (Swisdak, 1994) were found to be the most reliable and will be used in this research. These simplified equations were used in several of the recent studies (Muszynski and Purcell, 2003a, Muszynski and Purcell, 2003b, Pham et al. 2008, Wu et al. 2009, Pham, 2010) and found to closely match with the experimental results.

An inbuilt loading function based on the Kingery and Bulmash equations in LS-DYNA will be used for the development of the 3-D numerical model in Chapter 5. The inbuilt solution accounts for both positive and negative phase, including the impulse parameters. In addition, Friedlander equation (Dewey, 2010) is built in for the blast pressure routing, using the natural decay function.

In the case of 1-D analytical solution d (Chapter 6), peak positive reflected overpressure (P_r^+), positive phase duration (t_d^+) and arrival time (t_d^-) will be the only parameters to use as the loading. A simplified loading, ignoring negative phase duration, will be used for the development. Considering the structural simplifications (1-D analysis for a one-way slab), it is applicable to ignore the negative phase of the loading. Simplified Kingery and Bulmash equations (Swisdak, 1994) will be used for the evaluation of

these parameters, as it is more applicable to use in for the development. Friedlander equation with natural decay function will be used for the blast pressure profile generation in the 1-D application, which will be more accurate than the triangular approximations.

CHAPTER 3

MATERIAL PROPERTIES AND MODELLING TECHNIQUES OF CONCRETE AND REINFORCING STEEL

3.1. Introduction

Interaction of blast waves with a structure will create loading profiles in the dynamic and impulsive range, which will alter the mechanical properties of materials with higher rates of loading. The loading rate is expressed as strain rate, which is the usual method of expressing higher rates of loading. Explosive loads have been found to induce strain rates in the range of 10 s^{-1} to 10000 s^{-1}. These high rates of loading can alter the mechanical properties of materials, thereby the dynamic response of the structure. Hence, in order to understand the response of structures subjected to explosive loading, both static and dynamic properties of materials (both concrete and steel) needs to be determined. More specifically, to understand the response of reinforced concrete structures subjected to blast loading, understanding the behaviour of constitutive relationships of materials is essential.

This chapter discusses the static and dynamic properties of both concrete and reinforcing steel along with the interaction between the reinforcement and concrete matrix. Several constitutive relationships used for the modelling of concrete and reinforcement will be evaluated for the prediction of blast loading response of reinforced concrete structures.

3.2. Mechanical properties of materials in quasi-static conditions

3.2.1. Quasi-static properties of concrete

Mechanical properties of concrete do tend to change with time, environmental conditions and loading history even in the quasi-static loading conditions. More specifically, compressive strength, tensile strength, elastic modulus, poison's ratio and stress-strain relationships of concrete will be discussed in the following sections.

3.2.1.1. Compressive strength (f'_c) of concrete

Compressive strength or uniaxial compressive strength is the universally accepted method of determining quality (strength) of hardened concrete. This is usually measured using either concrete cylinders or concrete cubes of various sizes, after 28 days of casting. The United Kingdom, Europe and most of the Ex-UK colonies use cubes while Australia, USA and France use cylinders. Several Scandinavian countries use both cylinders and cubes for the measurement of uniaxial compressive strength. Concrete cubes are of one standard size, 150×150×150 mm (European Committee for Standardisation, 2009a) while concrete cylinders of various sizes are used. American standards specify 150×300 mm cylinders (American Society for Testing and Materials, 2010) while Australian standards (2009) allow both 100×200 mm and 150x300 mm cylinders.

It is important to have a universal measure of uniaxial compressive strength for different concrete samples since, most other mechanical properties are defined based on the uniaxial compressive strength. However, in the absence of universally accepted standard procedures, researchers have worked on comparing the different methods of testing and defining conversion factors and equations for comparison. (Rong and Ho, 2002, Graybeal and Davis, 2008, Wong, 2013, Kumavat and Patel, 2014). The general tendency is to define a single conversion factor however, most of the researchers agree (Day, 2006, Aïtcin, 2011) that a straightforward conversion factor is not applicable. However, the most widely used and the most preferred method is to use the standard conversion factor is 0.8 given by the British Standards (European Committee for Standardisation, 2013, European Committee for Standardisation, 2004). An extract of conversion factors from Eurocode 2 (European Committee for Standardisation, 2004) is presented in Table 3.1.

Table 3.1: Compressive strengths of concrete cylinders [$(f'_c)_c$] and cubes [$(f'_c)_{cu}$] (Source: European Committee for Standardisation, 2004)

$(f'_c)_c$	12	16	20	25	30	35	40	45	50	55	60	70	80	90
$(f'_c)_{cu}$	15	20	25	30	37	45	50	55	60	67	75	85	95	105

3.2.1.2. Tensile strength of concrete

In most standard design practices, the tensile strength of concrete is ignored, which is fair considering the difference in strength in compression and tension. As for the tensile strength, different standard methods of testing have been adopted in different countries. The most common methods are the flexural tensile test and splitting tensile test. The direct tensile strength is no longer used because of the difficulties in sample preparation. Standards Australia (2000), American Society for Testing and Materials (1996) and European Committee for Standardisation (2009b) specify the flexural tensile test.

Instead of conducting laboratory testing, researchers have developed simplified formulae for the tensile strength of concrete. All the formulae are based on the uniaxial compressive strength (f'_c) of concrete. However, due to the larger range of compressive strengths available, different formulae predict different values for tensile strength of concrete. Aïtcin (2011) compiled a list of available formulae for both splitting tensile strength and flexural tensile strength of concrete. An updated list of equations is presented in Table 3.2 and Table 3.3, respectively.

Table 3.2: Equations for predicting splitting tensile strength of concrete

Researcher/Standard	Splitting tensile strength (f_{st})(MPa)	Effective range of compressive strength (MPa)
CEB-FIP (1978)	$f_{st} = 0.273 f'^{0.67}_c$	No limitation
Carrasquillo et al. (1981)	$f_{st} = 0.54 f'^{0.5}_c$	$21 \leq f'_c \leq 83$
Raphael (1984)	$f_{st} = 0.313 f'^{0.5}_c$	$f'_c \leq 57$
ACI 363 (1984)	$f_{st} = 0.59 f'^{0.55}_c$	$21 \leq f'_c \leq 83$
Ahmad and Shah (1985)	$f_{st} = 0.462 f'^{0.55}_c$	$f'_c \leq 84$
Burg and Ost (1992)	$f_{st} = 0.61 f'^{0.5}_c$	$85 \leq f'_c \leq 130$
BS EN 1992 (2004)	$f_r = 0.3 f'^{0.67}_c$	No limitation
AS 3600 (2009)	$f_{st} = 0.36 f'^{0.5}_c$	$20 \leq f'_c \leq 100$
ACI 318 (2011)	$f_{st} = 0.56 f'^{0.5}_c$	No Limitation

Table 3.3: Equations for predicting the flexural tensile strength of concrete

Researcher/Standard	Modulus of rupture (f_r)(MPa)	Effective range of compressive strength (MPa)
Carrasquillo et al. (1981)	$f_r = 0.94f'^{0.5}_c$	$21 \leq f'_c \leq 83$
Burg and Ost (1992)	$f_r = 1.03f'^{0.5}_c$	$85 \leq f'_c \leq 130$
Khayat et al. (1995)	$f_r = 0.23 + 0.12f'_c - 2.18 \times 10^{-4}(f'_c)^2$	No limitation
ASTM C78 (2002)	$f_r = 0.74f'^{0.5}_c$	No Limitation
AS 3600 (2009)	$f_r = 0.60f'^{0.5}_c$	$20 \leq f'_c \leq 100$
ACI 318 (2011)	$f_r = 0.62f'^{0.5}_c$	No Limitation

AS 3600 (2009) equations are applicable to concrete compressive strengths between 20 MPa to 100 MPa. This covers the range expected for reinforced concrete facade panels. Hence, splitting tensile strength (f'_{st}) and flexural tensile strength (or modulus of rupture) (f_r) values proposed by AS 3600 is used as the reference values for this study.

3.2.1.3. Elastic (tangent) modulus of concrete

Normal strength concrete is considered as an elastic material until about 30-40% of compressive strength capacity whereas in higher strength concretes, this value is higher. Therefore, prediction of elastic modulus depends on the uniaxial compressive strength of concrete (f'_c). It is more appropriate to use the tangent modulus for this property rather than elastic modulus itself. Tangent modulus is the initial gradient of stress-strain curve measured from a compressive test. As shown in Figure 3.1, in the early stage of the compressive capacity, the stress-strain relationship is considered reasonably linear. The gradient of that linear portion is defined as the initial tangent modulus or elastic modulus of concrete.

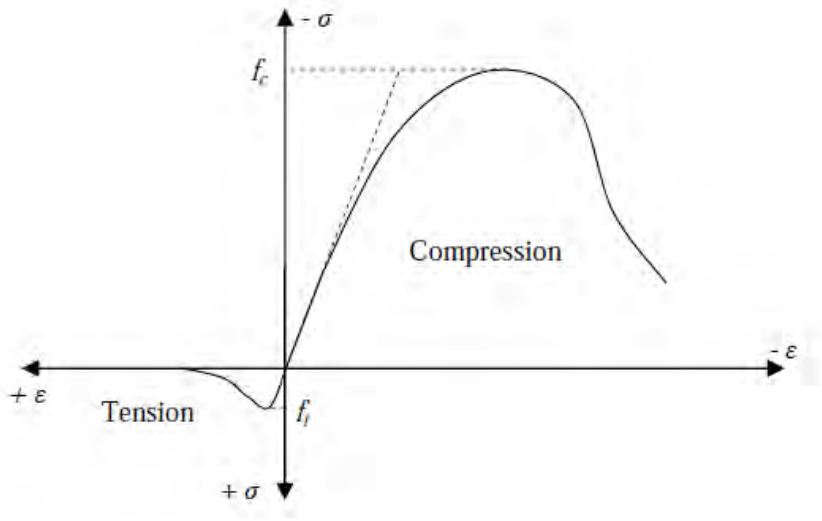

Figure 3.1: Stress-strain relationship of concrete (Source: Bangash, 1989)

The elastic modulus of concrete can be evaluated theoretically or using a standard compressive strength test. Derivation of the elastic modulus of concrete using the theoretical approach is considered extremely hard due to the difference in raw materials, mixing and curing times.

In the empirical approach, elastic modulus is estimated using the compressive strength of concrete. It is a firm belief that compressive strength is directly related to the elastic modulus of concrete, suggesting the same parameters influence the compressive strength and elastic modulus in a concrete mix. Various researchers have derived different formulations for elastic modulus of concrete, on the basis of experimental results. The formulations provided by the standards are also different from each other as shown in Table 3.4, which is a combined extract from Aïtcin (2011) and Pham (2010) with some details updated to the newer version of standards.

Table 3.4: Equations for predicting elastic modulus of concrete

Researcher/Standard	Modulus of Elasticity (GPa)	Strength Range (MPa)
Carrasquillo et al. (1981) ACI 363R-92 (1984)	$E_c = 3.32\left(f'_c\right)^{0.5} + 6.9$ $E_c = \left(3.32\left(f'_c\right)^{0.5} + 6.9\right)\left(\rho/2346\right)$	$21 \le f'_c \le 83$ ρ (density kgm^{-3})
AIJ (1985)	$E_c = 21\left(f'_c/20\right)^{0.5}\left(\rho/2300\right)^{1.5}$	No limitation
CAS A23.3(1990)	$E_c = 5\left(f'_c\right)^{0.5}$	High Strength
CEB (1990)	$E_c = 10(f'_c + 8)^{0.33}$	High Strength
Gardner and Zhao (1991)	$E_c = 9(f'_c)^{0.33}$	$f'_c \ge 27$
NS 3473 (2003)	$E_c = 9.5\left(f'_c\right)^{0.33}\left(\rho/2400\right)^{1.5}$	No limitation
BS EN 1992 (2004)	$E_c = 22\left(f'_c/10\right)^{0.3}$	No limitation
AS 3600 (2009)	$E_c = 0.043 \times 10^{-3}\rho^{1.5}\left(f'_c\right)^{0.5}$	$f'_c \le 40$
	$E_c = \left(0.043\left(f'_c\right)^{0.5} + 0.12\right)(\rho^{1.5} \times 10^{-3})$	$40 < f'_c \le 100$
ACI 318 (2011)	$E_c = 4.73\left(f'_c\right)^{0.5}$	Normal Strength

As shown in Table 3.4, all the elastic modulus relationships are based on the compressive strength of concrete. In order to cater for the lightweight concrete, some equations include the density as well. As it is applicable to wide range of concrete strengths, AS 3600 (Standards Australia, 2009) guidelines for evaluating the tangent modulus of concrete was used in this study. In addition, AS3600 has two different equations for two strength ranges as well as density included in the equation. This density term is applicable to reinforced concrete facade systems where lightweight concrete is used.

3.2.1.4. Poisson's ratio (υ)

Poisson's ratio is the negative value of the transverse to axial strain of a material, tested under uniaxial stress conditions. Most design codes and researchers agreed to use a scalar value for poison's ratio, instead of a relationship of strength. Figure 3.2 shows the

variation of Poisson's ratio, recorded for different stress levels of concrete for three different concrete strengths. The value is consistent until stresses reach the capacity of at least 80%, at which the apparent Poisson's ratio begins to increase. The value recorded for three concrete strengths varies between 0.19 and 0.24.

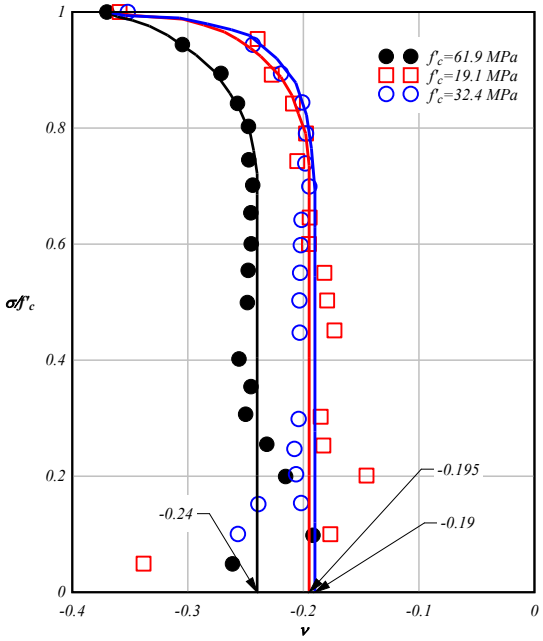

Figure 3.2: Relationship between stress-strength ratio and Poisson's ratio (Source: Chen, 2007)

If the exact value is required for a specific batch of concrete, Australian Standards (1997) define the testing method for the determination of Poisson's ratio. Alternatively, a representative value of 0.2 could be used as specified in AS3600 (2009), where the value is found to be consistent up to 80% of the compression capacity.

3.2.1.5. Fracture energy (G_f)

Fracture energy is defined as the specific energy to propagate a tensile crack of unit area (Comite Euro-International du Beton, 1990). Although there are several methods proposed by several researchers for the determination of fracture energy of concrete, including the simple three (3) point bending test (Peterson, 1980), the most widely used method to estimate the fracture energy is based on the maximum aggregate size and compressive strength, specified in CEB-FIP model code (1990) as in Equation 3.1.

$$G_f = G_{f0}\left(f'_c/10\right)^{0.7} \left(Nmm/mm^2\right) \quad (3.1)$$

Where;

G_{f0} = Base fracture energy based on the maximum aggregate size

f'_c = Compressive strength of concrete is MPa

The base fracture energy based on the maximum aggregate size is given in Table 3.5. For different values of maximum aggregate sizes, linear interpolation is permitted between the values.

Table 3.5: Base fracture energy for reinforced concrete (Source: Comite Euro-International du Beton, 1990)

Maximum Aggregate size (mm)	Base fracture energy (G_{f0}) (Nmm/mm^2)
8	0.025
16	0.030
32	0.058

3.2.1.6. Stress-strain relationship

Concrete in general exhibits a very complex behaviour involving inelasticity, cracking and strain softening even under quasi-static loading conditions. Therefore, predicting a universally acceptable stress-strain relationship is extremely difficult. In order to predict the stress-strain behaviour of concrete, various researchers have proposed many stress-strain relationships (Scott et al. 1982, Dilger et al. 1984, Soroushian and Obaseki, 1986, Mander et al. 1988, Attard and Setunge, 1996, Mendis et al. 2000) either using theoretical or empirical methods. Some of the more significant stress-strain relationships for concrete are as follows.

As suggested by Neville (1995), Desayi and Krishnan (1964) defined the most classical equation for the stress-strain relationship of concrete (Cited in Pham, 2010) as shown in Equation 3.2.

$$\sigma = \frac{E\varepsilon}{1 + \left(\frac{\varepsilon}{\varepsilon_o}\right)^2} \tag{3.2}$$

Where;

σ = Stress

ε = Strain

ε_o = Strain at maximum stress

E = Initial tangent modules, assumed twice the secant modulus as $2\sigma_{max}/\varepsilon_o$

Scott et al. (1982) presented a stress-strain model (hereafter the Scott model) which can be used with both confined and unconfined concrete as shown in Equations 3.3 and 3.4. The relationship consists of a parabolic ascending branch, a linear descending branch and a linear residual branch. The confinement parameter (K) was assumed to be equal to unity for unconfined concrete. The Scott model requires only the compressive strength of concrete to determine the stress-strain relationship of unconfined concrete while details of confining reinforcement (hoop reinforcement) are required to determine the stress-strain relationship for confined concrete.

$$f_c = Kf'_c\left[\frac{2\varepsilon}{0.002K} - \left(\frac{\varepsilon}{0.002K}\right)^2\right] \qquad for\ \varepsilon < 0.002K \tag{3.3}$$

$$f_c = Kf'_c[1 - Z_m(\varepsilon - 0.002K)] \geq f_{res} \qquad for\ \varepsilon > 0.002K \tag{3.4}$$

Where;

f_{res} $= 0.2Kf'_c$

K $= 1 + \frac{\rho_{sh} f_{yh}}{f'_c}$

Z_m $= \frac{0.5}{\frac{3 + 0.29f'_c}{145f'_c - 1000} + \frac{3}{4}\rho_{sh}\sqrt{\frac{h''}{s}} - 0.002K}$

f_{yh} = Yield strength of hoop reinforcement

ρ_{sh} = Volumetric ratio of hoop reinforcement

h" = Width of concrete core

s = Spacing of hoop reinforcement along the length of the member

Mander et al. (1988) also proposed a stress-strain curve (hereafter the Mander's model) for confined and unconfined concrete based on the experimental investigation of Watstein (1953). Initial developments of Popovics (1973, Cited in Fu et al. 1991a) was used for the development of Mander's model, which require three independent

parameters for the definition, compressive strength, secant modulus and strain at peak stress, as given in Equation 3.5.

$$f_c = \frac{f'_{cc} x r}{r - 1 + x^r} \tag{3.5}$$

Where;

$$x = {\varepsilon_{cc}}/{\varepsilon_c}$$

$$\varepsilon_{cc} = \varepsilon_{co}\left[1 + 5\left(\frac{f'_{cc}}{f'_{co}}\right) - 1\right]$$

$$r = \frac{E_c}{E_c - E_{sec}}$$

$$E_c = 5000\sqrt{f_{co}} \quad (MPa)$$

$$E_{sec} = {f'_{cc}}/{\varepsilon_{cc}}$$

f'_{cc} = Compressive strength of confined concrete ($f'_{cc} = Kf'_c$)

ε_c = Longitudinal compressive strain of concrete

K = Confinement coefficient as in Appendix A (unity for unconfined concrete)

Mendis et al. (2000) proposed a modified version of Scott model, which could be used to predict the stress-strain relationship of both normal strength concrete and high strength concrete up to 100 MPa. This model was developed using both Scott model and confinement parameter, defined by the Mander's model. The Modified Scott model has been validated to use for both confined and unconfined concrete (Mendis et al. 2000) and given in Equations 3.6 and 3.7 as,

$$f_c = Kf'_c\left[\frac{2\varepsilon}{\varepsilon_{cc}} - \left(\frac{\varepsilon}{\varepsilon_{cc}}\right)^2\right] \qquad for\ \varepsilon < \varepsilon_{cc} \tag{3.6}$$

$$f_c = Kf'_c[1 - Z_m(\varepsilon - \varepsilon_{cc})] \geq f_{res} \qquad for\ \varepsilon > \varepsilon_{cc} \tag{3.7}$$

Where;

$f_{res} = RKf'_c$

$\varepsilon_{cc} = (0.24K^3 + 0.76)\varepsilon_c$

$\varepsilon_c = \frac{4.26}{\sqrt[4]{f'_c}}\frac{f'_c}{E_c}$

$$Z_m = Z\frac{0.5}{\frac{3 + 0.29f'_c}{145f'_c - 1000} + \frac{3}{4}\rho_s\sqrt{\frac{h''}{s_h}} - \varepsilon_{cc}}$$

$Z = 0.0018f'_c + 0.55$

R $= 0.28 - 0.0032f'_c$ $R \geq 0$

E_c $= 9500(f'_c)^{0.3}$ (MPa)

K = Confinement coefficient calculated as in Appendix A

s_h = Spacing of shear reinforcement (hoop spacing)

h" = Width of concrete core measured to outside of the hoop reinforcement

ρ_s = Volumetric ratio of hoop reinforcement

The general stress-strain behaviour of normal strength concrete (NSC) widely differs to the more enhanced high strength concrete (HSC) and reactive powder concrete (RPC). As stated by Pham (2010), in HSC, the stress-strain curve remains linear almost up to the compressive strength while softening of the material occurs much earlier in NSC. This is mainly due to the internal load transfer and micro-cracking behaviour differences between the two strength classes of concrete. In addition, strain at maximum stress is increasing slightly with the increase of compressive strength, as shown in Figure 3.3.

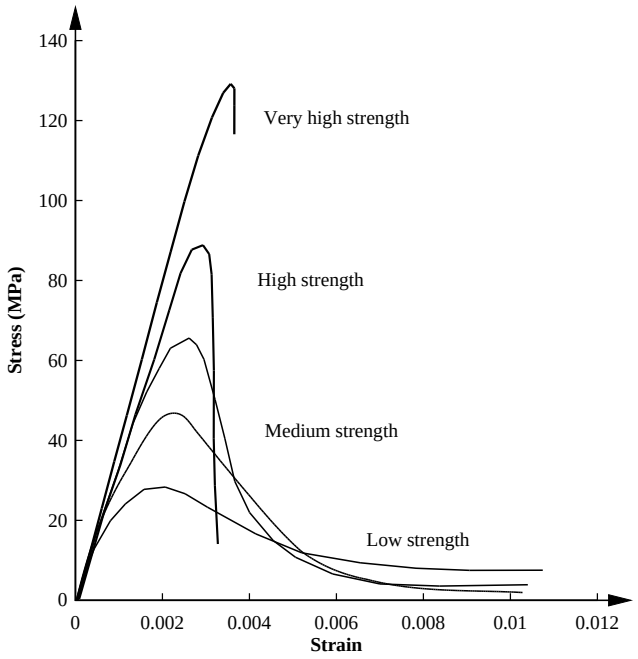

Figure 3.3: Uniaxial stress-strain curves for different concrete strengths (Source: Chen, 2007)

The ultimate strain at which the material fails become smaller with the increase in compressive strength, which indicates a reduction of ductility and possibility of sudden failure when the load exceeds the capacity. Furthermore, the descending branch of the stress-strain curve becomes steeper with the increase of compressive strength. The

failure patterns of HSC samples have shown smooth failure surfaces, indicating cracks passing through both the aggregate and concrete matrix, rather than failure at cement aggregate interface that is typical in NSC. These differences indicate different stress-strain relationships are required for HSC.

Thorenfeldt et al. (1987, Cited in Sengupta and Menon, 2010) proposed a stress-strain relationship for HSC, as shown in Equation 3.8. The relationship was based on the compressive strength of concrete, initial modulus, secant modulus and strain at maximum strength. According to Sengupta and Menon (2010), developments of the Thorenfeldt stress-strain relationship was based on the cube strength of concrete hence, cube strength should be taken as the characteristic strength of concrete.

$$f_c = f'_c \left[n\left(\varepsilon_c/\varepsilon_o\right) \right] \Big/ \left[n - 1 + \left(\varepsilon_c/\varepsilon_o\right)^{nk} \right] \tag{3.8}$$

Where;

k $= 1, if\ \varepsilon_c < \varepsilon_0\ or\ 0.67 + f_{ck}/77.5\ \ for\ \varepsilon_c > \varepsilon_0; k \geq 1$

n $= E_{ci}/(E_{ci} - E_s)$

E_{ci} = Initial modulus/Tangent modulus

E_s = Secant modulus (f_{ck}/ε_0)

f_c = Compressive stress

f_{ck} = Characteristic compressive Strength of concrete

ε_c = Compressive Strain

ε_0 = Strain corresponding to maximum stress

The Modified Scott Model (MSM) (Mendis et al. 2000) has been validated for both normal strength concrete and high strength concrete up to a compressive strength of 100 MPa. In addition, a comparison study conducted on the moment-curvature behaviour of reinforced concrete beam elements by Srikanth et al., (2007) revealed the superior performance of Modified Scott Model. On the basis of performance and ability to predict the behaviour of high strength concrete, Modified Scott Model was selected for 1-D analytical solution discussed in Chapter 6.

3.2.2. Quasi-static properties of reinforcing steel

Being an integral component of reinforced concrete, evaluation of the mechanical properties of reinforcing steel is important to understand the behaviour of reinforced

concrete. Unlike concrete, reinforcing steel is isotropic and considered to behave identically in both tension and compression under monotonic loading. Reinforcing steel is considered elastic for a certain range of strain and become plastic when that range is exceeded. A typical stress-strain relationship for steel reinforcement is shown in Figure 3.4.

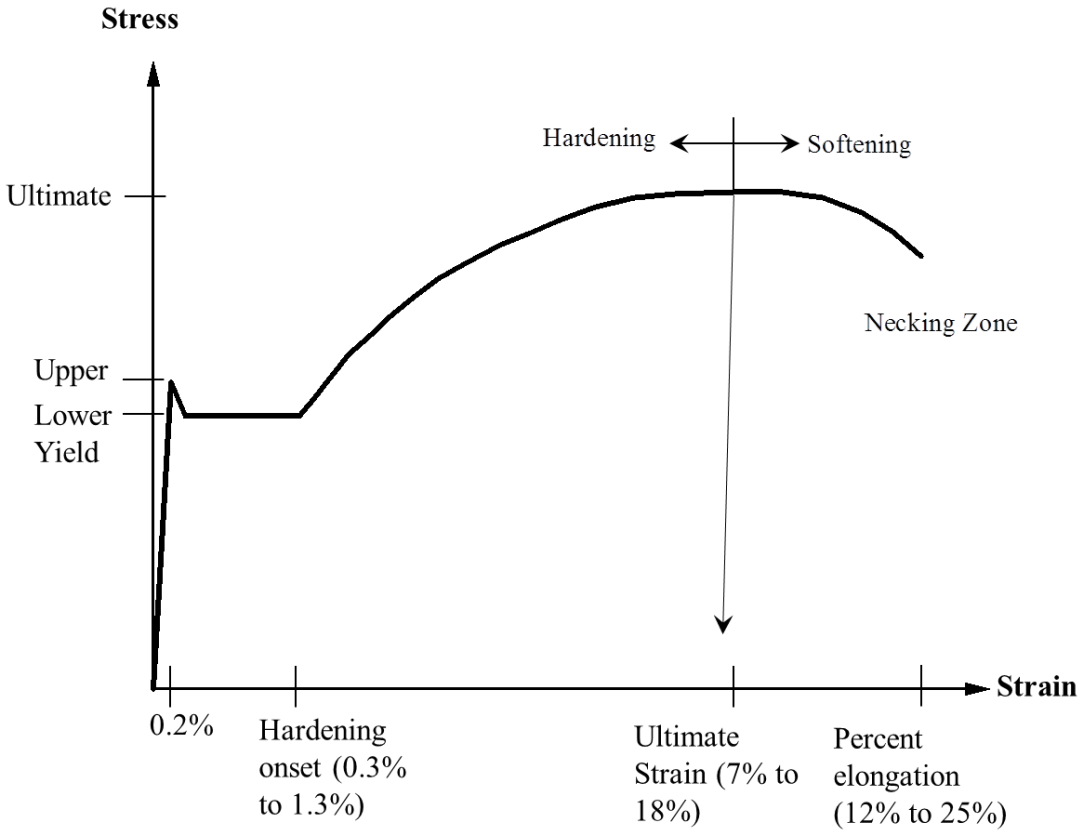

Figure 3.4: Typical stress-strain relationship for reinforcing steel (Source: Pham, 2010)

In most cases, the stress - strain relationship for reinforcing steel is idealised as bi-linear curves as shown in Figure 3.5. The idealisation is either considered as elastic-perfectly plastic or elastic-strain hardening plastic. However, in order to use for the design, these curves are further moderated with material safety factors.

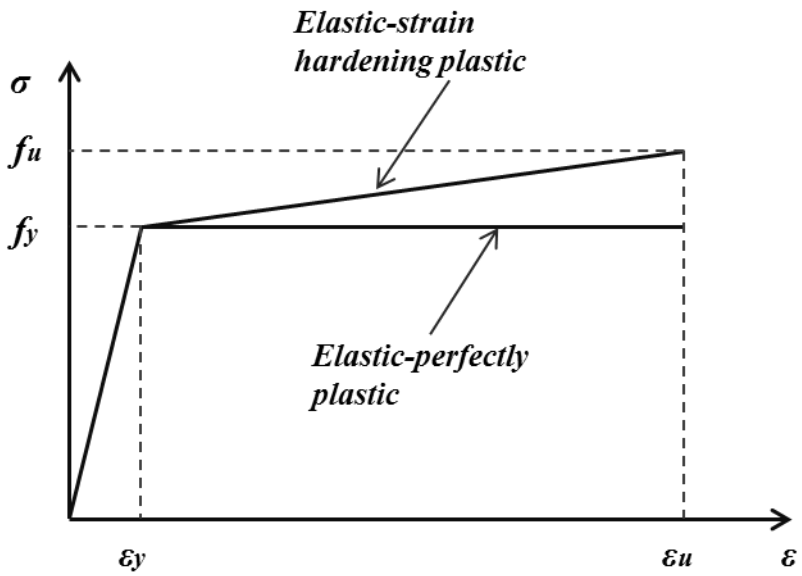

Figure 3.5: Idealised stress –strain curve for reinforcing steel (Source: EC 2, 2004)

Several quasi-static properties of reinforcing steel are discussed in this section including, yield strength, ultimate strength and ductility.

3.2.2.1. Yield strength (f_{sy})

The yield strength of reinforcing steel (f_{sy}/f_y) is the single most important parameter required for the reinforced concrete design. Yield strength defines the end of elastic limit for reinforcing bars which is achieved approximately with 0.2% strain, as shown in Figure 3.4. Among the different classes of steel available for design, 250 MPa (250N) and 500 MPa (500N, 500L) strength classes for round and deformed bars respectively, are the most widely used in the design of reinforcements, in Australia. However, recent developments in the reinforcement industry resulted in achieving yield strengths of 600 MPa or above. Although such strengths are not categorised in codes of practice, provisions have been made on how to use different strength classes in the design (Standards Australia, 2009).

3.2.2.2. Ultimate tensile strength (f_{su})

The ultimate tensile strength or the tensile strength of reinforcing steel defines the failure strength of the material. Once the ultimate strength is achieved, the material will undergo necking (in the case of tensile testing) and ultimately fail at a stress lower than the ultimate strength of the material. Although the ultimate tensile strength of

reinforcement is not used in the design of static members, it is used for the quality control of the material because of the ease of testing. Ultimate tensile strengths ranging between 300 MPa to 400 MPa for mild steel round bars and 550 MPa to 650 MPa for deformed tor steel bars are available for the design.

3.2.2.3. Ductility

Ductility is defined as the ability to undergo large permanent deformations without complete failure of a structural element and is a combined measure of ultimate tensile strength to yield strength ratio, and uniform elongation (Standards Australia, 2001). As for the reinforcement ductility, three ductility classes are available as low ductile reinforcement (Class L), Normal ductile reinforcement (Class N) and seismic or earthquake ductile reinforcement (Class E). However, only classes L and N are commonly used in Australia. Unless it is essential, use of normal ductile reinforcement is always encouraged over the low ductile reinforcement. Table 3.6 lists the ductility properties of different reinforcement classes specified in Australian Standards (2001).

Table 3.6: Ductility properties of different reinforcement classes (Source: Standards Australia, 2001)

Property	250N	500L	500N	300E	500E
Ultimate strength /Yield strength Ratio	≥1.08	≥1.03	≥1.08	≥1.15	≥1.15
Uniform Elongation (%)	≥5.0	≥1.5	≥5.0	≥15.0	≥10.0

3.3. Mechanical properties of materials under dynamic loading conditions

Structures can be subjected to different kinds of loading during their lifespan, including dynamic loading. Dynamic loading includes slow-moving winds to gale force winds, earthquakes, vehicle impacts, plane crashes and blast loads. Depending on the rate of loading (strain rate) these loads are classified as shown in Figure 3.6. Strain rates in the range of 10^{-6} s^{-1} to 10^{-5} s^{-1} are known as the quasi-static range and vehicle and plane crashes will have strain rates up to 10^{-1} s^{-1}. Earthquake induced loading can result in strain rates in the range of 10^{-4} s^{-1} to 10^{1} s^{-1}. The blast induced pressure and impulse loading, which is considered in this study, can induce strain rates up to 10^{4} s^{-1}, depending on the explosive charge weight (W) and standoff distance (R) combination.

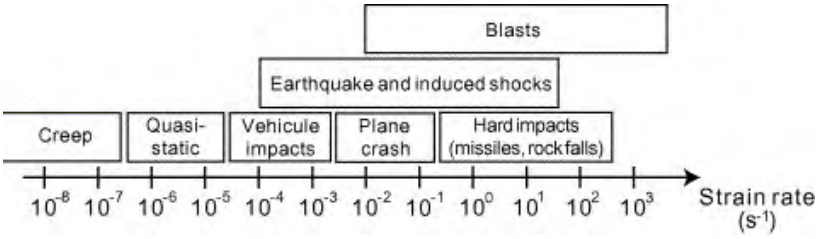

Figure 3.6: Different loading regimes based on the strain rate (Source: Hentz et al. 2004)

Response to higher rates of loading is different for different materials. In general brittle materials such as concrete will demonstrate a higher increase in strength than isotropic materials like steel. Rate enhancement properties for concrete and reinforcing steel are evaluated in the sections to follow.

3.3.1. Dynamic properties of concrete

The influence of higher rates of loading on the response of concrete structures is known for almost a century (Abrams, 1917), where higher compressive strengths have been observed with increased loading rates. Since then researchers derived different formulae and provided explanations for rate effects of concrete (Bischoff and Perry, 1991, Ross, 1989, Ross et al. 1996, Ross et al. 1995, Tedesco and Ross, 1993, Malvern et al. 1985, Takeda, 1985, Yon et al. 1992, Hughes and Gregory, 1972, Oh, 1987, Takeda and Tachikawa, 1962, Malvar and Crawford, 1998a, Malvar and Ross, 1998).

The most common method of illustrating the dynamic enhancement in strength is to express the ratio of dynamic strength to static strength, known as the dynamic increase factor (DIF) which depends on the rate of loading. The rate of loading, the independent variable in DIF, can be expressed in terms of direct loading rate, stress rate or the strain rate. Although all these three (3) terms are related to each other, simplification of loading rate to stress or strain rate can be applied only with certain specific conditions. However, in undertaking experiments, strain rate (strain) is measured more easily than the stress or the loading rate; hence DIF is normally presented as a variable of strain rate.

Although there are certain hypotheses provided for the rate enhancement of concrete, the most widely accepted is the explanation provided by Johansson (2000). Rate enhancement is due to two different scenarios, viscous effects and inertia/confinement

effects. The viscous effects are due to the pore pressure developments of free water trapped in micro-pores in hardened concrete. Viscous effects are considered applicable to a strain rate up to 30 s^{-1} in compression. The inertia and confinement effects are considered to be applicable beyond these limits. Many experiments have shown that the rate of change in DIF changes at 30 s^{-1} strain rate, as shown in Figure 3.7.

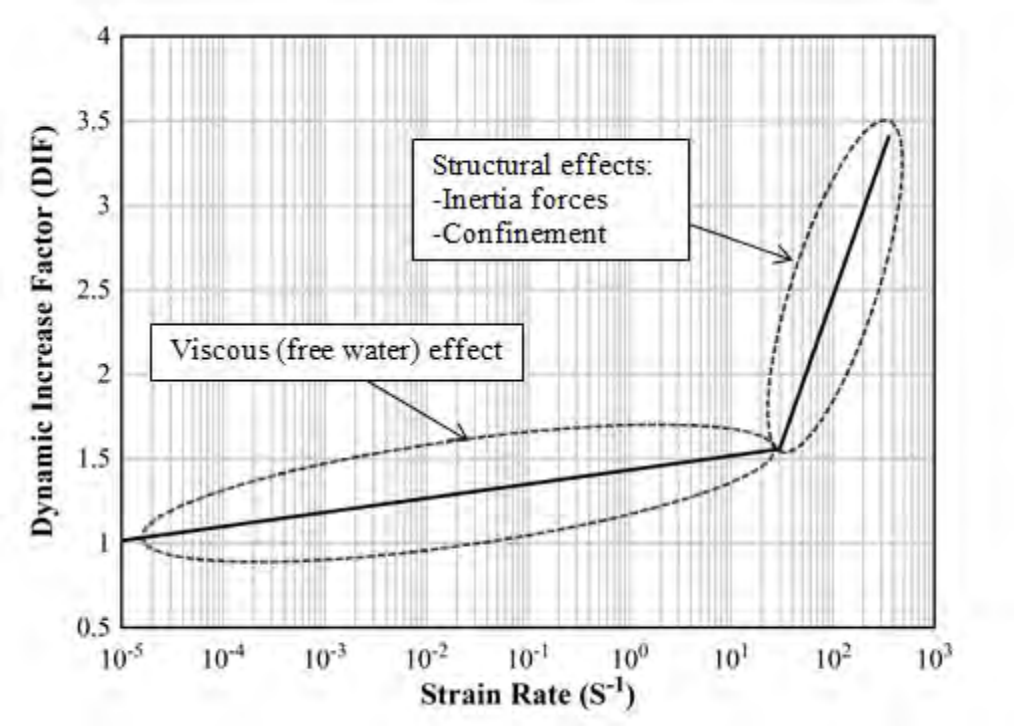

Figure 3.7: Viscous and structural effects of rate enhancement in concrete (Source: Johansson, 2000)

3.3.1.1. Compressive strength of concrete

Previous research

The earliest study of rate enhancement effects of concrete under compressive stress was recorded nearly 100 years ago (Abrams, 1917). Since then, various dynamic testing regimes were conducted on plain concrete samples in order to understand the process of dynamic increase in strength as well as the governing factors for the dynamic enhancements in compressive strength.

A comprehensive review on the rate enhancement of concrete under compressive loading (Fu et al. 1991a) has identified that earlier testing was limited to maximum strain rates up to 10 s^{-1}. Research in the 1930s' confirmed the Abrams's (1917)

observations where an increase in the rate of loading is accompanied by an increase in compressive strength of concrete. However, no quantification of loading rates or strength increases was performed. In 1953, Watstein first introduced the strain rate instead of the conventional loading rate that was used to define the rate enhancement effects. In his study, an 80% strength increase was observed by increasing the strain rate from 10^{-6} s^{-1} to 10 s^{-1}. In a book by Norris et al. (1959) rate enhancement factors of 1.33, 1.24 and 1.17 were defined for strain rates of 3 s^{-1}, 0.3 s^{-1} and 0.1 s^{-1} for all compressive strengths.

Variations of compressive strength gain of concrete during higher rates of loading were observed by several other researchers. Watstein's (1953) testing of concrete cylinders with drop hammer apparatus revealed similar strength gains of 84% and 85% for the two compressive strengths 17.4 MPa and 45.1 MPa.

Atchley and Furr (1967) tested sixty (60) concrete cylinders with different nominal strengths of 17.4 MPa, 25.7 MPa and 34.7 MPa at stress rates in the range of 0.05 MPa/s to 118055 MPa/s (roughly 5×10^{-6} s^{-1} to 5 s^{-1} in strain rates). Although an increase in strength was observed for all three concretes, no significant variations were observed for different strengths. Subsequently, two empirical equations were proposed for the dynamic strength of concrete for the stress rates from 13.9 MPa/s to 6944 MPa/s and 6944 MPa/s to 69444 MPa/s, respectively, irrespective of the compressive strength of concrete. Maximum strength gains of 25% and 38% were predicted for the two stress rate ranges using these empirical equations.

Testing carried out at Kyoto University in the early1980's (Wakabayashi et al. 1980) found that dynamic compressive strength can be predicted using the logarithm of strain rate. Thirty (30) cylindrical samples of 25 MPa concrete exhibited average strength gains of 14% and 24% respectively for two strain rates of 0.005 s^{-1} and 0.05 s^{-1}, in comparison with quasi-static strain rate (2×10^{-5} s^{-1} in this study). In general, all researchers have identified the compressive strength gain with the increased strain rate, although no significant variation was observed with the compressive strength of concrete.

Other than the compressive strength and parameters directly related to compressive strength (Such as Elastic modulus), some researchers have considered the options of aggregate type and strength, curing times and procedures and moisture content of

concrete as well for the rate enhancement in concrete. As shown in Cowell's experimental study (1966), moisture content in hardened concrete plays a significant role in defining the dynamic enhancement of compressive strength. A significant enhancement in compressive strength (8%-14%) has been observed with the wet condition of the hardened concrete, over dry condition. Similar observations (about 12% increase in strength) were observed with the dynamic testing conducted by Spooner (1971). Tests made with concrete prisms and cylinders (Kaplan, 1980) also confirmed the influence of moisture content on the rate enhancement of concrete, although no quantified results were presented. All three studies concluded that rate enhancement depends on the moisture content of hardened concrete, which also helps explain the Johansson hypothesis (Johansson, 2000) defined for the rate enhancement of concrete (Figure 3.7).

The influence of aggregate strength, size and shape on the rate enhancement properties of compressive strength of concrete has been investigated (Sparks and Menzies, 1973) with gravel, limestone and weak Lytag aggregate. A higher increase in strength was observed with Lytag aggregate concrete (16%) compared to limestone aggregate concrete (4%) when subjected to 10 MPa/s loading rate. A similar study conducted on 102 mm cubes subjected to impact loads by a ballistic pendulum (Green, 1964) has shown shape and size of the aggregates and curing conditions determine the magnitude of the effects of strain rates.

Bischoff and Perry (1991) accumulated sixty (60) years of quantified test results for dynamic compressive strength of concrete and graphically represented the results as shown in Figure 3.8. A wide scatter of data presented in the semi-log scale confirms the difficulty of predicting the dynamic compressive strength of concrete. Most of these tests were conducted using drop hammer testing or ballistic pendulum swing hence, measurement of strain and strain rate were difficult.

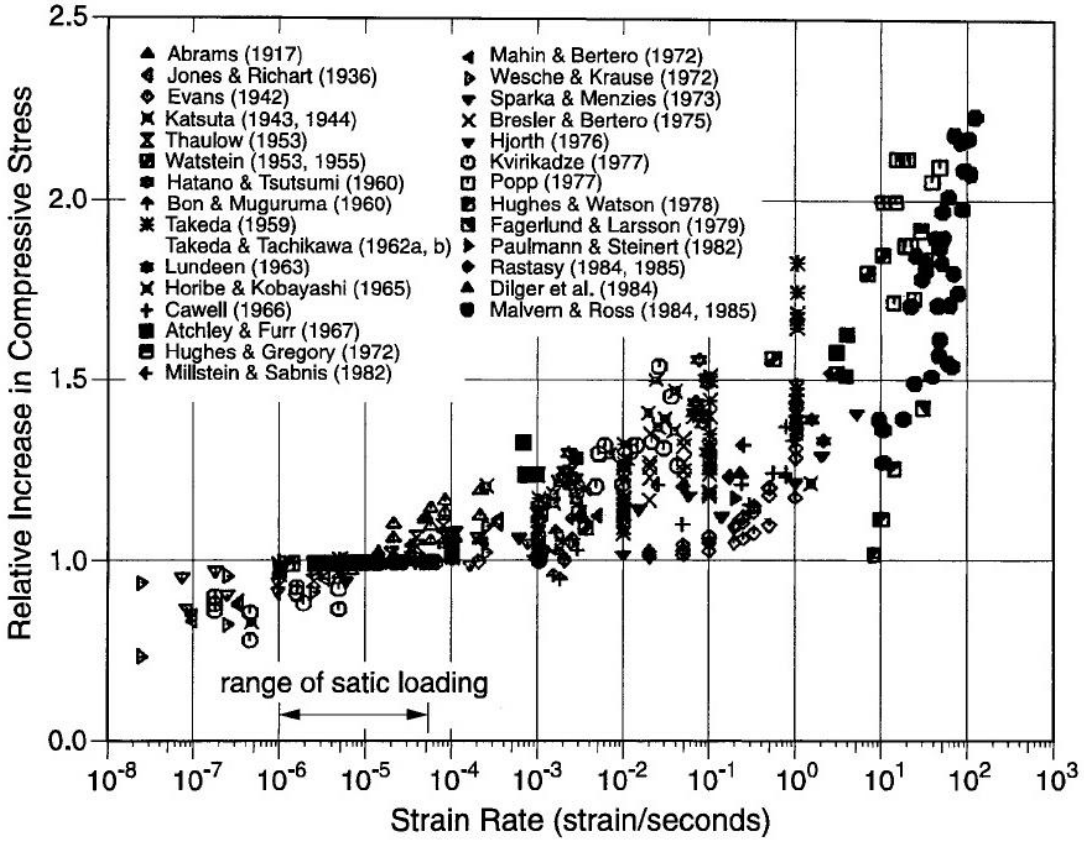

Figure 3.8: Rate enhancement effects on compressive strength of concrete (Source: Bischoff and Perry, 1991)

Prediction equations

Among the several empirical equations to predict the dynamic compressive strength of concrete (or dynamic increase factor in compression), the CEB-FIP (1990) formulation is widely accepted for strain rates up to 300 s^{-1}. The CEB formulation consists of two different equations for viscous effects and structural effects, in semi-logarithmic scale as given in Equations 3.9 and 3.10.

$$f'_c/f'_{cs} = DIF_{comp} = \left(\dot{\varepsilon}/\dot{\varepsilon}_s\right)^{1.026\alpha} \qquad for\ \dot{\varepsilon} \leq 30\ S^{-1} \tag{3.9}$$

$$f'_c/f'_{cs} = DIF_{comp} = \gamma\left(\dot{\varepsilon}/\dot{\varepsilon}_s\right)^{1/3} \qquad for\ \dot{\varepsilon} > 30\ S^{-1} \tag{3.10}$$

Where;

$\acute{\varepsilon}$ = Strain rate

$\acute{\varepsilon}_s$ = Quasi-static strain rate (30×10^{-6} s^{-1})

f_{co} = 10 MPa or 1450 psi

f_{cs} = Quasi-static compressive strength

$\log \gamma = 6.156\alpha - 2$

$\alpha = 1/(5+9f_{cs}/f_{co})$

The relationships were presented as a ratio of quasi-static compressive strength (f'_c), which was much more convenient in terms of the designer's perspective. A similar study (Malvar and Crawford, 1998a) to Bischoff and Perry (1991) revealed that the proposed CEB (1990) formulation predicts the dynamic enhancement of compressive strength of concrete accurately.

This formulation was widely accepted for normal strength concrete. However, DIF estimations of this formulation for high performance concretes, such as high strength concrete (HSC) and reactive powder concrete (RPC) were found to be over-predicted (Ngo, 2005).

The CEB formulation was also limited to 300 s^{-1}, which can be considered as a middle range strain rate for explosive loading. An experimental study (Grote et al. 2001) carried out to determine the compressive behaviour of concrete at very high strain rates with split Hopkinson pressure bar (SHPB) testing and plate impact testing showed dynamic increase factors up to 3.5 for concrete in compression. Prediction equations for the dynamic increase factor were presented (Equations 3.11 and 3.12) with curve fitting for two different ranges of strain rates, as illustrated in Figure 3.9.

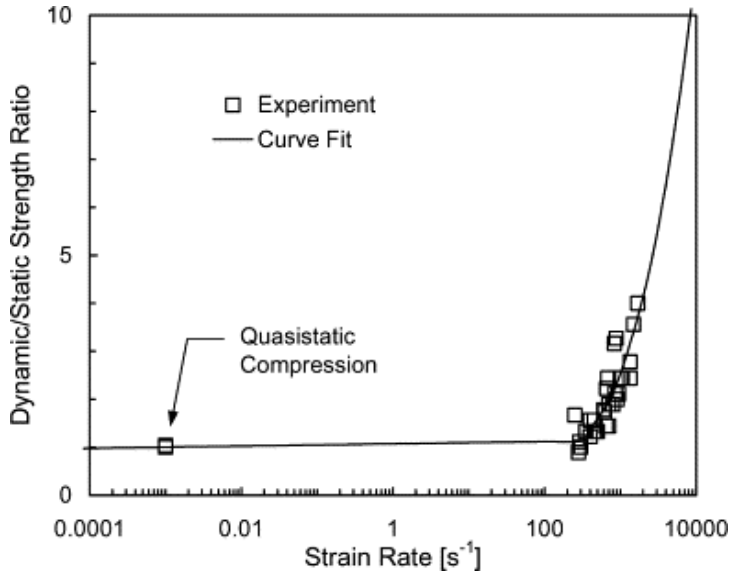

Figure 3.9: Strain rate dependence of the compressive strength of concrete at high strain rates (Source: Grote et al. 2001)

The initial linear section of the curve fit extends to 250 s^{-1}, compared to 30 s^{-1} in the CEB formulation, which was predicted using the Equation 3.11. The curvilinear section was proposed with a third order fit of strain rate and extrapolated beyond the 1700 s^{-1}. Prediction curves are limited to a single compressive strength value of 46 MPa. The prediction equation for strain rates beyond 250 s^{-1} is predicted using the Equation 3.12.

$$DIF_{comp} = 0.0235log\dot{\varepsilon} + 1.07 \qquad \dot{\varepsilon} \leq 250s^{-1} \qquad (3.11)$$

$$DIF_{comp} = 0.882(log\dot{\varepsilon})^3 - 4.48(log\dot{\varepsilon})^2 + 7.22(log\dot{\varepsilon}) - 2.64 \qquad \dot{\varepsilon} > 250s^{-1} \qquad (3.12)$$

Ngo (2005) investigated the behaviour of normal strength, high strength and reactive powder concrete under the effects of high strain rates using the split Hopkinson pressure bar (SHPB) test. The initial results on normal strength and high strength concrete revealed a slightly higher prediction when using the CEB formulation (1990) for compressive strength. Adjustments were made to the CEB formulation, is given in Equations 3.6 and 3.7 for the 'α' parameter, and given in Equation 3.13 with the rest of the parameters and equations kept as is.

$$\alpha = 1/(5 + 10f_{cs}/f_{co}) \qquad (3.13)$$

Both the CEB formulation and Ngo's proposed equation (Equation 3.13) failed to capture the dynamic strength of reactive powder concrete (RPC), which had a quasi-static compressive strength of 160 MPa. Among the three samples tested, strain rates

were recorded up to 267 s^{-1}, and a maximum DIF of 1.5, which was much lower than the CEB formulation and the modified CEB formulation. Hence, a new DIF equation was proposed (Ngo, 2005) based on the experimental results as in Equations 3.14 and 3.15, for reactive powder concrete.

$$f'_c / f'_{cs} = DIF_{comp} = \left(\dot{\varepsilon} / \dot{\varepsilon}_s\right)^{1.026\alpha} \qquad for\ \dot{\varepsilon} \le \dot{\varepsilon}_1\ s^{-1} \tag{3.14}$$

$$f'_c / f'_{cs} = DIF_{comp} = A_1 ln(\dot{\varepsilon}) - A_2 \qquad for\ \dot{\varepsilon} > \dot{\varepsilon}_1\ s^{-1} \tag{3.15}$$

Where;

α = $1/(20+f_{cs}/2)$

$\acute{\varepsilon}_1$ = $0.0022(f'_{cs})^2 - 0.1989 f'_{cs} + 46.137$

A_1 = $-0.0004\, f'_{cs} + 0.9866$

A_2 = $-0.0128\, f'_{cs} + 2.1396$

$\acute{\varepsilon}$ = Strain rate

$\acute{\varepsilon}_s$ = Quasi-static strain rate (30×10^{-6} s^{-1})

These formulations are similar to the CEB formulation until a strain rate of $\acute{\varepsilon}_1$ (which was 30 s^{-1} for CEB formulation). The second part of the bi-linear curve was proposed with a different form of an equation. The Ngo's equations also consider the dependency of slope change strain rate with the uniaxial quasi-static compressive strength of concrete.

As for this study, CEB formulation for the strain rate enhancement of compressive strength of concrete will be used. This formulation has been validated by many of the researchers. In addition, this formulation is applicable to a large range of strain rates (up to 300/s), which covers a large range of strain rates within the blast loading regime (10^{-2}/s to 10^{3}/s). It is quite rare to experience strain rates beyond 300/s for conventional explosive events (Detonation of high explosives) as well. Therefore, CEB formulation for the strain rate enhancement of compressive strength of concrete is selected for this study.

3.3.1.2. Tensile strength of concrete

As in most brittle materials, tensile strength is not the most considered material property in concrete. In most structural designs for static loading, tensile strength is ignored considering all the tensile stresses will be taken by the reinforcing steel. However, in

dynamic loading, specifically impulsive loading, ignoring the tensile strength will underestimate the capacity of reinforced concrete elements significantly. More importantly, different failure mechanisms such as direct shear failure in reinforced concrete elements, which is rare or non-existent in static loading but common in dynamic loading (Shi et al. 2005, Zineddin and Krauthammer, 2007), depends significantly on the tensile strength of the material. As noted in low strength concretes for compressive strength of concrete, dynamic enhancement is much larger with the tensile strength of concrete (Fu et al. 1991b), even reaching seven (Malvar and Crawford, 1998a) in certain experiments. This increase in tensile strength reduces the possibility of spalling and formation of flying debris. Furthermore, the enhancement in tensile strength could significantly alter the behaviour of reinforced concrete sections subjected to explosive and ballistic loading, acting primarily as an over-reinforced section (Pham, 2010).

The tensile strength of concrete is measured either as splitting tensile strength (Brazilian test) or direct tensile strength as discussed in section 3.2.1.2. The same approach is used to measure the dynamic tensile strength of concrete as well. Cowell (1966) and Wakabayashi (1980) used splitting cylinder testing to investigate the dynamic enhancement of tensile strength, while Komlos (1969), Takeda and Tachikawa (1971) used direct uniaxial tension. In all cases, higher strengths were recorded with the increased strain rate, especially by Cowell with an 18-65% increase and Takeda and Tachikawa with a 70% increase. These were considerably larger strength increases than what was achieved for compressive strengths for similar samples and strain rates.

Several formulations have been proposed for the determination of dynamic increase factors for concrete in tension (Evans, 1974, Mihashi and Izumi, 1977, Cited in Fu et al. 1991b). However, the CEB formulation (1990) is widely accepted as in the case of formulation for DIF for compressive strength of concrete. The formulation consists of two bi-linear curves on semi-log scale with lower tensile strengths predicting higher DIFs as shown in Equations 3.16 and 3.17, respectively.

$$f'_t/f'_{ts} = DIF_{tens} = \left(\dot{\varepsilon}/\dot{\varepsilon}_s\right)^{1.016\delta} \qquad for\ \dot{\varepsilon} \leq 30\ S^{-1} \tag{3.16}$$

$$f'_t/f'_{ts} = DIF_{tens} = \beta\left(\dot{\varepsilon}/\dot{\varepsilon}_s\right)^{1/3} \qquad for\ \dot{\varepsilon} > 30\ S^{-1} \tag{3.17}$$

Where;

$\log \beta = 7.11\delta - 2.33$

$\delta = 1/(10+6f_{cs}/f_{co})$

$\dot{\varepsilon}$ = Strain rate (up to 300 s^{-1})

$\dot{\varepsilon}_s$ = Quasi-static strain rate (3×10^{-6} s^{-1})

f_{co} = 10 MPa or 1450 psi

f_{cs} = Quasi-static compressive strength

Malvar and Crawford (1998a) revisitted earlier experimental studies and found that the turning point of the CEB formulation for DIF in tension does not match adequately with the experimental results. Also, the proposed maximum strain rate of 300 s^{-1} in the CEB formulation was reduced to 160 s^{-1} for the corrected formulation, which is shown in Equations 3.18 and 3.19. Figure 3.10 and Figure 3.11 illustrate the original CEB formulation plotted with the available experimental results and proposed formulation with the available experimental results, respectively.

$$f'_t/f'_{ts} = DIF_{tens} = \left(\dot{\varepsilon}/\dot{\varepsilon}_s\right)^{\delta} \qquad for\ \dot{\varepsilon} \leq 1\ s^{-1} \tag{3.18}$$

$$f'_t/f'_{ts} = DIF_{tens} = \beta\left(\dot{\varepsilon}/\dot{\varepsilon}_s\right)^{1/3} \qquad for\ \dot{\varepsilon} > 1\ s^{-1} \tag{3.19}$$

Where;

$\log \beta = 6\delta - 2$

$\delta = 1/(1+8f_{cs}/f_{co})$

$\dot{\varepsilon}$ = Strain rate (up to 160 s^{-1})

$\dot{\varepsilon}_s$ = Quasi-static strain rate (1×10^{-6} s^{-1})

f_{co} = 10 MPa or 1450 psi

f_{cs} = Quasi-static compressive strength

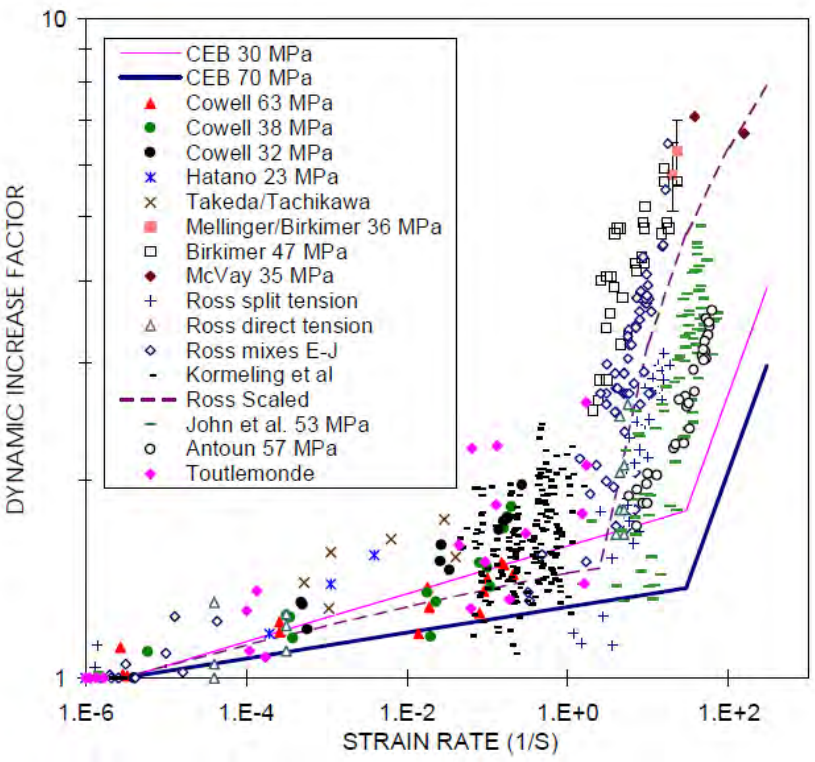

Figure 3.10: Comparison of CEB formulation for tension DIF in concrete with available experimental results (Source: Malvar and Crawford, 1998a)

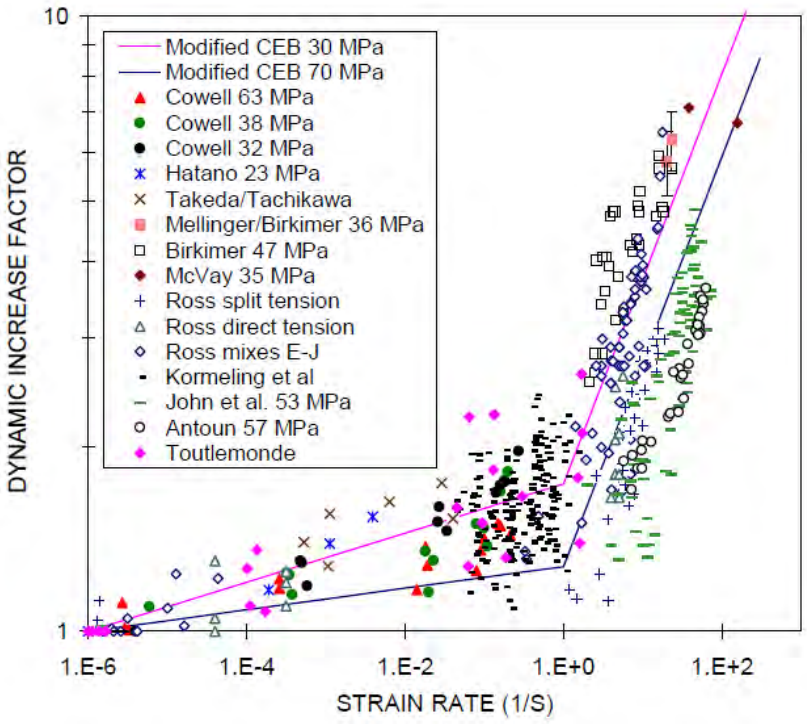

Figure 3.11: Comparison of modified CEB formulation for tension DIF in concrete with available experimental results (Source: Malvar and Crawford, 1998a)

Committee Euro-International du Beton published an updated version of CEB-FIP model code in 2010, where a completely different formulation was introduced for the dynamic increase factor for tensile strength of concrete. These relationships are overly simplified where dependency of compressive strength on DIF was ignored as shown in Equation 3.20 and 3.21.

$$f'_t/f'_{ts} = DIF_{tens} = \left(\dot{\varepsilon}/\dot{\varepsilon}_s\right)^{0.018} \qquad for\ \dot{\varepsilon} \leq 10S^{-1} \tag{3.20}$$

$$f'_t/f'_{ts} = DIF_{tens} = 0.0062\left(\dot{\varepsilon}/\dot{\varepsilon}_s\right)^{1/3} \qquad for\ \dot{\varepsilon} > 10\,S^{-1} \tag{3.21}$$

Comparison of 1990 CEB formulation (Comite Euro-International du Beton, 1990) and Malvar and Crawford formulation (1998a) in Figure 3.10 and Figure 3.11 indicate a better correlation of experimental results with the Malvar and Crawford formulation. Although there are some discrepancies, Malvar and Crawford formulation predicts the rate enhancement better than the original CEB formulation for concrete in tension. Hence, the Malvar and Crawford (1998a) formulation for DIF in tensile strength of concrete was utilised for the scope of this study.

3.3.1.3. Stress-strain relationship

Stress-strain characteristics of concrete under increased strain rates can be considerably different from that of quasi-static conditions due to the possible enhancements in compressive strength, elastic modulus and strain at ultimate stress. The differences in stress-strain curves under dynamic and static conditions were identified as early as the 1950's (Watstein, 1953) through the experimental investigation of concrete cylinders. Takeda and Tachikawa (1971) proposed a relationship between stress, strain and strain rate through experimental testing of concrete cylinders with strain rates ranging from 1×10^{-6} s^{-1} to 1 s^{-1}, as given in Equation 3.22. The same relationship is illustrated in the three-dimensional plot in Figure 3.12.

$$f_c = \int_0^S \alpha(\dot{\varepsilon})^{\beta-1} d\varepsilon \tag{3.22}$$

Where;

α, β = Functions of constant strain rate

f_c = Compressive stress at a given strain and strain rate

The α and β functions were defined for different strain rates ranging from 0.251 to 0.007 and 1.008 to 1.165 respectively. Equation 3.22 and Figure 3.12 (Fu et al. 1991a) indicated a fairly good agreement for strains between 0.00025 and 0.0025, in comparison to experimental results.

Wakabayashi et al. (1980) identified that only the ascending branch of the stress-strain curve will change with the increased rate of loading. This was based on the observations that strain at maximum stress will not change with increased strain rates, during the experimental investigation.

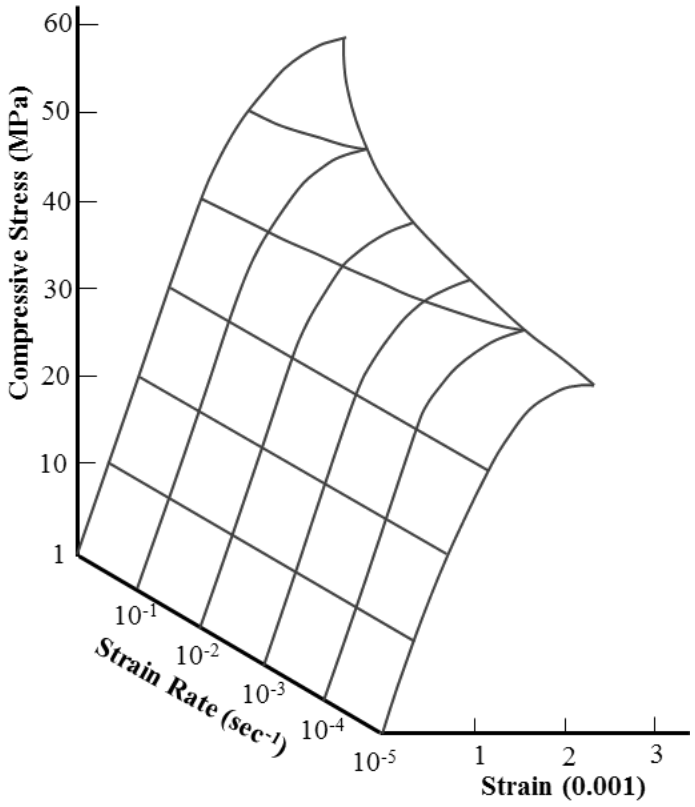

Figure 3.12 : Relationship between stress, strain and strain rate for concrete in compression (Source: Takeda and Tachikawa, 1971)

More detailed investigations on rate dependent stress-strain relationships were carried out in 1980's where stress-strain relationships were developed for confined concrete (Scott et al. 1982, Dilger et al. 1984, Soroushian and Obaseki, 1986, Mander et al. 1988). In which, Mander's model (1988) is considered to be capable of representing the rate-dependent stress-strain behaviour in confined concrete, at a specified range of loading rates (Pham, 2010). In order to adjust the Mander's stress-strain relationship

(Equation 3.8) to higher strain rates, three dynamic increase factors were introduced as in Equations 3.23, 3.24 and 3.25 for compressive strength (D_f), Elastic modulus (D_E) and strain at peak stress (D_ε) respectively.

$$D_f = \frac{1 + \left[\frac{\dot{\varepsilon}}{0.035(f'_c)^2}\right]^{1/6}}{1 + \left[\frac{0.00001}{0.035(f'_c)^2}\right]^{1/6}} \tag{3.23}$$

$$D_E = \frac{1 + \left[\frac{\dot{\varepsilon}}{0.035(f'_c)^3}\right]^{1/6}}{1 + \left[\frac{0.00001}{0.035(f'_c)^3}\right]^{1/6}} \tag{3.24}$$

$$D_\varepsilon = \frac{1}{3D_f}\left(1 + \sqrt{\frac{1 + 3{D_f}^2}{D_E}}\right) \tag{3.25}$$

The modified Scott model (Mendis et al. 2000) (Equations 3.3 and 3.4) is also capable of representing the rate enhancement effects in stress-strain relationship. The stress-strain relationship was modified using a modification factor for the rate enhancement, based on the Equations 3.3 and 3.4.

Ngo (2005) proposed a rate dependent stress-strain relationship as shown in Equations 3.26 and 3.27, based on an experimental study on high rates of loading on normal strength, high strength and reactive powder concrete. The proposed curves were similar to that of the modified Scott model and named the strain-rate dependent concrete model (SDCM).

$$f_c = K_{cd} f'_c \left[\frac{2\varepsilon}{\varepsilon_{cd}} - \left(\frac{\varepsilon}{\varepsilon_{cd}}\right)^2\right] \qquad for\ \varepsilon \le \varepsilon_{cd} \tag{3.26}$$

$$f_c = K_{cd} f'_c [1 - Z_d(\varepsilon - \varepsilon_{cd})] \qquad for\ \varepsilon > \varepsilon_{cd} \tag{3.27}$$

Where;

K_{cd} = Dynamic increase factor for compressive stress

ε_{cd} = Dynamic increase factor of strain at peak stress

$$Z_d = Z\frac{0.5(1 + 0.005f'_{cs})}{\frac{3 + 0.29f'_{cs}}{145f'_{cs} - 1000} - \varepsilon_{cs}} \tag{3.28}$$

In high performance concretes, the denominator of Equation 3.36 could become Zero or negative indicating a very steep decline. However, in case the denominator becomes

negative, the softening slope is defined as ten times the quasi-static compressive strength of concrete ($10f'_c$). Although this relationship lacks the incorporation of confinement effects, which could be achieved using the recommendations given in the modified Scott model.

The modified Scott model will be used for the development of the 1-D analytical solution, which is equipped with the rate enhancement effects on the stress-strain relationship.

3.3.2. Dynamic properties of reinforcing steel

As observed in concrete, rate enhancement also has been observed with reinforcing steel. Since steel being an isotropic material, identical tensile and compressive behaviours are assumed for the material. There was a significant interest on determining dynamic properties of steel (not limited to reinforcing steel) (Norris et al. 1959, Keenan and Feldman, 1960, Cowell, 1966, Cowell, 1969, Sozen, 1974, Wakabayashi et al. 1980, Soroushian and Obaseki, 1986, Soroushian and Choi, 1987, Malvar, 1998). In a review of earlier experimental results, Sozen (1974) observed the same pattern of low strength steel exhibit higher dynamic enhancement than that of higher strength steel, that was observed in concrete. On his review of past experimental results, Fu (1991b) made the following observations with respect to reinforcing steel bars at elevated strain rates.

- Behaviour in both tension and compression are similar even for elevated strain rates.
- Increased strain rate has little or no effect on the modulus of Elasticity and percentage elongation at failure (ultimate strain).
- Both yield strength and ultimate strength increase with increased strain rates. However, the increment depends on the static yield strength of steel, where lower strength reinforcement has higher strength gains and higher strength reinforcement has lower strength gains, similar to observations in concrete.
- Due to no difference observed in percentage elongation in failure (ultimate strain), ductility is reduced marginally.

3.3.2.1. Yield strength

Being the most important design parameter, the yield strength of steel was the most investigated property under the effects of elevated strain rates. Cowell (1969) observed strength increases of 25%, 33%, 38% and 53% at 0.03 s^{-1}, 0.1 s^{-1}, 0.3 s^{-1} and 1 s^{-1} strain rates respectively, compared to 1×10^{-5} s^{-1} strain rate for structural steel sections of 264 MPa (A36 steel). For the same strain rates, 350 MPa steel has shown strength increases of 10%, 13%, 17% and 19% only. Similar results were observed (Norris et al. 1959) with the 330 MPa steel and 278 MPa steel, tested with similar strain rates. Enhancements of 10%, 14%, 18% and 23% for 278 MPa steel and 9%, 12%, 17% and 21% for 330 MPa steel were observed. Wakabayashi (1980) performed tensile testing on both circular round bars and deformed bars of similar strength classes and found no difference in enhancement between two types of steel.

A formulation to estimate the dynamic enhancement of yield strength of steel was presented in 1986 (Liu and Owen) as shown in Equation 3.29.

$$DIF_{yield} = {f_y}/{f_{ys}} = \lambda log\left({\dot{\varepsilon}}/{\dot{\varepsilon}_s}\right) + 1 \tag{3.29}$$

Where;

λ = Material parameter (0.03)

$\acute{\varepsilon}_s$ = Quasi-static strain rate (0.01 s^{-1})

Soroushian and Obaseki (1986) also proposed a formulation for the dynamic increase factor for yield strength of steel, which was altered to the following formation in 1987 (Soroushian and Choi) (Equation 3.30).

$$DIF_{yield} = \left(-0.451\times10^{-6}f_y + 1.46\right) + \left(-9.20\times10^{-7}f_y + 0.0927\right)log_{10}\dot{\varepsilon} \tag{3.30}$$

Malvar and Crawford (1998b) presented a formula for DIF of the yield strength of reinforcing steel reviewing earlier experimental studies. The proposed formula, as given in Equation 3.31, can be used to estimate the DIF for a wide range of reinforcing steel from 290 MPa to 710 MPa. Figure 3.13 indicates the behaviour of DIF for yield strength of reinforcing steel using the Malvar and Crawford prediction formula and Figure 3.14 indicates the comparison of three (3) proposed equations for 500 MPa steel. Liu and Owen's (1986) predictions were available only for strain rates greater than 1×10^{-3} s^{-1} and has the smallest prediction among three equations. Although Soroushian

and Choi's predictions are available for smaller strain rates (less than 1×10^{-4} s^{-1}), calculations were limited to the smallest strain rate that could be used for the Malvar and Crawford's formulation. Soroushian and Choi recorded the highest predictions for DIF followed by Malvar and Crawford and Liu and Owen.

$$DIF_{yield} = \left(\dot{\varepsilon}/_{10^{-4}}\right)^{\alpha} \tag{3.31}$$

Where;

α $= 0.074 - 0.040\left(f_y/_{414}\right)$

f_y = Yield strength of reinforcing steel

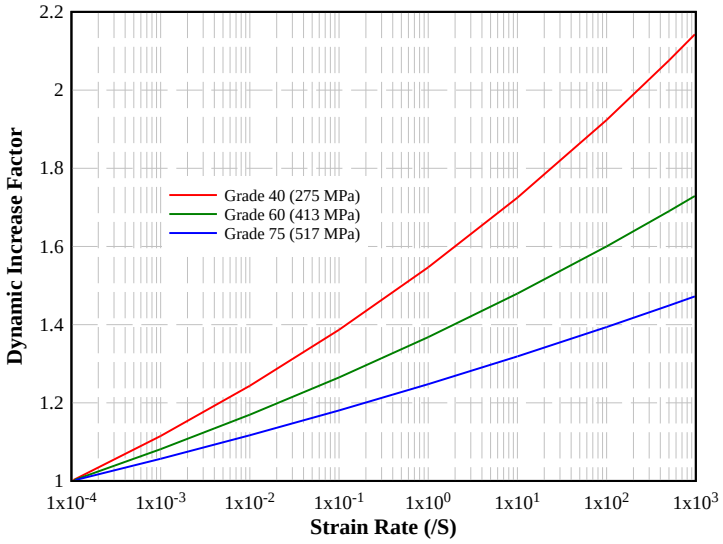

Figure 3.13: DIF for yield strength of reinforcing steel (Source: Malvar and Crawford, 1998b)

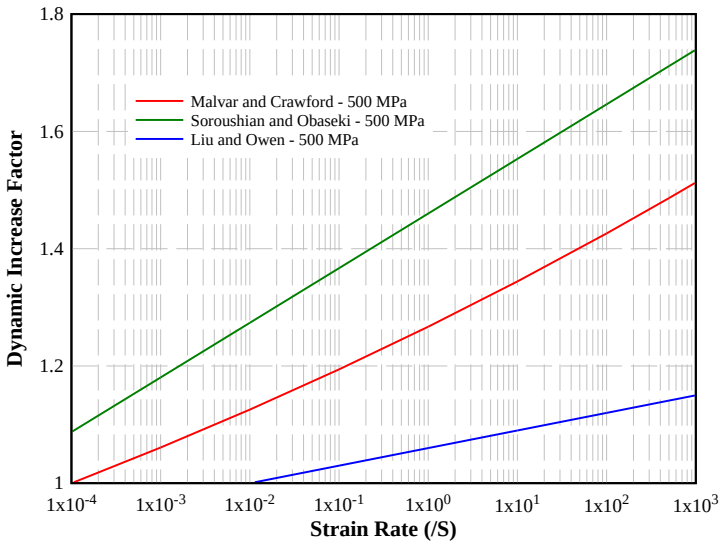

Figure 3.14: Comparison of DIF for yield strength of reinforcing steel from different formulae

3.3.2.2. Ultimate strength

Several researchers (Soroushian and Obaseki, 1986, Soroushian and Choi, 1987, Malvar and Crawford, 1998b) have investigated the enhancement of ultimate strength of reinforcing steel at elevated strain rates. Both Soroushian and Choi (1987) (Equation 3.32) and Malvar and Crawford (1998b) (Equation 3.33) presented formulae of DIF for ultimate strength of reinforcing bars, which were similar in formation to their yield strength formation. A comparison of the two equations for 500 MPa reinforcing steel is shown in Figure 3.15. Soroushian and Choi's predictions for DIF were smaller than Malvar and Crawford's predictions for strain rates less than 4×10^{-3} s^{-1} and larger afterwards.

$$DIF_{ultimate} = \left(-7.71 \times 10^{-7} f_y + 1.15\right) + \left(-2.44 \times 10^{-7} f_y + 0.0497\right) log_{10}\dot{\varepsilon} \quad (3.32)$$

$$DIF_{ultimate} = \left({\dot{\varepsilon}}/{10^{-4}}\right)^{\alpha} \quad (3.33)$$

Where;

α $= 0.019 - 0.009\left({f_y}/{414}\right)$

f_y = Yield strength of reinforcing steel

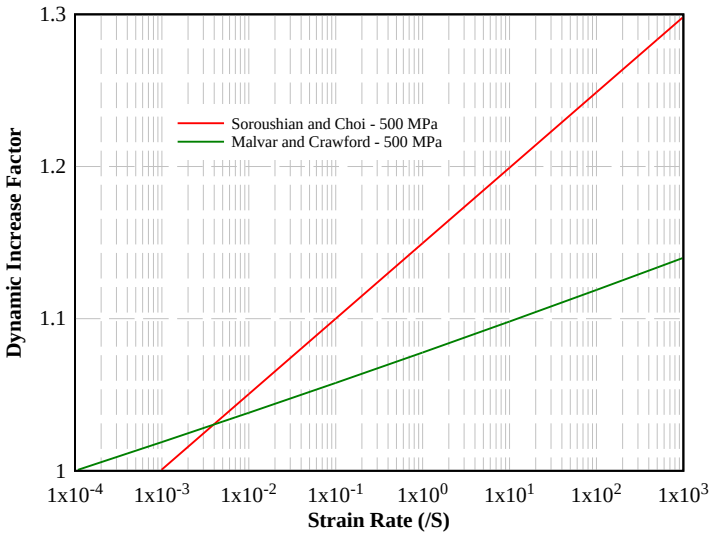

Figure 3.15: Comparison of DIF for ultimate strength of reinforcing steel from different formulae

The rate enhancement effects on the yield strength and the ultimate strength of reinforcing steel are not considered in the development of the 1-D analytical solution. The structural simplification of panel system to a 1-D system outweighs the implications of strain rate enhancement of reinforcing steel. However, In the case of LS-DYNA, 3-D numerical model, rate enhancement on reinforcing steel is considered for one of the material models (among the two considered).

3.4. Constitutive relationships for concrete and reinforcing steel

The important material parameters such as uniaxial compressive strength *(f'_c),* uniaxial tensile strength *(f'_t),* Elastic modulus *(E_c)*, Poisson's ratio (υ) and fracture energy (G_f) for concrete and yield strength (f_{sy}) and ultimate strength (f_{su}) for reinforcing steel as well as rate dependence and strain rate enhancement for specific parameters were identified in the previous section. These parameters will be used for the development of the 1-D analytical solution in Chapter 6, where structures are simplified to 1-D elements. However, in general applications, structural elements are subjected to multi-dimensional stress conditions, where uniaxial material parameters are incapable of predicting the response accurately. In these instances, 3-D constitutive relationships will be used to represent the behaviour of concrete and reinforcing steel.

There are a number of constitutive relationships that were developed for different combinations of structures and loading, with their inherent strengths and weaknesses.

Selecting the appropriate constitutive relationship for modelling the concrete and steel reinforcing (For LS-DYNA, 3-D numerical model) is essential for the prediction of structural response. In this section, a review of significant constitutive relationships that are available for the numerical modelling of concrete and reinforcing steel is presented, along with their restrictions and applications.

3.4.1. Constitutive relationships for concrete

Constitutive relationships for concrete can be broadly categorised as elasticity based constitutive relationships and plasticity-based constitutive relationships. The following sections discuss the formulation of different elasticity and plasticity-based constitutive relationships for concrete.

3.4.1.1. Elasticity-based constitutive relationships

Despite their shortcomings, elasticity based constitutive relationships are the most commonly used for concrete in pre and post failure ranges (Chen, 2007). Elasticity-based constitutive relationships are of two forms; linear elasticity based on the multidimensional Hook's law and nonlinear elasticity based on the secant modulus.

The general formation of the linear elastic constitutive relationship written in the form of stress and strain tensors is given in Equation 3.34.

$$\sigma_{ij} = C_{ijkl}\epsilon_{kl} \tag{3.34}$$

Where;

C_{ijkl} = Material constants (81 different constants)

σ_{ij} = Stress tensor (Cartesian)

ϵ_{kl} = Strain tensor (Cartesian)

The linear elastic response assumes the initial strain-free state corresponding to an initial stress-free state and stress depends only on the strain and not the history of stress (Chen, 2007). Although linear elastic models are capable of capturing the response in low to moderate stress levels where brittle tensile failure is more prominent, poor responses have been observed with complex loading conditions such as load reversal and loading beyond the peak capacity.

The nonlinear elastic models are based on the secant moduli of the material, in which secant modulus differs with the level of stress. It was observed that altering the linear elastic formulation with a non-linear elastic formulation, significant improvement in response can be achieved (Chen, 2007). Nonlinear elastic models can be of the Cauchy type, hyper-elastic type or hypo-elastic (Chen and Saleeb, 1981) where hyper-elastic formulation is much more prominent with path independent reversible behaviour.

The Cauchy type formulation is presented in Equation 3.35 where the current state of stress depends only on the current state of deformation. The formulation is similar to linear elastic, although the difference is within the tensor function, given as F_{ij}. As in the linear elastic formulation, σ_{ij} and ϵ_{kl} are stress and strain tensors in three-dimensional Cartesian stress-strain domain.

$$\sigma_{ij} = F_{ij}\epsilon_{kl} \tag{3.35}$$

The Cauchy type formulation is also path independent reversible, hence does not depend on the stress history of the material. However, Chen (2007) observed that this formulation may generate energy under certain loading conditions, violating laws of thermodynamics.

The hyperelastic type formulation involves the existence of a strain energy density function and complementary energy density function as shown in Equations 3.36 to 3.39, along with the Hook's law in the secant modulus formation (Equation 3.40) (Chen, 2007).

$$\sigma_{ij} = \frac{\partial W}{\partial \epsilon_{ij}} \tag{3.36}$$

$$\in_{ij} = \frac{\partial \Omega}{\partial \sigma_{ij}} \tag{3.37}$$

Where;

$$W = \int_0^{\epsilon_{ij}} \sigma_{ij} d\epsilon_{ij} \tag{3.38}$$

$$\Omega = \int_0^{\sigma_{ij}} \epsilon_{ij} d\sigma_{ij} \tag{3.39}$$

$$\sigma_{ij} = C_{ijkl}\epsilon_{kl} \qquad and \qquad \epsilon_{ij} = D_{ijkl}\sigma_{kl} \tag{3.40}$$

The formation was found to be quite accurate for concrete sustaining proportional loading, however, failed to identify inelastic deformations, a shortcoming that is

apparent with unloading (Chen, 2007). A well-defined unloading criterion is capable of rectifying this shortcoming although this will result in complications in the formulation.

The hypo-elastic or incremental type formulation is where the current state of stress and the stress path that follows define the current state of strain and vice-versa. Hence, the hypo-elastic formulation offers a more general description of materials with limited stress memory. The incremental constitutive relationship for time independent materials is given as in Equation 3.41 (Chen, 2007).

$$\dot{\sigma}_{ij} = F_{ij}(\dot{\epsilon}_{kl}\sigma_{mn}) \tag{3.41}$$

According to Chen (2007), the hypo-elastic formulation has two inherent difficulties with the construction of constitutive relationship. The incremental formulation requires an anisotropic instantaneous stiffness matrix even for an isotropic material, in which 21 independent material constants need to be defined in each stress state. Furthermore, a separate unloading criterion needs to be defined for different loading conditions. Despite all these difficulties in the formulation, several simplified models were proposed for concrete using the incremental approach.

3.4.1.2. Plasticity-based constitutive relationships

During tri-axial compression, concrete stress is found to be flowing like a ductile material between yield and failure surfaces, suggesting plastic behaviour in concrete. However, developing a plastic constitutive relationship is difficult than the development of an elastic constitutive relationship. This is due to the additional requirements in the decomposition of total strain, elastic constitutive relationship, yield and failure surfaces and a flow rule between the yield and failure surfaces.

The total strain (ε) is decomposed to reversible elastic strain (ε^e) and non-reversible plastic strain (ε^p), as in Equation 3.42.

$$\varepsilon = \varepsilon^e + \varepsilon^p \tag{3.42}$$

For the reversible elastic strain (ε^e), one of the elastic constitutive relationships, linear or non-linear, defined earlier in the chapter can be used. The most preferred elasticity criteria are either linear elastic formulation as in Equation 3.34 or the Cauchy type non-linear elastic formulation as in Equation 3.35, due to the easiness in the definition (Pham, 2010).

The yield surface, as in yield point in one-dimensional stress conditions, defines the end of elastic limit. Unlike in uniaxial stress conditions, the definition of yield surface needs a yielding criterion based on the bi-axial or tri-axial stress conditions. Several yielding criteria were proposed and evaluated for materials in general. However, Mohr – Coulomb (Labuz and Zang, 2012), Drucker – Prager (Drucker, 1959), Bresler – Pister (1958) and Willam –Warnke (1975) are the most commonly used yield criteria for concrete. Along with the yield surface, failure surface can also be defined using one of these criteria, which will define the complete disintegration of concrete matrix after cracking.

In order to construct the stress-strain relationship within the plastic range, i.e. between the yield surface and failure surface, a flow rule is defined. Flow rule is defined as the normality of the plastic-deformation-rate vector to the yield surface. In order to minimise the complexity, a simplified flow rule known as associated flow rule was defined based on the assumption the plastic-strain-increment vector was assumed to be normal to the yield surface at current stress state. Although there were several non-associated flow rules proposed for concrete, associated flow rule is applied predominantly for practical reasons (Chen, 2007).

For constitutive relationships, the plastic behaviour of concrete is categorised either as perfect plasticity, work-hardening plasticity or the endochronic plasticity depending on the definition of failure surface. All three plasticity conditions, initial pre-yield estimation and post failure estimation, are based on either linear or non-linear elastic relationships.

Elastic perfectly plastic constitutive relationships have three distinctive functions, initial elastic response function, the perfect plastic function and possible elastic unloading function. A simplified stress-strain relationship for a perfectly plastic constitutive model is shown in Figure 3.16.

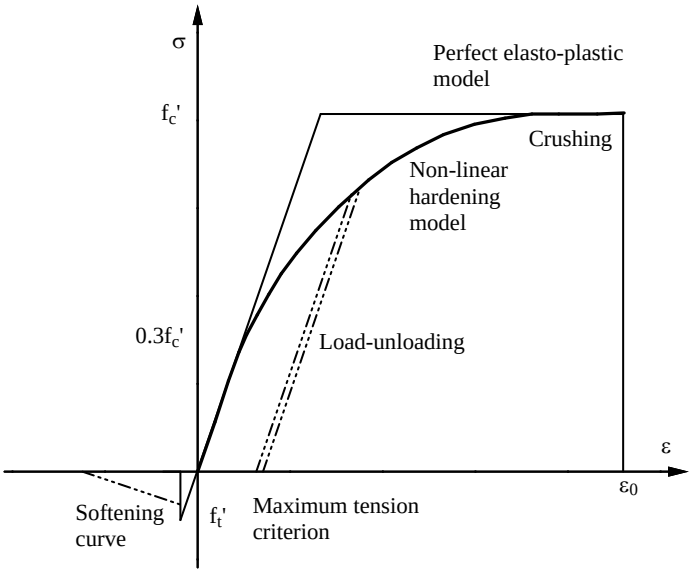

Figure 3.16: Idealised stress-strain curve for perfectly plastic concrete

The work hardening plasticity model uses the strain or the work hardening theory of plasticity. Instead of a single yield surface, a series of subsequent yield surfaces known as loading surfaces is defined as shown in Figure 3.17. This constitutive relationship is considered as a combination of perfect plasticity and strain hardening. Once the stress reaches the initial yield surface, a subsequent new yield surface is developed which becomes the new initial yield surface. If the material is unloaded from and reloaded within the new yield surface, no additional permanent deformation will occur until the next loading surface is reached. Once the final loading surface, better known as the failure surface is reached, concrete is considered crushed and subsequent capacity drops down to the residual strength of the material.

As in the perfect plasticity, the work hardening plasticity model also lacks the softening behaviour which was observed with cracking of concrete. Both these models predict the stress to drop suddenly to residual strength once the failure surface is reached, instead of gradual softening of the material. As an improvement on both perfect plasticity and work-hardening plasticity, endochronic plasticity is introduced (Valanis, 1970).

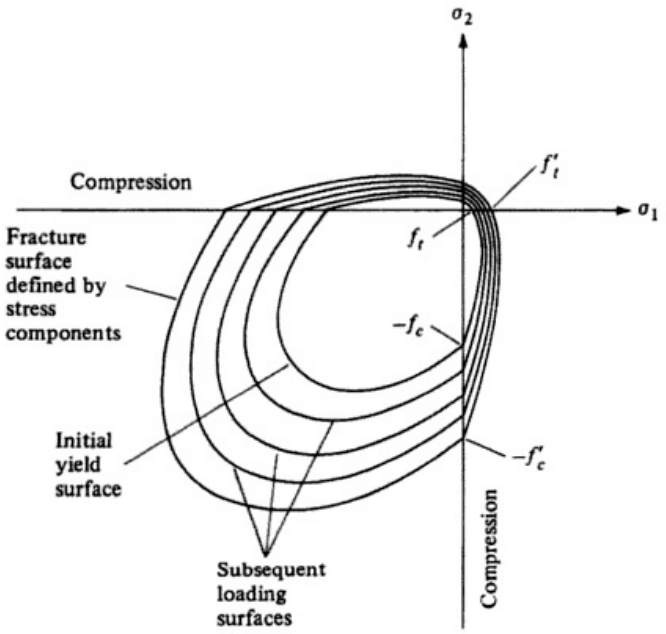

Figure 3.17: Loading surfaces of concrete in biaxial stress plane for work-hardening-plasticity model (Source: Chen, 2007)

The classical plastic theories, perfect and work hardening plasticity, assume the existence of yield surface, loading surfaces and failure surface along with a hardening rule. Although a material usually behaves as a continuous material, elasto-plastic models can be viewed as a discontinuous material model which separates the material response to different stages. The endochronic plasticity theory which is based on the definition of intrinsic time is formulated by a convolution integral between the strain tensor and a scalar function of the intrinsic time called memory kernel (Erlicher and Point, 2006).

The endochronic theory of plasticity was initially developed to describe the mechanical behaviour of metals (Valanis, 1970). Bazanth et al. (1976, 1977, 1978) and extended the theory to other materials such as rock, sand, plain and reinforced concrete, under various loading conditions. The concrete models developed using the endochronic plasticity was able to represent the experimentally observed effects such as inelasticity, strain softening and hardening, degradation of elastic moduli, aging and rate dependency (Chen, 2007).

In the case of numerical modelling using LS-DYNA, most of the numerical models are developed using the Cauchy type formulation. Development, formulation and capabilities of selected material models will be discussed in Section 3.5.

3.4.2. Constitutive relationships for reinforcing steel

Steel has a well-established stress-strain relationship, which has been verified for different structural elements and loading conditions. However, as in the case of concrete elements, the stress-strain relationship alone could not establish the complex loading conditions experienced in general steel structures. On the contrary, reinforcement in concrete is designed specifically to carry axial forces (shear to a minor extent), which could be explained using the uniaxial stress-strain relationship of the material.

As in concrete, constitutive relationships for reinforcing steel can also be categorised as elastic or plastic, although the latter is more preferred. A number of researchers have developed constitutive relationships for reinforcing steel (Ramberg and Osgood, 1943, Menegotto and Pinto, 1973, Stanton and McNiven, 1979, Filippou et al. 1983, Chang and Mander, 1994) which dates back to the early 1940's (Ramberg and Osgood, 1943, Cited in Lowes, 2000). The Ramberg and Osgood (1943) model is a non-linear elastic model with limited memory on stress-strain behaviour, defined specifically for monotonic loading.

Most of the constitutive relationships developed after the 1980's were based on the Menegotto and Pinto (1973), which is presented in Equation 3.43.

$$\sigma^* = b\varepsilon^* + \frac{(1-b)\varepsilon^*}{\left(1+\varepsilon^{*R}\right)^{1/R}} \tag{3.43}$$

Where;

σ^* = Effective stress

ε^* = Effective strain

b = Ratio of initial tangent modulus to the final tangent modulus

R = Unloading parameter

Several modified versions of the Menegotto and Pinto (1973) model were proposed (Stanton and McNiven, 1979, Filippou et al. 1983) but Chang and Mander (1994) proposed a more sophisticated constitutive relationship. Although all four models were

found to be reasonably accurate in comparison with the experimental results (Lowes, 2000), the Chang and Mander (1994) model was found to be more accurate than others.

Although identical responses were assumed for both tension and compression (symmetric response), Dodd and Restrepo-Posada (1995) found the behaviour to be slightly asymmetric, as shown in Figure 3.18. However, this asymmetric behaviour was rectified introducing the stress and strain as natural stress and natural strain as shown in Equations 3.44 and 3.45. Subsequently Dodd and Restrepo-Posada (1995) as well as Balan et al. (1998) proposed constitutive relationships for reinforcing steel based on the natural stress and strain.

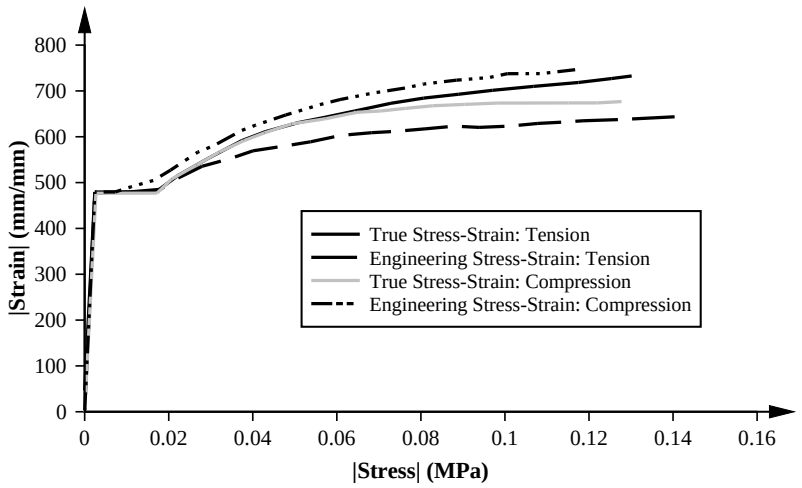

Figure 3.18: Engineering and true stress-strain history for reinforcing steel subjected to monotonic compression and tension (Source: Dodd and Restrepo-Posada, 1995)

$$\bar{\sigma} = ln(1 + \sigma) \tag{3.44}$$

$$\bar{\varepsilon} = ln(1 + \varepsilon) \tag{3.45}$$

Even with the inherent problems of asymmetric stress-strain relationship and complex formulation, the Chang and Mander (1994) model is widely used in modelling reinforcing steel. However, for simplified models such as one-dimensional (1-D) models, the Menegotto and Pinto (1973) the stress-strain relationship is commonly utilized as well.

In the case of numerical modelling using LS-DYNA, most of the reinforcement material models are defined using the uniaxial stress-strain relationships. Development,

formulation and applicability of selected reinforcement material models (in LS-DYNA) will be discussed in Section 3.6.

3.5. Material models for Concrete in LS-DYNA

Reinforced concrete is a heterogeneous material in nature. However, treating concrete as a heterogeneous material requires advanced finite element techniques such as Discrete Element Modelling (DEM) (Hentz et al. 2004), which require higher than usual computational demand. Due to this extreme computational demand, reinforced concrete is treated as a homogeneous material in finite element modelling. Despite this widely accepted assumption not applicable on a micro-scale, compatible results have been observed with macro-scale modelling of reinforced concrete structure (Hentz et al. 2004).

Various macro-scale material models have been proposed for different applications and capabilities for different finite element programs. Among the finite element (FE) programs that are used to model the blast loading response of the concrete structures, ABAQUS, ANSYS AUTODYN and LS-DYNA set the industry standard in the field. Even among the three FE programs LS-DYNA was found to be the most preferred choice, highlighted in Chapter 4, due to the vast variety of material models available and easy application procedure of explosive loading.

A list of available concrete material models is presented in Table 3.7, along with their advantages and drawbacks. All concrete material models, including the material models that are incapable of representing concrete at elevated strain rates are also included, with a reference to their theoretical formulation.

The selection of material models was based on the capabilities of the material model and recommendations of the past literature, which will be discussed in Chapter 4. Selected material models will be used in the development of the finite element program for this research and detailed in Chapter 5, along with the theoretical formulation of these material models.

Table 3.7: Concrete material models in LS-DYNA and their capabilities

LS-DYNA material ID	Material Name	Model Features/Strengths/Capabilities	Rate dependent	Reference
MAT_005	Soil and foam	Elastic perfectly plastic material model. Suitable for highly confined concrete and soil materials. Lacks material softening.	No	(Livermore Software Technology Corporation, 2013)
MAT_014	Soil and foam failure	Extension of soil and foam material to include failure. Advised only to use with high confining pressures.	No	(Livermore Software Technology Corporation, 2013)
MAT_016	Pseudo tensor	Simple Input. Specifically formulated to analyse structures subjected to impulsive loading. Can be formulated using the uniaxial compressive strength only. Capable of representing damage accumulation (ver II).	No	(Livermore Software Technology Corporation, 2013) (Khoe and Weerheijm, 2012)
MAT_017	Orientated crack	Elasto-plastic material model, including a yield and failure surfaces based on Von-Mises criterion. Able to represent tensile cracking.	No	(Livermore Software Technology Corporation, 2013)
MAT_025	Geological Cap	Two invariant* model. Able to model plastic compaction and shear dilation. Definition needs a high number of parameters.	No	(Livermore Software Technology Corporation, 2013) (Simo et al. 1990)
MAT_072	Concrete Damage	Specifically designed to analyse structures subjected to impulsive loading. Extension of MAT_016. Need to define a large number of parameters. Separate volumetric and deviatoric responses. Include damage accumulation.	Yes	(Livermore Software Technology Corporation, 2013) (Malvar et al. 1997)

MAT_072R3	Concrete Damage REL3	Extension of MAT_072 to include automatic parameter generation. Require compressive strength only for the definition.	Yes	(Livermore Software Technology Corporation, 2013) (Schwer and Malvar, 2005)
MAT_078	Soil Concrete	Separate volumetric and deviatoric response defined as user inputs. Failure conditions are also included.	No	(Livermore Software Technology Corporation, 2013)
MAT_080	Ramberg-Osgood	Used for one-dimensional simulations, with the shear predominant response. Elastic volumetric behaviour is assumed. Specific for seismic analysis.	No	(Livermore Software Technology Corporation, 2013)
MAT_084	Winfrith Concrete	Smeared crack and smeared reinforcement (optional) model. Relatively simple with or without defining volumetric response. Optional tensile crack visualization is available.	Yes	(Livermore Software Technology Corporation, 2013) (Broadhouse and Neilson, 1987)
MAT_096	Brittle Damage	Anisotropic brittle damage model. Progressive degradation of shear and tensile strength. Material softening included. Smeared reinforcement.	No	(Livermore Software Technology Corporation, 2013) (Govindjee et al. 1995)
MAT_111	Johnson-Holmquist	Suitable for materials subjected to large strains and high pressures. An accumulative damage function is also available.	Yes	(Livermore Software Technology Corporation, 2013) (Holmquist et al. 1993)
MAT_145	Schwer Murray Cap	Three invariant* extension of MAT_025. Strain softening and damage accumulation possible. Includes viscoplastic rate effects.	Yes	(Livermore Software Technology Corporation, 2013) (Schwer and Murray, 1994)
MAT_159	CSCM Concrete	Developed specifically for the evaluation of high-velocity impacts of concrete structures. Separate brittle and ductile damage. Simple	Yes	(Livermore Software Technology Corporation, 2013) (Murray et al.

		input (only compressive strength). Three invariant* model. Based on MAT_025.		2007)
MAT_272	RHT	Specifically formulated to analyse the structures subjected to impulsive loading. Automatic parameter generation available. New to LS-DYNA	Yes	(Livermore Software Technology Corporation, 2013) (Riedel et al. 1999)
MAT_273	Concrete damage plastic	Plastic damage model with rate effects. Specifically formulated for dynamic analysis. Automatic parameter generation available. New to LS-DYNA	Yes	(Livermore Software Technology Corporation, 2013, Grassl and Jirásek, 2006)

* - Three deviatoric stress invariants J_1, J_2 and J_3, where $J_1 = s_{kk} = 0$, $J_2 = \frac{1}{3}I_1^2 - I_2$ and $J_3 = \frac{2}{27}I_1^3 - \frac{1}{3}I_1I_2 + I_3$. Three principle stress invariants I_1, I_2 and I_3 are defined as $I_1 = \sigma_1 + \sigma_2 + \sigma_3$, $I_2 = \sigma_1\sigma_2 + \sigma_2\sigma_3 + \sigma_3\sigma_1$ and $I_3 = \sigma_1\sigma_2\sigma_3$. Deviatoric stress invariants define the plasticity in material while principle stress invariants define the elasticity.

Among the concrete material models, several were incapable of representing the rate enhancement properties of concrete. The Concrete Damage Model, Winfrith Concrete Model, Continuous Surface Cap Model (CSCM) and RHT material model were identified in the literature as the material models that are capable of representing concrete in impulsive loading regime. All four material models are equipped with strain hardening and softening, rate enhancement and damage accumulation and prediction which are essential in the analysis of structures subjected to explosive loading. However, the RHT material model was limited to ANSYS AUTODYN finite element program until late 2013, resulting in limited research on the capabilities of the RHT material model in LS-DYNA. The other three material models, Concrete Damage, Winfrith and CSCM concrete were selected for the development of the 3-D numerical model discussed in Chapter 5.

Markovich et al. (2011) proposed an improved calibration to the Concrete Damage model based on the past experimental results (Attard and Setunge, 1996). This new formulation was found to give improved stress-strain response of concrete under the dynamic loading conditions. However, these modifications were not incorporated in the original concrete damage model with automatic parameter generation. Therefore, a manual input concrete damage model was also used along with the original concrete damage model, the Winfrith concrete model and CSCM concrete model for the development of the 3-D numerical model. This manual input concrete damage model will be named as BGU concrete model for this study.

3.6. Material models for reinforcing steel in LS-DYNA

As an integral part of reinforced concrete, modelling of reinforcement as accurately as possible is important in finite element modelling. Axial forces are the predominant method of stress transfer in reinforcement along with shear stresses to a certain extent. Hence, constitutive relationships should be capable of predicting both axial and shear behaviour of reinforcing steel.

LS-DYNA is equipped with a large number material models that are capable of representing metal plasticity. However, most of these material models are limited to solid element formulation. LS-DYNA material models that are capable of representing steel reinforcement (beam elements) are listed in Table 3.8 along with the advantages and disadvantages of each material model.

Table 3.8: Reinforcing steel material models in LS-DYNA and their capabilities

LS-DYNA material ID	Material Name	Model Features/Strengths/Capabilities	Rate dependent	Reference
MAT_003	Plastic Kinematic	Suitable for both isotropic and kinematic hardening materials. Extremely cost effective. Suitable for most metals	Yes	(Livermore Software Technology Corporation, 2013)
MAT_024	Piecewise Linear Plasticity	Arbitrary stress-strain curve and arbitrary rate dependency. Failure options available. Thermal and stochastic options available. Need manual definitions in case of arbitrary stress-strain curve.	Yes	(Livermore Software Technology Corporation, 2013)
MAT_028	Resultant Plasticity	Elastic perfectly plastic material model (beams). Similar to MAT_003 without the tangent modulus. Simple and cost effective.	No	(Livermore Software Technology Corporation, 2013)
MAT_081	Plasticity With Damage	Elasto-visco-plastic material. Arbitrary stress-strain curve and strain rate enhancement. Damage prediction. Optional failure conditions.	Yes	(Livermore Software Technology Corporation, 2013)
MAT_098	Simplified Johnson Cook	A simplified version of Johnson cook, without thermal and damage effects.	Yes	(Johnson and Cook, 1983) (Livermore Software Technology Corporation, 2013)

Among the reinforcement material models in LS-DYNA, all material models except for MAT_028 are capable of strain rate enhancement, either arbitrarily (manual input) or using an inbuilt function. MAT_024 is an improvement on MAT_003 with the ability to define arbitrary stress-strain curve, which is quite useful when requiring actual stress-strain curves for the material. However, the arbitrary stress-strain curve comes with arbitrary strain rate enhancement factors, which also have to be defined manually. Similar to MAT_024, MAT_081 also has the ability to define arbitrary stress-strain curve, with similar limitations.

MAT_003 is defined with yield strength, elastic modulus and tangent modulus (after yielding) is capable of predicting strain hardening plasticity. In case tangent modulus is not available, the material will be represented as an elastic-perfectly plastic material. The Plastic Kinematic material model is also capable of representing the rate enhancement behaviour with Cowper-Symonds equation.

The Johnson Cook (JC) model was simplified to represent the beam and shell elements where the original version is incapable. The simplified version is incapable of handling thermal and damage effects, which is not essential in the case of structures subjected to explosive loading. The simplifications enabled improvement of analysis times up to 50%, in comparison with the original JC model (with shell and solid elements). Furthermore, four different strain rate enhancement options are available with simplified JC model.

Among the available reinforcing steel material models, the plastic kinematic material (MAT_003) model and simplified Johnson Cook (MAT_098) material model were selected for the numerical model development. These two material models were selected based on their available strength parameters for the materials, material model capabilities and recommendations of previous studies. A detailed description of these two material formulations and keyword definitions is presented in Chapter 5.

3.7. Summary

A detailed review of static properties, dynamic properties and constitutive relationships of concrete and reinforcing steel was presented in this section. Estimation of quasi-static properties using experimental tests and prediction of different material parameters using the compressive strength of concrete (f'_c) was discussed in detail. Determination of

quasi-static properties for reinforcing steel was also discussed along with the importance of each parameter. Behaviour of concrete and reinforcing steel when subjected to dynamic loading conditions was also assessed. The effects of higher strain rates of the material properties and estimation of dynamic increase factors for different material parameters are reviewed as well. Following material properties, parameters and stress-strain relationships were selected for the development of the 1-D analytical solution. Chapter 6 presents the full details of the development of the1-D analytical solution.

- The Modified Scott model as the stress-strain relationship for concrete with confinement delivered through Mander's coefficient (Appendix A-I).
- CEB-FIP model code (1990, 2010) for the strain rate enhancement of compressive strength of concrete.
- Tensile strength of concrete ignored.
- AS 3600 (2009) formulation for elastic modulus and Poisson's ratio of concrete.
- Idealised elastic-perfectly plastic stress-strain relationship for reinforcing steel.

Constitutive relationships for concrete and reinforcing steel were discussed along with the different types of formulations, their advantages and disadvantages. Finally, four concrete material models and two reinforcing steel material models were selected for numerical model development based on their capabilities and behaviour under dynamic loading conditions. Following material models, material properties and rate enhancement factors were selected for the development of the 3-D numerical model. Full details of the development are given in Chapter 5.

- The Concrete damage model, The Winfrith concrete model, the CSCM concrete material model and manually calibrated concrete damage model (Markovich et al. 2011) as concrete material models.
- CEB-FIP model code (1990, 2010) for the strain rate enhancement of compressive strength of concrete.
- Malvar and Crawford (1998a) for the strain rate enhancement of tensile strength of concrete.
- CEB-FIP (1990, 2010) for the fracture energy of concrete.
- The Plastic Kinematic model and the Simplified Johnson-Cook model for the reinforcing steel.

CHAPTER 4

REINFORCED CONCRETE SLAB AND WALL PANELS SUBJECTED TO EXPLOSIVE LOADING – REVIEW OF RECENT STUDIES AND DESIGN GUIDELINES

Reinforced concrete has been used in protective construction for more than 50 years with the earliest quantitative experimental records dating back to late 1950s' and early 1960s' (United States Army Corps of Engineers, 2008). Many of these government funded studies mainly originating in the United States Department of Defence (USDoD) had limited capabilities in terms of capturing loading effects, structural and material behaviour. However, recent developments in computers, information technology and sophisticated gauging instrumentation have resulted in more accurate and comprehensive experimental results. Furthermore, these detailed experimental procedures are capable of identifying the structural and material behaviour failure models of reinforced concrete wall and slab panels subjected to explosive loading more clearly.

Concrete has been typically categorised as either one-dimensional (1-D) elements such as beams and columns, or two-dimensional (2-D) elements such as slabs and walls. When subjected to blast loading 2-D elements have greater exposure to damage than the 1-D element because of the larger loading area and higher slenderness ratios. This chapter reviews the recent experimental studies on reinforced concrete panel systems subjected to explosive loading and associated failure models. Furthermore, a detailed review of the existing code design guidelines on the explosive resistant design of reinforced concrete structures is also presented.

4.1. Experimental studies of reinforced concrete panels subjected to explosive loading

A number of experimental studies have been conducted on the blast loading of concrete panels with various charge weights ranging from 0.1 kg to 6000 kg of equivalent TNT masses. The standoff distance-charge weight combinations were selected depending on the intent of the study. For example, close range (near field) and contact charges tend to

be used to investigate local effects, while far range (far field) explosions are used to study global effects. Although there is no exact scaled distance value specified, 0.70 $kg/m^{1/3}$ is used as the cut off value for close range scaled distance (Z) based on the response of the panels.

4.1.1. Close range studies

A detailed summary of experimental studies on concrete panels exposed to close range explosions or contact detonations ($Z \approx 0$) is presented in Table 4.1, along with the key findings of each study. The close range response can be brittle or ductile in nature hence, the critical output parameters may vary depending on the response. However, for comparison purposes, the format of the table was kept uniform without distinguishing the brittle or ductile nature of the response.

As Table 4.1 indicates, minimisation of local damage against explosive loading was the main focus area among the researchers. High performance concretes (HSC and RPC) and fibre inclusions (i.e. steel, glass, carbon) have been studied in detail and some empirical equations to quantify local damage in terms of spalling and scabbing diameters and depths were derived.

The following sub-sections discuss the main effects of different material types and properties on panel response observed during the experimental studies highlighted in Table 4.1. Prediction equations for local damage (spalling and scabbing) are also highlighted.

Table 4.1: Recent experimental studies of close range explosive loading on concrete panels

Reference	Test identifier	Panel size			Concrete Strength (MPa)	Reinforcement			Charge weight (kg TNT)	Standoff distance (m)	Peak pressure (kPa)	Peak Impulse (kPa.ms)	Peak displacement (mm) Inward/outward	Comments
		L (m)	*W (m)*	*T (m)*										
Yamaguchi et al. (2011)	A	0.6	0.6	0.05	41.5	T5@120 (50mm slabs) T10@120 (100mm slabs)	-	Polypropylene fibre	0.2	Contact Charges	–	–	–	Spalling damage of FRC was considered. Spalling diameter and depth depend on scaled thickness [d] and flexural toughness of the concrete material. The amount of spalling is considerably reduced compared to normal concrete samples.
	B			0.1	38.7		-		0.1					
	C			0.1	41.6		-		0.1					
	D			0.1	41.6		-		0.2					
	E			0.1	57.8		4%		0.1					
	F			0.1	59.9		2%		0.1					
	G			0.1	59.9		4%		0.2					
	H			0.05	70.6		4%		0.2					
	I			0.05	59.4		4%		0.2					
	J			0.1	54.6		4%		0.1					
	K			0.1	54.6		4%		0.2					
	L			0.1	76.0		4%		0.1					
	M			0.1	76.0		4%		0.2					
Wang et al. (2008)	1	3.0	3.0	0.3	–	T13@200mm			1	0	–	–	–	Spalling and crater formed in all panels. Section breached in panel 2 and 3. (Hole through the section)
	2								2	0	–	–	–	
	3								3	0.05	–	–	–	

Zhou et al. (2008)	1	1.3	1.0	0.1	50	T16@75mm T16@150mm	0.545	0.1	–	–	–	450×300 mm area of spalling up to 50 mm deep in RC panel and 100×200 mm area is detached (spalled) in SFRC panel, but no fragmentation.
	2				170/ RPC SFRC	No Reinforcement					9	
Riisgaard et al. (2006)	1	0.6	0.6	0.05	- / FRC	T5(1800)@ 10 mm and aramid lacing reinforcing	1.3	0.09	---	---	18 mm (plastic)	No damage observed for reinforcement or lacing in both tests. Scabbing and spalling observed in both panels.
	2	1.2	1.2	0.05			4.5	0.13	---	---	60 mm (plastic)	
Yusof et al. (2010)	1	0.6	0.6	0.1	32	T10@200mm	1	0.3	–	–	–	Full depth shear cracks at supports and crushing of RC panel. Minor damage with hairline cracks in SFRC panel
	2				41/ SFRC	T10@200 and 1.5% of steel fibres (1100)					4	
Wu et al. (2009)	1	2.0	1.0	0.1	151.6/ FRC	---	3.4	0.75	–	–	13.2	Flexural cracking with 4.2 mm permanent deflection in the unreinforced panel. Crushing of concrete and the panel was broken into two halves parallel to support in reinforced panel
	2					T12@100 (major) T12@200 (minor)	20.1	1	–	–	>100	
Eric Musselman (2007)	C1	1.83	1.83	0.165	43.5	13@150 in both directions	22.5	1.83	–	–	–	Cracks were formed to coincide with the reinforcement bars. Material with Type A fibres behaved marginally better.
	C2						33.8	1.83	6.27×10^4	3757	–	
	T2-A				43.3/ CFRP	10@300 single leg stirrups	33.8	0.98	–	–	50.8[a]	
	T2-B						33.8	0.98	–	–	57.2[a]	

Tabatabaei et al. (2012)	A1	1.83	1.83	0.165	51/ CFRP (A)	T13@152, 2 layers. 1.5% of CFRP type A	34	1.7	N/R	N/R	12.7 [a]	Type B fibres (100mm long) have performed slightly better than Type A (75x9mm) fibres. Lesser spalling loss in type B as well. Better spalling resistance in both types compared to NSC.
	A2								N/R	N/R	11.4 [a]	
	B1				51/ CFRP (B)	T13@152, 2 layers. 1% of CFRP type B			N/R	N/R	10.2 [a]	
	B2								N/R	N/R	12.7[a]	
Pantelides et al. (2012) Garfield T.T (2011)	A4-6	1.2	1.2	0.152	51	10mm@305[b]	6.2	1.02	–	–	82	Thicker panels responded well with very negligible damage. Panels where peak displacements were not recorded due to failure. Fibre inclusion made a significant impact when combined with conventional reinforcements. The spacing of reinforcement is more important than the reinforcement ratio.
	A4-10			0.254		13mm@305[b]	13.2	0.97			31	
	D4-6			0.152		10mm@152[c]	6.2	1.04			9	
	D4-10			0.254		13mm@152 [c]	13.2	0.97			12	
	D4-14			0.356		16mm@152 [c]	13.2	0.97			2	
	CON1			0.152		16mm@152 [c]	6.2	1.02			11	
	CON2			0.152		16mm@152 [c]	7.4	3.05			–	
	CON3			0.152		16mm@152 [c]	6.2	1.02			43	
	CON4			0.152		16mm@152 [c]	13.1	1.02			–	
	B4-6			0.152		No Rebar[d]	6.2	1.02			N/R	
	B4-10			0.254		No Rebar[d]	13.1	1.02			N/R	
	C4-6	1.2	1.2	0.152	46/ GFRC	10mm@152[bd]	6.2	1.04	–	–	5	
	C4-10			0.254		13mm@152[bd]	6.2	0.97			1.5	
	C4-14			0.356		16mm@152[bd]	13.2	0.97			0.3	
	CON5			0.152		No Rebar[d]	6.2	1.04			N/R	

Wang et al. (2012)	A	0.75	0.75	0.03	39.5[e]	T6@75mm One layer Both directions (600 MPa)	0.13	0.3	–	–	9	No pressure measurements due to close range explosions. Spalling in all panels. Panel F perforated.
	B	0.75	0.75	0.03			0.19	0.3			26	
	C	1.00	1.00	0.04			0.31	0.4			15	
	D	1.00	1.00	0.04			0.46	0.4			35	
	E	1.25	1.25	0.05			0.64	0.5			19	
	F	1.25	1.25	0.05			0.94	0.5			40	
Yi et al. (2012)	NSC1	1.0	1.0	0.15	25.6	T10@82 mm (400 MPa) 2 layers, both directions	15.9	1.5	–	–	Over 25	The author claims pressure / impulse differences due to weather conditions. RPC has shown marginally better resistance over HSC, although the main reo was omitted. Both HSC and RPC were much better compared to NSC. 3 significant modes of vibrations, second showing highest amplitude.
											12.26[a]	
	NSC2								–	–	18.57	
											5.79[a]	
	HSC1				202.1/ HSC	T10@82 mm (400 MPa) 2 layers, both directions			–	–	10.52	
											1.86[a]	
	HSC2								1.69 ×10^4	3870	15.14	
											5.86 [a]	
	RPC1				202.9/ RPC	No main Reo, 2% of steel fibre			–	–	10.73	
											3.20 [a]	
	RPC2								2.19 ×10^4	2830	13.09	
											5.41 [a]	

[a] – Permanent Deflection
[b] – 13mm diameter steel reinforcement bars of 420 MPa
[c] – GFRP bars with a tensile strength of 717 MPa
[d] – 8.9kg of polypropylene fibre (per m^3), a sinusoidal shape, 51mm long and 0.9mm diameter
[e] – Measured with concrete cubes. Equivalent cylinder strength 30.8 MPa

4.1.1.1. Compressive strength of concrete

Concrete compressive strengths ranging from 25 MPa to 200 MPa have been used in previous testing of panels. The main focus of these studies was to investigate the spalling and scabbing resistance hence, high performance concretes were introduced in the form of HSC and RPC to enhance the tensile strength (Zhou et al., 2008, Wu et al., 2009, Yi et al., 2012). High strength panels responded well compared to lower strength panels with reduced maximum deflections and lesser scabbing. A comparison of NSC of 25 MPa with HSC and RPC of 200 MPa by Yi et al. (2012) showed improved resistance when subjected to same explosive loading. Maximum transverse deflection of the HSC and RPC panels were reduced to half the value of NSC panel. A similar study conducted on 50 MPa NSC and 170 MPa RPC panels (Zhou et al., 2008) revealed the enhanced performance of the RPC panel with less 15% of spalling (area), although this improvement could be due to the inclusion of fibres in the concrete mix. In addition, NSC of higher strengths (e.g. 50 MPa) performed better than NSC of lower strengths (e.g.30 MPa) with lesser spalling and scabbing when subjected to similar explosive loading (similar scaled distances (Z)). Overall, concrete with higher compressive strengths has performed better than lower strength concretes.

4.1.1.2. Reinforcement and fibre inclusions

Tested concrete sections were reinforced either with conventional reinforcement bars, fibre inclusions or a combination of conventional reinforcement and fibre inclusions. Conventional reinforcement bars of different strengths and different materials were used for the testing of panels. Steel reinforcing bars of 400 MPa to 600 MPa were used with different diameters and reinforcement ratios. Closely spaced reinforcement was found to be more effective in resisting scabbing and spalling damage than higher reinforcement ratios (Garfield et al., 2011, Pantelides et al., 2012).

Polymer reinforcing materials were also evaluated using the close range detonations (Pantelides et al., 2012, Garfield, 2011), as a replacement to reinforcing steel with normal strength concrete. Glass Fibre Reinforcing Polymer (GFRP) bars of 717 MPa were used to replace the 420 MPa steel reinforcing bars and found to be more resilient to transverse displacement. However, as expected, conventional steel reinforcement was found to be more ductile.

Fibre inclusion is considered as a method to improve the spalling and scabbing resistance of concrete panels. Fibre inclusions improve the tensile strength of concrete, in turn increasing the spalling and scabbing resistance. Most studies, except Wang et al. (2008, 2012), used fibre inclusions, either carbon, steel or glass fibres, as a method of improving the scabbing and spalling resistance. It was observed that fibre inclusions improve the spalling and deflection resistance comparatively when used in conjunction with conventional reinforcement bars. However, use of fibres without main reinforcement bars in RPC found to have improved resistance against deflection than HSC of similar strengths and conventional reinforcement bars.

A different strategy to include fibres in the concrete, such as lacing reinforcement, along with prestressing and conventional reinforcement was the focus of another study (Riisgaard et al., 2006). Scabbing and spalling were observed with relatively large, close range detonations but, limited to cover concrete. Although this procedure improves the scabbing and spalling resistance considerably, the process was labour intensive and costly.

In general, the inclusion of fibres in the form of carbon, glass or steel found to improve the deflection and spalling resistance, used in conjunction with conventional reinforcement bars for NSCs. In contrast, just the inclusion of fibres without conventional reinforcement bars found to be the most effective with HSC and RPC.

4.1.1.3. Boundary/Support conditions

Almost all the experimental studies listed in Table 4.1 used simplified support conditions, either using timber planks or steel members to prevent transverse movement. There is a distinct lack of studies in the testing of proper connection mechanisms with close range explosive loading for precast concrete panels, even though precast and prestressed concrete is highly popular in the construction industry. The importance of proper fixing assemblies and flexible facade systems has been highlighted in other applications such as earthquake and wind resistance applications (Quintero-Febres and Wight, 2001, Sekulovic et al., 2002, Azad et al., 2012, Abtahi et al., 2012, Samali et al., 2014), but hasn't been considered in blast resisting concrete applications, up to date.

4.1.2. Far range studies

Table 4.2 summarises the experimental studies of concrete panels subjected to far range explosive detonations. Unlike the close range studies, pressure time histories were recorded for most of the far range studies along with other response parameters. Several studies were conducted in shock tube facilities where a pressure pulse is generated either using small explosive detonation or mechanical device. The entries in Table 4.2 are arranged based on the ascending scaled distance (Z), with shock tube testing listed at the end.

The main focus areas for far range studies were reinforcement strength and layout, concrete material improvements and failure mechanisms. Use of flexible connections as a passive measure of mitigating blast loads was also assessed. The importance of conventional reinforcement in mitigating explosive damage was highlighted, even with fibre inclusions in concrete.

Again the sub-sections to follow discuss the main effects of different material types and properties on panel response observed during the experimental studies highlighted in Table 4.2.

Table 4.2: Recent experimental studies of far range explosive loading on concrete panels

Reference	Test identifier	Panel size			Concrete Strength (MPa)	Reinforcement	Charge weight (kg TNT)	Standoff distance (m)	Peak pressure (kPa)	Peak Impulse (kPa.ms)	Peak displacement (mm) Inward/outward	Comments
		L (m)	*W* (m)	*T* (m)								
Wu and Sheikh (2012)	N/A	2.0	0.4	0.1	32	T12@326 (500) T12@89.5	8.2	1.5	832[a]	326[a]	38.9 33.6[b]	Testing was performed as a control specimen for structures against blast loading.
Wu et al. (2009)	N1 N2 N3 N4	2.0	1.0	0.1	39.5	T16@100mm (major plane) T16@200mm (minor plane)	1.00 8.14 3.44 8.21	3 3 1.4 1.5	420 2390 6380 –	186 715 705 –	1.5 10.5 13.9 38.9	N1, N2 – no cracking. N3 - minor tensile cracks N4 - post plastic tensile cracks.
Pham T. (2010)	A B1[c] B2[c] B3[c] B4[c] B5[c]	1.5 1.7	1.0 1.0	0.08 0.08	46 43	N5@100mm both faces (630 MPa)	5.5	2.0	2488	791	38.5/ 10 28.9/14.5 24.4/22.5 24.5/19.2 23.7/11.5 25.7/15.7	All panels were cracked in both tension and compression. B1-B5 shown lesser deflection than A. B4 panel's connection was broken
Muszynski et al. (2003a, 2003b)	A1 A2 B1 B2	– – 2.70 2.70	– – 2.48 2.48	– – 0.2 0.2	19.3 19.3 28 28	T9.5@300 mm T9.5@300 mm T9@300 mm T9@300 mm	860 860 830 830	24 24 14.6 14.6	– 3407 – –	– 5241 – –	77 81 73 73	Scabbing and stress fracture in exterior face from the centre towards corners. No spalling was observed.

Schenker et al. (2005, 2008)	A	1.3	1.2	0.2	30	T6.5@100 mm	100	10	–	–	–	Severe cracking in the exterior face of panel A, no spalling detected. Time histories of displacement, velocity and acceleration derived.
	B1	3m span			30	–	1000	20	638	–	–	
	B2				100/ HSC							
Ngo et al. (2007)	RC1	2.0	1.0	0.1	39.8	N16@200 mm	6000	40	735	2867	142[b]	Severe damage, breaching of section. 8 mm crack in exterior face Panels HSC1 & 2had minor cracks and no spalling while HSC 3 had major cracks in mid span and spalling with 32 mm permanent inward deflection.
	HSC1			0.1	164/ HSC	15.2 (1800) tendons @ 100 and 200		30	1513	3771	50.4/37	
	HSC2			0.1				40	735	2867	27.1/20.7	
	HSC3			0.075				40	735	2867	72.6/54.8	
Lan et al. (2005)		0.81	0.81	0.05	42.6 / SFRC	0.5% to 1.5% of 0.5 mm and 0.75 mm diameter steel fibres	8, 20 or 30 kg	5 m	---	---	---	Blast resistance with different fibre percentage inclusions and different fibre configurations. 1% of (weight) fibre inclusion has yielded best results. Crack patterns are similar to a plate loaded with uniform pressure
		0.81	0.81	0.05								
		0.96	0.96	0.05								
		0.96	0.96	0.05								
Barnett et al. (2010)	A	3.5	1.3	0.1	-/UHP FRC	[d]/ SFRC 2%	100kg	9	N/R	N/R	110, 20[b]	Panels A and B were able to recover deformation after the explosion. Panels C and D were broken half during the testing. No spalling was observed in any of the panels
	B					[d]/ SFRC 2%		7			210, 50[b]	
	C					[e]/ SFRC 2%		12			180,180[b]	
	D					[e]/ SFRC 4%		12			90, 90[b]	

Tanapornrawe ekit et al. (2007, 2008)	N/A	2.19	1.19	0.14	40	N16@120mm	5000	40	–	–	36 /5	Minor cracks in exterior face. Spalling at right support due to clearing effects.
Cramsey et al. (2007) Naito et al. (2008)	CON1 CON2 CON3 CON4	9.35	2.44	0.159	52.1	T13@304 both Directions (420 MPa)	–	–	55-220	476-993	56.8 92.4 139.4 177.9	Four Control panels as part of a major study. Charge weight or standoff is not reported for security reasons
Dunkman et al. (2009)	PT1-1 PT1-2 PT1-3 PT2-1 PT2-2 PT2-3	2.57	1.03	0.89	32.4	T13@304 and 3, 13mm un-bonded strand (post tension) T13@304 and 3, 13mm bonded strand (pre tension)	N/A Shock tube	N/A Shock tube	43.4 71.7 75.8 43.4 71.7 75.8	290 552 1310 290 552 1310	4.32/21.3 27.2/28.4 94.5/14.5 5.56/20.1 24.4/26.9 66.0/14.7	Only two panels with repetitive testing. Pre tensioned panel performed better. Post tensioned panel weakened quicker than pre tensioned panel with repetitive loading
Robert et al. (2009)	DM1 DM2 DM3 DM4 DM5	1.625	0.858	0.101	106.9/ HSC	T10@101mm[f] T10@304mm[f] (572 MPa) T10@101mm T10@304mm (469 MPa)	N/A Shock tube	N/A Shock tube	385 387 395 371 391	7730 7497 7784 5794 7424	121.9 132.1 152.4 152.4 152.4	All panels suffered spalling in the back face while only NSC panels suffered scabbing in exposed face. High strength Vanadium reinforcement plays a major role in minimising the deflection in both NSC and HSC panels, but it was more evident in NSC panels.
	DM6 DM7 DM8 DM9 DM10				27.6	T10@101mm[f] T10@304mm[f] (572 MPa) T10@101mm T10@304mm (469 MPa)			391 358 383 352 309	7347 6963 7467 6667 5691	136.1 119.4 147.3 221.0 101.6	

Agardh et al. (1997)	A3 B3 B3[g] C3 D1 D2 D3	1.2	1.2	0.06	63.2 / SFRC	T14(400)@ 80 mm and 0.7% inclusion of steel fibres	N/A Shock tube	N/A Shock tube	320 200 430 800 1370 1130 1260	Not recorded	4.5 3.1 9.5 22 --- 23 ---	Flexible end conditions with 27% clamping. Time dependent parameters as well as peak measurements for pressure, deflection, velocity, acceleration, stress and stress were recorded.

[a] – Incident overpressure (or calculated based on incident overpressure)
[b] – Permanent Deflection
[c] – Different fixing assemblies used
[d] – Steel reinforcement used, not reported
[e] – No steel reinforcement
[f] – High strength vanadium alloy steel
[g] – Repetitive testing on the same B3 panel

4.1.2.1. Compressive strength of concrete

Panels with compressive strengths of 19.3 MPa to 164 MPa were tested with different panel dimensions, standoff distances and charge weights. Unlike in close range studies, the tensile strength of concrete was not a significant factor in determining the response and damage mechanism of the panel. This partly explains why more attention was given to conventional reinforced concrete rather than high strength variants. Except for some studies by Schenker et al. (2005), Schenker et al. (2008), Ngo et al. (2007a,b), and Barnett et al. (2010) who focussed on HSC materials as a method of improving the blast resistance in far range response. Schenker et al. (2005, 2008) tested 100 MPa HSC panels with 1000 kg of TNT at a standoff distance of 20 m. Ngo et al. (2007b) evaluated the effects of prestressing and HSC in combination with large charge weights (6000 kg of TNT) and observed the superior performance in comparison with the 40 MPa concrete. Overall, high-performance concrete panels have performed well in comparison with NSC concrete panels, similar to close range studies.

4.1.2.2. Reinforcement and fibre inclusion

Reinforcement in different forms, such as conventional reinforcement bars, prestressing tendons, fibre inclusion within the concrete matrix or a combination was evaluated for the far range blast performance. Conventional reinforcing was preferred for far range studies due to the less likelihood of local failure modes (spalling and scabbing). Different bar sizes and reinforcement ratios were used for the panel construction where larger reinforcement ratios are displaying better resistance. Barnett et al. (2010) used high strength Vanadium reinforcement (572 MPa) as a replacement for conventional steel reinforcement (469 MPa) and displayed better resistance with reduced deflections and tensile cracking.

A combination of conventional reinforcement with prestressing tendons was assessed for far range blast performance in several studies (Ngo et al., 2007b, Dunkman et al., 2009). Dunkman et al. (2009) evaluated the performance of pre-tensioning and post-tensioning for blast resistance. Pre-tensioned panels exhibit lesser deflection and lesser pre-stress relaxation than the post-tensioned panel. The combination of HSC and pre-tensioning (Ngo et al., 2007b) revealed better performance with reduced deflections and tensile cracking in comparison to conventional steel reinforcement.

Lesser number of research studies was found utilising fibre inclusions within the concrete matrix in comparison to close range studies. However, in some work, steel fibres of different sizes, shapes and percentages were introduced with or without conventional reinforcing bars. In the case of using steel fibres without reinforcing it was found that cross-section was weakened and complete failure of panels were observed (Barnett et al., 2010). Hence, it can be considered that the use of steel fibres along with conventional reinforcement is better than using steel fibres alone, in far range blast resistant applications.

4.1.2.3. Boundary/support conditions

In general, wall panels were tested with simplified connections/support conditions. However, with slab panels, the tendency was to provide overly simple supports by means of timber planks or steel members fundamentally to prevent transverse movement. The use of flexible support/boundary conditions was evaluated by two researchers for far range studies where one was in a shock tube facility with hydraulic jacketing as the supports (Ågårdh, 1997). The other study uses the bolted, dowel and angle cleat connections.

Although no conclusions were reported on the fixing flexibility for the shock tube tests (Ågårdh, 1997), improvement in resistance to ultimate deflection was observed with the bolted connections (Pham, 2010). Comparison of two connection types, dowel and angle cleat connections reveal that angle cleat connections perform much better than dowel connected panels with reduced deflections and crack widths. Comparison of dowel connected panels with different support fixities (via the number of bolts and angle cleat thicknesses) showed that increased transverse flexibility results in reduced deflections. Improvement in resistance was also visible with the number of tensile cracks and crack widths within the section. In the meantime, allowing too much flexibility has resulted in catastrophic failures via fixing mechanisms.

Overall, transversely flexible connections seem to be an excellent passive solution for mitigation of blast loading effects on panel systems. However, not enough quantitative studies were conducted to prove the value of this hypothesis, although these flexible and energy dissipation connections have been used to minimise the effects of wind and earthquake loads (Precast/Prestress Concrete Institute, 2007, Azad et al., 2012, Abtahi et al., 2012, Samali et al., 2014).

4.1.3. Summary of experimental studies

The following observations were made based on the reviewed experimental studies.

Close range experimental studies

- Minimising the localised damage of panels by improving the tensile strength of concrete was the main focus of close range experimental studies. High-performance concrete in the form of HSC and RPC were generally used to mitigate spalling and scabbing with compressive strength in excess of 200 MPa.
- Steel, carbon or glass fibres were introduced to the concrete matrix to minimise the local damage by improving the tensile strength in NSC. Steel fibres incorporated to RPC concrete mixes found to be extremely resilient against localised damage.
- Closely spaced reinforcement (bars) layout within the concrete section was found to be an effective method in reducing localised damage where both spalling and scabbing can be limited to cover concrete. Lacing reinforcement in the form of steel or polymer is found to be similarly effective in resisting localised damage.

Far range experimental studies

- Use of high-performance concrete in far range studies was limited as panel performances were evaluated by global failure mechanisms. However, resistance to transverse deflection has been increased in instances where high-performance concrete was used.
- Fibre inclusions alone (without conventional reinforcement bars) found to be catastrophic in the case of far range studies as panels weren't able to develop the required global resistance with NSC. However, with high performance concretes, the inclusion of fibres in the concrete matrix without conventional reinforcement performed as equally as with conventional reinforcement (without fibres).
- Closely spaced reinforcement layout, rather than reinforcement percentage, found to improve the far range performance of the panels.

- Replacement of steel (bar) reinforcement with glass fibre (bar) and alloy reinforcement (bar) found to be effective in minimising transverse deflection. However, steel reinforcement found to be more ductile and suitable for far range blast resistant applications.
- Among the passive blast damage mitigation measures, transversely flexible support/fixing assemblies were found to minimise flexural damage to the panel. Although flexible supports/fixing assemblies minimise the damage to panel elements, these are susceptible to failure under the applied load, due to the extended flexibility. This will be evaluated thoroughly during this thesis using analytical and 3-D finite element modelling.

Resisting far range explosive loads are a major priority nowadays as the improved security measures limit the possibility of close range explosions to structural elements. Proper reinforcing was identified as one of the best ways to limit the damage and prevent catastrophic failures of reinforced concrete structures. Guidance is provided in UFC 3-340 (United States Army Corps of Engineers, 2008) for the design of reinforcement to resist the blast loads.

4.2. Numerical studies of reinforced concrete panels subjected to explosive loading

Finite element modelling (FEM) is a good alternative to conventional high-cost experimental studies, provided that the FE modeller can replicate the actual material and structural response. When it comes to concrete and explosive loading, both are considered extreme cases in FEM. LS-DYNA (Livermore Software Technology Corporation, 2013a) and AUTODYN (ANSYS Inc, 2013) have been preferred over similar FE programs, partly due to the available material models and inbuilt blast loading functions (Randers-Pehrson and Bannister, 1997). As in experimental studies, FEM studies were also divided into two major groups, close range and far range based on the scaled distance and panel response.

4.2.1. Close range studies

A detailed summary of close range FEM studies is presented in Table 4.3. Concrete elements subjected to close range explosive loads will undergo large plastic deformation. Hence, the concrete material models used should be able to capture the

post peak softening behaviour (Wu et al., 2012), in order to predict the response accurately. Available material models (Concrete Damage, RHT, Drucker-Prager, CSCM, Winfrith concrete) were found to be capable of capturing the close range behaviour of reinforced concrete with reasonable accuracy (Wang et al., 2008, Zhou et al., 2008, Riisgaard et al., 2006, Pantelides et al., 2012). However, with HSC and RPC, the FEM results are not always consistent with the available experimental results (Zhou et al., 2008) as most of the material models in the FEM have been developed and calibrated to NSC rather than high performance concretes.

4.2.1.1. Concrete material modelling

As highlighted in Table 4.3, different concrete material models were used for different concrete strengths and types. Modelling of conventional reinforced concrete for blast loading response wasn't a major concern, although local damage prediction was not entirely convincing (Zhou et al., 2008). In the case of modelling engineered cement composites, (HSC, NSC and SFRC) results weren't always within the applicable error margin.

The modified Drucker-Prager concrete material model has been utilised with ANSYS AUTODYN for the modelling of both NSC and HSC with steel fibres (Zhou et al., 2008). However, results were under predicted in both concrete types. All other numerical studies used LS-DYNA as the FEM tool. However, different material models were used for concrete in each of those studies. The concrete damage, pseudo tensor, CSCM and user developed model were used achieving different accuracy levels.

4.2.1.2. Reinforcement material modelling

Similar to concrete material models, different reinforcement material models were used with reinforcement as well. The Plastic Kinematic reinforcement model and the Johnson Cook (simplified) model were the most common material models used for close range studies. A perfect bond between reinforcement and concrete matrix has been assumed with reinforcement material model, either through node sharing or through keyword definition.

On the other hand, an increase in tensile strength of concrete was used as modelling reinforcements in certain studies (Xu and Lu, 2006). The developed model has been validated for 2% of reinforcement area, although accuracy levels were not presented.

Table 4.3: Recent Numerical simulation studies of close range explosive loading on concrete panels

Reference	Test identifier	Finite element modeller	Concrete Strength (MPa) / material model	Reinforcement/material model	Charge weight (kg TNT) Emp/ Num	Standoff distance (m)	Peak pressure (kPa)	Peak Impulse (kPa.ms)	Peak displacement (mm)Inward/ outward	Comments
Wang et al. (2008)		LS-DYNA	- / Concrete Damage	T13@200mm/ Plastic kinematic	Vary/ Num	Vary	–	–	–	Effects of contact charges and close in detonations were observed with 12 different simulations
Zhou et al. (2008)		AUTODYN	50/ modified Drucker-Prager	T16@75mm (Bottom) T16@150mm(Top)Johnson Cook	0.545 / Num	0.1	206000	–	–	Maximum deflection is underestimated up to 30% (NSC and SFRC) and time to peak is under predicted up to 25% (SFRC). Minimal of damage observed as in the experimental results. Two predominant failure modes have been identified.
			170/ Modified Drucker-Prager (SFRC)	–						
Xu and Lu (2006)		LS-DYNA	40/ pseudo-tensor	2% of concrete area	Vary	Vary	–	–	–	A parametric analysis with different standoff distances and charge weights for three slab panels

Riisgaard et al. (2006)		LS-DYNA	– (SFRC)	–	–	–	–	–	The effects of aramid fibres were evaluated with 50% reduction of fibres
Eric Musselman (2007)	2A	LS-DYNA	43.3/ Plasticity Compression	–	33.5	0.98	N/R	N/R	–	A complete user input material model was used with available test data (stress-strain curve, dynamic increase factors, etc.) Numerical results were not encouraging as the displacement of panel continues to increase.
	2B		Tension (CFRP)		33.5	0.98	N/R	N/R	–	
Pantelides et al. (2012) Garfield T.T (2011)		LS-DYNA	46/ CSCM concrete	No Reinforcement	6.2/ NUM	1.00	N/R	N/R	N/R	Only a preliminary model. No comparison was made with experimental results

4.2.1.3. Connection/support conditions

Support conditions/connection mechanisms in most FE studies were limited to simplified supports. These simplified supports were modelled either using the inbuilt end conditions (pin, fixed, roller or other combination of 3-dimensional space). In certain studies, the experimental procedure was replicated with FE modelling. However, most of these were limited to simple supports where the edges were clamped using the steel sections or supported on rigid edges.

A comparison of different support conditions were evaluated (Wang et al., 2008) with small contact charges. The authors claim that the change in support conditions had only a minor difference in the response of panels. However, no FE analyses were carried out on connection performance or quantification of the support reactions/connection forces on reinforced concrete panels subjected to close range explosive loads.

4.2.2. Far range studies

A detailed summary of far range FEM studies conducted on RC wall and slab panels is presented in Table 4.4. As observed in experimental studies, more studies were undertaken on conventional reinforced concrete rather than engineered cement composites for far range studies. As seen in Table 4.4, LS-DYNA was preferred for the far range analysis of RC structures subjected to explosive loading over other FEM programs.

4.2.2.1. Concrete material modelling

The Concrete Damage Model (CDM) with automatic parameter generation and the Winfrith concrete model (WCM) were preferred over the other material models as the concrete material model. These two material models were preferred in both NSC and HSC applications. The preference is largely due to the easiness in model parameter definition and capabilities of the models.

Acceptable results within the specified error margin were observed for both RC and HSC materials. The quality of the results observed in far range studies was better than those for the close range studies, for both NSC and HSC applications. This is partly due to the global nature of panel behaviour and lack of local failure modes (spalling and scabbing).

4.2.2.2. Reinforcement material modelling

The Plastic Kinematic (PK) reinforcement model was preferred for reinforcement modelling in far range numerical modelling studies. Preference for the Plastic Kinematic model was due to its ability to fit experimental stress-strain curves and lower computational costs. A perfect bond between reinforcement and concrete matrix is assumed with the reinforcement material models, similar to close range studies.

As an alternative, the tensile strength of concrete was increased instead of modelling reinforcement in certain studies (Schenker et al., 2005). However, accuracy of increasing the tensile strength of concrete hasn't been validated in this study.

4.2.2.3. Connection/support conditions and cladding panels

Use of flexible support conditions as a passive method of damage mitigation was studied by several researchers (Tanapornraweekit et al., 2007, Raman, 2008, Pham et al., 2008, Pham, 2010). Pham (2010) investigated the behaviour of flexible support conditions in RC cladding panels subjected to explosive loading. Reduced maximum deflections were observed with transversely flexible support conditions. However, these supports suffer large transverse deflections due to reduced support stiffness, which proved to be a costly exercise considering the large support deflections. Except for support deflection, reduced panel deflections (relative deflection), reduced crack widths and support reactions were identified as positives of this study.

Table 4.4: Recent Numerical simulation studies of far range explosive loading on concrete panels

Reference	Test identifier	Finite element modeller	Concrete Strength (MPa) / material model	Reinforcement/material model	Charge weight (kg TNT) Emp/ Num	Standoff distance (m)	Peak pressure (kPa)	Peak Impulse (kPa.ms)	Peak displacement (mm)Inward/ outward	Comments
Pham T. (2010)	A B2	LS-DYNA	46/ Concrete Damage 43/ Concrete Damage	N5@100 mm/ Plastic-Kinematic	5.5/ [a]	2	–	–	36.4/9.4 25.6/15.8	Approximate results have been observed with panel deflections. No other results were presented.
Tai et al. (2011)	A B C D	LS-DYNA	17.2/ Johnson Holmsquist concrete	Plastic Kinematic	1 3 5 10 (Num)	2.50	–	–	2.4/1.9 6.1/4.0 9.9/6.1 18.2/10.4	Higher reinforcement ratios resulted in support shear failure while lower ratios yield, flexural or shear damage in mid span.
Schenker et al. (2005)	B	LS-DYNA	30/-	Not modelled, Increase tensile strength	1000	20	–	–	–	Support conditions were modelled as non-slipping and frictionless as two cases. Preliminary analysis or results not presented
Tanapornra weekit et al. (2007, 2008, 2008)		LS-DYNA	40/ Concrete-Damage	N16@120 mm/Plastic-kinematic	5000/ Emp	40	663	5147	36/5	Failure in tension. Compressive stresses up to 60% in concrete. 40-60% of stresses in reinforcement.

Vasudevan A.K (2013)	A1	LS-DYNA	27.6/ Concrete Damage, Winfrith concrete	T10@101 T10@304 (572 MPa)	N/A[a]	N/A[a]	352	6667	[b]	0.5 inch mesh performed well with experimental observations for NSC panels (both material models) while for HSC, Winfrith showed better calibration and concrete damage model was too stiff. Crack propagation of 1 inch model was (Winfrith) matching with experimental results.
	B1			T10@101 T10@304 (469MPa)			358	6963		
	A2		106.9/ Concrete Damage, Winfrith concrete	T10@101 T10@304 (572 MPa)			385	7730		
	B2			T10@101 T10@304 (469MPa)			391	7434		
Agardh et al. (1997)	A1 B1 B1 C1 D2 D3	LS-DYNA ABAQUS	63.2/ Winfrith Concrete (SFRC)	–	–	–	–	–	3.4/3.4[c] 1.5/1.4[c] 4.8/4.8[c] 10/21[c] 15.5/fail[c] 18/fail[c]	The fixed part of the panel was modelled with elastic material and kept simply supported to have matching frequencies. Time dependent parameters of acceleration, velocity, displacement and strain rate were recorded

[a] – reflected pressure measured was used as a manual loading curve
[b] - A comparison study was made with mesh sensitivity and two material models
[c] – Two values were for LS-DYNA and ABAQUS numerical results
Emp – Empirical blast load
Num – Numerical (physical) modelling of explosives

4.2.3. Summary of numerical studies

The following observations were made based on the reviewed finite element studies.

Close range studies

- Selected concrete material models failed to capture the local failure modes associated with close range explosive loading. The inability of material models to represent material fragmentation was highlighted in many of the close range studies. No specific preference was given to any concrete material model. Similarly, reinforcement material models were given no specific preference as well

Far range studies

- Available material models for concrete are found to be capable of predicting the global failure modes accurately for both NSC and HSC applications. The concrete damage model (CDM) and the Winfrith concrete model (WCM) were given the preference as a concrete material model.
- The plastic kinematic (PK) model was given the preference among the reinforcement material models.
- Effects of flexible support conditions were given considerable attention with far range explosive loads and found to improve the deflection and crack resistance. However, support deflection found to be a concern with overly flexible supports.

4.3. Failure mode behaviour of reinforced concrete panels subjected to explosive loading

The failure modes of a structure depend on both loading and structural characteristics, which can be broadly categorised as local and global failure modes. The type of failure mode depends on the explosive loading characteristics of pressure, impulse and loading rate and structural characteristics such as geometry, boundary conditions and material properties. As for the explosive loading classification, ***far range*** loading is normally associated with global failure modes such as flexure and shear while ***close range*** loading is associated with local failure modes such as spalling and scabbing.

4.3.1. Local failure modes

Local failure modes are typically associated with close range explosive events and contact detonations. After the explosive detonation, a compressive stress wave is generated by the high pressure pulse applied on the face of the element. Depending on the strength of the compressive wave, localised ‘cratering’ can occur on the exposed face, which is also known as spalling.

A compressive stress wave will travel through the thickness of the structure and partially reflect at the back face as a tensile stress wave. The generated stress wave may cause tensile failure on the rear face of the structure, resulting in scabbing. Flying debris (projectiles) observed after an explosive event is predominantly due to the scabbing damage to the structure.

In the case of extremely high explosive events, spalling in the front face and scabbing in the rear face can merge. In the case of merged spalling and scabbing, a typical cross-section is said to be breached. A graphical representation of a cross-section experiencing spalling, scabbing and section breaching is shown in Figures 4.1 a, b, and c respectively.

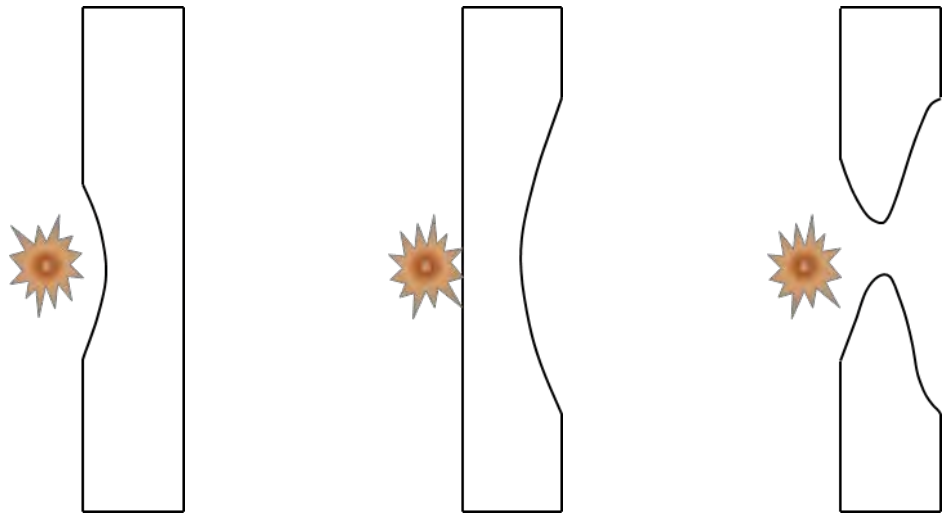

(a). Spalling (b). Scabbing (c). Section breach

Figure 4.1: Local failure modes of RC panels exposed to explosive loading (Source: Nyström, 2008)

4.3.2. Global failure modes

The global failure modes of RC panels subjected to explosive loading can be broadly categorised as membrane, flexural or shear. A graphical representation of these failure modes including sub-categories are presented in Figure 4.2.a to 4.2.f.

As shown in Figure 4.2.a, membrane type failures occur when the in-plane forces are applied to the structural element with supports capable of restraining the in-plane forces. Membrane type failures can be compressive or tensile depending on the sense of the loading.

Flexural failures are associated with plastic hinge formations where structures become mechanisms. These flexural failure modes can be sub-categorised as flexural failures with plastic hinge formations (Figure 4.2.b) and flexural failures with support slipping off (Figure 4.2.e). These failure mechanisms in RC structures can be identified with excessive tensile cracking and large transverse deformations, irrespective of the subcategory.

Shear failures of RC structures subjected to explosive loading can be of two types, diagonal shear failures (Figure 4.2.c) or direct shear failures (Figure 4.2.d). Diagonal shear failure, or more properly known as diagonal tension failure, can occur as in statically loaded RC sections where enough shear reinforcement is not provided. Unlike in membrane and flexural failures, no significant deformations are observed prior to failure.

Direct shear failures are rare in RC structures under static loading, but common with short duration impulsive loading such as explosive loading. Direct shear failures are commonly associated with geometric discontinuities such as thickness changes or existing cracks or loading discontinuities. In the case of explosive loading, direct shear failures are often observed in early stages of loading prior to significant bending deformations. In order to observe the direct shear response in structural analysis, higher modes of vibration should be included in the numerical analysis tools (Pham, 2010).

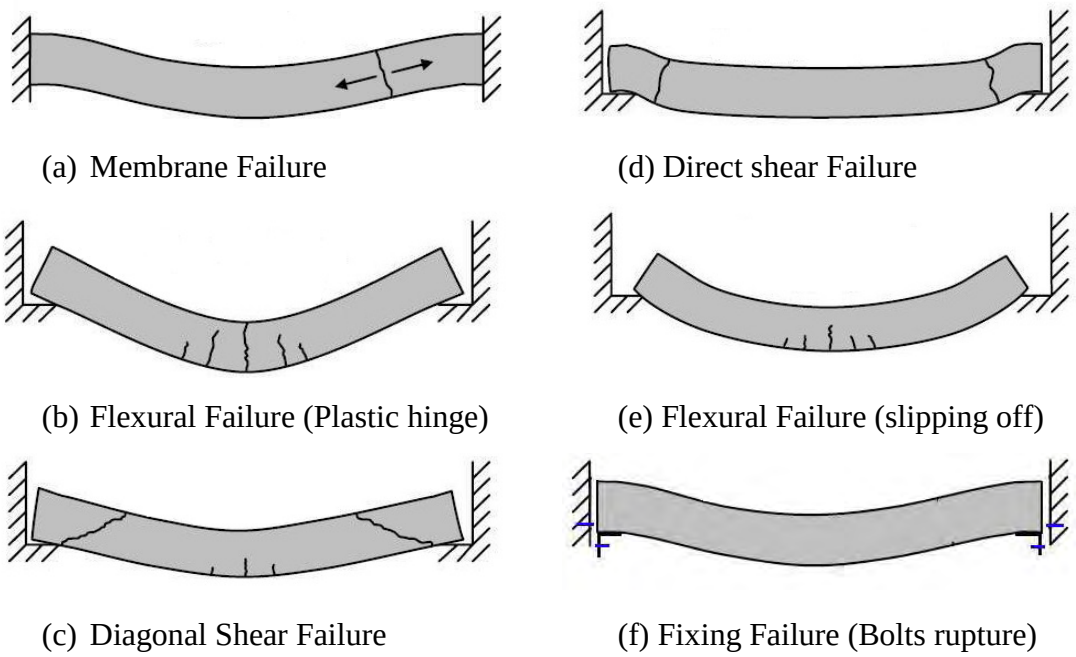

Figure 4.2: Global failure modes of RC panels exposed to explosive loading (Source: Nyström, 2008)

4.4. Review of design guidelines

Reinforced concrete is used for the construction of almost all types of structures and design procedures are covered by different codes of practices. (AS 3600, EC 2, ACI 318) However, none of these design codes provide comprehensive guidelines for the design of reinforced concrete structures subjected to explosive loading. Although, there are provisions provided with the equivalent static analysis and design procedures for dynamically applied loads (American Concrete Institute, 2011), there is no consideration of the explosive resistance design requirements of the reinforced concrete elements.

Although the explosive design is omitted from major design codes, there are several specific design guidelines for explosive related design. These design guidelines were specifically formulated for the design of military and storage facilities for explosive related design for different construction materials. Design guidelines for explosive related designs are listed in Table 4.5 below.

Table 4.5: Design codes for explosive related design

Year	Code/ Guidelines	Organization	Remarks
1986	TM5-855 Foundations of protective design for conventional weapons	United States Army Corps of Engineers	Replaced by TM5-1300.
1990	TM5-1300 Structures to resist the effects of accidental explosions	United States Department of Defence	Replaced by UFC 3-340.
2003	FEMA 427 Primer for design of commercial building to mitigate terrorist attacks	United states Federal Emergency Management Agency	Present design guidelines with how to minimise the damage to structures by eliminating the possibility of occurrence.
2004	PCI designers notebook Blast considerations	Prestress/Precast Concrete Institute	Highlight general design methods specific to precast and glass facade systems.
2008	Unified Facilities Criteria (UFC 3-340) Structures to resist the effects of accidental explosions	United States Department of Defence	The most comprehensive design guide up to date.
2010	Design of blast resistant buildings in petrochemical facilities	American Society of Civil Engineers	Highlight mitigation procedures rather than design and refers to UFC 3-340.

Among the available documentation, UFC 3-340 presents the most advanced design guidelines for protective construction of both steel and concrete. It presents guidelines and design charts for evaluating the potential threat to design the structure to withstand the potential threat. This documentation was initially used for the purpose of the design of protective construction used in facilities for development, testing, production, storage, maintenance, modification, inspection, demilitarisation and disposal of explosive materials. However, with the new release in 2008, this manual is used as a design guide for commercial and critical civilian structures as well.

UFC 3-340 consists of five major sections which cover, load evaluation including fragmental impact and shock loads, dynamic analysis principles including dynamic properties of materials, design of reinforced concrete structures, design of steel structures and special considerations for explosive design facilities. In this review,

procedures for reinforced concrete design of panel elements (slabs and walls) will be evaluated.

The design of slab panels has been divided into two main categories, conventional RC slab panels and panels with lacing reinforcement. The concept of lacing reinforcement was developed to use in protective structures such as blast barriers. Therefore, the application of lacing reinforcement in general civilian and commercial structures is economically unviable. Therefore, this review is limited to non-laced slab and wall panels.

4.4.1. Rate effects of materials

Different strength parameters of concrete and steel have different rate enhancement factors (DIF), as discussed in Chapter 3. UFC 3-340 (United States Army Corps of Engineers, 2008) defines these rate enhancement factors as shown in Table 4.6 in terms of dynamic yield strength (f_{dy}) and dynamic ultimate strength (f_{du}) for steel and dynamic compressive strength (f'_{dc}) for concrete. These DIF values were taken from DIF curves generated from experimental studies with maximum strain rates up to 300/S for concrete and 100/S for reinforcing steel. Different values are assigned for the far range design and the close range design. However, with the very high strain rates observed in close range explosive events (beyond 300/S), these DIF values are found to be conservative. Although these values are found to be conservative, considering the different material strengths, unpredictability in explosive loading and strain rate measurements, use of conservative DIF values is justified. In the case of more accurate estimation, rate enhancement curves are also provided for different strength classes of concrete and reinforcing steel as shown in Figures 4.3 and 4.4 respectively.

Table 4.6: Dynamic increase factors for concrete and reinforcing steel (UFC 3-340, 2008)

Type of Stress	Far Design Range			Close-in Design Range		
	Reinforcing Bars		Concrete	Reinforcing bars		Concrete
	f_{dy}/f_y	f_{du}/f_u	f'_{dc}/f'_c	f_{dy}/f_y	f_{du}/f_u	f'_{dc}/f'_c
Bending	1.17	1.05	1.19	1.23	1.05	1.25
Diagonal tension	1.00	----	1.00	1.10	1.00	1.00
Direct Shear	1.10	1.00	1.10	1.10	1.00	1.10
Bond	1.17	1.05	1.00	1.23	1.05	1.00
Compression	1.10	----	1.12	1.13	----	1.16

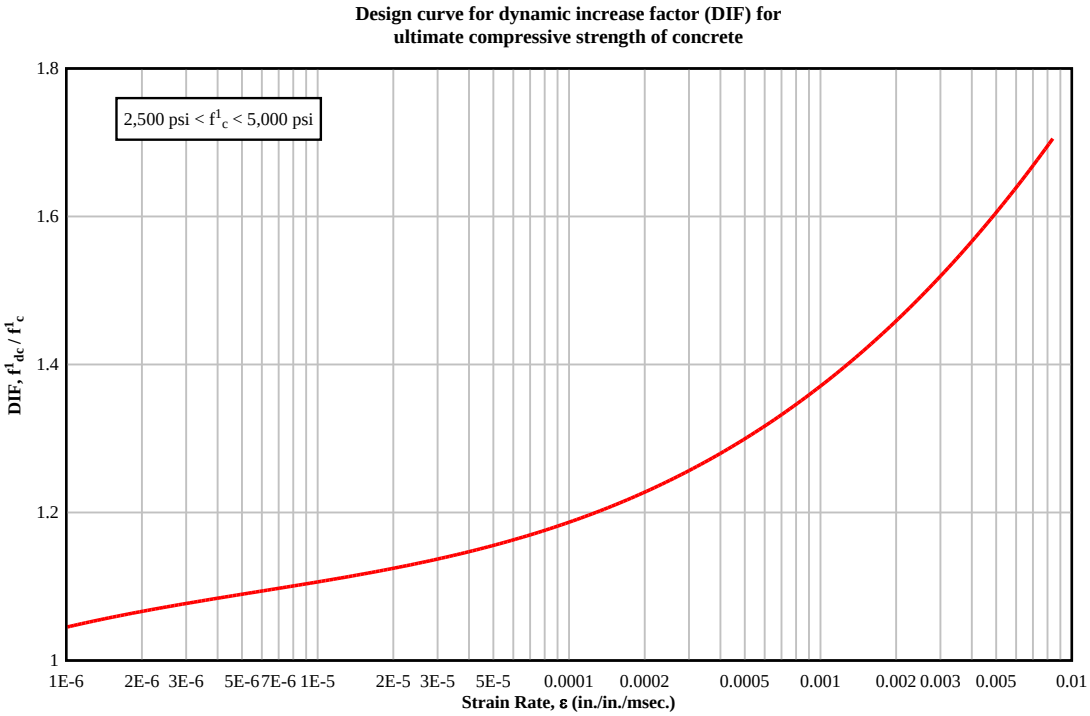

Figure 4.3: Dynamic increase factor for compressive strength of concrete (Source: UFC 3-340, 2008)

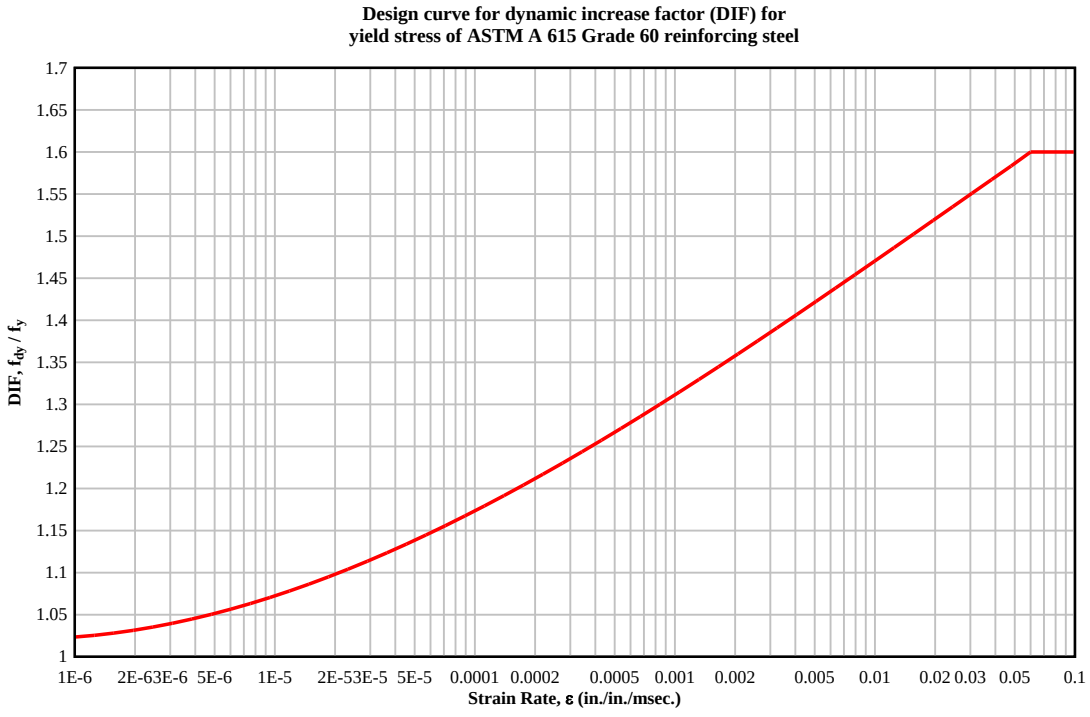

Figure 4.4: Dynamic increase factor for yield strength of reinforcement (Source: UFC 3-340, 2008)

4.4.2. Design categories and cross-sections types

Depending on the blast output and the permissible deformations, three types of RC cross-sections can be utilised in the design or analysis of explosive resistant concrete panels, named Type I, Type II and Type III.

A graphical illustration of the three cross-section types is presented in Figure 4.5.

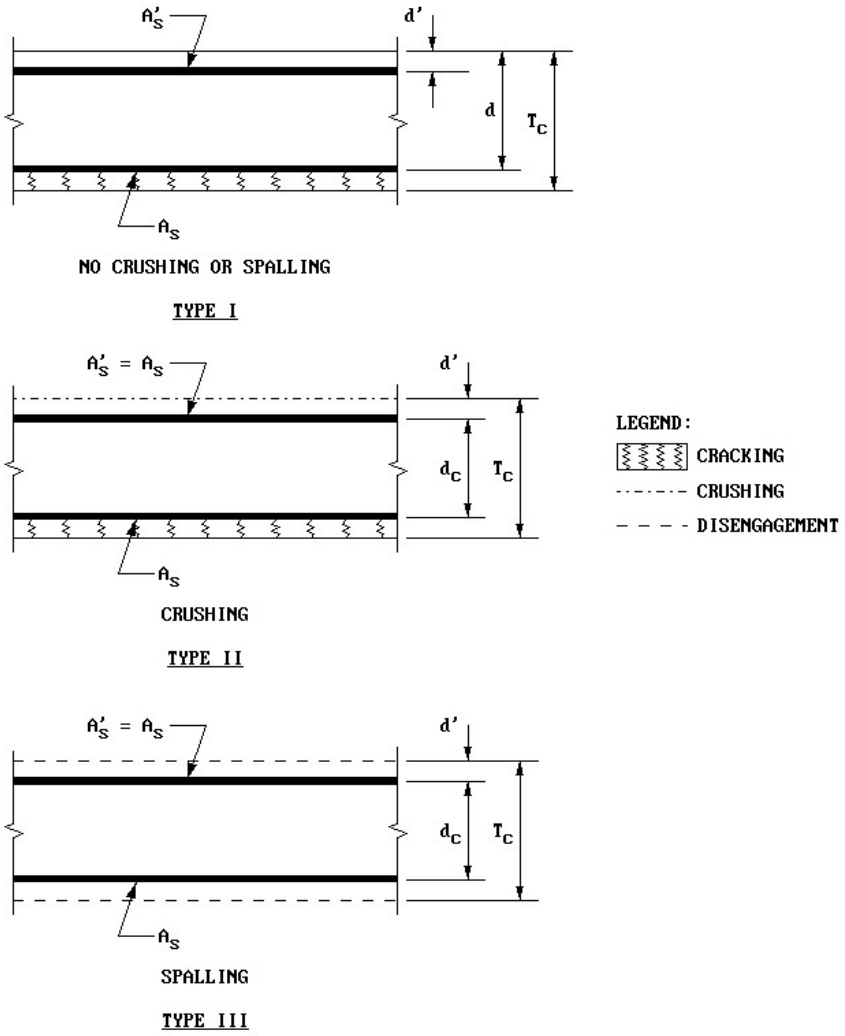

Figure 4.5: Types of RC cross-section available for design (Source: UFC 3-340, 2008)

4.4.2.1. Type I cross-sections

The whole concrete section is considered effective in resisting the applied moment. Therefore, Type I sections exhibit the maximum strength of a selected cross-section. Type I cross-sections are typically used in far range explosive loads with limited deflections where the maximum allowed support rotation is limited to 2^o, where support

rotation is defined as the inverse tangent of maximum deflection divided by half the span length (Equation 4.1). This type of cross-section can be designed either as singly reinforced or doubly reinforced, although it is encouraged to use doubly reinforced sections to cater for rebound forces. Shear reinforcement is considered not essential for this type of cross-section. The support rotation is given as,

$$\theta = tan^{-1}\left(\frac{\delta}{L/2}\right) \tag{4.1}$$

Where;

θ = Support rotation

δ = Maximum deflection

L = Span length

4.4.2.2. Type II cross-sections

Concrete in the compression zone of the maximum moment region is considered crushed, hence not effective in resisting moment for Type II cross-sections. As a result, compression reinforcement is essential in carrying the moment applied from the potential explosion and should be equal to the amount of tensile reinforcement. Although both cover layers of concrete are cracked, they considered to remain intact for this Type II cross-section.

Support rotation up to 6^o is allowed for Type II cross-sections. As concrete is not effective in resisting compressive forces, shear reinforcement of some form should be provided in order to fully develop the compressive strength of steel without bucking. This type of cross-section is typically used in far range designs with large deformations.

4.4.2.3. Type III cross-sections

Type II and Type III cross-sections have the same moment carrying capacity, although Type III sections are allowed to deform more than the Type II sections. The additional deformation of up to 12^o of support rotation is allowed for this type of cross-section. As a result, both cover layers of concrete are considered as completely disintegrated. As of Type-II sections, reinforcement in both tension and compression layers are equal and flexural capacity will depend on the amount of reinforcement. Closely spaced shear reinforcement is essential in order to attain full moment capacity as no lateral resistance

is provided by the concrete. Type III cross-sections are typically used in close range applications like blast barriers.

4.4.3. Dynamic design stresses

The magnitude of stresses produced in the reinforcement of an element responding in the elastic range can be related directly to the strains. However, in the plastic design range, stresses cannot be directly related to the strains. Hence, design stresses are estimated using the deflection of the element, in this case, support rotation. The average dynamic design stress is therefore expressed as a function of dynamic yield strength *(f_{dy})*, dynamic ultimate strength *(f_{du})* and support rotation *(θ_m)* as given in Table 4.7.

Table 4.7: Dynamic design stresses for concrete and reinforcing steel (Source: UFC 3-340, 2008)

Type of Stress	Type of Reinforcement	Maximum Support Rotation θ_m (Degrees)	Dynamic Design Stress	
			Reinforcements, f_{ds}	Concrete, f'_{dc}
Bending	Tension and compression	$0 < \theta_m \leq 2$	f_{dy}(1)	f'_{dc}
		$2 < \theta_m \leq 6$	$f_{dy} + (f_{du} - f_{dy})/4$ (2)	
		$6 < \theta_m \leq 12$	$(f_{dy} + f_{du})/2$ (2)	
Diagonal Tension	Stirrups	$0 < \theta_m \leq 2$	f_{dy}	f'_{dc}
		$2 < \theta_m \leq 6$	f_{dy}	f'_{dc}
		$6 < \theta_m \leq 12$	f_{dy}	f'_{dc}
Diagonal Tension	Lacing	$0 < \theta_m \leq 2$	f_{dy}(1)	f'_{dc}
		$2 < \theta_m \leq 6$	$f_{dy} + (f_{du} - f_{dy})/4$	f'_{dc}
		$6 < \theta_m \leq 12$	$(f_{dy} + f_{du})/2$	f'_{dc}
Direct Shear	Diagonal Bars	$0 < \theta_m \leq 2$	f_{dy}(1)	f'_{dc}
		$2 < \theta_m \leq 6$	$f_{dy} + (f_{du} - f_{dy})/4$ (3)	
		$6 < \theta_m \leq 12$	$(f_{dy} + f_{du})/2$ (3)	
Compression	Column	(4)	f_{dy}	f'_{dc}

(1) Tension reinforcement only
(2) Concrete crushed and not effective ins resisting moment
(3) Concrete is considered not effective and shear is resisted by reinforcement only
(4) Capacity is not a function of support rotation

4.4.4. Ultimate moment capacity

Ultimate moment capacity depends on the type of cross-section available for design. Therefore, ultimate moment capacity is evaluated separately for different cross-section

types. All the equations in this section and sections to follow (Sections 4.4.4 to 4.4.9) use the imperial unit system (US system).

4.4.4.1. Type I cross-sections

The moment capacity of a Type I cross-section without compression reinforcement is given by,

$$M_u = \frac{A_s f_{ds}}{b}\left(d - \frac{a}{2}\right) \tag{4.2}$$

Where;

a = $A_s f_{ds}/0.85 b f'_{dc}$

f_{ds} = Dynamic design stress of reinforcement (Table 4.7)

f'_{dc} = Dynamic design strength of concrete (Table 4.7)

The moment capacity of a Type I cross-section with compression reinforcement is given by,

$$M_u = \left[(A_s - A'_s)\frac{f_{ds}}{b}\right]\left[d - \frac{a}{2}\right] + \left(\frac{A'_s f_{ds}}{b}\right)(d - d') \tag{4.3}$$

Where;

a = $(A_s - A'_s) f_{ds}/0.85 b f'_{dc}$

A_s = Area of tensile steel,

A'_s = Area of compressive steel

b = Width of the cross-section,

d = Effective depth for tensile reinforcement and

d' = Effective depth for compressive reinforcement

The moment capacity defined by UFC 3-340 and ACI 318 are identical for Type I cross-sections. However, the capacity reduction factor is omitted in the UFC 3-340 design, which is assumed to be built into the loading and yield line prediction for the slab and wall panels.

4.4.4.2. Type II and III cross-sections

Type II and III have identical moment carrying capacities as shown in Equation 4.4.

$$M_u = \frac{A_s f_{ds} d_c}{b} \tag{4.4}$$

Detailing guidelines are provided in separate clauses of UFC 3-340. Alternatively ACI-318 guidelines can also be used as both UFC 3-340 and ACI-318 have similar detailing guidelines. However, use of large bar sizes (#14 (43 mm diameter) and above), bundled bars and wielding of bars are discouraged for ductility reasons. However, provisions were given for the use of bundled bars up to 3, if unavoidable.

4.4.5. Ultimate shear capacity – Diagonal shear

Diagonal shear capacity is considered a combination of shear capacity of unreinforced concrete and capacity of shear reinforcement. In order to determine the shear capacity from reinforcement, ultimate shear stress and shear capacity of unreinforced concrete should be determined, as highlighted below.

4.4.5.1. Ultimate shear stress

Ultimate shear stress depends on the type of cross-section available for design, other than loading and geometric properties.

Ultimate shear stress for a Type I cross-section is given by,

$$v_u = {V_u}/{bd} \tag{4.5}$$

Ultimate shear stress for Type II and Type III cross-sections are given by,

$$v_u = {V_u}/{bd_c} \tag{4.6}$$

Where;

$$d_c = d - d'$$

V_u = Design shear force

b = Width of the section

d = Effective depth for tension reinforcement

d' = effective depth for compressive reinforcement

The design shear force V_u is calculated either at the face of the support or d or d_c away from the support depending on the type of cross-section available and possibility of extending diagonal tensile cracks through the support. Design shear stress v_u should not exceed $10(f'_{dc})^{1/2}$ for cross-sections using stirrups. In case v_u exceeds this value, dimensions of the cross-section should be altered.

4.4.5.2. Shear capacity of unreinforced concrete

Shear stress permitted for unreinforced concrete section subjected to flexural stresses is given by,

$$v_c = 2(f'_{dc})^{1/2} \tag{4.7}$$

$$v_c = \left[1.9(f'_{dc})^{1/2} + 2500\rho\right] \leq 3.5(f'_{dc})^{1/2} \tag{4.8}$$

Where;

ρ = Tensile reinforcement ratio at the location where shear stress is calculated

Two additional equations were proposed for the combined axial and flexural actions as in Equations 4.9 and 4.10 for tensile and compressive stresses respectively. Tensile forces are considered negative for the calculation of shear stresses.

$$v_c = 2\left[1 + N_u/500A_g\right](f'_{dc})^{1/2} \geq 0 \tag{4.9}$$

$$v_c = 2\left[1 + N_u/2000A_g\right](f'_{dc})^{1/2} \tag{4.10}$$

Where;

N_u = Axial force applied at the same location as design shear force

It is advised that a time history analysis should be performed prior to using Equations 4.9 and 4.10 as a simple analysis will not yield the exact timing of shear force and axial force. In the case where time history analysis is not performed, it is recommended that enhancement due to compression forces must be ignored and reduction due to tensile forces must be included. However, both these assumptions are conservative.

4.4.5.3. Design shear stress

Design shear stresses were defined based on the type of cross-section available for design, applied shear stress and the type of structural action, as in Table 4.8. Design shear stress is further categorised according to the scaled distance. This classification is specifically used to determine the occurrence of possible spalling, which will reduce the shear capacity of the section.

4.4.5.4. Design of shear reinforcement

Whenever the ultimate shear stress *(v_u)* exceeds ultimate shear capacity *(v_c)*, shear reinforcement must be provided either in the form of stirrups or lacing reinforcement. However, for the scope of this thesis only stirrups are considered for the shear reinforcement. The area of stirrups *(A_v)* required is calculated using Equation 4.11 given below.

$$A_v = {[(v_u - v_c)b_s S_s]}/{\varphi f_{ds}} \tag{4.11}$$

Where;

φ = Capacity reduction factor (0.85)

b_s = Width of the section (strip)

S_s = Spacing of stirrups parallel to main reinforcemnt

In order to ensure the required ductility is attained, specific guidelines are given for the bending of stirrups. Other than the guidelines given in UFC 3-340, stirrups should comply with the ACI-318 guideline as well.

Table 4.8: Minimum design shear stresses for slabs (Source: UFC 3-340, 2008)

Design Range (ft/lb$^{1/3}$)	Type of Cross-section	Type of Structural Action	Type of Shear Reinforcement	Excess Shear Stress *(v_u-v_c)*		
				$v_u \leq v_c$	$v_c < v_u \leq 1.85v_c$	$v_u > 1.85v_c$
Z ≥ 3.0	Type I	Flexure	Stirrups	*0*	v_u-v_c	v_u-v_c
	Type II	Flexure	Stirrups	*0.85v_c*	*0.85v_c*	v_u-v_c
	Type II & Type III	Tension Membrane	Stirrups	*0.85v_c*	*0.85v_c*	v_u-v_c
Z < 3.0	Type I*	Flexure	Stirrups or Lacing	*0.85v_c*	*0.85v_c*	v_u-v_c
	Type II & Type III	Flexure or Tension Membrane	Stirrups or Lacing	*0.85v_c*	*0.85v_c*	v_u-v_c

*- Verify spalling is prevented

4.4.6. Ultimate shear capacity – Direct shear

Direct shear failure is categorised as a rapid propagation of a vertical crack through the depth of the member. These failures are more common close to supports and geometric discontinuities of structures.

4.4.6.1. Direct shear capacity of unreinforced concrete

The direct shear capacity of concrete is defined as a function of support rotation (indirectly cross-section type). If support rotation is greater than 2^o, ($\theta \geq 2^o$) or if the section is in net tension, direct shear capacity *(V_d)* of concrete is considered zero. If support rotation is less than 2^o ($\theta < 2^o$) or if a simple support is used, direct shear capacity is given as in Equation 4.12.

$$V_d = 0.16 f'_c bd \tag{4.12}$$

4.4.6.2. Design of shear reinforcement

Similar to diagonal shear, when the applied shear stress (shear force in direct shear) is greater than the shear capacity, shear reinforcement must be provided. However, providing stirrups close to supports and geometrical discontinuities is difficult due to the congested reinforcement details. Therefore, diagonal reinforcing bars were introduced as the reinforcing for direct shear. Reinforcement for direct shear is essential for Type II and Type III cross-sections. The required area of diagonal bars *(A_d)* to restrain the applied direct shear force is given by,

$$A_d = {(V_s b - V_d)}\Big/{f_{ds} \sin(\alpha)} \tag{4.13}$$

Where;

V_s = Applied shear force per unit width,

α = Angle between the diagonal and longitudinal reinforcement

4.4.7. Tensile membrane capacity

RC slabs with sufficient lateral restraints attain large deflections ($\theta > 6^o$), and can harvest tension membrane actions within the section and achieve support rotations up to 12^o. However, in order to develop tensile membrane actions, sufficient reinforcement should be provided in excess of flexural and shear reinforcement. For a given deflection *(X)*, the tensile membrane capacity *(r_T)* of a one-way slab is given by,

$$r_T = X\left[8T_y \Big/ L_y^2\right] \tag{4.14}$$

Where;

$$T_y = (A_s)_y f_{ds}$$

$(A_s)_y$ = Area of longitudinal reinforcement

L_y = clear span

A similar equation is available for two-way slabs as well where reinforcement in both directions is considered. If a Type III section is designed, sufficient reinforcement should be provided to achieve the deflection limit ($6^o < \theta \leq 12^o$).

4.4.8. Spalling and scabbing resistance

Direct spalling is due to a compression stress wave travelling through a concrete element, reaching the back face and reflecting as a tensile stress wave. Spalling occurs when applied tensile stress is greater than the tensile strength of the material. The spalling prediction was based on the observations of spalling tests. Two empirical equations were proposed for the spalling threshold and breaching threshold. A plot of spalling threshold and breaching threshold is given in Figure 4.6.

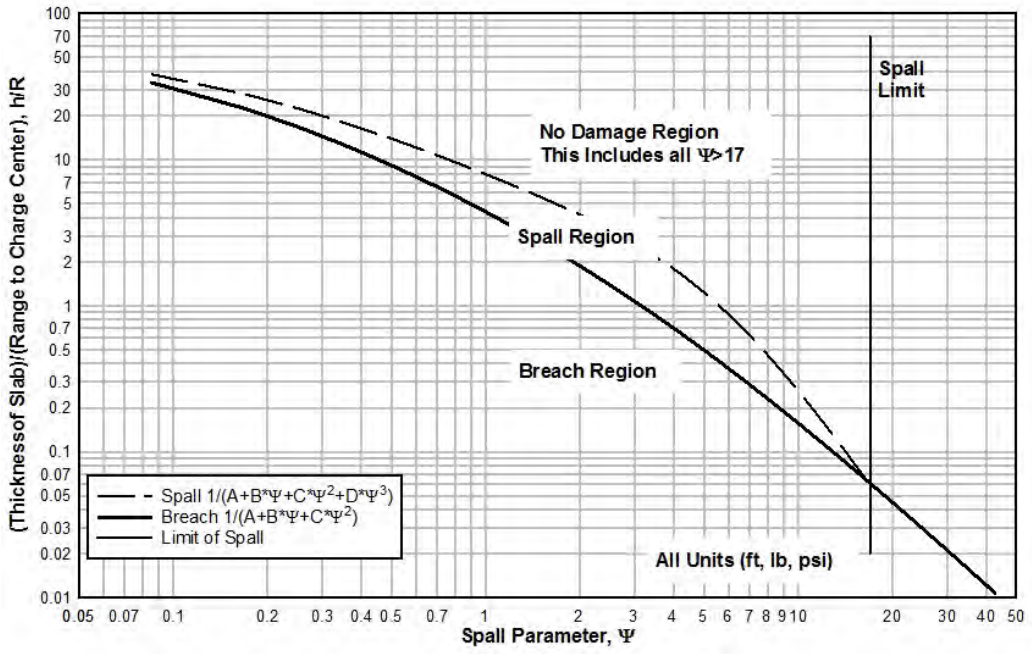

Figure 4.6: Threshold spall and breach curves for slabs subjected to high explosive bursts in Air (standoff and contact charges) (Source: UFC 3-340, 2008)

Spalling threshold of RC slabs subjected to explosive loading is given by,

$$\frac{h}{R} = \frac{1}{a + b\psi + c\psi^2 + d\psi^3} \tag{4.15}$$

Where;

h = Concrete thickness (feet)

R = Range from slab face to charge centre of gravity (feet)

ψ = Spall parameter

a = 0.01633; b = 0.98009; c = -0.64804; d = 2.21259

Breaching threshold of RC slabs subjected to explosive loading is given by,

$$\frac{h}{R} = \frac{1}{a + b\psi + c\psi^2} \tag{4.16}$$

Where;

a = 0.01526; b = 1.41191; c = 3.42685

Spall parameter was defined for different explosive scenarios including contact detonations and free air detonations, shape charges and enclosed charges as well. The spall parameter (ψ) for free air detonations (non-contact detonations) is given as,

$$\psi = R^{0.926} f'^{0.266}_c W^{-0.353}_{adj} \left(\frac{W_{adj}}{W_{adj} + W_c}\right)^{0.333} \tag{4.17}$$

And, spall parameter (ψ) for contact charges is given as,

$$\psi = 0.527 R^{0.972} f'^{0.308}_c W^{-0.341}_{adj} \tag{4.18}$$

Where;

W_{adj} = Shape adjusted charge weight (lb)

W_c = Weight of steel casing

$$W_{adj} = B_f C_f W \tag{4.19}$$

Where;

B_f = Blast configuration factor, 1 for surface blasts and 0.5 for free air blasts

C_f = Cylindrical charge shape factor

$$C_f = \begin{cases} 1 + 2\left(\frac{LD}{\pi(3LD^2/16)^{0.667}} - 1\right)\left(1 - \frac{R}{2W^{0.333}}\right) & for\ L > D\ and\ R/W^{0.333} < 2 \\ 1.0 & for\ all\ other\ case \end{cases} \quad (4.20)$$

Where;

L = Length of the cylindrical charge weight

D = Diameter of the cylindrical charge weight

Two equations defined for the spall and breaching parameters were based on experimental testing of scaled down and full scale tests. Therefore, a range for each of the parameters (material and geometrical) used during the testing is also provided, as shown in Table 4.9. Although a range for these parameters was given, use of spall prediction in full-scale panels rather than scaled down panels is recommended due to the rate enhancement effects used in the spall parameter *(ψ)* definition.

Table 4.9: Parametric ranges for spall prediction (Source, UFC 3-340, 2008)

Parameter	Max.	Min.	Avg.
Range, R, in	360	0.10	21.0
Charge weight, W, lb	2299	0.03	24.4
Case length, in	60	0.80	8.80
Case Diameter, in	18	0.80	4.00
Case thickens, in	0.62	0.00	0.05
Scaled Distance, Z, in/lb$^{1/3}$	12.1	0.008	0.70
Concrete Thickness, T, in	84	2.00	9.23
Compressive strength, f'_c, psi	13815	1535	5067
Reinforcement Spacing, S, in	11.8	1.25	7.16
Reinforcement Ratio, ρ	0.025	0.0005	0.0054

4.4.9. Summary of design guidelines

Three different cross-sections named Type I, Type II and Type III were defined based on the probable damage to the section for a selected charge weight-standoff combination. Type I has the highest flexural capacity, although it has the cross-section that can sustain the lowest damage with reference to 2^o of support rotation. Type II and III cross-sections possess the same capacity, although the latter can sustain additional damage up to 12^o of support rotation, with additional reinforcement.

Concrete shear strength is considered only for Type I cross-sections where both cover concretes remain uncracked. Although cover concrete is cracked, the concrete core

remains intact in both Type II and Type III cross-sections, which is not considered in the shear capacity. Considerable shear resistance can be attained at least from Type II cross-section where the whole section is considered to remain intact.

Loading is categorised as close range ($Z \leq 3$ ft/lb$^{1/3}$ or 1.2 m/kg$^{1/3}$) and far range depending on the potential charge weight, standoff distance combination. Both design procedures and capacities of cross-sections are different for the two ranges. However, the close range and far range classification and available cross-sections were interpreted differently by authors (Garfield, 2011) as in Table 4.10.

Table 4.10: Modified Scaled distance classification and cross-section availability (Source: Garfield, 2011)

Cross-section	Range classification	Applicable scaled distance			
		Garfield T. (2011)		UFC 3-340 (2008)	
		Imperial (ft/lb$^{1/3}$)	Metric (m/kg$^{1/3}$)	Imperial (ft/lb$^{1/3}$)	Metric (m/kg$^{1/3}$)
Type I	Far range	$Z > 2$	$Z > 0.8$	$Z > 3$	$Z > 1.2$
Type II	Intermediate range	$1 < Z \leq 2$	$0.4 < Z \leq 0.8$	$Z \leq 3$	$Z \leq 1.2$
Type III	Close range	$Z \leq 1$	$Z \leq 0.4$		

However, experimental studies conducted on RC panels, show spalling is exhibited even in sections exposed to scaled distances around 1 m/kg$^{1/3}$, which could not be designed as Type I sections.

Rate enhancement factors (DIF) were defined based on the average strain rates of about 2×10^{-4} S^{-1}, which is considerably lower than the strain rates observed in experimental studies. However, use of tabulated values for DIF is more convenient than calculating separately for different loading scenarios.

Minimum strengths which could be used for the materials were also defined in separate clauses of UFC 3-340. The minimum yield strength of 60000 psi (413 MPa) for reinforcing steel and minimum compressive strength of 4000 psi (27.5 MPa) was recommended for the protective design. Furthermore, the use of larger bar sizes (#14 and larger), bundled bars and welding of the bars were discouraged.

UFC 3-340 provides practical and considerably straightforward design procedures for the rather complex art of protective construction. The flexural capacity of all three cross-section types is applicable while shear capacity prediction of both Type II and Type III cross-sections are conservative along with the rate enhancement predictions. Despite the conservativeness, UFC 3-340 remains the only design guideline available protective design guideline for reinforced concrete.

Appendices A-II and A-III provide example design calculation and spalling and section breach threshold calculation respectively, for a facade panel which will be used in numerical and analytical model developments.

CHAPTER 5

NUMERICAL MODEL DEVELOPMENT USING EXPLOSIVE FIELD TESTS

5.1. Introduction

The development of a finite element model (FEM) is detailed in this chapter. The calibrated and verified numerical model will then be used as the analysis tool to investigate the performance of reinforced concrete cladding panels subjected to explosive loading over a range of variables.

An initial description of the experimental data used for the FEM calibration and verification will be presented. The experimental studies cover three different types of boundary/support conditions typically encountered in construction (two of which are specifically used with reinforced concrete cladding panels), three different concrete compressive strengths and two different reinforcement layouts. The explosive charge weights range from 0.13kg to 5.5kg of equivalent TNT for the selected experimental tests.

A detailed description and justification of element and material formulation, material models, boundary and loading conditions is then given. A comprehensive account of the different modelling and simplification techniques utilised and their impacts will be further discussed. Finally, a comparison of the numerical results with the available experimental results is presented. The developed model which exhibits an optimum calibration with experimental results was selected for further verification and parametric studies.

5.2. Explosive Field Tests of University of Melbourne

A large scale experimental study was conducted by Pham (2010) to investigate the blast loading performance of reinforced concrete cladding panels. Concrete panel dimensions were utilised from realistic cladding panels (Brookes, 1998), and scaled down by a factor of 0.5. Test panels were fixed to a high strength concrete bunker (Figure 5.1.a and5.1.b) prior to testing. The connections were of either angle cleat type or the dowel

type (explained later). All six panels were subjected to 5kg of Ammonite charges, which is equivalent to 5.5kg of TNT, at a clear standoff distance of 2 m. Figure 5.1 illustrates the testing procedure carried out including the safety bunker used for the measuring equipment.

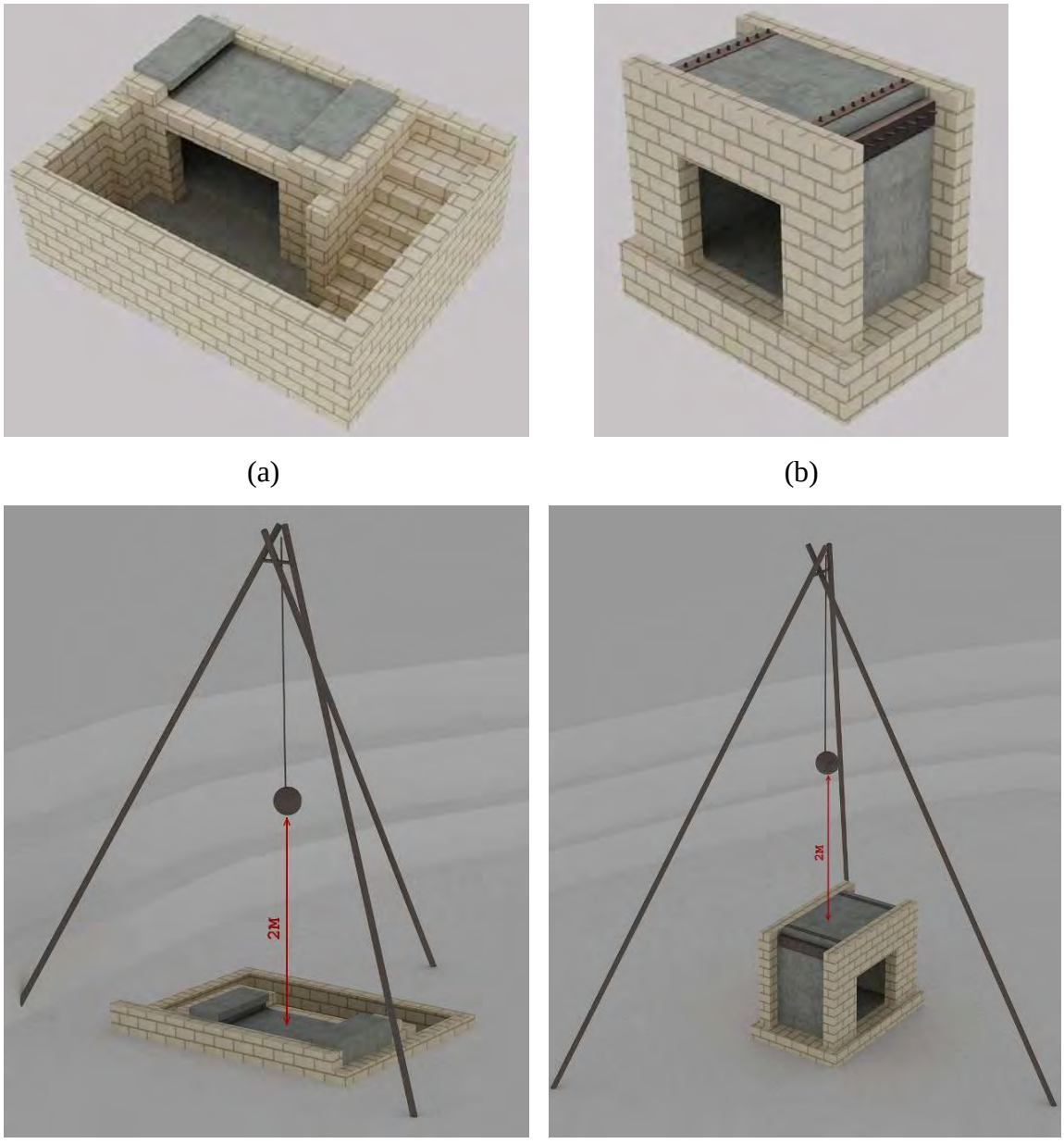

Figure 5.1: (a) Type A test bunker with panel installed, (b) Type B test bunker with panel installed, (c) Type A test bunker with charge weight installed and (d) Type B test bunker with charge weight installed (Source: Pham, 2010)

Two different HSC bunkers were constructed to install the two panel types, one for dowel connected panel (Type A, Figure 5.1.a) and one for angle cleat connected panels (Type B, Figure 5.1.b). The different bunkers were used due to different

connection/fixing configurations. Once the panel was fixed to the bunker, measuring instruments were installed. The Type A bunker was also filled with sand to level with the panel, in order to minimise the clearing effects on the edges of the panel. However, Type B panels were not covered as it was used for repetitive testing up to five times (Five angle cleat connected panels).

5.2.1. Test Specimens

Five precast concrete panels of 1700 (Long) ×1000 (Wide) ×80 (Thick) mm and one panel of 1500 (L) ×1000 (W) ×80 (T) mm were cast for the experimental evaluation. The 1700mm panels were connected to the test bunkers using the angle cleat connections (as in Figure 5.1.(b)), in a way such that the effective length of the specimen would be equal to that of the Type A panel. Connection detail of the Type A panel is illustrated in Figure 5.1.(a).

Table 5.1: Geometry and connection details of test panels (Source: Pham, 2010)

Panel ID	Dim.(mm) (L×W×T)	Concrete Strength (MPa)	Reinforcement (f_y=630 MPa and ρ = 0.00245)	Connection		Number of bolts	
				Type	Dim (mm)	Hor.	Ver.
A1	1500×1000×80	46	N5@100 mm both faces and directions	Dowel (Plate)	1000×260×20	N/A	8M18
B1	1700×1000×80	43	As above	Angle cleat	100×100×8	9M20	9M20
B2	1700×1000×80	43	As above	Angle cleat	100×100×10	9M20	9M20
B3	1700×1000×80	43	As above	Angle cleat	100×100×10	9M12	9M20
B4	1700×1000×80	43	As above	Angle cleat	100×100×10	3M12	9M20
B5	1700×1000×80	43	As above	Angle cleat	100×100×10	3M16	9M20

All six specimens were reinforced with N5 reinforcing bars of 630MPa at 100mm intervals, in both longitudinal and transverse directions. This reinforcement arrangement was used in both tensile and compression layers with a reinforcement ratio of 0.00245. Table 5.1 illustrates the dimensions, material properties and connection details of the six panels. Additional details on fixing assemblies including bolt configuration are given in Section 5.2.3.

5.2.2. Material Properties

Test panels were cast using the same mix proportions, but with different batches of concrete. Hence, different compressive strengths of 46 MPa for the dowel-type panel (Type A) and 43 MPa for the angle cleat type panels (Type B) were resulted. The compressive strengths were measured on the test day using the standard cylinder testing process according to AS1012.9 (1999).

Mechanical properties of steel reinforcement, steel fixing assemblies and bolting materials were measured according to BSEN 10002-1 (2001). A summary of material properties for both concrete and steel is presented in Table 5.2.

Table 5.2: Material Properties and testing standards

Material		Property	Standard	Strength
Concrete	Type A	Compressive strength (f'_c)	AS 1012.9	46 MPa
	Type B			43 MPa
Reinforcement		Yield strength (f_y)	BSEN 10002-1:1992	630 MPa
		Tensile strength (f_u)		660 MPa
		Ultimate elongation		14.4%
Bolts		Tensile strength (f_u)	BSEN 10002-1:1992	800 MPa
Steel angles and Plates		Yield strength (f_y)	BSEN 10002-1:1992	300 MPa
		Tensile strength (f_u)		360 MPa

5.2.3. Fixing assemblies

Two typical fixing assemblies used in different design guidelines were selected for the study, namely dowel connection and angle cleat connection (Brookes, 1998). These fixing assemblies are given in Figure 5.2.

Dowel type assembly Angle cleat type assembly

Figure 5.2: Typical fixing assemblies for concrete panels (Source: Brookes, 1998)

In this study, slightly modified connection details were utilised. A steel plate was embedded as the dowel instead of a typical threaded bar for dowel connections. No modifications on angle cleat connections were performed except for the introduction of bolts as restraining mechanism. Details of the two fixing assemblies utilised are given in Figures 5.3 and 5.4 respectively.

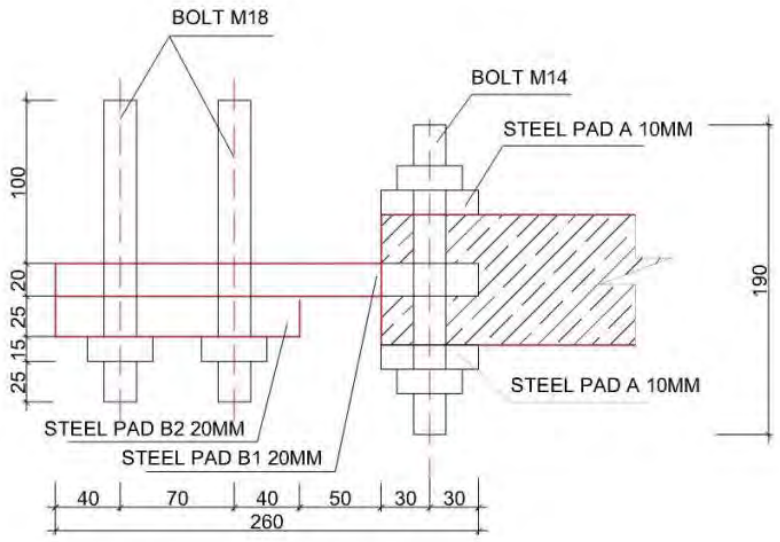

Figure 5.3: Dowel type fixing assembly (Source: Pham, 2010)

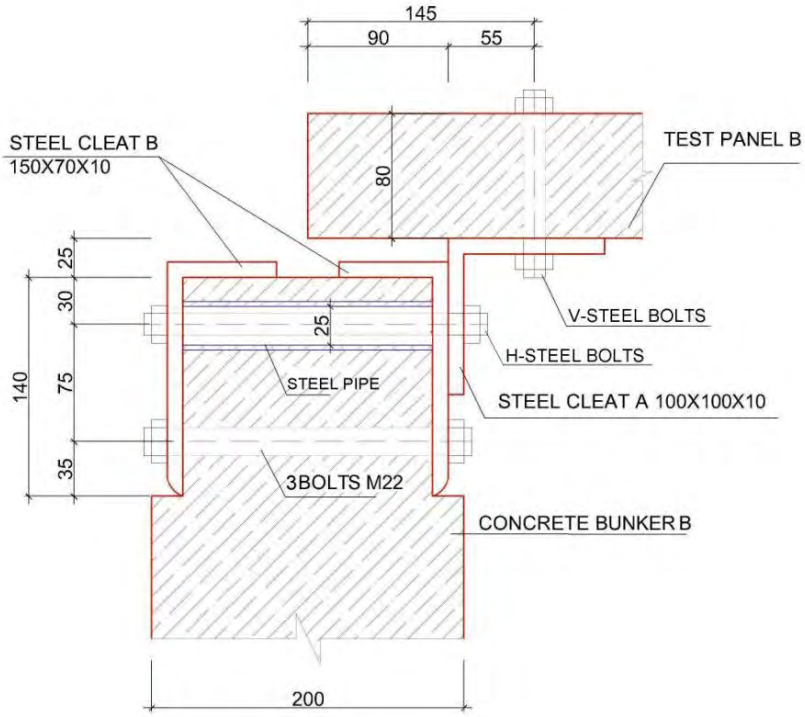

Figure 5.4: Angle cleat type fixing assembly (Source: Pham, 2010)

Constructed panels were connected to test bunkers made of 98MPa HSC through the selected fixing assemblies. The perimeter walls of the bunkers were constructed with brick veneer as shown in Figure 5.1. Once the panels were fixed to the test bunkers, both panel types were considered to have the same effective length of 1440 mm. Before testing, measures were taken to reduce the clearing effects of the explosives, such as the top surface of the panel being in line with the ground surface.

5.2.4. Explosive materials

Ammonite was used as the explosive material for the blast pressure generation, with a TNT equivalence of 1.1. Ammonite is considered as a civilian explosive, which is an approximately 80/20 mix of TNT and Ammonium Nitrate. All six panels were tested with 5 kg of Ammonite (considered as 5.5 kg of Equivalent TNT) spherical explosive charges at 2 m clear distance, each having a diameter of 213 mm (a standoff distance of 2.1065 m). This combination of charge weight-standoff distance accounts for a scaled distance of 1.193 m/kg$^{1/3}$, which is considered as a medium-far range explosive loading.

5.2.5. Test Procedure

Three initial blast trials of 0.1 kg, 0.5 kg and 5 kg at standoff distances of 1 m, 1 m and 2 m were conducted to calibrate the explosives and measuring instruments. Three spherical explosive charges that used were of 58 mm, 99 mm and 213 mm in diameter respectively.

Six identical 5 kg Ammonite charges of 213 mm diameter were used for the testing of six panels. Panels were tested as slabs and explosive charges were mounted 2 m vertically from the top surface of the panel (Figures 5.1.a and 5.1.b). Explosive charges were detonated using electrical detonators connected to the explosive from a safe distance of 400 m.

Blast pressure measurements were recorded only for the initial trials, where time-dependent pressure measurements were recorded for the initial 0.5 kg and 5 kg ammonite charges. The initial detonation of 0.1 kg charge was used as an equipment calibration detonation and was not reported. Pressure and impulse measurements were not recorded during the panel testing due to the equipment safety requirements. Two mechanical devices were installed to measure the mid-point and support deflection response, which were limited to the maximum and residual displacements. After the detonation, crack patterns were recorded for both surfaces of each panel.

5.2.6. Test results

5.2.6.1. Blast pressure histories

Blast pressure measurements (reflected) were recorded for the 0.5 kg and 5 kg ammonite charges, using pressure transducers installed for the initial trials. The impulse time history for the reflected pressure was generated integrating the reflected pressure time history. Table 5.3 summarises the pressure and impulse for the two explosive events. Similar pressure and impulse combinations were assumed for the actual panel tests as no measurements were taken during the six explosive trials.

Table 5.3: Summary of blast pressure and Impulse

Charge weight* (kg)	Standoff Distance (m)	Scaled Distance ($m/kg^{1/3}$)	Peak reflected pressure (kPa)	Peak Reflected impulse (kPa.ms)
0.55	1.0495	1.281	1709	332
5.5	2.1065	1.193	2488	791

*: Equivalent TNT weight

5.2.6.2. Panel displacements

Ultimate and residual panel displacements were measured for all six blast trials. Both inward and outward measurements were taken at the panel centre as well as at the support. A summary of maximum displacement values recorded for the six panels is listed in Table 5.4.

Table 5.4: Displacement Summary for test panels

Panel ID	Central Displacement		Support Displacement	
	Inward (mm)	*Rebound* (mm)	*Inward* (mm)	*Rebound* (mm)
A1	38.5	10	3.50	0.00
B1	28.9	14.5	4.80	3.90
B2	24.4	22.5	1.70	1.00
B3	24.5	19.2	1.90	1.30
B4	23.7	11.5	5.50 (10)	3.40 (5.9)
B5	25.7	15.7	3.80	3.20

Note: Values within brackets were measured from the failed fixing assemblies

5.2.6.3. Post blast crack survey results

A comprehensive crack survey was carried out on the test panels after testing while attached to the test bunkers. Crack widths, location and lengths of individual cracks were measured and recorded for all the test panels. Cracks in both front and back faces were recorded. A summary of crack width and locations are summarised in Table 5.5.

Table 5.5: Crack pattern summary

Panel	Surface	No. of cracks	Angle (degree)	Crack width (mm)	Crack span full length	Distance to centre (mm)
A1	Top	1	0.00	1.74	Yes	0
	Bottom	3	0.00	2.60	Yes	27
B1	Top	3	0.00	0.02	Yes	-132
	Bottom	5	0.00	0.87	Yes	111
B2	Top	3	0.00	0.18	Yes	0
	Bottom	5	0.00	0.77	Yes	0
B3	Top	1	0.00	0.10	Yes	0
	Bottom	5	0.00	0.73	Yes	-53
B4	Top	1	0.00	0.02	Yes	0
	Bottom	3	4.50	0.66	Yes	-265
B5	Top	2	0.00	0.03	Yes	0
	Bottom	4	0.00	0.48	Yes	0

Note: (-) for distance is when the crack is located left of the centreline of the slab

In general, each panel was observed with three to five cracks on the bottom surface of the panel and one to three cracks on the exposed surface of the panel. Panel A1 suffered moderate to severe cracking. The largest crack widths of 2.6 mm and 1.7 mm were recorded on the bottom and top surfaces respectively. The cracks on the bottom surface were found to be tensile in nature and the single crack found on the exposed surface was compressive with the crushing of concrete.

All Type B panels exhibited minor tensile cracking on both surfaces where crack widths of less than 1 mm were recorded. The largest crack width of 0.87 mm was recorded in Panel B1 and smallest of 0.48 mm was recorded in Panel B5 for the bottom surface. All tensile cracks on the exposed surface were less than 0.2 mm wide, which were due to the rebound of the panel, after the initial downward deflection. These crack patterns (compressive) were compared with stress patterns predicted by the finite element model as a method of verification, later in the chapter. No local damage was recorded in either Panel A1 or Panels B1 to B5.

5.3. Explosive Field tests by National University of Defence Technology, China

A recent experimental study conducted with scaled down concrete panels by Wang et al. (2012) to observe the scalability of blast resistance of reinforced concrete panels will also be used as a verification for the developed finite element models. Six square reinforced concrete panels of varying dimensions were exposed to explosive charges of 0.13 kg to 0.94 kg. The standoff distances were selected to match the charge weights to achieve scaled distances of 0.518 m/ $kg^{1/3}$ and 0.591 m/$kg^{1/3}$.

5.3.1. Test specimens

Six scaled down panels with cube strengths of 39.5 MPa concrete, were tested with varying charge weights. All square panels had a length to depth ratio of 25. The panels were rigidly clamped at two ends with the other two left unsupported as shown in Figure 5.5.(a). A detail of the fixing assembly is illustrated in Figure 5.5.(b). The top surface of the concrete panel was clamped to the test frame using a timber plank in order to prevent the movement of the panel during the testing. These supports were idealised as fixed supports in the verification of the finite element model. Panel dimensions, material strengths, reinforcement details and explosive charge weight details are listed in Table 5.6.

(a) (b)

Figure 5.5: Fixing assembly detail for test panels (Source: Wang et al., 2012)

Table 5.6: Details of Test Specimens (Source: Wang et al., 2012)

Panel ID	Dim. (mm) (L×W×T)	Conc. Str. (MPa)	Reinforce-ment	Explosive Charges			
				Wgt (kg)	Std. off (m)	Dia. (mm)	Hgt. (mm)
A	750×750×30	39.5 (Cube strength)	T(600)@ 75 mm, both direction, single layer	0.13	0.3	23.5	46.9
B	750×750×30			0.19	0.3	26.6	53.3
C	1000×1000×40			0.31	0.4	31.4	62.7
D	1000×1000×40			0.46	0.4	35.8	71.5
E	1250×1250×50			0.64	0.5	39.9	79.9
F	1250×1250×50			0.94	0.5	45.4	90.8

Note: Explosive charges were cylindrical in shape. Diameter (Dia.) and Height (Hgt) is listed in the last two columns of Table 5.6

5.3.2. Material Properties

A summary of material properties used is given in Table 5.7.

Table 5.7: Material Properties (Source: Wang et al., 2012)

Material	Property	Strength (MPa)
Concrete	Compressive Strength (f'_c)	39.5 (31.6 equivalent cylinder strength)
	Elastic modulus (E_c)	28300
	Tensile Strength (f_t)	4.2
Reinforcing Steel	Yield Strength (f_y)	600
	Elastic Modulus (E_s)	200,000

Tri-nitro-toluene (TNT) was used as the explosive material hence, a TNT equivalency of unity was used.

5.3.3. Test Procedure

The idealised boundary condition is described as fixed with timber restraining the vertical deflection and rotation in support. Panels (A-F) were tested sequentially with six different charge weights having the dimensions given in Table 5.6.

Blast pressure measurements were not recorded for any of the six tests conducted. However, responses of the reinforced concrete panels were recorded in terms of mid-panel deflection (maximum) and the spalling and scabbing dimensions.

5.3.4. Test results

5.3.4.1. Panel Displacements

The maximum mid-panel displacements were measured for all six specimens and are presented in Table 5.8. The measurements were limited to maximum downward deflections only, as neither deflection time history nor the rebound deflections were recorded. Normalised deflection (deflection to thickness ratio) is also presented along with the mid-panel deflection.

Table 5.8: Panel Deflection summary

Panel ID	Deflection (δ) (mm)	(δ/t)
A	9	0.30
B	26	0.87
C	15	0.375
D	35	0.875
E	19	0.38
F	40	0.80

5.3.4.2. Local damage in panels

Local damage in panels by means of concrete spalling (spalling radius) were measured after each detonation and presented in Table 5.9. Spalling radius was defined as the measured spalling area fit to a circular shape with radius of this area, defined as the spalling radius. No measurements were recorded for scabbing. Normalised spalling radius (spalling radius to thickness ratio) is also presented.

Table 5.9: Panel spalling summary

Panel ID	Spall radius (r) (mm)	(r/t)
A	50	1.67
B	85	2.83
C	90	2.25
D	120	3.0
E	120	2.4
F	185	3.7

All panels suffered local damage either in the form of scabbing or spalling. Flexural cracks were also observed in all panels, which were not documented in any great detail. Only panel F suffered extensive local damage which perforated the cross-section. The damage observed is justifiable as this panel was exposed to the biggest charge weight. In general, larger panels exhibited higher damage and increased mid-panel deflections due to the size effect.

5.4. Summary of explosive field tests

The study conducted by the University of Melbourne used a constant standoff distance of 1.193 m/kg$^{1/3}$, which is considered a medium-far range explosive event. Standoff combinations of 0.518 m/kg$^{1/3}$ and 0.591 m/kg$^{1/3}$ were selected for the study conducted by the National University of Defence Technology, China, which is considered as close range explosive events. These two studies cover both close range and far range explosive events. In addition, one of these experimental studies (Pham, 2010) is a dedicated experimental study on facade panels with actual fixing assemblies, and none of the other experimental studies was directly addressing the facade systems.

These studies also feature three different compressive strengths of concrete, 39.5 MPa (cube strength), 43 MPa and 46 MPa (Cylinder strength). Conversion of cube strength of 39.5 MPa to cylinder strength yields equivalent cylinder strength of 31.6 MPa as the compressive strength. This range (i.e. 30 – 46 MPa), is within the range specified by the UFC 3-340 (f'_c > 27.6 MPa) (United States Army Corps of Engineers, 2008) for the construction of protective structures. In addition, the two studies have different reinforcing arrangements, i.e. single layer and two layers.

The connection details include two typical connections used in facade systems and one idealised connection. In addition, the angle cleat type connection features different fixities representing a range of different stiffness' in connections.

These two studies with the variables discussed above can be utilised for the calibration and validation of the numerical model.

5.5. Finite Element Modelling with LS-DYNA

Among the currently available finite element (FE) modelling packages LS-DYNA (2013) was selected as the FE package for this study, based on the reviews conducted in Chapters 3 and 4. It was observed in many previous studies that LS-DYNA was preferred over other finite element programs for numerical modelling of both close range and far range explosives. In comparison with other leading FE packages for modelling high energy related problems, LS-DYNA has the added advantage of inbuilt loading function for the air blast loading (Randers-Pehrson and Bannister, 1997). Considering the material models, LS-DYNA is built with most of the leading concrete and reinforcement material models, which is essential in this study. Some of these concrete material models are capable of automatic parameter generation for the stress-strain relationships for concrete, using the uniaxial compressive strength (f'_c). This is an added advantage in case the stress-strain relationship for concrete is unknown. Furthermore, the current version of LS-DYNA is built with an improved reinforcement coupling algorithm, which eradicates the problems associated with the energy balance of the system. Considering all these factors and those discussed in previous chapters, availability and the user familiarity, LS-DYNA was selected as the FE modeller for this study.

LS-DYNA is based on the keyword format for the creation and control of the FE model. The keyword pre-processor LS-PrePost is used for the numerical model building.

5.5.1. Geometry and Meshing

Geometry of the panel systems (both dowel connected (Type A) and angle cleat connected (Type B)) were selected to closely match the exact geometry of the experimental study, minimising the approximations and assumptions. All elements related to cladding panels and connection assemblies were modelled including the connecting bolts. In order to cater for the lack of fixity for the model, all contacts that

involve the bunker are defined as rigid-wall types, which will be discussed later in the chapter.

Meshing is one of the most important aspects of finite element modelling. Theoretically, finer meshes produce more accurate results, although analysis times and computer usage increase rapidly with the higher number of elements. A preliminary analysis was carried out with the Type A panel for meshing and accuracy using different element sizes. Element sizes (solid) were varied from 5 mm to 20 mm in the thickness direction and 10 mm to 40 mm in length and width directions. Accuracy by means of error percentages for mid and support deflections, peak reflected pressure and analysis times were recorded for the formulation.

Each model consists of 6744 beam elements (for reinforcements and connecting bolts) and 2600 solid elements for the steel plate sections, in addition to the hexahedral solid elements which represent the concrete panel. The analysis was carried out on a computer with 8 Gigabytes of Random Access Memory (RAM) and Intel Pentium Core i5 (2.27 Mhz) processor. The initial mesh sensitivity study was limited to a 20 ms analysis of explosive loading (5.5 kg of TNT at a standoff distance of 2.1065 m), where convergence was observed for most of the panels. Actual analysis times varied from 25 mins for the 40mm mesh model to almost 5 hours for the 5 mm model.

Table 5.10: Mesh sensitivity analysis for numerical model development

Mesh Size			No. of elements	Analysis Time	Peak reflected Pressure (kPa)	Mid-Point Def. (mm) (error)	Support Def. (mm) (error)
X (mm)	Y (mm)	Z (mm)					
10	10	5	244544	04:52:23	2540.9	No conv.	4.32 (23%)
10	10	10	126944	01:56:54	2540.3	No conv.	1.94 (-45%)
20	10	10	68144	01:09:05	2540.6	32.4 (-16%)	2.66 (-24%)
10	20	10	68144	01:10:54	2541.7	31.5 (-18%)	1.91 (-45%)
20	20	10	38744	00:45:31	2541.9	31.3 (-19%)	3.24 (-7%)
20	20	20	24344	00:29:44	2540.7	28.5 (-26%)	2.20 (-37%)
20	40	20	16844	00:25:10	2544.7	26.2 (-32%)	2.23 (-36%)

No conv.: No convergence observed, deflection kept increasing

No significant variation was observed for mid-panel peak reflected pressure, as seen in Table 5.10. This is due to the fact that the inbuilt blast pressure prediction methodology (discussed later) is independent of the mesh size of the target structure. Although, no definite pattern was observed with support deflection, mid-panel deflection was increased with the reduction in element size. In comparison with the deflection recorded during the experimental study, three panels of 20 mm element size (10 mm in the thickness direction) were found to have the best correlation, in terms of mid-panel deflection. Among these three mesh sizes, 20×20×10 mm mesh predicts the support deflection with greater accuracy than other two mesh sizes. Considering the deflection results and analysis times observed in numerical simulations, the mesh size of 20×20×10 mm was selected for further analysis. Maximum deflections in both mid-panel and support were found to be within the acceptable limit of 20% error margin (Li and Hao, 2011) for the selected mesh size.

5.5.2. Material modelling

Material modelling is an important aspect of the finite element formulation. A proficient material model should be able to represent the material as exactly as it behaves in reality. However, material models will behave as predicted only with certain conditions due to approximations, assumptions and importantly mesh size as well. Hence, it is important to understand the material model behaviour to match with the required outcome.

5.5.2.1. Concrete material models

Three different concrete material models were selected for the initial calibration of the finite element model, named as the Concrete Damage Model (CDM) (MAT_072R3), the Winfrith Concrete Model (WCM) (MAT_084) and the Continuous Surface Cap Model (CSCM) (MAT_159) as discussed in Chapter 3. These material models were successfully used previously in representing concrete under the effects of explosive loading (Wang et al., 2008, Garfield et al., 2011, Pantelides et al., 2012, Pham, 2010, Tanapornraweekit et al., 2007, Pham et al., 2008, Raman et al., 2013, Vasudevan, 2013, Ågårdh, 1997). In addition, all three material models are capable of strain rate enhancement, confining effects, shear dilation, strain hardening and post peak softening. Furthermore, all three material models were simple input material models, where stress-strain relationships were generated using the uniaxial compressive strength of concrete

(f'_c). Besides the simple input concrete models, a manually calibrated version of the Concrete Damage Model (Markovich et al., 2011) was also used along with the other three models. Theoretical formulation of material models and application of material models will be discussed in this section.

5.5.2.1.1. Concrete Damage Model (MAT_072R3)

The three invariant Concrete Damage Model (CDM) was initially developed using the two invariant Pseudo Tensor (MAT_016) model and was introduced to DYNA3D in 1994 as an extension to Pseudo Tensor material model (Malvar et al., 1995). The second version of CDM was introduced in 1996 (Malvar et al.), which is considered as the basis for the current version of CDM (MAT_072R3 in LS-DYNA). The current version of CDM was released in 1999, which includes the automatic parameter generation using the uniaxial compressive strength of concrete (f'_c). The automatic parameter generation has made the CDM one of the easiest to use concrete material models in dynamic and impulsive loading regimes.

Theoretical formulation and keyword implementation of the CDM is freely accessible via the LS-DYNA Theory manual (Livermore Software Technology Corporation, 2013c) and LS-DYNA keyword user manual (Livermore Software Technology Corporation, 2013d), respectively.

5.5.2.1.2. Continuous Surface Cap Model (MAT_159)

The continuous surface cap model (CSCM) was developed in the early 1990s with the intention of assessing the safety of roadside structures and introduced to LS-DYNA in 2005. As in the CDM, the CSCM is also capable of automatic parameter generation through the uniaxial compressive strength ($f'c$). However, theoretical formulation of the CSCM is significantly different to that of the CDM, which is accessible freely via the LS-DYNA Theory manual (Livermore Software Technology Corporation, 2013c). Keyword definition and the implementation procedure for the CSCM material model is presented in LS-DYNA keyword user manual (Livermore Software Technology Corporation, 2013b).

5.5.2.1.3. Winfrith Concrete Model (MAT_084/085)

The Winfrith Concrete Model (WCM) was originally developed in the 1980s in order to assess reinforced concrete structures subjected to impact loading. The same version was later introduced to LS-DYNA in 1991 (Wu et al., 2012). The theoretical formulation of the WCM is presented in LS-DYNA Theory manual (Livermore Software Technology Corporation, 2013c) while keyword definition and implementation is presented in LS-DYNA Keyword user manual (Livermore Software Technology Corporation, 2013b).

5.5.2.1.4. Concrete Damage Model with manual calibration (MAT_072)

Markovich et. al (2011) studied the softening behaviour of the CDM with different confinement pressures and observed that the softening behaviour is under-predicted, in comparison with the experimental results (Attard and Setunge, 1996). Modifications were proposed for the automatic parameter generation for the three stress surfaces, softening parameters and volumetric response parameters. Since the automatic parameter generation was not available for the proposed model, parameters were generated using the proposed set of equations. The volumetric response was modelled using the relationship proposed by Unossen (2000). The material model will be identified as the Ben-Gurion University (BGU) concrete model for the rest of this thesis.

The triaxial behavior of the CDM and the BGU concrete model was compared with the Attard and Setunge (1996) triaxial tests on 50 MPa and 100 MPa concretes as shown in Figures 5.6 and 5.7 respectively. A comparison of absorbed energy revealed better agreement between the test results and the BGU formulation, especially with low confining stresses. Although the BGU model has not been used for the simulation of concrete structures subjected to explosive loading, material model calibration results indicate better performance than the original CDM. Hence, the BGU concrete model was also used as a concrete material model in initial calibration.

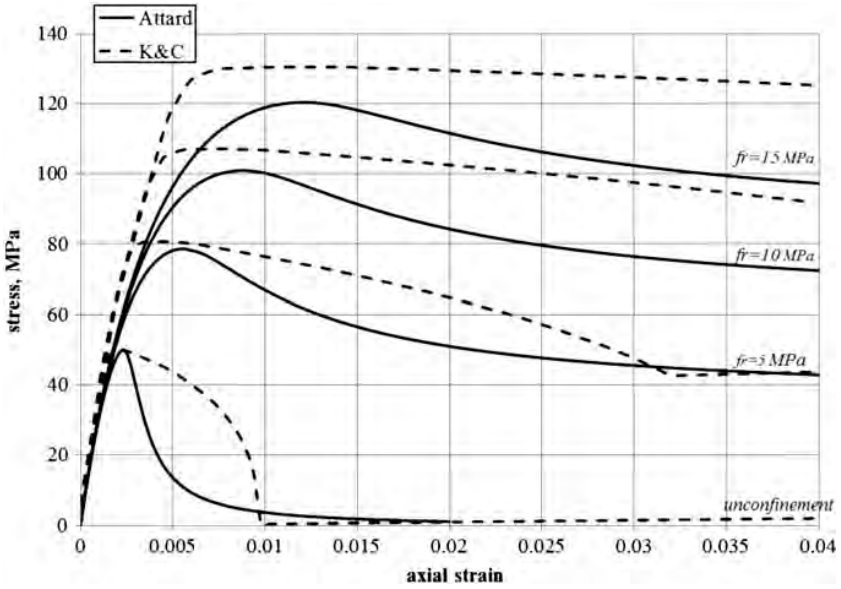

Figure 5.6: Comparison of BGU model with CDM and experimental and experimental results for 50 MPa concrete (Source: Markovich et al., 2011)

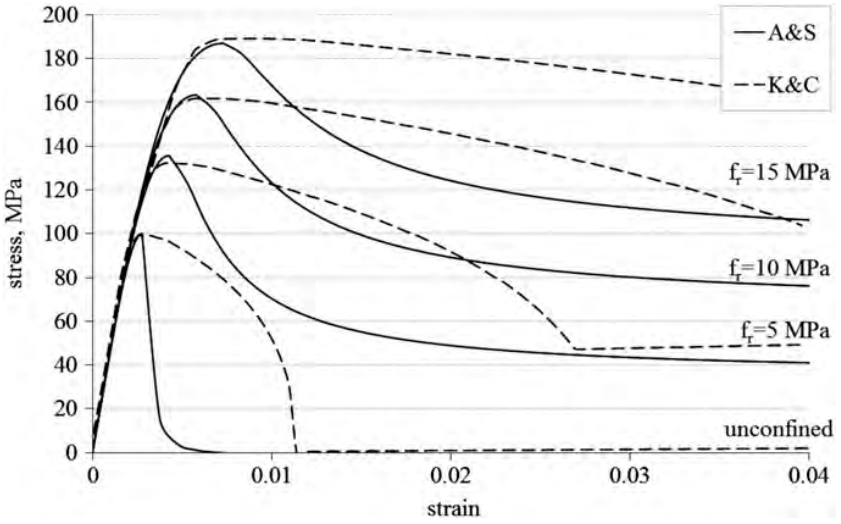

Figure 5.7: Comparison of BGU model with CDM and experimental and experimental results for 100 MPa concrete (Source: Markovich et al., 2011)

5.5.2.2. Reinforcement material models

Two different material models, Plastic Kinematic (PK) (MAT_003) and simplified Johnson-Cook (SJC) (MAT_098), were selected for the representation of reinforcement. Although the Johnson-Cook model is limited to solid and shell elements, a simplified version of the same model is capable of modelling beam elements as well.

5.5.2.2.1. Plastic Kinematic Model (PK) (MAT_003)

The Plastic kinematic material model is one of the most efficient metal plasticity models in LS-DYNA. Although this model lacks a failure criterion and strain softening effects, this is the most suitable material model to be used when exact stress-strain relationships are not available. The Plastic kinematic model is based purely on the yield strength (f_y) and elastic modulus of steel (E_s). If the tangent modulus is defined, strain hardening will occur, otherwise perfect plasticity is assumed. In the case of strain hardening considered, both isotropic hardening and kinematic hardening options are available to use.

The PK model is also equipped with rate enhancement options, delivered via the Cowper-Symonds (1957) rate enhancement model. The rate enhancement is applied multiplying the yield strength of material with rate enhancement factor as in Equation 5.1.

$$k = 1 + \left(\frac{\dot{\varepsilon}}{C}\right)^{1/p} \tag{5.1}$$

Where;

$\dot{\varepsilon}$ = Strain rate

C, P = Material constants

The Plastic kinematic model was used as the reinforcement material model in reinforced concrete structures subjected to explosive loading (Tanapornraweekit et al., 2007, Pham et al., 2008, Raman, 2008, Wang et al., 2008, Tai et al., 2011, Vasudevan, 2013). This material model is useful, especially in the case of scarcity in available stress-strain relationships, where yield strength, density and elastic modulus are the only known material parameters.

5.5.2.2.2. Simplified Johnson-Cook (SJC) model (MAT_098)

Originally defined for the analysis of metals subjected to large strains and high temperatures (Johnson and Cook, 1983), the simplified version of the Johnson-Cook (SJC) material model is defined specifically to be used in beam and truss elements, where the original JC material model is incapable. As for the simplification, damage accumulation and thermal effects have been omitted, which makes the analysis up to 50% faster than the original JC model (Livermore Software Technology Corporation,

2013a,b). The SJC model uses the following relationship (Equation 5.2) to represent the stress (as a function of strain).

$$\sigma_y = \left(A + B\bar{\varepsilon}^{p^n}\right)(1 + ln\dot{\varepsilon}*) \quad (5.2)$$

Where;

A, B, n = Material constants

$\bar{\varepsilon}^p$ = Effective plastic strain

$\dot{\varepsilon}*$ = Effective total strain rate (strain rate / quasi-static threshold rate)

In the case of 1-D elements (beams and trusses), both effective plastic strain and strain rate are based on the axial strains in compression or tension.

The Johnson-Cook material model has been used to model reinforcement in blast resistance applications (Zhou et al., 2008), using the full version of JC model in ANSYS AUTODYN. Given the calibre and capabilities of the material model, the SJC model was used for the development of the numerical model in this research.

5.5.2.3. Material models for structural steel sections

Two types of structural steel sections, plate and angle cleat, were utilised in this study. Among the limited number of material models capable of using, the PK model was selected as the best option for numerical modelling of structural steel sections. The definition of the material model was similar to the reinforcement model used in the previous section, but the strength parameters, yield strength and Poisson's ratio were altered accordingly.

5.5.2.4. Material models for high strength bolts

The PK model, altered to match the properties of class 800 bolts was used as the material model for the bolt material. It is being noted that only the tensile strength of bolting material was measured during the experimental evaluation, hence the yield strength of the material was not available for definition. According to the Steel designer's Handbook (Gorenc et al., 2012) the yield strength for class 800 snug tight bolts were found to be of 640 MPa (Minimum yield strength). Therefore, the yield strength of 640 MPa, Tensile strength of 800 MPa and Poison's ratio of 0.2 was used for the high strength bolt material model definition.

5.5.3. Element formulation

Finite element formulation requires a definition of the section, either beam, shell or solid as the section for the appropriate part. In LS-DYNA, this is achieved by 'SECTION' keyword definition. Based on the type of formulation, i.e. beam, different integration rules, cross-sectional properties and nodal thicknesses were defined.

Two cross-section types were required in this study for beams and solids as no shell elements were available in the model. Among the different definitions available for the beam and solid element formulations, the Hughes-Liu formulation (Livermore Software Technology Corporation, 2013a,b) with cross-section integration for beams and constant stress element formulation (Livermore Software Technology Corporation, 2013a,b) for solids were used.

5.5.3.1. Beam element formulation

The SECTION_BEAM keyword was used for the definition of beam elements, where element formulation was selected as Hughes-Liu with cross-section integration. This type of formulation required a third node for the integration, perpendicular to the axis of the member which was defined during the meshing.

Cross-section type was selected as tubular (CST=1) since it represents the circular cross- section. For circular cross-section, the shear correction factor was equal to unity and diameters for two nodes were defined accordingly for both reinforcement and bolt cross-sections.

5.5.3.2. Solid element formulation

Solid elements were defined for concrete and structural steel sections. Solid element type 164, commonly known as constant stress solid, was used for both types of sections. Solid element type 164 is an 8 node, hexahedral element with Lagrange type formulation. The constant stress solid element is extremely efficient with computer usage and accurate to be used in the dynamic finite element analysis. Increased accuracy is observed with finer meshing, which comes with the disadvantage of increased analysis times.

5.5.4. Reinforcement/Connecting bolt coupling

Reinforcement coupling was achieved via an inbuilt keyword of ALE_COUPLING_NODAL_CONSTRAINED. This keyword is updated in the latest version of LS-DYNA (Version 9.7R7.00) instead of the CONSTRAINED_LARGRANGE_IN_SOLID keyword. This updated version was found to be more suitable for high energy related problems with energy conservation. The keyword is assembled with several coupling options for fluid-structure interaction. However, constrained acceleration and velocity is the only option available for reinforcement coupling. A perfect bond between reinforcement and concrete is assumed for the selected definition. Reinforcement/connecting bolts were defined as slaves and concrete panel/structural steel sections were defined as the master elements, accordingly. Part ID defined during the meshing was used as the slave and master types.

5.5.5. Contact definitions

Interaction between elements in a numerical model is defined by contact definitions. For the current finite element model developed, Type A panels required four contact definitions, two between steel plates and concrete with the other two between the bunker and the steel plates. Type B panels also required four contact definitions, similar to Type A panels. Since the bunker was not modelled, the contact definition between steel angles and the bunker was treated differently (i.e. as a rigid wall) which is discussed later in the chapter.

5.5.5.1. Steel/Concrete contacts

Contacts between the concrete panel and steel sections were defined as surface to surface contacts. These definitions allow separation when subjected to tensile forces in the interface. Although panels were cast with connection assemblies built into the section, friction and any tensile force transfer between the members were ignored. As in reinforcement coupling, definitions required master and slave sections, which were used as part IDs for the definition.

5.5.5.2. Bunker/Steel plate contacts

The surface of the steel section in contact with the bunker surface was defined as the rigid-wall surface and the appropriate surface nodes were selected and defined as slave

nodes. The stiffness scaling factor, which is defined as the stiffness ratio between the slave and the master, was not used since, the stiffness provided by bunker material could not be estimated.

5.5.6. Blast load application

Blast pressure generation was performed through the inbuilt LOAD_BLAST_ENHANCED keyword. Charge weight (as an equivalent weight of TNT), coordinates of the charge centre and the time of detonation were required for the definition of this keyword. Since all the models were built as symmetrical about *X* and *Y* axes, the definition of *Z* coordinate was the only requirement. The unit system of gram, millimetre, millisecond and mega Pascal (UNIT=8) was used for the definitions which was consistent with other definitions of the model. Spherical free air blast (BLAST = 2) was selected as the type of blast. Detonation time of blast (TBO) was defined negative, in order to minimise the analysis time, allowing the back calculation for the arrival time of blast wave. Death time for blast pressure (DEATH) was defined as 10 ms since, the negative pressure was negligible after 10 ms for selected charge weight-standoff distance combination. Table 5.11shows the definitions for blast pressure generation keyword.

Table 5.11: Keyword definitions for Blast load generation

Property	Definition	Value
bid	Unique identification number for blast load	1
m	Mass of equivalent TNT charge	5500 g
xbo	X coordinate of charge centre	0
ybo	Y coordinate of charge centre	0
zbo	Z coordinate of charge centre (standoff of 2106.5 mm)	2146.5 mm
tbo	Blast initiation time	-1.25 ms
blast	Blast type (Spherical selected)	2
Death	Blast pressure keyword termination time	10 ms

The blast load generation keyword is then coupled with LOAD_BLAST_SEGEMENT_SET keyword to apply the blast loading to the targeted

structure. The top surface of the concrete panel was selected as the surface accepting the blast load.

5.5.7. Analysis control

Analysis control was achieved through seven different control keywords. Most of these keywords were used with default definitions, except for termination time and energy control. Initial analysis was performed for 60 ms, until the critical deflection times were identified, then was curtailed to 30 ms. During the 30 ms interval, both maximum downward and rebound deflections were observed.

Hourglass energy, stonewall energy, sliding interface energy and Rayleigh energy (damping energy) dissipation options were included in the energy balance equations. The default LS-DYNA hourglass energy option was used with hourglass coefficient of 0.1. The time step safety factor of 0.8 was used for this study, which is lower than the recommended maximum of 0.9. Although the use of lower time step safety factor results in longer analysis time, it minimises the iteration errors thus improving accuracy. Default control definitions were used for the contact, damping and accuracy control.

5.5.8. Output control

Output control is one of the important things in numerical modelling, where output can be presented in different methods. All the output control keywords of LS-DYNA is listed under the database keyword group. In the case of explosive load related problem, it is essential to record the blast pressure time history. The BLSTFOR keyword definition is capable of recording the pressure time history for every element on the surface defined for the acceptance of blast load. The time interval between two outputs needs to be defined for the keyword.

The D3PLOT keyword is used to record almost all the variables for the output. Use of this keyword required the definition of time interval between outputs as in BLSTFOR keyword. Smaller time intervals defined for the D3PLOT and BLSTFOR keywords will yield more detailed output. Definition of smaller time intervals has a major disadvantage in output file size. Since both these output types will generate graphical outputs, these files require a much larger storage space for the analysis results. D3PLOT and BLSTFOR files were saved with time intervals of 0.1 ms for this study.

LS-DYNA provides another solution for output control and data management in terms of ASCII files. Since the small size of the files, small time intervals can be used and more accurate results can be obtained. However, these keywords need to be defined separately depending on the requirements, hence used for selected nodes and elements only. Nodal and element output results for selected nodes and elements, material summaries and global statics defining energy were saved in different ASCII files with a time interval of 0.001 ms.

5.6. Numerical model calibration

The finite element model calibration was performed using the available experimental results, comprehensively described earlier in the chapter (Pham, 2010). More specifically, Panel A1 and B2 were modelled and calibrated with all available material model combinations, and Panels B1, B3, B4 and B5 were then used only as a comparison and verification of the derived model. The verification involved an assessment of the numerical model outputs using blast pressure, mid-point and support deflections for panels as indicators.

5.6.1. Blast pressure and impulse

A comparison of pressure time histories was performed for the Panel A1 and Panel B2 against the experimental pressure time history recorded. The original model definition was to use 0.1 ms intervals for blast pressure histories. However, two curves for each numerical model with reducing the time interval between outputs to 0.01 ms and original definition of 0.1 ms were used for the comparison, as shown in Figure 5.8.

Panels A1 and B2 recorded exactly similar pressure time histories at similar time intervals. Hence, Figure 5.8 failed to illustrate the pressure time histories for the panel A1 for both time intervals, as these coincide with panel B2 results.

The pressure transducer used to record the pressure time history was installed just in front of the panel surface. Therefore, several sub-peaks were observed in the experimental pressure time history, due to the rebound of the blast wave from the panel surface. However, numerical prediction is based on the pressure measured on the surface of the panel hence, no sub-peaks were witnessed during the numerical investigation.

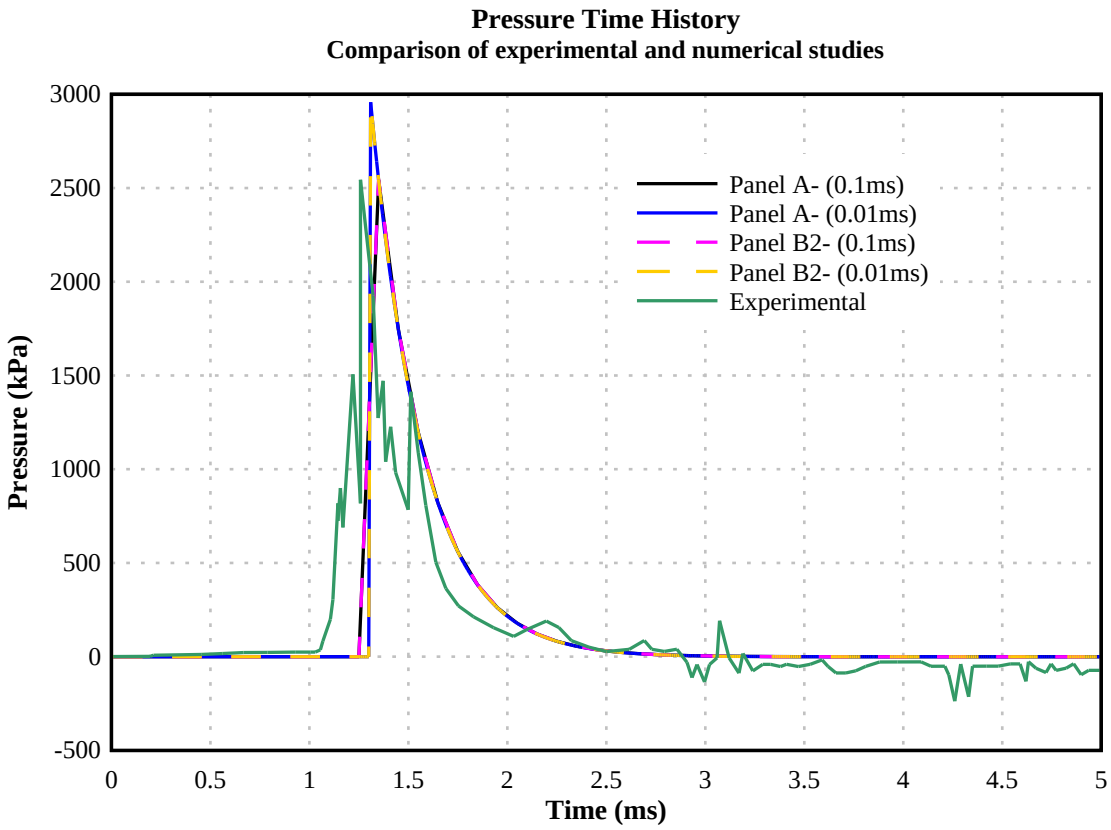

Figure 5.8: Comparison of experimental and numerical pressure time histories

The maximum reflected pressure depends on the interval between pressure recordings. A larger time interval results in smaller file size with the disadvantage of not being able to record the maximum. Maximum pressure recorded in the experimental study was 2541 kPa while 2959 kPa was recorded in the numerical study for 0.01 ms interval and 2544 kPa for 0.1 ms interval. This clearly explains the time interval dependency of the blast pressure profile. Therefore, blast pressure time history was recorded with 0.01ms time interval, although which results in a maximum of 2959 kPa.

Similar arrival times are observed with experimental and numerical simulations, after the initial time interval of -1.25 ms (Blast initiation time (tbo), Section 5.5.6) was removed from the pressure time history. Arrival time of 1.08 ms was recorded with experimental study in comparison with 1.25 ms and 1.31 ms recorded in numerical evaluations for 0.1 ms and 0.01 ms time intervals. However, the time to peak values of 1.26 ms, 1.35 ms and 1.32 ms were recorded for experimental, numerical with 0.1 ms and 0.01 ms, respectively. These numbers are compatible with the Kingery and Bulmash (1984) arrival time prediction of 1.17 ms for the selected charge weight-standoff combination.

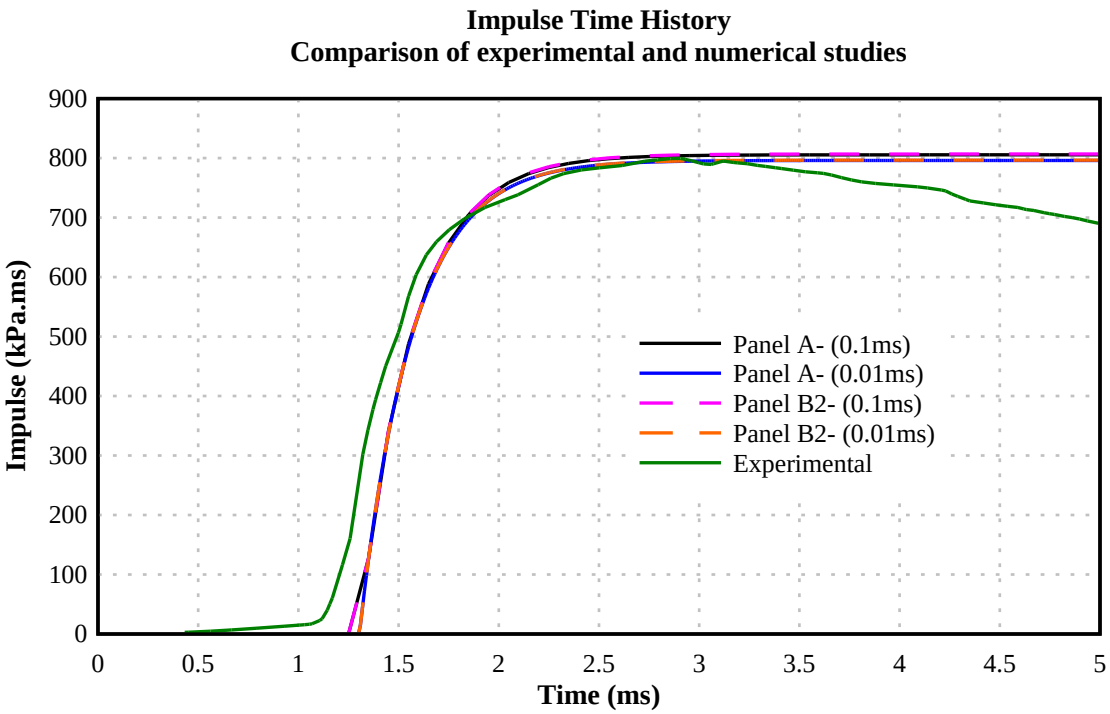

Figure 5.9: Comparison of impulse time history

Comparison of experimental and numerical predictions for impulse time history is presented in Figure 5.9. Similar to pressure time history, a small discrepancy in arrival time is observed in impulse time history as well. However, peak impulse and time to peak impulse have shown comparable results. Peak impulse of 788.95 kPa.ms was observed at 2.92 ms during the experimental evaluation. Peak impulse and time to peak impulse of 805.45 kPa.ms and 3.04 ms were recorded respectively, for both Panel A1 and panel B2 with 0.1 ms time interval. Similarly, 795.98 kPa.ms and 3.07 ms were recorded with 0.01 ms time interval.

A comparison of peak pressure, peak impulse, time to peak for pressure and impulse between experimental and two numerical values are presented in Table 5.12. Although a better comparison was observed in pressure time history for 0.1 ms time interval, 0.01 ms interval predicted the impulse time history more closely. The only reason to observe a closer peak reflected pressure with 0.1 ms was due to the missed peak value because of the larger time interval.

Table 5.12: Maximum pressure and impulse comparison

Experimental /Numerical	Panel A1/Panel B2			
	Pressure (kPa)	Time to peak (ms)	Impulse (kPa.ms)	Time to peak (ms)
Experimental	2541	1.25	788.95	2.92
Numerical (0.1 ms)	2544	1.35	805.45	3.04
Numerical (0.01 ms)	2959	1.32	795.98	3.07

5.6.2. Panel deflections – Mid-Point

The deflection time histories of the panel mid-point for numerical simulations were compared with ultimate deflection recorded during the experimental evaluation. Note that as mentioned previously, deflection time histories were not recorded during the experimental evaluation.

5.6.2.1. Panel A1

The time history plot for mid-panel deflection for different material model combinations is shown in Figure 5.10. A maximum mid-panel deflection of 38.5 mm was recorded for panel A1 during the experimental procedure, which is shown as a black dotted line. None of the material model combinations were able to achieve the 38.5 mm maximum deflection, as all the material model combinations under-predicted the maximum deflection. The closest value of 34.8 mm was recorded for the combination of CDM (concrete) and SJC (reinforcement) material models, followed by the WCM/SJC combination and WCM/PK combination. Table 5.13 shows the full comparison of mid-panel deflection of the numerical model with experimental results.

The CDM with SJC model combination was the only material combination to achieve an error of less than 10%, closely followed by the WCM and SJC model combination with 11.4% variation in mid-panel displacement. The BGU model was found to be stiffer exhibiting least defection in comparison with other concrete material models. The CSCM and SJC model combination exhibit error percentage of 18.2%, which is marginally inside the maximum acceptable error percentage of 20%. On the other hand, CSCM – PK material combination exhibit an error percentage of 22.3%. In general, all material models under-predicted the mid-panel displacement for Panel A1.

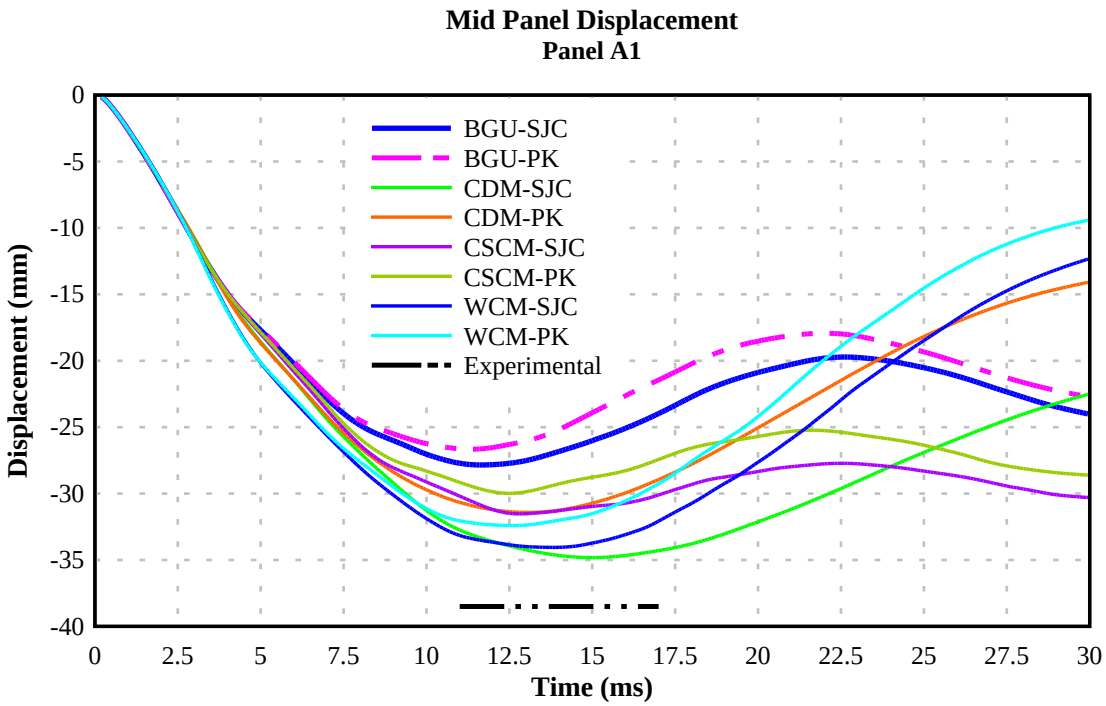

Figure 5.10: Comparison of mid-panel displacement – Panel A1

Table 5.13: Comparison of ultimate mid-panel displacement for Panel A1 with different material models

Identifier	Concrete material model	Reinforcement material model	Maximum Mid-panel displacement	Difference	Error (%)
EXP	N/A	N/A	38.5	N/A	N/A
BGU-SJC	MAT_072	MAT_098	27.8	-10.7	-27.8
BGU-PK	MAT_072	MAT_003	26.7	-11.8	-30.6
CDM-SJC	MAT_072R3	MAT_098	34.8	-3.7	-9.6
CDM-PK	MAT_072R3	MAT_003	32.3	-6.2	-16.1
CSCM-SJC	MAT_159	MAT_098	31.5	-7.0	-18.2
CSCM-PK	MAT_159	MAT_003	30.0	-8.5	-22.1
WCM-SJC	MAT_084/085	MAT_098	34.1	-4.4	-11.4
WCM-PK	MAT_084/085	MAT_003	32.4	-6.1	-15.8

Once the panel reaches the maximum deflection, different material model combinations predicted the rebound differently. The CSCM concrete model exhibits the least rebound irrespective of reinforcement model. The WCM model and the CDM concrete model

with PK reinforcement model represent rebound better than other material model combinations. This is due to the individual capabilities of concrete and reinforcement material models, especially the strain hardening and softening behaviours.

5.6.2.2. Panel B2

The mid-panel deflection time history for Panel B2 is presented in Figure 5.11. A maximum mid-panel deflection of 24.4 mm was recorded during the experimental study is presented as a black dotted line in Figure 5.11. Close approximations were achieved with most material model combinations for mid deflections in Panel B2. As in panel A1, the BGU concrete model exhibited stiffer response compared to all other material model combinations. The closest approximation was recorded with the CSCM/PK material model combination with 24.8 mm deflection, followed by the CDM/PK model combination with 25.4 mm deflection. A comparison of ultimate mid deflection, along with error percentages for Panel B2 with different material combinations is presented in Table 5.14.

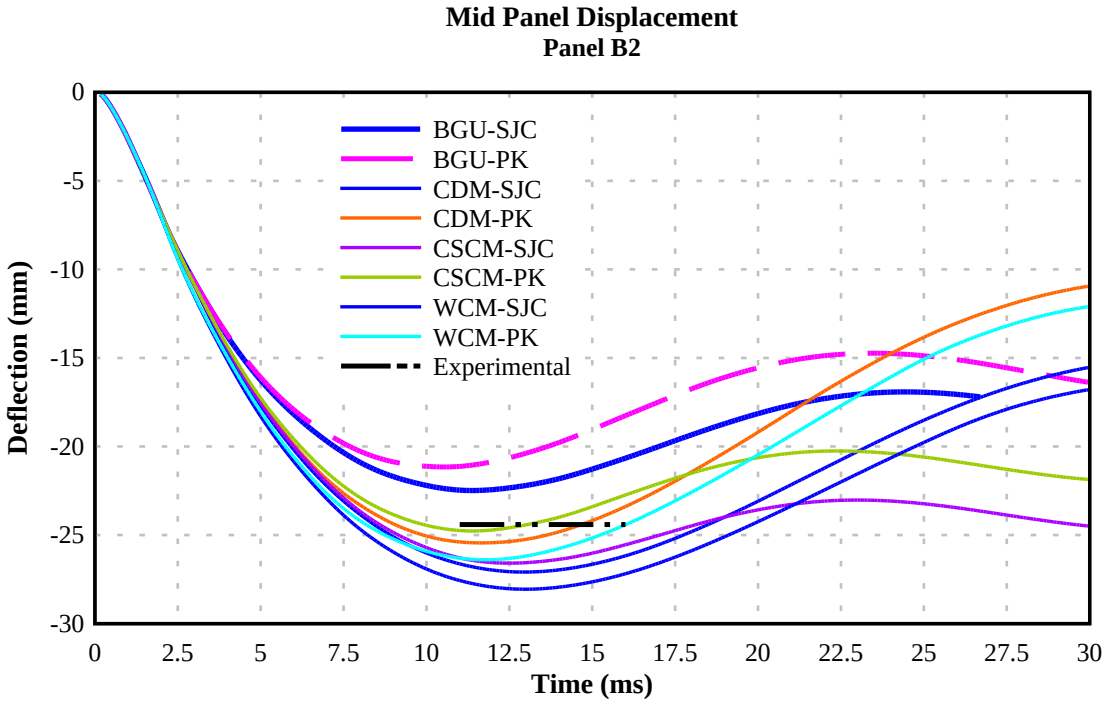

Figure 5.11: Comparison of mid-panel displacement – Panel B2

Different material model combinations predicted the rebound differently, beyond the maximum deflection, similar to panel A1. The CSCM concrete material model exhibits the least rebound, irrespective of the reinforcement material combination. The CDM/PK

and WCM/PK material model combination represent the rebound better than other material combinations, suggesting better post peak strain hardening and softening behaviour.

Table 5.14: Comparison of ultimate mid-panel displacement for Panel B2 with different material models

Identifier	Concrete material model	Reinforcement material model	Maximum mid-panel displacement	Difference	Error (%)
EXP	N/A	N/A	24.4	N/A	N/A
BGU-SJC	MAT_072	MAT_098	22.5	-1.9	-7.8
BGU-PK	MAT_072	MAT_003	21.2	-3.2	-13.1
CDM-SJC	MAT_072R3	MAT_098	27.1	2.7	11.1
CDM-PK	MAT_072R3	MAT_003	25.4	1.0	4.1
CSCM-SJC	MAT_159	MAT_098	26.5	2.1	8.6
CSCM-PK	MAT_159	MAT_003	24.8	0.4	1.6
WCM-SJC	MAT_084/085	MAT_098	28.1	3.7	15.2
WCM-PK	MAT_084/085	MAT_003	26.4	2.0	8.2

A better correlation between experimental and numerical simulations was observed with Panel B2. All material model combinations recorded smaller error percentages than Panel A1, maximum being 15.2%. All concrete material models, except the BGU concrete model, showed a more flexible response than the experimental response. This is in contrast to the Panel A1, where deflection was under-predicted for all material model combinations. The time for maximum deflection varies from 10.5 ms to 13 ms for the different model combinations with WCM/SCJ model combination corresponding to the maximum.

5.6.3. Panel deflections – Support

The maximum deflection at supports (fixing assemblies) was also recorded during the experimental evaluation for both panels and was also used as a method of calibration for the developed numerical model. The deflection was measured perpendicular to the surface of the panel, similar to the maximum mid-panel deflection.

5.6.3.1. Panel A1

Figure 5.12 exhibits the deflection time history for support deflection for different material model combinations. Time to achieve the peak support deflection is consistent for the BGU and CDM models with mid-panel deflection shown in Figure 5.11. The CSCM and WCM models exhibited indifferent deflection time history curves. However, all model combinations found a converging point in deflection time history around the 20 ms. The BGU and CDM models were able to recover from the initial downward deflection and able to register positive rebound deflections.

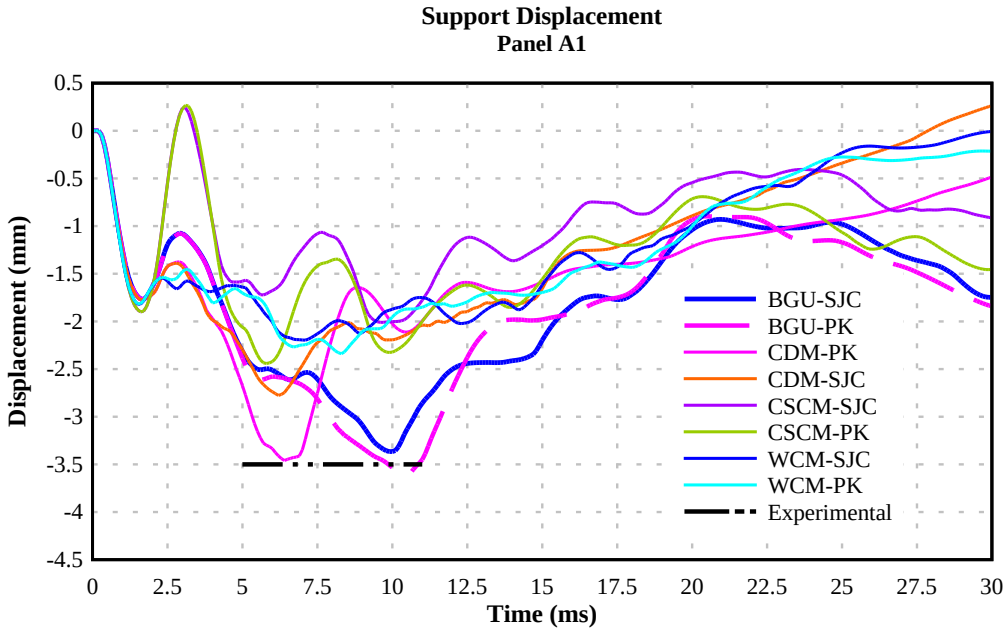

Figure 5.12: Comparison of panel support displacement– Panel A1

A maximum support deflection of 3.5 mm was recorded for Panel A1 during the experimental evaluation. The BGU/SJC, BGU/PK and CDM/PK model combinations showed similar values for the support deflection, with error percentages less than 4%, as shown in Table 5.15. The CDM and SJC model combination recorded a maximum support displacement of 2.78 mm, giving a 20.6% error percentage, which is just outside the margin of acceptable error percentage. All other model combinations had error percentages greater than 30%, which are well outside the margin of acceptable accuracy.

Table 5.15: Comparison of ultimate support displacement for Panel A1 with different material models

Identifier	Concrete material model	Reinforcement material model	Maximum Support displacement	Difference	Error (%)
EXP	N/A	N/A	3.50	N/A	N/A
BGU-SJC	MAT_072	MAT_098	3.37	-0.13	-3.71
BGU-PK	MAT_072	MAT_003	3.62	0.12	3.43
CDM-SJC	MAT_072R3	MAT_098	2.78	-0.72	-20.6
CDM-PK	MAT_072R3	MAT_003	3.46	-0.04	-1.14
CSCM-SJC	MAT_159	MAT_098	2.01	-1.49	-42.6
CSCM-PK	MAT_159	MAT_003	2.45	-1.05	-30.0
WCM-SJC	MAT_084/085	MAT_098	2.20	-1.30	-37.1
WCM-PK	MAT_084/085	MAT_003	2.34	-1.16	-33.1

5.6.3.2. Panel B2

Deflection time history for the Panel B2 is presented in Figure 5.13. A uniform deflection time history, in comparison with Panel A1 in Figure 5.12, was observed for all the material models until peak and followed by two different paths for the four concrete models. No significant influence was observed from the reinforcement material model as CDM and WCM models showed a significant rebound in the supports. The rebound action of CSCM and BGU concrete models was such that even half of original downward deflection was not regained. Although behaving differently, none of the material combinations were able to record rebound deflections above the original position, within the selected analysis time of 30 ms. All material model combinations reach a deflection of 1.4 mm however, fail to achieve 1.7 mm, which was recorded during the experimental evaluation.

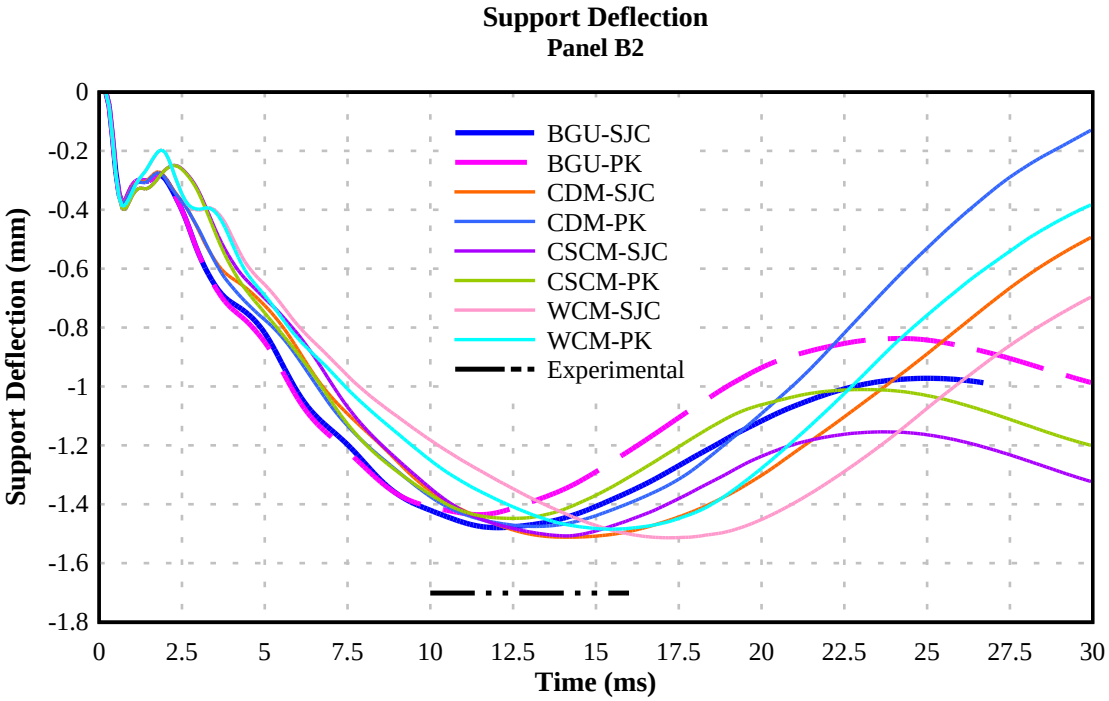

Figure 5.13: Comparison of panel displacement (support) – Panel B2

Table 5.16: Comparison of ultimate support displacement for Panel B2 with different material models

Identifier	Concrete material model	Reinforcement material model	Support displacement	Difference	Error (%)
EXP	N/A	N/A	1.70	N/A	N/A
BGU-SJC	MAT_072	MAT_098	1.48	-0.22	-12.9
BGU-PK	MAT_072	MAT_003	1.43	-0.27	-15.9
CDM-SJC	MAT_072R3	MAT_098	1.51	-0.19	-11.2
CDM-PK	MAT_072R3	MAT_003	1.47	-0.23	-13.5
CSCM-SJC	MAT_159	MAT_098	1.51	-0.19	-11.2
CSCM-PK	MAT_159	MAT_003	1.45	-0.25	-14.7
WCM-SJC	MAT_084/085	MAT_098	1.51	-0.19	-11.2
WCM-PK	MAT_084/085	MAT_003	1.48	-0.22	-12.9

As illustrated in Table 5.16, all material combinations recorded error percentages between 11 and 16, which was well within the acceptable limit of 20% for high explosive related simulations. Three concrete material models CDM, CSCM and WCM had recorded the minimum error percentage of 11.2. Interestingly, all three were

recorded with the SJC reinforcement model. Again, the BGU concrete model was found to be too stiff with the support deflection for Panel B2.

5.6.4. Compressive stress of concrete

Stress and strain measurements were not recorded during the experimental study. However, compressive stress of concrete was recorded in the numerical study for the identification of failure mechanism of panels and therefore comparison with the actual compressive strength could be made. The middle 1/3 on the exposed surface of the panel was selected for evaluation of compressive stress of concrete, which was the most probable location for maximum compressive stresses.

5.6.4.1. Panel A1

A summary of maximum compressive stress recorded and stress time history are shown in Table 5.17 and Figure 5.14, respectively. Crack patterns observed on the exposed surface of the test panel and a stress plot of exposed face is also presented in Figures 5.15 and 5.16, respectively.

Table 5.17: Maximum compressive stress in concrete for different material combinations – Panel A1

Panel Identifier	Time to maximum stress (ms)	Maximum stress (σ)(MPa)	Stress (σ) / Compressive Strength (f'_c)
BGU-SJC	11.9	49.95	1.09
BGU-PK	12.4	49.71	1.08
CDM-SJC	9.8	48.22	1.05
CDM-PK	9.4	49.99	1.09
CSCM-SJC	7.1	54.04	1.17
CSCM-PK	7.4	57.14	1.24
WCM-SJC	14.5	56.14	1.22
WCM-PK	9.8	57.81	1.26

Table 5.17 indicates that different material combinations returned different compressive stresses for the same structure. However, all the material model combinations exhibited stresses higher than the compressive strength (46 MPa) of the material. The increased

value can be attributed to the strain rate enhancement effect. A maximum of 57.81 MPa was recorded with WCM / PK model combination while the minimum of 48.22 was found for the CDM / SJC combination. The CSCM /SJC combination reached the maximum at 7.1 ms and WCM/SJC was the slowest at 14.5 ms, more than double the time for the quickest of CSCM/SJC combination. No comparisons could be made with experimental results as no stress-strain measurements were recorded.

Figure 5.14 illustrates the time history plot for the maximum compressive stress in concrete for different material model combinations. Stress response seemed to be similar for every material model combination until 2.5 ms, which was the positive phase duration of loading. Once the positive phase loading ended, model combinations selected different stress paths. No significant difference was observed with reinforcement material models as both models exhibit identical stress values for the same concrete model. The BGU concrete model was the first to reach the tensile stresses recorded around 22.5 ms, followed by the CDM/PK and WCM models.

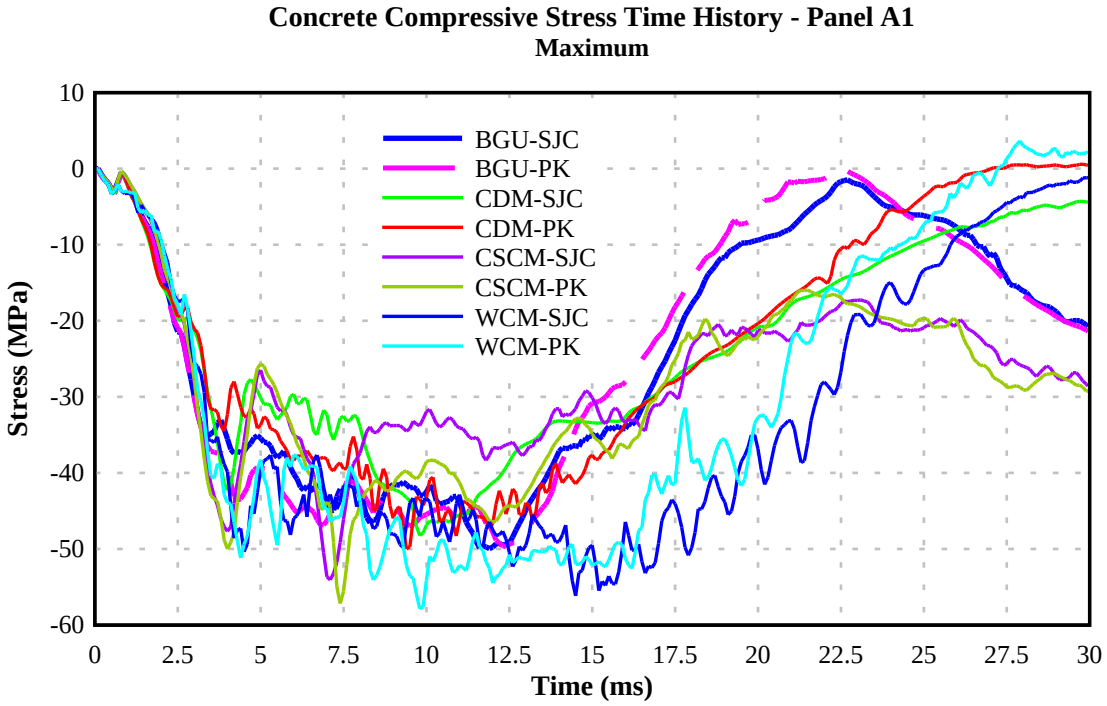

Figure 5.14: Stress time history for maximum stress element (concrete) – Panel A1

Figure 5.15 illustrates the crack pattern of the concrete panel from the exposed face of the Panel A1 along with stress plots for the concrete panel for CDM/PK material model

combination in Figure 5.16. Most of the material model combinations exhibit similar response as indicated Appendix B-I for other material model combinations.

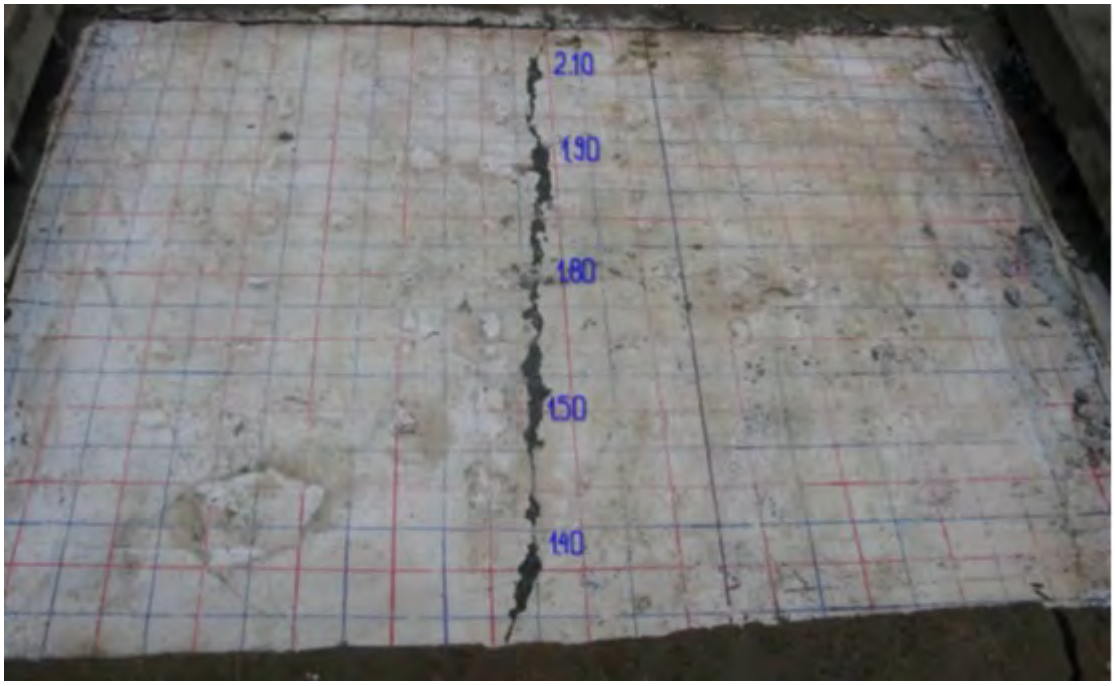

Figure 5.15: Crack pattern (compression) on exposed face – Panel A1

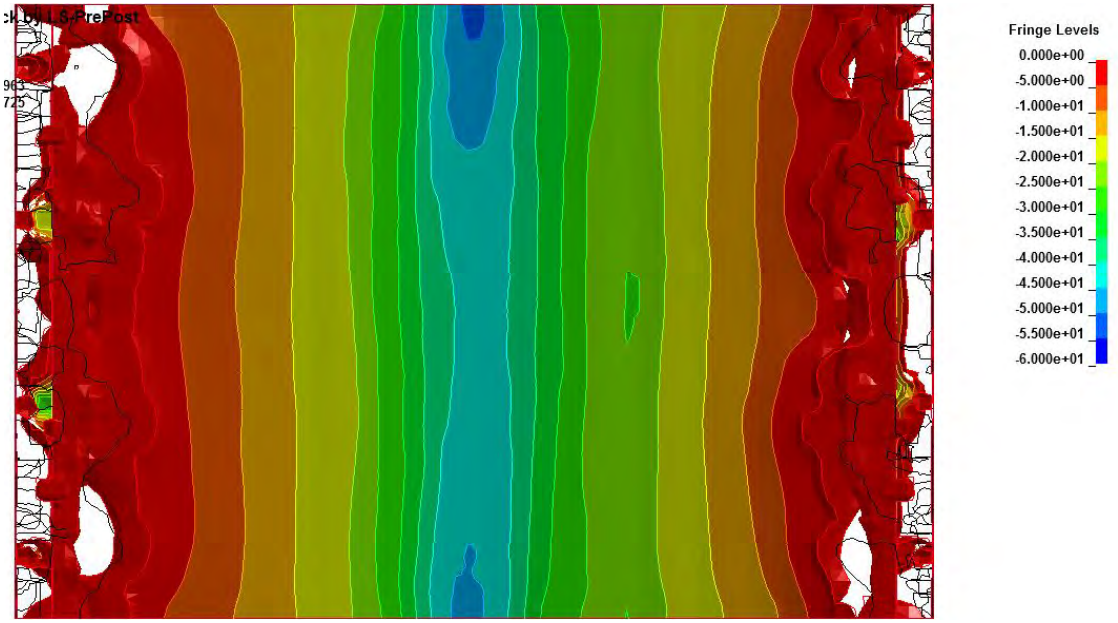

Figure 5.16: Stress plot for the exposed face at the time of maximum stress – Panel A1 for CDM/PK material model combination

As shown in Figure 5.15, a compression crack was formed in mid-panel and minor crushing of concrete was observed. Crack width measurements vary from 1.4 mm to 2.1

mm, suggesting the crack initiation and propagation from one free edge to other free edge. The stress plot shown in Figure 5.16 indicates a higher stress concentration close to one free edge, with magnitude exceeding the compressive capacity of concrete, which can be considered as an initiation of compressive cracking.

5.6.4.2. Panel B2

A summary of maximum compressive stress observed in the Panel B2 and the time history plot for the maximum stress element is presented in Table 5.18 and Figure 5.17, respectively. The crack pattern of the exposed face observed during the experimental study and relevant stress plot for CDM/SJC material model combination is also shown in Figures 5.18 and 5.19. Stress plots of Panel B2 for other material model combinations are presented separately in Appendix B-II.

Table 5.18: Maximum compressive stress in concrete for different material combinations – Panel B2

Panel Identifier	Time to maximum stress (ms)	Maximum stress (σ)(MPa)	Stress (σ) / Compressive Strength (f'_c)
BGU-SJC	2.7	34.67	0.81
BGU-PK	2.7	34.5	0.80
CDM-SJC	4.4	36.35	0.85
CDM-PK	5.0	38.27	0.89
CSCM-SJC	3.8	33.57	0.78
CSCM-PK	4.3	34.61	0.80
WCM-SJC	7.1	38.66	0.90
WCM-PK	5.7	44.43	1.03

As illustrated in Table 5.18 and Figure 5.17, the maximum compressive stress recorded in concrete did not reach the compressive strength (43 MPa) for the majority of material model combinations. The only exception is the WCM/PK model combination where the maximum stress of 44.43 MPa was recorded. The smallest maximum of 33.57 MPa was recorded with the CSCM/SJC combination closely followed by the BGU/PK and CSCM/PK combinations.

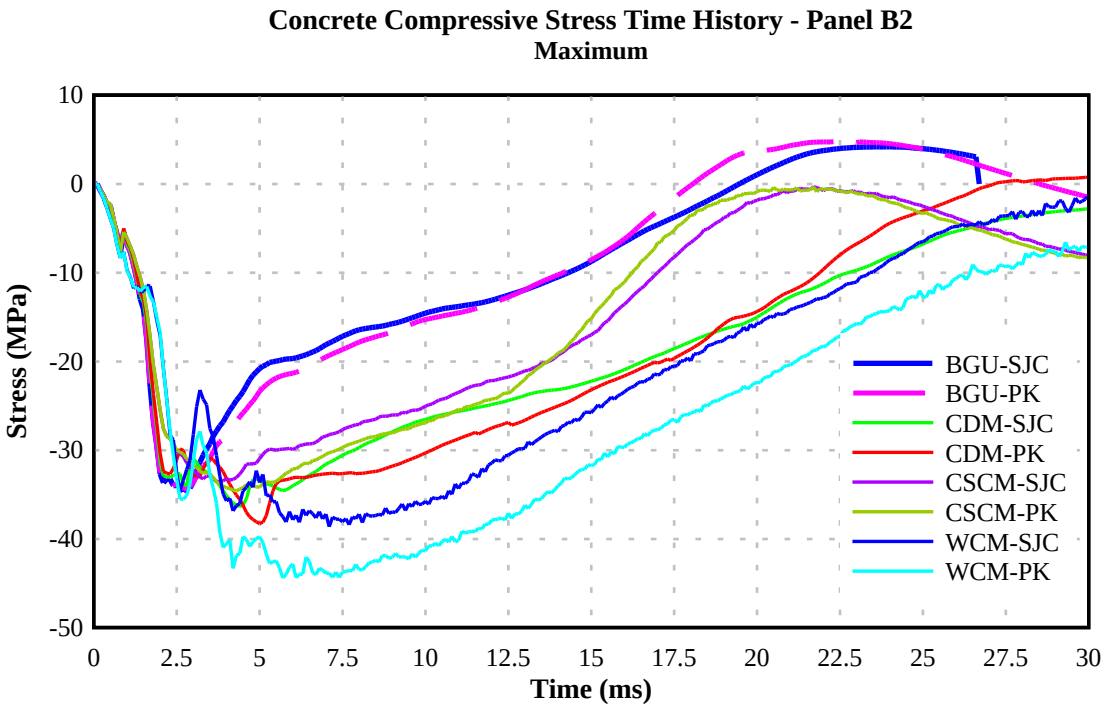

Figure 5.17: Stress time history of maximum stress element (concrete) – Panel B2

The time to maximum stress was much smaller than that of Panel A1 for all combinations, with the quickest being the BGU concrete at 2.7 ms and slowest the WCM/SJC combination at 7.1 ms. As in Panel A1, no measurements of stress or strain were taken during the experimental evaluation hence, no comparisons could be made.

The maximum stress response of all model combinations was identical until 2.5 ms, which is close to the positive phase duration of blast pressure loading, similar to Panel A1. At the end of the positive phase duration, different concrete material models started following different stress paths. No significant variations were observed with different reinforcement models, as long as the concrete material model remains same, except for the WCM. The BGU concrete model was the first to reach the tensile stress around 18 ms. The CDM/PK combination was the only other material model to reach tensile stress on the maximum compressive element around 27 ms. None of the other combinations reached the tensile stress within the analysis time of 30 ms.

It is reasonable to witness similar response in panels for the loading phase, as all concrete models use the same volumetric prediction using the same equation of state. Minor differences are due to the variations in deviatoric response and different reinforcement models. The BGU concrete model was the first to reach rebound

deflection as seen in Figure 5.11. Hence, it is realistic to assume BGU concrete model to reach the tensile stresses first, as seen in Figure 5.17.

Figure 5.18 illustrates the crack pattern observed during the experimental study for exposed face of the Panel B2. Three tensile cracks were formed with only one extending between the edges of the panel. The other two cracks were terminated close to the middle of the panel. No compressive damage (either local or bending) was observed in the panel. Tensile cracks on the exposed face were found to be caused by rebound deflection of the panel.

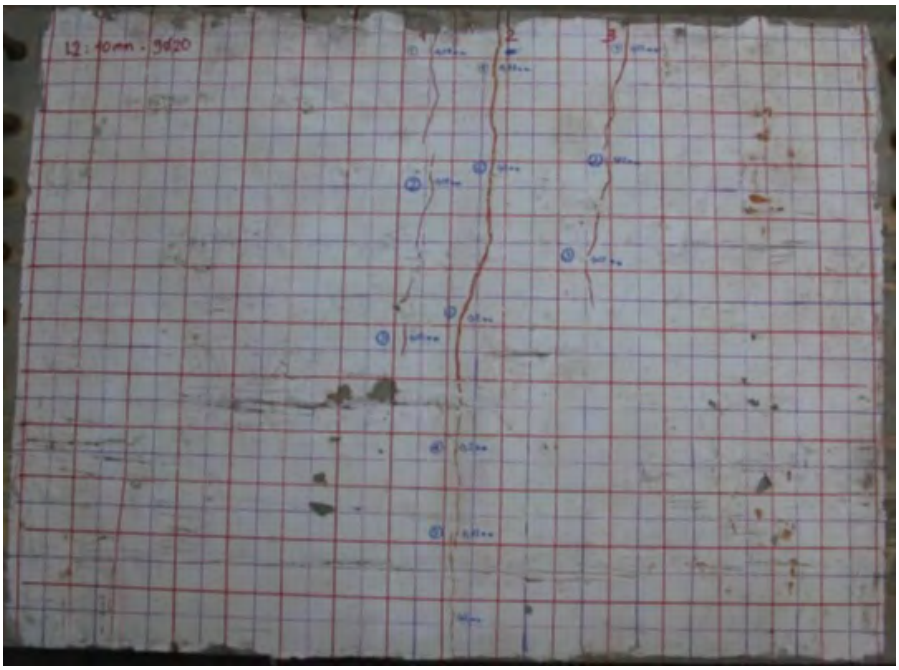

Figure 5.18: Crack pattern on exposed face – Panel B2

The stress plot (CDM/SJC material model combination) of the exposed face of the Panel B2 is presented in Figure 5.19 at the time of maximum compressive stress. Similar stress distributions were observed in all material model combinations as illustrated in Figures B.9 to B.16 presented in Appendix B-II. Unlike in Panel A1, a perfectly symmetrical stress plot was observed without any stress concentrations exceeding the compressive strength of concrete. Hence, it is safe to assume that angle cleat connected panels had a limited possibility of compression failures than the dowel connected panels.

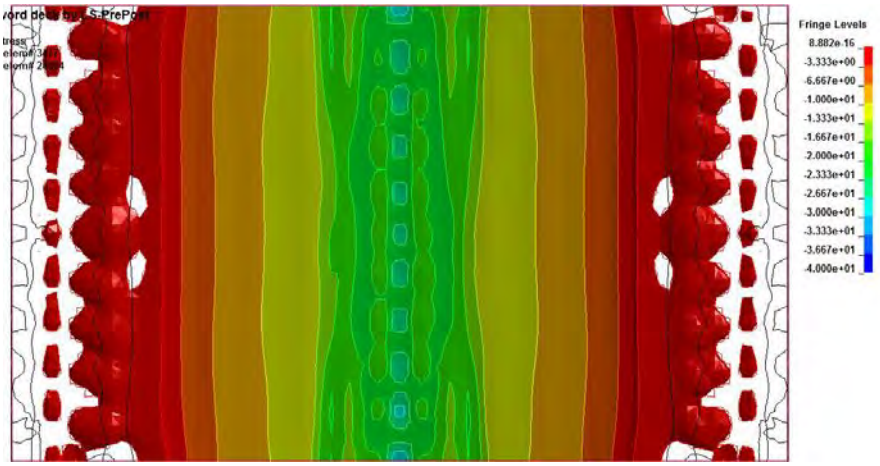

Figure 5.19: Stress plot for the exposed face at the time of maximum stress – Panel B2 for CDM/SJC material model combination

5.6.5. Axial stress in reinforcement

Although no measurements were taken during the experimental evaluation, axial stress in reinforcement was recorded in the numerical study. The tensile stresses are marked as positive while compressive stresses are marked as negative as illustrated in Figures 5.20 and 5.21. Results are presented for both Panels A1 and B2, discussing the influence of reinforcement stresses with cracking and crack width of concrete.

5.6.5.1. Panel A1

Maximum values of reinforcement stress time histories recorded for Panel A1 are presented in Figure 5.20. Two reinforcement models represent similar axial stress time histories irrespective of the concrete models. The SJC reinforcement model, reached a threshold stress close to 660 MPa for all four concrete material models at 3 ms, and remained consistent until 12 ms. The maximum stress of 660 was slightly higher than the yield strength (630 MPa) of reinforcing material. The PK reinforcement model indicated a similar response, with the maximum stress of 630 MPa. All four concrete material models displayed a similar response for maximum reinforcement stress.

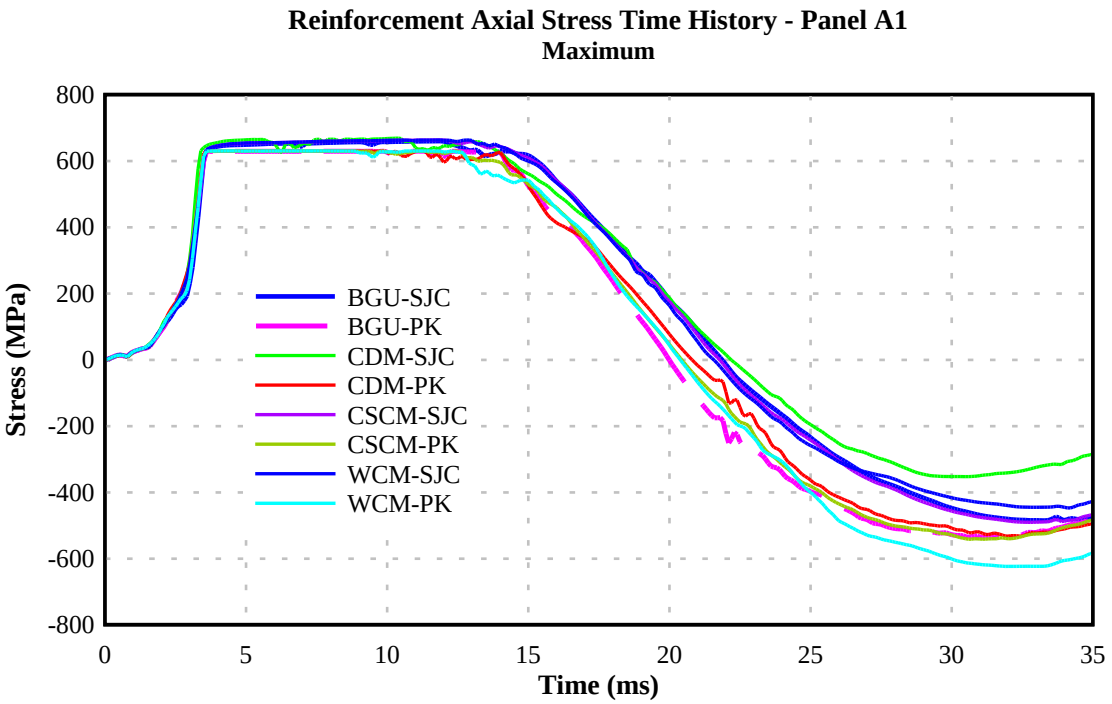

Figure 5.20: Reinforcement axial stress of Panel A1

All material model combinations reach negative stresses in reinforcement (compressive stress) after 20 ms of analysis time. The BGU/PK model combination was the first to achieve compressive stresses, which is acceptable considering this material combination was the first to reach the rebound deflections. The largest compressive stress (in reinforcement) was observed in the WCM/PK model combination, almost reaching the yield strength of 630 MPa. However, it is more realistic to observe compressive stresses less than the yield strength of reinforcement.

5.6.5.2. Panel B2

Figure 5.21 illustrates the maximum axial stress for reinforcement in Panel B2. A stress distribution identical to that observed in Panel A1 is observed with Panel B2 for different material model combinations. Maximum stress of 630 MPa of PK material model and 660 MPa for SJC material model was observed across all four concrete material models.

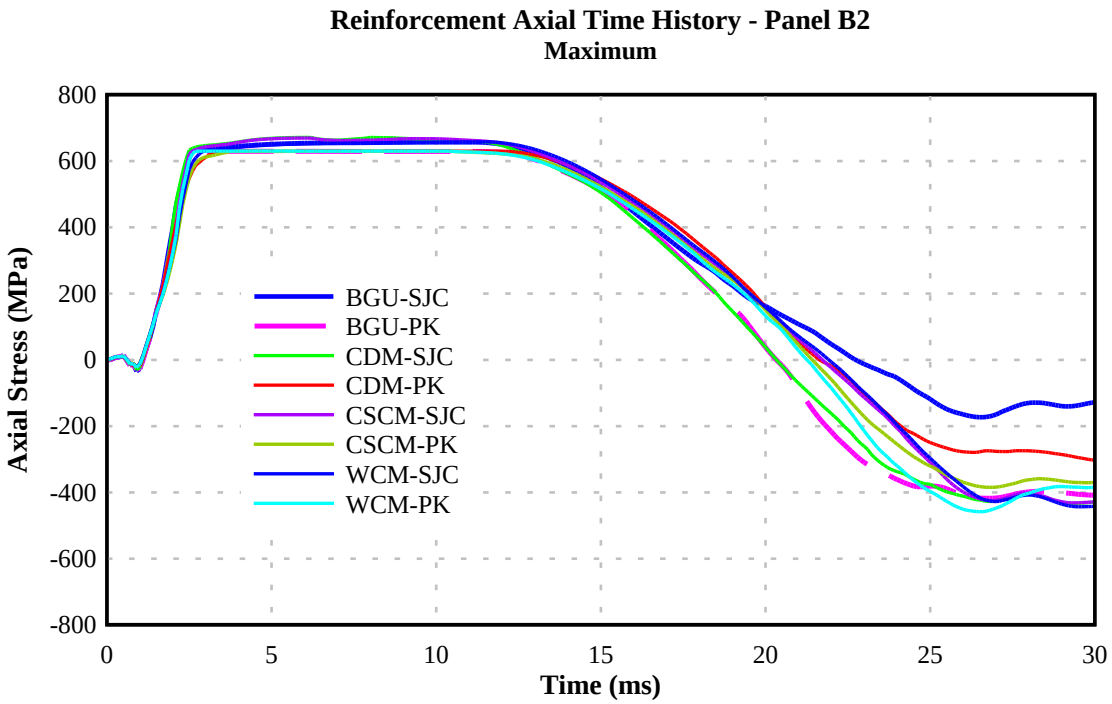

Figure 5.21: Reinforcement axial stress of Panel B2

Reinforcements reached compressive stresses between 20 ms and 23 ms of analysis time for all material model combinations, which is similar to the observations in Panel A1. The BGU/PK model combination was the first to reach compressive stresses. However, the intensity of compressive stresses in reinforcement was smaller than that of Panel A1, reaching a maximum of 440 MPa in WCM/PK model combination. This is acceptable considering the lower compressive stresses in concrete in Panel B2 (Figure 5.19 and Table 5.18) and the WCM/PK model reaching the maximum in panel A1 as well.

Overall, all material model combinations express similar reinforcement stresses in the tensile region, while different behaviours were observed in the compressive region. Panel A1 experience higher compressive stresses than Panel B2, which is to be expected considering the larger deflection and higher compressive stresses in concrete. Comparison between different material model combinations for reinforcement stress does not reveal conclusive evidence of what material model combination is better replicating the experimental results.

5.6.6. Model calibration summary

The numerical model calibration was performed with different aspects such as blast pressure, mid-panel and support deflections, crack pattern and failure mechanisms. The blast pressure was not dependent on the material model combinations used. Inbuilt keyword LOAD_BLAST_ENHANCED was used to generate the blast pressure while LOAD_BLAST_SEGEMENT_SET was used to transform the structure to accept the blast load. These keywords were able to predict the blast pressure and impulse with economical computer use and acceptable accuracy. Hence, the above mentioned keywords will be used with the calibrated model for parametric study.

A summary of calibration parameters along with error percentages for different material model combinations is presented in Table 5.19. (This is a summary presentation of Tables 5.13 to 5.18 for ease of comparison). Figure 5.22 plots the error percentages recorded for different material model combinations for maximum mid-panel and support deflections. Two dark lines at positive 20 and negative 20 indicates the acceptable error margins.

Table 5.19: Summary of calibration results

Material model combination	Panel A1					Panel B2				
	Mid def.	Error (%)	Sup. def.	Error (%)	Max stress	Mid def.	Error (%)	Sup. def.	Error (%)	Max stress
BGU-SJC	27.8	-27.8	3.37	-3.71	49.9	22.5	-7.8	1.48	-12.9	34.7
BGU-PK	26.7	-30.6	3.62	3.43	49.7	21.2	-13.1	1.43	-15.9	34.5
CDM-SJC	34.8	-9.6	2.78	-20.6	48.2	27.1	11.1	1.51	-11.2	36.4
CDM-PK	32.3	-16.1	3.46	-1.14	50.0	25.4	4.1	1.47	-13.5	38.3
CSCM-SJC	31.5	-18.2	2.01	-42.6	54.0	26.5	8.6	1.51	-11.2	33.6
CSCM-PK	30.0	-22.1	2.45	-30.0	57.1	24.8	1.6	1.45	-14.7	34.6
WCM-SJC	34.1	-11.4	2.20	-37.1	56.1	28.1	15.2	1.51	-11.2	38.7
WCM-PK	32.4	-15.8	2.34	-33.1	57.8	26.4	8.2	1.48	-12.9	44.4

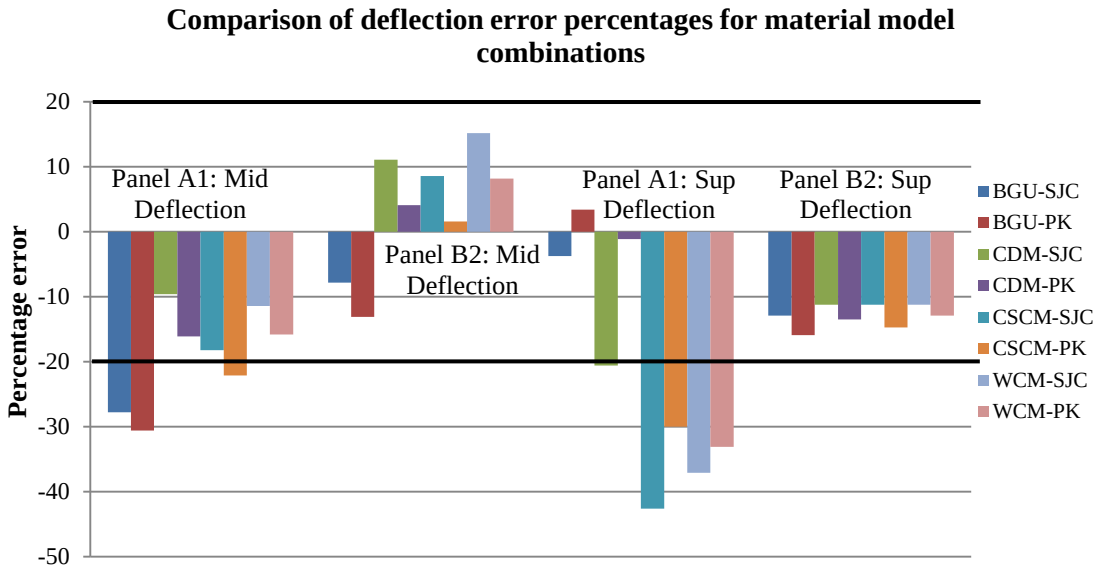

Figure 5.22: Comparison of error percentages for different material model combinations

Comparison of error percentages of Panel A1 and Panel B2 suggest that Panel B2 predictions are significantly better than that of Panel A1, for all material model combinations. Panel A1 exhibits larger deflection and higher stresses than the Panel B2 during the experimental evaluation. Although same was observed with numerical modelling, more rigid performance was observed with Panel A1. The rigid response suggests the shortcomings of material models in predicting the softening behaviour under higher rates of loading.

It is clear that the concrete damage model (CDM) exhibits the best combination of error percentages in comparison with the selected experimental results. Although, smaller error percentages are common for both the plastic kinematic (PK) and simplified Johnson-Cook (SJC) reinforcement models, better calibration was observed with the PK reinforcement model. The CDM has been validated for different loading conditions, including explosive loading, and automatic parameter generation is based on these calibration results. Therefore, it is common to experience smaller error percentages with the CDM. Considering the CDM as the concrete material model, the PK reinforcement model experience better calibration results in comparison with the SJC model. Hence, CDM/PK material model combination was selected for the validation and further analysis along with the inbuilt blast loading function.

5.7. Numerical model verification

The remaining experimental test results from the University of Melbourne (Pham, 2010) (Panels B1, B3, B4 and B5) and the National University of Defence Technology, China (Panels A-F) were used for the verification of the developed numerical model. The verification will utilise the CDM/PK material model combinations selected in the previous sections.

5.7.1. Verification of test results from the University of Melbourne

The verifications are performed using comparisons to recorded mid-panel and support deflections. Additional parameters such as reinforcement and bolt stresses are discussed where appropriate. All Panels (B1, B3, B4 and B5) were modelled using the CDM/PK material model combination selected in Section 5.6. The loading remained same as calibration tests where the exact same combination of charge weight-standoff distance was used. A scaled distance of 1.193 m/kg$^{1/3}$ was resulted from this combination, which is considered as a mid to far range explosive loading.

5.7.1.1. Panel Deflection – Mid-point

Figure 5.23 illustrates the mid-panel deflection time history comparisons for Panels B1, B3, B4 and B5 with maximum deflections recorded during the experimental evaluation. The experimental values are presented as short straight lines since the maximum values were the only measurements recorded (no time history plots recorded).

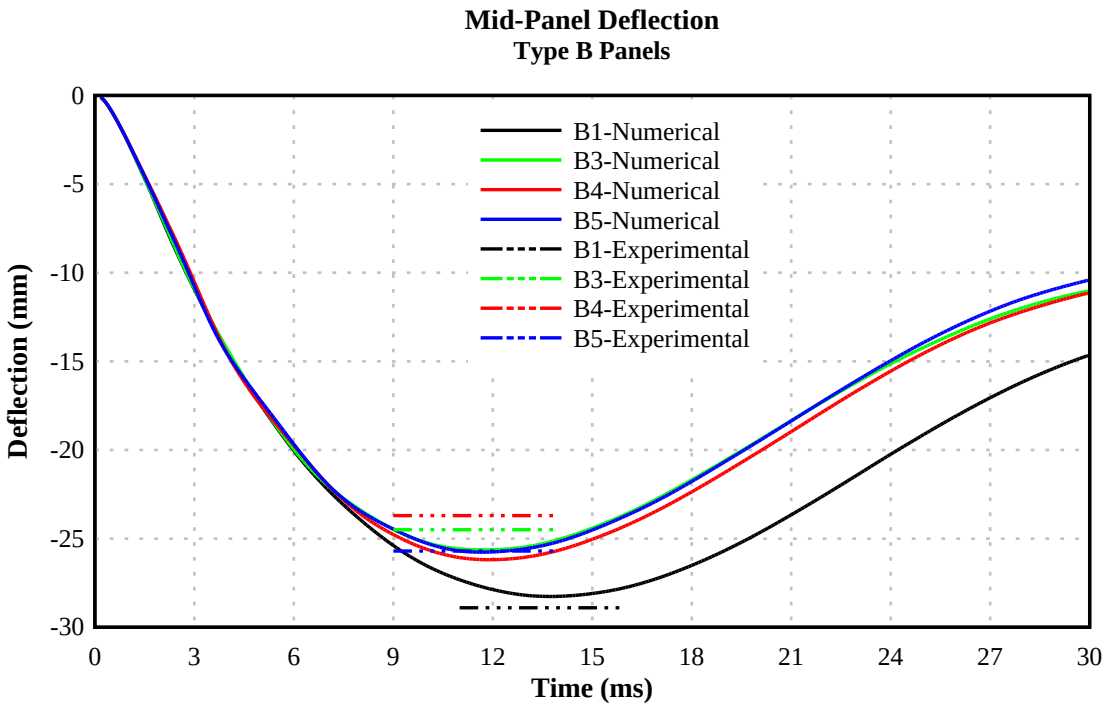

Figure 5.23: Mid-panel deflection of Type B panels

Panel B1, was found to be more flexible in comparison to other three panels, having higher deflection (28.3 mm) and larger duration (13.7 ms) to reach the maximum. This is due to the thinner angle section (8 mm) used. Panels, B3, B4 and B5 were observed to have similar numerical deflection time histories for the verification trials using the selected (calibrated) material model combinations and loading function. Recall the number and size of connecting bolts being the only difference between these panels, yet no significant variation was observed with mid-panel deflection. All three panels (B3, B4 and B5) recorded deflections in the range of 25 mm around 11.5 ms time duration.

A more detailed comparison of mid-panel deflections between experimental and numerical studies along with the error percentage is presented in Table 5.20. All four panels showed excellent correlation between experimental and numerical maximum deflections, all within the acceptable error margin of 20% for higher energy related problems.

Table 5.20: Maximum mid-panel deflections for Type B panels

Panel ID	Maximum mid-panel deflection (mm)		Error (%)
	Experimental	Numerical	
B1	28.9	28.3	-2.07
B3	24.5	25.63	4.61
B4	23.7	26.19	10.51
B5	25.7	25.76	0.23

5.7.1.2. Panel Deflection – Support

The support deflection time history for Panels B1, B3, B4 and B5 is shown in Figure 5.24. As in mid-panel deflection comparisons, experimental maximum values are shown in dashed straight lines.

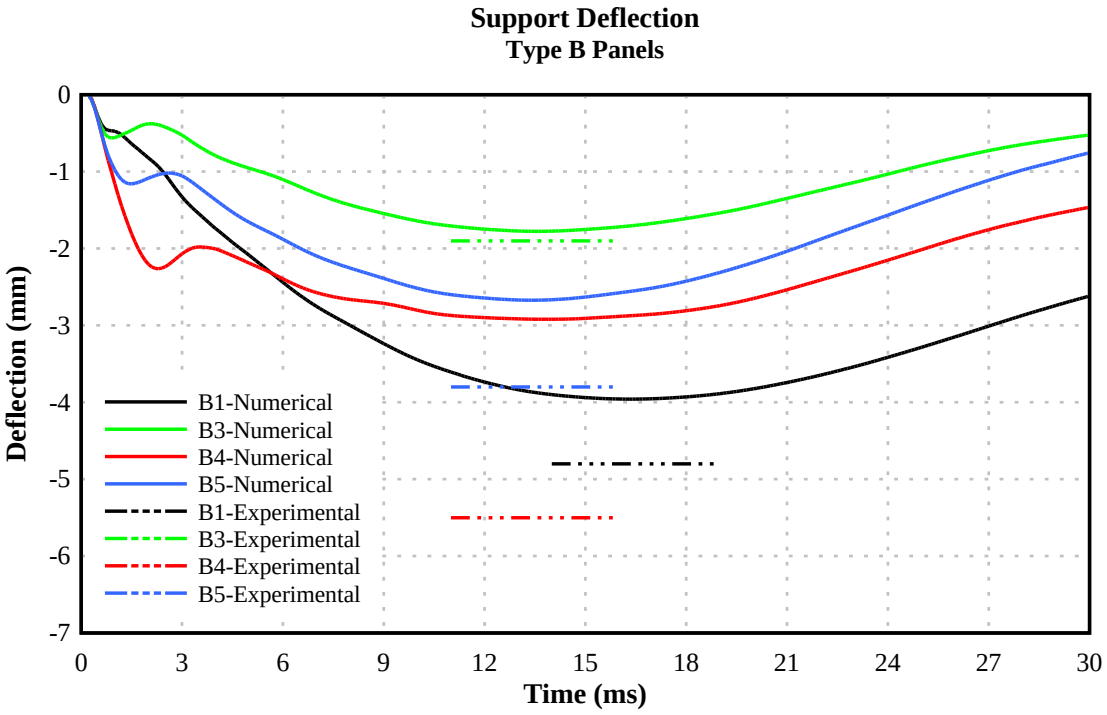

Figure 5.24: Support Deflection of Type B panels

The reduction in angle cleat thickness to 8 mm seems to have changed the response of the Panel B1 in comparison with 10 mm cleated panels. The other three panels exhibit similar responses with only a small change in direction around 2 ms and reaching the maximum close to 13.5 ms. The direction change was also observed in Panel B1,

although this was not as distinct as the other panels due to the lesser resistance against transverse deflection. Panel B4, which showed damage to the connecting bolts during the experimental study, reached a maximum deflection of 2.92 mm.

Table 5.21: Maximum support deflections for Type B panels

Panel ID	Maximum mid-panel deflection (mm)		Error (%)
	Experimental	Numerical	
B1	4.80	3.96	-17.5
B3	1.90	1.78	-6.32
B4*	5.50	2.92	-46.91
B5	3.80	2.67	-29.73

*: Fixing assemblies were broken during the experimental evaluation

A comparison of maximum deflection in experimental and numerical studies is shown in Table 5.21, along with error percentages. All four panels under predicted the support deflection, B4 and B5 collecting error percentages of 46.9% and 29.7% respectively, well above the maximum allowable limits. In comparison Panel B2 (used earlier in the calibration) only had an error percentage of 13.5%. The response of Panel B4 is understandable as the fixing assembly was broken during the experimental study and measurements were taken from the failed supports. Panels B1 and B2 exhibit reasonably accurate results with error percentages of 17.5% and 6.3%, respectively. High error percentages in support deflections are understandable as these measurements are within generally 1-2 mm of each other and a difference of 0.1 mm is approximately 5% variation in deflection (apart from Panel B4). In addition, mechanical device used for the deflection measurement also had a measuring accuracy of 0.1 mm, which accounts for approximately 5% of support deflection.

Support deflection does not seem to have the strongest compatibility with the experimental results for the selected material combinations. Two panels exhibit reasonable accuracy as in model calibrations and two below the acceptable error margins (although one panel had a broken fixing assembly). Therefore, a lower accuracy in Panel B4 was expected.

5.7.1.3. Compressive stress in concrete

The maximum compressive stress time histories for Type B panels are shown in Figure 5.25 and a comparison of maximum stress recorded with different panels is presented in Table 5.22. In addition, the maximum compressive stress plots for Panels B1, B3, B4 and B5 are presented in Figures B.17 to B.20 in Appendix B-III.

Panels B3, B4 and B5 followed similar stress paths, while panel B1 followed a different stress path to others. All three panels except Panel B1 reached the tensile stress between 23 ms and 25 ms for the maximum compressive stress element. Panels B1 and B4 recorded the smallest maximum values for the compressive strength of concrete. This can be due to the fixity of the supports, where these panels had higher inbuilt flexibility than the other two panels (i.e. either as thinner plate element (B1) or as reduced number of connecting bolts (B4)). This is clear evidence that use of flexible support conditions results in lower stresses in concrete elements when subjected to transient dynamic loading. However, allowing more flexibility could be catastrophic, as seen in Panel B4 where the fixing assembly was broken during the experimental testing.

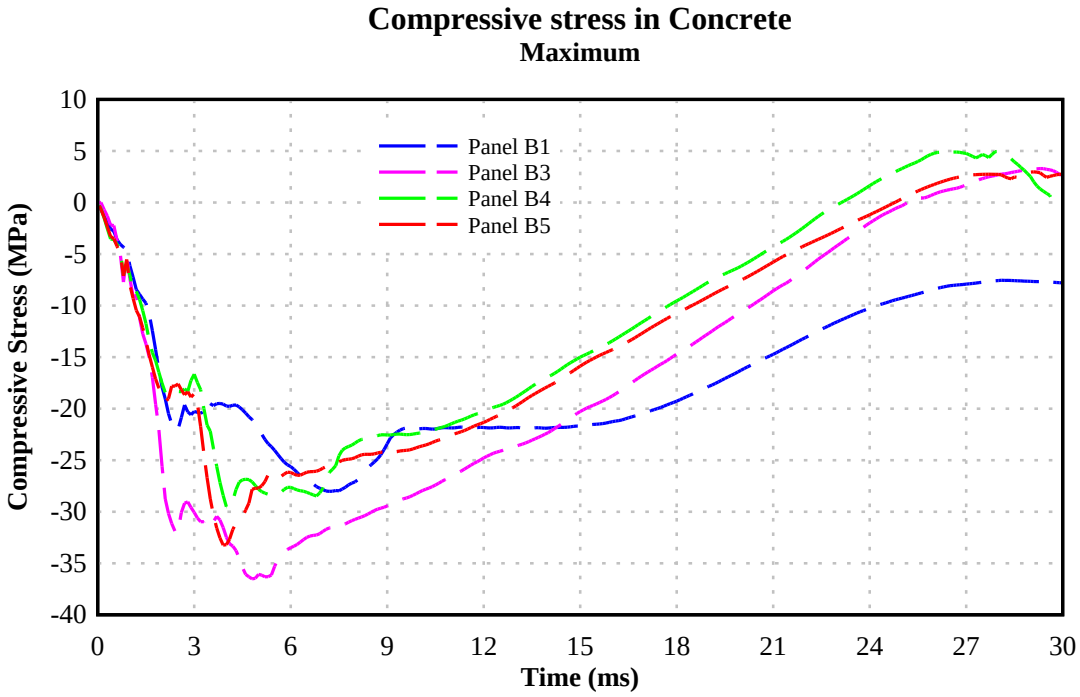

Figure 5.25: Maximum compressive stress of concrete –Type B panels

Table 5.22 illustrates the maximum stress reached in the concrete, time to reach maximum and maximum stress reached as a ratio of the compressive strength of

concrete. All Type B panels had the same compressive strength of 46 MPa. As seen in the experiments, none of the panels reach the compressive strength of concrete. Panel B1 having a thinner plate element showed the minimum stress levels in concrete only reaching 65% of the capacity, closely followed by Panel B4 with 69% of the capacity. Maximum stress was recorded in Panel B3, which had the minimum flexibility in the fixing assemblies. No pattern was identified for the time to reach maximum with the flexibility of the support. Panel B5 reached the maximum earliest at 3.9 ms from the start of the analysis and B1 was the last at 7.2 ms.

Table 5.22: Maximum stress of concrete –Type B panels

Panel Identifier	Time to maximum stress (ms)	Maximum stress (σ)(MPa)	Stress (σ) / Compressive Strength (F_c)
B1	7.2	28.03	0.65
B3	4.8	36.52	0.84
B4	4.1	29.59	0.68
B5	3.9	33.24	0.77

5.7.1.4. Axial stress of reinforcement

As in model calibrations, no comparisons could be made with the experimental study for the axial stress of reinforcement. A similar axial stress time history observed for the calibration of Panel B2 was observed with the other Type B panels as shown in Figure 5.26. All four panels reached the yield strength around 3 ms and yielded until 13 ms of analysis time, except Panel B1, which yielded a further 3 ms. The higher deflection and bigger crack widths on Panel B1 suggest a higher yielding time for reinforcement as well.

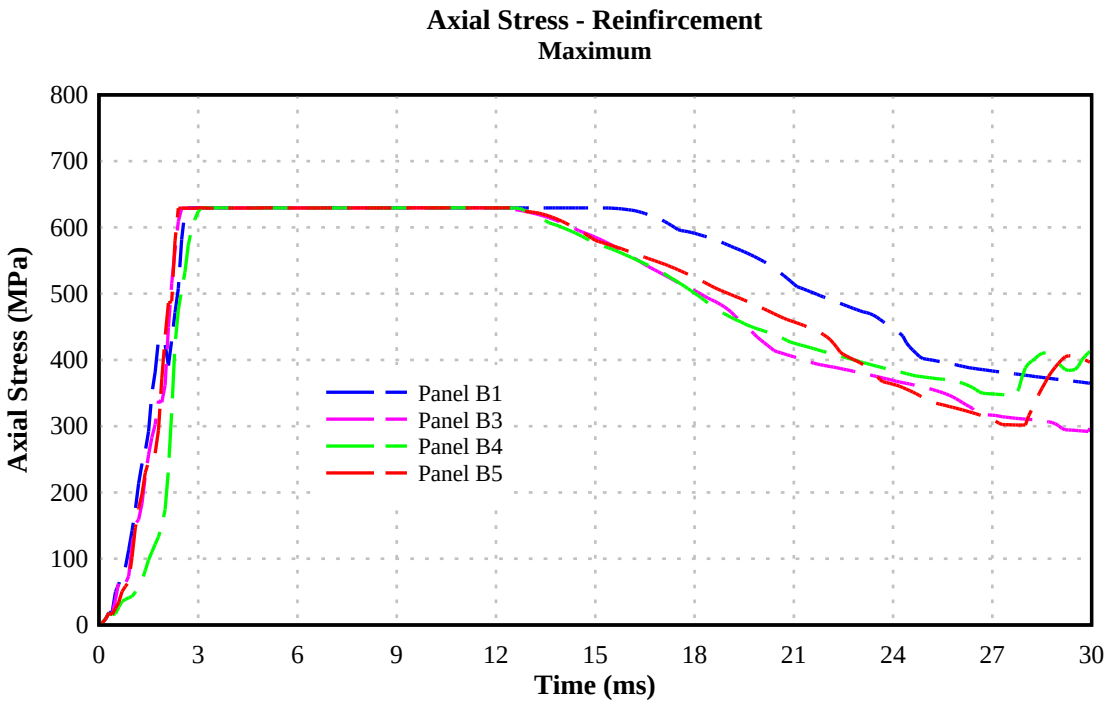

Figure 5.26: Maximum stress in reinforcement – Type B panels

5.7.1.5. Stresses in horizontal bolts

The Type B panels were connected to the test bunkers through structural angle section and a series of bolts as discussed earlier in the chapter. Although no measurements were taken for the stresses and strains of the connecting bolts and sections, failure of horizontal bolts in Panel B4 was used as a guideline to verify the results of the panels. Horizontal bolts in Type B panels transfer the loads predominantly in shear with the connection configuration used. However, evidence shows that those bolts failed in combined action of transverse shear and axial tension, as shown in Figure 5.27. Hence, both axial and shear stresses from the numerical evaluation are presented.

(a) (b)

Figure 5.27: Failed fixing bolts for (a) left and (b) right supports

Figure 5.28 illustrates the axial stress time history of bolts for the Type B panels. Panel B1 showed the smallest maximum stress of 24.8 MPa and Panel B4 had the largest of 339.4 MPa. Reduced bolt numbers and sizes in Panel B4 (9M20 to 3M12) resulted in higher stresses and more flexible response from the panel. Panel B3, which used the same M12 bolts as Panel B4, recorded a maximum of 160.9 MPa. However, Panel B3 was equipped with 9M12 bolts compared to 3M12 bolts in Panel B4. Panel B5, which used 3M16 bolts as horizontal bolts, reached a maximum of 134.4 MPa.

Although fixing assemblies in Panel B4 were found to be broken during the experimental study, recorded axial stresses were not high enough to cause failure in the bolts. However, a significant increase of more than two times the maximum axial stress of next highest (B3) was recorded with the Panel B4.

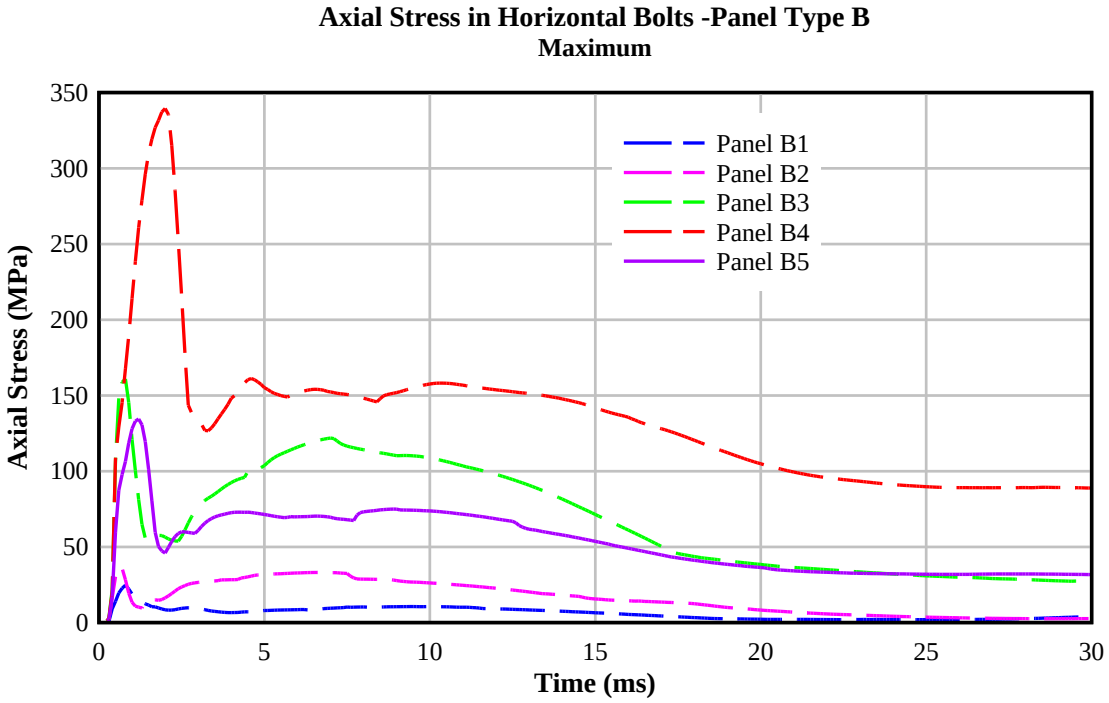

Figure 5.28: Axial stress time history of bolts (maximum) for Type B panels

Figure 5.29 illustrates the shear stress force history of bolts for the Type B panels. All panels showed a sudden decrease in shear stress, after the initial peak value. Similar stresses in the range of 450 MPa were recorded with panels B3, B4 and B5 while panels B1 and B2 exhibited 188.4 MPa and 231.1 MPa respectively. As in axial stress, the maximum was recorded with Panel B4 of 457.4 MPa. However, this was still less than the strength of the bolting material (Yield Strength of 640 MPa) in order to fail in shear.

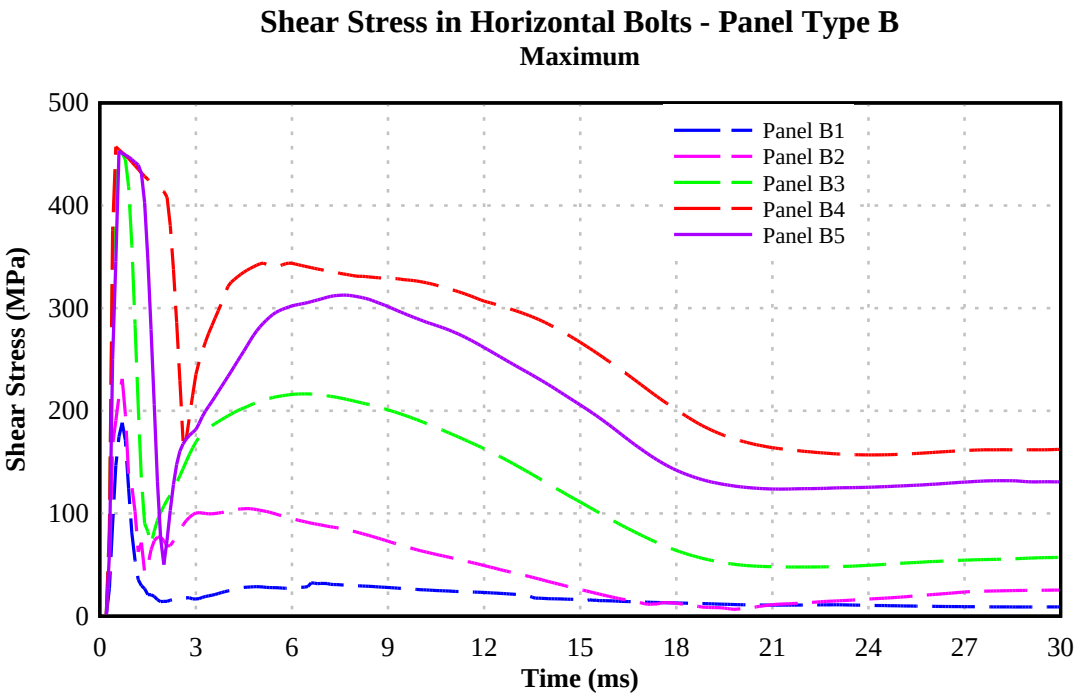

Figure 5.29: Shear stress time history of bolts (maximum) for Type B panels

Overall, bolt stresses in Panel B4 were found to be higher than bolt stresses for the other panels. However, no individual stress was high enough to fail the bolt elements. A combination of shear, axial and bending stresses could result in failure of bolt elements although this could not be visualised via the material model and LS-DYNA finite element module itself.

5.7.2. Verification of test results from National University of Defence Technology, China

As a verification measure for close range explosive loads, experimental data from the study carried out by the National University of Defence Technology, China (Wang et al., 2012) was used. Six scaled down reinforced concrete panels were tested with varying charge weights, as discussed earlier in Section 5.3. Panel deflection and spalling dimensions (damage parameters in the numerical model) were used for the verification. Additional details such as reinforcement stress were presented as necessary for the study. No pressure and impulse measurements were taken during the study hence, no results were presented for the pressure and impulse time histories.

5.7.2.1. Mid-panel deflection.

Maximum mid-panel deflection was recorded for the six reinforced concrete panels using the developed numerical model. Deflection time history for the mid-panel deflection and relevant experimental values are presented in Figure 5.30 and Table 5.23 respectively.

Two similar sets of curves were observed for the two scaled distances used. Panels A, C and E subjected to an explosive loading from scaled distances of 0.59 m/kg$^{1/3}$, showed lesser deflection than Panels B, D and F with scaled distance of 0.51 m/kg$^{1/3}$. This response is expected due to the two different blast pressures generated from two different scaled distances. Panels A, C and E rebounded from the initial downward deflection rapidly compared to Panels B, D and F. The higher flexibility in Panels B, D and F was attributed to the accumulation of damage due to the higher initial pressure pulse, weakening the cross-section.

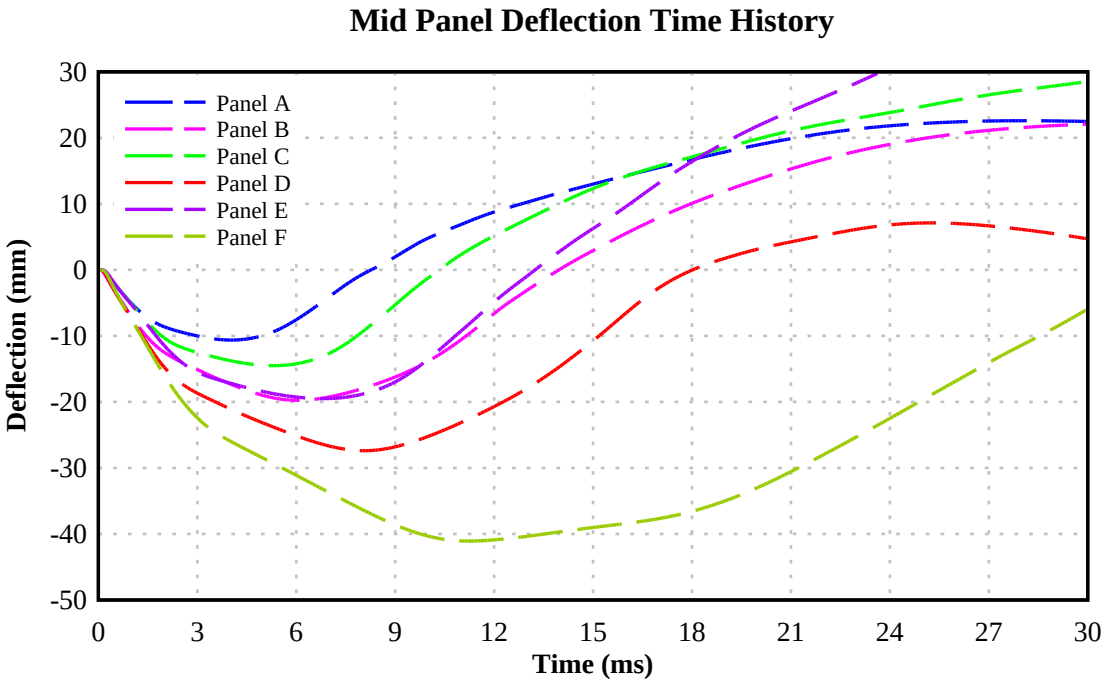

Figure 5.30: Mid-panel deflection time history

Larger panels were found to be more flexible among panels subjected to similar explosive loading. The time to reach the maximum also increased with the panel size, where the smallest recorded for Panel A at 4 ms and largest for Panel F at 11.2 ms. All panels were able to rebound reaching a positive outward deflection, except Panel F,

within the selected analysis time. This was partially due to size effects, fixity of the supports and mainly due to the higher intensity in pressure pulse.

As indicated in Table 5.23 maximum deflection recorded during the experimental study was found to be well predicted by the numerical analysis for most of the panels. However, three panels under-predicted the actual maximum deflection and other three over predicted. All except Panel D recorded error percentages within the allowable limit of 20%. Panels A, C and E with higher scaled distance showed a more rigid response than the Panels B, D and F, as expected with smaller intensity in explosive loading. Among the different size panels, larger panels provided better calibration with small error percentages as seen with Panels E and F.

Table 5.23: Maximum mid-panel deflection comparison

Panel ID	Maximum mid-panel deflection (mm)		Error (%)
	Experimental	Numerical	
A	9	10.6	17.8
C	15	14.5	-3.3
E	19	19.5	2.63
B	26	19.8	-14.6
D	35	27.4	-21.7
F	40	41.1	2.75

5.7.2.2. Spalling diameter and local damage

The spalling radius measurements taken after the explosive trials were used as a method of verifying the test results. The numerical model is unable to directly predict the local spalling damage. Numerical erosion techniques have been used to predict the spalling of concrete, although known to have problems with mass and energy balance of the system. Hence, an indirect method is used to predict the spalling diameter, as a damage parameter defined with the CDM. Although damage parameter is a combination of brittle and ductile damage, the local damage was selected for the results in this section.

The damage parameter is an accumulating scalar function, valued between zero and two. Values up to one are considered to be recoverable (elastic) damage and beyond one is non-recoverable (plastic) damage. Theoretically, the damage parameter reaching two represents complete disintegration of the material. However in practicality, values above

1.95 are considered completely damaged. Hence, the fringe levels for the plots were rearranged to highlight the damage parameter higher than 1.95.

Figures 5.31 and 5.32 illustrate the damage to the bottom face of the panel during the experimental evaluation for Panel D and relevant damage parameter (effective plastic strain) plot for the same panel, respectively. Refer to Appendix B-IV for other spalling damage and damage parameter plots.

Figure 5.31: Spalling damage of Panel D – Experimental

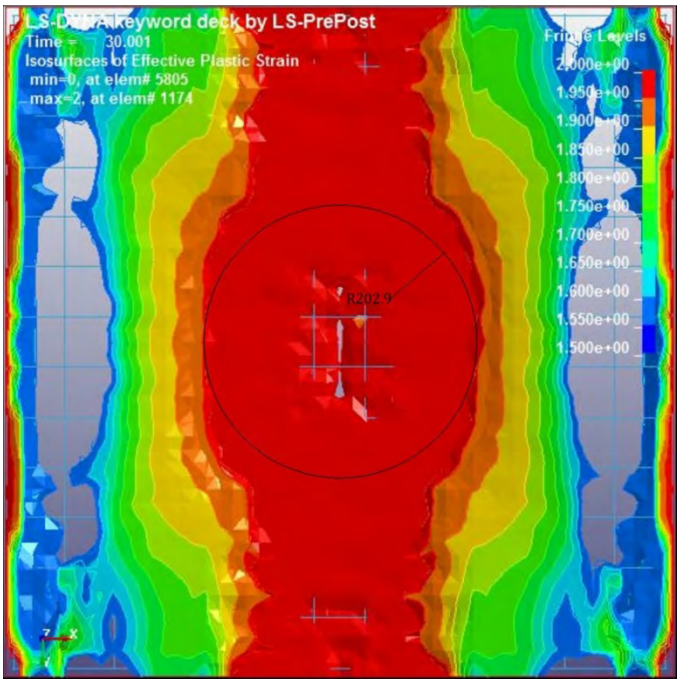

Figure 5.32: Damage Parameter plot for Panel D

Fringe levels for the plot in Figure 5.32 were rearranged from 1.5 to 2.0 so that the elements which exhibit damage parameter greater than 1.95 could be highlighted. The area close to the centre of the panel was considered to be spalling. Since the panel was supported only by two edges, damage accumulated close to free edges was due to the bending. In order to isolate the spalling damage, a circular area was highlighted in the panel centre, with maximum possible radius having damage parameter greater than 1.95 as the spalling damage radius. Since the damage parameter was defined on an element by element basis, the selected damage parameter radius was found to be larger than the experimental value. A comparison of experimental and numerical spall radius and respective error percentages are presented in Table 5.24.

Table 5.24: Comparison of Spall Radius – Experimental and Numerical

Panel ID	Spall radius (mm)		Error (%)
	Experimental	Numerical	
A	50	96.6	93.8
C	90	141.9	57.7
E	120	203.0	69.2
B	85	110.9	30.5
D	120	202.9	69.1
F	185	305.4	65.1

Numerical prediction of spall radius was found to be overestimated with errors ranging up to 93.8%. Panel B was found to give the best matching result for the damage parameter and still 30% larger than the experimental spall radius. The worst result was observed with Panel A, which had a two-fold over prediction. Surprisingly both, best and worst results were observed with the same size panel (750 mm) for different charge weights. The rest of the panels over predicted the spall radius by about 65% on average. Hence, the use of damage parameter as a method of predicting the spall damage of the panel was not convincing. The originally developed finite element model (selected material model combination, element formulation and size) was not calibrated for the spalling, since no spalling was observed with the original experimental details (Pham, 2010) selected. Hence, use of damage parameter as a method of predicting spalling damage needs to be considered, especially with the close range scaled distances.

5.7.3. Model verification summary

Two separate experimental studies with different dimensions, compressive strengths, loading and support conditions were selected for the verification of the calibrated FE model. The mid-panel deflection, support deflection, concrete stresses and spalling dimensions were considered as the parameters for the verification of numerical model with the experimental results. Following conclusions were made based on the model verification results.

- Among the 10 panels selected for the numerical model validation, 9 panels exhibit error percentages lesser than 18% for the maximum mid-panel deflection. Other panel also exhibits an error percentage less than 22%.
- Two panels out of four exhibit error margin smaller than 20% for the maximum support deflection.
- Maximum compressive stress records suggest no compressive cracking within the concrete section, which is confirmed by the crack survey conducted on test panels (experimental).
- Tensile cracking (experimental) on both faces of the panel suggest yielding of reinforcement, which was confirmed in the numerical model for all panels.
- Axial and shear stresses in connecting bolts suggest no failure in bolts, although connecting bolts in Panel B4 were broken during the experimental evaluation.
- Spalling predictions using the damage parameter found to over predict the local damage up to 90% in certain panels. Hence, use of damage parameter as a verification method was deemed not applicable in this instance.

The developed numerical model was verified using two different sources of experimental results and was found to be adequately matching with respect to mid-panel deflection and support deflection. However, use of spalling dimensions was not optimal in this instance. On the other hand failure mechanisms observed in test panels were found to be in good agreement with the predictions of the numerical model, especially with cracking of concrete and yielding of reinforcement. Hence, the developed numerical model can be considered calibrated and verified to be used in different strengths, dimensions, loading conditions and boundary conditions.

CHAPTER 6

DEVELOPMENT, CALIBRATION AND VERIFICATION OF 1-D ANALYSIS PROGRAM FOR EVALUATION OF REINFORCED CONCRETE ONE-WAY SLABS

6.1. Introduction

Various analysis tools are being used to predict the behaviour of reinforced concrete beam and one-way slab elements subjected to explosive loading. These include simplified single degree of freedom (SDOF) methods, empirical developments based on experimental results or complex procedures such as multi degree of freedom analysis (MDOF) and use of numerical analysis tools such as ANSYS AUTODYN or LS-DYNA. Chapter 5 utilised LS-DYNA to develop a numerical analysis tool. As already highlighted in this thesis, all these methods have their inherent advantages and disadvantages with varying difficulty in implementation.

The SDOF method is the simplest form of analysis for RC structures subjected to explosive loading. The actual structure is replaced by an equivalent mass and weightless spring system which represent the resistance to applied loading. These simplified form of models also have their variations due to linear and non-linear elasticity, elastoplasticity or even damping. (Ngo et al., 2007a,b). SDOF models are found to be accurate in predicting flexural and diagonal shear responses. In fact, most of the predictions and design guidelines in the UFC 3-340 (United States Army Corps of Engineers, 2008) are based on the SDOF models. The major drawback with the SDOF system is the inability to incorporate higher modes of vibrations, which are essential in predicting direct shear response (Krauthammer et al., 1993a).

Empirical relationships have been proposed based on experimental studies for different measurable attributes such as maximum deflection or spalling dimensions (Morishita et al., 2000, Yamaguchi et al., 2011, Wang et al., 2012). However, these relationships are specific to the selected study and therefore, the applicability in general is limited.

MDOF analysis arises when a structure is discretised into several equivalent lumped masses and weightless spring system prior to analysis. The MDOF is an advancement of the SDOF method. Discretisation to several masses and springs enables direct shear prediction which is lacking in SDOF method, as well as providing improved accuracy of flexural and diagonal shear prediction. MDOF systems are typically used in the analysis of structures subjected to seismic actions (Park et al., 1985). This method has also been successfully used in RC elements subjected to impact loads (Krauthammer et al., 1993a, Krauthammer et al., 1993b) and explosive loading (Pham, 2010). Although the MDOF method is effective in predicting the response of a structure, the procedure is tedious and requires sound mathematical knowledge for implementation.

As illustrated in Chapter 5, use of Finite Element Modelling (FEM) is considered as one of the most accurate methods to predict the response of structural elements subjected to explosive loading. However, use of FEM to evaluate the response of an RC structure subjected to explosive loading requires unique skills, can become time consuming and expensive.

Several analytical solutions have been proposed for the analysis of RC beams and one-way panels subjected to transient dynamic loading. Ghaboussi et al., (1984) presented an analysis tool to predict the combined effects of flexural actions in RC beams and one-way slabs, subjected to impacts loads. Krauthammer (Krauthammer et al., 1993a, Krauthammer et al., 1993b) also developed and validated an analysis tool for RC structures subjected to impact loading with considerations for constitutive failure options including shear moment interaction. A similar study was performed on RC beams and one-way slabs subjected to explosive loading with simplified loading conditions (Pham, 2010).

The primary objective here is to develop an accurate and relatively simplified analysis tool yet can be used with basic knowledge of structural engineering for the analysis of reinforced concrete beam and one-way panel elements subjected to explosive loading. An analytical solution is developed idealising to a 1-D, MDOF system. The development is primarily based on the differential formulation of Timoshenko beam theory (Timoshenko, 1921). Constitutive relationships for flexure, diagonal and direct shear were included in the development. The loading is based on the Kingery and Bulmash (Kingery and Bulmash, 1984) equations for spherical charge weights. The

developed model is validated with prior experimental results prior to using in parametric studies.

6.2. Structural modelling of beam elements

Two classical beam theories available for the structural formulation of beam elements are known as the Euler-Bernoulli beam theory (EBBT) and Timoshenko beam theory (TBT). The EBBT is also known as the classical beam theory due to the assumption used in the development, which is the main difference between two theories. In assuming "plane sections remain plane and normal to the longitudinal axis after bending" the EBBT ignores the possible shear deformation. Although this assumption is accurate for thinner sections with a larger span to thickness ratios in quasi-static loading, predictions in thicker elements and loading in the dynamic and impulsive regime are found to be inaccurate. Furthermore, the EBBT is more suitable for predicting small deflections within the elastic limit while the TBT is suitable for both small and large deflections with post plastic prediction capabilities with its second order formulation. Therefore, the TBT is more suitable for analysing the structures subjected to explosive loading (Krauthammer et al., 1993a).

The development of this 1-D analytical tool is based on the differential formulation of the TBT, as shown in Figure 6.1. The structure is discretised to a limited number of nodes based on the thickness and the speed of sound through the material, with each element having a length of Δx *(dx)*. The governing equilibrium equations for the TBT are given in Equations 6.1 and 6.2.

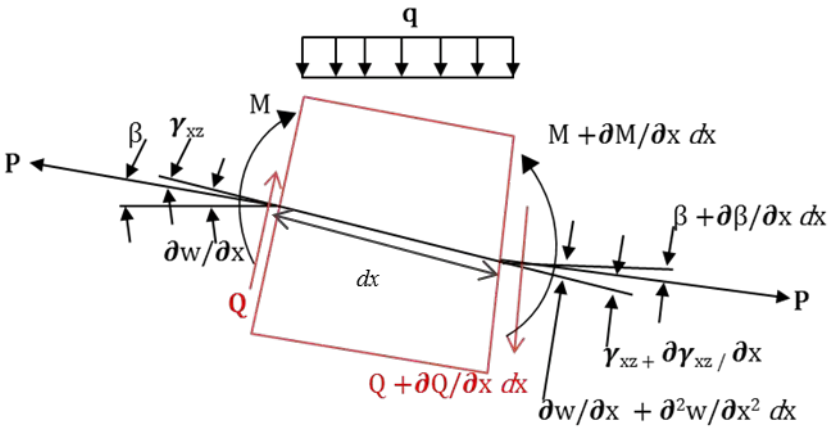

Figure 6.1: Timoshenko beam differential element (Source: Krauthammer et al., 1993)

$$\frac{\partial M_{(x,t)}}{\partial x} - Q_{(x,t)} = -\rho_m I \frac{\partial^2 \beta_{(x,t)}}{\partial t^2} \tag{6.1}$$

$$\frac{\partial Q_{(x,t)}}{\partial x} + q_{(x,t)} + P_{(x,t)} \frac{\partial \beta_{(x,t)}}{\partial x} = \rho_m A \frac{\partial^2 w_{(x,t)}}{\partial t^2} \tag{6.2}$$

Where;

M = *Bending moment*

Q = *Shear force*

β = *Angle of bending rotation*

w = *Transverse displacement*

I = *Moment of inertia*

A = *Cross sectional area*

ρ_m = *Material density*

q = *Uniformly distributed load transverse to the beam*

P = *Axial force applied at the centroid of the cross-section*

x = *Location of the element along the member*

t = *time*

In addition, two further compatibility conditions exist as given in Equations 6.3 and 6.4. These two compatibility conditions are derived using the deformation diagram given in Figure 6.2.

$$\gamma_{xz(x,t)} = \frac{\partial w_{(x,t)}}{\partial x} - \beta_{(x,t)} \tag{6.3}$$

$$\varphi_{(x,t)} = -\frac{\partial \beta_{(x,t)}}{\partial x} \tag{6.4}$$

Where;

$\gamma_{(xz)}$ = *Shear strain*

φ = *Curvature of the section*

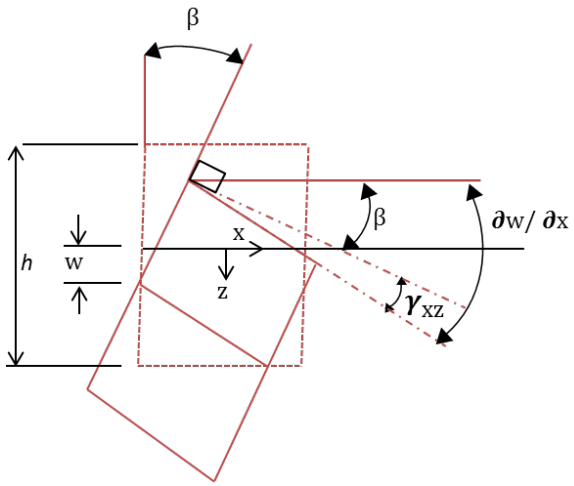

Figure 6.2: Deformations of a Timoshenko beam element (Source: Krauthammer et al., 1993)

Shear force (Q) and Bending moment (M) can be expressed as functions of Shear strain (γ_{xz}) and curvature of the cross-section (φ) respectively as shown in Equations 6.5 and 6.6 respectively.

$$Q_{(x,t)} = \mathrm{K}Af_1(\gamma_{xz}) \tag{6.5}$$

$$M_{(x,t)} = f_2(\varphi) \tag{6.6}$$

Equation 6.5 is known as the shear force-strain relationship for diagonal shear and Equation 6.6 as the moment-curvature relationship for a given cross-section. The modification factor (K) was defined as the deformation correction coefficient, which can be calculated if the shear stress distribution through the cross-section is known. Determination of the deformation correction factor is relatively simple in the static loading domain. However, the stress distribution will vary with the mode of vibration (Mindlin, 1951). Being a second order theory, the TBT can predict two modes of vibrations, lower mode or the flexure-shear mode and higher mode or thickness-shear mode (Mindlin, 1951). The governing value for flexure-shear modes is given as $\pi^2/12$, which will be used during this study.

Other than the moment-curvature relationship and shear force-strain relationship, two other functions are required for an accurate implementation of the TBT for dynamic loading conditions. These relationships are known as the shear force-slip relationship

for direct shear and force-displacement relationship for supports. All of these relationships will be discussed in detail in the sections to follow.

6.3. Flexural response modelling

The flexural behaviour of RC beams and one-way panels is governed by the moment-curvature relationship. The moment - curvature relationship of 1-D concrete elements is developed based on several simplified assumptions. The stresses experienced in 1-D concrete elements are assumed to be uniaxial. This assumption was found to be realistic for beams and one-way slabs where cross-sectional dimensions are considerably smaller than the length. The plain sections law, commonly known as Euler-Bernoulli theorem, is also assumed for the flexural behaviour. This assumption recommends a linear strain distribution within the cross-section, throughout the analysis. Although this assumption is found to be realistic, several deviations of this assumption have been documented (Park and Pauly, 1975).

A perfect bond between reinforcement and concrete is assumed. This assumption along with the plain sections law allows the reinforcement stresses to be estimated using the compressive strain of concrete. The contribution from concrete tensile strength was neglected and all the tensile stresses are assumed to be carried only by the steel reinforcements. This assumption is reasonable for concrete which is week and brittle under tensile stresses once cracking has occurred at advanced stages of loading.

In addition to the above assumptions, the moment-curvature relationship requires stress-strain relationships for concrete and reinforcing steel. As discussed in Sections 3.2.1.6 and 3.3.1.3, the Modified Scott Model (MSM) for concrete and Plastic Kinematic model (elastic-perfectly plastic) for steel were selected for the construction of moment-curvature relationship. The Mander's coefficient (Mander et al., 1988) defined for confined concrete was also used for this development (Refer to Appendix A-I for the derivation and definitions).

The moment-curvature relationship was developed with the above assumptions and equilibrium of forces in tension and compression within the section. Each point in the relationship corresponds to a value of compressive strain in the extreme fibre of concrete (ε_c). Strain compatibility and distribution of forces for a given compressive strain are presented in Figure 6.3.

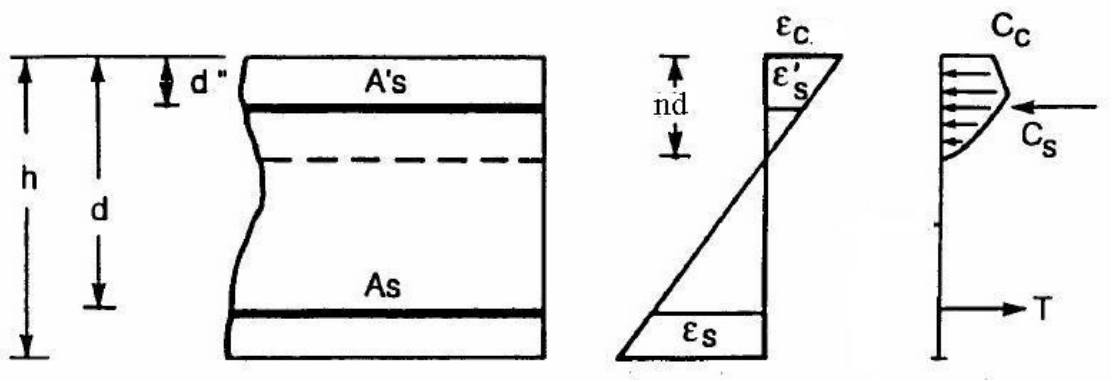

Figure 6.3: Strain compatibility and distribution of forces on a cross-section for moment-curvature relationship (Assadi-Lamouki and Krauthammer, 1988)

The initial step is to assume the compressive strain in the outermost fibre and calculate the neutral axis depth until the compressive forces and tensile forces are in equilibrium. Once the equilibrium is achieved, bending moment (M) and the curvature (φ) corresponding to the assumed strain is calculated, and the assumed strain is increased until one of the failure conditions is achieved. Failure conditions for the moment-curvature relationship include failure strain of concrete (ε_{cu}), maximum curvature (φ_{max}) or the failure strain of reinforcement (ε_{su}). A graphical representation of solution procedure for the moment-curvature relationship is illustrated in the flow chart in Figure 6.4. The complete theoretical formulation of the MSM is presented in Appendix C-I.

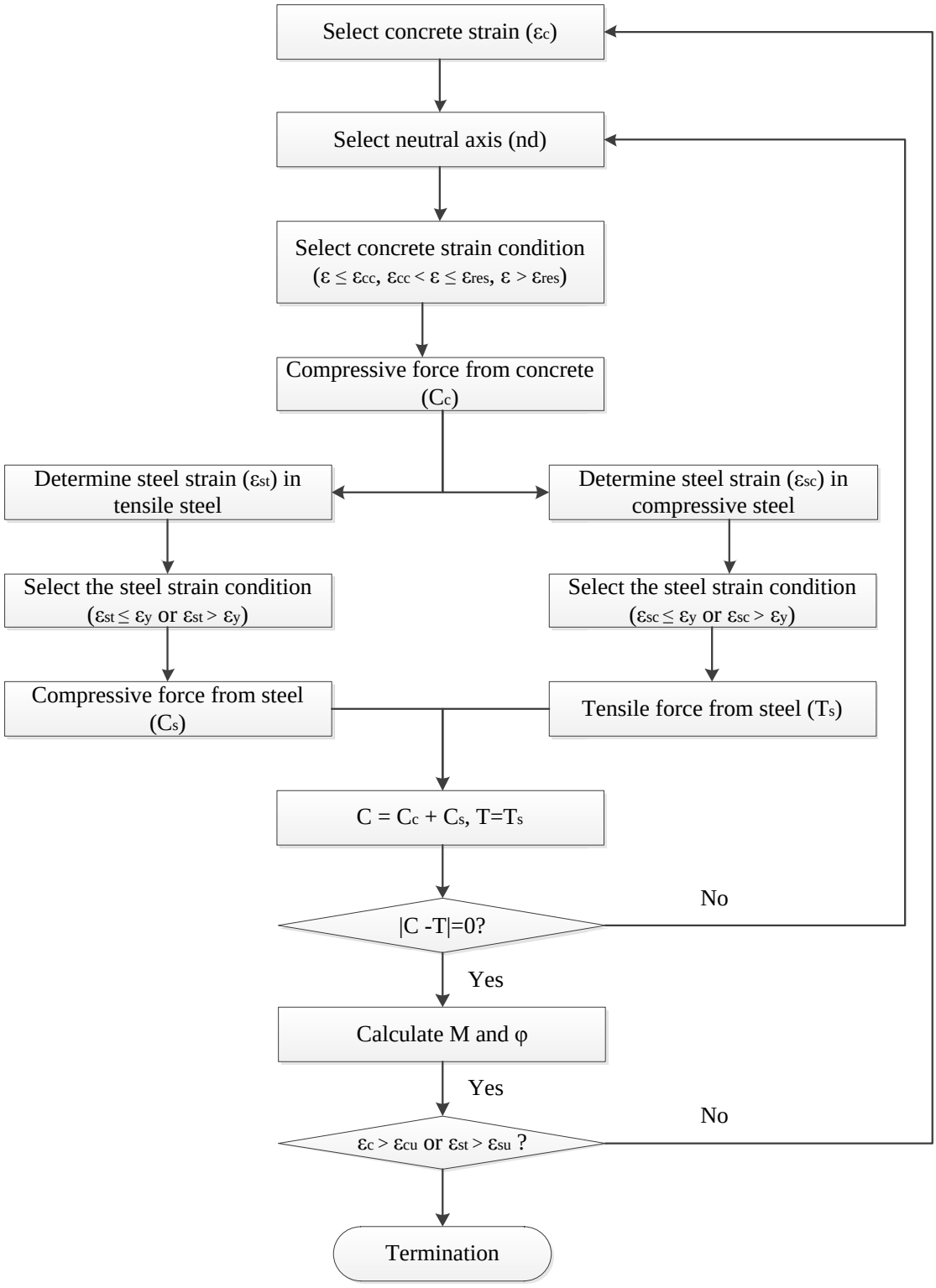

Figure 6.4: Flow chart for the solution procedure for moment-curvature relationship of RC cross-section

The moment-curvature relationship was coded to a computer application using the version 12.8 of PGI visual FORTRAN (The Portland Group, 2011). The relevant coding is presented in Appendix C-IV.

6.4. Shear response modelling

The Shear response in reinforced concrete elements can be categorised into two major types, named as diagonal shear and direct shear. The diagonal shear response is associated with tensile cracks developing at an angle to the axis of the member. These cracks can result in brittle failure unless adequate shear reinforcement is provided. The direct shear response is associated with the concentration of shear stresses such as at supports and fixing assemblies, geometric discontinuities or close to concentrated loads. Direct shear failures can be usually identified as cracks propagating perpendicular to the axis of the member. The direct shear response is characterised by transverse shearing, usually known as slip between adjoining segments of the structure.

6.4.1. Diagonal shear response modelling

Several analytical solutions, compression field theory (CFT) (Vecchio and Collins, 1981), rotating angle softened truss model (RA-STM) (Pang and Hsu, 1995), fixed angle softened truss model (FA-STM) (Pang and Hsu, 1996) and softened membrane model (SMM)(Hsu and Zhu, 2002), were proposed for the non-linear shear behaviour prediction for reinforced concrete elements. All these analytical solutions were exceptional in representing the ascending section (up to the peak value, Figure 6.5) of the shear stress-strain curve. However, none of the analytical solutions are able to adequately predict the softening behaviour except for the SMM (Hsu and Zhu, 2002). Therefore, the SMM was selected as the solution for diagonal shear behaviour for this analysis. A small summary of the SMM and procedure for development of shear force-strain relationship is given in the following section.

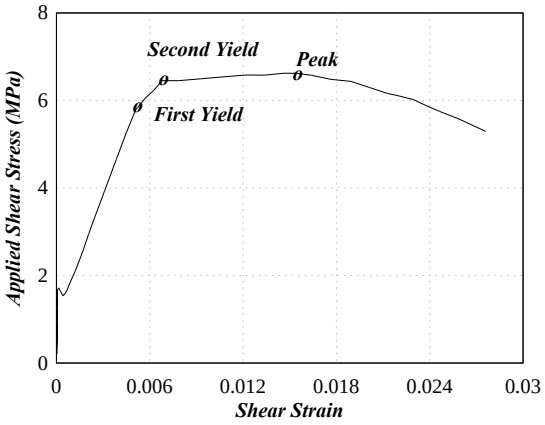

Figure 6.5: Typical shear stress-strain curve for concrete (Hsu and Zhu, 2002)

Developments of the SMM were based on the RA-STM and FA-STM for the purposes of minimising the limitations of its predecessors, especially in the softening range of shear stress-strain relationship. The SMM was defined as the rational theory satisfying Navier's three principles of mechanics of materials, stress compatibility, strain compatibility and constitutive material laws. The stress and strain compatibility equations were directly imported from FA-STM while constitutive relationships were imported with different interpretations.

The solution algorithm for the SMM involves a similar iteration procedure as for the flexural response in the MSM (Figure 6.6). Initially, three independent strains, smeared strain in principle direction 1 (ε_1), smeared strain in principle direction 2 (ε_2) and smeared shear strain in the 2-1 coordinate system (γ_{21}) are assumed. These three strains are varied with a step by step process with an interval of 1×10^{-6} until the convergence is achieved. When the convergence criterion is achieved, corresponding shear stress and strain are calculated and stored and the solution process is advanced to the next set of strains. The solution is continued until the shear stress-strain curve softens below 75% of the maximum shear capacity or the smeared strain reaches a predefined threshold, based on the compressive strength of concrete. A flow chart of the solution algorithm is shown in Figure 6.6, which was initially defined in the original SMM formulation (Hsu and Zhu, 2002). The complete theoretical formulation of the SMM is presented in Appendix C-II and Appendix C-IV presents the relevant FORTRAN coding for the SMM formulation.

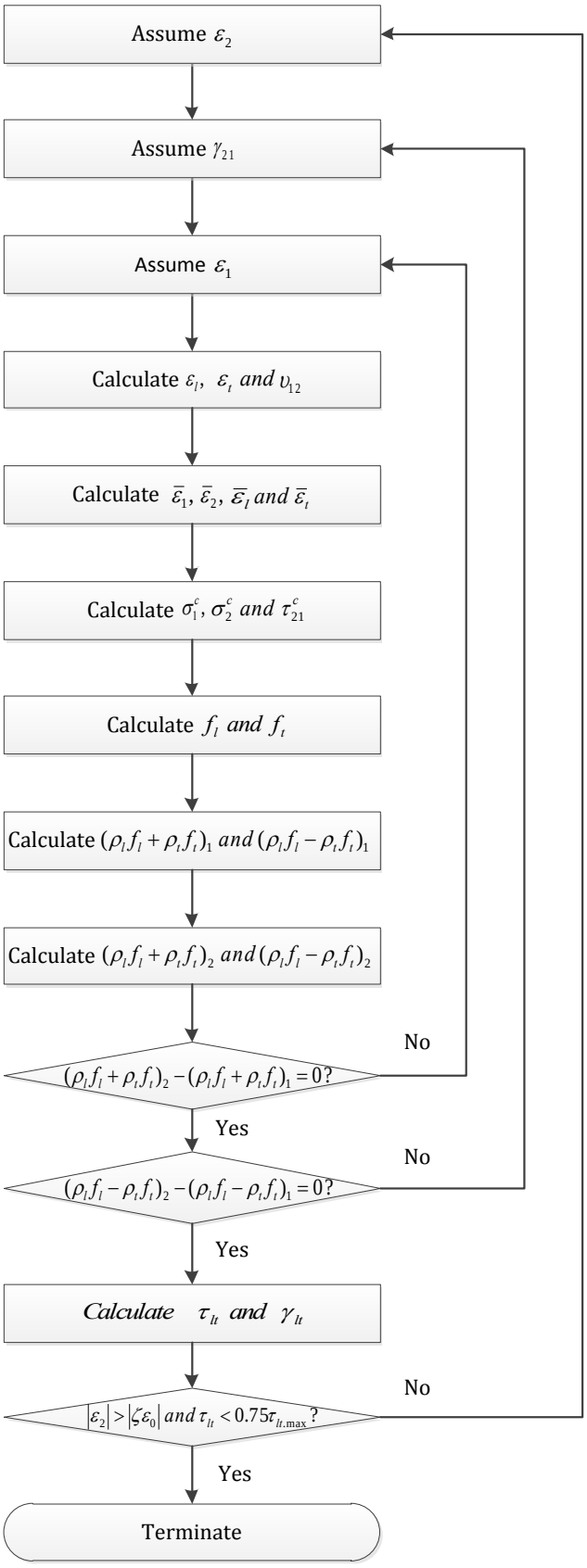

Figure 6.6: Flow chart for the solution procedure for shear stress-strain relationship of RC cross-section

6.4.2. Direct shear response

In geometrical discontinuities or force concentrations, shear stress may cause a sliding type failure perpendicular to the axis of the member. It has been documented that (Park and Pauly, 1975) this behaviour is critical when the flexural member having small shear span to effective depth ratios, or when higher stresses have to be transferred through a weak section like a pre-cracked section. However, this kind of failure has been observed even without pre-existing cracks and with a higher shear span to effective depth ratios (Kiger et al., 1980, Slawson, 1984).

The empirical relationship proposed for the shear-slip action by Hawkins (Hawkins, 1982) is employed during this study. The proposed model is based on experimental data and material behaviour neglecting axial forces. The Hawkins shear-slip relationship consists of five straight lines defining different stresses and applicable deflection levels, as shown in Figure 6.7.

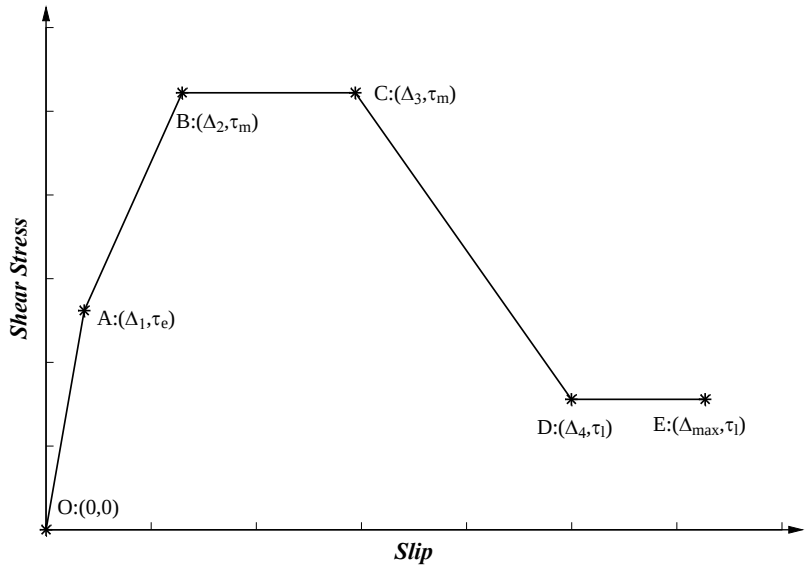

Figure 6.7: Hawkin's Shear stress-slip relationship (Source: Hawkins, 1982)

The original equations defining the model parameters are in the imperial unit system and were transformed to the metric system and presented in Appendix C-III. Values of Δ_1, Δ_2, and Δ_3 correspond to slip deflections of 0.1016 mm, 0.3048 mm and 0.6096 mm respectively. Δ_3 and Δ_{max} values are calculated based on the empirical relationships given in Appendix C-III. Relevant FORTRAN coding for the Hawkin's shear-slip relationship is presented in Appendix C-IV.

Achieving a slip deflection of Δ_{max} is defined as the failure criterion under the direct shear response. In addition, the shear stress-slip relationship was transformed to shear force-slip relationship, which is simpler to use with the TBT. The transformation was straightforward as the Hawkins shear-slip relationship was based on the average shear stresses.

6.4.3. Shear moment interaction

It is well known that a given cross-section cannot simultaneously resist both ultimate shear force and bending moment (Vecchio and Collins, 1988). A study of rectangular RC cross-section on bending shear interaction reveals that in locations where ultimate moment does not exceed half the ultimate moment capacity, the section is capable of developing almost up to ultimate shear capacity and vice versa (Krauthammer et al., 1993a). However, at locations where both high moment and shear occur simultaneously, such as in cantilevers, sections tend to fail without reaching the full capacity (either in shear or flexure) of the section, as shown in Figure 6.8.

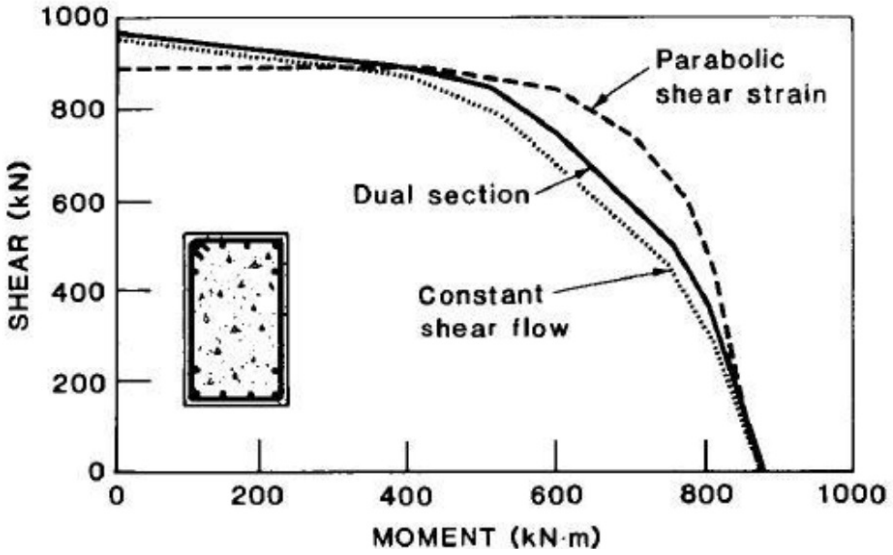

Figure 6.8: Shear moment interaction diagrams for comparing approximate procedures (Vecchio and Collins, 1988)

In general, there is a possibility that shear-moment interaction may affect the carrying capacity of concrete. However, the interaction may be ignored in certain specific loading conditions such as impulsive loading (Feldman et al., 1962, Slawson, 1984). On the other hand, implementation of the moment-shear interaction in a 1-D analysis for

dynamic and impulsive loading is not feasible as both moment and shear capacities can vary with the time and location. On the basis of the above arguments, shear moment interaction is ignored during this study.

6.5. Strain rate enhancement

Materials subjected to higher rates of loading exhibit enhanced carrying capacities than the same material subjected to equivalent static loading. This phenomenon is known as strain rate enhancement and was discussed in detail in Chapter 3. As observed, different strength related attributes can enhance in different proportions. However, due to the vast scatter and wide range of experimental results, a bilinear logarithmic fit was proposed to (tensile and compressive strengths of concrete) relate the strain rate enhancement (Malvar and Crawford, 1998a,b). As with any logarithmic relationship, an order of magnitude value instead of the exact strain rate enhancement will prove sufficient.

6.5.1. Procedure for determination of strain rate for 1-D structures

There are two simplified methods to determine the strain rate in a 1-D structural element. The first method involves several assumptions including simplifying the structure as a simply supported beam with a rectangular cross-section. The loading is also assumed to be static uniformly distributed with an intensity of q. Assuming elastic stress-strain distribution, bending stress and strain at the outermost fibre can be defined as in Equations 6.7 and 6.8. In addition, the neutral axis of the section is assumed to coincide with the geometrical neutral axis of the section ($h/2$).

$$\sigma = \frac{M_{max}}{I}\frac{h}{2} = \frac{qL^2}{8}\frac{h}{2I} = 0.0625\frac{qL^2h}{I} \tag{6.7}$$

$$\varepsilon = \frac{\sigma}{E} = 0.0625\frac{qL^2h}{EI} \tag{6.8}$$

Where;

L = Length of the beam

h = Thickness of the section

I = Moment of inertia of the section

EI = Flexural stiffness (assumed to be constant for both cracked and uncracked concrete)

$$EI = \frac{M}{\varphi} = \frac{(M)_y}{(\varphi)_y} \tag{6.9}$$

Where;

$(M)_y$ = Yielding moment (Corresponds to initial cracking)

$(\varphi)_y$ = Yielding curvature

Combining Equations 6.8 and 6.9 and differentiating the equation assuming the uniformly distributed loading *(q)* is dynamic; the strain rate can be defined as in Equation 6.10.

$$\frac{\partial \varepsilon}{\partial t} = \dot{\varepsilon} = 0.0625 \frac{\partial q}{\partial t} L^2 h \frac{(\varphi)_y}{(M)_y} \tag{6.10}$$

The rate of loading ∂q/∂t is determined from the loading time history. The maximum value of loading rate determined from the loading time history will be used as the representative value for the entire duration. Similarly, strain rate for a simply supported beam with a dynamic point load in the middle can be written as in Equation 6.11.

$$\frac{\partial \varepsilon}{\partial t} = \dot{\varepsilon} = 0.125 \frac{\partial P}{\partial t} L^2 h \frac{(\varphi)_y}{(M)_y} \tag{6.11}$$

Where;

P = Dynamic point load applied at the middle of the span

Krauthammer et al. (1990) implemented this procedure and observed strain rates similar to those observed during the experimental evaluation. However, implementation of this procedure in an analysis requires the definition of different rate determination procedures for different loading configurations. In the case of a point load, the strain rate depends on the loading position as well, which makes the implementation even more difficult. In addition, the same strain rate needs to be applied for bond strength, diagonal shear and direct shear.

The second procedure is to implement strain rate from the rate of change in curvature and shear strain. In this approach, strain rate for each attribute (bending and diagonal shear) is calculated for each analysis point and the maximum value is applied to each attribute for the entire beam. Although it is possible to accommodate strain rate and applicable strain rate enhancement for each node in the analysis, a 1-D analysis solution

does not possess similar accuracy levels due to its simplifications and approximations. Hence, the maximum value is implemented. The strain rate for flexure is calculated based on the rate of change in curvature and rate of change in shear strain was used for the diagonal shear resistance, as shown in Equation 6.12.

$$\frac{\partial \varepsilon}{\partial t} = \dot{\varepsilon} = \left(\frac{\partial \varphi}{\partial t}\right) \; or \; \left(\frac{\partial \gamma}{\partial t}\right) \tag{6.12}$$

This procedure possesses several advantages over the first approach as it does not depend on the type or location of the loading, structural shape and applicable even after the load vanishes. Implementation of this procedure in a numerical solution is more straightforward than the first approach and with lesser assumptions and simplifications. Hence, the second method, strain rates based on the rate of change in curvature and shear strain is implemented in this analysis.

6.5.2. Implementation of strain rate enhancements for 1-D structures

As discussed earlier, strain rates are determined based on the different parameters of the structural response, i.e. rate of change in curvature and shear strain rate. The strain rate enhancements are also implemented on the basis of those attributes. Rate enhancement curves proposed for compressive strength of concrete by Malvar and Crawford (1998a,b) were used to calculate the DIFs for both flexure and diagonal shear, as these equations represent better calibration with experimental results, as discussed in Chapter 3.

The Hawkins (1982) direct shear prediction does not involve any strain related parameters hence, the dynamic enhancement was required to be implemented differently. The stress rate could be implemented however, which might not be compatible with the strain rates used with flexural and diagonal shear. On the other hand, Krauthammer et al. (1990) proposed a DIF value of 1.4 (40% increase) for the direct shear response. This modification was found to be compatible with the experimental results. Therefore, a single DIF value of 1.4 was implemented for the direct shear response.

6.6. Boundary conditions

Application of Timoshenko beam equations on beams with finite length requires the definition of boundary conditions, which is not required with beams with infinite length.

In the equivalent static analysis, simplified boundary conditions such as pinned or fixed supports can predict the response of the structure close to reality. Implementation of these simplified boundary conditions is also straightforward. However, in reality, idealised boundary conditions do not exist and a realistic solution cannot be expected from these simplified boundary conditions. Hence, several boundary conditions, including the simplified boundaries, are defined in Tables 6.1 and 6.2 for the purpose of analysis of 1-D structural elements.

All these boundary conditions were defined based on the allowable rotation and transverse deflection of the support. Each beam element requires the definition of two boundary conditions for each end (support) and the overall stability of the structure needs to be checked prior to further analysis. Boundary conditions selected for the analysis for bending rotation and transverse deflection are given in Table 6.1 and 6.2 respectively.

Table 6.1: Boundary conditions related to bending rotation

Name	Function	Description
Free rotation	$M_b = 0$	The support node is free to rotate under the applied loading. Rotation value is directly calculated from the analytical solution and moment is vanished
Fixed rotation	$\beta_b = 0$	No rotation is allowed at the support, hence rotation is vanished and applied moment exists.
Liner rotational spring	$M_b = K_r(\beta_b)$	Both bending rotation and moment exist. Linear approximation between support rotation and applied bending moment is assumed.
Non–linear rotational spring	$M_b = f_r(\beta_b)$	The moment is approximated from a pre-defined function of support rotation. Both moment and rotation exist.

Table 6.2: Boundary conditions related to transverse deflection

Name	Function	Description
Free translation	$Q_b = 0$	The support node is free to translate under the applied loading. Translation is directly calculated from the analytical solution and shear force is vanished
Fixed translation	$W_b = 0$	No translation is allowed at the support, hence translation is vanished and applied shear force exists.
Liner translational spring	$Q_b = K_t(W_b)$	Both translation and shear force exist. Linear approximation between translation and applied shear force is assumed.
Non–linear translational spring	$Q_b = f_t(W_b)$	The shear force is approximated from a pre-defined function of support translation (slip). Both shear force and transverse deflection exist.

6.7. Failure conditions

Failure conditions can be classified as a partial failure and complete failure.

6.7.1. Partial failure conditions

Partial failure of the structure is assumed to occur when the maximum carrying capacity of each attribute (flexure, diagonal shear or direct shear) is reached. Three different partial failure conditions can be defined for flexure, diagonal shear and direct shear as follows.

Applied moment reaching maximum moment capacity is assumed to fail the section in flexure. This condition corresponds to the maximum moment of the moment-curvature relationship, not the maximum value of curvature.

$$M_a = M_{max} \tag{6.13}$$

Applied shear force reaching the maximum shear capacity is assumed to fail the section in diagonal shear. This condition corresponds to maximum shear capacity which does not necessarily mean the maximum shear strain.

$$Q_a = Q_{max} \tag{6.14}$$

Applied shear stress reaching the maximum direct shear capacity of the Hawkins shear - slip relationship is considered to fail the section in direct shear. This condition corresponds to maximum direct shear capacity which does not necessarily mean the maximum allowable slip.

$$Q_a = \tau_m A_c \tag{6.15}$$

Reaching one of these conditions will hinder the load carrying capacity of the structure. However, if support conditions permit, the structure will be able to transfer additional loads with rearranging load transfer mechanisms until the complete failure is occurred.

6.7.2. Complete failure conditions

As in partial failure conditions, three different complete failure conditions can be defined for the three carrying capacities. All three attributes, flexure, diagonal shear and direct shear are considered to have post peak residual capacities; hence considering complete failure with maximum allowable deformations (curvature, shear strain or slip) is more applicable. Furthermore, this will allow the structure to reach the maximum capacity in one attribute (e.g. flexure) and complete failure in same or other type of attributes (e.g. diagonal shear or direct shear)

Reaching the maximum allowable curvature is considered a complete failure in flexure.

$$\varphi_a = \varphi_{max} \tag{6.16}$$

Reaching the maximum allowable shear strain is considered a complete failure in diagonal shear.

$$\gamma_a = \gamma_{max} \tag{6.17}$$

Reaching the maximum allowable shear slip is considered a complete failure in direct shear. The maximum slip is defined using the Hawkins shear slip model (Hawkins, 1982).

$$\Delta_a = \Delta_{max} \tag{6.18}$$

Reaching any of the above mentioned failure conditions is considered to result in a complete failure of the structure. If any of these conditions reach during an analysis, the analysis process is terminated and the failure method is presented.

6.8. Loading and application of loading

This computational tool is intended to be used in evaluating the response of the reinforced concrete beam and one-way panels subjected to explosive loading. Both user-defined pressure time histories as well as program calculated pressure time histories can be used as the loading. In the case of a user-defined pressure time history, a piecewise linear pressure-time history is used to define the loading function.

In the case of program calculated pressure time history, the Kingery and Bulmash (Kingery and Bulmash, 1984) equations discussed in Chapter 2 are used to define the peak reflected pressure and positive phase duration. The option of using the pressure time history as a triangular distribution or using the Friedlander exponential decay function (Freidlander, 1946, Cited in Dewey, 2010) is provided.

The Timoshenko beam equations (Equations 6.1 and 6.2) are defined based on uniformly distributed loading. However, the uniformity of the loading should only be within the element considered for the analysis. Therefore, it is possible to apply different load intensities for different elements within the same time interval, considering different arrival times. However, for 1-D analysis, uniform loading for every element, within the same time interval will provide reasonable accuracy.

Considering the charge weight-standoff combinations, this analysis solution will be most accurate for far range studies, as it does not consider local failure modes. The pressure intensity variation within the elements of the beam or slab for far range explosive events will be minimal. Therefore, constant pressure intensity is considered for all elements within the same time interval. The determined pressure profile is converted to a uniformly distributed load prior to application in the Timoshenko beam equations.

6.9. Implementation of numerical solution

The Timoshenko beam with linear elastic material models allows closed form solutions with simplified boundary conditions. However, with material and structural nonlinearities, numerical modelling seems to be the only option available for achieving an accurate solution, especially in conjunction with complex boundary conditions. Finite element and finite difference techniques are considered feasible for obtaining a

numerical solution with structural and material nonlinearities and complex boundary conditions.

Both finite element and finite difference techniques rely on discretising the overall domain to small sub domains. The solution procedure is compiled to each sub domain and until the required convergence accuracy is reached. The solution of each sub domain is assembled sequentially to obtain an approximate solution to the problem. This procedure is similar in both finite element and finite difference algorithms.

A solution of a Timoshenko beam problem can be obtained from either finite element or finite difference procedures. Although finite element procedures available for linear elastic Timoshenko beam formulations, a finite difference scheme was used for this study. Finite element formulations are based on matrices for stiffness and mass, which requires higher computational resources. In addition, these matrices need to be updated at every time interval, which will extend the analysis time. Furthermore, in post peak failure analysis, numerical instabilities can occur with the formation of negative stiffness matrices (Krauthammer et al., 1993a).

The finite difference scheme holds several advantages over finite element scheme in case of dynamic Timoshenko beam equations. The finite difference method can also have numerical stabilities with large time steps. However, these instabilities are easy to overcome by defining smaller time steps, which may increase the analysis time. Therefore, finite difference method was selected for the scope of this study.

6.9.1. Finite difference method

The finite difference method is considered as one of the simplest and earliest known methods for solving partial derivatives. The continuous function of given variables is divided into a system of discrete elements and the partial derivatives of each node are expressed in terms of neighbouring nodes (linear multistep method). Alternatively, the Taylor series expansion can be used to derive an algebraic equation to express partial derivatives. In both methods, in order to derive a solution for a boundary value problem, the number of algebraic equations defined should be equal to number of unknowns in the system of equations (Krauthammer et al., 1993b). The Taylor series expansion was used to transform partial derivatives to algebraic equations for the scope of this study.

Taylor series expansion can be used to represent partial differential equations with respect to space as well as time. Defining the parameters of a node (i.e. bending moment) using the same or related parameters of close by nodes is known as space related Taylor series expansion. Defining the parameters of the node using the same or related parameters of the same node of previous time steps is known as the time related Taylor series expansion. In the case of using the TBT to analyse blast loading response of RC structures, both space and time related Taylor series expansions will be used.

The following sections discuss the construction of both space and time related Taylor series expansions that will be used in solving the Timoshenko beam equations.

A function of location and time is defined as *F(x,t)*. Using the Taylor series expansion, value of function *F* at a neighbouring node at the same time, *F(x+Δx,t)* can be defined using partial derivatives as,

$$F(x+\Delta x,t) = F(x,t) + \Delta x\frac{\partial F(x,t)}{\partial x} + \frac{(\Delta x)^2}{2!}\frac{\partial^2 F(x,t)}{\partial x^2} + \cdots + \frac{(\Delta x)^{(n-1)}}{(n-1)!}\frac{\partial^{n-1} F(x,t)}{\partial x^{n-1}} + O[(\Delta x)^n] \quad (6.19)$$

Being an infinite series, the Taylor series expansion possesses infinite number of terms. However, the formulation given in Equation 6.19 is truncated at the n^{th} term, representing the rest as error function, $O[(\Delta x)^n]$. Accuracy of the prediction depends on the number of terms used in the formulation. An algebraic equation for the first partial derivative ($\partial F/\partial x$) can be obtained rearranging the Equation 6.20. This procedure is known as the forward difference scheme of Taylor series expansion.

$$\frac{\partial F(x,t)}{\partial x} = \frac{F(x+\Delta x,t) - F(x,t)}{(\Delta x)} - \frac{(\Delta x)}{2!}\frac{\partial^2 F(x,t)}{\partial x^2} - \cdots - \frac{(\Delta x)^{(n-2)}}{(n-1)!}\frac{\partial^{n-1} F(x,t)}{\partial x^{n-1}} - O[(\Delta x)^{n-1}] \quad (6.20)$$

Similarly, the first partial derivative ($\partial F/\partial x$) can be written in terms of other neighbouring node *(x=x-Δx)* as in Equation 6.21. This procedure is known as the backward difference scheme of Taylor series expansion.

$$\frac{\partial F(x,t)}{\partial x} = \frac{F(x,t) - F(x-\Delta x,t)}{(\Delta x)} - \frac{(-\Delta x)}{2!}\frac{\partial^2 F(x,t)}{\partial x^2} - \cdots + \frac{(-\Delta x)^{(n-2)}}{(n-1)!}\frac{\partial^{n-1} F(x,t)}{\partial x^{n-1}} - O[(\Delta x)^{n-1}] \quad (6.21)$$

The addition of Equations 6.20 and 6.21 will define a new equation, which will be based on the values of function at both front *(x=x+Δx)* and back nodes *(x=x-Δx)*. This

procedure is known as the central differential scheme for Taylor series expansion and gives Equation 6.22.

$$\frac{\partial F(x,t)}{\partial x} = \frac{F(x+\Delta x,t) - F(x-\Delta x,t)}{2(\Delta x)} - \frac{2(\Delta x)^2}{3!}\frac{\partial^3 F(x,t)}{\partial x^3} - \frac{2(\Delta x)^4}{5!}\frac{\partial^5 F(x,t)}{\partial x^5} \dots + \frac{2(-\Delta x)^{(n-2)}}{(n-1)!}\frac{\partial^{n-1} F(x,t)}{\partial x^{n-1}} - O[(\Delta x)^{n-1}] \quad (6.22)$$

In order to obtain an accurate solution, the distance between nodes *(Δx)* should be defined as a small value. Therefore, higher order terms including power of two or more can be omitted and a solution up to second order in accuracy arises, as shown in Equation 6.23. This second order accurate first order partial derivative will be used to represent middle nodes (excluding left and right supports) of the beam/panel element.

$$\frac{\partial F(x,t)}{\partial x} = \frac{F(x+\Delta x,t) - F(x-\Delta x,t)}{2(\Delta x)} \quad (6.23)$$

Equation 6.23 cannot be used in boundary elements as it requires values of both left and right of the selected node. If the centre difference scheme is to be used with boundary elements, mirror nodes have to be defined at each of the boundaries which require additional mirror node definitions. As a solution, the forward difference scheme with left support and backward difference scheme with right support can be used. However, as given in Equations 6.20 and 6.21, the first order truncation error will be available which is not compatible with the centre difference scheme which has a second order truncation error. As a solution, the Taylor series expansion can be written in terms of second node to the right or left depending on the forward or backward difference schemes, as shown in Equation 6.24 (Forward difference scheme with second order accuracy).

$$\frac{\partial F(x,t)}{\partial x} = \frac{F(x+2\Delta x,t) - F(x,t)}{(2\Delta x)} - \frac{(2\Delta x)}{2!}\frac{\partial^2 F(x,t)}{\partial x^2} - O[(\Delta x)^2] \quad (6.24)$$

Similarly, rearranging Equation 6.20 to second order accurate terms and substituting twice the rearranged equation from Equation 6.24 will yield a second order forward difference scheme for a first order partial derivative as in Equation 6.25 (omitting second order truncation error).

$$\frac{\partial F(x,t)}{\partial x} = \frac{-3F(x,t) + 4F(x+\Delta x,t) - F(x+2\Delta x,t)}{(2\Delta x)} \tag{6.25}$$

The second order accurate, first order partial derivative for backward difference scheme can be developed similarly as shown in Equation 6.26.

$$\frac{\partial F(x,t)}{\partial x} = \frac{3F(x,t) - 4F(x-\Delta x,t) + F(x-2\Delta x,t)}{(2\Delta x)} \tag{6.26}$$

However, it was argued that in order to match the second order accuracy of centre difference scheme, forward and backward difference schemes should at least have fourth order truncation errors (Krauthammer et al., 1993a). Therefore, in order to match the accuracy levels of three partial differential schemes, first order forward and backward partial differential equations are transformed to fourth order accurate algebraic equations as in Equations 6.27 and 6.28, respectively.

$$\frac{\partial F(x,t)}{\partial x} = \frac{-25F(x,t) + 48F(x+\Delta x,t) - 36F(x+2\Delta x,t) + 16F(x+3\Delta x,t) - 3F(x+4\Delta x,t)}{(12\Delta x)} \tag{6.27}$$

$$\frac{\partial F(x,t)}{\partial x} = \frac{25F(x,t) - 48F(x-\Delta x,t) + 36F(x-2\Delta x,t) - 16F(x-3\Delta x,t) + 3F(x-4\Delta x,t)}{(12\Delta x)} \tag{6.28}$$

The partial differentials given in Timoshenko beam equations (Equations 6.1 and 6.2) were transformed to algebraic equations using the Equations 6.23, 6.27 and 6.28 for general nodes (except left and right supports), left support and right support, respectively.

6.9.2. Explicit partial differential formulation

The solution of dynamic equilibrium equations can be of two major types, explicit and implicit formulations. In the case of solving dynamic Timoshenko equations (Equations 6.1 and 6.2), explicit formulation is considered applicable for this study. For the use of explicit formulation, geometrical derivatives *(∂F/∂x)* are found to be of the first order and evaluated as in the previous section. Since geometrical derivatives are of first order, higher approximations can be utilised easily for obtaining more accurate forward or

backward difference equations. Furthermore, non-linear material behaviour can be easily incorporated to the system without the use of material constitutive laws.

The time related derivatives for the TBT is found to be of second order derivatives ($\partial^2\beta/\partial t^2$ and $\partial^2 w/\partial t^2$). However, the centre difference scheme can be used for all the nodes as no geometrical boundaries are available for the time related parameters. Using the same general function used in Section 6.9.1, the time related second order partial differential equation can be derived as in Equation 6.29.

$$\frac{\partial^2 F(x,t)}{\partial t^2} = \frac{F(x,t+\Delta t) - 2F(x,t) + F(x,t-\Delta t)}{(\Delta t)^2} \tag{6.29}$$

Equation 6.29 is also found to be second order accurate with truncation errors in the order of $[(\Delta x)^2]$. Hence Equation 6.29 can be used directly in Equations 6.1 and 6.2 without compromising the accuracy.

Finally, Equations 6.1 and 6.2 can be transformed to the explicit formulation where all the unknown terms are assembled to the left side of the equations and all the known terms are assembled to the right side of the equation. Three different algebraic equations are defined for each dynamic Timoshenko equation (Equation 6.1 and 6.2), from centre difference, backward difference and forward difference schemes. Timoshenko beam equations transformed to algebraic equations using centre difference scheme is shown in Equations 6.30 and 6.31, which are used for the general nodes (except left and right boundary nodes).

$$\beta(x,t+\Delta t) = 2\beta(x,t) - \beta(x,t-\Delta t) - \frac{(\Delta t)^2}{\rho_m I}\left[\frac{M(x+\Delta x,t) - M(x-\Delta x,t)}{2\Delta x} - Q(x,t)\right] \tag{6.30}$$

$$w(x,t+\Delta t) = 2w(x,t) - w(x,t-\Delta t) - \frac{(\Delta t)^2}{\rho_m A}\left[\begin{array}{l}\dfrac{Q(x+\Delta x,t) - Q(x-\Delta x,t)}{2\Delta x} + q(x,t) + \\ P(x,t)\left(\dfrac{\beta(x+\Delta x,t) - \beta(x-\Delta x,t)}{2\Delta x}\right)\end{array}\right] \tag{6.31}$$

Where, all the terms have the meaning as defined as in Equations 6.1 and 6.2. Similarly, Equations 6.1 and 6.2 can be written in forward difference scheme as shown in Equations 6.32 and 6.33, which are used to solve the equilibrium of left support.

$$\beta(x,t+\Delta t) = 2\beta(x,t) - \beta(x,t-\Delta t) - \frac{(\Delta t)^2}{\rho_m I}\left[\left(\frac{\begin{matrix}-25M(x,t)+48M(x+\Delta x,t)-36M(x+2\Delta x,t)\\+16M(x+3\Delta x,t)-3M(x+4\Delta x,t)\end{matrix}}{12\Delta x}\right) - Q(x,t)\right] \tag{6.32}$$

$$w(x,t+\Delta t) = 2w(x,t) - w(x,t-\Delta t) - \frac{(\Delta t)^2}{\rho_m A}\left[\begin{matrix}\left(\frac{\begin{matrix}-25Q(x,t)+48Q(x+\Delta x,t)-36Q(x+2\Delta x,t)\\+16Q(x+3\Delta x,t)-3Q(x+4\Delta x,t)\end{matrix}}{12\Delta x}\right)+q(x,t)+\\ P(x,t)\left(\frac{\begin{matrix}-25\beta(x,t)+48\beta(x+\Delta x,t)-36\beta(x+2\Delta x,t)\\+16\beta(x+3\Delta x,t)-3\beta(x+4\Delta x,t)\end{matrix}}{12\Delta x}\right)\end{matrix}\right] \tag{6.33}$$

Equations 6.34 and 6.35 defined using the backward difference scheme is used for the right support.

$$\beta(x,t+\Delta t) = 2\beta(x,t) - \beta(x,t-\Delta t) - \frac{(\Delta t)^2}{\rho_m I}\left[\left(\frac{\begin{matrix}25M(x,t)-48M(x-\Delta x,t)+36M(x-2\Delta x,t)\\-16M(x-3\Delta x,t)+3M(x-4\Delta x,t)\end{matrix}}{12\Delta x}\right) - Q(x,t)\right] \tag{6.34}$$

$$w(x,t+\Delta t) = 2w(x,t) - w(x,t-\Delta t) - \frac{(\Delta t)^2}{\rho_m A}\left[\begin{matrix}\left(\frac{\begin{matrix}25Q(x,t)-48Q(x-\Delta x,t)+36Q(x-2\Delta x,t)\\-16Q(x-3\Delta x,t)+3Q(x-4\Delta x,t)\end{matrix}}{12\Delta x}\right)+q(x,t)+\\ P(x,t)\left(\frac{\begin{matrix}25\beta(x,t)-48\beta(x-\Delta x,t)+36\beta(x-2\Delta x,t)\\-16\beta(x-3\Delta x,t)+3\beta(x-4\Delta x,t)\end{matrix}}{12\Delta x}\right)\end{matrix}\right] \tag{6.35}$$

Transforming Equations 6.1 and 6.2 to explicit finite difference formulation, bending rotation (β) and transverse deflection (w) can be readily calculated using already known parameters. Equations 6.32-6.35 are used as applicable for left and right supports and Equations 6.30 and 6.31 are used for rest of the nodes. Use of forward and backward difference schemes for modelling supports nullified the requirement of imaginary nodes which is extremely difficult to formulate with non-idealised boundary conditions.

6.10. Solution algorithm

The partial differential equations of the dynamic TBT are transformed to algebraic equations as shown in the previous section. Deformation characteristics, curvature and transverse deformation, for the next time step can be calculated directly using the explicit finite difference formulation of current time. The stepwise procedure followed for solving Timoshenko beam equations is summarised in the following section.

1. Constitutive relationships, moment-curvature, shear force strain and shear stress slip, are established based on the user inputs as discussed in section 6.4. Loading parameters were also calculated if user defined loading is not available.
2. The beam or one-way panel element is discretised to finite number of sections along the length of the member, each having a length of Δx, as shown as in Figure 6.1. The value of Δx should be compatible with the convergence and stability criteria discussed in Section 6.11.
3. Time step size, Δt, is established based on the Δx and material sound speed to comply with the convergence and stability criteria discussed in Section 6.11.
4. Establish boundary conditions for left and right supports (Both moment and angle of rotation (M-β) and shear force-slip for both supports (V-γ)).
5. Initial conditions, by means of initial curvatures, loading prior to blast loading and corresponding response and boundary conditions are applied to the first two steps. This includes bending and shear forces and corresponding deformations. If no initial loading is considered, values for first two steps are set to zero for all parameters (β, w, γ, φ, M and Q).
6. The transformed equations of motion (Equations 6.30 to 6.35 where applicable) were used to determine the angle of bending rotation and transverse deflection for the next time step $(\beta(x,t+\Delta t)$ *and* $w(x,t+\Delta t))$.
7. Curvature (φ) and shear strain (γ_{xz}) of the cross-section is calculated for all nodal points. Equations 6.3 and 6.4 transformed as in Equations 6.36 to 6.41 will be used to determine those parameters for a general node (6.36 and 6.37), left support (6.38 and 6.39) and right support (6.40 and 6.41).

$$\varphi(x,t) = -\left(\frac{\beta(x+\Delta x,t)-\beta(x-\Delta x,t)}{(2\Delta x)}\right) \tag{6.36}$$

$$\gamma_{xz}(x,t) = \frac{w(x+\Delta x,t) - w(x-\Delta x,t)}{(2\Delta x)} - \beta(x,t) \tag{6.37}$$

$$\varphi(x,t) = -\left(\frac{\begin{matrix}-25\beta(x,t) + 48\beta(x+\Delta x,t) - 36\beta(x+2\Delta x,t) \\ +16\beta(x+3\Delta x,t) - 3\beta(x+4\Delta x,t)\end{matrix}}{(12\Delta x)}\right) \tag{6.38}$$

$$\gamma_{xz}(x,t) = \left(\frac{\begin{matrix}-25w(x,t) + 48w(x+\Delta x,t) - 36w(x+2\Delta x,t) \\ +16w(x+3\Delta x,t) - 3w(x+4\Delta x,t)\end{matrix}}{(12\Delta x)}\right) - \beta(x,t) \tag{6.39}$$

$$\varphi(x,t) = -\left(\frac{\begin{matrix}25\beta(x,t) - 48\beta(x-\Delta x,t) + 36\beta(x-2\Delta x,t) \\ -16\beta(x-3\Delta x,t) + 3\beta(x-4\Delta x,t)\end{matrix}}{(12\Delta x)}\right) \tag{6.40}$$

$$\gamma_{xz}(x,t) = \left(\frac{\begin{matrix}25w(x,t) - 48w(x-\Delta x,t) + 36w(x-2\Delta x,t) \\ -16w(x-3\Delta x,t) + 3w(x-4\Delta x,t)\end{matrix}}{(12\Delta x)}\right) - \beta(x,t) \tag{6.41}$$

8. Strain rate in terms of ($\partial\varphi/\partial t$) and ($\partial\gamma_{xz}/\partial t$) is calculated separately for flexure and shear. Identify the maximum value for strain rate in both flexure and shear and calculate the DIFs accordingly for both flexure and shear. These two factors will be the DIFs for this time step. A constant DIF of 1.4 is assumed for direct shear.
9. Corresponding bending moment and shear forces are calculated for all the nodes based on the curvature and shear strain. Dynamic enhancement factors calculated in the previous step will also be used when calculating these values.
10. Values for boundary nodes are updated according to the user defined boundary conditions.
11. The structure is checked for failure as described in the previous sections. If partial failure occurs, failure mode, location and time were noted and analysis is carried out until the full failure or the analysis time is reached.
12. If the structure does not fail all the values for nodes are updated, where values for time t becomes the values for time t-Δt and newly calculated vales of time t+Δt becomes the values for time t. Once the values are updated, solution process repeated from step 5 onwards.

13. If the structure fails (complete failure), failure mode and time is noted and results are saved for further analysis, if necessary.

The flow chart of the solution algorithm is represented in Figure 6.9. Theoretical development discussed in this chapter is programmed using the PGI visual FORTRAN (Version 12.8) programming language, which is presented in Appendix C-IV.

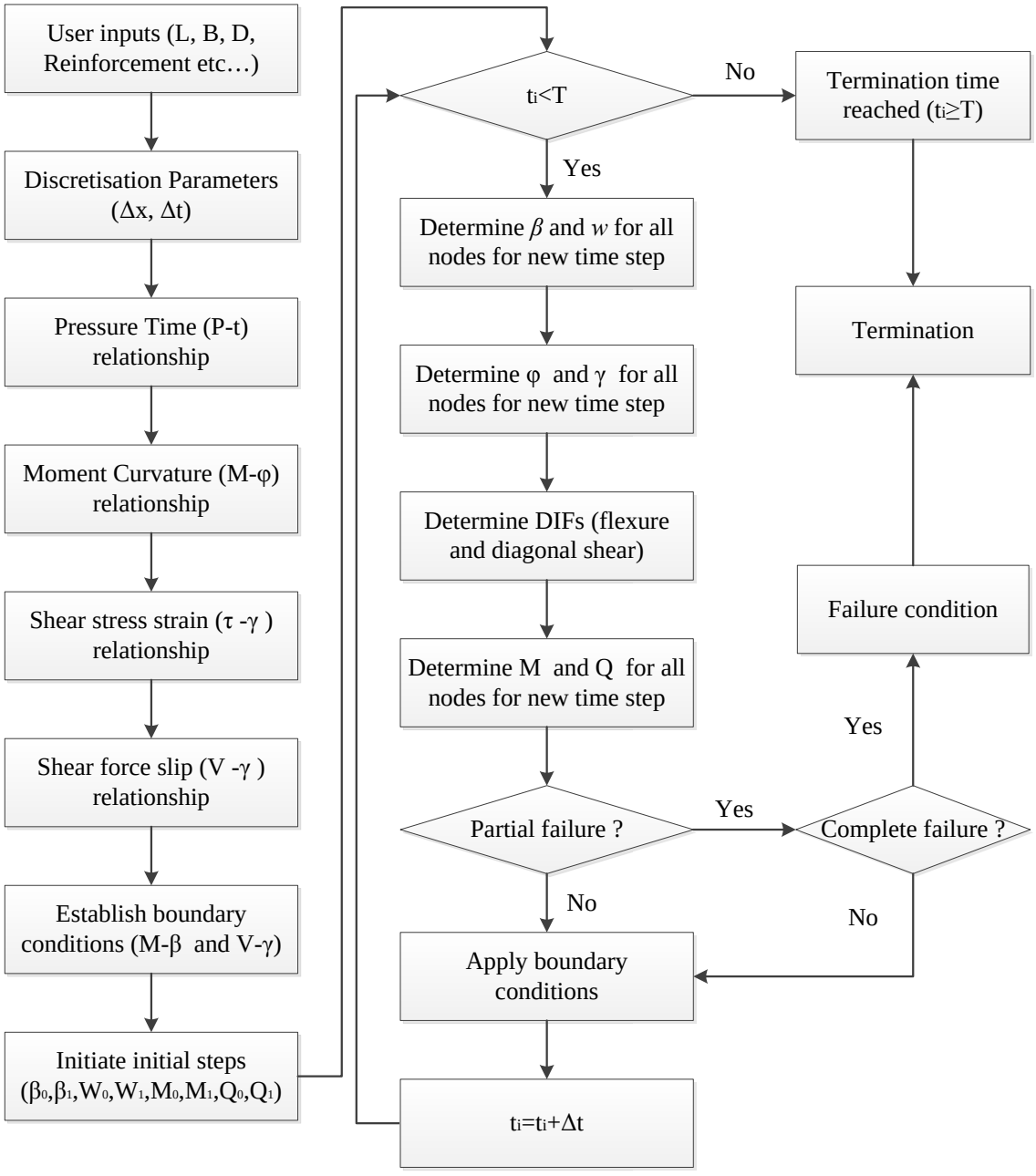

Figure 6.9: Program flow chart for the explicit finite difference solution using TBT

6.11. Stability and convergence criteria

In order to achieve accurate results, stability and convergence need to be considered when using numerical methods to solve engineering problems. In case stability conditions are not satisfied, errors will accumulate throughout the solution process and the results obtained using such programs will not be accurate. As in many finite element and finite difference programs, mesh size and the time step size will define the stability of a numerical solution. Therefore, the same principle will be used as the stability criteria for this numerical solution.

The primary consideration of limiting the time step is to prevent the information (i.e. disturbances) from travelling from one node to next closest node within a single time step. Hence, the limiting value of time step is calculated as,

$$\Delta t < \Delta t_{max} = \frac{\Delta x}{C_L} \tag{6.42}$$

Where;

Δx = Node spacing (mm)

C_L = Highest velocity of the disturbance propagation (mm/ms) (Equation 6.43)

$$C_L = \left[\frac{E(1-\nu)}{(1+\nu)(1-2\nu)\rho_m}\right]^{1/2} \tag{6.43}$$

Where;

E = Elastic modulus of concrete,

ν = Poisson's ratio

ρ_m = Mass density

A satisfying Δt value will guarantee a stable solution process.

Equation 6.43 is valid only for elastic materials however, values obtained from Equation 6.43 will provide a stable analysis process for any of the materials with strain softening capabilities. As seen in many of the concrete materials, materials tend to soften with tensile and compressive cracking, which results in reduced disturbance propagation velocities. A reduced disturbance propagation velocity will define a larger time step than the original definition. Hence, the time step obtained from the Equation

6.42 will be the smallest time step, which will ensure the stability of the solution process.

Another important aspect of accuracy and convergence is the number of nodes in the system. As seen in SDOF methods, a single node (element or mass) can represent only one mode of deflection whereas multiple nodes represent multiple modes of deflections. As indicated by Krauthammer et al., (1993a,b), the number of nodes indicates a frequency of vibration for the selected structural elements. Furthermore, the number of nodes is exactly similar to the number of model shapes that can be predicted by a proposed structural model. Through Fourier analysis, Ross (1983) pointed out that under uniform dynamic loading, frequencies below 100000 rad/s could cover up to 95% contribution of the frequency content of the load.

It is well known that higher frequency loading will have little or no effect on the flexural or shear response of a beam element, which are the properties to consider as structural engineers. Hence, as specified by Krauthammer (1993a), a minimum of 25 nodes (24 segments) were considered for the solution. 25 nodes will corresponds to 25 different modes of vibrations which covers up to 90000 rad/s, which will be more than adequate for flexural and shear response prediction. Therefore, based on the above criterion, maximum nodal distance (segmental length, Δx) is defined as L/24, in which L is the span length.

The TBT is capable of representing both flexural and shear responses. Therefore, any shear disturbances should not travel more than the thickness of the section within the specified time step. Therefore, Δx is bounded by the thickness of the member as well. Although this condition is not essential for conventional RC beams where thickness is substantial, will govern the one-way slab elements with small thicknesses. Therefore, the maximum nodal distance is defined as in Equation 6.44, which will guarantee a stable and accurate numerical solution.

$$\Delta x = minumum\ of \begin{cases} L/24 \\ h \end{cases} \tag{6.44}$$

6.12. Calibration and verification of analytical solution

The developed analytical solution was transformed to a numerical algorithm as described in Section 6.9.1. This numerical algorithm was programmed to a numerical

analysis tool using the FORTRAN programming language. The Program consists of eight different modules for input, moment-curvature, Mander's coefficient, shear stress-strain, shear slip, blast pressure, finite difference and interpolation function.

6.12.1. Verification of Test results

The University of Melbourne experimental tests, discussed in Chapter 5, (Pham, 2010) consist of one dowel connected panel and a five angle cleat connected panels. Significant horizontal deformation (along the axis of the member) was not observed with any of the Type B panels hence, horizontal translations of all Type B panels were fixed in boundary nodes. However, Panel A has shown significant axial deformations through bolt shear which needs to be taken in to account for the boundary conditions.

Analysis of panels with two connection types, dowel and angle cleat connections, require definitions of translational and rotational stiffness for both boundary nodes. However, the flexural resistance provided by the fasteners (i.e. the plate element in dowel connection and angle section in angle cleat connection) is several orders of magnitudes lower than the flexural stiffness of the connection. According to the LRFC manual (American Institute of Steel Construction, 1994), a flexural stiffness of a connection less than 20% of the connecting beam is considered as a partially restrained (free to rotate) member and flexural stiffness in ignored. Therefore, translational stiffness (K_z) is the only required calculation for both panels.

6.12.1.1. Panel boundary stiffness (K_z)

Translational stiffness (K_z) of the connection consists of two distinct stiffness parameters, the shear stiffness of the bolt (K_s) and flexural (translational) stiffness (K_b) of the angle section. Considering the angle cleat connected panels, these two values can be considered as two springs connected series to each other. The combined stiffness of this mechanism (K_z) can be defined using the Equation 6.45 given below.

$$1/K_z = 1/K_s + 1/K_b \tag{6.45}$$

Shear stiffness of a bolt can be defined as in Equation 6.46, where G, A and L is defined as shear modulus of bolting material, shear area of the bolt and initial length of the bolt shear plane, respectively. However, this equation is not applicable for every cross-sectional shape and modification is required for different cross-section types. A

modification factor of 32/37 is applicable for circular sections (Hoogenboom and Spaan, 2005), which is the shape of the bolt.

$$K_s = {}^{(GA)}/_{L} \tag{6.46}$$

Flexural stiffness of the angle section is defined as in Equation 6.47, where the flange of the panel is assumed to be fixed at the connected edge and free to rotate at other edge.

$$K_b = {}^{(3EI)}/_{L_f{}^3} \tag{6.47}$$

Where;

E = Elastic modulus

I = Moment of Inertia

L_f = Effective length of the flange

The flexural (translational) stiffness of the dowel connection can be defined similarly as in Equation 6.47, where effective flange length and the numerical coefficient (3 in equation 6.47) need to be modified. In angle cleat connections, the flange section behaves as a fixed-pin connection having a flexural stiffness of *3EI/L* whereas the dowel connection panel behaves as a cantilever hence, having a flexural strength of *EI/L* for the plate section.

Bolts in the dowel connection will transfer significant axial forces resulting in axial elongation. Therefore, axial stiffness of the bolting material is calculated using hooks law for axial forces using the Equation 6.48 and combined translational stiffness is calculated using Equation 6.45. L_b in Equation 6.48 is defined as the length of the bolt shank up to the fastener (nut) and A_t is the tensile area of the bolts.

$$K_a = {}^{(EA_t)}/_{L_b} \tag{6.48}$$

For all six panels investigated, translational stiffness is calculated and presented in Table 6.3. Panel A1 exhibits the maximum translational stiffness while Panel B1 possesses the smallest. No significant difference in stiffness is seen with Panels B2 to B5, where values between 66.8 kN/mm to 68.3 kN/mm are observed for all four panels. Even though Panel A1 exhibited the largest translational stiffness, it recorded the maximum support deflections during the experimental study (Chapter 5).

Panels B1 to B5 were selected for the analysis using the developed analytical tool as the development is incapable of allowing horizontal deformation. Therefore, Panel A1 was omitted from the analysis.

Table 6.3: Connection stiffness parameters

Panel ID	A_t (mm^2)	A_s (mm^2)	I (mm^4)	K_b (N/mm)	K_a (N/mm)	K_s (N/mm)	K_z (N/mm)
A1	2035.8	-	666667	77160	9047787	-	76508
B1	-	2827.4	42667	35117	-	195627824	35060
B2	-	2827.4	83333	68587	-	195627824	68371
B3	-	1017.9	83333	68587	-	70426017	67991
B4	-	339.3	83333	68587	-	23475339	66830
B5	-	603.2	83333	68587	-	41733936	67587

6.12.1.2. Constitutive relationships

Figure 6.10.a to Figure 6.10.c exhibit the moment-curvature relationship, shear stress-strain relationship and shear stress-slip relationship for Type B panels, derived using the constitutive relationships discussed earlier. All five panels were constructed of the same cross-section dimensions, hence the same constitutive relationships are available for all five cross-sections.

An ultimate bending moment of 9 kNm was recorded for the cross-section. A maximum section rotation (curvature) of 3.7×10^{-4} radians was associated with the maximum bending moment. A yielding moment of 8 kNm was observed with curvature of 6×10^{-5} radians, which is compatible with AS 3600 (that would give a calculated value of 8.01kNm without capacity reduction factors) (Standards Australia, 2009).

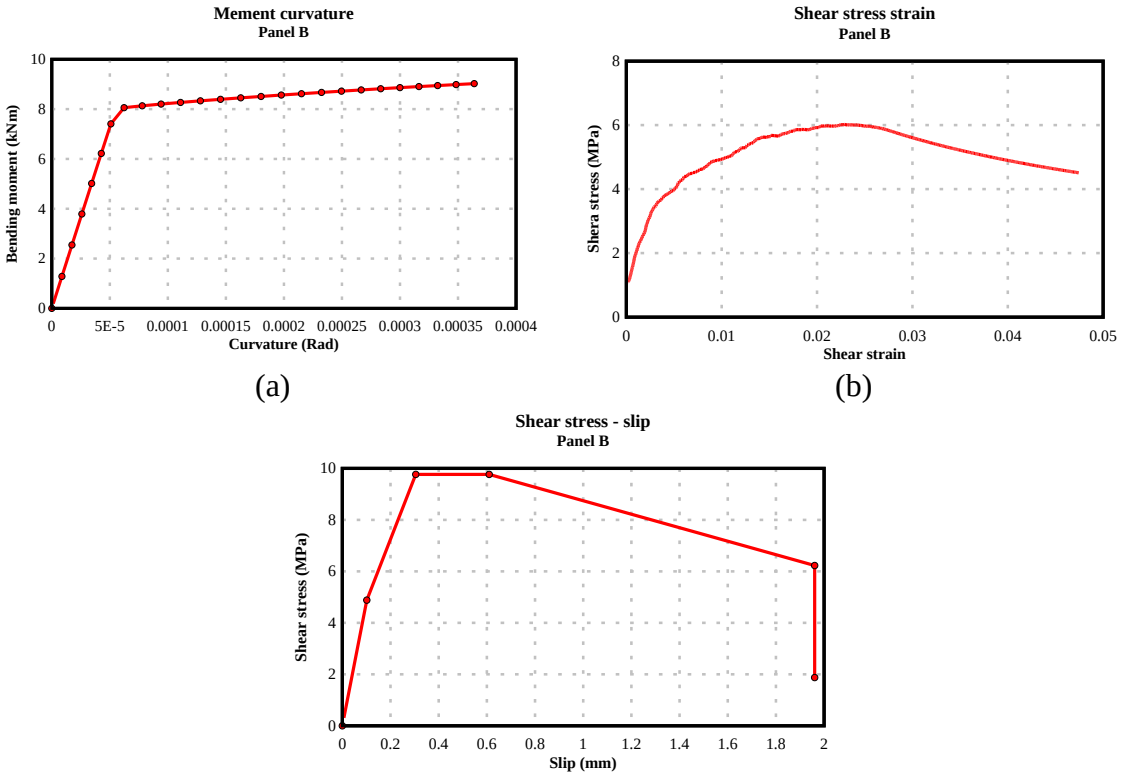

Figure 6.10: (a). Moment-curvature, (b) shear stress-strain and (c) Shear slip relationships for Panel B

Shear stress-strain variation is presented in Figure 6.10.b where a maximum shear stress of 6.02 MPa was observed. A shear strain of 0.0229 was found to correspond with the maximum shear stress. A failure shear strain of 0.047 was also observed for the selected cross-section and reinforcement detail.

Figure 6.10.c shows the variation of shear stress-slip relationship for the selected cross-section. A maximum shear stress of 9.767 MPa was required to achieve a shear slip 0.3 mm, which was highly unlikely due to the thinner cross-section. Interestingly, failure slip deflection was found to be less than the residual slip deflection, hence shear stress-slip curve was terminated at the failure slip deformation of 1.96 mm.

6.12.1.3. Panel deflections

The maximum mid-panel deflection, maximum support deflection and maximum relative deflection obtained from the 1-D analysis for Panels B1 to B5 are listed in Table 6.4 below. Experimental deflections and percentage error between experimental value and analytical prediction are also presented in the same table. For easy

comparison, values in the tables are also presented in Figure 6.11.(a) to Figure 6.11.(c) for maximum mid-panel deflection, maximum support deflection and maximum relative deflection.

Table 6.4: Comparison of experimental and analytical panel deflections

Panel ID	Mid deflection			Support Deflection			Relative Deflection		
	1-D	Exp.	Error%	1-D	Exp.	Error%	1-D	Exp.	Error%
B1	30.45	28.9	5.36	3.34	3.5	-4.57	27.42	25.4	7.95
B2	24.78	24.4	1.56	1.82	1.7	7.06	23.07	22.7	1.63
B3	24.78	24.5	1.14	1.82	1.9	-4.21	23.07	22.6	2.08
B4	24.82	23.7	4.72	1.86	5.5	-66.18	23.04	18.2	26.6
B5	24.81	25.7	-3.46	1.85	3.8	-51.31	22.99	21.9	4.98

Exp.: Experimental Value

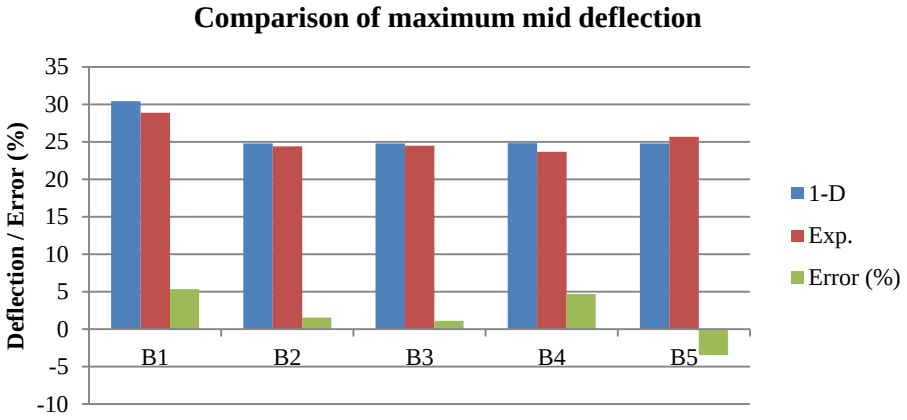

(a)

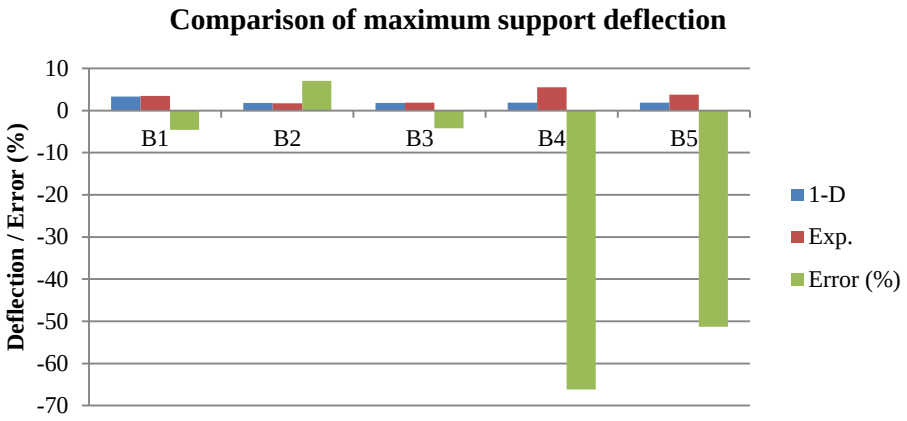

(b)

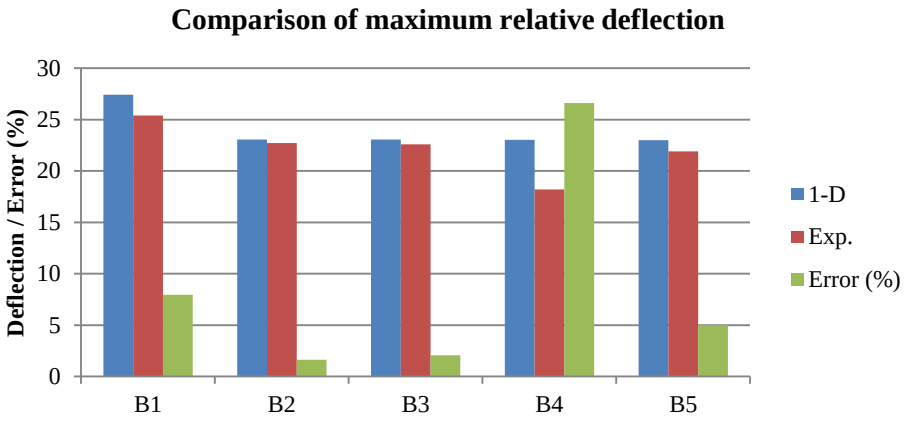

(c)

Figure 6.11: Comparison of experimental and 1-D analytical deflection predictions

An excellent correlation between experimental and analytical prediction was observed for mid-panel deflections for all five panels, as shown in Figure 6.11.(a). The maximum error percentage of 5.36 was observed with Panel B1, which exhibits the lowest translational stiffness with a thinner (8mm) angle section. Panels B2 to B5 did not exhibit any significant difference in maximum mid deflection. Although panels B4 and B5 fixing assemblies were significantly weakened with lesser number of blots, panel deflections did not reflect any variation.

Comparison of support deflection is presented in Figure 6.11.(b) along with error percentages. Panels B2-B5 showed similar response where almost no difference in support deflection was observed with the 1-D analysis. All these panels had similar connection stiffness as shown in Table 6.4 hence, the result is acceptable. Comparison with experimental results reveals significant discrepancies with error percentages as high as 66%. However, this 66% error was observed with Panel B4 where supports were damaged during the experiment. The best comparison of support deflection was observed with Panels B1, B2 and B3 where error percentages were less than 8%.

Figure 6.11.(c) shows the relative deflection of the panel resetting the support deflection to zero. Since time history results were available for the 1-D analytical solution, relative deflection was calculated subtracting the maximum support deflection time history from the maximum panel deflection time history, rather than the maximum values. Excellent verification results with error percentages less than 8% was observed with all panels except for Panel B4, where an error percentage of 26.6 was observed.

In summary, the developed 1-D analytical solution was able to predict the maximum deflection of reinforced concrete cladding panels subjected to explosive loading more accurately. However, support deflection remains a problem with higher than acceptable error percentages, in some cases. Reduction in support stiffness due to lesser bolts does not reflect in support deflection results. However, considering the maximum deflection and overall performance, the 1-D analysis program can predict reasonably accurate results for reinforced concrete cladding panels subjected to explosive loading.

6.12.2. Verification of test results from National University of Defence Technology, China

As discussed in detail in Section 5.2, test results from National University of Defence Technology, China (Wang et al., 2012) were also used to verify the developed 1-D analytical solution. All six panels, A to F, were used for the verification. These panels were tested under rigid boundary conditions where both support rotation and translation fixed. Therefore, no connection stiffness definitions were required.

Constitutive relationship outputs similar to those observed in Section 6.12.1.2 were witnessed for these six test panels as well. Therefore, constitutive relationship outputs were not presented in this section.

6.12.2.1. Panel deflections

Comparison of panel deflections for the experimental and 1-D analytical procedures is presented in Table 6.5 and Figure 6.12. Each entry in Table 6.5 for analytical prediction is presented with an error percentage where the error is defined as the difference between prediction and experimental deflection, as a percentage of experimental deflection. Error percentage is also plotted in Figure 6.12.

All six panels have under predicted the maximum deflection, with varying degrees of error percentages. However, all panels were within an error percentage of 20%, which is considered acceptable for high energy related applications. Among the two standoff distances, panels with scaled distance of 0.591 $m/kg^{1/3}$ (Panels A, C and E) have shown better calibration with smaller error percentages.

Table 6.5: Comparison of experimental results with 1-D predictions

Panel ID	Maximum Deflection		
	Experimental	Analytical	Error%
A	9	8.42	-6.44
B	26	21.74	-19.6
C	15	14.23	-5.13
D	35	29.89	-14.6
E	19	18.74	-1.37
F	40	37.43	-6.42

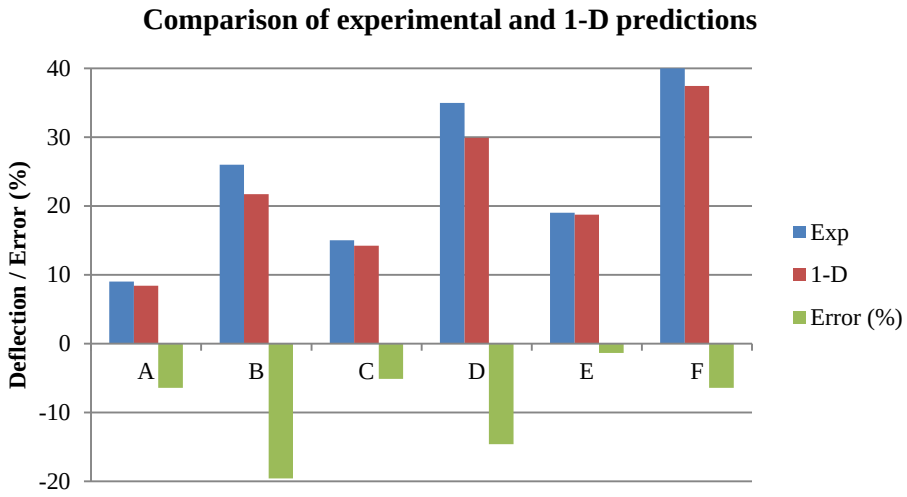

Figure 6.12: Comparison of experimental and 1-D analytical predictions

Similarly, accuracy levels have increased with increased panel size for both scaled distances, where Panels A and B were 750 mm, C and D were 1000 mm and E and F were 1250 mm in planner dimension. This is due to the large deflections observed with large span lengths during the experimental evaluation.

6.12.3. Comparison of 1-D analytical results and LS-DYNA numerical results

A comparison of 1-D analytical and LS-DYNA numerical results was performed for the selected experimental results, as shown in Table 6.6. In addition, maximum deflections and error percentages are plotted in Figures 6.13 to 6.15 for easy comparison.

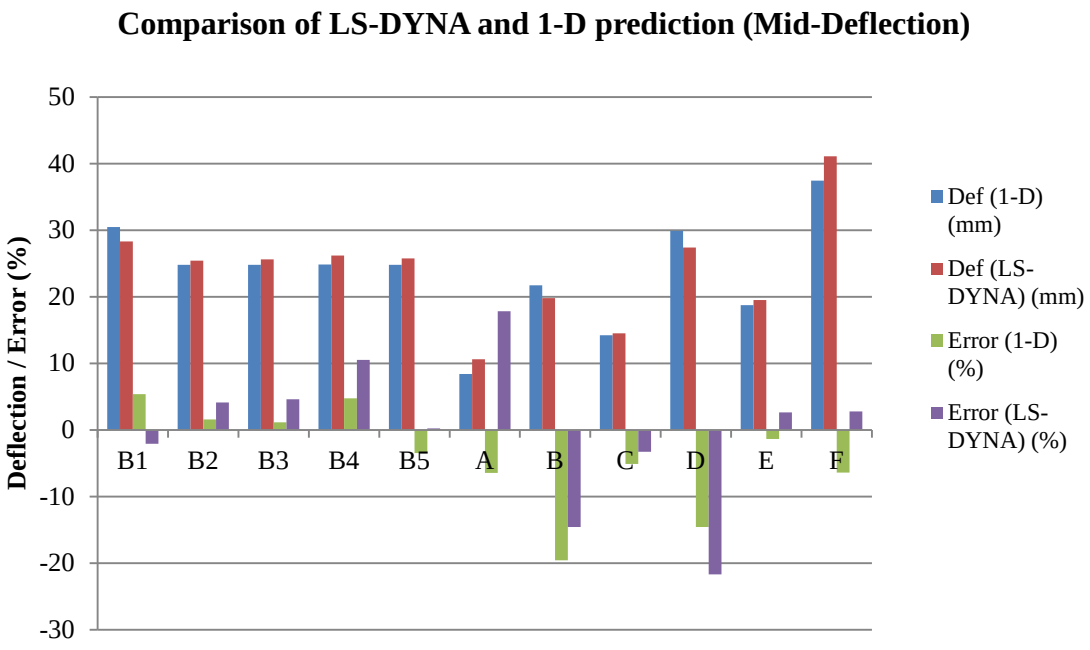

Figure 6.13: Comparison of LS-DYNA and 1-D predictions for maximum mid deflection

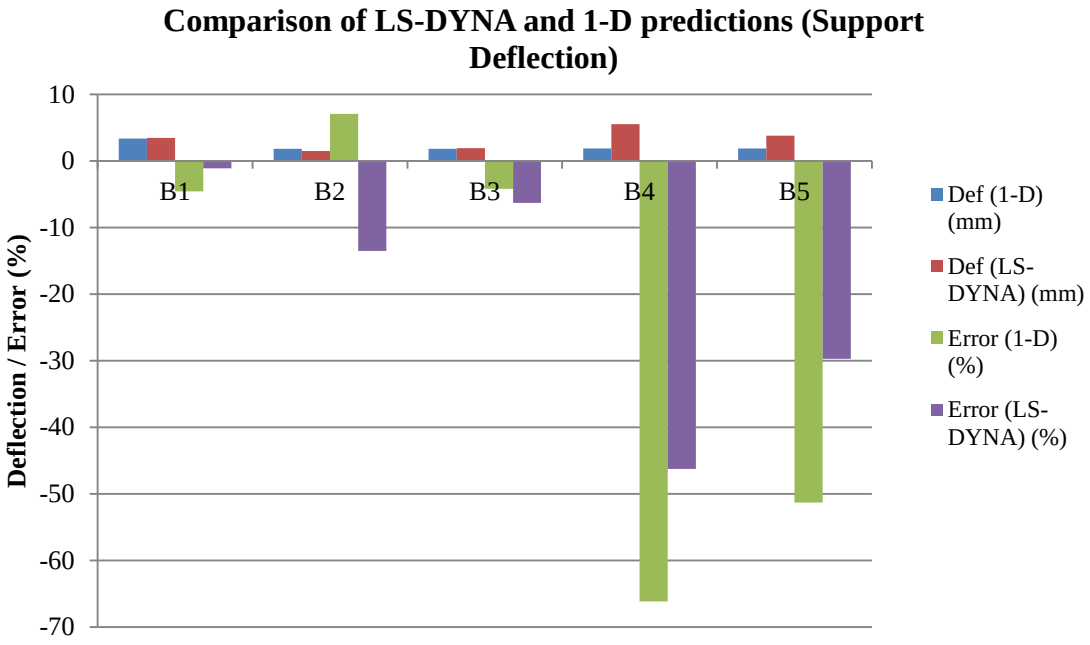

Figure 6.14: Comparison of LS-DYNA and 1-D predictions for maximum support deflection

Table 6.6: Comparison of 1-D analytical and LS-DYNA results

Panel ID	Maximum Deflection				Support Deflection				Relative Deflection			
	1-D Analytical		LS-DYNA		1-D Analytical		LS-DYNA		1-D Analytical		LS-DYNA	
	Deflection (mm)	Error (%)	Deflection (mm)	Error (%)	Deflection (mm)	Error (%)	Deflection (mm)	Error (%)	Deflection (mm)	Error (%)	Deflection (mm)	Error (%)
The University of Melbourne explosive field tests (Pham, 2010)												
B1	30.45	5.36	28.3	-2.07	3.34	-4.57	3.46	-1.14	27.42	2.57	23.57	2.19
B2	24.78	1.56	25.4	4.1	1.82	7.06	1.47	-13.5	23.07	1.63	23.97	5.59
B3	24.78	1.14	25.63	4.61	1.82	-4.21	1.90	-6.32	23.07	2.08	23.84	5.49
B4*	24.82	4.72	26.19	10.51	1.86	-66.18	5.50	-46.29	23.04	26.6	20.76	14.07
B5	24.81	-3.46	25.76	0.23	1.85	-51.31	3.81	-29.73	22.99	4.98	22.07	7.76
The National University of Defence Technology explosive field tests (Wang et al., 2012)												
A	8.42	-6.44	10.6	17.8	N/A				N/A			
B	21.74	-19.6	19.8	-14.6								
C	14.23	-5.13	14.5	-3.3								
D	29.89	-14.6	27.4	-21.7								
E	18.74	-1.37	19.5	2.63								
F	37.43	-6.42	41.1	2.75								

*: Fixing assemblies were broken during the experimental investigation. Measurements were taken from broken fixing assemblies

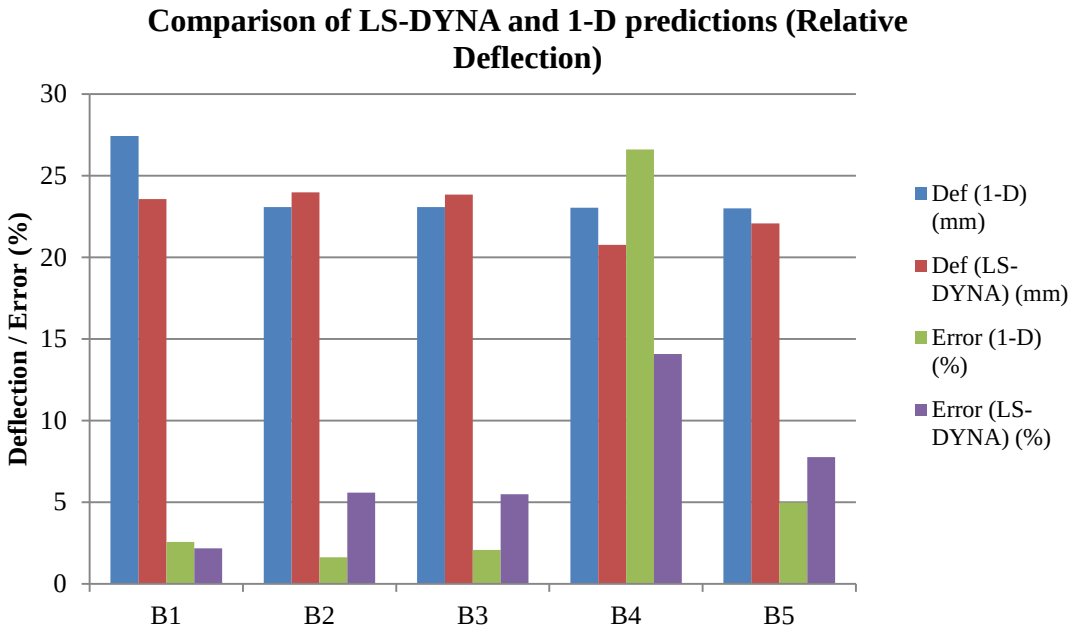

Figure 6.15: Comparison of LS-DYNA and 1-D predictions for maximum support deflection

Maximum mid-panel deflection

Comparison of maximum mid-panel deflection prediction using the developed 1-D analytical solution and LS-DYNA 3-D numerical model is presented in Figure 6.13, along with the relevant error percentages, in comparison with experimental values. Considerably better results were observed with the 1-D analytical solution for maximum mid-panel deflection over LS-DYNA. Results were further improved when comparing the University of Melbourne (Pham, 2010) test results. 1-D solution predicted the maximum mid-panel deflection with error percentages less than 6% for those test results in comparison with 10.51% observed with LS-DYNA predictions.

The National University of Defence Technology (Wang et al., 2012) test results exhibit similar trend in comparison with LS-DYNA and 1-D prediction results. However, error percentages were slightly higher on this instance. The maximum error percentage of 19.6 was observed with the 1-D solution where as 21.7% was observed with LS-DYNA predictions. In addition, all 1-D predictions were associated with negative error percentages, whereas LS-DYNA had both positive and negative error percentages.

Overall, the 1-D analytical solution was considerably better in predicting the maximum mid-panel deflection in comparison with the LS-DYNA finite element model. Furthermore, considering the complexity and computational cost, the 1-D analytical solution is more preferable than the FEM solution.

Maximum support deflection

Comparison of maximum support deflection and corresponding error percentages for the 1-D analytical solution and the 3-D finite element solution is presented in Figure 6.14, in addition to the values given in Table 6.6. This comparison is only available for the University of Melbourne (Pham, 2010) test results.

Slightly better results were observed with the 1-D analytical solution for Panels B1 to B3 whereas Panels B4 and B5 were better predicted with the LS-DYNA 3-D finite element model. Error percentages as high as 66% were observed (Panel B4) with the 1-D analytical solution. However, for this specific test results, support deflection was measured from a broken fixing assembly.

Maximum relative deflection

Similar results as in the maximum mid-panel deflections were observed with the maximum relative deflection as shown in Table 6.6 and Figure 6.15. All panels, except B4, in which fixing assemblies were broken during the experimental evaluation, were predicted with error percentages less than 5%. Relative deflection was predicted with an error of 27%, even in the case of Panel B4. In comparison with LS-DYNA, better predictions were observed with Panels B1 to B3 using the 1-D analytical solution. In case of Panels B4 and B5, LS-DYNA finite element model predicted the relative deflection better.

6.13. Summary

An analytical solution developed to predict the response of reinforced concrete one-way slab panels subjected to explosive loading was discussed in this chapter. The 1-D analytical solution was verified using deflection as the criterion for two independent experimental programs using a total of 11 different reinforced concrete panels. The following conclusions were made on the model verification results.

- The 1-D analytical solution was able to predict the maximum (mid-panel) deflections with reasonable error margins. These error margins are within the acceptable 20% margin for all 11 panels considered.

- A comparison of the maximum support deflection revealed mixed results. Some of the predictions were well within the acceptable range with less than 10% error (Panels B1, B2 and B3) and some are well above (beyond 50%) the acceptable error margin (Panels B4 and B5).

- Relative displacement, taken as the difference between mid-panel and support deflection, exhibit similar error margins as in the maximum mid-panel deflection. Error percentages were less than 5% in Panels B1, B2, B3 and B5.

- Considerably smaller error percentages were observed for 1-D analytical solution over LS-DYNA for mid panel deflection, in 7 of the 11 panels used for the verification.

- Similar responses were observed for the maximum support deflection and the maximum relative deflection between LS-DYNA and 1-D solution. Out of the five panels, 1-D solution predicted better results for three panels and LS-DYNA for the other two panels.

The analytical solution was developed as an alternative to the Finite Element (FE) programs, where considerable mastery is required in both FE applications and structural engineering. In addition, the 1-D analytical solution has insignificant initiation and analysis time requirements compared to LS-DYNA solution times and shows promising results although, it has some limitations to current applications.

In overall comparison, the 1-D analytical solution and the LS-DYNA numerical model predictions were in same accuracy domains. However, in comparison of initiation time, analysis time and computer usage, 1-D analytical solution predictions are found to be more optimal than the LS-DYNA numerical model.

CHAPTER 7

PARAMETRIC STUDIES: REINFORCED CONCRETE FACADE SYSTEMS

7.1. Introduction

A comprehensive parametric study conducted on the performance of reinforced concrete facade systems subjected to explosive loading is presented in this chapter. The developed LS-DYNA, 3-D finite element model (Chapter 5) and 1-D analysis tool (Chapter 6) were used with different geometric configurations of panels for the evaluation.

Flexible connections were initially assessed to evaluate the damage mitigation in blast loaded facade systems. Angle cleat connections as well as dowel connections (as in Figures 5.2, 5.3 and 5.4) were considered for the study. The effect of bolt size (diameter) and cleat thickness was varied for angle cleat connections while bolt size was the variable used for dowel connections. Variation of plate thickness was not evaluated for dowel connections due to the simplified connection configuration (see Section 5.2.3).

As discussed in Chapter 5, longitudinal deformations in fixing assemblies of dowel connected panels were incompatible with the 1-D analysis tool. Therefore, only the LS-DYNA, 3-D finite element model was used in this case.

The performance of reinforced concrete cladding panels with openings was evaluated using the developed LS-DYNA, 3-D numerical model. Opening size with and without opening stiffening, longitudinal and transverse locations of the openings were used as variables.

Finally, architectural cladding panels with initial curvatures were evaluated for explosive loading performance, only using the LS-DYNA, 3-D finite element model. Curvatures in both longitudinal and transverse directions, as well as convex and concave shapes, were used for the evaluation. Curvature (1/R) to span (S) ratios

between 3 to 30 for longitudinal direction (long span) curvatures and 2 to 20 for transverse direction (shorter span) curvatures was selected.

The parametric study was conducted with a charge weight-standoff distance combination of 5.5 kg of equivalent TNT charge and 2.1065 m standoff distance respectively. This combination accounts for a scaled distance of 1.193 m/kg$^{1/3}$. Considering the minimum scaled distance of 1.2 m/kg1/3 specified in UFC 3-340 (United States Army Corps of Engineers, 2008) for far range (far field) explosive loading, and comparability with explosive field tests (Pham, 2010), this charge weight-standoff distance combination was used for the evaluation.

It is fair to consider higher explosive loads yielding a different response from the facade systems. However, considering the purpose and type of cross-section (Type I, II or III, see Section 4.4.2) available to resist the explosive loading, the Type III cross section is the only suitable cross section available for the design of facade systems. The Type III cross section is limited to use in the far range explosive design, with a minimum scaled distance (Z) of 1.2 m/kg$^{1/3}$ (3.0 ft/lb$^{1/3}$) (UFC 3-340). Therefore, a single explosive load of 5.5 kg equivalent TNT charge weight at 2.1065 m standoff distance is considered for the parametric study. However, different scaled distances ranging from 0.5 m/kg $^{1/3}$ to 3 m/kg$^{1/3}$ was considered for a selected set of panels in Section 7.3.1, which could be used as a reference for other scaled distances.

7.2. Flexible connections for reinforced concrete facade systems in blast load mitigation

The performance of two types of reinforced concrete cladding connections was evaluated for the explosive loading performance. The connection details used for the experimental procedure, dowel and angle cleat connections, (Pham, 2010; see Figures 5.2, 5.3 and 5.4) were also used for the parametric study. These two connections were evaluated against a constant explosive load of 5.5 kg of equivalent TNT charge at a standoff distance of 2.1065 m, as discussed in the previous section.

The dimensions of both Type A and Type B panels were retained as in the experimental study. Different parameters of the two connections, including cleat thickness and bolt diameter, were varied to achieve different connection configurations. Connection and overall panel performances were evaluated on the basis of panel deflections and

component stresses for these connection configurations. Both the LS-DYNA finite element model and the 1-D analytical solution were utilised for this evaluation. In addition to the details provided in here, time history plots for relevant parameters are presented in Appendix D-I.

7.2.1. Angle cleat connection

Angle cleat connections are preferred for both top and bottom end connections due to the easiness in construction (Brookes, 1998). A typical connection consists of a steel angle section and a set of high-strength bolts, where the two legs of the angle section connect the structure and facade panel (Figure 5.4). These high strength bolts in each leg of angle section hold the panel against the supporting structure, transferring the load applied, safely to the main structure. The bolt configuration used for this study is presented in Figure 7.1. In this section, different connection configurations were evaluated to understand the explosive loading performance of reinforced concrete facade panel systems with flexible connections.

The connection stiffness for the 1-D analytical solution was calculated using the method proposed in Section 6.12.1.1. The whole connection was modelled with LS-DYNA for the parametric study as discussed in Section 5.5.5.

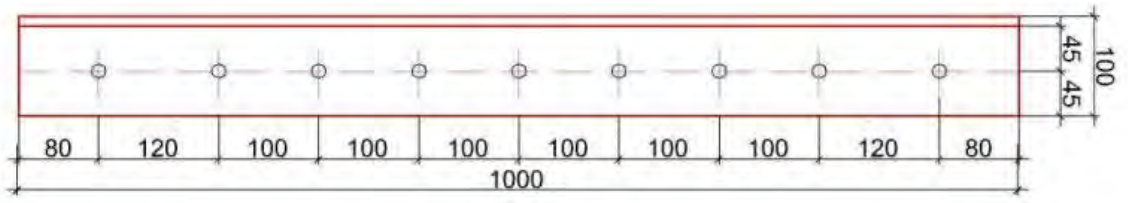

Figure 7.1: Bolt configuration for angle cleat connections

7.2.1.1. Bolt size (diameter)

Explosive loading performance of reinforced concrete facade panels of similar dimensions and configurations to experimental trials were evaluated with different bolt sizes. Bolt sizes varying from 10 mm to 40 mm were used for the study with exact bolt configuration (location and number) as in experiments (see Figures 5.4 and 7.1). Maximum mid-panel deflection, maximum support deflection, axial and shear forces of connecting bolts, effective stress in angle cleat section and maximum compressive stress in the concrete section were used as evaluation parameters.

Effect on maximum mid-panel deflection

The variation of maximum mid-panel deflection is presented in Figure 7.2. The change in bolt diameter did not influence the mid-panel deflection as both the LS-DYNA and the 1-D analytical solution predicted similar trends. Although 1-D analytical prediction for mid deflection was slightly lower than LS-DYNA, with the difference being within 1 mm of each other for all considered bolt diameters.

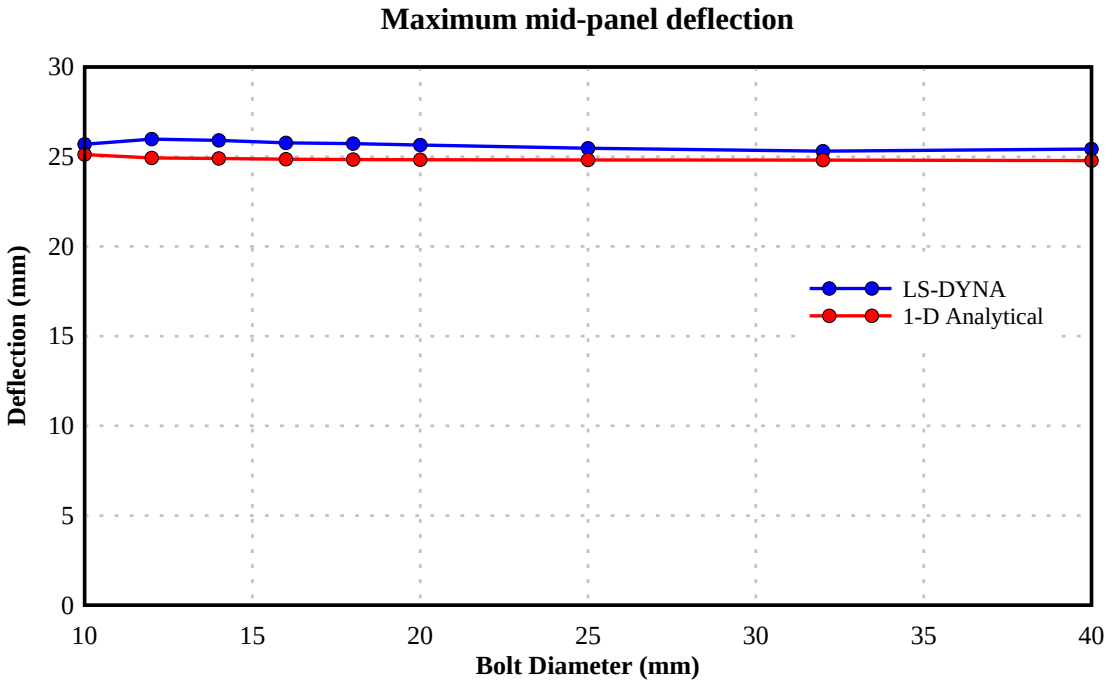

Figure 7.2: Maximum mid-panel deflection with bolt diameter-Angle cleat connections

Effect on support deflection

Figure 7.3 shows the variation of maximum support deflection with bolt diameters. Similar trends were observed with both LS-DYNA and 1-D analytical predictions. Except for the small drop in deflection between 10 mm and 12 mm bolts, support deflection remained constant throughout the bolt diameter change. Unlike in mid-panel deflection, the 1-D analytical prediction was slightly higher than the LS-DYNA prediction. However, the difference was less than 0.3 mm of each other for all considered bolt diameters.

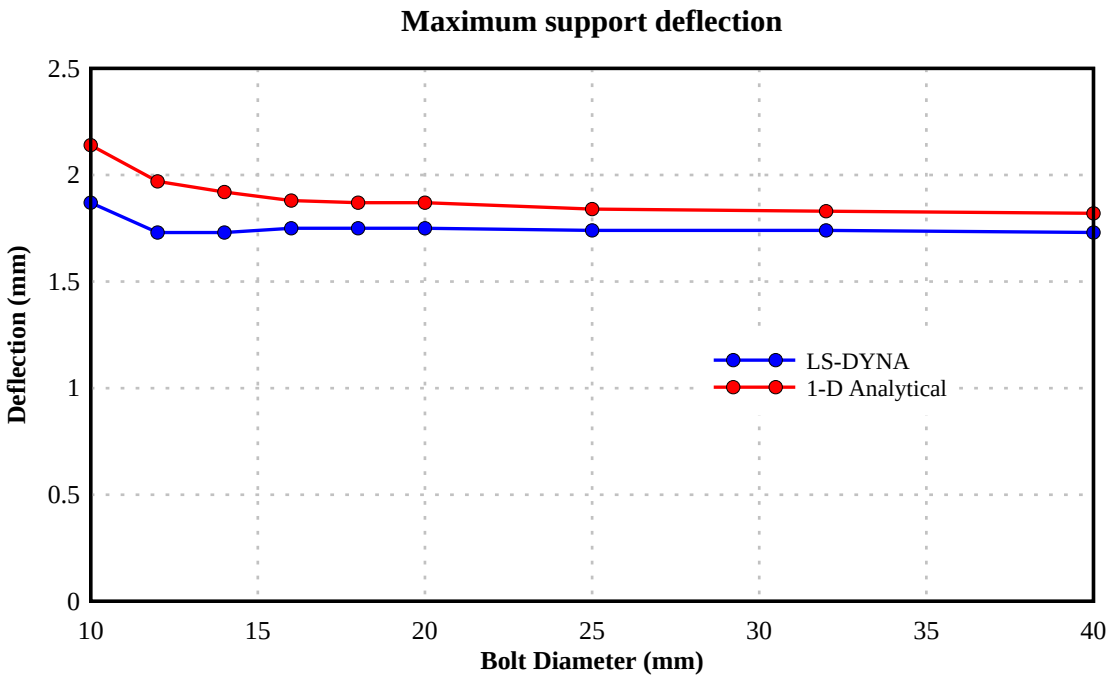

Figure 7.3: Maximum support deflection with bolt diameter-Angle cleat connections

Effect on relative deflection

Variation of relative deflection, the difference between maximum mid-panel deflection and maximum support deflection, is presented in Figure 7.4. No significant variation in relative deflection was observed, similar to both mid-panel deflection and support deflection. Furthermore, similar predictions between the LS-DYNA and the 1-D analytical solution is observed. The LS-DYNA prediction and 1-D analytical prediction was within 1 mm of each other for all considered bolt diameters.

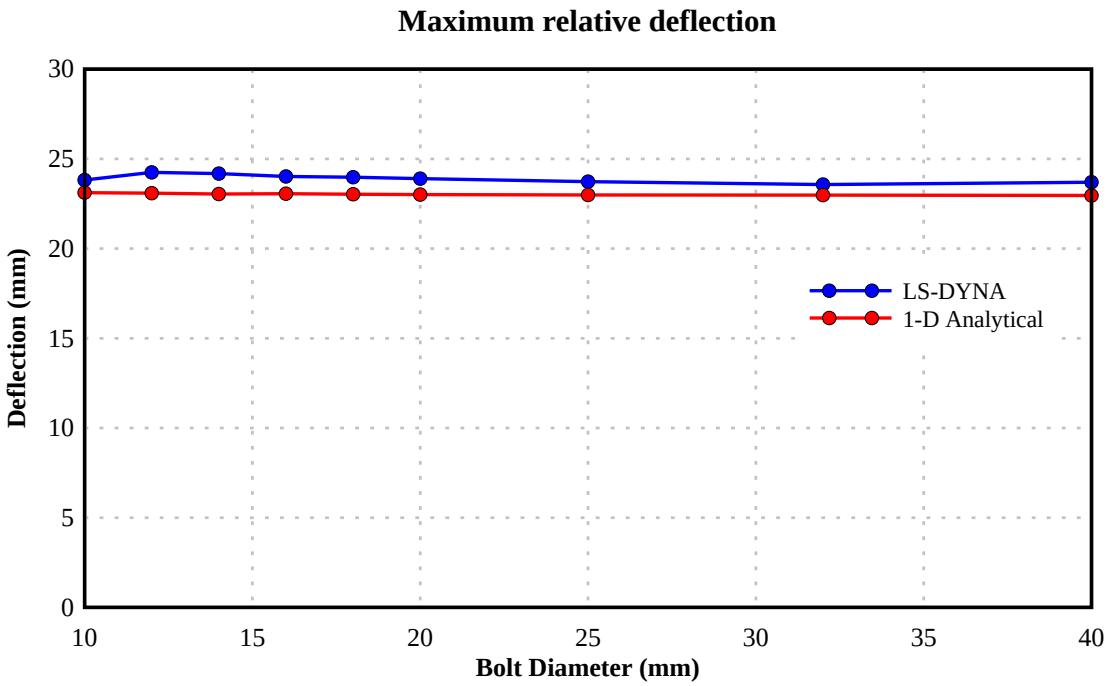

Figure 7.4: Maximum relative deflection with bolt diameter-Angle cleat connections

Effect on axial stress and shear stress in connecting bolts

Figure 7.5 describes the variation of axial stress and shear stress of connecting bolts. Evaluation of stresses involved only the LS-DYNA, 3-D finite element model as the 1-D analytical solution was a simplified analysis tool used for deflection and failure mode prediction. Shear stress is more than twice as high as axial stress for every selected bolt diameter. As expected, both shear and axial stresses reduce in magnitude with diameter change. This Reduction was purely due to the larger cross-sectional area available for stress (load) transfer even though shear and axial forces increase with the bolt diameter.

Axial stresses as low as 6 MPa were observed with large diameter bolts (M40). Conversely, shear stresses in connecting bolts did not fall below 90 MPa, which was also recorded for the M40 bolts. Maximum values of 221 MPa and 454 MPa for axial and shear stresses were witnessed with smaller diameter (M10) bolts, where higher stresses were due to the smaller bolt size. However, these numbers are significantly smaller than the tensile strength of the bolting material (800 MPa). Overall, these results suggest the use of smaller bolt sizes could result in higher bolt stresses, where smaller variation in explosive charges can lead to connection failures.

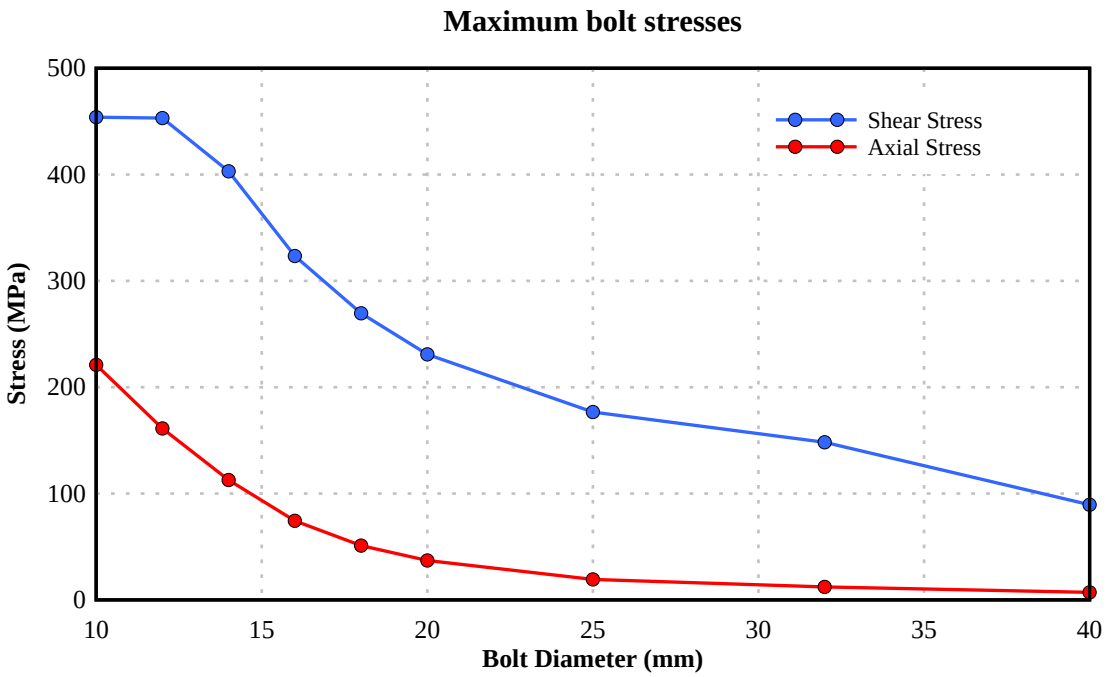

Figure 7.5: Maximum stresses in connecting bolts with bolt diameter-Angle cleat connections

Effect on maximum compressive stress in concrete

The variation of maximum compressive stress in concrete is presented in Figure 7.6, using the LS-DYNA, 3-D finite element model. A gradual increase in compressive stress was witnessed between the bolt diameters of 10 mm and 20 mm. The maximum compressive stress of 38.8 MPa recorded at bolt diameter of 20 mm, which is approximately 90% of the compressive strength of concrete (43 MPa). Further increase in bolt diameter provided a slight decline in the maximum compressive stress. A slight increase in compressive stress was observed with 40 mm bolts, which was not enough to reach the maximum.

Fluctuations in compressive stress can be explained by the variation of support stiffness. Smaller bolt diameters result in lower support stiffness which yields to transverse support deflection. These deflections dissipate the applied loading which reduces the flexural action within the concrete section, reducing the compressive stresses. Fluctuations in compressive stress beyond the 25 mm diameter are explainable only with a rebound of the panel resulting in localised stress concentrations.

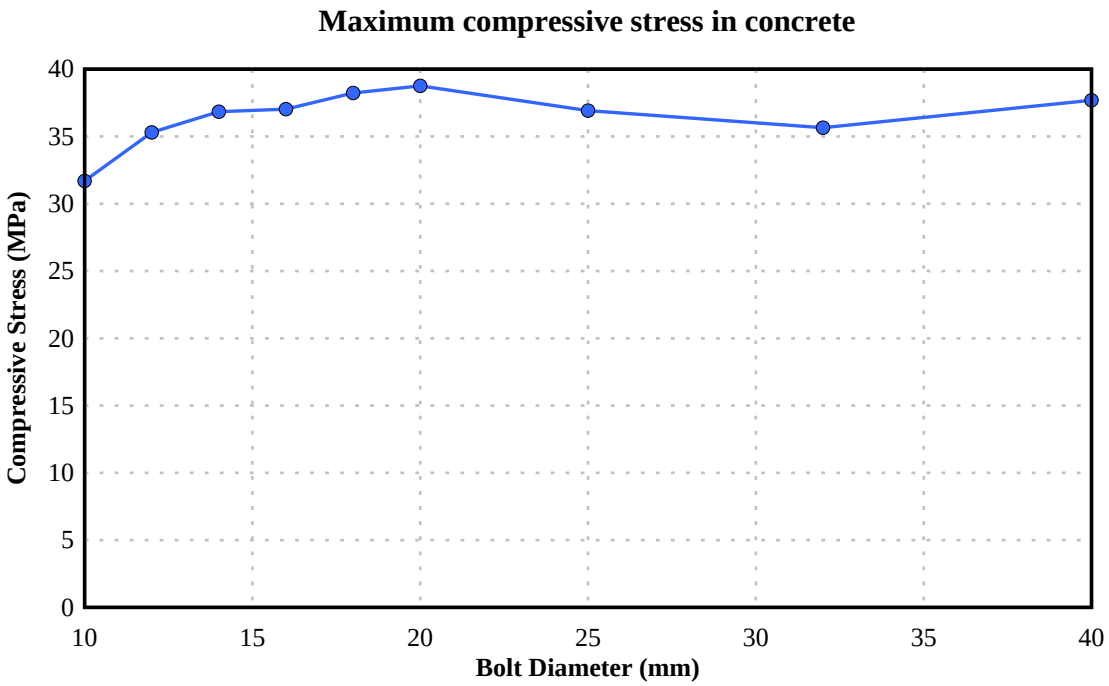

Figure 7.6: Maximum compressive stress with bolt diameter-Angle cleat connections

Effect on effective stress in connecting cleat

Figure 7.7 demonstrates the variation of maximum effective stress in connecting cleats. A monolithic rise in the effective stress of angle cleats was observed with the increment of bolt diameter. However, effective stress in connecting bolts did not reach the yield strength (300 MPa) of angle cleat sections, for the selected diameter range. Maximum effective stresses between 128.23 MPa and 237.47 MPa were observed in the selected diameter range.

Smaller bolt sizes resulting in smaller translational resistance is demonstrated with the effective stresses in angle cleats. This rise in stiffness resulted in an increase in force transfer, which escalates the effective stress in the angle section. Monolithic gains in effective stress further suggest the rise in translational stiffness resulting in increased forces in fixing assemblies.

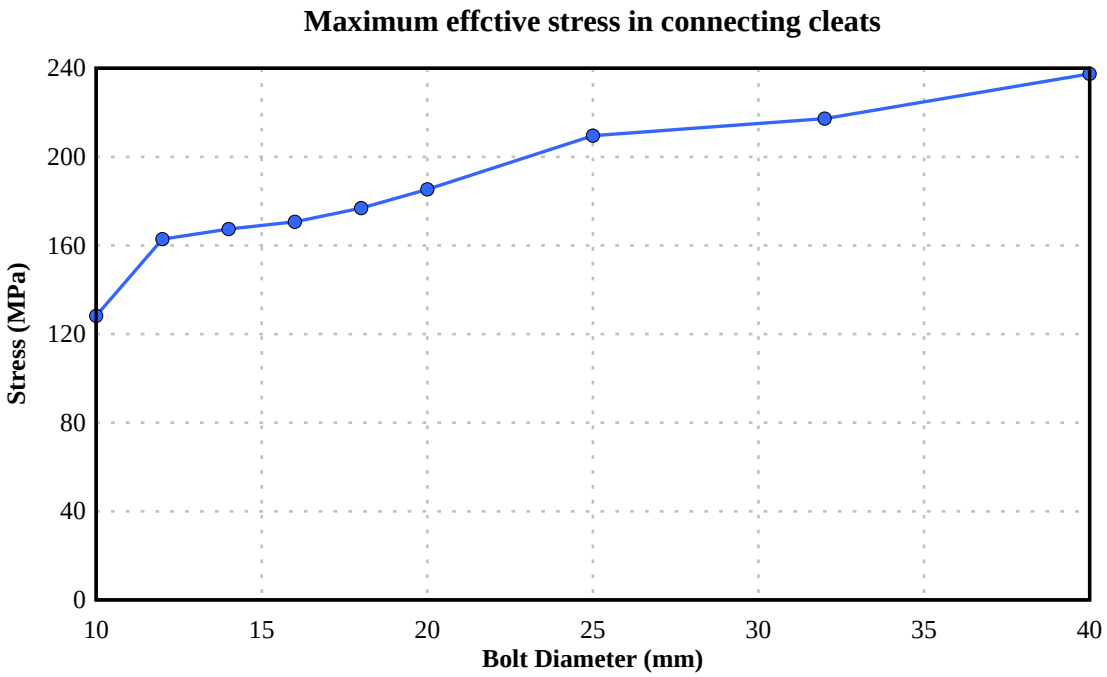

Figure 7.7: Maximum effective stresses in connecting cleats with bolt diameter-Angle cleat connections

Overall conclusions

Use of smaller bolt diameters was found to be effective in reducing the forces transferred through fixing assemblies, although this does not affect the panel deflections significantly. This phenomenon is clearly visible with effective stress in connecting cleats and to a certain level in concrete stresses. However, use of smaller bolt diameters has the disadvantage of increased stresses within the bolt section.

Bolt diameters between 16-20 mm are found to be the most effective for angle cleat connections for the selected panel size, explosive charge and standoff distance combination. Although selected bolt sizes did not influence the panel deflections, stresses in different components of the panel and fixing assemblies varied significantly. Stresses in bolts were smaller with large bolt diameters while stresses in steel cleats were smaller with small bolt diameters. Although compressive stresses in concrete were largest with mid-size bolt diameters (16-25 mm), the compressive strength of the panel was not reached. Hence, it is advisable to use mid-size bolts with the selected bolt configuration.

7.2.1.2. Cleat thickness

This section describes the assessment of transversely flexible connections by variation of cleat thickness in explosive resistant reinforced concrete facade systems. Angle sections with thicknesses varying from 5 mm to 15 mm were used for the evaluation. Since the panels were scaled down panels (Scale factor of 2, described in Section 5.2), cleat thicknesses too have been scaled down to achieve consistent stiffness ratios. Hence, these cleat thicknesses represent an actual thickness range of 10 mm to 30 mm respectively, which is frequently used in industry.

Effect on maximum mid-panel deflection

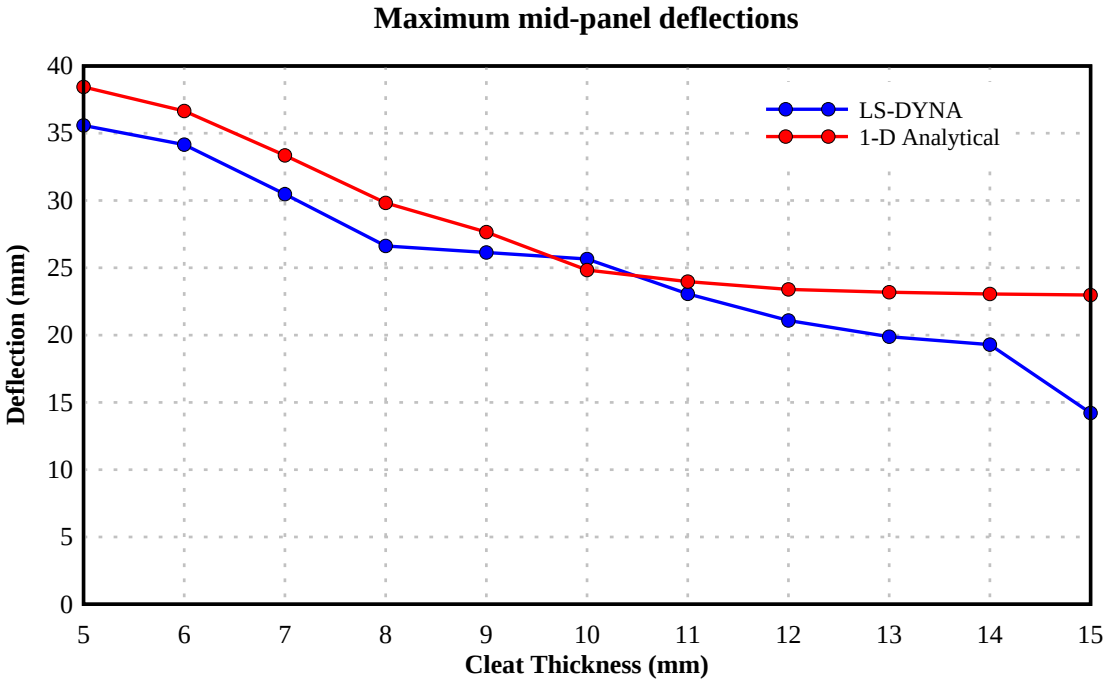

Figure 7.8: Maximum mid-panel deflection with cleat thickness-Angle cleat connections

The variation of maximum mid-panel deflection using both LS-DYNA and the 1-D solution is presented in Figure 7.8. A gradual decrease in mid-panel deflection was observed with the cleat thickness increase with LS-DYNA. A similar response was also observed with the 1-D analytical solution until a cleat thickness of 11 mm and remained approximately constant beyond. The 1-D analytical solution gives slightly higher mid-panel deflection than the LS-DYNA for all cleat thicknesses except 10mm. The maximum difference between the two panels of 8.76 mm was observed with the 15 mm

cleat section. The difference between the two predictions remained below 4 mm for all other selected cleat thicknesses.

Effect on maximum support deflection

Figure 7.9 illustrates the variation of support deflection for different cleat thicknesses. A similar response to mid-panel deflection (Figure 7.8) was witnessed with support deflection as well. Both LS-DYNA and 1-D analytical solution showed similar prediction paths. The largest difference between LS-DYNA and 1-D analysis of 0.83 mm was observed with 5 mm cleat thickness, where maximum deflections were also observed.

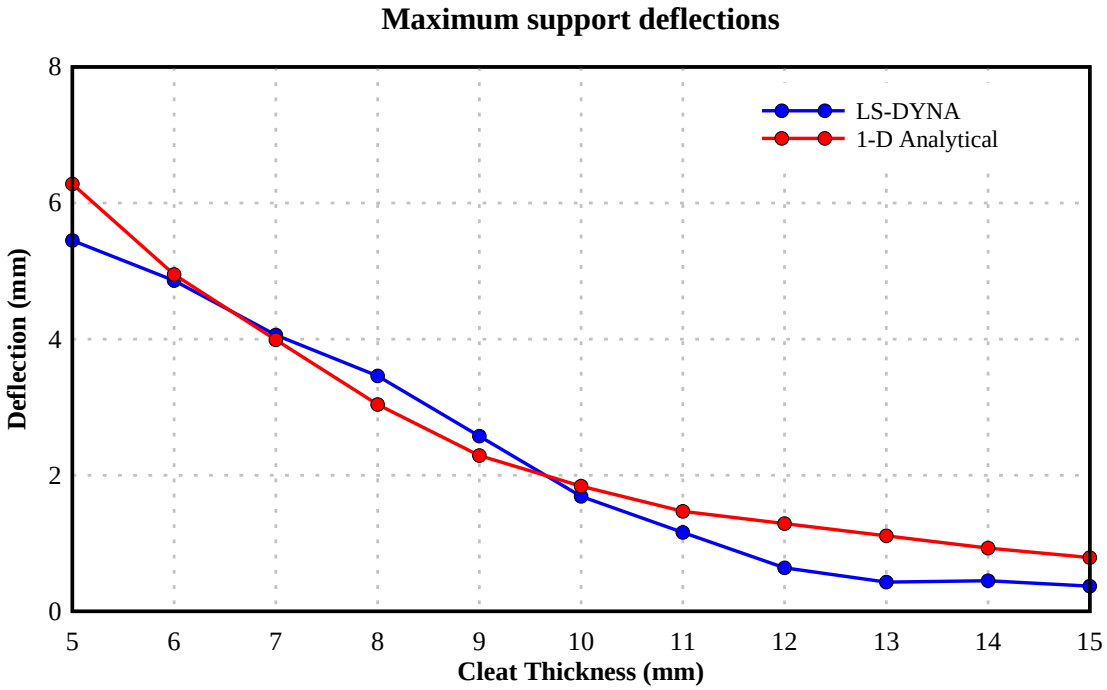

Figure 7.9: Maximum support deflection with cleat thickness-Angle cleat connections

Effect on relative deflection

The variation of relative deflection is presented in Figure 7.10. Both LS-DYNA and 1-D predictions for relative deflection were very similar to mid-panel deflection variation (Figure 7.8). A slight gradual decrease in deflection was observed with LS-DYNA for the cleat thicknesses less than 10 mm. The largest difference between two methods of 8.58 mm was observed with 15 mm cleat thickness. The 1-D prediction remained above the LS-DYNA prediction for all cleat thicknesses except for 10 mm, similar to the maximum mid-panel deflection.

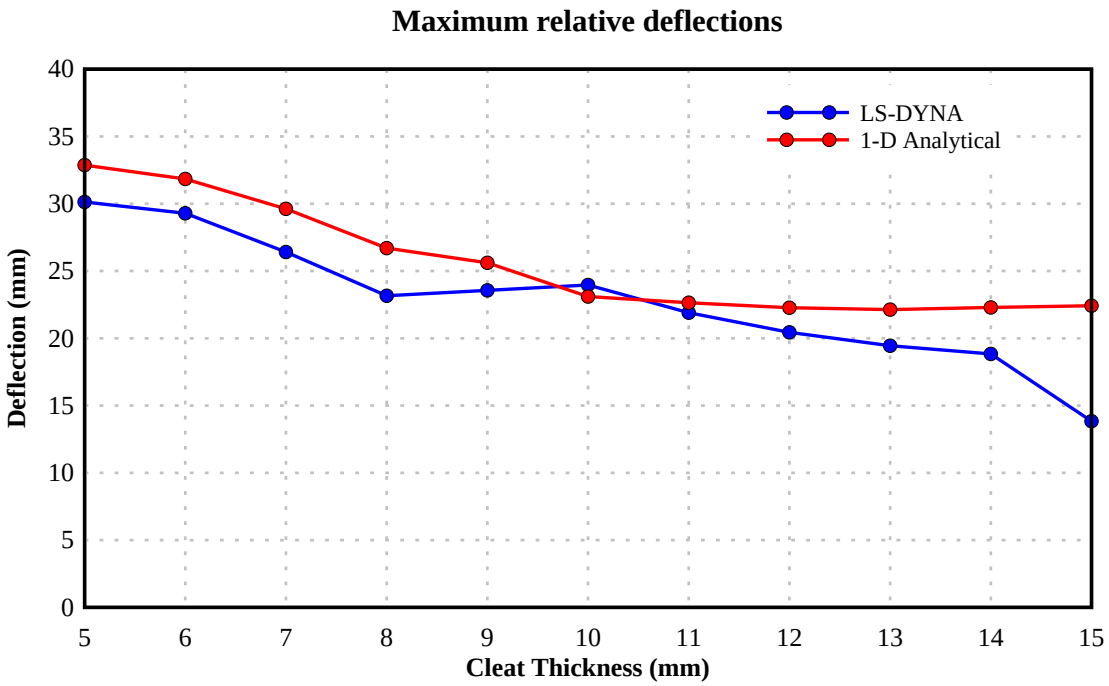

Figure 7.10: Maximum relative deflection with cleat thickness-Angle cleat connections

Use of thinner angle sections has shown to alter the behaviour of the panel considerably, allowing significant support deflection in the transverse direction. The energy dissipated during this process will ease the forces transferred as a flexural action within the section. Therefore, the panel will be able to safely transfer the reduced flexural action with lesser deflection. However, use of thinner sections as supports could escalate the rotational flexibility. This rise in rotational flexibility has the capacity to increase the mid-panel deformation, as indicated in Figure 7.8.

Effect on axial and shear stress in connecting bolts

The variation of axial and shear stresses of connecting bolts is presented in Figure 7.11. Both shear stress and axial stress were considered, although axial stress is significantly small in comparison to shear stress. Analysis results are limited to LS-DYNA, 3-D finite element model as the 1-D model is developed only for deflection and failure mode predictions.

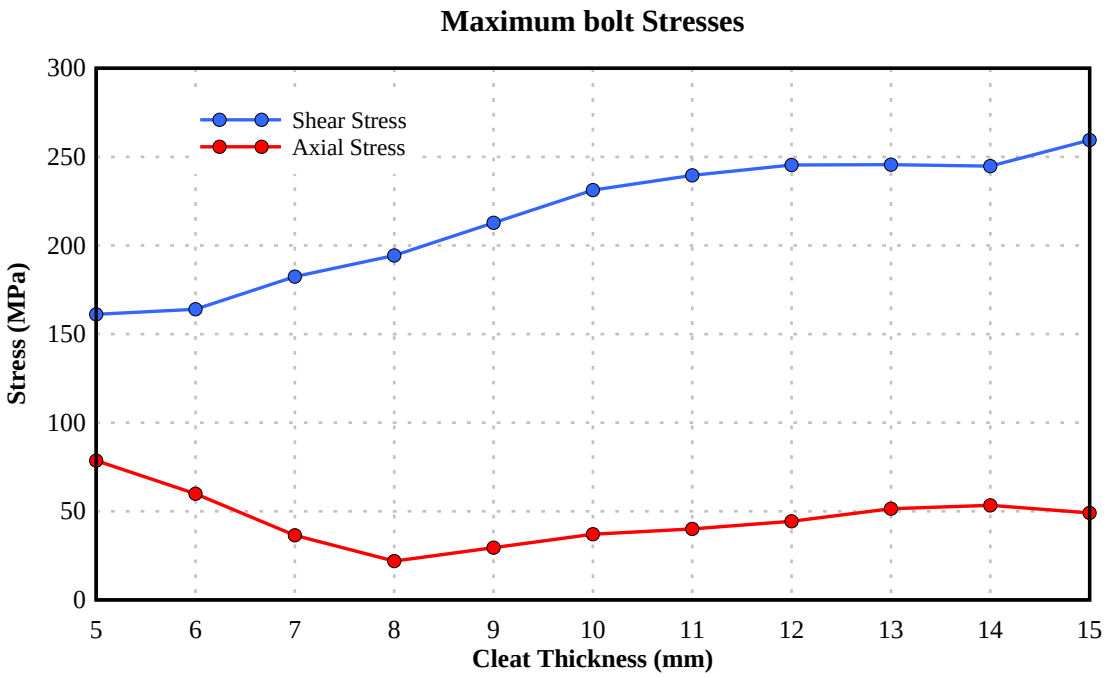

Figure 7.11: Maximum stresses in connecting bolts with cleat thickness-Angle cleat connections

Shear stress in connecting bolts demonstrates a monolithic gain with increased cleat thickness. However, none of the bolts reached at least half of their capacity (640 MPa yield strength and 800 MPa tensile strength), where a maximum of 259.5 MPa was recorded. The monotonic rise in shear stress is due to the gain in support resistance, which eventually results in higher shear stresses in bolts.

Axial stresses in connecting bolts have shown a different pattern to shear stress where the maximum axial stress being recorded with the thinnest cleat thickness of 5 mm. This has declined rapidly from the maximum of 79.8 MPa to a minimum of 21.8 MPa within a thickness increment of 3 mm (8 mm cleat). Since then, a gradual rise of axial stress was witnessed up to 15 mm, which is the largest cleat thickness considered for this analysis. However, this gradual increase is not sufficient to reach the maximum reached with 5 mm cleat thickness.

Comparison of maximum axial and shear stresses (in bolts) reveals that use of thinner angle sections can reduce the shear force in connecting bolts. However, the axial force will be dependent on the combination of flexural stiffness of panel and support sections. In comparison, maximum shear stresses transferred by bolts in angle cleat connections are significantly higher than axial stresses.

Effect on maximum compressive stress in concrete

The maximum compressive stress recorded is plotted against the cleat thickness as presented in Figure 7.12. Compressive stresses were recorded using only the LS-DYNA, 3-D finite element model, similar to the stresses in connecting bolts in the previous section. A variation similar to axial stresses in connecting bolts was observed for the maximum compressive stresses in concrete. The thinnest cleat section of 5 mm recorded a compressive stress of 32.1 MPa, which eventually dropped down to a minimum of 26.3 MPa. Since reaching the minimum, a steady increase in compressive stress was witnessed where a peak of 53.5 MPa was recorded in 15 mm thick section. The 15 mm cleat thickness was the only instance where compressive stress exceeded the compressive strength of concrete (43 MPa).

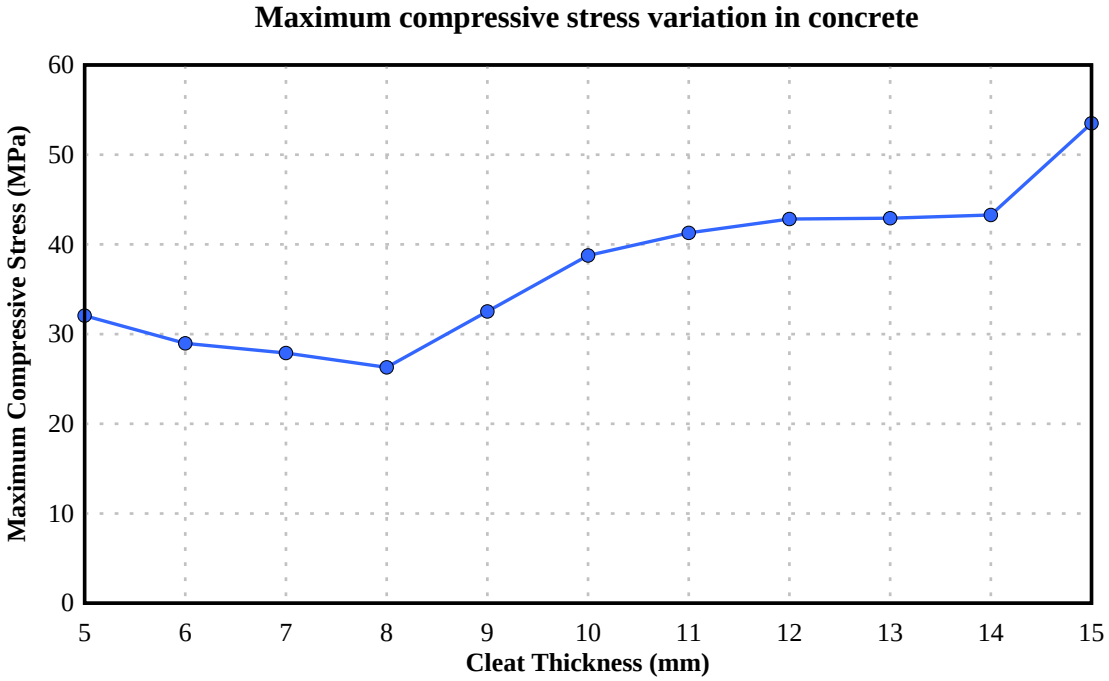

Figure 7.12: Maximum compressive stress in concrete with the variation of cleat thickness –Angle cleat connections

The variation of maximum compressive stress within the concrete section can be explained by the same argument which explains the axial stresses in connecting bolts. Higher concrete stresses and large mid-panel deflections were observed with thinner angle sections (8 mm or less) due to the obvious weaker rotational stiffness at the supports. However, both rotational stiffness and translational stiffness rise with the increased cleat thickness, resulting in panel cross-section experiencing increased

flexural loading. This results in an escalation of compressive stresses in concrete. The 8 mm thick cleat section appears as the optimal thickness as it exhibits a balanced combination of rotational and translational stiffness, which induces the minimum compressive stresses within the concrete section.

Effect on effective stress in connecting cleat

Figure 7.13 shows the variation of maximum effective stress in connecting cleats with the cleat thickness using the LS-DYNA, 3-D finite element model. A rapid decline between 6 mm and 7 mm followed by a steady decrease in effective stress was observed.

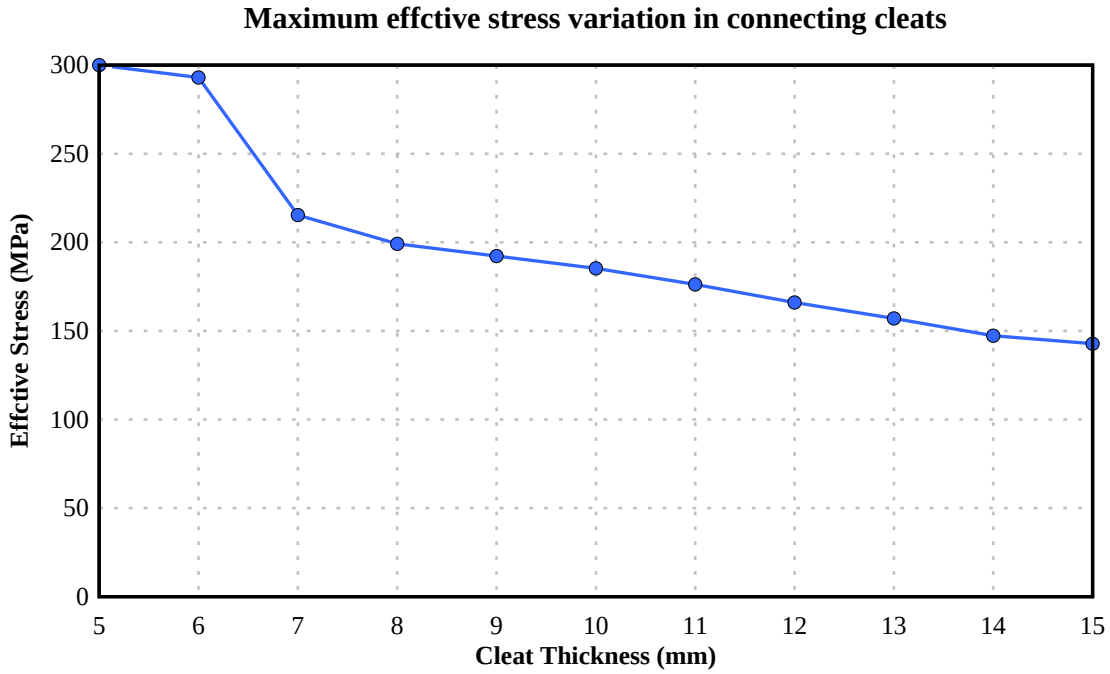

Figure 7.13: Maximum effective stresses in connecting cleats with cleat thickness-Angle cleat connections

The maximum effective stress of 300 MPa was registered for the thinnest angle section of 5 mm. This maximum stress was equivalent to the yield strength of the material (300 MPa). Although material yield strength was reached, yielding was limited to a localised area around the connecting bolts. The smallest maximum of 142.8 MPa was witnessed with 15 mm cleat section, which was less than half the maximum effective stress achieved.

Overall conclusions

Larger cleat thicknesses improved the resistance against transverse deflection in supports and mid-panel. The results were evident in both the LS-DYNA and the 1-D solutions. In addition, effective stresses have decreased with increase in cleat thicknesses. Conversely, compressive stress in the concrete panel and shear stress in connecting bolts have increased with the cleat thickness. Therefore, the use of mid-size angle cleat sections (8-12 mm) is advisable considering the performance of the panel. Considering the scale down factor of 2, cleat thicknesses of 16-24 mm is desirable for full-scale panels with similar explosive charges.

7.2.2. Dowel connection

The dowel type fixing assemblies is typically used in bottom end connections of facade systems (Brookes, 1998). These connections consist of threaded bars built into the panel cross-section, where forces are transferred to supports using the dowel action. However, these connections were simplified using a steel plate embedded in the concrete section during the experimental evaluation (see Figures 5.2 and 5.3). Figure 7.14 illustrates the bolt configuration used for dowel connection in this study. Bolt size was the only parameter varied for this evaluation, due to the simplification of connection configuration during the experimental evaluation.

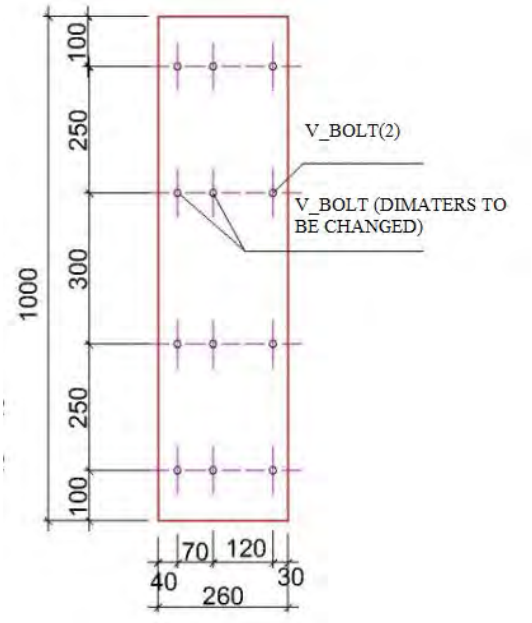

Figure 7.14: Bolt configuration for dowel connection (Source: Pham, 2010)

7.2.2.1. Bolt size (Diameter)

The parametric study was conducted varying the bolt diameter between 10 mm and 40 mm. All other parameters including the loading were kept similar to that of the experimental study and numerical model development. Panel deflections, stresses in the panel and connection mechanisms were evaluated as the panel performance parameters. Unlike in angle cleat connections, the parametric study was limited to LS-DYNA, 3-D finite element model because the 1-D analytical solution was only capable of modelling rigid horizontal supports.

Effect on maximum mid-panel, support and relative deflections

The variation of maximum mid-panel (central), support and relative deflections are presented in Figure 7.15. All three parameters were plotted on the same graph (different scales) as no comparison could be made with the 1-D solution.

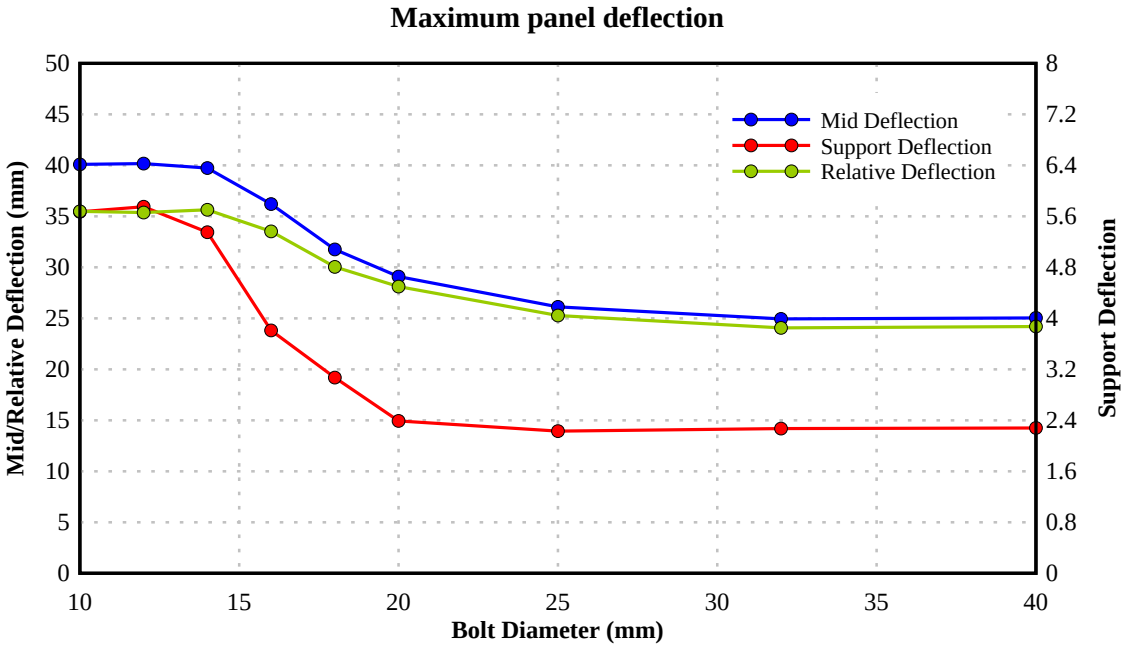

Figure 7.15: Maximum deflections with bolt diameter-Dowel connections

Three identical curves were observed with the three deflection parameters. Each curve can be broadly categorised into three different phases, a stable initial phase, gradual decreasing phase and a constant final phase. The initial stable phase is between the bolt diameters of 10 mm and 15 mm, where deflections remained approximately constant. Maximum deflections of 40.2 mm, 5.8 mm and 35.6 mm were observed in this initial

phase for the mid-panel, support and relative deflections, respectively. A gradual decrease in deflection was visualised following the initial stable phase, up to bolt diameters of 25 mm. The final stable phase, where deflections remain fairly constant, was observed for bolt diameters beyond 25 mm.

The variation of support deflection indicates significant transverse deflection with smaller bolt sizes. Along with the transverse support deflection, large central and relative deflections suggest significant horizontal (shear) deformation through connecting bolts. These large deflections point to the shear and axial flexibility of the fixing assembly with smaller bolt diameters. Decline in maximum deflections (in mid-panel, support and relative deflections) beyond 15 mm diameter bolts is an indication of gain in axial and shear resistance of fixing assemblies. However, this gain in resistance did not result in a reduction of deflection beyond the diameters of 25 mm. This phenomenon could be explained by increased support resistance tipping the scales between support resistance and panel stiffness. Hence, a further increase in bolt diameter will not result in reduced deflections.

Effect on axial and shear stress in connecting bolts

Figure 7.16 depicts the variation of axial and shear stresses of connecting bolts for dowel connections. As shown in Figure 7.16, axial stresses indicate yielding of bolts with stresses reaching 640 MPa. Yielding occurs with bolt diameters up to 18 mm before gradually declining to a minimum of 261 MPa. On the other hand, axial stress exhibits a slight increase up to a bolt diameter of 25 mm with a maximum of 450 MPa before falling down to a minimum of 267.3 MPa.

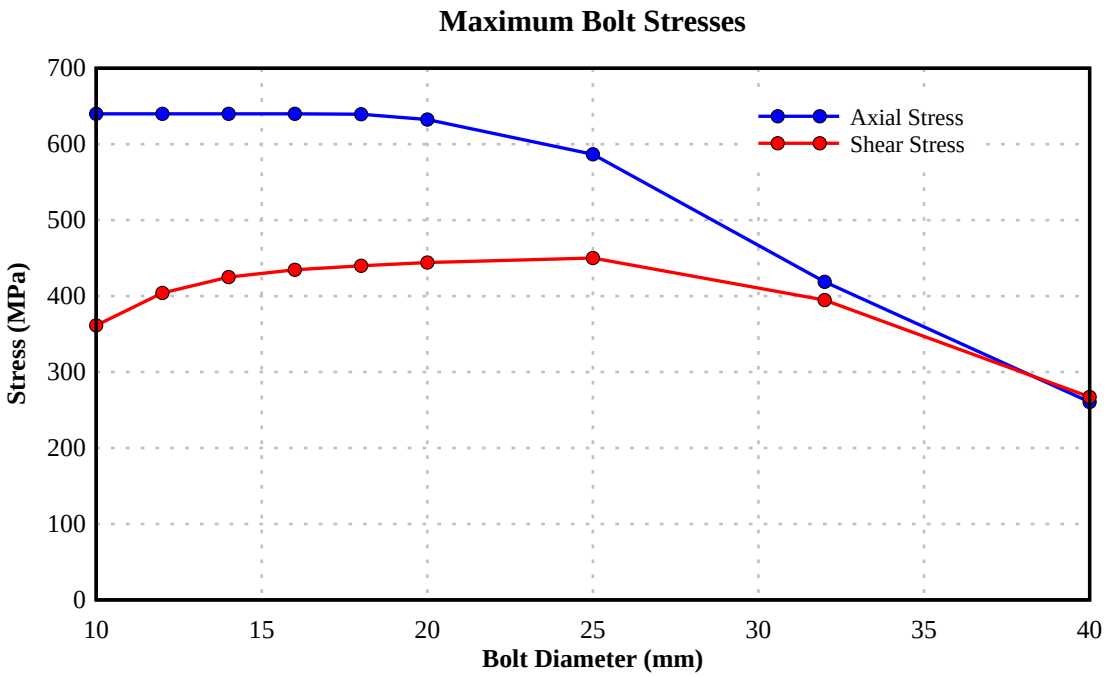

Figure 7.16: Maximum bolt stresses with bolt diameter-Dowel connections

Unlike in angle cleat connections, the configuration of the dowel connection allows the connecting bolts to transfer significant axial and shear stresses. Axial stresses reaching yield strength was observed with smaller bolt diameters. This explains the presence of large transverse deflections in supports in excess of 5 mm. Bolt diameters above 18 mm were able to resist the applied load without permanent damage (yield) to bolts, after which axial stresses have declined significantly. This is due to the expanded cross-section (bolt) available for resisting the applied loading.

Shear resistance of connections was improved with the increase in bolt diameters. This increased resistance can be observed in terms of shear stresses in connecting bolts, even with the expanded cross-section. However, beyond 25 mm diameter, rise in support shear force was comparatively lesser than the rise in available cross-section. Hence, decrement in shear stress was observed beyond 25 mm diameter bolts.

This variation in bolt stresses confirms the deflection variation observed in Figure 7.15. Large deflections associated with smaller bolt diameters were due to the flexibility in fixing assemblies, whereas an increase in bolt diameter reduces the flexibility and maximum deflections. However, the increase in bolt diameters beyond 25 mm has resulted in constant deflections.

Effect on maximum compressive stress in concrete

The variation of maximum compressive stress with change in bolt diameter is shown in Figure 7.17. A gradual rise in compressive stress is observed with the increase of bolt diameter, where smaller bolts resulting in lower compressive stresses. The minimum compressive stress of 31.4 MPa was witnessed with 12 mm diameter bolts whereas the maximum of 66.4 MPa was recorded with 32 mm diameter bolts. These maximum stresses were witnessed close to the middle of the panel suggesting probable compression failures.

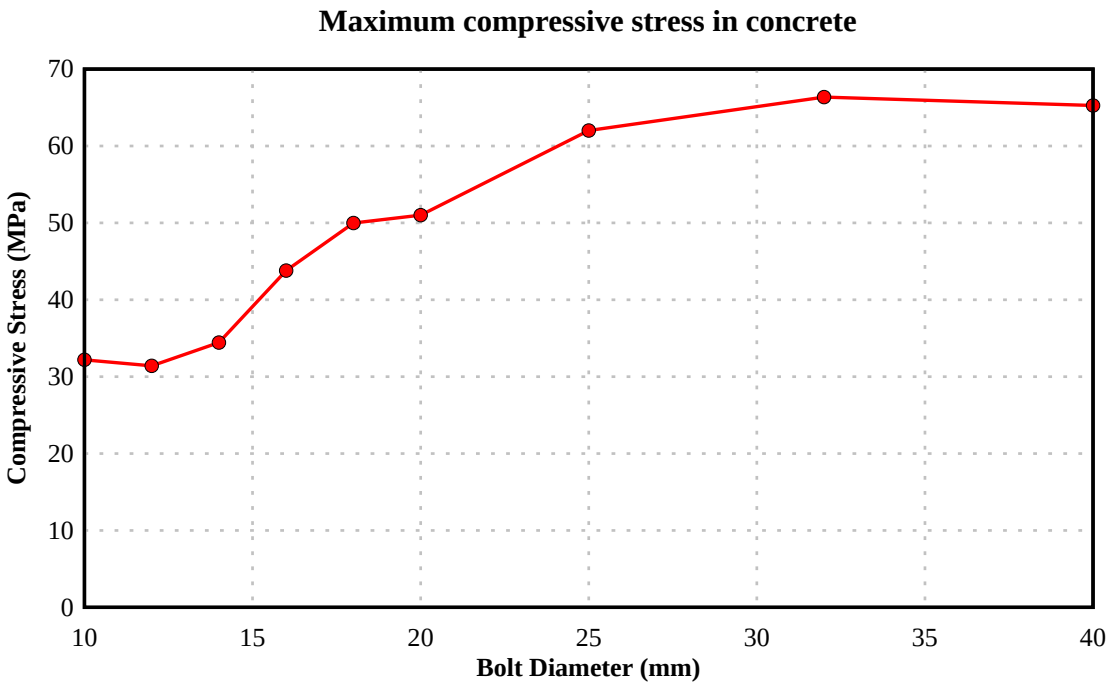

Figure 7.17: Maximum compressive stresses of concrete with bolt diameter-Dowel connections

These higher compressive stresses (beyond compressive strength) could be due to two reasons, strain rate enhancement and gain in support stiffness. As discussed in Chapter 3, higher rates of loading can yield to higher compressive stresses. On the other hand, the rise in flexural and translational stiffness can lead to a rigid response from the panel. Therefore, flexural action within the concrete section is increased, which leads to higher compressive stresses. In addition, these high compressive stresses were recorded with small mid-panel deflections, which confirm the involvement of strain rates. As further evidence, Panel A1 suffered compression cracks using 18 mm bolts during the

experimental evaluation and confirmed in the numerical evaluation (Chapter 5), which confirms the observations in this parametric study.

One would argue that smaller deflections lead to lesser stresses. However, this argument is valid only within the quasi-static domain where strain rates are small. Therefore, this variation in compressive stress is due to a combination of strain rate effects and stiffness increase in fixing assemblies.

Effect on effective stress in connecting cleat

Figure 7.18 demonstrates the effective stress variation in the steel plate section. Lower stresses were observed for smaller bolt diameters with the lowest of 271.9 MPa. This lowest stress was witnessed with 10 mm diameter bolts. A gradual increase in stress was observed for effective stress until a bolt diameter of 16 mm, where effective stress reaches yield strength (300 MPa) of the steel section. Effective stress remains at yield strength for bolt diameters larger than 16 mm in this instance. The gain in stiffness due to the larger bolt diameters has increased the forces transferred through supports, resulting in localised yielding of the steel section.

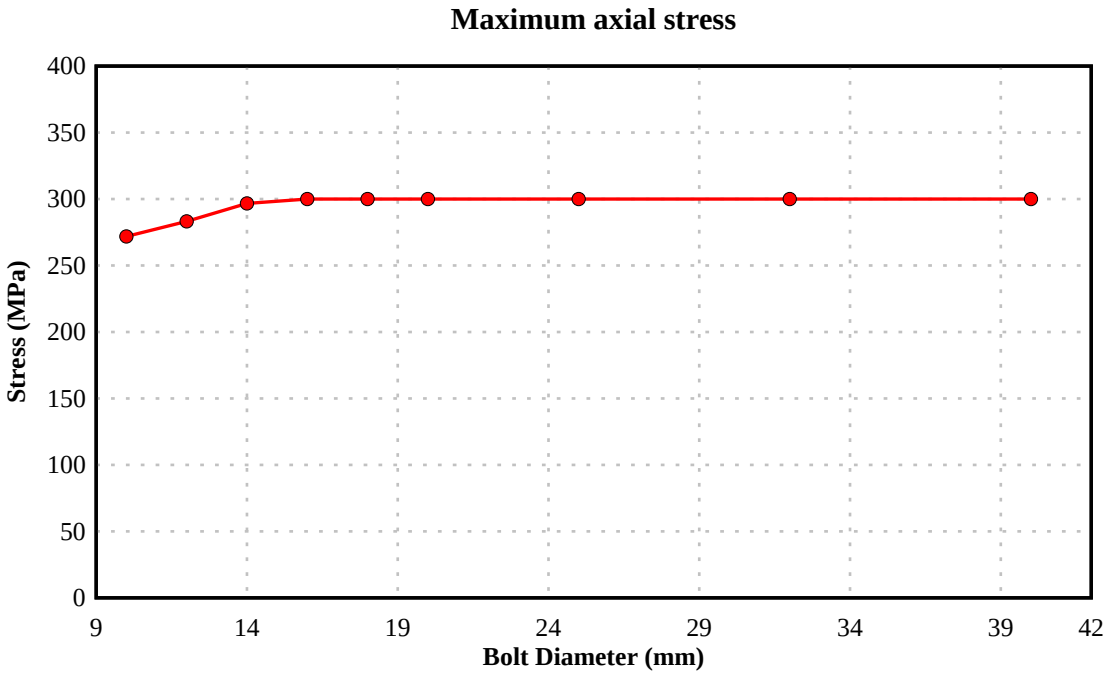

Figure 7.18: Maximum effective stress in connecting cleats with the variation of bolt diameter – Dowel connections

Overall conclusions

Overall, larger bolt diameters have reduced the maximum deflections (mid-panel, relative and support) of the panel. Similarly, large bolt diameters have shown reduced stresses within the bolt section. However, these larger bolt diameters have increased the compressive stress in concrete and effective stress in the steel plate section. Interestingly, at least one combination of failure stresses (partial failure) was reached for every bolt diameter considered, for the selected combination of loading and panel thickness, although these were localised concentrations. Considering all stresses and deflections, bolt diameters between 16-25 mm would result in the least possibility of complete failure of the section although, partial failures may occur.

7.2.3. Summary: Facade panels with flexible support conditions

The applicability of flexible connections in blast effects mitigation of reinforced concrete facade systems was evaluated in this section. The LS-DYNA, 3-D numerical model and the 1-D analytical solution was used for the evaluation. Use of different bolt diameters and cleat thicknesses were evaluated. The performance of each connection configuration/fixing assembly was evaluated based on the maximum deflection and maximum stresses in different structural components. The following observations were made based on the parametric study results.

- The variation in bolt diameter did not have any significant influence on Type B (angle cleat connected) panels, in terms of maximum deflection. However, larger bolt diameters resulted in reduced deflections in Type A (dowel connected) panels.
- Thicker cleat sections (Type B panels) influenced similarly as larger bolt diameters in Type A panels, where reduced deflections were observed with thicker cleat sections.
- Increase in bolt diameter (Type A and Type B) and increase in cleat thickness (Type B) influenced similarly with increased compressive stresses.
- Smaller bolt diameters (Type A and Type B) have resulted in smaller effective stresses in connecting cleats/plates. Localised yielding of thinner cleat sections ($t \leq 8$ mm) was also observed in Type B panels.

- Smaller bolt diameters resulted in elevated shear and axial stresses in connecting bolts (Type A and Type B). The effects are more significant in Type A panels.
- Thinner cleat sections resulted in reduced bolt stresses (axial and shear) in both Type A and Type B panels.
- The possible failure modes include both connection failures and panel failures. Bolt rupture and yielding of fixing assemblies were found to be plausible connection failure mechanisms for the considered scaled distance (see Figure 4.2).
- Flexural failure by means of tensile cracks and crushing (compression failure) of concrete was observed. However, no significant stress concentrations were observed to suggest diagonal or direct shear failures for the selected scaled distance (see Figure 4.2).

Based on the overall performance (deflections and stresses) of the panels for different connection configurations, following conclusions were made for optimum bolt diameter and cleat thickness.

- Bolt diameters between 10-40 mm did not have a significant influence on the deflection of ***angle cleat connected*** panels. Bolt diameters between 16-25 mm would result in minimum stress levels in all structural components.
- Cleat thicknesses between 8-12 mm would result in minimum stress levels and optimum deflections in ***angle cleat connected*** panels. Therefore, considering the scale down factor of 2, cleat thicknesses between 16-24 mm would result in optimum stress levels and deflections for full-scale panels (span of 3 m).
- In ***dowel connected*** panels, at least one stress component reached failure stress (partial failure) for every bolt diameter considered. However, the least possibility of failure was observed with bolt diameters between 18-25 mm.
- Considering dowel and angle cleat connected panels, the angle cleat connected panels were found to be more stable in blast resistant applications. It is therefore recommended to use angle cleat connections over dowel connections for blast resistant facade systems.

7.3. Reinforced concrete facade panels with openings subjected to explosive loading

Openings in reinforced concrete panel elements (slabs and walls) are an integral part of modern day construction. These openings provide access as well as serve the purpose of openings for services. These openings can be classified into two major categories depending on the size and their intended use. Smaller openings are used mainly for installation of services such as heating, cooling and electrical whereas larger openings are mainly used as access control and additionally as natural lighting.

The design of reinforced concrete wall and slab panels with openings for conventional loading is performed using different design codes worldwide (i.e. Canadian Standard Association, 1990, Standards Australia, 2009, American Concrete Institute, 2011). These design codes provide guidelines on locations and sizing of openings within a reinforced concrete panel element and design of reinforcements. According to simplified ACI-318 guidelines (American Concrete Institute, 2011), any reinforced concrete panel is capable of having an unstiffened opening up to 300 mm. Openings larger than 300 mm will need specific design of reinforcements. Furthermore, no limitations are imposed on the dimensions of the openings as long as a prior analysis is performed for ultimate and serviceability conditions.

In the case of explosive resistant design of reinforced concrete panel elements, only a limited number of design guidelines are available. The Unified Facilities Criteria (UFC 3-340) (United States Army Corps of Engineers, 2008) is the only comprehensive design guideline available to serve this purpose. The design of reinforced concrete structural panels with openings is also included in the UFC 3-340. These guidelines are to be used in conjunction with ACI-318 (American Concrete Institute, 2011) guidelines for opening size and reinforcement detailing. However, none of these provides any direct guidelines on the design of reinforced concrete facade panels with openings. Hence, openings in facade panels are treated as openings in slab panels, considering the effects of explosive loading.

Reinforced concrete facade panels are evaluated with different opening sizes and reinforcement configurations with different explosive loading configurations. Both stiffened and unstiffened openings are considered where unstiffened opening sizes were

determined using the ACI 318 (American Concrete Institute, 2011) guidelines. Two typical connection mechanisms (angle cleat and dowel) used for the experimental evaluation are used in this parametric study as well.

In most of the cases, openings are fitted with glazing. Considering the shatter resistances in glass and concrete, no significant difference in the loading or the structural behaviour can be expected from a glazed opening and openings without glazing. However, in the case of laminated or toughened glazing, loading and structural behaviour may vary depending on the thickness of the glazing. However, for the purpose of this analysis, the resistance provided by glazing and subsequent attaching mechanisms is ignored, assuming all the panels were fitted with conventional glazing.

7.3.1. Scaled distance-deflection curves for reinforced concrete facade panels with openings

Three different panel geometries; a solid panel without opening, a panel with a 300×280 mm unstiffened opening and 580×600 mm stiffened opening was used for the analysis (as in Figure 7.19). Both dowel connected (Type A) and angle cleat connected (Type B) panels were considered, hence six different panel configurations were considered in the analysis (Figure 7.19.(a) to (f)). The two solid panels were identical to the panels used for experimental evaluation and the other panels had the same geometric properties except for the openings. An unstiffened opening size of 300 mm was selected as it was the maximum opening size recommended by ACI 318. The 600 mm opening was stiffened by redistributing the same amount of reinforcement that was terminated due to opening (as in Figure 7.19.(e) and (f)). In addition, redistributed reinforcement was extended beyond the openings for a maximum of development length specified in ACI 318. All these openings were centrally located within the panel.

A set of scaled distance-deflection curves for reinforced concrete cladding panels with openings subjected to explosive loading is illustrated in Figure 7.20. Instead of scaled distance directly, maximum deflection is plotted against the reciprocal of scale distance (1/Z) as the increase in reciprocal indicates an increase in loading. Scaled distances ranging between 0.5 m/kg$^{1/3}$ and 3 m/kg$^{1/3}$ were selected for the analysis.

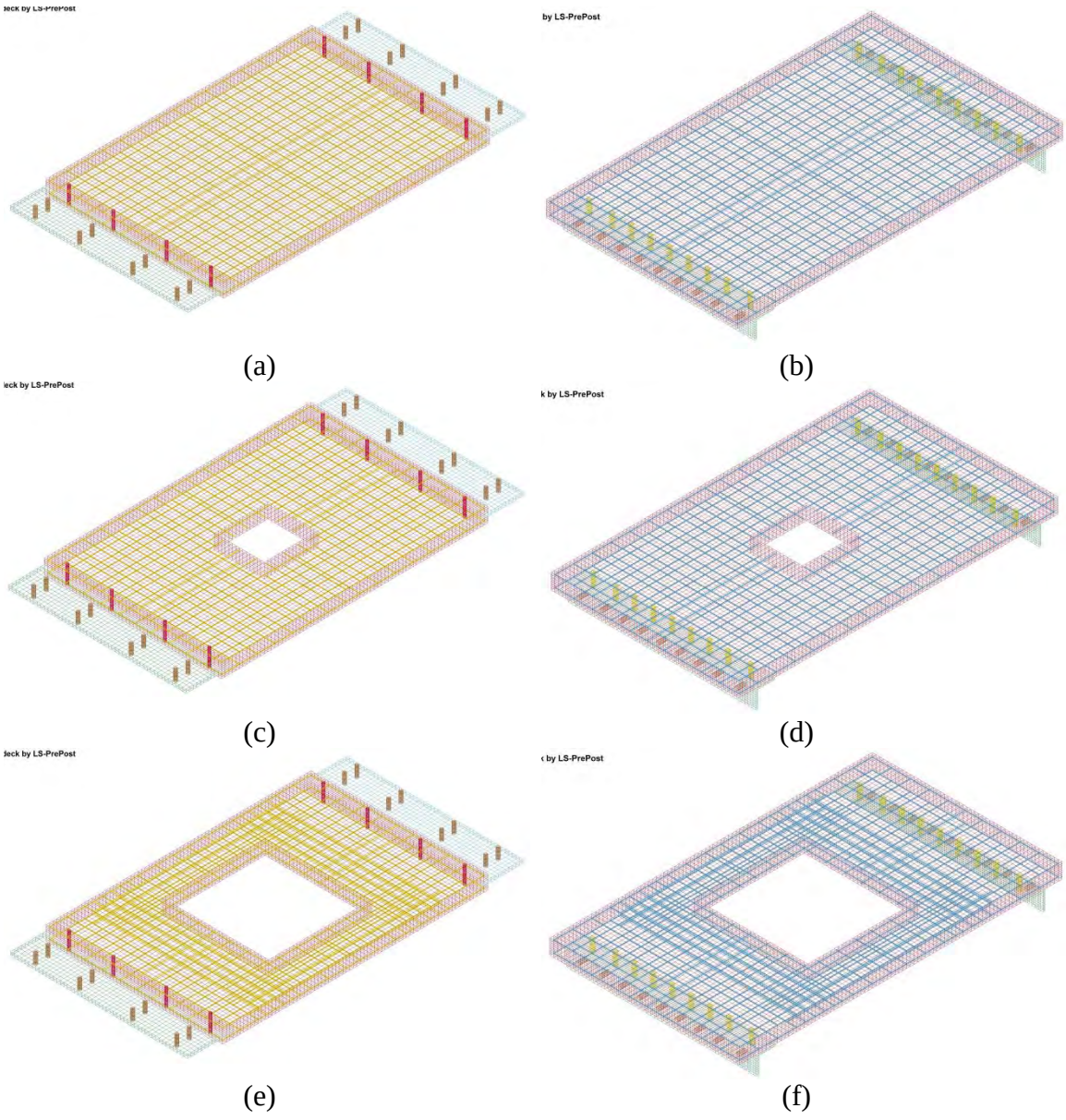

Figure 7.19: (a): Dowel connected panel without opening, (b): Angle cleat connected panel without opening, (c): Dowel connected panel with unstiffened opening, (d): Angle cleat connected panel with unstiffened opening (e): Dowel connected panel with stiffened opening and (f): Angle cleat connected panel with stiffened opening (rotated front view)

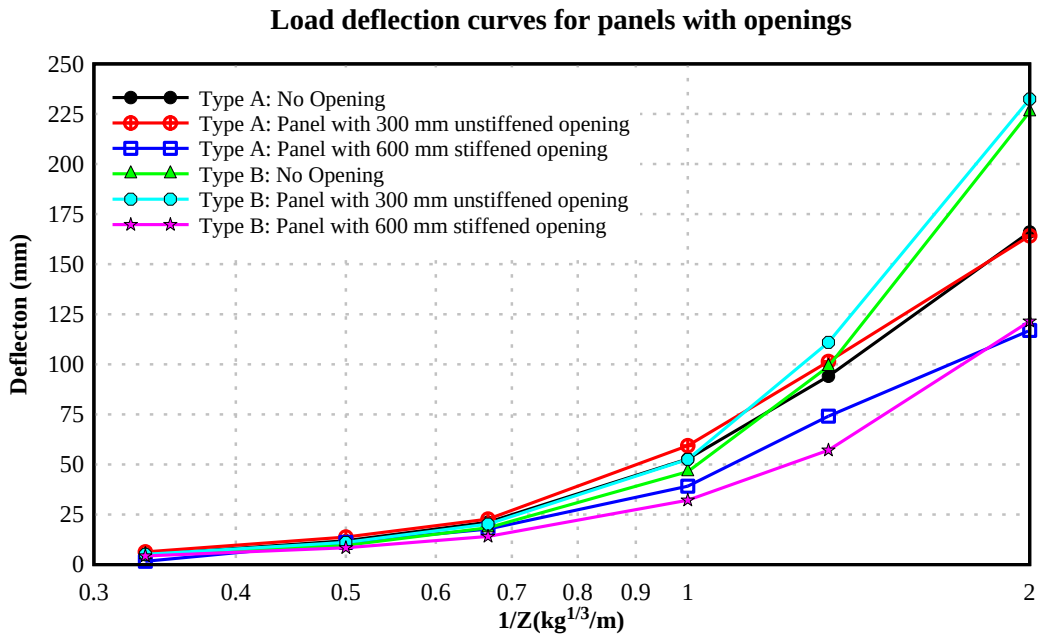

Figure 7.20: Scaled distance-deflection curves for panels with openings

As illustrated in Figure 7.20, three distinct sets of curve behaviours can be identified. Exponential growth in deflection was witnessed with an increase in the reciprocal of scaled distance (1/Z) for all panels with different magnitudes. No significant difference was visible between the Type B solid panel and Type B panel with unstiffened opening. A similar trend was noticed with Type A panels where deflections of similar magnitude were observed between solid panel and panels with the unstiffened opening. Irrespective of the type of connection, panels with stiffened openings experience similar deflections.

Stiffened panels responded to applied explosive loading showing improved resistance compared to both panels without openings and panels with unstiffened openings. This response can be expected from panels with stiffened openings as a similar amount of reinforcement and reduced loading surface available in comparison with solid panels. In the meantime, reduction in cross-sectional area may result in increased concrete stresses and possible compression failures.

7.3.2. Evaluation of explosive resistance of panels with unstiffened openings

Unstiffened openings of different sizes and locations were evaluated with an explosive load of 5.5 kg of equivalent TNT charge at a standoff distance of 2.1465 m (2 m clear distance) standoff distance. This combination of charge weight-standoff distance accounts for a scaled distance of 1.193 m/kg$^{1/3}$. Considering the minimum scaled

distance of 1.2 m/kg$^{1/3}$ specified in UFC 3-340 (United States Army Corps of Engineers, 2008) for far range (far field) explosive loading, and comparability with explosive field tests (Pham, 2010), this charge weight-standoff distance combination was used for this evaluation.

In addition to the results given in the following sections, time history plots for the maximum compressive strength and maximum mid-panel deflection are presented in Appendix D-II.

7.3.2.1. Opening size

Unstiffened openings starting from 40×60 mm to a maximum of 300×280 were positioned at the centre of the 1000×1500 mm panel, as shown in Figure 7.21.(a) to Figure 7.21.(f). Openings in all panels were placed as such that at least one reinforcement bar is interrupted in the major direction. The explosive source was placed coinciding with the centre of the panel and centre of the opening. Maximum panel deflections and maximum compressive stress in the concrete were plotted against the opening ratio (size of the opening as a percentage of the total panel area). The effective stress in connecting cleat/plate and stresses in bolts were ignored as varying opening sizes can alter the forces in fixing assemblies.

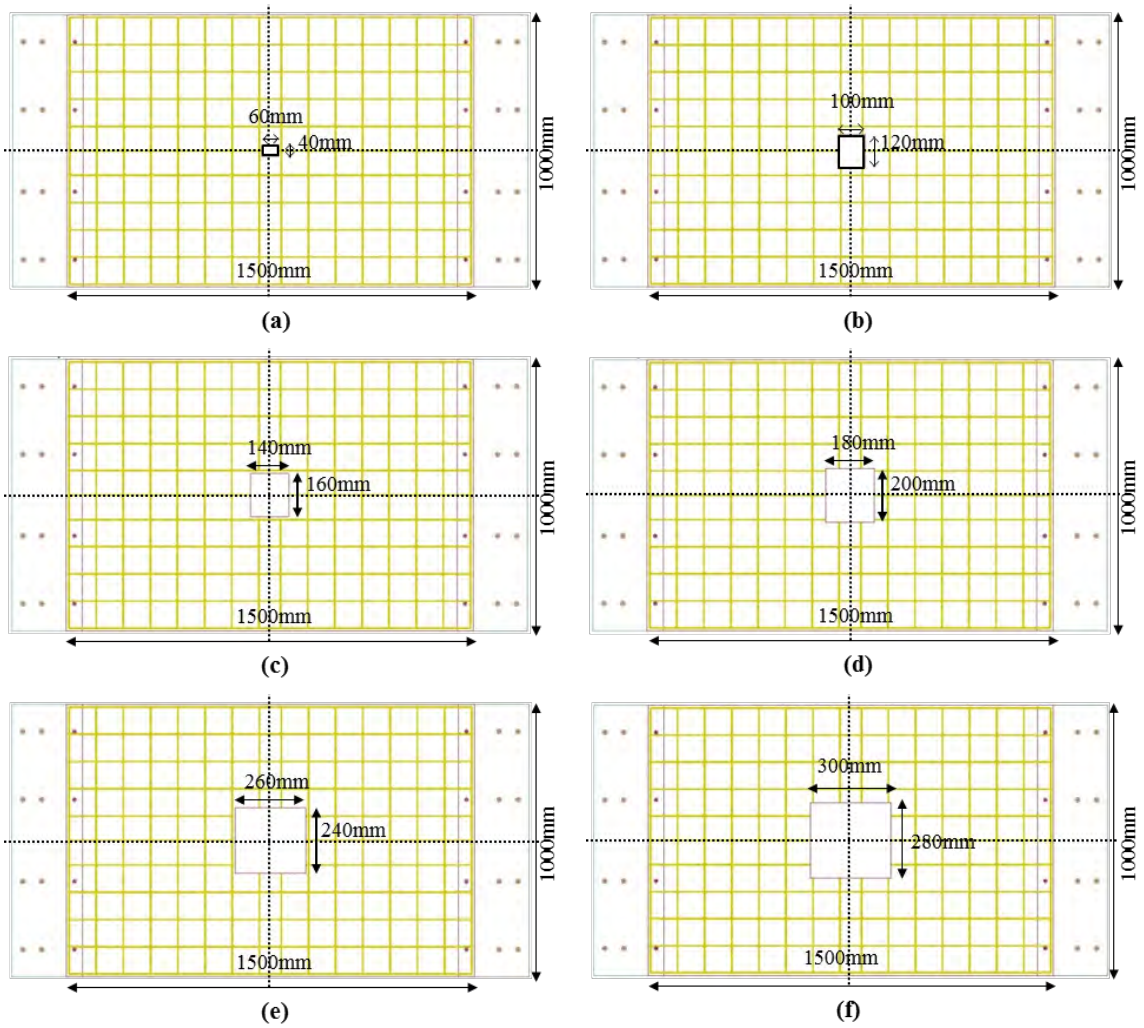

Figure 7.21: Details of opening sizes and reinforcement configuration-unstiffened openings (rotated front view)

Effect on maximum mid-panel deflection

Figure 7.22 illustrates the variation of maximum deflection with a change in unstiffened opening size. Both Type A and Type B panel exhibited a similar deflection response to the introduction of an opening. As in the experimental evaluation and numerical verification, Type A panels predict the deflection slightly higher than the Type B panels. Although a slight increase in maximum deflection was observed with opening size, variation as opening ratio increased was insignificant.

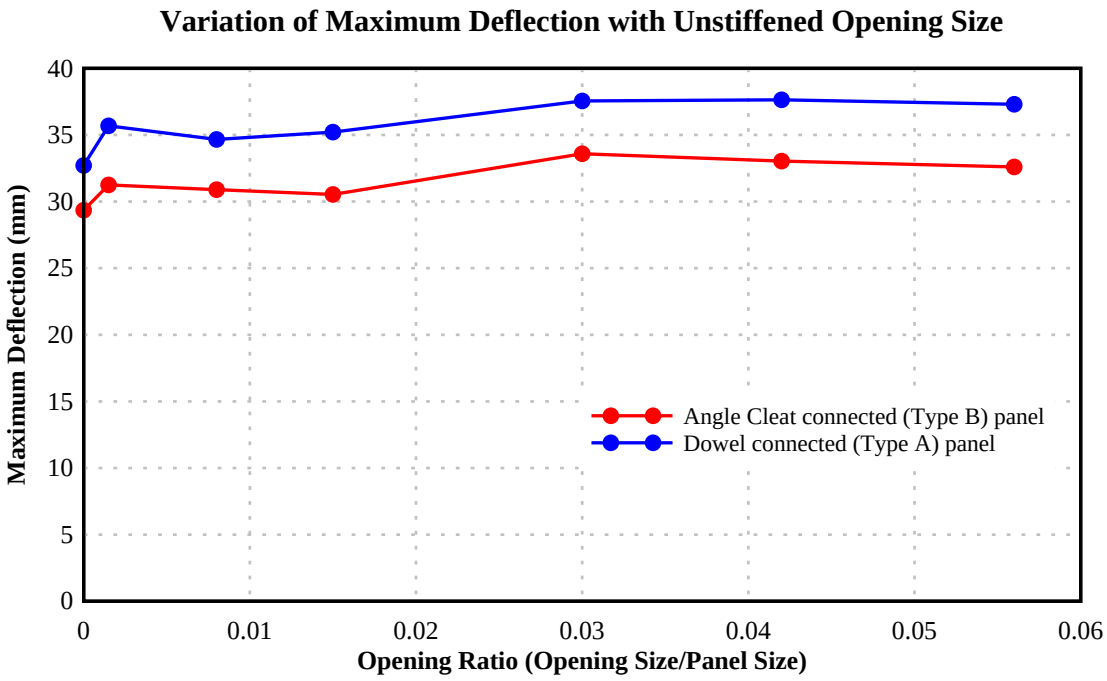

Figure 7.22: Variation of maximum deflection with unstiffened opening size

Effect on maximum compressive stress in concrete

The variation of maximum compressive stress in concrete for panels with unstiffened openings is shown in Figure 7.23. A noticeable rise in maximum compressive stress was observed with the increase in opening percentage for both Type A and Type B panels. Comparison between the two panel types, Type A panels exhibited larger stresses than Type B panels. Compressive stresses higher than the compressive strength of concrete (46 MPa) was observed for all opening sizes in Type A panels, including the solid panel. Most Type B panels, excluding solid panel and a panel with 40×60 mm opening, experience compressive stresses higher than the compressive strength of concrete. However, these maximum stresses were localised in the middle section of the panel.

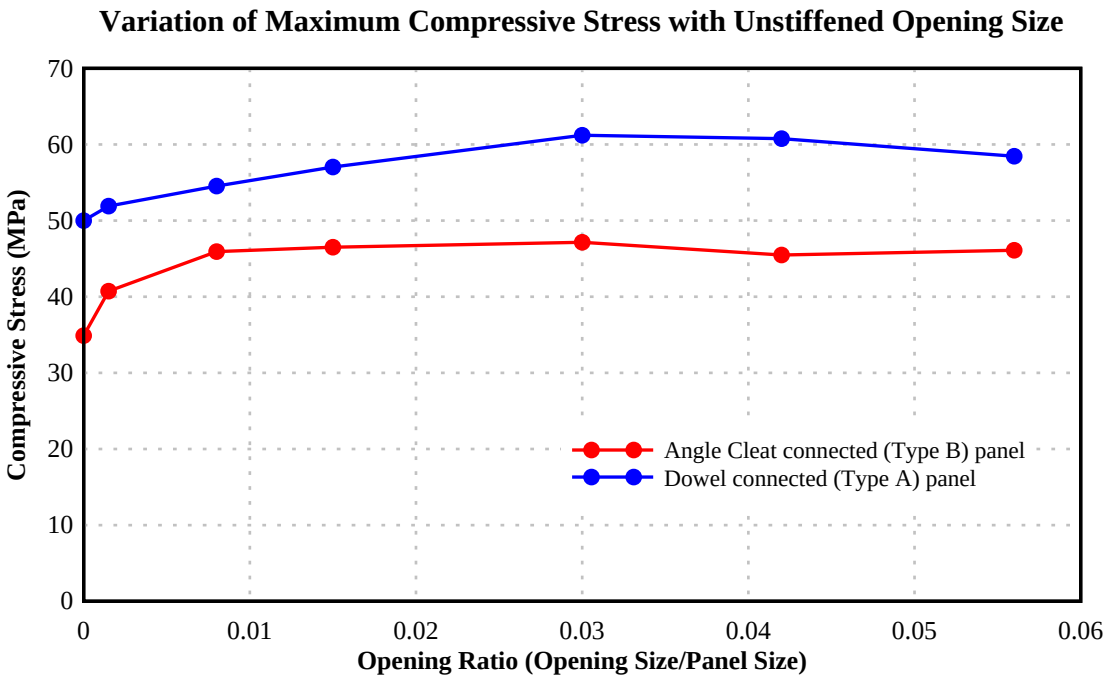

Figure 7.23: Variation of maximum compressive stress in concrete with unstiffened opening size

The largest value of maximum compressive stress was observed with 0.03 opening ratio, which corresponds to an opening of 220×200 mm. Both Type A and Type B panels experienced maximum compressive stresses with this opening. The opening size of 220×200 mm corresponds to the smallest opening size where three discontinued reinforcement bars exist in the main direction (in each layer) (Figure 7.19).

Although the introduction of unstiffened openings does not make a significant impact on the transverse deflection, compressive stresses in concrete have increased noticeably. All the stress concentrations were recorded close to the middle of the panel, where the opening was introduced. The introduction of unstiffened openings has resulted in a minor loss of resistance for both panel types considering the support rotation (θ) ($2\Delta_{max}/L$) and the maximum compressive stress within the concrete section.

7.3.2.2. Longitudinal location of the opening

The position of an unstiffened opening of 300×280 was varied from the centre of the panel and the support, for both Type A and Type B panels, as a parametric evaluation of opening location, as shown in Figure 7.24.

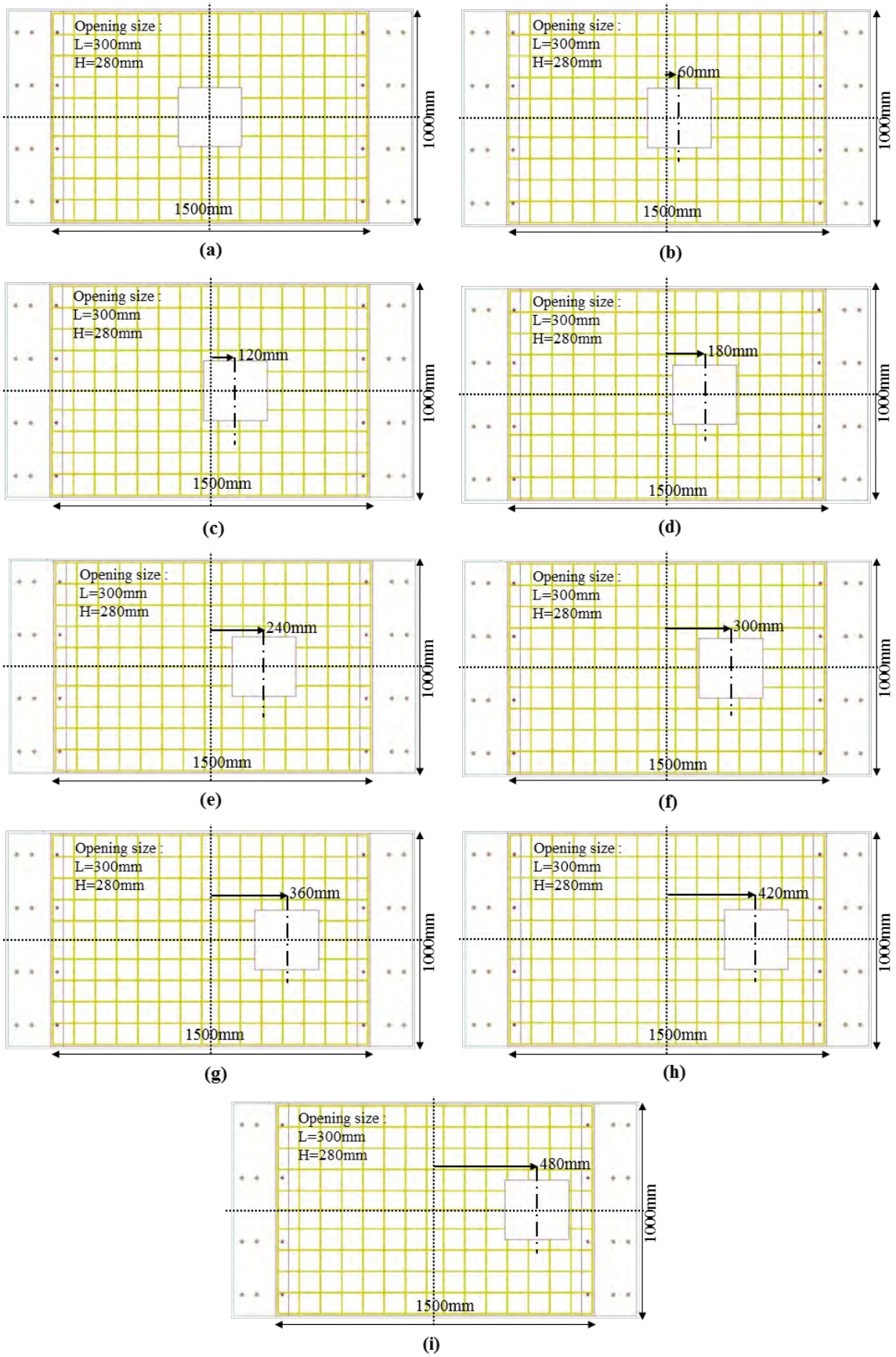

Figure 7.24: Details of unstiffened opening location-Longitudinal direction (rotated front view)

A minimum of three reinforcement bars in each layer in each direction was curtailed by the opening, occasionally curtailing four reinforcement bars in the transverse direction (Figure 7.24.(a)). Maximum deflection and maximum compressive stress recorded were plotted against the location (distance from the centre of the panel to the centre of the opening) normalised by the span length of the panel.

Effect on maximum mid-panel deflection

The variation of maximum mid-panel deflection against the normalised location of the unstiffened opening is presented in Figure 7.25. Both dowel connected (Type A) and angle cleat connected (Type B) panels were considered. An initial increase in maximum deflection was witnessed in both panel types until the centre of opening reached 1/6 of the span, away from the centre of the panel. This location records the maximum deflection for both Type A and Type B panels. The value of maximum deflection decreased from this location onwards, reaching the lowest at the normalised opening location of 1/3. The maximum deflection was recorded near the opening for all opening locations except the last two normalised opening locations in each curve. Maximum deflection was recorded in the centre of the panel in those two instances.

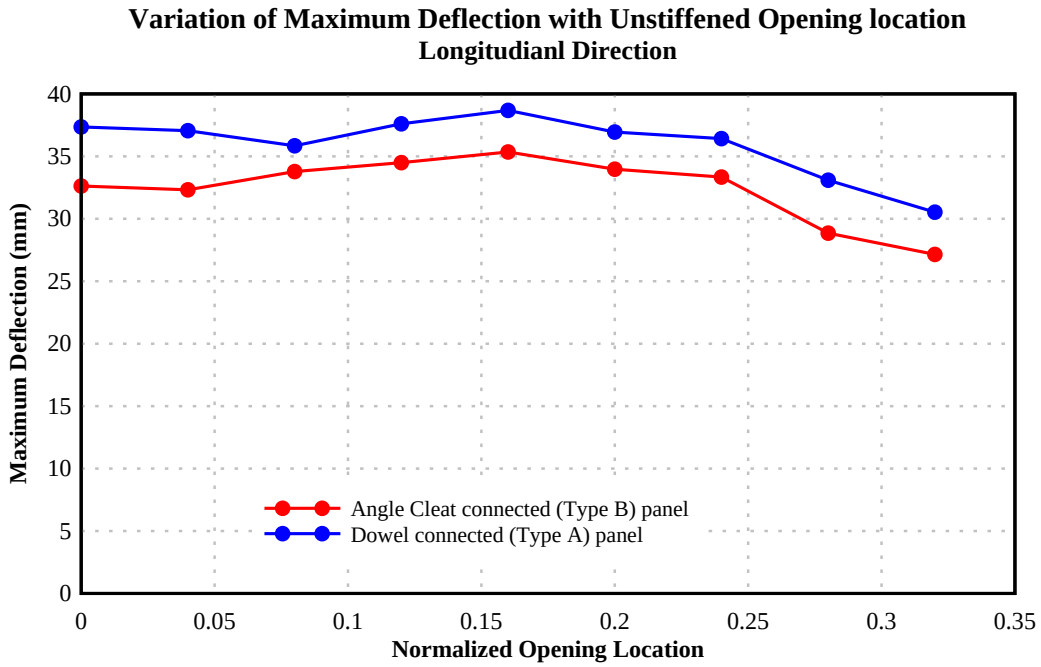

Figure 7.25: Variation of maximum deflection with normalised location of unstiffened opening-Longitudinal direction

Initially, charge centre, panel centre and the centre of the opening is placed in line with each other. Hence, much of the pressure and impulse generated from the loading are released through the opening, which explains the smaller (about 2 mm, compared to maximum) deflection at the beginning of the curves. However, moving the opening away from the panel centre will escalate the loading on the panel. This increase in loading will push the panel further increasing the transverse deflection, despite weakest cross-section being further away from the panel centre. The location of the maximum deflection coincides with the centreline of the opening suggesting the maximum deflection occurring in the weakest cross-section. For opening placed beyond the 1/6 of span from the panel centre, effects of loading increase are nullified as weaker cross-section move further away from the charge centre. Observing the maximum deflection near the middle of the panel instead of near the opening also suggests this phenomenon.

Effect on maximum compressive stress in concrete

Figure 7.26 depicts the variation of maximum compressive stress in concrete with unstiffened opening location, in the longitudinal direction. Maximum compressive stress follows a similar pattern to maximum deflection observed in Figure 7.25. The largest compressive stress was recorded when the opening (centre) was placed 1/8 of span length in Type B panels and 1/12 of span length in Type A panels. This variation of compressive stress can be explained by the same argument as in maximum transverse deflection in the previous section.

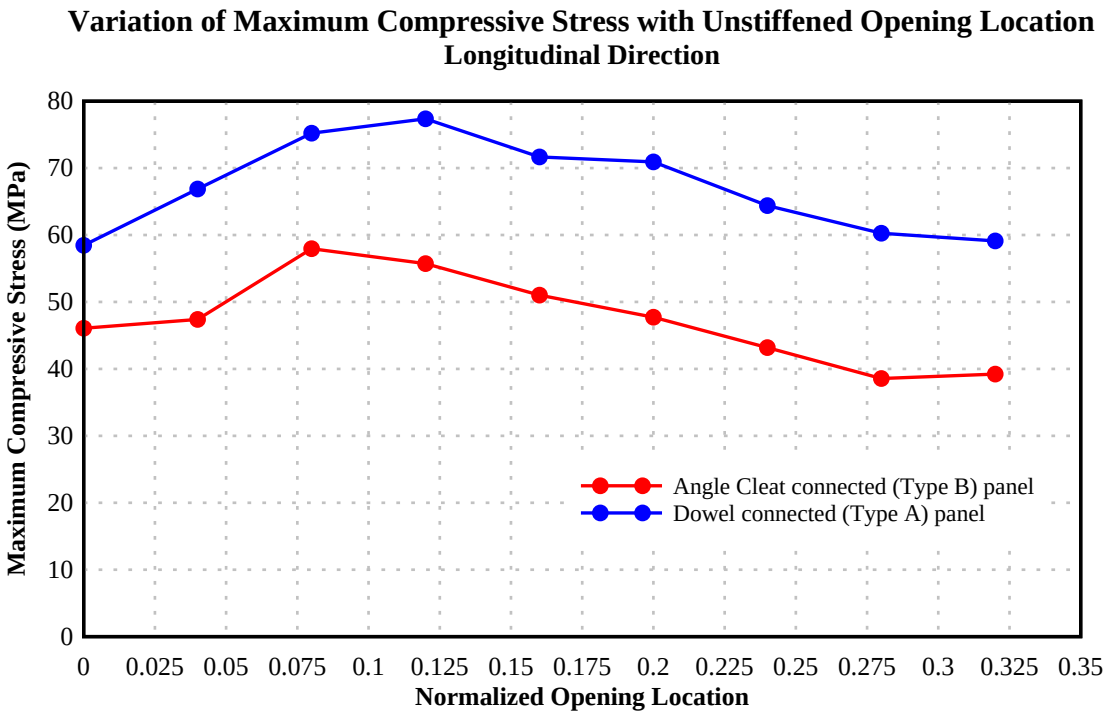

Figure 7.26: Variation of maximum compressive stress with normalised location of unstiffened opening - Longitudinal direction

Considering both maximum compressive stress and maximum transverse deflection, unstiffened openings are best to be placed closer to the fixing assemblies or centre of the panel for optimum performance.

7.3.2.3. Transverse location of the opening

An unstiffened opening of 300×280 mm was positioned between panel centre and the unsupported edge of the panel (transverse direction) as shown in Figure 7.27. The size of the opening was selected to replicate the maximum allowable unstiffened opening size. Three reinforcement bars in each layer for long span direction and four reinforcement bars in each layer for short span direction were discontinued due to the opening, except in one instance. The exception was when centre of the opening was located 240 mm away from centreline of the panel where only two reinforcement bars in longer span direction was curtailed. This curtailment of reinforcement was common for both panel types. Maximum mid-panel deflection and maximum compressive stress in concrete were plotted against the normalised opening location, similar to the previous section. However, normalisation was performed using the transverse span length in this instance, as the opening location was varied along the transverse direction.

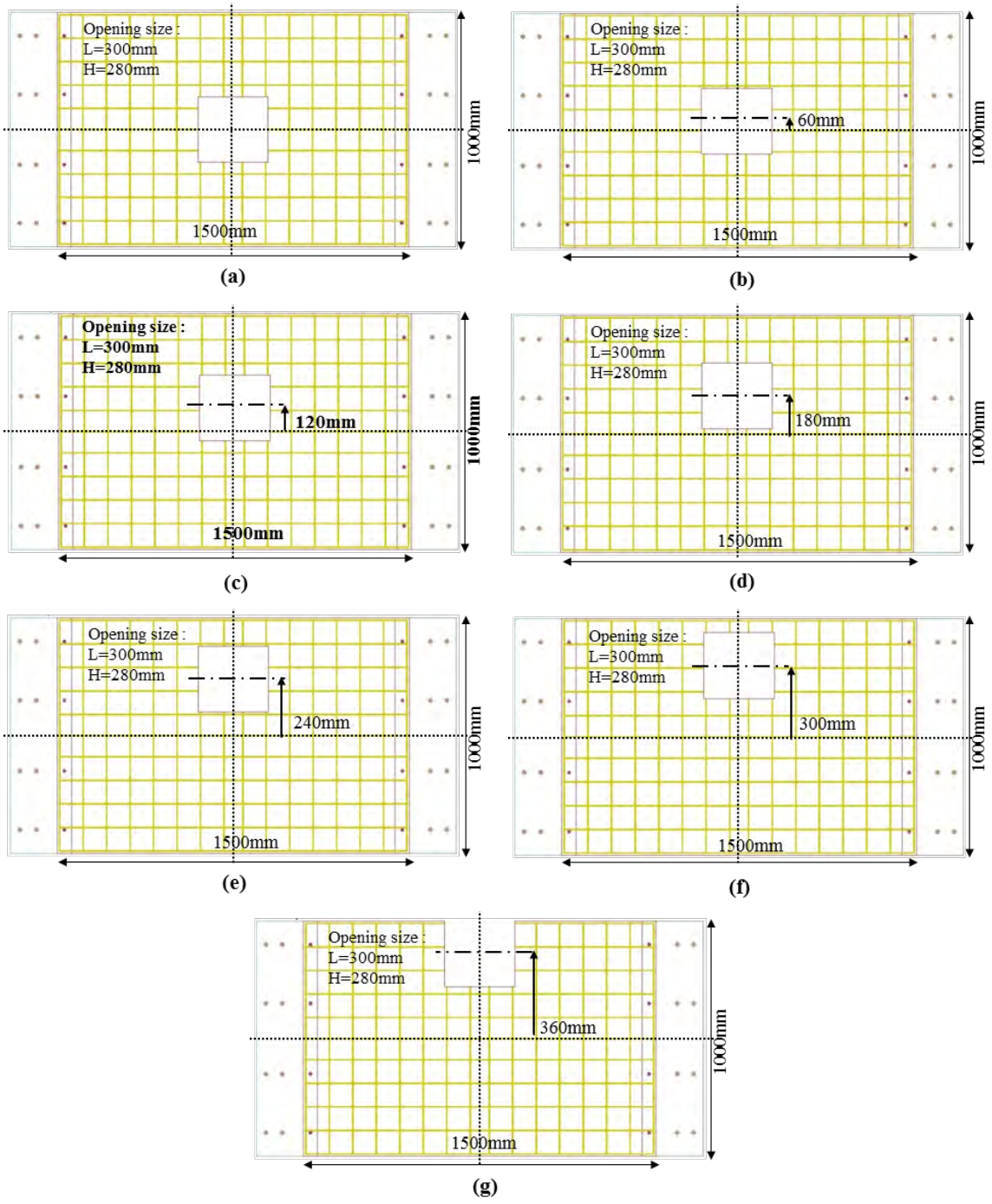

Figure 7.27: Details of unstiffened opening location-Transverse direction (rotated front view)

Effect on maximum mid-panel deflection

The variation of maximum mid-panel deflection against the normalised location of unstiffened opening for both Type A and Type B panels is presented in Figure 7.28. Neither panel type exhibited any significant variation in maximum deflection except at

the normalised opening ratio of 0.24. This positioning of opening affects the minimum number of reinforcements to be curtailed (3 bars compared to 4 in each layer), which is highlighted as a sudden drop in deflection in Figure 7.28. The final position of each curve represents the edge of opening coinciding with an edge of the panel, which results in an unconfined opening. However, no variation was observed.

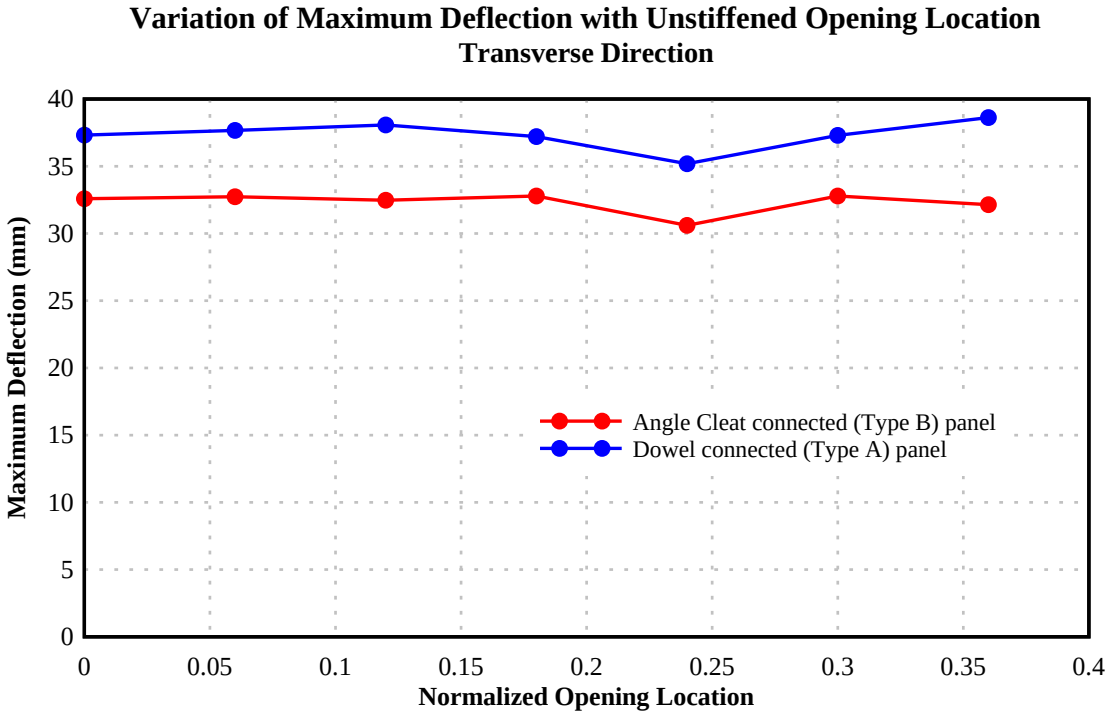

Figure 7.28: Variation of maximum deflection with normalised location of unstiffened opening-Transverse direction

Effect on maximum compressive stress in concrete

The variation of maximum compressive stress in concrete with the normalised location of unstiffened opening for both Type A and Type B panels is illustrated in Figure 7.29. After a small initial descent, the maximum compressive stress in concrete has increased gradually with the relocation of the opening towards the edge of the panel. This was common for both panel types. The number of curtailed reinforcement bars has not had any impact on maximum compressive stress as both curves exhibit gradual increases.

A gradual increase in maximum concrete stress was observed with the transverse location of the unstiffened opening. Although this was not visible in the maximum deflection, an increase in the maximum compressive stress is due to the increased loading received with the relocation of opening. Both Type A and Type B panels exhibit

similar variations. Even though compressive stresses beyond compressive strength (46 MPa) were witnessed with both panel types, these stress concentrations were limited to a small thickness of the panel, suggesting localised compression failures.

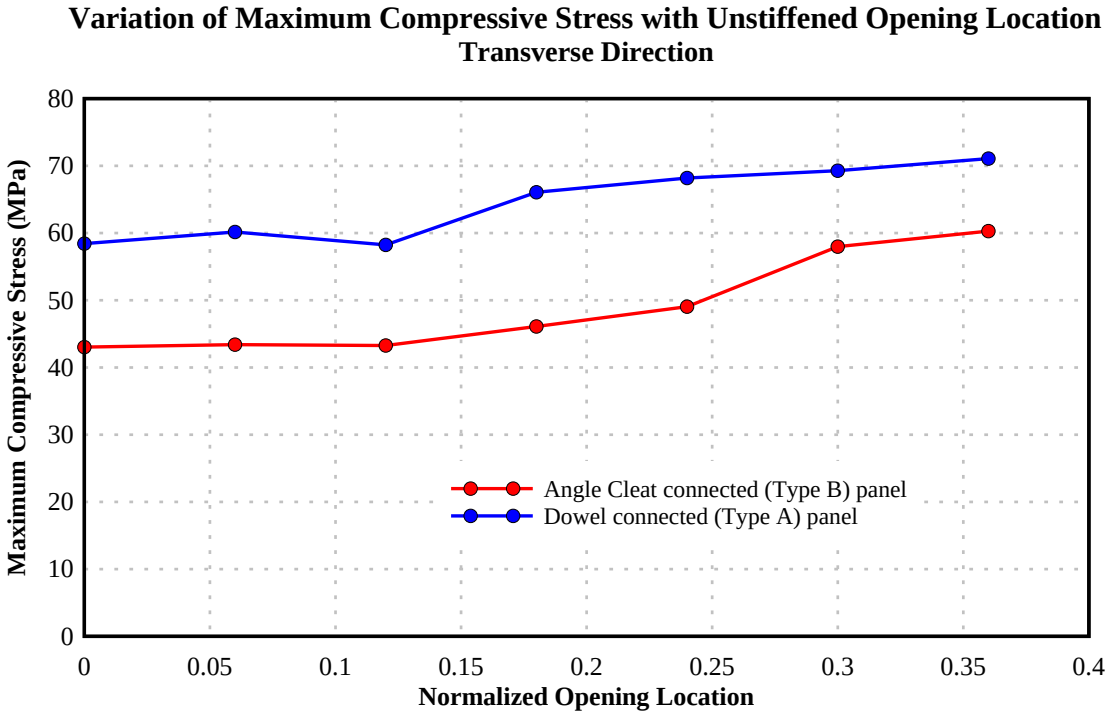

Figure 7.29: Variation of maximum compressive stress with normalised location of unstiffened opening-Transverse direction

7.3.3. Evaluation of explosive resistance of panels with stiffened openings

Stiffened openings of different sizes and locations were evaluated with similar loading conditions as discussed with unstiffened openings in Section 7.3.2. In addition to the results given in the following sections, time history plots for the maximum compressive strength and maximum mid-panel deflection are presented in Appendix D-II.

7.3.3.1. Opening size

Opening sizes varying from 300×280 mm to 580×600 mm placed in the centre of the panel for the evaluation of stiffened opening size against the applied explosive loading. Details of opening and reinforcement configuration are given in Figure 7.30.(a) to Figure 7.30.(g) The minimum opening size of 300×280 mm was selected as it was the maximum opening size which could be used without additional stiffening. On the other hand, the maximum opening size of 580×600 mm was selected to limit the

reinforcement congestion in panel edges. The variation of maximum deflection and maximum compressive stress was selected as evaluation parameters similar to panels with unstiffened openings discussed in the previous section.

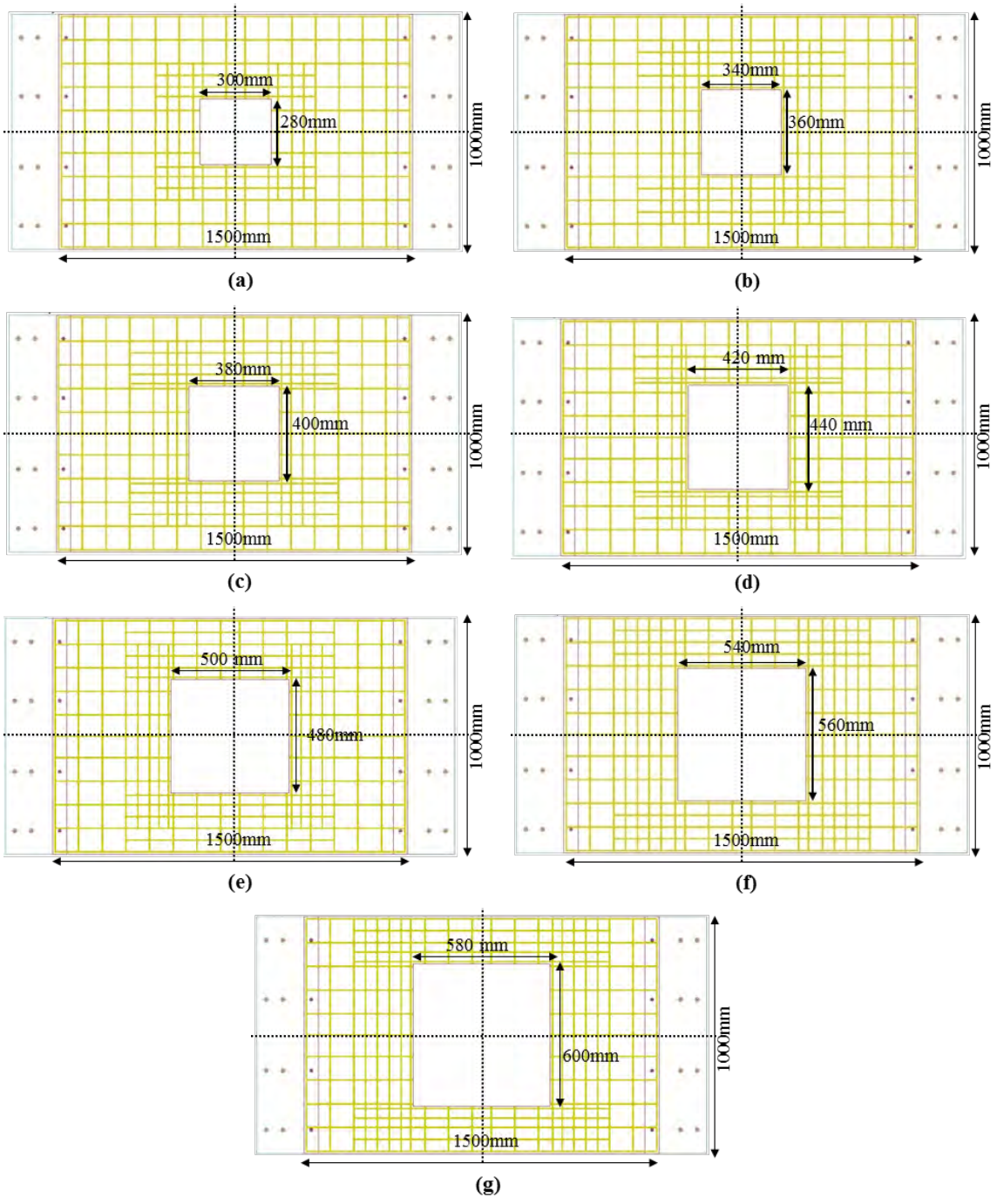

Figure 7.30: Details of opening sizes and reinforcement configuration-stiffened openings (rotated front view)

Effect on maximum deflection

Figure 7.31 depicts the variation of maximum deflection with stiffened opening size for both panel Type A and Type B panels. The opening area was normalised using the area of the panel as in the previous section. A gradual descent in deflection was observed with the increase in opening size for both panel types. This drop is primarily due to the loss of pressure and impulse through the increased opening.

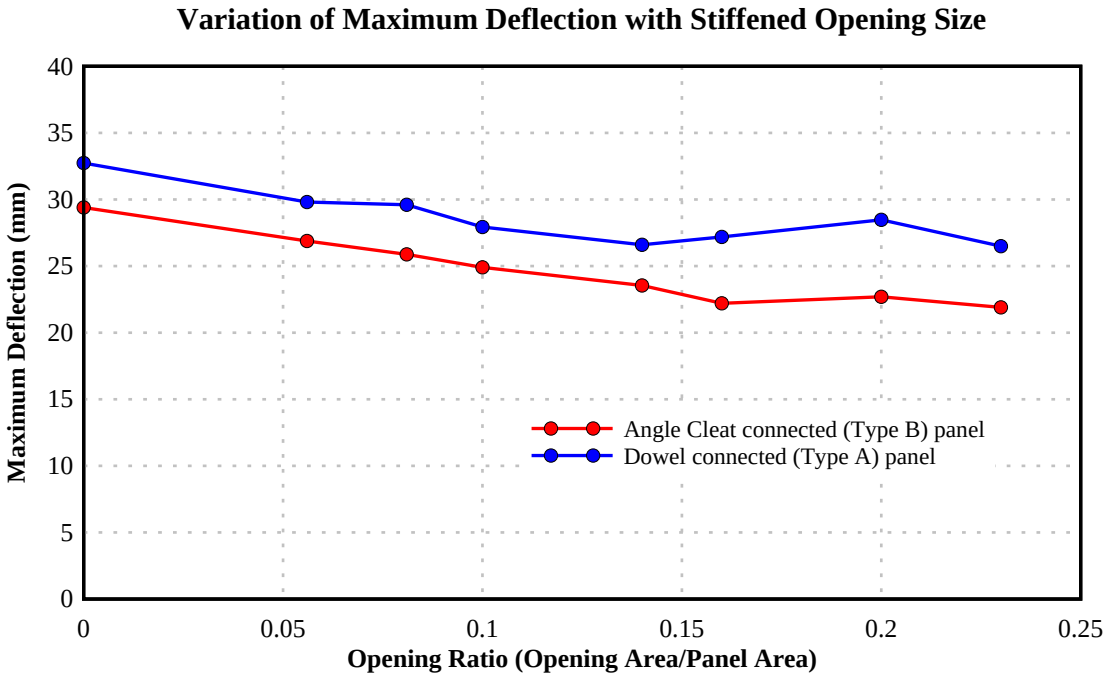

Figure 7.31: Variation of maximum deflection with stiffened opening size

Effect on maximum compressive stress

The variation of maximum compressive stress with the stiffened opening size is presented in Figure 7.32. A slight increase in maximum compressive stress was observed with the stiffened opening size, in contrast to the maximum mid-panel deflection. The variation is more significant in Type B panels compared to Type A panels. However, the maximum compressive stress in Type B panels did not reach the stress levels of Type A panels for the selected opening sizes.

In conclusion, the introduction of a stiffened opening has resulted in an increased state of compressive stress, although the maximum deflection has decreased. Reduced load due to the increased opening is responsible for reduced deflection. However, narrowing

of cross-section has escalated the maximum compressive stress, even though the loading on the panel has been reduced.

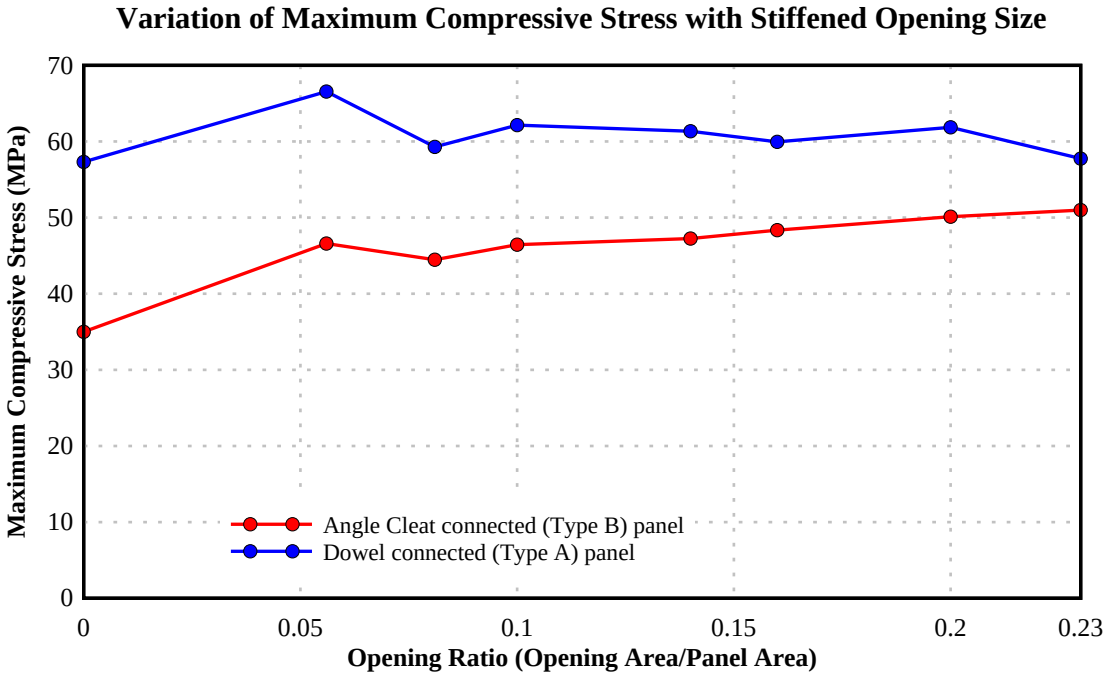

Figure 7.32: Variation of maximum compressive stress with stiffened opening size

7.3.3.2. Longitudinal location of the opening

The position of the stiffened opening of 300×280 mm was varied between panel centre and the support for Type A and Type B panels to evaluate the optimum opening location, as shown in Figure 7.33.(a) to Figure 7.33.(i). The smaller size opening was selected as this size resulted in the largest maximum deflection and smaller size allowed more flexibility in relocation. Furthermore, the smaller opening size resulted in less congested reinforcement layout and offers a comparison with the same size unstiffened opening discussed in previous sections. Stiffening around the opening was achieved by relocating the curtailed reinforcement with the addition of development lengths. Additional reinforcement bars were introduced to maintain the symmetry of reinforcement layout, when necessary.

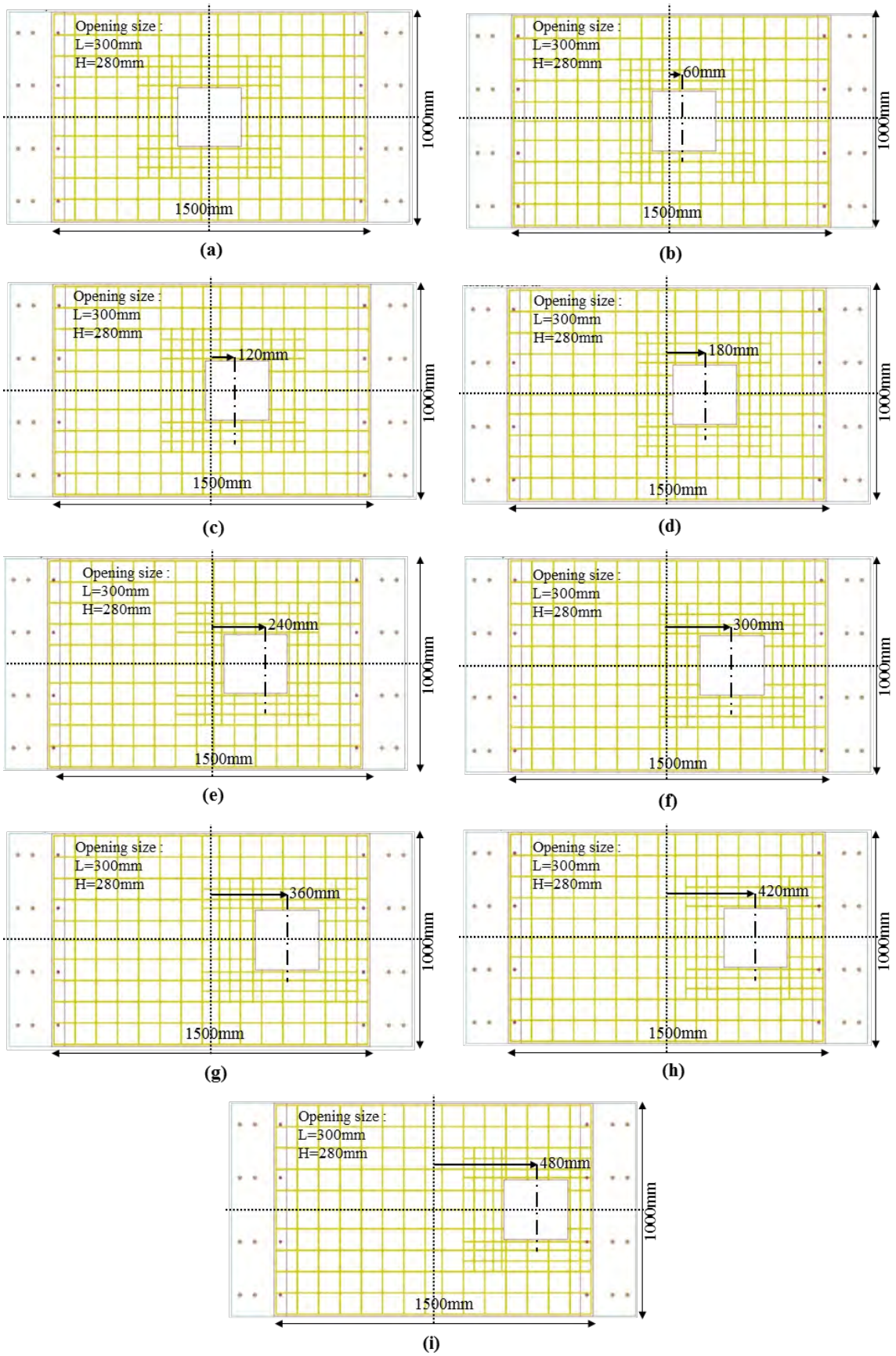

Figure 7.33: Details of stiffened opening location-Longitudinal direction (rotated front view)

Effect on maximum mid-panel deflection

The variation of maximum mid-panel deflection with the opening position is presented in Figure 7.34. The opening location was normalised by the span length of the panel, similar to the procedure used in unstiffened panels. Relocation of opening away from the centre resulted in a slight initial increase of maximum transverse deflection, in both panel types. This increase in deflection was visible until the centre of the opening is about 1/8 of the span length (180 mm offset), where the maximum was reached. Following the maximum, a slight reduction in deflection was observed. The maximum deflection fell below the value of panel with a central opening for Type A panels, whereas Type B panels never reached the same with skewed openings.

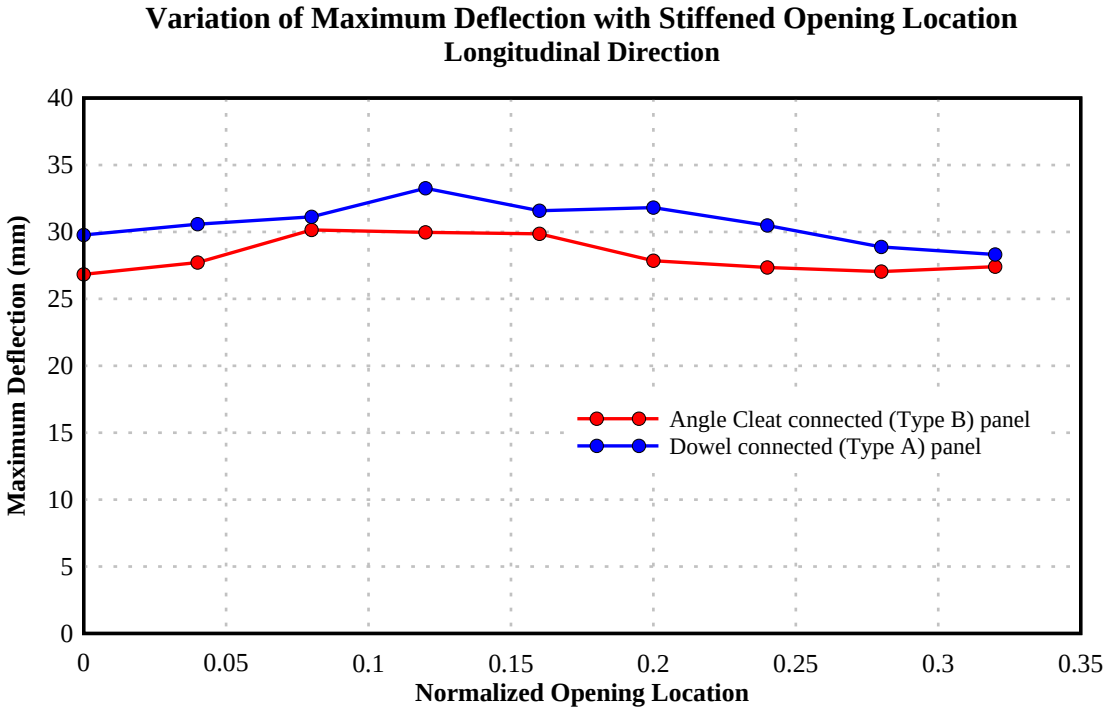

Figure 7.34: Variation of maximum deflection with normalised location of stiffened opening-Longitudinal direction

Effect on maximum compressive stress

Similarly, maximum compressive stress in concrete was recorded for skewed opening locations as shown in Figure 7.35. Unlike in the maximum deflection, a slightly different response was observed with Type A and Type B panels. A gradual ascend in maximum compressive stress followed by a gradual descent was witnessed with the repositioning of the opening in Type B panels. In contrast, a gradual descent was

observed in Type A panels. Maximum compressive stresses smaller than the value observed with central opening were witnessed when openings repositioned closer to the supports.

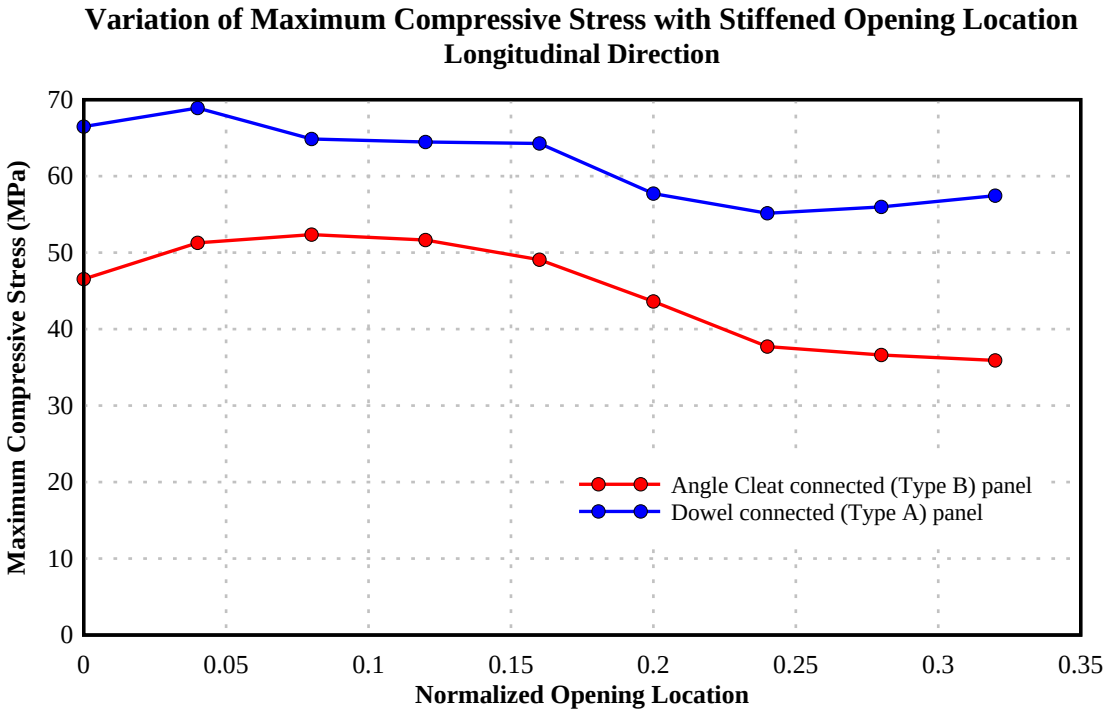

Figure 7.35: Variation of maximum compressive stress with normalised location of stiffened opening-Longitudinal direction

Overall, openings placed in the middle 1/3 of the distance between panel centre and the support have resulted in increased maximum deflection and maximum compressive stresses. The percentage of loading passed through the opening is reduced when the opening is moved away from the centre of the panel as charge centre in coinciding with the panel centre. In the meantime, if the weakest cross section is close to maximum loading, an increase in maximum deflection and maximum stresses can be expected, as noted in this instance. However, when the opening is moved further away from the panel centre, deflection and stresses will be reduced as the weakest cross section is away from the highest loading location. It should be noted that this phenomenon is valid only for charge weights aligned with the centre of the panel.

7.3.3.3. Transverse location of the opening

The position of a 300×280 mm opening was varied between the panel centre and unsupported edge to observe the response of stiffened panel location when subjected to explosive loading, as shown in Figure 7.36.(a) to Figure 7.36.(g).

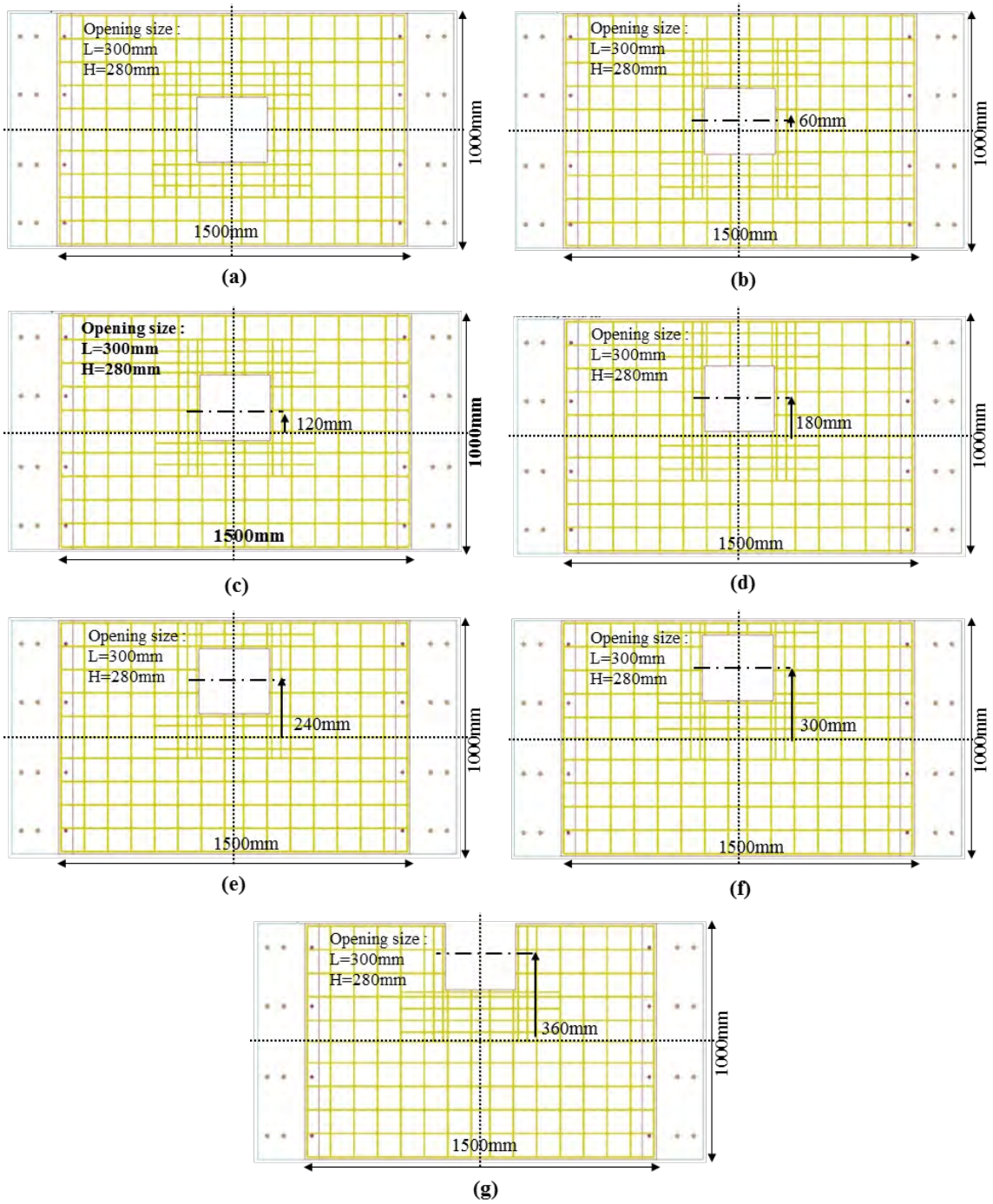

Figure 7.36: Details of stiffened opening location-Transverse direction (rotated front view)

Stiffening of openings was achieved as described in the previous section through repositioning the curtailed reinforcement with additional lengths for stress development. A symmetrical reinforcing arrangement was utilised for stiffening unless not enough space was available to provide the required number of reinforcement bars. Particularly in the case of unconfined opening where the wall of the opening coincides with the edge of the panel, all reinforcement bars were relocated to a single side. Both Type A and Type B panels were considered measuring maximum transverse deflection and maximum compressive stress of concrete as the resistance parameters.

Effect on maximum mid-panel deflection

As shown in Figure 7.37, a very slight increase in maximum deflection was witnessed with both panel types when the stiffened opening was repositioned in shorter span direction. The deflection was lowest when the opening centre coincided with the panel centre. When the opening is relocated along the centreline of the panel towards the unsupported edge, loading is amplified resulting in increased deflection. Weakening of cross-section is limited in stiffened openings as the opening was small compared to the panel size and all curtailed reinforcement was relocated within the cross-section. Therefore, no abrupt variations in maximum deflection were observed for change in the opening location in the transverse direction.

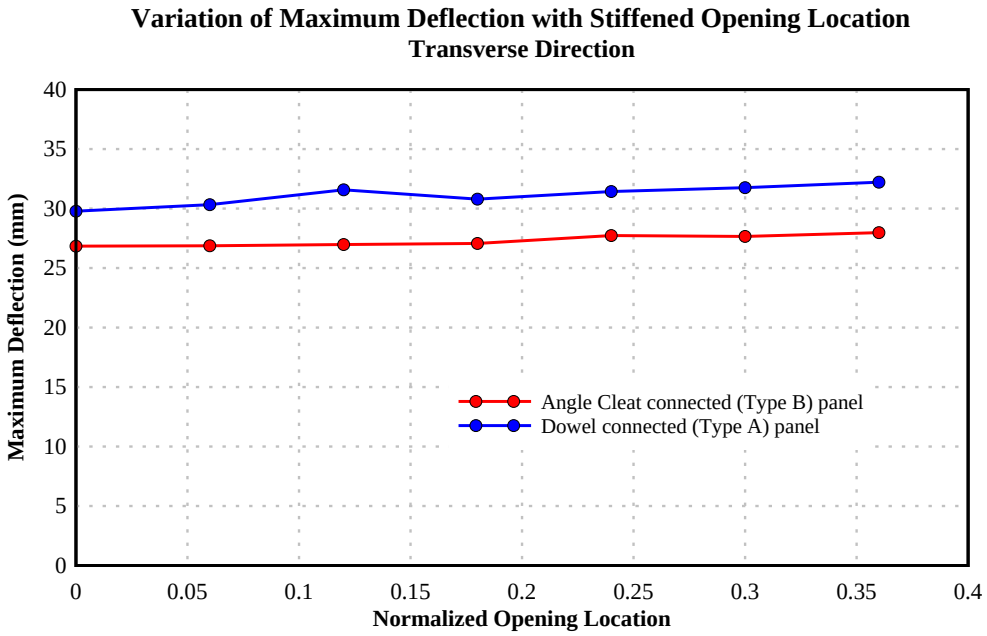

Figure 7.37: Variation of maximum deflection with normalised location of stiffened opening-Transverse direction

Effect on maximum compressive stress

As illustrated in Figure 7.38, a gradual increase in maximum compressive stress was observed with the relocation of the opening in the transverse direction. The variation is similar to the maximum mid-panel deflection but, more significant. Comparing two panel types, the variation in the Type B panel was more prominent when the opening was closer to the edge of the panel. The maximum compressive stress has exceeded the compressive strength of the material in all opening locations in both panel types. Overall, the increase in loading due to the relocation of the opening is responsible for this behaviour.

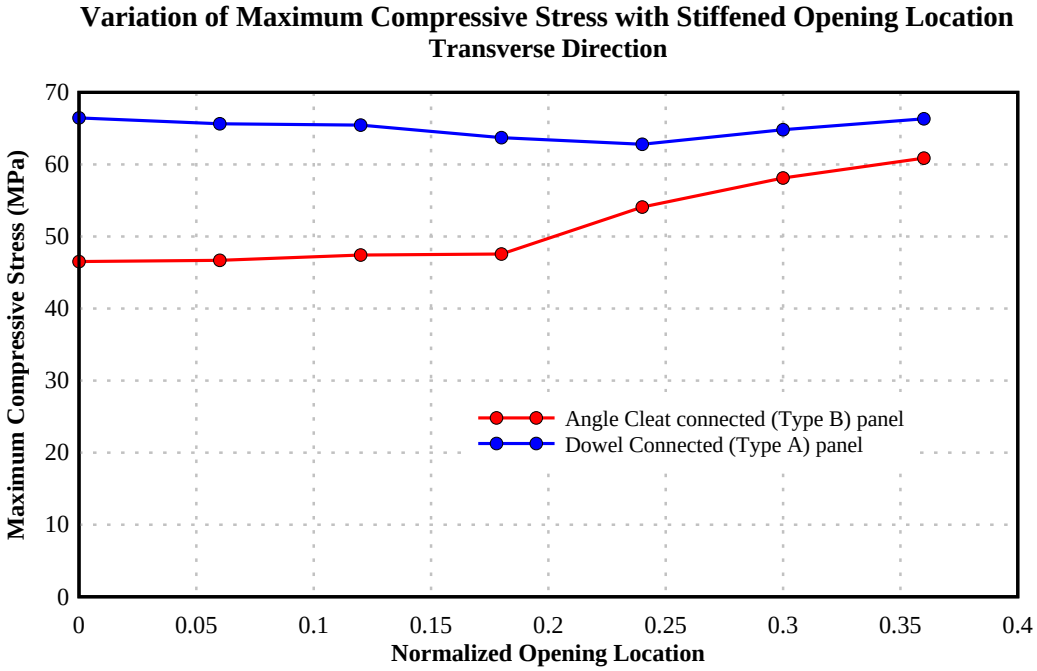

Figure 7.38: Variation of maximum compressive stress with normalised location of stiffened opening-Transverse direction

7.3.4. Summary: Openings in facade panels

The performance of reinforced concrete facade panels with openings subjected to explosive loading was evaluated. Different stiffened and unstiffened opening sizes were considered in the evaluation. Both Type A and Type B panels were considered as well. The performance of the panels was evaluated based on the maximum mid-panel deflection and maximum compressive stress. The following conclusions were made based on the observations of parametric study results.

Unstiffened openings

- Larger unstiffened openings result in an increase in maximum deflection and maximum compressive stress in both Type A and Type B panels. This increase is observed even with reduced explosive impact due to the large opening.
- Unstiffened openings placed in the middle 1/3 of the distance between panel centre and support exhibit larger compressive stresses and slightly larger deflections. This is due to the combination of increased loading and having weakest cross section close to the position of largest loading.
- The position of the opening in transverse direction does not affect the panel performance as in longitudinal direction, although a slight increase in compressive stress was observed.
- The existence of unstiffened openings increased the possibility of flexural failures. Increase in maximum mid-panel deflection and maximum compressive stress confirm the possible flexural failures.

Stiffened openings

- Larger stiffened openings in facade panels had improved the panel performance, resulting in reduced maximum deflection and the maximum compressive stress, as a result of reduced loading.
- Stiffened openings placed in the middle 1/3 of the distance between panel centre and support increased the maximum deflections and the maximum compressive stress, similar to unstiffened openings. However, the effects are less significant with stiffened openings, compared to unstiffened openings.
- Relocation of stiffened openings in transverse direction increases the maximum compressive stress and the maximum deflection slightly. This is due to the increased loading due to the relocation of the opening.

Comparatively, the introduction of stiffened openings improves the panel performance, whereas unstiffened openings reduce the panel resistance. However, when the same size, stiffened and unstiffened openings are relocated in longitudinal and transverse directions, effects are more significant in stiffened panels, with respect to the maximum deflection and the maximum compressive stress. Variations are similar in both panel types, although Type A panels exhibit slightly higher deflection and compressive stress.

7.4. Performance of reinforced concrete facade panels with initial curvatures

Concrete was largely considered as a heavy, cold and grey material with no architectural features except for the fixed image of rapid urbanisation in the 1960s (Huyge and Schoofs, 2009). Since then, concrete has made significant progress in both technical and architectural aspects, becoming more beautiful and lively while getting stronger and lighter. As for the call for more free-form features in structures, single and double curvature panels were introduced, which were mainly used as non-load-bearing facade systems in buildings (Huyge and Schoofs, 2009).

Steel, aluminum, glass and composites were preferred for these architectural features over reinforced concrete, mostly due to constructability issues. Even with the constructability issues, prefabricated concrete panels with curvatures have been used in facade systems in building, especially with single curvatures. These panels were either cast as full-size panels or assembled with smaller sections, which can represent the curvatures in facade systems.

Evaluation of blast loading performance of reinforced concrete facade panels is limited to plain flat panels. Only a handful of studies were available in literature even for conventional reinforced concrete facade panels (Pan and Watson, 1996, Pan and Watson, 1998, Mays et al., 1999, Pan et al., 2001, Starr and Krauthammer, 2005, Pham et al., 2008, Pham, 2010). Turkmen (2002) and Shen et. al (2010) observed the blast loading response of laminated composite shells with initial curvatures and curved aluminum foam panels, respectively. However, no studies were conducted to evaluate the performance of reinforced concrete cladding panels with initial curvatures subjected to explosive loading.

A parametric study was carried out with the developed LS-DYNA, 3-D numerical model, discussed in Chapter 5. Panel dimensions and material properties were kept identical to the experimental tests (Pham, 2010) including the loading of 5.5 kg of equivalent TNT at 2 m clear standoff distance. Single curvature panels with span length (L) to the radius of curvature (R) ratios ranging from 0.033 to 0.5 were selected. Curvatures in both shorter and longer span directions were modelled separately with both types of supports discussed in Section 5.2, with minor modifications to match the

curvatures. Both convex (outward curvature) and concave (inward curvature) panels were used for the evaluation. Although the concave panels are not used in abundance, were used in this instance for the purpose of evaluating the possibility of internal explosions. In addition to the details presented in this section, time history plots for the maximum mid-panel deflection and maximum compressive stress are presented in Appendix D-III.

7.4.1. Panels with curvatures in longer span direction

Ten panels, each having different curvatures, were modelled for each type of connection (dowel and angle cleat types) discussed in Chapter 5. For every convex panel, an identical concave panel was also modelled, totalling twenty panels for each type of connection. An analogy of convex and concave curvatures in longer span direction is presented in Figure 7.39.(a) and Figure 7.39.(b) respectively. Figure 7.40.(a) to Figure 7.40.(k) shows the schematic diagrams for all positive (convex) curvatures (for Type A panels) including the reinforcement. An identical set of panels was modelled for negative curvatures (concave). This procedure was repeated for both Type A and Type B panels. Maximum deflection and maximum compressive stress were evaluated as performance parameters, similar to the previous sections.

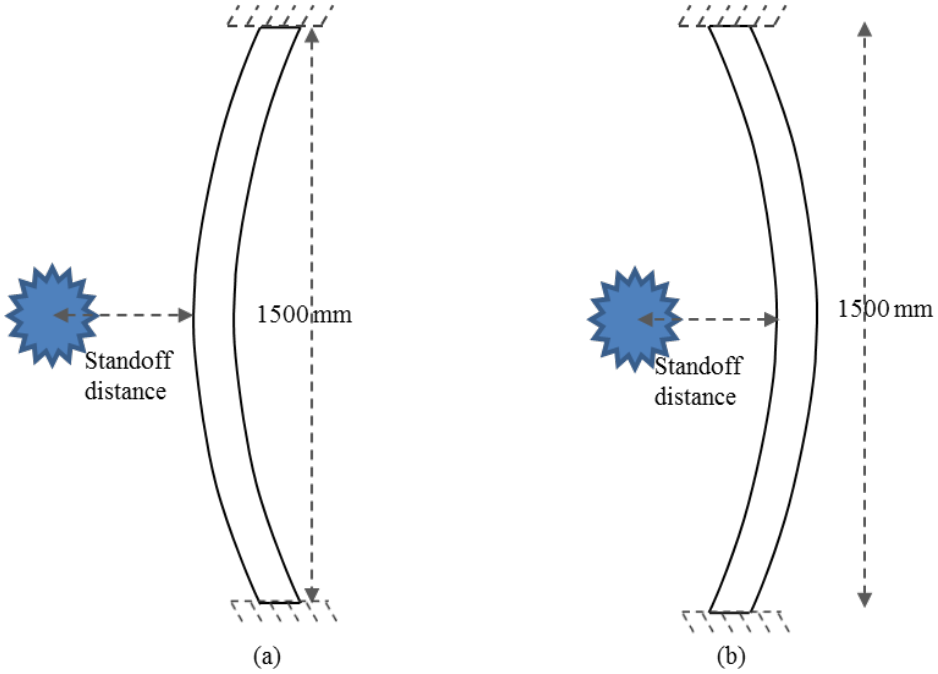

Figure 7.39: Analogy of (a). convex and (b). concave panels in longer span (longitudinal) direction (side on view)

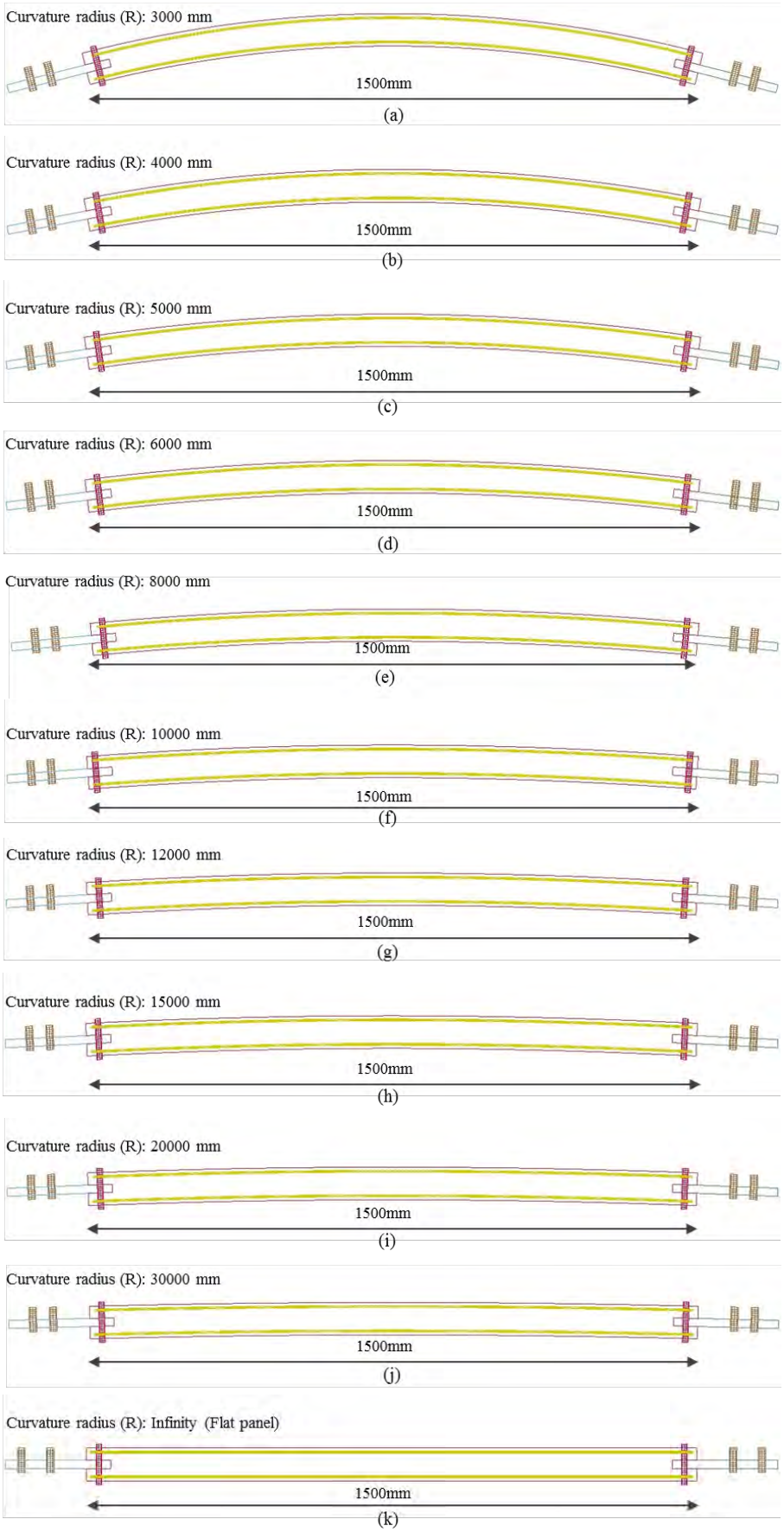

Figure 7.40: Details of curved panels-Longitudinal direction (rotated side on view)

Effect on maximum deflection

The variation of maximum deflection with span (L) to the radius of curvature (R) ratio for both Type A and Type B panels is shown in Figure 7.41. Concave panels are considered to have a negative curvature for the comparison. Span (L) to the radius of curvature (R) ratios between -0.5 and 0.5 are considered which corresponds to a curvature radius of 3 m in negative and positive directions. LS-DYNA, 3-D numerical models developed for flat panels in Chapter 5 were also considered as having a span to the radius of a curvature ratio of 0 (infinite radius).

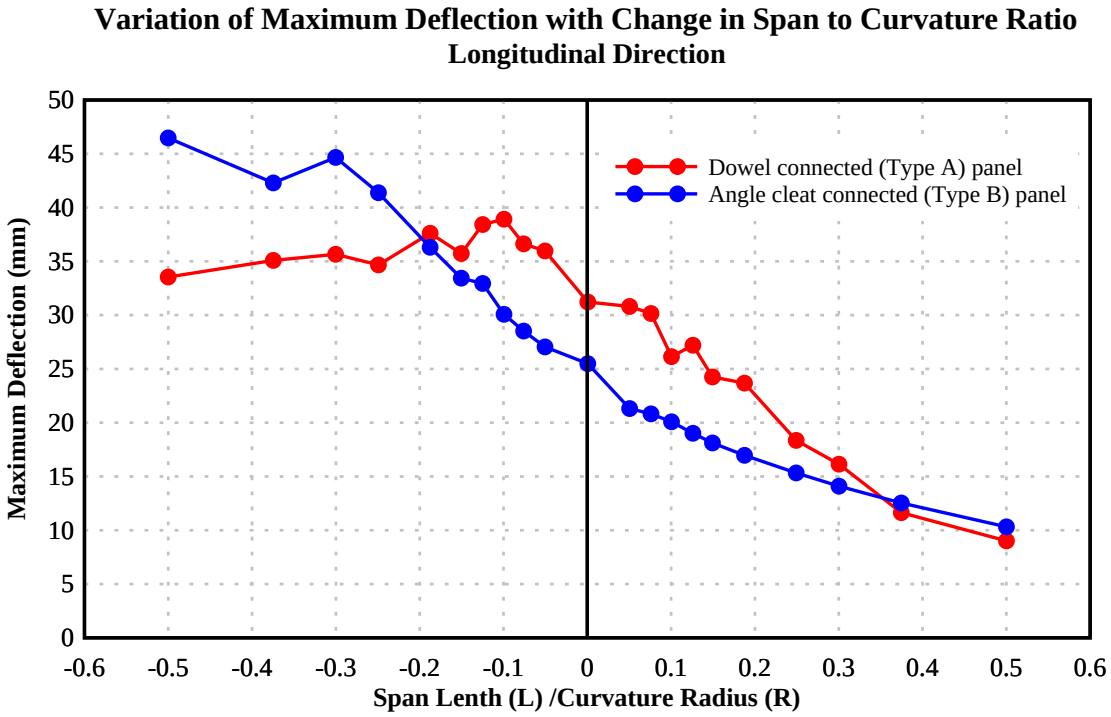

Figure 7.41: Variation of mid-panel deflection with span to curvature radius ratio- Longitudinal curvature

The introduction of a curvature in the longitudinal direction has changed the panel response significantly. The maximum mid panel deflection increased monolithically when the curvature is reduced in Type B panels, where the smallest mid-panel deflection was observed with an L/R ratio of 0.5. The increase was observed even with the negative curvatures, where the largest mid-panel deflection of 46.47 mm was witnessed with the L/R ratio of -0.5. Type A panels exhibit the same monolithic increase in deflection until an L/R ratio of -0.1 (15 m radius concave panel), where the

maximum deflection of 38.93 mm was recorded. Beyond this L/R ratio, deflection reduced gradually up to 33.54 mm.

In general, positive curvatures (convex) have shown a positive response for both Type A and Type B panels while the negative response is witnessed with Type B concave panels. Type A panels reveal a more stable response for negative curvatures as well with only a smaller variation in deflection with curvature changes.

Effect on maximum compressive stress

Figure 7.42 shows the variation of compressive stress in concrete with the change in span length (L) to curvature radius (R) ratio.

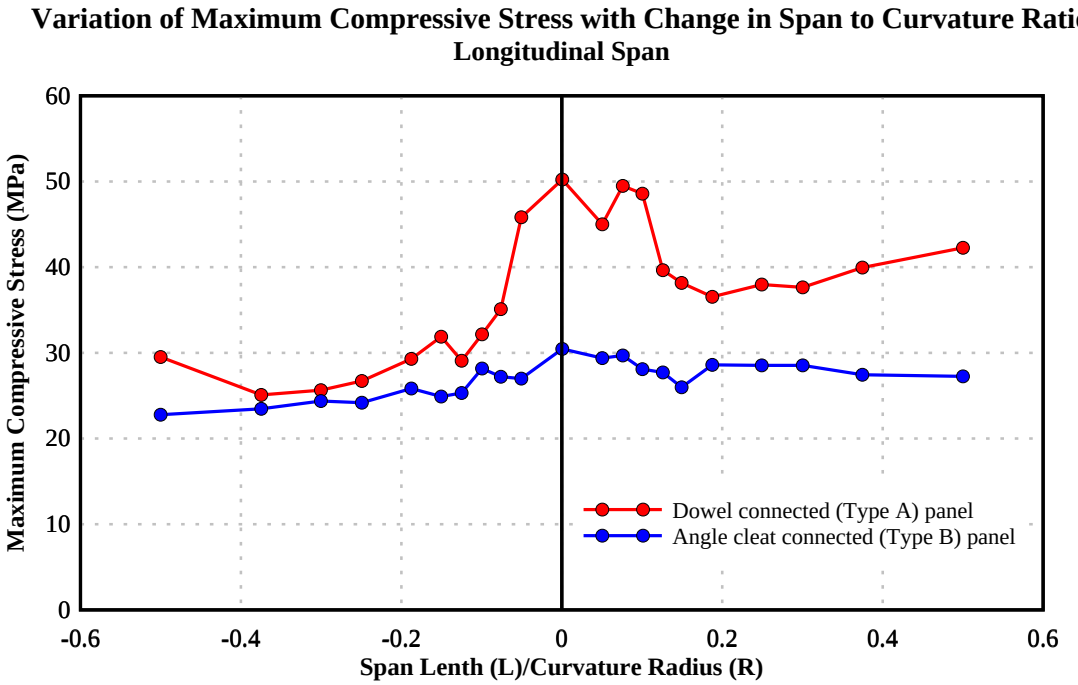

Figure 7.42: Variation of compressive stress in concrete with change in span to radius of curvature ratio

A considerably different stress response was observed between Type A and Type B panels. The introduction of curvature has reduced the maximum compressive stress in both panel types irrespective of the curvature. However, the effects are more significant in Type A panels. The largest compressive stress was observed in flat panels (L/R=0) for both panel types. The maximum compressive stress in Type A panels remained above the values in Type B panels for all L/R ratios. Maximum compressive stresses were observed close to the unsupported edge of the panel for all curvatures.

Overall, the introduction of a convex shaped curvature in facade panels has reduced the deflection and compressive stress considerably. Observations were identical in both Type A and Type B panels. However, negative curvatures worked differently, allowing the panel to deflect more than the flat panel. However, the stress response was beneficial as in convex panels. The arching action is a possible explanation for this behaviour (convex panels) in Type B panels as angle cleat connections were able to resist the horizontal deflection. However, dowel connected panels do not have the privilege of rigid horizontal supports as these connections allow horizontal deformation. However, the shape of the panel allows for redistribution of blast pressure, which can alter the response.

7.4.2. Panels with curvatures in shorter span direction

Eight panels, each having different curvatures in short span direction, were modelled based on the numerical model developed and validated in Chapter 5. An identical concave panel was also modelled for each convex panel, modelling 16 independent panels with span to curvature radius ratios ranging from -0.5 to 0.5. Concave panels were considered to have a negative curvature as in the previous section. Considering dowel and angle cleat connected panels, 32 independent panels were considered for the study. Figure 7.43.(a) and Figure 7.43.(b) represent the analogy of shorter span (transverse) curvature panel testing for convex and concave panels respectively. Figure 7.44.(a) to Figure 7.44.(i) illustrate the panels with convex (positive) curvatures for Type A panels. The maximum mid-panel deflection and the maximum compressive stress were evaluated as performance parameters.

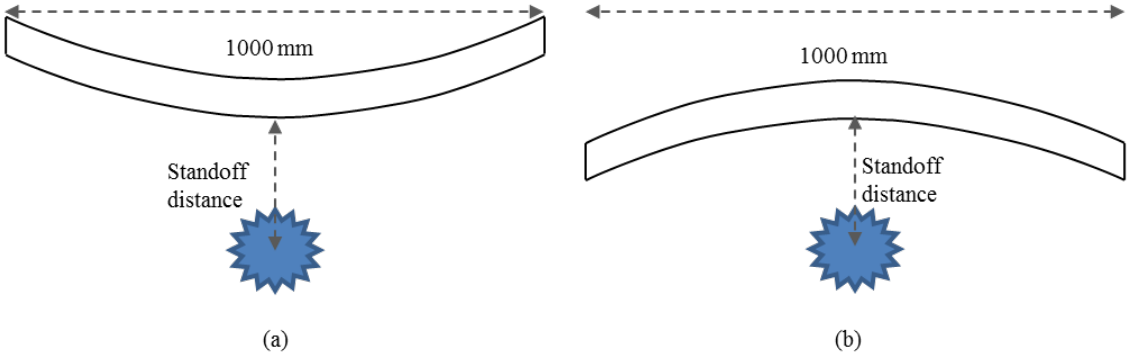

Figure 7.43: Analogy of (a). convex and (b). concave panels in the shorter span (transverse) direction (plan view)

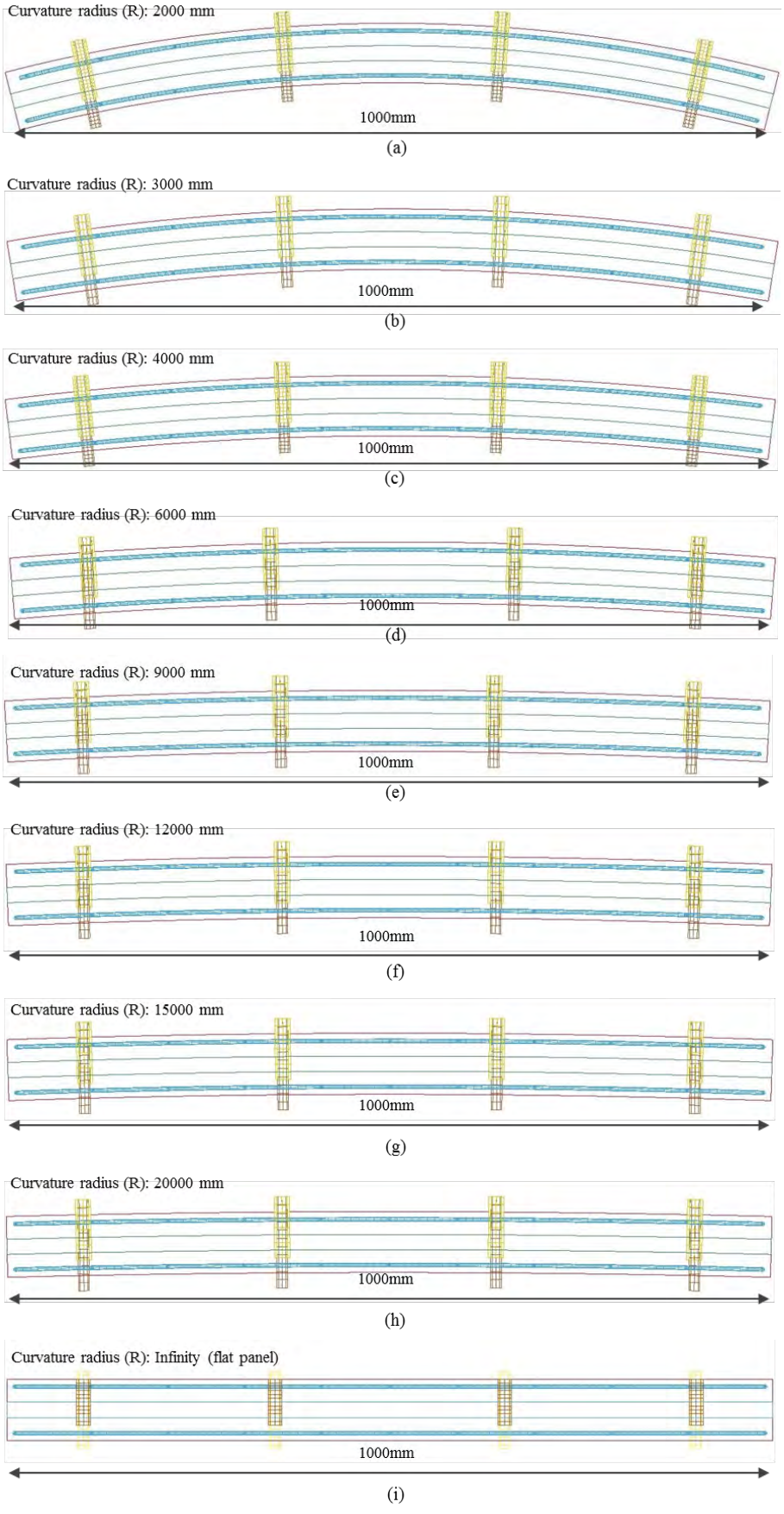

Figure 7.44: Details of curved panels-Transverse direction (plan view)

Effect on maximum deflection

The variation of maximum mid-panel deflection with the span to curvature radius (L/R) ratio is shown in Figure 7.45. The introduction of a curvature in the transverse direction has improved the resistance against the transverse deflection of the panel, irrespective of the curvature direction. Maximum deflections were associated with the flat panel (in Type A) or panels with least curvatures (In Type B). Both panel types exhibited a similar response when exposed to the explosive loading generated from 5.5 kg of TNT at 2 m clear distance.

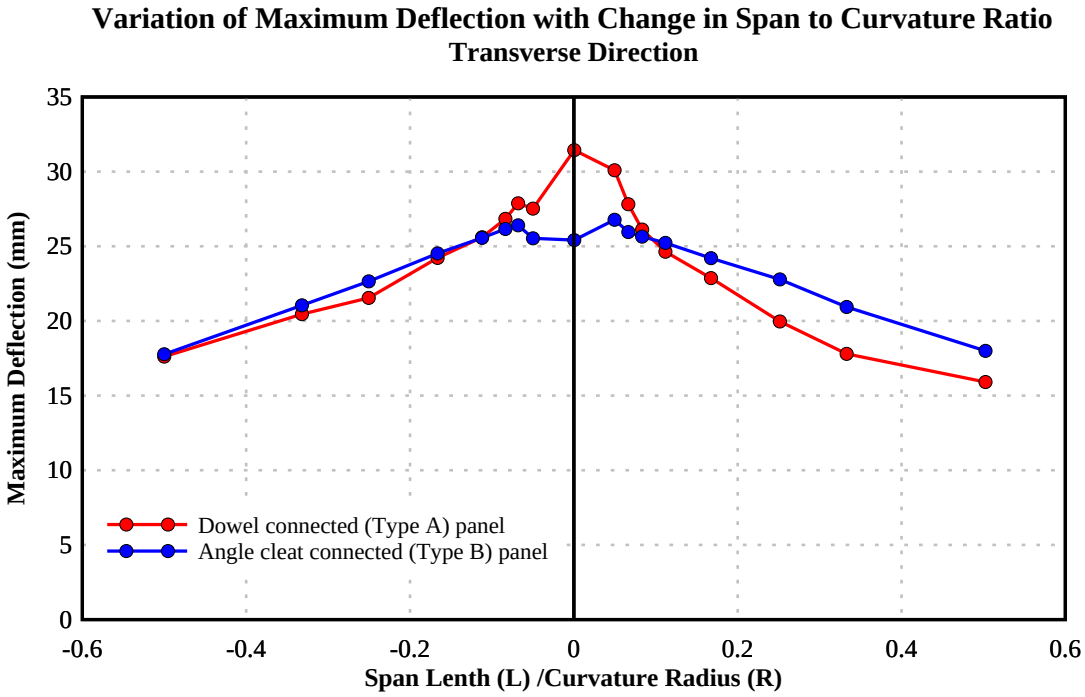

Figure 7.45: Variation of mid-panel deflection with span to radius of curvature ratio (shorter span)

Effect on maximum compressive stress of concrete

The variation of maximum compressive stress in concrete with span to the radius of curvature ratio (L/R) for shorter span direction is presented in Figure 7.46. The introduction of a curvature has increased the maximum compressive stress within the section significantly, irrespective of the curvature direction. The effects were immediate in dowel connected Type A panels as the maximum compressive stresses rise by 30 MPa with the smallest of curvatures. However, the response was more gradual in Type B panels where, two-fold increase in the maximum compressive stress was observed

with L/R ratios reaching 0.2. Overall, both panels experienced compressive stresses well above the compressive strength of concrete (46 MPa) with either positive or negative curvatures. However, compressive stresses with negative curvatures were slightly higher than with the positive curvatures. It should be noted that these stresses were limited to a small thickness within the panel.

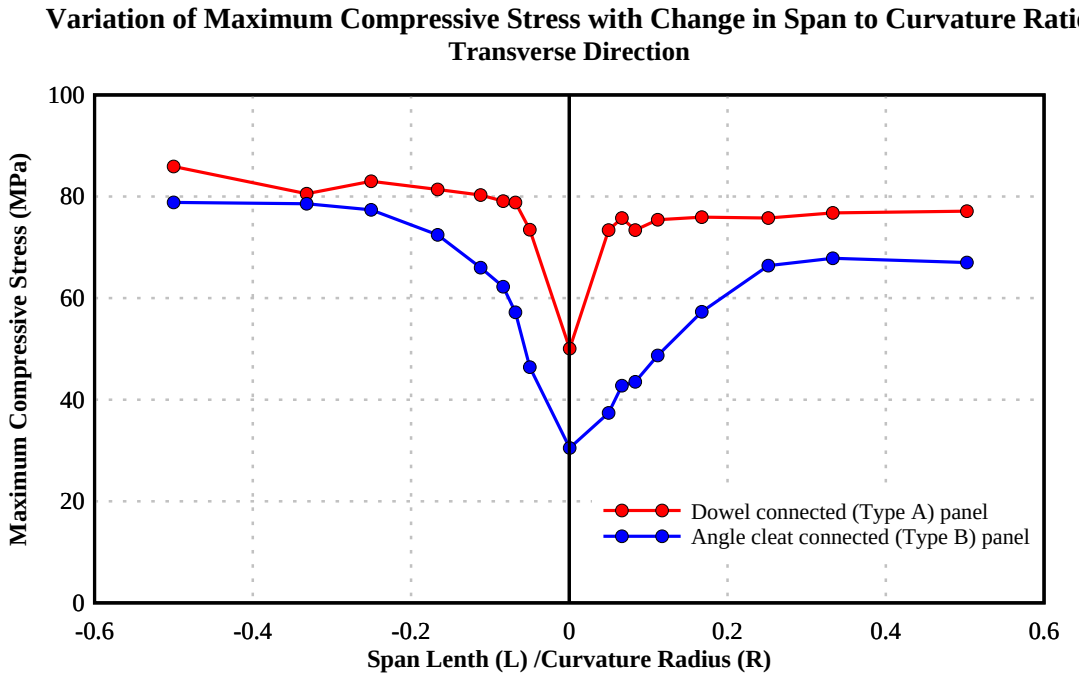

Figure 7.46: Variation of Maximum compressive stress in concrete with change in span to radius of curvature ratio (shorter span)

In contrast to the curvatures in the longitudinal direction, maximum stresses were observed closer to the middle of the panel with transverse curvatures.

Overall, incorporating curvatures in the short span direction have improved the resistance against transverse deflection for both positive and negative curvatures. However, a significant increase in maximum stress was also observed with the transverse curvatures, although stresses were limited to the surface of the panel. Panels behaved as thick plates when having large curvatures in the transverse direction, experiencing a rigid response. Hence, large compressive stresses and small deflections were observed with these curvatures. In addition, curvatures account for redistribution of blast pressure within the panel section displaying slightly larger compressive stresses with negative curvatures.

7.4.3. Summary: Facade panels with built-in curvatures

The performance of reinforced concrete panels with built in curvatures subjected to explosive loading was evaluated and is discussed in this section. Both convex (positive curvatures) and concave (negative curvatures) panels with the span to curvature radius ratios (L/R) between 0.05 and 0.5 were considered. All 73 panels were single curvature panels where 40 in longer span direction, 32 in shorter span direction and one flat panel. Following conclusions were made based on the maximum deflection and the maximum compressive stress responses observed.

- The introduction of convex (positive) curvatures, either in shorter or longer span direction, has improved the deflection resistance of the panel, irrespective of the connection type (dowel or angle cleat).
- Negative curvatures in the longer span direction reduce the deflection resistance while negative curvatures in the short span direction behave otherwise.
- Curvatures in the longer span direction reduce the maximum compressive stress within the concrete section, whereas curvatures in the short span direction increase the values up to twice in certain curvatures.

In summary, panels with built in curvatures (positive) have performed better against the applied explosive loading, especially positive curvatures in longer span direction. Curvatures in shorter span direction (both positive and negative) are also preferable in reducing the maximum deflection. However, this could result in higher compressive stresses within the concrete section.

CHAPTER 8

CONCLUSIONS AND RECOMMENDATIONS

The objective of this research was set to comprehensively evaluate the performance of reinforced concrete facade systems subjected to explosive loading. In order to achieve this objective, a 3-D finite element model and a 1-D analytical solution were developed and verified using experimental test results. LS-DYNA was used to develop the 3-D finite element model, in which the latest material models and keyword combinations were utilised. The 1-D analytical solution was developed based on the differential formulation of the Timoshenko beam theory (TBT), which is capable of predicting both flexural and shear (direct shear and diagonal shear) responses of reinforced concrete facade systems.

Finally, a comprehensive parametric study was conducted using the LS-DYNA, 3-D finite element model and the 1-D analytical solution. Stiffness in fixing assemblies, effects of opening, opening size and opening locations within the panel and architectural concrete facade panels with built-in curvatures were given particular attention.

8.1. Conclusions

The main results and conclusions of this study are categorised into three major sections, 3-D finite element solution, 1-D analytical solution and the parametric study.

8.1.1. 3-D finite element model

Details of the derived 3-D model were presented in Chapter 5 and a summary of outcomes were given in Sections 5.6.6 and 5.7.3. More specific conclusion are set out below.

- The Concrete Damage (CD) and Plastic Kinematic (PK) material model combination exhibited better overall calibration with the experimental results, even though different material model combinations demonstrated better results with individual aspects of calibration. The maximum and minimum error percentages of -16.1% and -1.14% were recorded for the mid panel deflection and support deflection of Panel A1, respectively.

- The selected material model combination, mesh size and control keywords were able to predict the maximum mid-panel deflection and maximum relative deflection with reasonable accuracy where a maximum error percentage of 21.7% was observed with Panel D. Among the 11 panels used for the verification, 10 panels exhibited error percentages less than 20%.
- In comparison, significantly larger error percentages were observed for support deflection, the maximum being 46.91% in Panel B4. Among the panels used for support deflection verification, two panels were observed with error percentage less than 7% while other two were associated with error percentages greater than 29%.
- The blast pressure profile delivered through the inbuilt keyword function was found to be in agreement with the experimental results, even though it uses only a fraction of the computational time than the numerical modelling of the explosion and associated air medium.
- Different mechanisms were utilised to deliver strain rate enhancement in different material models. A definition of rate enhancement through an externally defined curve using the CEB formulation for concrete in compression and Malvar and Crawford formulation for concrete in tension in the CDM exhibited comparable results with inbuilt rate enhancement mechanisms of the other material models.
- The method used for predicting localised damage using the internal damage parameter found to be incompatible with the selected material model combination and mesh sizing. Significant over-prediction of spalling dimensions was observed with the selected local damage prediction method.

8.1.2. 1-D analytical solution

Details of the derived 1-D analytical solution were presented in Chapter 5 and a summary of outcomes were given in Section 6.13. More specific conclusion are set out below.

- The developed 1-D analytical solution is capable of predicting the structural behaviour of reinforced concrete facade systems subjected to explosive loading with reasonable accuracy. The maximum error percentage of -19.6% was

observed for mid-panel deflection in Panel B. However, 9 of the 11 test panels exhibited error percentages less than 7%.

- In comparison, the maximum support deflection experienced significantly larger error percentages with the maximum being 66.18% in Panel B4. However, Panels B1, B2 and B3 all experienced error percentage less than 7.1% for support deflection.
- A maximum error percentage of 26.6% was recorded for the maximum relative deflection in Panel B4. In contrast, all other panels (B1 to B3 and B5) experienced error percentages less than 8%.
- Both flexural and shear behaviour was predicted within an acceptable error margin. Hence, the use of the Modified Scott Model (MSM) and the Mander's coefficient in predicting flexural behaviour as well as the Softened Membrane Model (SMM) and the Hawkin's shear slip relationship in predicting shear behaviour in rate sensitive applications is assured to yield accurate results.
- The Step by step update of rate enhancement properties has yielded comparatively better results. However, this step by step update was available only for flexural and diagonal shear responses as only a single enhancement factor of 1.4 was used for direct shear modelling.
- Along with idealised boundary conditions, non-idealised boundary conditions were also incorporated in the analytical solution, which is essential in determining the support deflections. However, the method used for evaluating boundary (support) stiffness did not yield ideal results for dowelled connections. However, the proposed method for stiffness determination yielded comparable results for angle cleat connections.
- Similar accuracy levels were observed for the maximum support deflection and the maximum relative deflection in both the 1-D analytical solution and the LS-DYNA, 3-D numerical model. Slightly better results were observed with the 1-D analytical solution for the maximum mid-panel deflection.

8.1.3. Parametric Study

The parametric study was conducted on three different aspects of facade systems namely, connection stiffness, openings and architectural facade systems with inbuilt curvatures. Conclusions derived for each parameter are presented in subsections below.

8.1.3.1. Connection Stiffness

Conclusions derived for the connection stiffness of the two typical panel connection types, angle cleat and dowel, are presented in the following sections. Overall, it was found that the angle cleat connections performed better than the dowel connections.

Angle cleat connected panels

- No significant variation was observed on the maximum mid-panel deflection, support deflection and relative deflection when changing the bolt diameter in angle cleat connections. However, thinner cleat sections have resulted in a significant drop in maximum mid-panel, support and relative deflection. The rate of drop in deflection stabilised above the 10 mm cleat thickness.
- Allowing transverse flexibility via smaller bolt diameters resulted in increased stresses within the bolt section, especially for bolt diameters smaller than 20 mm. For example, shear stresses doubled and axial stresses quadrupled when bolt diameter was changed from 20 mm to 10 mm. Conversely, thinner plate sections resulted in reduced stresses within the bolt cross section.
- The transverse flexibility by means of smaller bolt diameters have resulted in reduced compressive stresses within the concrete section. Although a small decrease was observed for bolt diameters larger than 20 mm, compressive stresses stabilised beyond the diameter of 20 mm. In contrast, increasing the cleat thickness from 5 mm to 8 mm resulted in a decrease in compressive stress.
- Similarly, effective stress within the cleat section has increased with the increase in bolt diameter. However, an increased support stiffness due to increased cleat thickness had the contrasting effect to the escalation of bolt diameters.
- Overall, bolt diameters between 16-20 mm and cleat thicknesses between 8-12 mm resulted in the best performance for angle cleat connections. Although, the largest compressive stresses were recorded for bolt diameters within this range, these stresses did not reach the compressive strength of the concrete.

Dowel connected panels

- In contrast to angle cleat connected panels, maximum mid-panel, support and relative displacements have decreased significantly with the increase in bolt

diameter up to 25 mm. All three displacement parameters have stabilised beyond the 25 mm diameter bolts.

- The bolt stresses (both shear and axial) were larger with smaller bolt diameters, especially due to the size effect of the bolts. However, the size effect was insignificant beyond the diameters of 25 and above.
- The observed maximum compressive stress within the concrete section escalated with the increase in bolt diameters, similar to the observation in angle cleat connected (Type B) panels.
- The effective stress in connecting cleats was found to escalate with the increase of bolt diameter, similar to angle cleat connected panels. However, yield capacity of the cleat section was breached with bolt diameters greater than 16 mm.
- Overall, small bolt diameters were found to be more effective in reducing the stresses with the panel section and large bolt diameters were found to be effective in limiting deflections. It is recommended that medium size bolts (16-25 mm range) to be used in blast resistant connection detailing, especially with dowel type connections.

8.1.3.2. Panels with openings

- Although the use of unstiffened openings is allowed up to 300 mm, it is advisable to minimise the use of unstiffened openings, if the blast resistance is considered. The presence of unstiffened openings tends to escalate the deflection as well as concrete stresses around the opening.
- The presence of stiffened openings up to 1/4 of panel area improved the panel performance with reduced deflections, without any variation in stresses. This is primarily due to the loss of loading through the opening.
- It is best to avoid openings in middle 1/3 of the distance between panel centre and support (longer span). This placing of openings will increase the panel deflection as well as stresses within the concrete section.
- Transverse location of the unstiffened openings does not interfere with the panel performance significantly. However, best results were observed with stiffened openings placed closer to the panel centre.

8.1.3.3. Architectural facade panels with built-in curvature

- The introduction of a positive curvature in the longer span direction (support to support) has improved the performance with respect to panel deflections. This is similar for both dowel and angle cleat connected panels.
- The presence of curvatures in the longer span direction (support to support) minimises the compressive stresses within the concrete section irrespective of the direction (positive or negative).
- Curvatures in shorter span direction are extremely efficient in reducing the maximum deflection, irrespective of the positive or negative curvatures. However, localised stress concentrations can yield to the failure of the section.

8.2. Recommendations and future research

The following recommendations are made for future research based on the behaviours identified during this study.

8.2.1. Explosive field tests

- During the literature review, it was identified that the available experimental data do not hold enough time-dependent measurements. All deflection measurements were recorded as maximum values rather than time-dependent deflections. Although these maximum deflection measurements can be used for the calibration of numerical and analytical tools, use of time-dependent deflection parameters would be more accurate.
- Strain measurements in concrete, as well as reinforcing steel, will yield much more information for the understanding of the subject. These strain measurements can yield valuable information on stress/strain, strain rate and even force transfer mechanism when enough measurements were taken.
- Use of proper fixing assemblies is encouraged in explosive field tests. This will effectively improve the understanding of flexible fixing assemblies in blast resistant applications. In addition, force/strain measurements in connection mechanisms will yield valuable information for flexible connection designs.

8.2.2. 3-D finite element model

Although the developed 3-D model was found to adequately model the test results, it is recommended that the following is considered.

- None of the material models available in LS-DYNA was able to capture localised damage associated with spalling and scabbing accurately. It is essential to improve/alter the method of local damage prediction in material models.
- Inbuilt loading functions were able to predict blast pressure-time profiles accurately for spherical charges. However, use of the same equations with different shaped charges could yield to erroneous results. Although there are other methods available for predicting blast pressures in LS-DYNA, all of them are mesh sensitive and higher computer capacities are required. A simplified method of predicting blast pressures for different shaped charges, at least for a more common shape like a cylinder is advised.

8.2.3. 1-D analytical solution

Although the developed 1-D analytical solution was able to adequately replicate the test results, it is considered that following is considered.

- The proposed analytical solution is equipped with several boundary conditions. However, it is possible to introduce load deflection relationships as boundary conditions, where a simple experiment will yield the behaviour of fixing assembly, which could be used directly in the solution.
- This solution does not consider the possibility of shear-moment interaction within the cross section. Incorporating shear-moment interaction will enable this tool to be used in a wide variety of applications.
- Although step by step rate enhancement was delivered in this application, it was applied on the moment and shear forces, instead of flexural or shear stresses. Therefore, it is worthwhile to investigate the concept of applying rate enhancement directly on stresses.
- The Hawkins shear slip method was applied with a constant rate enhancement factor (DIF). Although it was proven to be accurate with experimental results, a modification for the direct shear prediction method is recommended.

- This analytical solution can be improved to investigate different panel configurations, including openings and curvatures. However, modelling any discontinuities in reinforcement will be a significant task for this application.

REFERENCES

ABAQUS 2013. ABAQUS Analysis User's Guide. Dassault Systems.

Abrams, D. A. 1917. Effect of rate of application of load on the compressive strength of concrete. ASTM J, 17.

Abtahi, P., Samali, B., Zobec, M. & Ngo, T. 2012. Application of flexible façade systems in reducing the lateral displacement of concrete frames subjected to seismic loads. From Materials to Structures: Advancement through Innovation, 241.

Ågårdh, L. 1997. Fe-modelling of fibre reinforced concrete slabs subjected to blast load. Journal de Physique, 4, 723-728.

Ahmad, S. & Shah, S. 1985. Structural properties of high-strength concrete and its implications for precast concrete. PCI Journal, 30, 92-119.

Aïtcin, P.-C. 2011. High performance concrete, CRC Press.

American Concrete Institute 1984. State of the Art report on High Strength Concrete. ACI Journal Proceedings, 81, 364-411.

American Concrete Institute 2011. 318-11. Building Code Requirements for Structural Concrete and Commentary (ACI 318-11).

American Institute of Steel Construction 1994. Manual of steel construction. Load and Resistance Factor Design.

American Society for Testing and Materials 1996. ASTM C496: Standard Test Method for Splitting Tensile Strength of Cylindrical Concrete Specimens. American Society for Testing and Materials.

American Society for Testing and Materials 2002. ASTM C78-2002: Specification for Flexural-Strength Test. American Society for Testing and Materials.

American Society for Testing and Materials 2010. ASTM C39: Standard Test Method for Compressive Strength of Cylindrical Concrete Specimens. American Society for Testing and Materials.

American Society of Civil Engineers 2002. ASCE 7: Minimum Design Loads for Building and Other Structures. American Society of Civil Engineers.

Anderson, F. E., Hansen, R. J., Murphy, H. L., Newmark, N. M. & White, M. P. 1985. Design of structures to resist nuclear weapons effects, American society of civil engineers.

Anderson, J. 2001. Fundamentals of aerodynamics, McGraw-Hill.

ANSYS Inc 2013. ANSYS Autodyn User's Manual. Southpointe, 275, Technology Drive, Canonsburg: ANSYS Inc.

Architectural Institute of Japan 1985. Standard for Structural Calculation of Reinforced Concrete Structures. Architectural Institute of Japan.

Assadi-Lamouki, A. & Krauthammer, T. 1988. Development of improved Timoshenko beam and Mindlin plate theories for the analysis of reinforced concrete structures subjected to impulsive loads. University of Minnesota, Minneapolis.

Atchley, B. L. & Furr, H. L. Strength and energy absorption capabilities of plain concrete under dynamic and static loadings. ACI Journal Proceedings, 1967. ACI.

Atkatsh, R. S., Chan, K. K., Stultz, K. G., Dillworth, R. & Maranda, M. L. 1994. EPSA-II Theoretical Guidebook. Revision G. New York: Weidlinger Associates.

Attard, M. & Setunge, S. 1996. Stress-strain relationship of confined and unconfined concrete. ACI Materials Journal, 93.

Azad, A., Samali, B., Ngo, T., Nguyen, C., Samali, B., Attard, M. M. & Song, C. 2012. Dynamic behaviour of flexible facade systems in tall buildings subjected to wind loads. From Materials to Structures: Advancement through Innovation, 431.

Baker, W. E. 1973. Explosions in air, University of Texas Press Austin.

Baker, W. E., Cox, P., Kulesz, J., Strehlow, R. & Westine, P. 1983. Explosion hazards and evaluation, Elsevier.

Balan, T. A., Filippou, F. C. & Popov, E. P. 1998. Hysteretic model of ordinary and high-strength reinforcing steel. Journal of Structural Engineering, 124, 288-297.

Bangash, M. Y. H. 1989. Concrete and concrete structures: numerical modelling and applications.

Barnett, S. J., Millard, S. G., Schleyer, G. K. & Tyas, A. 2010. Blast tests of fibre-reinforced concrete panels. Construction Materials (Proceedings of the ICE), 163.

Baum, J. D., Luo, H. & Loehner, R. Numerical simulation of blast in the world trade center. AIAA, Aerospace Sciences Meeting and Exhibit, 33rd, Reno, NV, 1995.

Bažant, Z. 1978. Endochronic inelasticity and incremental plasticity. International Journal of Solids and Structures, 14, 691-714.

Bazant, Z. P. & Asghari, A. A. 1977. Constitutive law for nonlinear creep of concrete. Journal of the Engineering Mechanics Division, 103, 113-124.

Bazant, Z. P. & Bhat, P. D. 1976. Endochronic theory of inelasticity and failure of concrete. Journal of the Engineering Mechanics Division, 102, 701-722.

Belytschko, T., Lu, Y. Y. & Gu, L. 1994. Element-free Galerkin methods. International journal for numerical methods in engineering, 37, 229-256.

Ben-Dor, G. 2007. Shock wave reflection phenomena, Springer.

Bethe, H. A., Fuchs, K., Hirshfelder, J. O., Magee, J. L., Peleris, R. E. & Neumann, J. v. 1947. Blast wave. Los Alamos Scientific Laboratory, University of California, New mexico.

Bischoff, P. & Perry, S. 1991. Compressive behaviour of concrete at high strain rates. Materials and structures, 24, 425-450.

Brannon, R. M. & Leelavanichkul, S. 2009. Survey of Four Damage Models for Concrete. Sandia National Laboratories, Albuquerque, New Mexico.

Bresler, B. & Bertero, V. 1975. Influence of high strain rate and cyclic loading on behaviour of unconfined and confined concrete in compression. Second Canadian Conference on Earthquake Engineering.

Bresler, B. & Pister, K. S. Strength of Concrete Under Combined Stresses*. ACI Journal Proceedings, 1958. ACI.

Britt, J. & Lumsden, M. 1994. Internal Blast and Thermal Environment from Internal and External Explosions: A User's Guide for the BLASTX Code, Version 3.0. Science Applications International Corporation, St. Joseph, Louisiana, SAIC, 405-94.

Broadhouse, B. 1995. The Winfrith concrete model in LS-DYNA3D. Report: SPD/D (95), 363.

Broadhouse, B. & Attwood, G. Finite element analysis of the impact response of reinforced concrete structures using dyna3d. Transactions of the 12. international

conference on Structural Mechanics in Reactor Technology (SMiRT). Volume J: Structural dynamics and extreme loads analysis, 1993.

Broadhouse, B. & Neilson, A. 1987. Modelling reinforced concrete structures in dyna3d. UKAEA Atomic Energy Establishment, Winfrith (UK). Safety and Engineering Science Div.

Brode, H. L. 1955. Numerical solutions of spherical blast waves. Journal of Applied physics, 26, 766-775.

Brookes, A. 1998. Cladding of buildings, Taylor & Francis.

Buchan, P. & Chen, J. 2007. Blast resistance of FRP composites and polymer strengthened concrete and masonry structures–A state-of-the-art review. Composites Part B: Engineering, 38, 509-522.

Budge, K. G. & Peery, J. S. 1993. RHALE: a MMALE shock physics code written in C++. International Journal of Impact Engineering, 14, 107-120.

Burg, R. G. & Ost, B. W. 1992. Engineering properties of commercially available high-strength concretes.

Canadian Standard Association 1990. CAS 23.3: Design of Concrete Structures. Canadian Standard Association.

Carrasquilio, R. L. & Nilson, A. H. Properties of high strength concrete subject to short-term loads. ACI Journal Proceedings, 1981. ACI.

Chang, G. A. & Mander, J. B. 1994. Seismic energy based fatigue damage analysis of bridge columns: part 1-evaluation of seismic capacity.

Chen, W.-F. 2007. Plasticity in reinforced concrete, J. Ross Publishing.

Chen, W.-F. & Saleeb, A. F. 1981. Constitutive equations for engineering materials, Wiley New York.

Comite Euro-International du Beton 1978. CEB-FIP model code for concrete structures. du Beton, Comite Euro-Internationale de la Précontrainte, Fédération.

Comite Euro-International du Beton 1990. CEB FIP Model Code 1990. Model code for concrete structures. Thomas telford Ltd.

Comite Euro-International du Beton 2010. CEB FIP Model Code 2010. Model code for concrete structures.

Corley, W., Sozen, M., Thornton, C. & Mlakar, P. 1996. The Oklahoma City bombing: Improving building performance through multi-hazard mitigation. Federal Emergency Management Agency Mitigation Directorate, FEMA Report, 277.

Cowell, W. 1969. DYNAMIC TESTS ON SELECTED STRUCTURAL STEELS. Defence Technical Information Centre.

Cowell, W. L. 1966. Dynamic Properties of Plain Portland Cement Concrete Defense Technical Information Centre.

Cowper, G. R. & Symonds, P. S. 1957. Strain-hardening and strain-rate effects in the impact loading of cantilever beams. DTIC Document.

Cramsey, N. & Naito, C. 2007. Analytical assessment of blast resistance of precast, prestressed concrete components. April, 2007: Airport Research Laboratory

Crawford, J. E., Wu, Y., Choi, H.-J., Magallanes, J. M. & Lan, S. 2012. Use and validation of the release III K&C concrete material model in LS-DYNA. Karagozian & Case, Glendale, CA: Karagozian & Case.

Day, K. W. 2006. Concrete mix design, quality control and specification, CRC Press.

Department of the Army 1967. FM 5-25: Explosives and Demolition. US Army Corps of Engineers.

Desayi, P. & Krishnan, S. Equation for the stress-strain curve of concrete. ACI Journal Proceedings, 1964. ACI.

Design, S. o. C. E. T. C. o. B. R. 2010. Design of Blast-resistant Buildings in Petrochemical Facilities, ASCE Publications.

Dewey, J. M. The shape of the blast wave: studies of the Friedlander equation. 21st international symposium on military aspects of blast and shock, Israel, 2010.

Dilger, W., Koch, R. & Kowalczyk, R. Ductility of plain and confined concrete under different strain rates. ACI Journal Proceedings, 1984. ACI.

Ding, P. & Buijk, A. 2005. Simulation of Under Water Explosion using MSC. Dytran. Ann Arbor, 1001, 48105.

Dodd, L. & Restrepo-Posada, J. 1995. Model for predicting cyclic behaviour of reinforcing steel. Journal of Structural Engineering, 121, 433-445.

Drucker, D. C. 1959. A definition of a stable inelastic material. ASME Journal of Applied Mechanics, 26, 101-195.

Dunkman, D. A., Yousef, A. E. A., Karve, P. M. & Williamson, E. B. Blast Performance of Prestressed Concrete Panels. Structures Congress 2009@ Don't Mess with Structural Engineers: Expanding Our Role, 2009. ASCE, 1-10.

El-Dakhakhni, W., Mekky, W. & Rezaei, S. C. 2009. Validity of SDOF models for analysing two-way reinforced concrete panels under blast loading. Journal of Performance of Constructed Facilities, 24, 311-325.

Erlicher, S. & Point, N. 2006. Endochronic theory, non-linear kinematic hardening rule and generalized plasticity: a new interpretation based on generalized normality assumption. International journal of solids and structures, 43, 4175-4200.

European Committee for Standardization 2001. BS EN 10002-1:2001 Tensile testing of metallic materials. Method of test at ambient temperature. British Standards Institution.

European Committee for Standardization 2004. BS EN 1992-1-2:2004 Design of concrete structures. General rules. Structural fire design. British Standards Institution.

European Committee for Standardization 2006. Actions on Structures. EN 1991-1.

European Committee for Standardization 2009a. BS EN 12390-3: Testing hardened concrete. Compressive strength of test specimens. British Standards Institute.

European Committee for Standardization 2009b. BS EN 12390-5: Testing hardened concrete. Flexural strength of test specimens. British Standards Institute.

European Committee for Standardization 2013. BS EN 206: Concrete. Specification, performance, production and conformity. British Standards Institution.

Evans, A. 1974. Slow crack growth in brittle materials under dynamic loading conditions. International Journal of Fracture, 10, 251-259.

Federal Emergency Management Agency 2003. Primer for Design of Commercial Buildings to Mitigate Terrorist Attacks. FEMA 427. Federal Emergency Management Agency.

Feldman, A., Keenan, W. & Siess, C. P. 1962. Investigation of resistance and behaviour of reinforced concrete members subjected to dynamic loading, part III. DTIC Document.

Filippou, F. C., Popov, E. P. & Bertero, V. V. 1983. Effects of bond deterioration on hysteretic behaviour of reinforced concrete joints.

Freidlander, F. G. The diffraction of sound pulses. I. Diffraction by a semi-infinite plate. Royal society of London, 1946. 322-344.

Fu, H., Erki, M. & Seckin, M. 1991a. Review of effects of loading rate on concrete in compression. Journal of structural engineering, 117, 3645-3659.

Fu, H., Erki, M. & Seckin, M. 1991b. Review of effects of loading rate on reinforced concrete. Journal of structural engineering, 117, 3660-3679.

Gardner, N. J. & Zhao, J. W. 1991. Mechanical Properties of concrete for calculating long term deformations. Second Canadian Conference on cement and Concrete. Vancouver, Canada.

Garfield, T., Richins, W. D., Larson, T. K., Pantelides, C. P. & Blakeley, J. E. 2011. Performance of RC and FRC Wall Panels Reinforced with Mild Steel and GFRP Composites in Blast Events. Procedia Engineering, 10, 3534-3539.

Garfield, T. T. 2011. Performance of Reinforced Concrete Panels During Blast Loading. Master of Science, The University of Utah.

Ghaboussi, J., Millavec, W. A. & Isenberg, J. 1984. R/C structures under impulsive loading. Journal of structural engineering, 110, 505-522.

Gingold, R. A. & Monaghan, J. J. 1977. Smoothed particle hydrodynamics: theory and application to non-spherical stars. Monthly notices of the royal astronomical society, 181, 375-389.

Goldstein, H., Jr, C. P. & Safko, j. 2001. Classical Mechanics, Addison-wesley.

Gorenc, B., Tinyou, R. & Syam, A. 2012. Steel designers' handbook, UNSW Press.

Govindjee, S., Kay, G. J. & Simo, J. C. 1995. Anisotropic modelling and numerical simulation of brittle damage in concrete. International Journal for Numerical Methods in Engineering, 38, 3611-3633.

Grassl, P. & Jirásek, M. 2006. Damage-plastic model for concrete failure. International journal of solids and structures, 43, 7166-7196.

Graybeal, B. & Davis, M. 2008. Cylinder or cube: strength testing of 80 to 200 MPa (11.6 to 29 ksi) ultra-high-performance fiber-reinforced concrete. ACI Materials Journal, 105.

Green, H. IMPACT STRENGTH OF CONCRETE. ICE Proceedings, 1964. Thomas Telford, 383-396.

Grote, D., Park, S. & Zhou, M. 2001. Dynamic behaviour of concrete at high strain rates and pressures: I. experimental characterization. International Journal of Impact Engineering, 25, 869-886.

Gunger, M. 1992. Progress on tasks under the sympathetic detonation program. WL/MN-TR-91-85, Orlando Technology, Shalimar, FL.

Hallquist, J. O. 1993. LS-DYNA3D theoretical manual. Livermore software technology corporation.

Hawkins, N. 1982. Direct shear resistance. Letter Report to US Navy, Reproduced in RN Murtha and TJ Holland, Analysis of WES FY82 Dynamic Shear Test Structures, Technical Memorandum, 51-83.

Hayes Jr, J. R., Woodson, S. C., Pekelnicky, R. G., Poland, C. D., Corley, W. G. & Sozen, M. 2005. Can strengthening for earthquake improve blast and progressive collapse resistance? Journal of Structural Engineering, 131, 1157-1177.

Henrych, J. & Major, R. 1979. The dynamics of explosion and its use, Elsevier Amsterdam.

Hentz, S., Donzé, F. V. & Daudeville, L. 2004. Discrete element modelling of concrete submitted to dynamic loading at high strain rates. Computers & structures, 82, 2509-2524.

Hikida, S., Bell, R. & Needham, C. 1988. The SHARC codes: documentation and sample problems. S-Cubed Technical Report SSS.

Holmquist, T. J., Johnson, G. R. & Cook, W. H. 1993. A computational constitutive model for glass subjected to large strains, high strain rates and high pressures. The 14th international symposium on Ballastics. Qucbec.

Hoogenboom, P. & Spaan, R. Shear Stiffness and Maximum Shear Stress of Tubular Members. The Fifteenth International Offshore and Polar Engineering Conference, 2005. International Society of Offshore and Polar Engineers.

Hopkinson, B. 1915. British Ordnance Board Minutes 13565.

Hsu, T. T. & Zhu, R. R. 2002. Softened membrane model for reinforced concrete elements in shear. ACI Structural Journal, 99.

Hughes, B. & Gregory, R. 1972. Concrete subjected to high rates of loading in compression. Magazine of Concrete Research, 24, 25-36.

Hussein, A. T. 2010. Nonlinear analysis of SDOF system under blast load. European Journal of Scientific Research, 45, 430-437.

Huyge, K. & Schoofs, A. 2009. Precast double curved concrete panels. Delft University of Technology.

Hyde, D. 1991. ConWep, conventional weapons effects program. US Army Engineer Waterways Experiment Station, USA.

Jacques, E., Lloyd, A. & Saatcioglu, M. 2012. Predicting Reinforced Concrete Response to Blast Loads. Canadian Journal of Civil Engineering.

Johansson, M. 2000. Structural Behaviour in Concrete Frame Corners of Civil Defence Shelters Non-linear Finite Element Analyses and Experiments. Doctor of Philosophy, Chalmers University of Technology.

Johnson, G. R. & Cook, W. H. A constitutive model and data for metals subjected to large strains, high strain rates and high temperatures. Proceedings of the 7th International Symposium on Ballistics, 1983. The Netherlands, 541-547.

Kaplan, S. A. 1980. Factors affecting the relationship between rate of loading and measured compressive strength of concrete. Magazine of Concrete Research, 32, 79-88.

Keenan, W. A. & Feldman, A. 1960. The Yield Strength of Intermediate Grade Reinforcing Bars Under Rapid Loading. Research Doctorate, Air force Weapons Centre

University of Illinois.

Khayat, K., Bickley, J. & Hooton, R. 1995. High-strength concrete properties derived from compressive strength values. Cement, Concrete and Aggregates, 17.

Khoe, Y. S. & Weerheijm, J. 2012. Limitations of smeared crack models for dynamic analysis of concrete. 12th International LS-DYNA users conference.

Kiger, S., Getchell, J., Slawson, T. & Hyde, D. 1980. Vulnerability of shallow-buried flat roof structures. US Army Engineer Waterways Experiment Station, Technical Report SL-80-7.

Kingery, C. 1966. Air blast parameters versus distance for hemispherical TNT surface bursts. DTIC Document.

Kingery, C. N. & Bulmash, G. 1984. Air blast parameters from TNT spherical air burst and hemispherical surface burst, Ballistic Research Laboratories.

Kingery, C. N., Bulmash, G. & Laboratory, U. A. B. R. 1984. Air blast parameters from TNT spherical air burst and hemispherical surface burst, Ballistic Research Laboratories.

Kinney, G. F. & Graham, K. J. 1985. Explosive shocks in air. Berlin and New York, Springer-Verlag, 1985, 282 p., 1.

Komlos, K. Factors affecting the stress-strain relation of concrete in uniaxial tension. ACI Journal Proceedings, 1969. ACI.

Krauthammer, T., Assadi-Lamouki, A. & Shanaa, H. 1993a. Analysis of impulsively loaded reinforced concrete structural elements—I. Theory. Computers & structures, 48, 851-860.

Krauthammer, T., Assadi-Lamouki, A. & Shanaa, H. 1993b. Analysis of impulsively loaded reinforced concrete structural elements—II. Implementation. Computers & structures, 48, 861-871.

Krauthammer, T., Astarlioglu, S., Blasko, J., Soh, T. & Ng, P. 2008. Pressure–impulse diagrams for the behaviour assessment of structural components. International Journal of Impact Engineering, 35, 771-783.

Krauthammer, T., Bazeos, N. & Holmquist, T. 1986. Modified SDOF analysis of RC box-type structures. Journal of Structural Engineering, 112, 726-744.

Krauthammer, T., Shahriar, S. & Shanaa, H. 1990. Response of reinforced concrete elements to severe impulsive loads. Journal of Structural Engineering, 116, 1061-1079.

Kumavat, H. R. & Patel, V. J. 2014. Factors Influencing the Strength Relationship of Concrete Cube and Standard Cylinder. International Journal of Innovative Technology and Exploring Engineering.

Labuz, J. F. & Zang, A. 2012. Mohr–Coulomb failure criterion. Rock mechanics and rock engineering, 1-5.

Lan, S., Lok, T. S. & Heng, L. 2005. Composite structural panels subjected to explosive loading. Construction and Building Materials, 19, 387-395.

Li, J. & Hao, H. 2011. A two-step numerical method for efficient analysis of structural response to blast load. International Journal of Protective Structures, 2, 103-126.

Liu, G. & Owen, D. 1986. Ultimate load behaviour of reinforced concrete plates and shells under dynamic transient loading. International journal for numerical methods in engineering, 22, 189-208.

Liu, M., Liu, G., Lam, K. & Zong, Z. 2003. Smoothed particle hydrodynamics for numerical simulation of underwater explosion. Computational Mechanics, 30, 106-118.

Livermore Software Technology Corporation 2006. LS-DYNA Theory manual. Livermore, California: Livermore Software Technology Corporation.

Livermore Software Technology Corporation 2013a. LS-DYNA Finite Element Program. R700 ed. Livermore, CA, USA: Livermore Software Technology Corporation.

Livermore Software Technology Corporation 2013b. LS-DYNA keyword user manual. Volume II-Material Models. Livermore, California: Livermore Software Technology Corporation.

Livermore Software Technology Corporation 2013c. LS-DYNA Theoty Manual (Draft). Livermore, California: Livermore Software Technology Corporation.

Livermore Software Technology Corporation 2013d. LS-DYNA keyword user manual. Volume I. Livermore, California: Livermore Software Technology Corporation.

Lowes, L. N. 2000. Finite element modelling of reinforced concrete beam-column bridge connections. Doctor of Philosophy, University of California, Berkeley.

Lumantarna, R., Lam, N. & Mendis, P. 2006. Analytical Model of Glazing Panel Subjected to Impact Loading. Australasian Conference on the Mechanics of Structures and Materials. Christchurch, New Zealand.

M.A. Yusof, N. M. N., A. Ismail, R.M. Sohaimi, M.F.M. Zain, N.G.N. Daud, N.C. Peng 2010. Development of blast resistant concrete. The journal of defence and security, 1.

Malvar, J. L., Crawford, J. E., simons, D. A. & Wesevich, J. W. 1995. A New Concrete Material Model for DYNA3D. 10th ASCE Engineering Mechanics Conference.

Malvar, L., Crawford, J., Wesevich, J. & Simons, D. 1996. A new concrete material model for DYNA3D-Release II: shear dilation and directional rate enhancements. A Report to Defense Nuclear Agency under Contract No. DNA001-91-C-0059.

Malvar, L. J. 1998. Review of static and dynamic properties of steel reinforcing bars. ACI Materials Journal, 95.

Malvar, L. J. & Crawford, J. E. 1998a. Dynamic increase factors for concrete. Defence Technical Information Centre.

Malvar, L. J. & Crawford, J. E. 1998b. Dynamic increase factors for steel reinforcing bars. Defence Technical Information Centre.

Malvar, L. J., Crawford, J. E., Wesevich, J. W. & Simons, D. 1997. A plasticity concrete material model for DYNA3D. International Journal of Impact Engineering, 19, 847-873.

Malvar, L. J. & Ross, C. A. 1998. Review of strain rate effects for concrete in tension. ACI Materials Journal, 95.

Malvern, L., Jenkins, D., Tang, T. & Ross, C. Dynamic compressive testing of concrete. Proceedings of 2nd symposium on the interaction of non-nuclear munitions with structures. Florida, USA, 1985. 194-199.

Mander, J. B., Priestley, M. J. & Park, R. 1988. Theoretical stress-strain model for confined concrete. Journal of structural engineering, 114, 1804-1826.

Markovich, N., Kochavi, E. & Ben-Dor, G. 2011. An improved calibration of the concrete damage model. Finite Elements in Analysis and Design, 47, 1280-1290.

Mays, G., Hetherington, J. & Rose, T. 1999. Response to blast loading of concrete wall panels with openings. Journal of Structural Engineering, 125, 1448.

Mays, G. C. & Smith, P. D. 1995. Blast effects on buildings: Design of buildings to optimize resistance to blast loading, Thomas Telford.

McGlaun, J. M., Thompson, S. & Elrick, M. 1990. CTH: a three-dimensional shock wave physics code. International Journal of Impact Engineering, 10, 351-360.

Mendis, P., Pendyala, R. & Setunge, S. 2000. Stress–strain model to predict the full-range moment curvature behaviour of high-strength concrete sections. Magazine of Concrete Research, 52, 227-234.

Menegotto, M. & Pinto, P. Method of analysis for cyclically loaded reinforced concrete plane frames including changes in geometry and non-elastic behaviour of elements under combined normal force and bending Proc. of IABSE symposium on resistance and ultimate deformability of structures acted on by well defined repeated loads, 1973. 15-22.

Mihashi, H. & Izumi, M. 1977. A stochastic theory for concrete fracture. Cement and Concrete Research, 7, 411-421.

Mills, C. The design of concrete structures to resist explosions and weapon effects. Pros. 1st Int. Conference for Hazard Protection, Edinburgh, 1987.

Mindlin, R. D. 1951. Influence of rotary inertia and shear on flexural motions of isotropic, elastic plates. J. of Appl. Mech., 18, 31-38.

Miyoshi, H. Numerical simulation of shaped charges using the SPH solver: jet formation and target penetration. Materials Science Forum, 2008. Trans Tech Publ, 65-70.

Morishita, M., Tanaka, H., Ito, T. & Yamaguchi, H. 2000. Damage of reinforced concrete slabs subjected to contact detonations. Struct. Eng.(Jpn. Soc. Civ. Eng.), 46, 1787-1797.

Murray, Y. D. 2007. User's manual for LS-DYNA concrete material model 159.

Murray, Y. D., Abu-Odeh, A. Y. & Bligh, R. P. 2007. Evaluation of LS-DYNA concrete material model 159. Federal Highway Administration.

Musselman, E. 2007. Characterizing Blast and Impact Resistance of Long Carbon Fibre Reinforced Concrete. Doctor of Philosophy, The Pennsylvania State University.

Muszynski, L. C. & Purcell, M. R. 2003a. Composite reinforcement to strengthen existing concrete structures against air blast. Journal of Composites for Construction, 7.

Muszynski, L. C. & Purcell, M. R. 2003b. Use of composite reinforcement to strengthen concrete and air-entrained concrete masonry walls against air blast. Journal of Composites for Construction, 7.

Naito, C. J., Dinan, R. J., Fisher, J. W. & Hoemann, J. M. 2008. Precast/Prestressed Concrete Experiments - Series 1 (Volume1). Airforce research laboratory.

Neville, A. M. 1995. Properties of concrete, New York, Longman Scientific & Technical.

Newmark, N. & Hansen, R. 1961. Design of blast resistant structures. Shock and vibration handbook, 3.

Ngo, T., Mendis, P., Gupta, A. & Ramsay, J. 2007a. Blast loading and blast effects on structures—an overview. Electronic Journal of Structural Engineering, 7, 76-91.

Ngo, T., Mendis, P. & Krauthammer, T. 2007b. Behaviour of ultrahigh-strength prestressed concrete panels subjected to blast loading. Journal of Structural Engineering, 133, 1582-1590.

Ngo, T. D. 2005. Behaviour of high strength concrete subject to impulsive loading. Doctor of Philosophy, University of Melbourne.

Nichols, A. 2007. User's Manual for ALE3D: An Arbitrary Lagrange/Eulerian 3D Code System. Lawrence Livermore National Laboratory.

Norris, C. H., Hansen, R. J., Holley, M. J., Biggs, J. M., Namyet, S. & Minami, J. K. 1959. Structural design for dynamic loads, McGraw-Hill.

Norwegian Standards 2003. NS 3473:2003 Concrete Structures - Design And Detailing Rules. Norwegian Standards.

Nyström, U. 2008. Concrete Structures Subjected to Blast and Fragment Impacts, Numerical Simulations of Reinforced and Fibre-reinforced Concrete. Chalmers University of Technology.

Oh, B. H. 1987. Behaviour of concrete under dynamic tensile loads. ACI Materials Journal, 84.

Ohashi, K., Kleine, H. & Takayama, K. Characteristics of blast waves generated by milligram charges. Proceedings of the 22nd International Symposium on Shock Waves, Forth Worth, Texas, 2001.

Ottosen, N. S. 1977. A failure criterion for concrete. Journal of the Engineering Mechanics Division, 103, 527-535.

Pan, Y. & Watson, A. 1996. Interaction between concrete cladding panels and fixings under blast loading. Cement and Concrete Composites, 18, 323-332.

Pan, Y. & Watson, A. 1998. Effect of panel stiffness on resistance of cladding panels to blast loading. Journal of engineering mechanics, 124, 414.

Pan, Y., Watson, A. & Hobbs, B. 2001. Transfer of impulsive loading on cladding panels to the fixing assemblies. International journal of impact engineering, 25

Pang, X.-B. D. & Hsu, T. T. 1995. Behaviour of reinforced concrete membrane elements in shear. ACI structural Journal, 92.

Pantelides, C., Garfield, T., Richins, W., Larson, T. & Blakeley, J. Behaviour of Concrete Panels Reinforced with Synthetic Fibers, Mild Steel, and GFRP Composites Subjected to Blasts. Structures Congress 2012, 2012. ASCE, 23-34.

Park, R. & Pauly, T. 1975. Reinforced Concrete Structures, John Wiley & Sons, Inc., USA.

Park, Y.-J., Ang, A. H.-S. & Wen, Y. K. 1985. Seismic damage analysis of reinforced concrete buildings. Journal of Structural Engineering, 111, 740-757.

Peterson, P. 1980. Fracture energy of concrete: Method of determination. Cement and Concrete research, 10, 79-89.

Pham, T. 2010. Blast loading response of reinforced concrete facade systems. Doctor of Philosophy, University of Melbourne.

Pham, T., Ngo, T. & Mendis, P. 2008. An investigation of the interaction between RC panels and fixings under blast loading. 20th Australian Conference on the Mechanics of Structures and Materials. Toowoomba, Australia: Taylor and Francis Group.

Pinelli, J.-P., Craig, J. I., Goodno, B. J. & Hsu, C.-C. 1993. Passive control of building response using energy dissipating cladding connections. Earthquake spectra, 9, 529-546.

Popovics, S. 1973. A numerical approach to the complete stress-strain curve of concrete. Cement and concrete research, 3, 583-599.

Precast/Prestress Concrete Institute 2004. Designer's Notebook: Blast consideration. In: INSTITUTE, P. P. C. (ed.). PCI.

Precast/Prestress Concrete Institute 2007. PCI Design Handbook: Precast and Prestressed Concrete, Chicago, IL, PCI.

Prochazka, P., Kravtsov, A. & Peskova, S. 2008. Blast impact on structures of underground parking. Undergr Spaces Des Eng Environ Asp, 102, 11-19.

Quintero-Febres, C. G. & Wight, J. K. 2001. Experimental study of reinforced concrete interior wide beam-column connections subjected to lateral loading. ACI Structural Journal, 98.

Raman, S., Pham, T., Mendis, P. & Ngo, T. 2013. Experimental investigation on the behaviour of RC panels retrofitted with polymer coatings under blast effects.

Ramberg, W. & Osgood, W. R. 1943. Description of stress-strain curves by three parameters, National advisory committee for aeronautics.

Randers-Pehrson, G. & Bannister, K. A. 1997. Airblast Loading Model for DYNA2D and DYNA3D. DTIC Document.

Rankine, W. J. M. 1870. On the thermodynamic theory of waves of finite longitudinal disturbances. Philosophical Transactions of the Royal Society of London

Raphael, J. M. Tensile strength of concrete. ACI Journal Proceedings, 1984. ACI.

Remennikov, A. 2002. Blast resistant consulting: A new challenge for structural engineers. Australian Journal of Structural Engineering, 4, 121.

Remennikov, A. M. & Rose, T. A. 2005. Modelling blast loads on buildings in complex city geometries. Computers & structures, 83, 2197-2205.

Riedel, W., Thoma, K., Hiermaier, S. & Schmolinske, E. Penetration of reinforced concrete by BETA-B-500 numerical analysis using a new macroscopic concrete model for hydrocodes. Proceedings of the 9th International Symposium on the Effects of Munitions with Structures, 1999.

Riisgaard, B., Gupta, A., Mendis, P. & Ngo, T. 2006. Enhancing the performance under close-in detonations with polymer reinforced CRC. Electronic journal of Structural engineering, 6, 75-79.

Robert, S. D. & Johnson, C. F. Blast Response of Conventional and High Performance Reinforced Concrete Panels. Structures Congress 2009@ don't Mess with Structural Engineers: Expanding Our Role, 2009. ASCE, 1-9.

Rong, H. W. & Ho, D. 2002. Stregth of concrete cubes and cylinders. Available: http://staff.science.nus.edu.sg/~scilooe/srp2002/sci_paper/CE/research%20paper/Ho%20Wei%20Rong.pdf.

Rose, T. 2003. Air3D user's guide. 7.0: RMCS. UK: Cranfield University.

Ross, C. A. 1989. Split-Hopkinson pressure-bar tests on concrete and mortar in tension and compression. ACI Materials Journal, 86.

Ross, C. A., Jerome, D. M., Tedesco, J. W. & Hughes, M. L. 1996. Moisture and strain rate effects on concrete strength. ACI Materials Journal, 93.

Ross, C. A., Tedesco, J. W. & Kuennen, S. T. 1995. Effects of strain rate on concrete strength. ACI Materials Journal, 92.

Ross, T. J. 1983. Direct shear failure in reinforced concrete beams under impulsive loading. DTIC Document.

Rubin, M. 1991. Simple, convenient isotropic failure surface. Journal of engineering mechanics, 117, 348-369.

Raman, S.N, Ngo, T & Mendis, P. 2008. Preliminary investigation on the behaviour of RC panels with polymer coating under blast loading. 20th Australian Conference on the Mechanics of Structures and Materials. Toowoomba, Australia: Taylor and Francis Group.

Sachs, P. G. 1944. The Dependence of Blast on Ambient Pressure and Temperature. Aberdeen Proving Ground, Maryland.

Samali, B., Abtahi, P. & Ngo, T. 2014. Evaluation of effect of sacrificial facade bracket elements in reducing dynamic response of structures subjected to seismic loads. World Conference on Structural Control and Monitoring. Barcelona, Spain.

Sandler, I. & Rubin, D. 1990. FUSE calculations of far-field water shock including surface and bottom effects. Weidlinger Associates, New York, Technical Report for SAIC Subcontract, 64.

Sandler, I. S., Baladi, G. Y. & DiMaggio, F. L. 1976. Generalized cap model for geological materials. Journal of the Geotechnical Engineering Division, 102, 683-699.

Schenker, A., Anteby, I., Gal, E., Kivity, Y., Nizri, E., Sadot, O., Michaelis, R., Levintant, O. & Ben-Dor, G. 2008. Full-scale field tests of concrete slabs subjected to blast loads. International journal of impact engineering, 35, 184-198.

Schenker, A., Anteby, I., Nizri, E., Ostraich, B., Kivity, Y., Sadot, O., Haham, O., Michaelis, R., Gal, E. & Ben-Dor, G. 2005. Foam-protected reinforced concrete structures under impact: Experimental and numerical studies. Journal of Structural Engineering, 131, 1233.

Schlamp, R. J., Hassig, P. J., Nguyen, C. T., Hatfield, D. W., Hookham, P. A. & Rosenblatt, M. 1995. MAZe User's Manual. Los Angeles. California: TRT Corporation.

Schwer, L. The Winfrith Concrete Model: Beauty or Beast? Insights into the Winfrith Concrete Model. 8th European LS-DYNA Users Conference, 2011.

Schwer, L. E. & Malvar, J. L. 2005. Simplified concrete modelling with MAT_CONCRETE_DAMAGE_REL3.

Schwer, L. E. & Murray, Y. D. 1994. A three-invariant smooth cap model with mixed hardening. International Journal for Numerical and Analytical Methods in Geomechanics, 18, 657-688.

Scott, B., Park, R. & Priestley, M. Stress-strain behaviour of concrete confined by overlapping hoops at low and high strain rates. ACI Journal Proceedings, 1982. ACI.

Sekulovic, M., Salatic, R. & Nefovska, M. 2002. Dynamic analysis of steel frames with flexible connections. Computers & structures, 80, 935-955.

Sengupta, A. K. & Menon, D. 2010. Prestress concrete structures. Available: http://nptel.ac.in/courses/IIT-MADRAS/PreStressed_Concrete_Structures/pdf/1_Introduction/1.6_Concrete_II.pdf [Accessed 10/06/2014].

Sevin, E., Knoop, S., Belytschko, T., Briggs, G., Hall, W., Hoffman, B., Krauthammer, T., Walter Moore, j., Myerchin, B. & Robertson, L. 1995. Protecting Buildings from Bomb Damage. Transfer of Blast-Effects Mitigation Technologies from Military to Civilian Applications.

Shen, J., Lu, G., Wang, Z. & Zhao, L. 2010. Experiments on curved sandwich panels under blast loading. International Journal of Impact Engineering, 37, 960-970.

Shi, Y., Liang, Z. & Dan, W. 2005. Failure mode analysis for RC slab under explosive loads [J]. Journal of Shenyang Architectural and Civil Engineering Institute, 3.

Simo, J. C., Ju, J. W., Pister, K. S. & Taylor, R. L. 1990. Softening response completeness condition and numerical algorithms for cap model International journal for numerical methods in engineering.

Slawson, T. 1984. Dynamic shear failure of shallow-buried flat-roofed reinforced concrete structures subjected to blast loading. DTIC Document.

Smith, P. D. & Hetherington, J. G. 1994. Blast and ballistic loading of structures, Butterworth-Heinemann Oxford, UK.

Smith, P. D. & Rose, T. A. 2006. Blast wave propagation in city streets—an overview. Progress in structural engineering and materials, 8, 16-28.

Soroushian, P. & Choi, K.-B. 1987. Steel mechanical properties at different strain rates. Journal of Structural Engineering, 113, 663-672.

Soroushian, P. & Obaseki, K. Strain rate-dependent interaction diagrams for reinforced concrete sections. ACI Journal Proceedings, 1986. ACI.

Sozen, M. A. 1974. Hysteresis in structural elements. Applied mechanics in earthquake engineering, 8, 63-98.

Sparks, P. R. & Menzies, J. 1973. The effect of rate of loading upon the static and fatigue strengths of plain concrete in compression*. Magazine of Concrete Research, 25, 73-80.

Spooner, D. 1971. Stress-strain-time relationships for concrete. Magazine of Concrete Research, 23, 127-131.

Srikanth, M., Kumar, G. R. & Giri, S. 2007. Moment curvature of reinforced concrete beams using various confinement models and experimental validation. Asian Journal of Civil Engineering (Building and Housing), 8, 247-265.

Standards Australia 1997. AS 1012.17: Methods of testing concrete. Determination of the static chord modulus of elasticity and Poisson's ratio of concrete elements. Standards Australia.

Standards Australia 2000. AS 1012.11: Methods of testing concrete. Determination of Modulus of Rupture. Standards Australia.

Standards Australia 2001. AS/NZS 4671: Steel Reinforcing Materials.

Standards Australia 2009. AS3600-2009: Concrete Structures. Part1: Permanent, Imposed and Other actions. Standards Australia.

Standards Australia 2011. Structural Design Actions. AS 1170: 2: Wind Actions. Standards Australia.

Standards Australia 2014. AS 1012.9: Methods of testing concrete. Compressive strength tests - Concrete, mortar and grout specimens. Standards Australia.

Stanton, J. F. & McNiven, H. D. 1979. The development of a mathematical model to predict the flexural response of reinforced concrete beams to cyclic loads, using system identification.

Starr, C. M. & Krauthammer, T. 2005. Cladding-structure interaction under impact loads. Journal of Structural Engineering, 131, 1178.

Swegle, J. & Attaway, S. 1995. On the feasibility of using smoothed particle hydrodynamics for underwater explosion calculations. Computational Mechanics, 17, 151-168.

Swisdak, M. 1994. Simplified Kingery airblast calculations. Naval Surface Warfare Center,Indian Head Division.

Tabatabaei, Z. S., Volz, J. S., Gliha, B. P. & Keener, D. I. 2012. Development of Long Carbon Fiber Reinforced Concrete for Dynamic Strengthening. Journal of Materials in Civil Engineering.

Tai, Y., Chu, T., Hu, H. & Wu, J. 2011. Dynamic response of a reinforced concrete slab subjected to air blast load. Theoretical and Applied Fracture Mechanics, 56, 140-147.

Takeda, J.-i. Strain Rate Effects on Concrete and Reinforcements, and their Contributions to Structures. MRS Proceedings, 1985. Cambridge Univ Press, 15.

Takeda, J. & Tachikawa, H. 1962. The mechanical properties of several kinds of concrete at compressive, tensile, and flexural tests in high rates of loading. Transactions of the Architectural Institute of Japan, 77, 1-6.

Takeda, J. & Tachikawa, H. Deformation and fracture of concrete subjected to dynamic load. Proceedings of the Conference on Mechanical Behaviour of Materials., 1971.

Tanapornraweekit, G., Haritos, N., Mendis, P. & Ngo, T. 2007. Modelling of reinforced concrete panel subjected to blast load by explicit non-linear FE code. Proceedings of the Earthquake Engineering in Australia conference.

Tedesco, J. W. & Ross, C. A. 1993. Experimental and numerical analysis of high strain rate splitting-tensile tests. ACI Materials journal, 90.

The Portland Group 2011. PGI Visual Fortran. 12.8 ed.

Thorenfeldt, E., Tomasziewicz, A. & Jensen, J. J. 1987. Mechanical Properties of HSC and Application in Design. Proceedings of the Symposium Utilisation of High Strength Concrete. Tapir, Trondheim.

Timoshenko, S. P. 1921. LXVI. On the correction for shear of the differential equation for transverse vibrations of prismatic bars. The London, Edinburgh, and Dublin Philosophical Magazine and Journal of Science, 41, 744-746.

Tu, Z. & Lu, Y. 2009. Evaluation of typical concrete material models used in hydrocodes for high dynamic response simulations. International Journal of Impact Engineering, 36, 132-146.

Türkmen, H. 2002. Structural response of laminated composite shells subjected to blast loading: comparison of experimental and theoretical methods. Journal of Sound and Vibration, 249, 663-678.

United States Army Corps of Engineers 1986. TM5-855-1: Fundamentals for Protective Design for Conventional Weapons. Fundamentals for Protective Design for Conventional Weapons. US Army Corps of Engineers, US Army Waterways Experiment Station.

United States Army Corps of Engineers 1990. Structures to resist the effect of accidental explosions. TM5-1300, . Washington D.C: United states department of Army, United states department of Navy, United states department of Air Force.

United States Army Corps of Engineers 2008. Unified Facilities Criteria (UFC). Structures to Resist the Effects of Accidental Explosions. US Army Corps of Engineers, Naval Facilities Engineering Command, Air Force Civil Engineering Support Agency.

United states Department of State 2010. Country report on Terrorism. Washington, DC: United states Department of State-office of the coordinator for counterterrorism.

Unosson, M. 2000. Numerical simulations of penetration and perforation of high performance concrete with 75 mm steel projectile. Defence Research Establishment, Weapons and Protection Division, Tumba, Sweden.

Valanis, K. C. 1970. A theory of viscoplasticity without a yield surface. Part 1. General theory. Defence technical information centre.

Vasudevan, A. K. 2013. Finite Element Analysis and Experimental Comparison of Doubly Reinforced Concrete Slabs Subjected to Blast Loads. Master of Science, The University of Missouri-Kansass.

Vecchio, F. & Collins, M. 1981. Stress-strain characteristics of reinforced concrete in pure shear. Final report, 211-225.

Vecchio, F. J. & Collins, M. P. 1988. Predicting the response of reinforced concrete beams subjected to shear using the modified compression field theory. ACI Structural Journal, 85.

Wakabayashi, M., Nakamura, T., Yoshida, N., Iwai, S. & Watanabe, Y. Dynamic loading effects on the structural performance of concrete and steel materials and beams. Proceedings of the seventh world conference on earthquake engineering, 1980. 271-278.

Wang, F., Wan, Y. K. M., Chong, O. Y. K., Lim, C. H. & Lim, E. T. M. 2008. Reinforced Concrete Slab Subjected to Close-in Explosion. 7th LS-DYNA user forum. Bamberg, Germany.

Wang, W., Zhang, D., Lu, F., Wang, S.-C. & Tang, F. 2012. Experimental study on scaling the explosion resistance of a one-way square reinforced concrete slab under a close-in blast loading. International journal of impact engineering, 49, 158-164.

Watstein, D. Effect of straining rate on the compressive strength and elastic properties of concrete. ACI Journal Proceedings, 1953. ACI.

Willam, K. & Warnke, E. Constitutive model for the triaxial behaviour of concrete. Proceedings, International Association for Bridge and Structural Engineering, 1975. ISMES, Bergamo, Italy, 174.

Windham, J. E., Zimmerman, H. D. & Walker, R. E. 1993. Improved ground shock predictions for fully buried conventional weapons. Sixth International Symposium on the Interaction of Conventional Munitions with Protective Structures. Panama City, Florida.

Wong, H. D. 2013. Cylinder Strength Versus Cube Strength. Available: http://www.devb.gov.hk/filemanager/en/content_850/5_cylinder_strength_versus_cube_strength.pdf.

Wu, C., Oehlers, D. J., Rebentrost, M., Leach, J. & Whittaker, A. S. 2009. Blast testing of ultra-high performance fibre and FRP-retrofitted concrete slabs. Engineering Structures, 31, 2060-2069.

Wu, C. & Sheikh, H. 2012. A Finite Element Modeling to Investigate the Mitigation of Blast Effects on Reinforced Concrete Panel Using Foam Cladding. International journal of impact engineering.

Wu, Y., Crawford, J. E. & Magallanes, J. M. Performance of LS-DYNA concrete constitutive models. 12th International LS-DYNA Users conference, 2012.

Xu, K. & Lu, Y. 2006. Numerical simulation study of spallation in reinforced concrete plates subjected to blast loading. Computers & structures, 84, 431-438.

Yamaguchi, M., Murakami, K., Takeda, K. & Mitsui, Y. 2011. Blast resistance of polyethylene fiber reinforced concrete to contact detonation. Journal of Advanced Concrete Technology, 9, 63-71.

Yi, N.-H., Kim, J.-H. J., Han, T.-S., Cho, Y.-G. & Lee, J. H. 2012. Blast-resistant characteristics of ultra-high strength concrete and reactive powder concrete. Construction and Building Materials, 28, 694-707.

Yon, J.-H., Hawkins, N. M. & Kobayashi, A. S. 1992. Strain-rate sensitivity of concrete mechanical properties. ACI Materials Journal, 89.

Zhou, X., Kuznetsov, V., Hao, H. & Waschl, J. 2008. Numerical prediction of concrete slab response to blast loading. International journal of impact engineering, 35, 1186-1200.

Zineddin, M. & Krauthammer, T. 2007. Dynamic response and behaviour of reinforced concrete slabs under impact loading. International Journal of Impact Engineering, 34, 1517-1534.

APPENDIX A-I

DETERMINATION OF CONFINEMENT COEFFICIENT (MANDER'S METHOD)

The ratio of confined to the unconfined compressive strength of concrete is given by,

$$K = 1 + A\frac{f_1}{f_c'} \qquad (A.1)$$

Effective confining stress for a rectangular cross section is given by,

$$f_1 = k_e \rho_s f_y \qquad (A.2)$$

Confinement effective coefficient for a rectangular cross section is given by,

$$k_e = \frac{A_e}{A_{cc}} \qquad (A.3)$$

Effectively confined area for a rectangular cross section is given by (Refer to Figure A.1),

$$A_e = \left[b_c d_c - \sum_{i=1}^{n} \frac{W_i^2}{6}\right]\left(1 - \frac{s'}{2b_c}\right)\left(1 - \frac{s'}{2d_c}\right) \qquad (A.4)$$

Core area for a rectangular cross section is given by (Refer to Figure A.1),

$$A_{cc} = b_c d_c (1 - \rho_{sl}) \qquad (A.5)$$

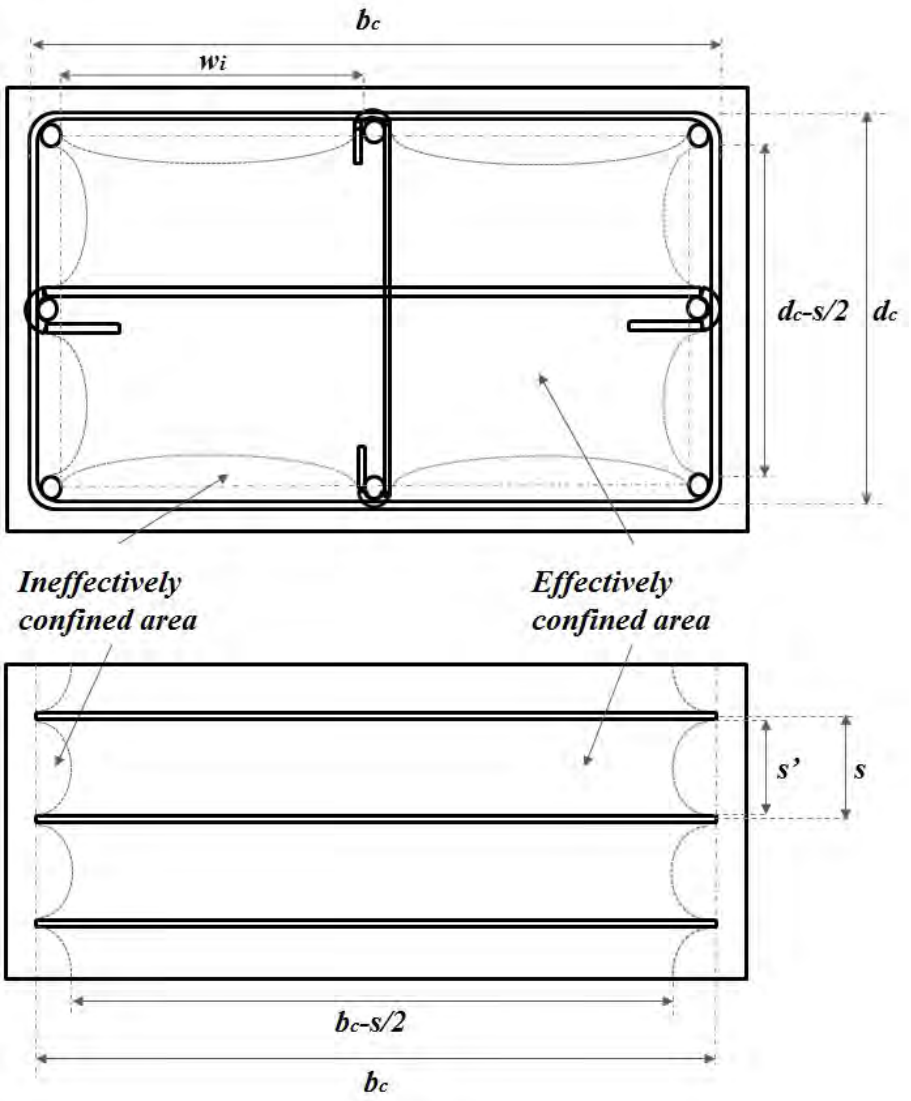

Figure A.1: Confined core concrete in rectangular sections

Notations and Definitions

A = 3.0

A_{cc} = Core area

A_e = Effectively confined area

b_c = Section core width (Centre to centre of hoops)

d_c = Section core depth (Centre to centre of hoops) (neutral axis depth in beams)

f_1 = Effective confining pressure

f_y = Yield strength of hoop reinforcement

K = Confinement Parameter

k_e = Confinement effective coefficient

n = Number of spacings between longitudinal bars

s' = Clear space between ties

W_i = i^{th} clear spacing between two longitudinal bars

ρ_s = Volumetric ratio of hoop reinforcement to concrete core area

ρ_{sl} = Ratio of longitudinal steel area to total core area

APPENDIX A-II

EXAMPLE CALCULATION USING UFC 3-340 FOR BLAST RESISTANT FACADE PANEL

Illustrative example: Panel A-1 (Pham, T. (2010))

These calculations illustrate the procedure for design of a one-way reinforced concrete section for the pressure time history relationship. Dimensions and the reinforcement configuration of constructed panels were selected to emulate the design process. All the calculations are in imperial units system as it will be easier to follow the UFC 3-340 (2008) design guidelines. Equations applied for the design process is referred back to equations given in this chapter where applicable.

Table A.1: Panel geometry and assumptions

Parameter	SI Units	Imperial Units (1 inch = 25 mm)
Panel Dimensions	1500 mm ×1000 mm × 80 mm	5 ft×3.33 ft×0.267 ft
Concrete Strength	46 MPa	6670 psi
Charge weight (cylindrical)	5.5 kg	12.125 lb
Standoff distance	2.1465 m	7.15 ft
Scaled Distance	1.216 m/kg$^{1/3}$	3.112 ft/lb$^{1/3}$
Maximum deflection criteria	3 times the elastic deflection (assumed)	

Design parameters

- Pressure time relationship

  Pressure time relationship is assumed as a triangular distribution having a maximum of Peak incident overpressure (P_{so}) and ignores the negative phase. The positive phase duration and the peak incident overpressure are determined using the scaled distance calculated and Figure 2.10 (Figure 2-7 in the UFC 3-340 (2008)).

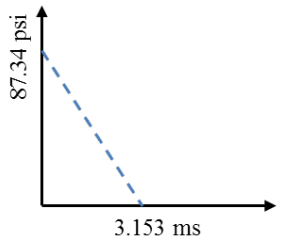

- Maximum deflection

  Assumed as 3 times the elastic deflection

- Cross section type

  Type I cross section with maximum allowable support rotation of 2^o

- Selected cross section

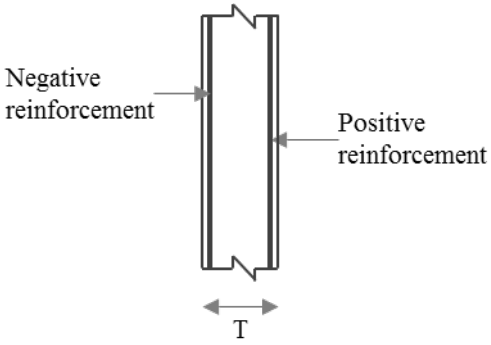

Section thickness : 80 mm (3.2 inch)

Minimum Cover : 7.5 mm (0.3 inch)

Reinforcement : 5 mm (0.2 inch) at 100 mm (4 inch) C/C

Concrete strength : 46 MPa (6670 psi)

Reinforcement strength: 630 MPa (91350 psi)

Dynamic increase factors, dynamic strength and dynamic design stresses

Dynamic increase factors, dynamic strength and dynamic design stresses are calculated used Table 4.6 (Table 4-1 in UFC 3-340) and Table 4.7 (Table 4-2 in UFC 3-340).

Table A.2: Rate enhancement factors and dynamic design stresses

Material/Parameter	Dynamic increase factors	Dynamic strength (psi)	Dynamic design stresses (psi)
Concrete			
Bending	1.19	7937.3	7937.3
Diagonal tension	1.00	6670	6670
Reinforcement			
Bending	1.17	106879.5	106879.5
Diagonal tension	1.00	91350	91350
Direct shear	1.10	100485	100485

Minimum steel ratios

Reinforcement and cover for both positive and negative directions are identical. Reinforcement in horizontal (transverse) direction is similar to that of vertical (longitudinal) direction.

Vertical reinforcement : 5 mm (0.2 inch) at 100 mm (4 inch) C/C

$$A_{sv} = 0.0314 \times \frac{12}{4} = 0.0942\ in^2/ft$$

$$Effective\ depth\ (d) = 3.2 - 0.3 - \frac{0.2}{2} = 2.8\ in$$

$$Reinforcement\ ratio\ (\rho_v) = \frac{0.0942}{12 \times 2.8} = 2.803 \times 10^{-3}$$

$$\rho_{v,min} = \frac{1.875\sqrt{f_c'}}{f_y} = \frac{1.875 \times \sqrt{6670}}{91350} = 1.676 \times 10^{-3}$$

$$< \rho_v \qquad Hence\ O.K$$

Horizontal Reinforcement : 5 mm (0.2 inch) at 100 mm (4 inch) C/C

$$A_{sh} = 0.0314 \times \frac{12}{4} = 0.0942\ in^2/ft$$

$$Effective\ depth\ (d) = 3.2 - 0.3 - \frac{0.2}{2} - 0.2 = 2.6\ in$$

$$Reinforcement\ ratio\ (\rho_h) = \frac{0.0942}{12 \times 2.6} = 3.019 \times 10^{-3}$$

$$\rho_{h,min} = \frac{1.25\sqrt{f_c'}}{f_y} = \frac{1.25 \times \sqrt{6670}}{91350} = 1.118 \times 10^{-3}$$

$$< \rho_h \qquad Hence\ O.K$$

Ultimate moment capacity of the section

- Depth of equivalent rectangular stress block

$$a = \frac{A_s f_{ds}}{0.85 b f_c'} = \frac{0.0942 \times 106879.5}{0.85 \times 12 \times 7937.3} = 0.124\ in$$

- Ultimate moment

$$M_u = \frac{A_s f_{ds}}{b}(d - a/2) = \frac{0.0942 \times 106879.5}{12}(2.8 - 0.124/2)$$
$$= 2297.2\ in - lb/in$$

Elastic modulus and modular ratio

$$Elastic\ modulus\ (E_c) = w^{1.5} \times 33(f_c')^{0.5} = 150^{1.5} \times 33 \times (6670)^{0.5}$$
$$= 4.95 \times 10^6\ psi$$

$$Modular\ ratio\ (n) = \frac{E_s}{E_c} = \frac{29 \times 10^6}{4.95 \times 10^6} = 5.86$$

Geometric section modulus and cracked section modulus

$$Geometric\ section\ modulus\ \left(I_g\right) = \frac{T^3}{12} = \frac{3.2^3}{12} = 2.731\ in^4/in$$

$$Average\ reinforcement\ ratio\ (\rho_{avg}) = \rho_v = 2.803 \times 10^{-3}$$

Using Figure 4-12 in UFC 3-340 (2008),

$$Coefficient\ for\ moment\ of\ Inertia\ in\ cracked\ section\ (F) = 0.0133$$

$$I_{cr} = F\left(d_{avg}\right)^3 = 0.0133(2.8)^3 = 0.262\ in^4/in$$

$$I_a = \frac{I_g + I_{cr}}{2} = \frac{2.731 + 0.262}{2} = 1.497\ in^4/in$$

Equivalent elastic stiffness

- Peak resistance

$$r_u = \frac{8M_p}{L^2} = \frac{8 \times 2297.2}{60^2} = 5.105\ psi$$

- Equivalent elastic unit stiffness

$$K_e = \frac{384EI}{5L^4} = \frac{384 \times 4.95 \times 10^6 \times 1.497}{5 \times 60^4} = 43.912\ in$$

- Load-Mass factor (Table 3-12 of UFC 3-340 (2008))

$$K_{LM,elastic} = 0.78$$

$$K_{LM,plastic} = 0.66$$

$$K_{LM,avg} = \frac{K_{LM,elastic} + K_{LM,plastic}}{2} = \frac{0.78 + 0.66}{2} = 0.72$$

- Unit mass of element

$$m = \frac{wT_c}{g} = \frac{150 \times 10^6}{32.2 \times 12^3} = 2695.8\ psi - ms^2/in$$

- Effective unit mass

  $m_e = K_{LM,avg} \times m = 0.72 \times 2695.8 = 1941\ psi - ms^2/in$

Natural period of vibration

$$T_N = 2\pi \left(\frac{m_e}{K_E}\right)^{0.5} = 2\pi \left(\frac{1941}{43.912}\right)^{0.5} = 41.77\ ms$$

Response chart parameters

$$P/r_u = 87.134/5.105 = 17.07$$

$$T/T_N = 3.153/41.77 = 0.0755$$

Using the Figure 3-65A or 3-65B in UFC 3-340 (2008),

$$X_m/X_E \approx 7 \geq 3\ (assumed);\ Hence\ section\ has\ to\ be\ redesigned.$$

Using the Figure 3-65A or 3-65B in UFC 3-340 (2008),

$$t_m/T_N = 0.61$$

$$t_m/t_0 = \frac{t_m/T}{T/T_N} = \frac{0.61}{0.0755} = 8.08 > 3;\ Hence\ section\ is\ not\ within\ the\ range\ of$$

$$0.1 < t_m/t_0 < 3\ and\ has\ to\ be\ redisgned\ with\ alternative\ dimensions.$$

This panel was constructed with the similar dimensions and same reinforcement configuration and tested under the exact same explosive charges. A maximum deflection of 38.5 mm has been recorded with the testing, which is about 1.5 times the 2^0 support rotation. Hence, it is beyond the applicability of Type I cross section assumed for the design. However, with similar dimensions, reinforcement configurations and charge weight standoff combination, but different fixing assemblies were able to resist the deflection within the 2^0 support rotation (Panels B1-B5, Pham, T. (2010). However, in the design process, both these panels are treated identical with pinned support conditions (or fixed, whatever applicable). However, partial fixities in supports are ignored, which has a considerable effect in these thinner, flexible panels, rather than thick, bulgy panels which UFC 3-340 is meant to be used for the design.

APPENDIX A-III

EXAMPLE CALCULATION USING UFC 3-340 FOR THE DETERMINATION OF SPALLING AND SECTION BREACH THRESHOLDS

Illustrative example: Panel B (Wang et al. (2012))

Table A.3: Panel details

Parameter	SI Units	Imperial Units
Panel Dimensions	750 mm ×750 mm × 30 mm	2.46 ft×2.46 ft×0.098 ft
Concrete Strength	Cube: 39.5 MPa	5727.5 psi
	Equivalent Cylinder: 31.2 MPa	4524 psi
Charge weight (cylindrical)	0.19 kg	0.423 lb
Charge diameter	26.6 mm	0.087 ft
Charge length	53.3 mm	0.175 ft
Standoff distance	0.3 m	0.984 ft
Casing for explosive	Not available	

Determination of spalling threshold

The cylindrical charge factor given as in equation 4.20,

$$C_f = \begin{cases} 1 + 2\left(\frac{LD}{\pi(3LD^2/16)^{0.667}} - 1\right)\left(1 - \frac{R}{2W^{0.333}}\right) & for\ L > D\ and\ \ R/W^{0.333} < 2 \\ 1.0 & for\ all\ other\ case \end{cases}$$

$L = 0.175\ ft; D = 0.087\ ft; R = 0.984\ ft\ and\ W = 0.423\ ft$

$L = 0.175\ ft > D = 0.087\ ft;\ R/W^{0.333} = 1.311\ ft/lb^{1/3}$

Therefore,

$$C_f = 1 + 2\left(\frac{LD}{\pi(3LD^2/16)^{0.667}} - 1\right)\left(1 - \frac{R}{2W^{0.333}}\right)$$

$$C_f = 1 + 2\left(\frac{0.175 \times 0.087}{\pi(3 \times 0.175 \times 0.087^2/16)^{0.667}} - 1\right)\left(1 - \frac{0.984}{2 \times 0.423^{0.333}}\right)$$

$$= 1 + 2(0.23)(0.345)$$

$$= 1.1587$$

Shape adjusted charge weight as given in equation 4.19,

$W_{adj} = B_f C_f W$

$B_f = 0.5\ (free\ air\ blast)$

$W_{adj} = 0.5 \times 1.1587 \times 0.423$

$W_{adj} = 0.5 \times 1.1587 \times 0.423$

$= 0.245$ lb

Spall parameter for free air blast is given in equation 4.17,

$$\psi = R^{0.926} f'^{0.266}_c W^{-0.353}_{adj} \left(\frac{W_{adj}}{W_{adj} + W_c}\right)^{0.333}$$

$$\psi = 0.984^{0.926} \times 4524^{0.266} \times 0.245^{-0.353} \left(\frac{0.245}{0.245 + 0}\right)^{0.333}$$

$= 15.188$

Using the Figure 4.6,

$h/R = 0.082$

$h = 0.082 \times 0.984$

$= 0.0807\ ft$

$= 0.0246\ m$

Hence, a minimum of 24.6 mm section is required to eliminate the possibility of spalling for the selected charge weight standoff combination. However, spalling has been observed with panel B during the experimental where a 30 mm panel section was utilized during the experimental investigation.

Determination of section breach threshold

Using the Figure 4.6,

$h/R = 0.073$

$h = 0.073 \times 0.984$

$= 0.0718\ ft$

$= 0.0219\ m$

Hence, a minimum of 21.9 mm section is required to eliminate the possibility of a section breach for the selected charge weight standoff combination. Section hasn't been

breached during the experimental evaluation with a 30 mm section, which confirms the UFC prediction equation for section breach threshold.

Table A.4 summarises the spalling and breaching threshold thicknesses for all six panels used during the Wang et al's (2009) experimental evaluation.

The panel A had a spall parameter (ψ) of 17.578, which is beyond the applicable maximum limit of 17, for the selected charge weight standoff combination. Therefore, the threshold thickness for spalling hasn't been calculated for Panel A. Among the other five panels, actual thicknesses of the panel were larger than the spalling threshold thicknesses in four panels where, panel F is the exception. This suggests that spalling should not be visible in panels B to E, although the spalling was visible in all six panels (Appendix B-IV).

Similar to the spalling threshold, the section breach threshold has also been calculated. All six panels had actual thicknesses greater than the required threshold thicknesses, suggesting no section breach should be visible. Acceptable predictions were observed as out of the six panels where, only one section was breached, which was observed with panel F (Appendix B-IV).

In fairness to the UFC, the minimum concrete thickness required to use this calculation hasn't been met in all six panels (minimum of 2 inches, Table 4.9). All other parameters were within the specified range to be used for the spalling and section breach threshold calculations. In addition, these calculations were limited to either spherical charge weights or cylindrical charge weights with the axis of explosive charge parallel to the panel surface. However, the orientation of the charge weights was not reported for these experimental tests, which were assumed to comply with the required orientation.

Table A.4: Summary of spalling and breaching threshold prediction

Panel ID	h (ft)	Explosive charge				C_f	W_{adj}	ψ	Spalling threshold		Breaching threshold	
		W (lb)	R (ft)	L (ft)	D (ft)				h/R	h (ft)	h/R	h (ft)
A	0.098	0.289	0.984	0.077	0.154	1.121	0.162	17.578	N/A	N/A	0.057	0.056
B	0.098	0.423	0.984	0.087	0.175	1.159	0.245	15.187	0.082	0.081	0.073	0.072
C	0.131	0.690	1.312	0.103	0.206	1.117	0.385	16.894	0.06	0.079	0.06	0.079
D	0.131	1.023	1.312	0.117	0.235	1.160	0.593	14.509	0.093	0.122	0.08	0.105
E	0.164	1.424	1.640	0.131	0.262	1.123	0.800	16.054	0.07	0.115	0.068	0.112
F	0.164	2.091	1.640	0.149	0.298	1.163	1.216	13.848	0.11	0.180	0.087	0.143

APPENDIX B-I

STRESS PLOTS FOR DIFFERENT MODEL COMBINATIONS – PANEL A1

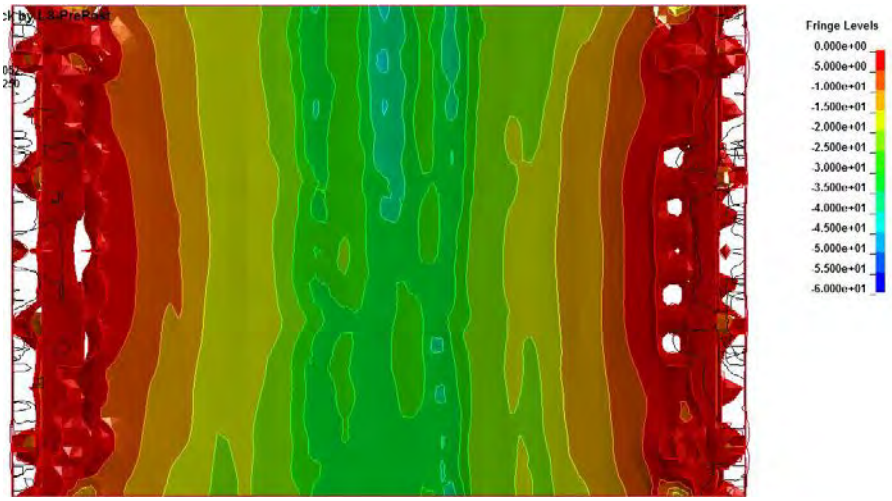

Figure B.1: Compressive stress plot for BGU/PK model combination

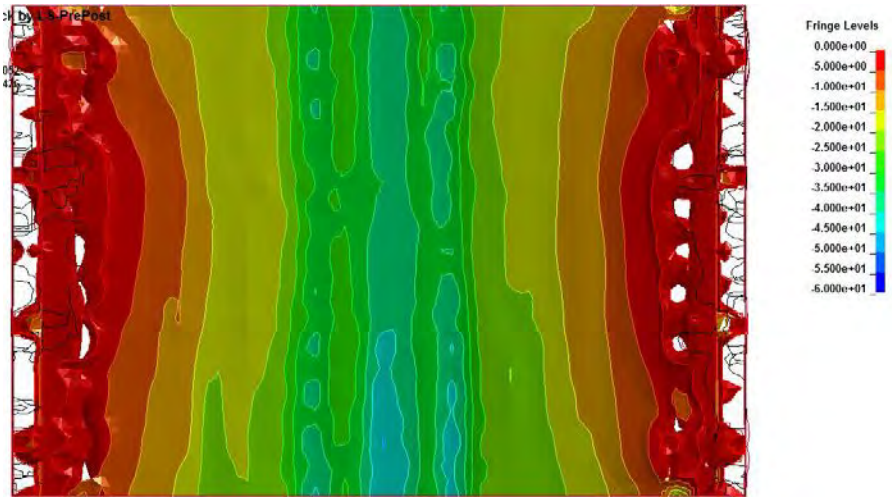

Figure B.2: Compressive stress plot for BGU/SJC model combination

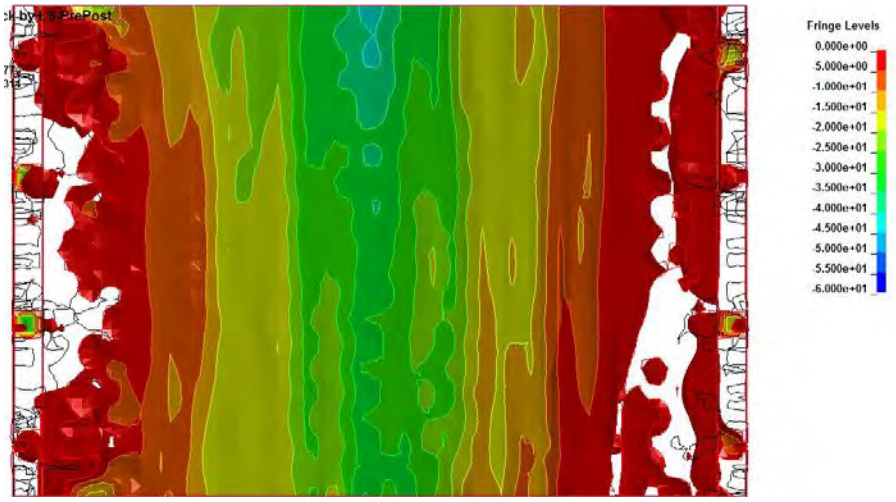

Figure B.3: Compressive stress plot for CDM/PK model combination

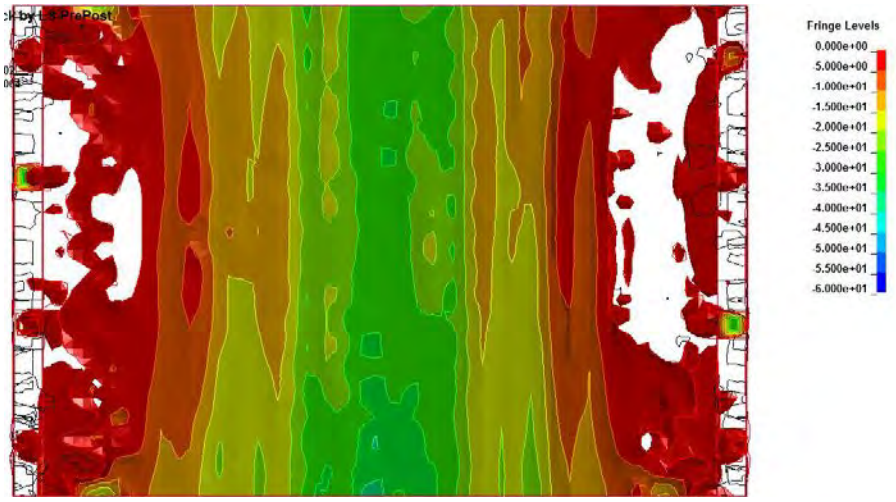

Figure B.4: Compressive stress plot for CDM/SJC model combination

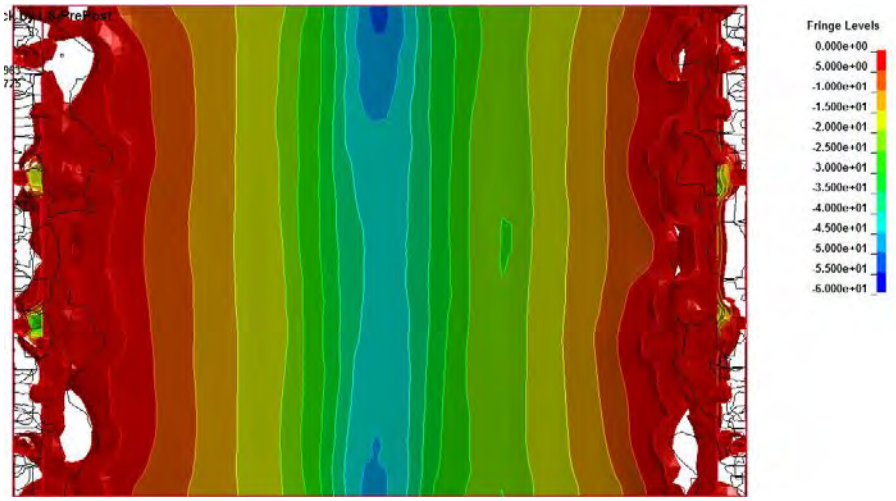

Figure B.5: Compressive stress plot for CSCM/PK model combination

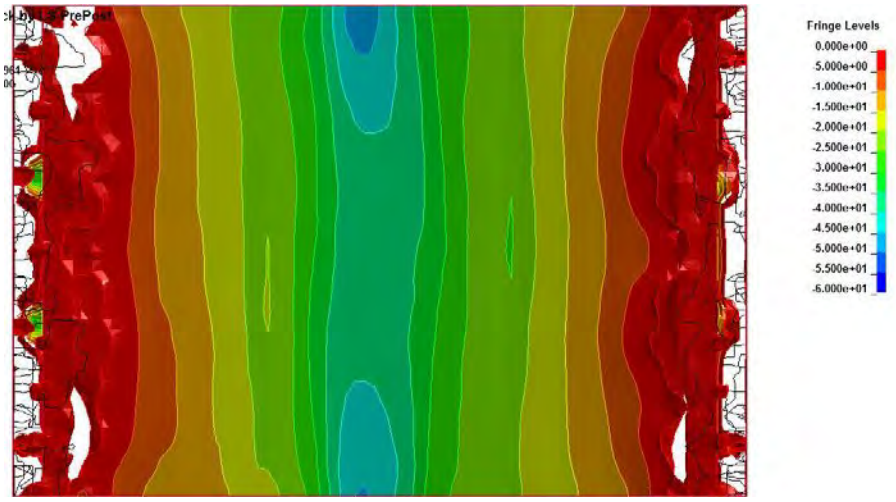

Figure B.6: Compressive stress plot for CSCM/SJC model combination

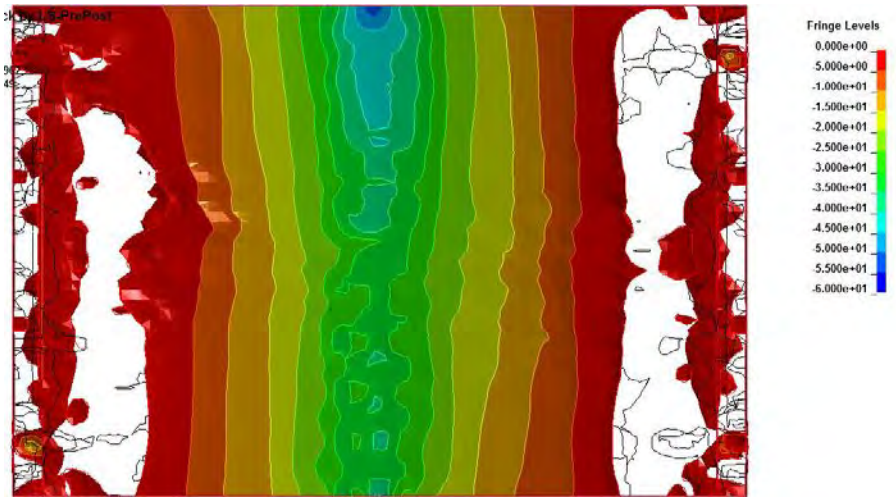

Figure B.7: Compressive stress plot for WCM/PK model combination

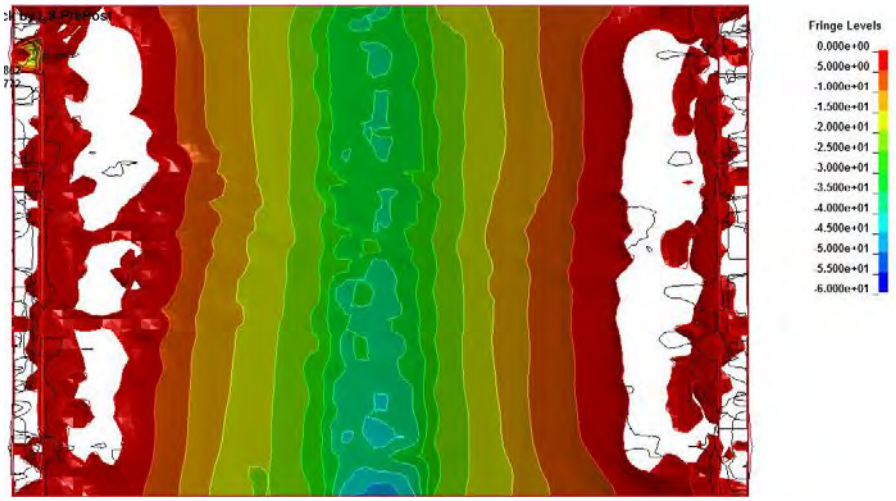

Figure B.8: Compressive stress plot for WCM/SJC model combination

APPENDIX B-II

STRESS PLOTS FOR DIFFERENT MODEL COMBINATIONS – PANEL B2

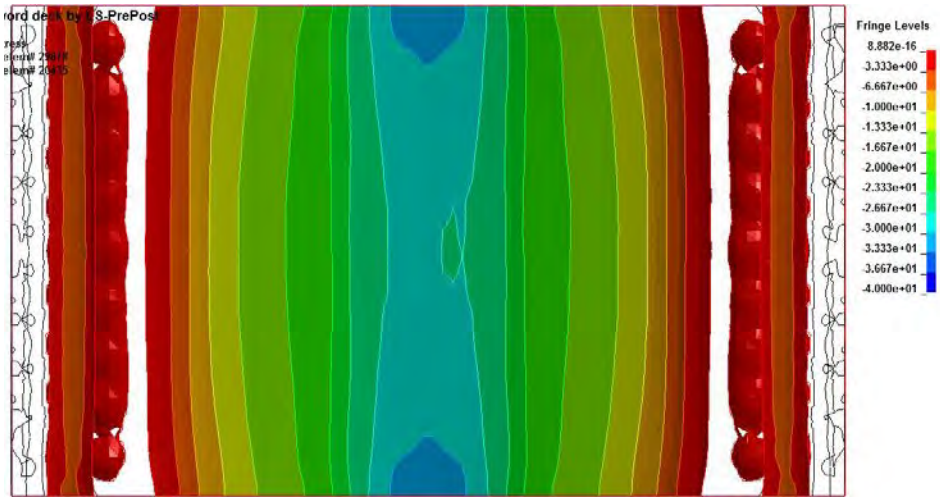

Figure B.9: Compressive stress plot for BGU/PK model combination

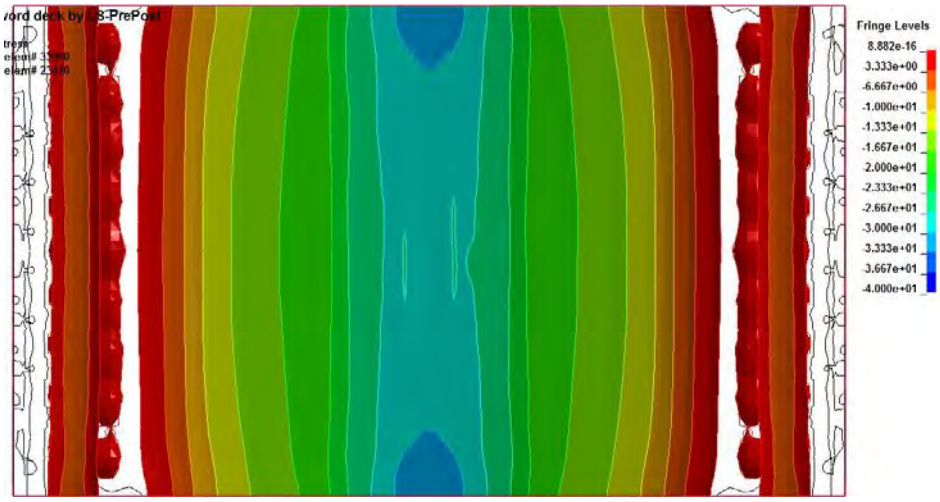

Figure B.10: Compressive stress plot for BGU/SJC model combination

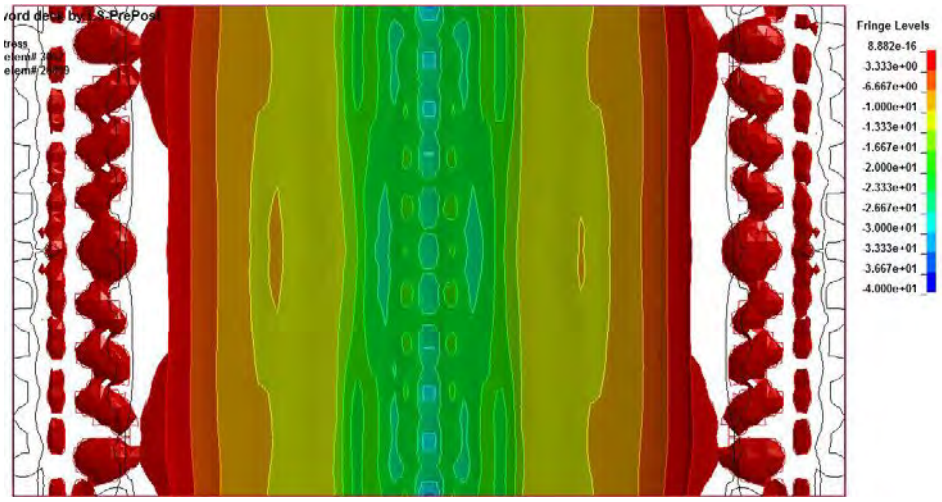

Figure B.11: Compressive stress plot for CDM/PK model combination

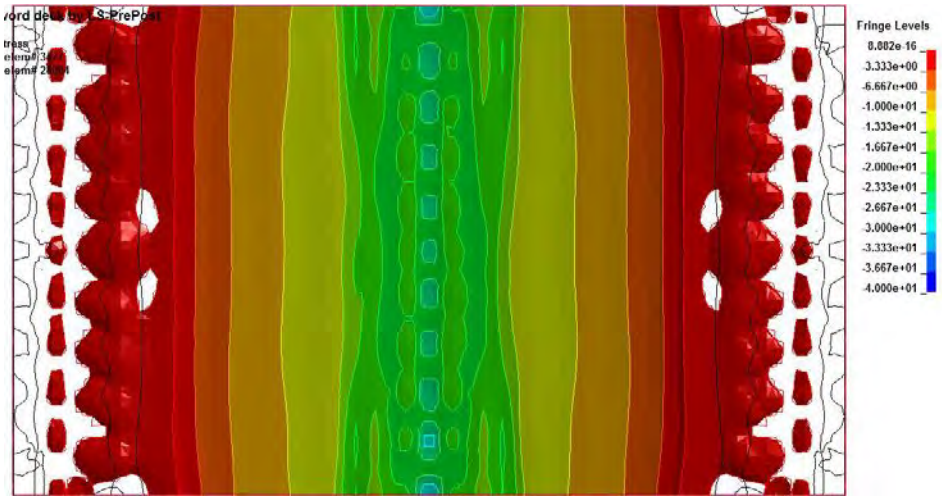

Figure B.12: Compressive stress plot for CDM/SJC model combination

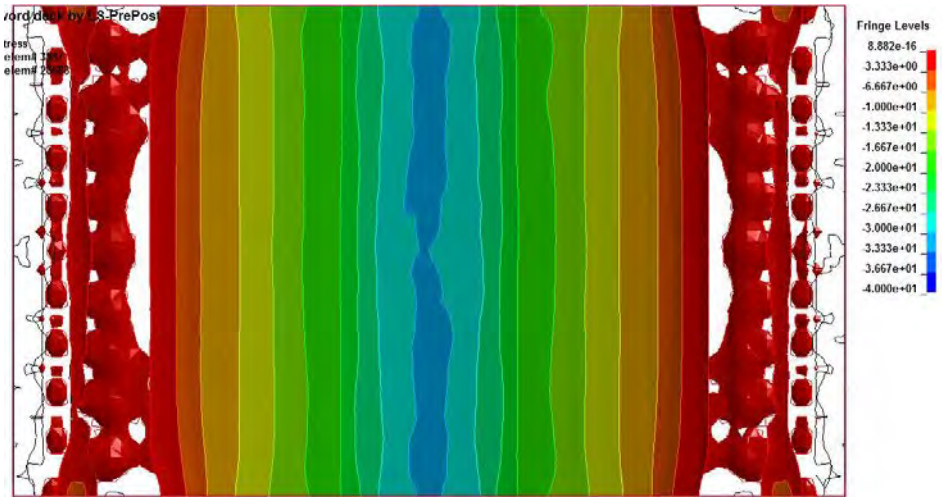

Figure B.13: Compressive stress plot for CSCM/PK model combination

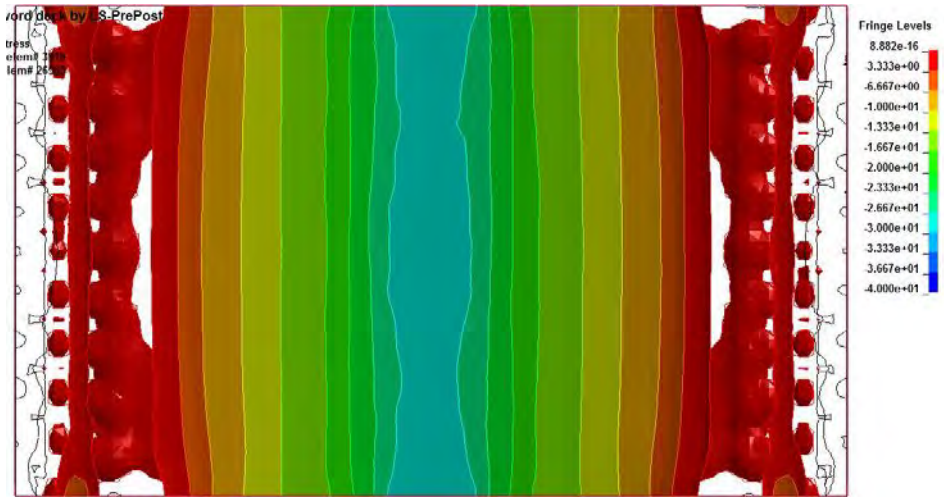

Figure B. 14: Compressive stress plot for CSCM/SJC model combination

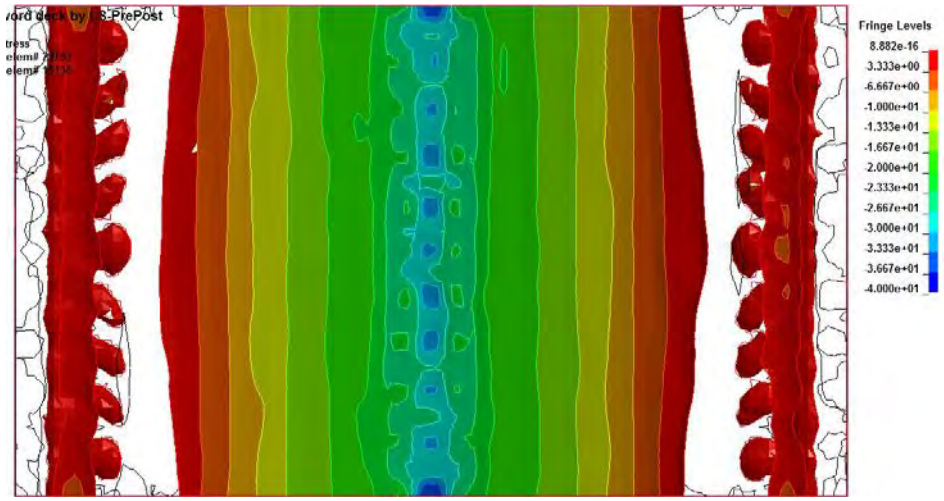

Figure B.15: Compressive stress plot for WCM/PK model combination

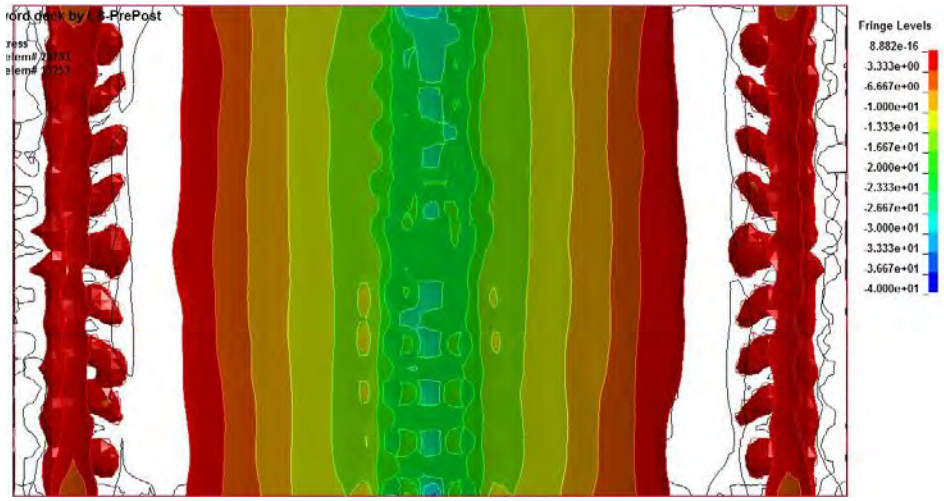

Figure B.16: Compressive stress plot for WCM/SJC model combination

APPENDIX B-III

STRESS PLOTS FOR NUMERICAL MODEL VALIDATION – PANELS B1, B3, B4 AND B5

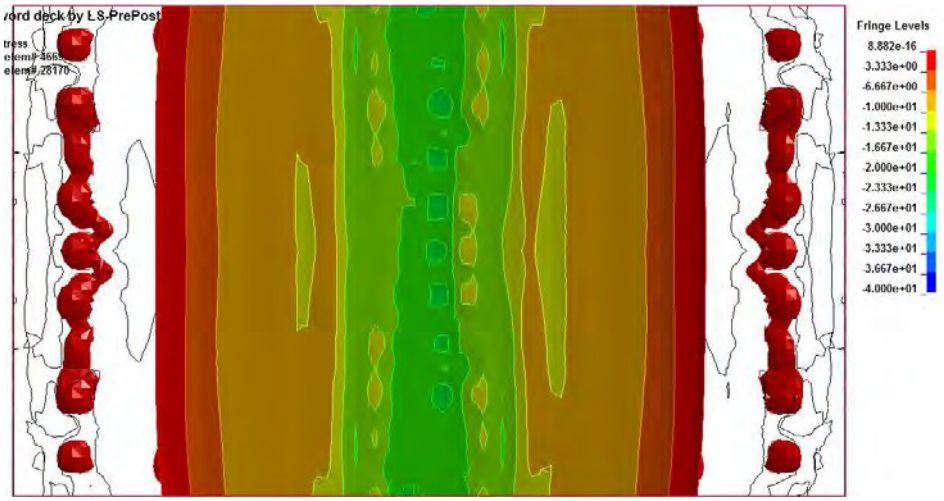

Figure B.17: Compressive stress plot for Panel B1

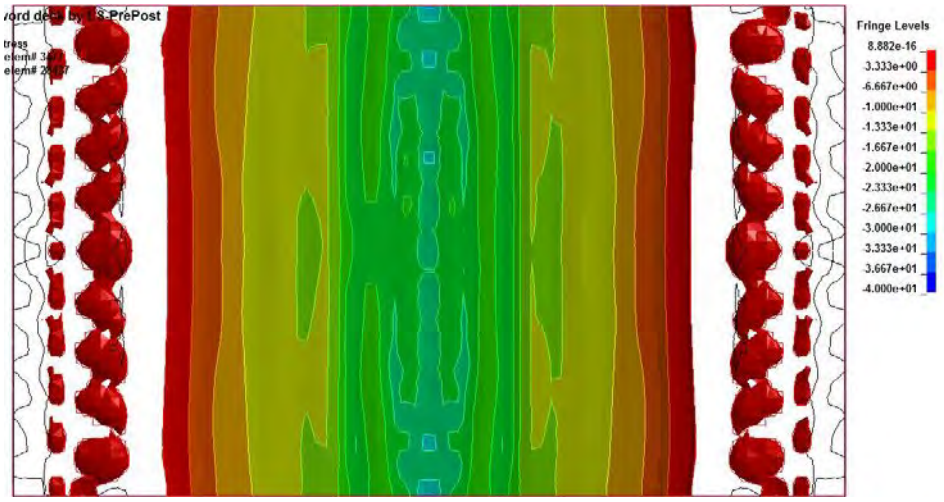

Figure B.18: Compressive stress plot for Panel B3

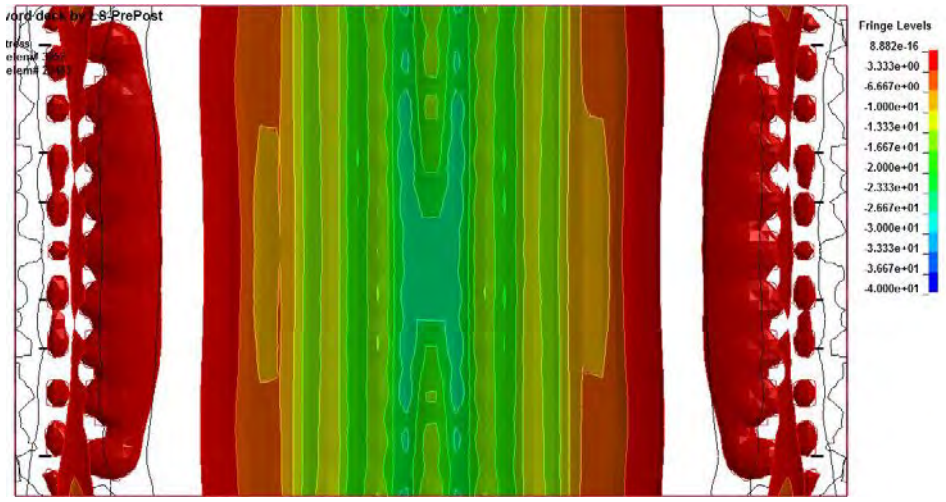

Figure B.19: Compressive stress plot for Panel B4

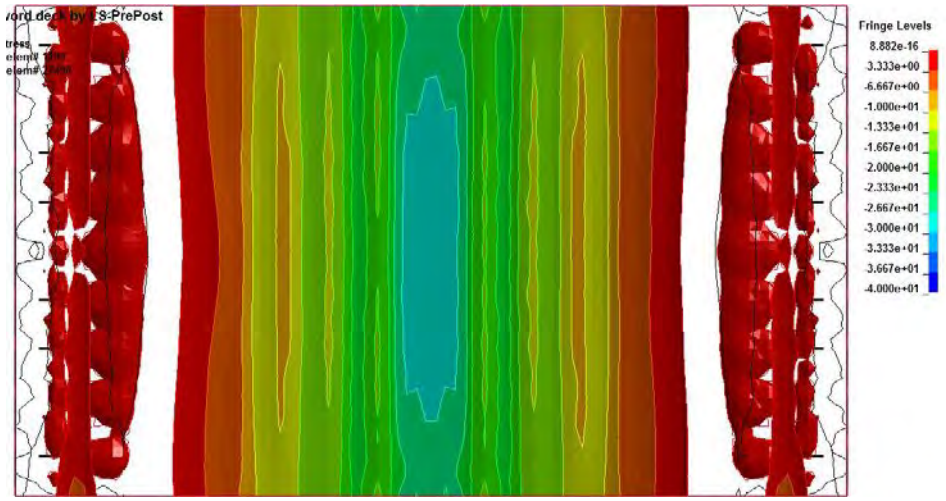

Figure B.20: Compressive stress plot for Panel B5

APPENDIX B-IV

SPALLING AND DAMAGE PARAMETER COMPARISON FOR NUMERICAL MODEL VALIDATION

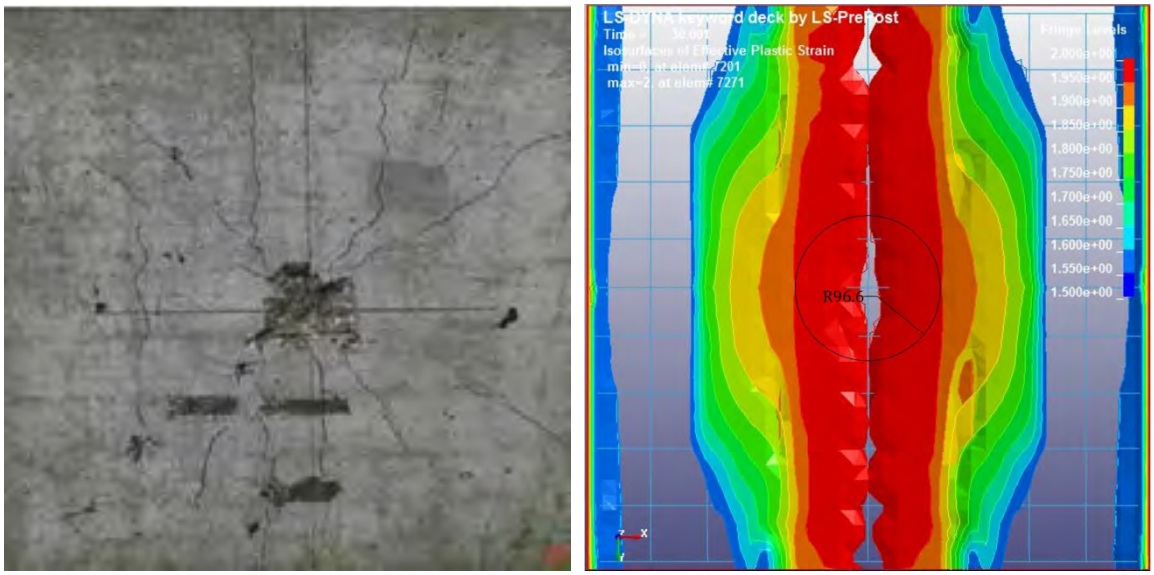

(a) (b)

Figure B.21: (a) Spalling damage and (b) Damage Parameter for Panel A

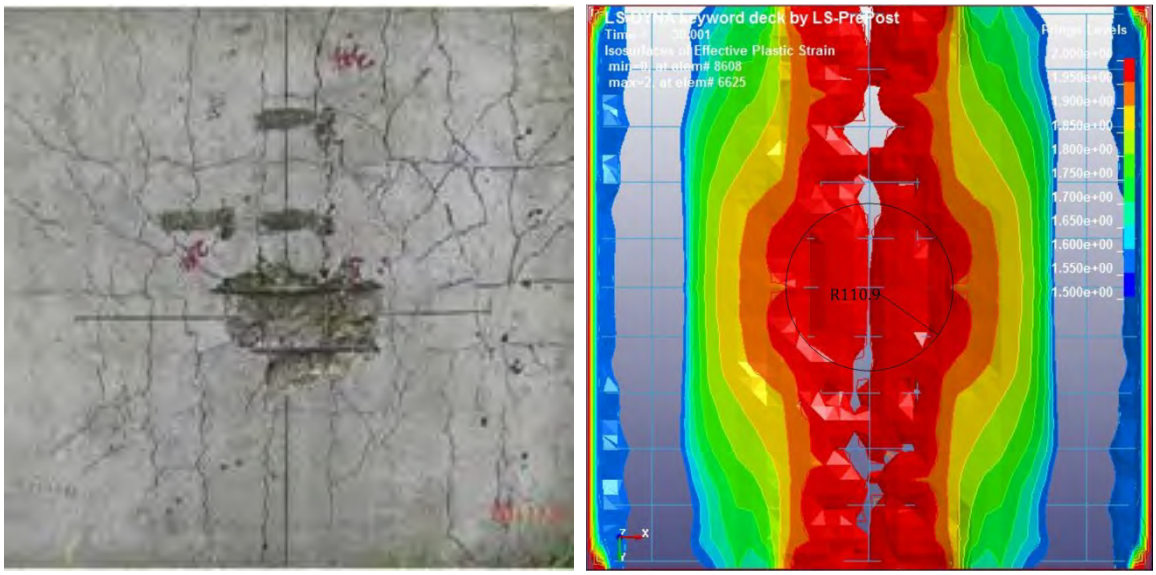

(a) (b)

Figure B.22: (a) Spalling damage and (b) Damage Parameter for Panel B

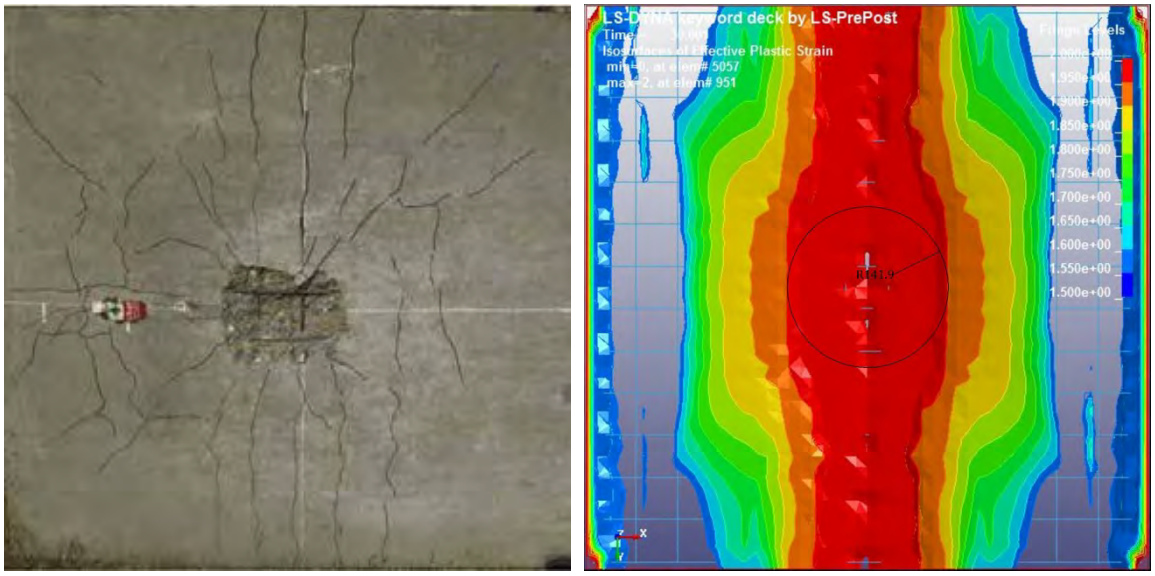

(a) (b)

Figure B.23: (a) Spalling damage and (b) Damage Parameter for Panel C

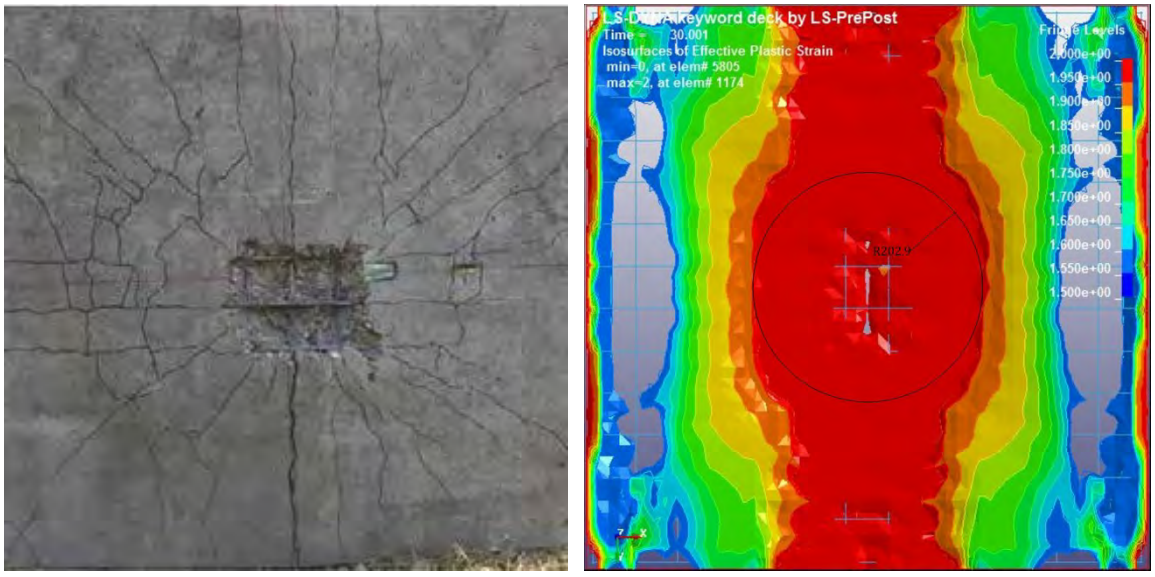

(a) (b)

Figure B.24: (a) Spalling damage and (b) Damage Parameter for Panel D

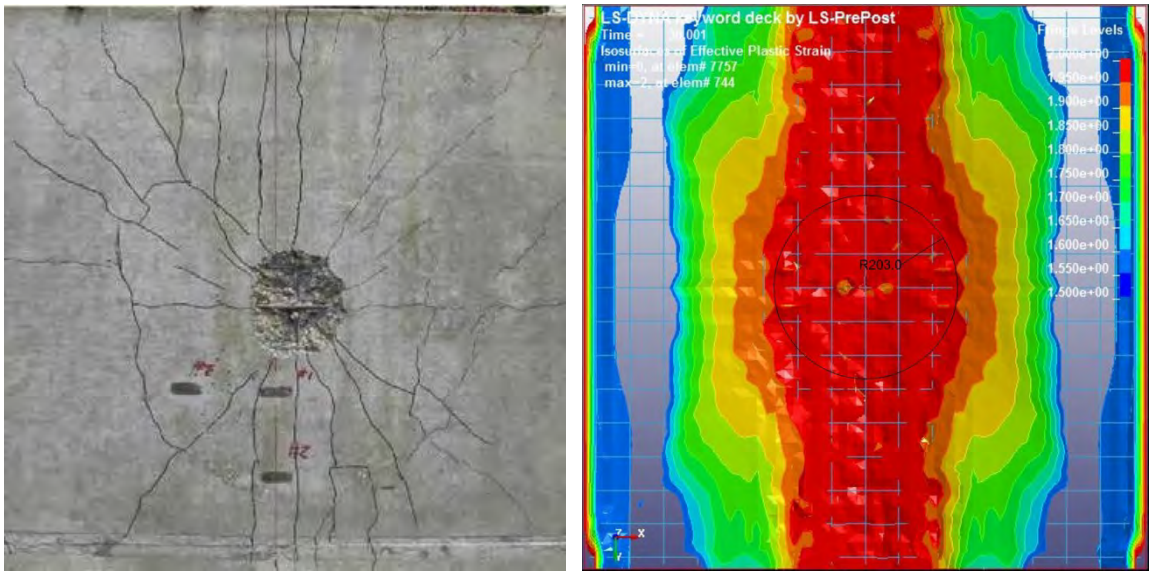

(a) (b)

Figure B.25: (a) Spalling damage and (b) Damage Parameter for Panel E

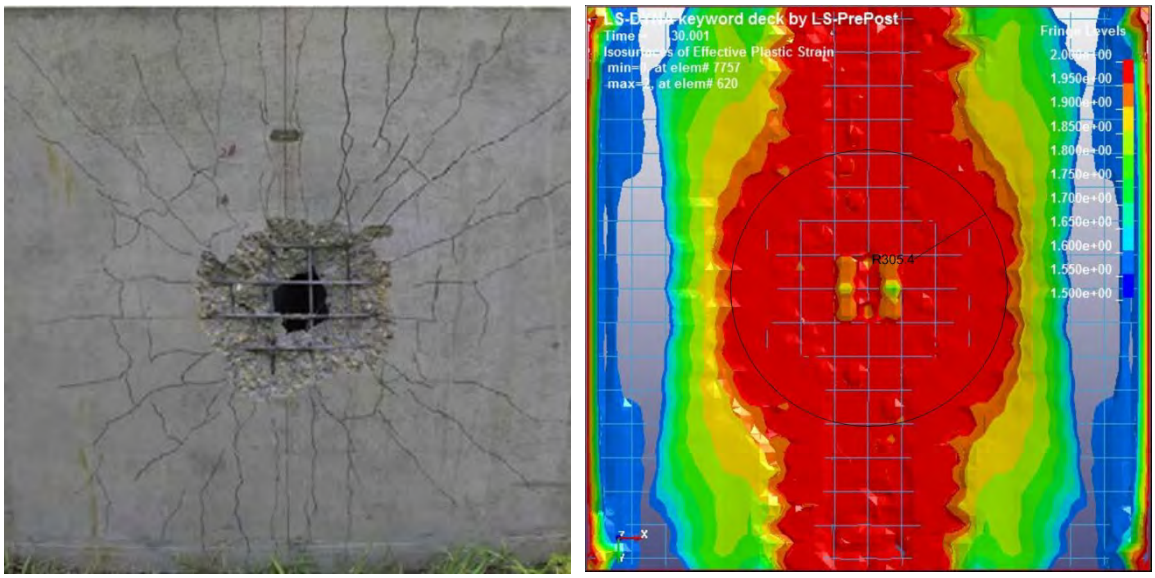

(a) (b)

Figure B.26: (a) Spalling damage and (b) Damage Parameter for Panel F

APPENDIX C-I

FORMULATION OF MODIFIED SCOTT MODEL FOR CONCRETE

The stress-strain relationship used for the definition of modified Scott model is presented in Figure C.1.

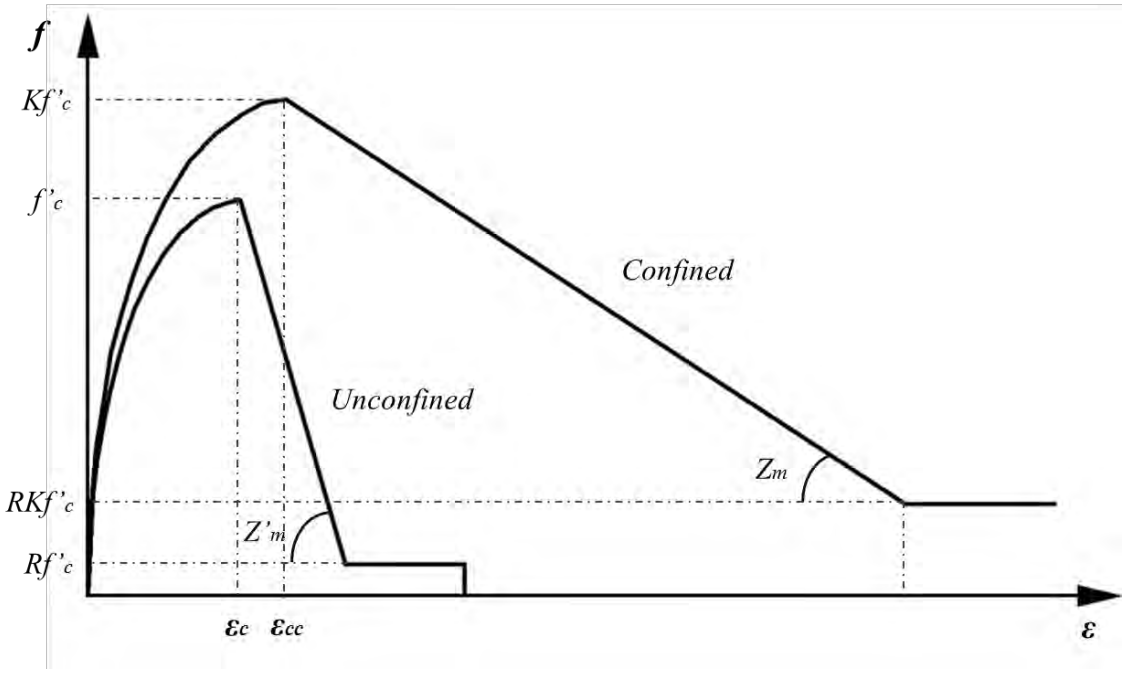

Figure C.1: Stress-strain diagram for the modified Scott model

The parabolic ascending portion of the curve for confined concrete is given by,

$$f = Kf_c' \left[\frac{2\varepsilon}{\varepsilon_{cc}} - \left(\frac{\varepsilon}{\varepsilon_{cc}}\right)^2\right] for\ \varepsilon \leq \varepsilon_{cc} \qquad (C.1)$$

The linear descending portion of the curve for confined concrete is given by,

$$f = Kf_c'[1 - Z_m(\varepsilon - \varepsilon_{cc})] \geq f_{res}\ for\ \varepsilon > \varepsilon_{cc} \qquad (C.2)$$

The residual stress for confined concrete is given by,

$$f_{res} = RKf_c' \qquad (C.3)$$

$$R = 0.28 - 0.0032f_c'\ , R \geq 0 \qquad (C.4)$$

The softening slope for confined concrete is given by,

$$Z_m = Z\frac{0.5}{\frac{3+0.29f_c'}{145f_c'-1000}+\frac{3}{4}\rho_s\sqrt{\frac{h''}{s_h}}-\varepsilon_{cc}} \quad (C.5)$$

$$Z = 0.018f_c' + 0.55 \quad (C.6)$$

Strain at maximum stress for confined concrete is given by,

$$\varepsilon_{cc} = (0.24K^3 + 0.76)\varepsilon_c \quad (C.7)$$

$$\varepsilon_c = \frac{4.26f_c'}{\sqrt[4]{f_c'}E_c} \quad (C.8)$$

$$E_c = 9500(f_c')^{0.3} \quad (C.9)$$

The parabolic ascending portion of the curve for unconfined concrete is given by,

$$f = f_c'\left[\frac{2\varepsilon}{\varepsilon_c}-\left(\frac{\varepsilon}{\varepsilon_c}\right)^2\right] for\ \varepsilon \le \varepsilon_c \quad (C.10)$$

The linear descending portion of the curve for unconfined concrete is given by,

$$f = f_c'[1 - Z_m'(\varepsilon - \varepsilon_c)] \ge f_{res}'\ for\ \varepsilon > \varepsilon_c \quad (C.11)$$

The residual stress for unconfined concrete is given by,

$$f_{res}' = f_c'(0.28 - 0.0032f_c') \ge 0 \quad (C.12)$$

The softening slope for unconfined concrete is given by,

$$Z_m' = Z\frac{0.5}{\frac{3+0.29f_c'}{145f_c'-1000}-\varepsilon_c} > 0 \quad (C.13)$$

Notations and Definitions

f = Stress

f_c' = Cylinder compressive strength of concrete

f_{res} = Residual stress of confined concrete

f_{res}' = Residual stress of unconfined concrete

h'' = Width of the concrete core

K = Confinement coefficient (Equation A.1)

R = Residual strength factor

s_h = Centre to centre spacing between hoop reinforcement

Z_m = Softening slope for confined concrete

Z_m' = Softening slope for unconfined concrete

ε = Strain

ε_{cc} = Strain at maximum stress for confined concrete

ε_c = Strain at maximum stress for unconfined concrete

ρ_s = Volumetric ratio of hoop reinforcement

APPENDIX C-II

FORMULATION OF SOFTENED MEMBRANE MODEL FOR CONCRETE

Stress equilibrium equations for the softening membrane model is given by,

$$\sigma_l = \sigma_2^c cos^2\alpha_2 + \sigma_1^c sin^2\alpha_2 + \tau_{21}^c 2sin\alpha_2 cos\alpha_2 + \rho_l f_l \quad (C.14)$$

$$\sigma_t = \sigma_2^c sin^2\alpha_2 + \sigma_1^c cos^2\alpha_2 - \tau_{21}^c 2sin\alpha_2 cos\alpha_2 + \rho_t f_t \quad (C.15)$$

$$\tau_{lt} = (-\sigma_2^c + \sigma_1^c) sin\alpha_2 cos\alpha_2 + \tau_{21}^c (cos^2\alpha_2 - sin^2\alpha_2) \quad (C.16)$$

Strain compatibility equations for the softening membrane model is given by,

$$\varepsilon_l = \varepsilon_2 cos^2\alpha_2 + \varepsilon_1 sin^2\alpha_2 + \frac{\gamma_{21}}{2} 2sin\alpha_2 cos\alpha_2 \quad (C.17)$$

$$\varepsilon_t = \varepsilon_1 cos^2\alpha_2 + \varepsilon_2 sin^2\alpha_2 - \frac{\gamma_{21}}{2} 2sin\alpha_2 cos\alpha_2 \quad (C.18)$$

$$\frac{\gamma_{lt}}{2} = (-\varepsilon_2 + \varepsilon_1) sin\alpha_2 cos\alpha_2 + \frac{\gamma_{21}}{2} (cos^2\alpha_2 - sin^2\alpha_2) \quad (C.19)$$

Coordinate system for steel bars and principal applied stresses is presented in Figure C.2.

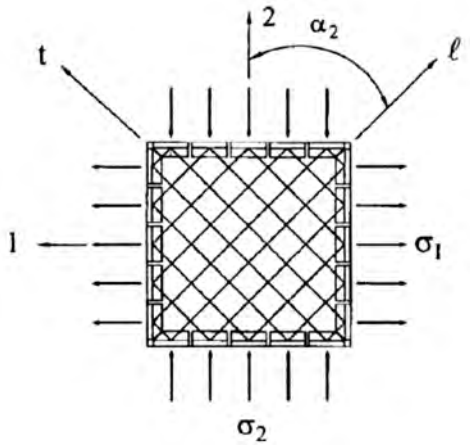

Figure C.2: Coordinate system for steel bars and principal applied stresses (Source: Hsu and Zhu, 2002)

In figure C.2, $l-t$ coordinate represents the direction of longitudinal and transverse steel bars, $2-1$ coordinate represents the direction of principal applies stresses σ_2 and σ_1 and α_2 is the angle between $l-t$ coordinate and $2-1$ coordinate.

The constitutive matrix of smeared concrete subjected to bi-axial loading, defined using the $2-1$ coordinate system is given by,

$$\begin{Bmatrix} \sigma_2^c \\ \sigma_1^c \\ \tau_{21}^c \end{Bmatrix} = \begin{bmatrix} E_2^c & \upsilon_{21}E_2^c & 0 \\ \upsilon_{12}E_1^c & E_1^c & 0 \\ 0 & 0 & G_{21}^c \end{bmatrix} \begin{Bmatrix} \varepsilon_2 \\ \varepsilon_1 \\ \gamma_{21} \end{Bmatrix} \qquad (C.20)$$

The constitutive matrix for steel reinforcing bars, which form the $l-t$ coordinate system is given by

$$\begin{Bmatrix} \rho_l f_l \\ \rho_t f_t \\ 0 \end{Bmatrix} = \begin{bmatrix} \rho_l E_l^s & 0 & 0 \\ 0 & \rho_t E_t^s & 0 \\ 0 & 0 & 0 \end{bmatrix} \begin{Bmatrix} \varepsilon_l \\ \varepsilon_t \\ 0 \end{Bmatrix} \qquad (C.21)$$

The constitutive relationship between uniaxial stress and strain in $2-1$ direction, considering Hsu/Zhu ratios is given by,

$$\varepsilon_1 = \frac{\sigma_1^c}{\bar{E}_1^c} - \upsilon_{12}\frac{\sigma_2^c}{\bar{E}_2^c} \qquad (C.22)$$

$$\varepsilon_2 = \frac{\sigma_2^c}{\bar{E}_2^c} - \upsilon_{21}\frac{\sigma_1^c}{\bar{E}_1^c} \qquad (C.23)$$

The constitutive relationship between bi-axial stress and strain in $2-1$ direction is given by,

$$\bar{\varepsilon_1} = \frac{\sigma_1^c}{\bar{E}_1^c} \qquad (C.24)$$

$$\bar{\varepsilon_2} = \frac{\sigma_2^c}{\bar{E}_2^c} \qquad (C.25)$$

The uniaxial strains using the bi-axial strain and Hsu/Zhu ratios is given by,

$$\varepsilon_1 = \bar{\varepsilon_1} - \upsilon_{12}\bar{\varepsilon_2} \qquad (C.26)$$

$$\varepsilon_2 = \bar{\varepsilon_2} - \upsilon_{21}\bar{\varepsilon_1} \qquad (C.27)$$

A graphical representation of uniaxial and bi-axial stress-strain is given in Figure C.3, blow.

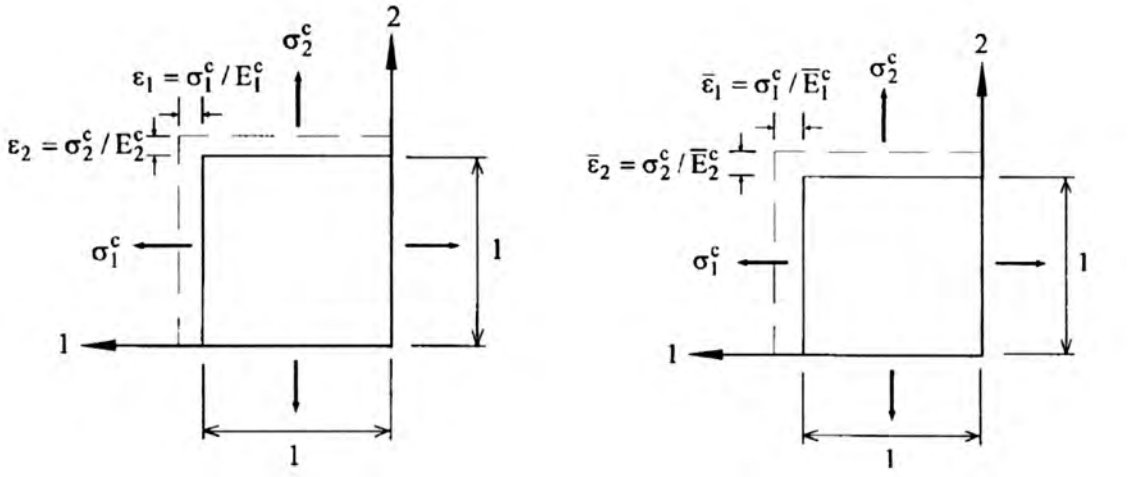

(a) **(b)**

Figure C.3: (a) bi-axial strain condition considering Hsu/Zhu ratios and (b) uniaxial strain condition neglecting Hsu/Zhu ratios for reinforced concrete sections (Source: Hsu and Zhu, 2002)

Bi-axial strains expressed in terms of uniaxial strain, rearranging the equations C.26 and C.27 and assuming non zero Hsu/Zhu ratios, is given by,

$$\bar{\varepsilon}_1 = \frac{1}{1 - v_{12}v_{21}}\varepsilon_1 + \frac{v_{12}}{1 - v_{12}v_{21}}\varepsilon_2 \qquad (C.28)$$

$$\bar{\varepsilon}_2 = \frac{v_{21}}{1 - v_{12}v_{21}}\varepsilon_1 + \frac{1}{1 - v_{12}v_{21}}\varepsilon_2 \qquad (C.29)$$

Substituting bi-axial strains in equation C.16,

$$\begin{Bmatrix} \sigma_2^c \\ \sigma_1^c \\ \tau_{21}^c \end{Bmatrix} = \begin{bmatrix} \frac{\bar{E}_2^c}{1 - v_{12}v_{21}} & \frac{v_{21}\bar{E}_2^c}{1 - v_{12}v_{21}} & 0 \\ \frac{v_{21}\bar{E}_1^c}{1 - v_{12}v_{21}} & \frac{\bar{E}_1^c}{1 - v_{12}v_{21}} & 0 \\ 0 & 0 & G_{21}^c \end{bmatrix} \begin{Bmatrix} \varepsilon_2 \\ \varepsilon_1 \\ \gamma_{21} \end{Bmatrix} \qquad (C.30)$$

Smeared (average) strains in steel bars in $l - t$ direction are given by,

$$\bar{\varepsilon}_l = \bar{\varepsilon}_2 cos^2\alpha_2 + \bar{\varepsilon}_1 sin^2\alpha_2 + \frac{\gamma_{21}}{2} 2sin\alpha_2 cos\alpha_2 \qquad (C.31)$$

$$\bar{\varepsilon}_t = \bar{\varepsilon}_1 cos^2\alpha_2 + \bar{\varepsilon}_2 sin^2\alpha_2 - \frac{\gamma_{21}}{2} 2 sin\alpha_2 cos\alpha_2 \quad (C.32)$$

Strain compatibility equations using Hsu/Zhu ratios and smeared strains along the $l-t$ direction is given by,

$$\varepsilon_l = \bar{\varepsilon}_l - v_{12}\bar{\varepsilon}_2 sin^2\alpha_2 - v_{21}\bar{\varepsilon}_1 cos^2\alpha_2 \quad (C.33)$$

$$\varepsilon_t = \bar{\varepsilon}_t - v_{12}\bar{\varepsilon}_2 cos^2\alpha_2 - v_{21}\bar{\varepsilon}_1 sin^2\alpha_2 \quad (C.34)$$

$$\bar{\varepsilon}_l = \frac{f_l}{\bar{E}_l^s} \quad (C.35)$$

$$\bar{\varepsilon}_t = \frac{f_t}{\bar{E}_t^s} \quad (C.36)$$

Equations C.33 and C.34 can be rearranged using equations C.35 and C.36 as,

$$\begin{Bmatrix} \rho_l f_l \\ \rho_t f_t \\ 0 \end{Bmatrix} = \begin{bmatrix} \rho_l \bar{E}_l^s & 0 & 0 \\ 0 & \rho_t \bar{E}_t^s & 0 \\ 0 & 0 & 0 \end{bmatrix} \begin{Bmatrix} \varepsilon_l \\ \varepsilon_t \\ 0 \end{Bmatrix} + \begin{Bmatrix} v_{12}(\rho_l \bar{E}_l^s \bar{\varepsilon}_2 sin^2\alpha_2) + v_{21}(\rho_l \bar{E}_l^s \bar{\varepsilon}_1 cos^2\alpha_2) \\ v_{12}(\rho_t \bar{E}_t^s \bar{\varepsilon}_2 cos^2\alpha_2) + v_{21}(\rho_t \bar{E}_t^s \bar{\varepsilon}_1 sin^2\alpha_2) \\ 0 \end{Bmatrix} \quad (C.37)$$

Constitutive relationships for compressive stress-strain in concrete is given by,

$$\sigma_2^c = \xi f_c' \left[1 - \left(\frac{\bar{\varepsilon}_2/\xi\,\varepsilon_0 - 1}{4/\xi - 1} \right)^2 \right] for\ \frac{\bar{\varepsilon}_2}{\xi \varepsilon_0} > 1 \quad (C.38)$$

$$\sigma_2^c = \xi f_c' \left[2\left(\frac{\bar{\varepsilon}_2}{\xi \varepsilon_0} \right) - \left(\frac{\bar{\varepsilon}_2}{\xi \varepsilon_0} \right)^2 \right] for\ \frac{\bar{\varepsilon}_2}{\xi \varepsilon_0} \leq 1 \quad (C.39)$$

$$\xi = \frac{5.8}{\sqrt{f_c'}} \frac{1}{\sqrt{1 + \frac{400\bar{\varepsilon}_1}{\eta'}}} \leq 0.9 \quad (C.40)$$

$$\eta = \frac{\rho_t f_{ty} - \sigma_t}{\rho_l f_{ly} - \sigma_l} \quad (C.41)$$

$$\eta' = \begin{cases} \eta & for\ \eta \leq 1 \\ 1/\eta & for\ \eta > 1 \end{cases} \quad (C.42)$$

Compressive stress-strain in concrete is graphically represented in Figure C.4.

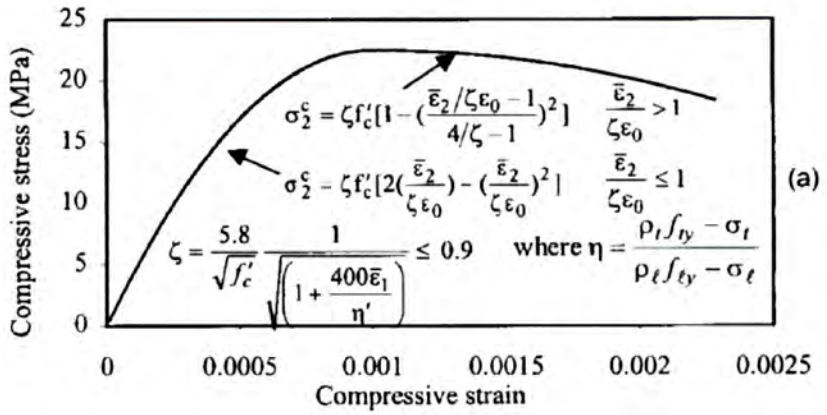

Figure C.4: Constitutive relationship for compressive stress-strain in concrete (Source: Hsu and Zhu, 2002)

Constitutive relationships for tensile stress-strain in concrete is given by,

$$\sigma_1^c = E_c \bar{\varepsilon}_1 \qquad for\ \bar{\varepsilon}_1 \le \varepsilon_{cr} \tag{C.43}$$

$$\sigma_1^c = f_{cr}\left(\frac{\varepsilon_{cr}}{\bar{\varepsilon}_1}\right)^{0.4} \qquad for\ \bar{\varepsilon}_1 \le \varepsilon_{cr} \tag{C.44}$$

$$E_c = 3875\sqrt{f_c'} \tag{C.45}$$

$$f_{cr} = 0.31\sqrt{f_c'} \tag{C.46}$$

$$\varepsilon_{cr} = \frac{f_{cr}}{E_c} = 0.00008 \tag{C.47}$$

Tensile stress-strain in concrete is graphically represented in Figure C.5.

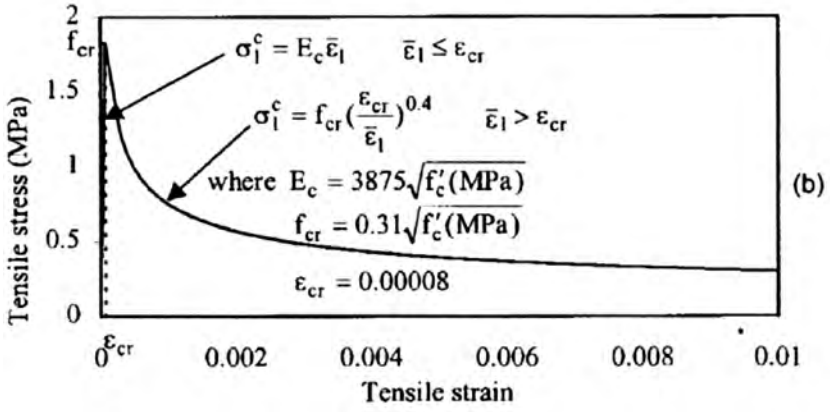

Figure C.5: Constitutive relationship for tensile stress-strain in concrete (Source: Hsu and Zhu, 2002)

Constitutive relationships for tensile stress-strain in reinforcing steel is given by,

$$f_s = f_y\left[(0.91 - 2B) + (0.002 + 0.25B)\frac{\bar{\varepsilon}_s}{\varepsilon_y}\right] \quad for\ \bar{\varepsilon}_s > \bar{\varepsilon}_n \qquad (C.48)$$

$$f_s = E_s\bar{\varepsilon}_s \qquad for\ \bar{\varepsilon}_s \leq \bar{\varepsilon}_n \qquad (C.49)$$

$$\bar{\varepsilon}_n = \varepsilon_y(0.93 - 2B) \qquad (C.50)$$

$$B = \frac{1}{\rho}\left(\frac{f_{cr}}{f_y}\right)^{1.5} \qquad (C.51)$$

Equations C.48 to C.51 are valid for both longitudinal and transverse directions and should be used separately for longitudinal and transverse directions. A graphical representation of stress-strain relationship for reinforcing steel is given in Figure C.6.

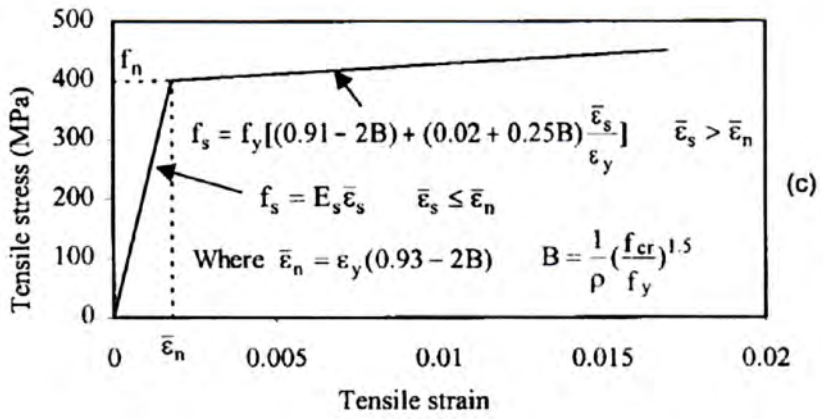

Figure C.6: Constitutive relationship for tensile stress-strain in reinforcing steel (Source: Hsu and Zhu, 2002)

Stress-strain relationship of concrete in shear is given by,

$$\tau_{21}^c = \frac{\sigma_2^c - \sigma_1^c}{2(\varepsilon_2 - \varepsilon_1)}\gamma_{21} \qquad (C.52)$$

$$v_{12} = \begin{cases} 0.2 + 850\varepsilon_{sf} & for\ \varepsilon_{sf} \leq \varepsilon_y \\ 1.9 & for\ \varepsilon_{sf} > \varepsilon_y \end{cases} \qquad (C.53)$$

$$v_{21} = 0 \qquad (C.54)$$

Notations and Definitions

$1-$ = Direction of applied principal tensile stress

$2-$ = Direction of applied principal compressive stress

E_c = Elastic modulus of concrete

E_1^c = Secant modulus of concrete in direction-1, considering Hsu/Zhu ratios

$\bar{E}_1^c$ = Secant modulus of concrete in direction-1, neglecting Hsu/Zhu ratios

E_2^c = Secant modulus of concrete in direction-2, considering Hsu/Zhu ratios

$\bar{E}_2^c$ = Secant modulus of concrete in direction-2, neglecting Hsu/Zhu ratios

E_s = Secant modulus of steel in direction -1, neglecting Hsu/Zhu ratios

E_l^s = Secant modulus of steel in direction –*l*, considering Hsu/Zhu ratios

$\bar{E}_l^s$ = Secant modulus of steel in direction –*l*, neglecting Hsu/Zhu ratios

E_t^s = Secant modulus of steel in direction –*t*, considering Hsu/Zhu ratios

$\bar{E}_t^s$ = Secant modulus of steel in direction –*t*, neglecting Hsu/Zhu ratios

f_c' = Cylinder compressive strength of concrete

f_{cr} = Cracking tensile strength of concrete

f_l = Smeared (average) steel stress in longitudinal direction (*l*-axis)

f_{ly} = Yield stress of longitudinal bare steel bars

f_n = Smeared (average) tensile steel stress at first yield

f_s = Smeared (average) stress in embedded mild steel bars, becomes f_l or f_t when applied to longitudinal and transverse steel, respectively

f_t = Smeared (average) steel stress in transverse direction (*t*-axis)

f_{ty} = Yield stress of transverse bare steel bars

f_y' = Yield stress of bare steel bars

l = Direction of longitudinal steel bars

t = Direction of transverse steel bars

G_{21}^c = Shear modulus of concrete in 2-1 coordinates of applied stresses

α_2 = Angle of applied principal compressive stress (2-axis) with respect to longitudinal steel bars (*l*-axis)

ε_0 = Concrete cylinder strain corresponding to peak cylinder strength

ε_1 = Smeared strain in 1-direction considering Hsu/Zhu ratios or strain in 1-direction

$\bar{\varepsilon}_1$ = Smeared (average) strain in 1-direction neglecting Hsu/Zhu ratios or uniaxial strain in 1-direction

ε_2 = Smeared (average) strain in 2-direction considering Hsu/Zhu ratios or bi-axial strain in 1-direction

$\bar{\varepsilon}_2$ = Smeared (average) strain in 2-direction neglecting Hsu/Zhu ratios or uniaxial strain in 1-direction

ε_{cr} = Cracking tensile strain of concrete

ε_l = Smeared (average) strain in l -direction considering Hsu/Zhu ratios or bi-axial strain in l -direction

$\bar{\varepsilon}_l$ = Smeared (average) strain in l -direction neglecting Hsu/Zhu ratios or uniaxial strain in l -direction

$\bar{\varepsilon}_n$ = Smeared (average) strain of steel bars at first yield neglecting Hsu/Zhu ratios or uniaxial strain in l -direction

$\bar{\varepsilon}_n$ = Smeared (average) strain in steel bars neglecting Hsu/Zhu ratios; becomes or when applied to the longitudinal and transverse steel, respectively

ε_{sf} = Smeared (average) tensile strain of steel bars that yields first

ε_t = Smeared (average) strain in t -direction considering Hsu/Zhu ratios or bi-axial strain in t-direction

$\bar{\varepsilon}_t$ = Smeared (average) strain in t -direction neglecting Hsu/Zhu ratios or uniaxial strain in t -direction

ε_y = Yield strain of steel

γ_{21} = Smeared (average) shear strain in 2-1 coordinate of applied stresses

γ_{lt} = Smeared (average) shear strain in *l-t* coordinate of steel bars

σ_1^c = Smeared (average) tensile stress of concrete in 1-direction

σ_2^c = Smeared (average) tensile stress of concrete in 2-direction

σ_l = Applied normal stress in *l*-direction of steel bars

σ_t = Applied normal stress in *t*-direction of steel bars

γ_{21}^c = Smeared (average) shear stress of concrete in 2-1 coordinates

γ_{lt} = Applied shear stress in *l-t* coordinate of steel bars

η = Parameter defined as $(\rho_t f_{ty} - \sigma_t)/(\rho_l f_{ly} - \sigma_l)$

η' = η or its reciprocal, whichever is less than unity; $\eta' \geq 0.2$

ρ_l = Steel ratio in longitudinal direction

ρ_t = Steel ratio in transverse direction

v_{12} = Hsu/Zhu ratio (ratio of resulting tensile strain to source compressive strain)

v_{21} = Hsu/Zhu ratio (ratio of resulting compressive strain to source tensile strain)

ξ = Softening coefficient of concrete in compression when peak stress-softened coefficient is equal to strain-softened coefficient

APPENDIX C-III

FORMULATION OF HAWKIN'S SHEAR SLIP MODEL FOR CONCRETE

The Hawkin's shear stress-slip relationship for direct shear response is presented Figure C.7.

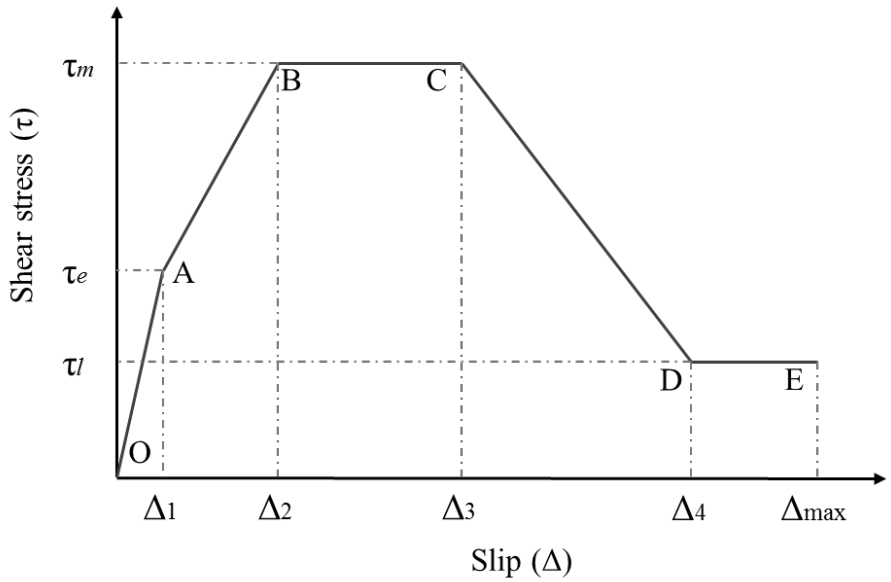

Figure C.7: Shear stress-slip diagram for the Hawkin's shear-slip model (Source: Hawkins, 1982)

This relationship was originally developed using the imperial unit system. However, for the scope of this thesis, these equations were converted to metric system using relevant conversion factors. Equations for both imperial and metric systems are presented in Table C.1

.

Table C.1: Equations for Hawkin's Shear stress-slip relationship

Imperial unit system (Psi, in)	**Metric unit system (MPa, mm)**
$\tau_c = 165 + 0.157 f_c'$	$\tau_c = 1.138 + 1.08 \times 10^{-3} f_c'$
$\tau_m = 8\sqrt{f_c'} + 0.8\rho_{vt} f_y$	$\tau_m = 0.664\sqrt{f_c'} + 5.517 \times 10^{-3}\rho_{vt} f_y$
$K_u = 2000 + 0.75 f_c'$	$K_u = 13.793 + 5.517 \times 10^{-3} f_c'$
$\Delta_{max} = 2\left(\frac{e^x - 1}{120}\right)$	$\Delta_{max} = 50.8\left(\frac{e^x - 1}{120}\right)$
$x = \frac{900}{2.86\sqrt{\frac{f_c'}{d_b}}}$	$x = \frac{5.2266}{\sqrt{\frac{f_c'}{d_b}}}$
$\tau_l = \frac{0.85 A_{sb} f_s'}{A_c}$	$\tau_l = \frac{5.862 \times 10^{-3} A_{sb} f_s'}{A_c}$

The **line segment OA** in Figure C.1 corresponds to the elastic region of the relationship where a slip dimension of Δ_1=0.004 in (0.1 mm). The limiting shear stress is given by,

$$\tau_e = \begin{cases} \tau_c & for\ \tau_c \leq \tau_m/2 \\ \tau_m/2 & for\ \tau_c > \tau_m/2 \end{cases} \qquad (C.55)$$

The **line segment AB** in Figure C.1corresponds to a slip dimension of Δ_2=0.012 in (0.3 mm). The limiting shear stress is given by,

$$\tau_m = 0.664\sqrt{f_c'} + 5.517 \times 10^{-3}\rho_{vt} f_y \qquad (C.56)$$

Reaching a shear stress of τ_m is considered a partial failure in this study.

The **line segment BC** in Figure C.1 corresponds to a slip dimension of Δ_3=0.024 in (0.6 mm) where shear stress remains constant.

The **line segment CD** in Figure C.1 corresponds to a slip dimension of Δ_4. Δ_4 is calculated case by case basis and does not have a pre-defined value. In order to calculate the value of Δ_4, slope of the line segment CD is given by,

$$K_u = 13.793 + 5.517 \times 10^{-3} f_c' \qquad (C.57)$$

The limiting shear stress corresponding to Δ_4 is given by,

$$\tau_l = \frac{5.862 \times 10^{-3} A_{sb} f_s'}{A_c} \qquad (C.58)$$

The **line segment DE** in Figure C.1 corresponds to a limiting deflection of Δ_{max} given by,

$$\Delta_{max} = 50.8\left(\frac{e^x - 1}{120}\right) \qquad (C.59)$$

$$x = \frac{5.2266}{\sqrt{\frac{f_c'}{d_b}}} \qquad (C.60)$$

Shear stress remains as τ_l along the line segment DE. Reaching the maximum deflection of Δ_{max} is considered a complete failure of of the element.

Notations and Definitions

A_{sb} = Area of bottom reinforcement
A_c = Cross sectional area
d_b = Diameter of bottom reinforcement
f_y = Yield strength of reinforcement crossing the shear plane
f_c' = Cylinder compressive strength of concrete
f_s' = Tensile strength of reinforcement crossing the shear plane
x = Exponential parameter for maximum deflection
Δ_{max} = Maximum deflection
ρ_{vt} = Reinforcement ration crossing the shear plane
τ_m = Maximum shear stress
τ_e = Elastic shear stress
τ_c = Limiting shear stress
τ_l = Residual shear stress

APPENDIX C-IV

FORTRAN CODING FOR THE 1-D ANALYTICAL SOLUTION

Input module

```
SUBROUTINE READINPUT(L,B,D,FC,K_B,K_S,K_T,AS_C,AS_T,FY_C,FY_T,FY_H,COV,&!D_C
     D_T,D_B,D_H,RO,V,R,W_TNT,S_RATE_B,S_RATE_S,T,BOUNDARY,&
     NO_T,NO_B,SP_H)
REAL(KIND=KIND(0.D0)) L, B, D, FC, K_B,K_S,K_T,AS_C, AS_T, FY_C, FY_T,FY_H,&
       COV, D_C, D_T, D_B, D_H, RO, V, R, W_TNT,S_RATE_B,S_RATE_S,&
       NO_T,NO_B,SP_H
INTEGER T, BOUNDARY
  INTEGER IOS,NPOS
  CHARACTER(LEN=100) FILELINE,WORKLINE
  CHARACTER(LEN=40) INPUTFILE
LOGICAL FILE_END,MATERIAL_FLAG,GEOMETRY_FLAG,REINFORCE_FLAG,LOAD_FLAG,MIXED_FLAG
  INPUTFILE='INPUTDATA'
  OPEN(11,FILE=INPUTFILE,STATUS='OLD',IOSTAT=IOS,FORM='FORMATTED')
  IF(IOS/=0)THEN
     PRINT*,' INPUTFILE NOT FOUND'
     STOP
  ENDIF
  FILE_END     =.FALSE.
  MATERIAL_FLAG =.FALSE.
  GEOMETRY_FLAG =.FALSE.
  REINFORCE_FLAG=.FALSE.
  LOAD_FLAG     =.FALSE.
  MIXED_FLAG    =.FALSE.
  FILE: DO WHILE(.NOT.FILE_END)
     READ(11,'(A)',IOSTAT=IOS)FILELINE
     IF(IOS/=0) EXIT FILE
     MATERIAL_FLAG=(INDEX(FILELINE,'M A T E R I A L  P A R A M E T E R S')>0)
     MATERIAL: DO WHILE(MATERIAL_FLAG)
        READ(11,'(A)',IOSTAT=IOS)FILELINE
        IF(IOS/=0)EXIT FILE
        NPOS=INDEX(FILELINE,'DENSITY=')
        IF(NPOS>0)THEN
           NPOS=NPOS+8
           READ(FILELINE(NPOS:),*)RO
        ENDIF
        NPOS=INDEX(FILELINE,'NU=')
        IF(NPOS>0)THEN
           NPOS=NPOS+3
           READ(FILELINE(NPOS:),*)V
        ENDIF
        NPOS=INDEX(FILELINE,'STRENGTH=')
        IF(NPOS>0)THEN
           NPOS=NPOS+9
           READ(FILELINE(NPOS:),*)FC
        ENDIF
        NPOS=INDEX(FILELINE,'BEAMSTIFF=')
        IF(NPOS>0)THEN
           NPOS=NPOS+10
           READ(FILELINE(NPOS:),*)K_B
        ENDIF
          NPOS=INDEX(FILELINE,'ROTASTIFF=')
        IF(NPOS>0)THEN
           NPOS=NPOS+10
           READ(FILELINE(NPOS:),*)K_S
        ENDIF
        NPOS=INDEX(FILELINE,'TRANSTIFF=')
        IF(NPOS>0)THEN
           NPOS=NPOS+10
           READ(FILELINE(NPOS:),*)K_T
        ENDIF
        MATERIAL_FLAG=(INDEX(FILELINE,'E N D  M A T E R I A L')==0)
     ENDDO MATERIAL
GEOMETRY_FLAG=(INDEX(FILELINE,'G E O M E T R Y  O F  T H E  M E M B E R')>0)
      GEOMETRY: DO WHILE(GEOMETRY_FLAG)
         READ(11,'(A)',IOSTAT=IOS)FILELINE
         IF(IOS/=0)EXIT FILE
         NPOS=INDEX(FILELINE,'LENGTH=')
         IF(NPOS>0)THEN
            NPOS=NPOS+7
            READ(FILELINE(NPOS:),*)L
         ENDIF
         NPOS=INDEX(FILELINE,'WIDTH=')
         IF(NPOS>0)THEN
            NPOS=NPOS+6
            READ(FILELINE(NPOS:),*)B
```

```
            ENDIF
            NPOS=INDEX(FILELINE,'DEPTH=')
            IF(NPOS>0)THEN
               NPOS=NPOS+6
               READ(FILELINE(NPOS:),*)D
            ENDIF
            GEOMETRY_FLAG=(INDEX(FILELINE,'E N D  G E O M E T R Y')==0)
         ENDDO GEOMETRY
REINFORCE_FLAG=(INDEX(FILELINE,'R E I N F O R C E M E N T  P A R A M E T E R S')>0)
         REINFORCE: DO WHILE(REINFORCE_FLAG)
            READ(11,'(A)',IOSTAT=IOS)FILELINE
            IF(IOS/=0)EXIT FILE
            NPOS=INDEX(FILELINE,'AREACOMPRESS=')
            IF(NPOS>0)THEN
               NPOS=NPOS+13
               READ(FILELINE(NPOS:),*)AS_C
            ENDIF
            NPOS=INDEX(FILELINE,'AREATENSILE=')
            IF(NPOS>0)THEN
               NPOS=NPOS+12
               READ(FILELINE(NPOS:),*)AS_T
            ENDIF
            NPOS=INDEX(FILELINE,'YIELDCOMPRESS=')
            IF(NPOS>0)THEN
               NPOS=NPOS+14
               READ(FILELINE(NPOS:),*)FY_C
            ENDIF
            NPOS=INDEX(FILELINE,'YIELDTENSILE=')
            IF(NPOS>0)THEN
               NPOS=NPOS+13
               READ(FILELINE(NPOS:),*)FY_T
            ENDIF
            NPOS=INDEX(FILELINE,'YIELDSHEAR=')
            IF(NPOS>0)THEN
               NPOS=NPOS+11
               READ(FILELINE(NPOS:),*)FY_H
            ENDIF
            NPOS=INDEX(FILELINE,'COVERREINFORCE=')
            IF(NPOS>0)THEN
               NPOS=NPOS+15
               READ(FILELINE(NPOS:),*)COV
            ENDIF
            NPOS=INDEX(FILELINE,'DIAMCOMPRESS=')
            IF(NPOS>0)THEN
               NPOS=NPOS+13
               READ(FILELINE(NPOS:),*)D_C
            ENDIF
            NPOS=INDEX(FILELINE,'DIAMTENSILE=')
            IF(NPOS>0)THEN
               NPOS=NPOS+12
               READ(FILELINE(NPOS:),*)D_T
            ENDIF
            NPOS=INDEX(FILELINE,'DIAMBOTTOM=')
            IF(NPOS>0)THEN
               NPOS=NPOS+11
               READ(FILELINE(NPOS:),*)D_B
            ENDIF
            NPOS=INDEX(FILELINE,'DIAMSHEAR=')
            IF(NPOS>0)THEN
               NPOS=NPOS+10
               READ(FILELINE(NPOS:),*)D_H
            ENDIF
REINFORCE_FLAG=(INDEX(FILELINE,'E N D  R E I N F O R C E M E N T')==0)
         END DO REINFORCE
   LOAD_FLAG=(INDEX(FILELINE,'E X P L O S I V E  L O A D')>0)
         LOAD: DO WHILE(LOAD_FLAG)
            READ(11,'(A)',IOSTAT=IOS)FILELINE
            IF(IOS/=0)EXIT FILE
            NPOS=INDEX(FILELINE,'STANDOFF=')
            IF(NPOS>0)THEN
               NPOS=NPOS+9
               READ(FILELINE(NPOS:),*)R
            ENDIF
            NPOS=INDEX(FILELINE,'CHARGEWEIGHT=')
            IF(NPOS>0)THEN
               NPOS=NPOS+13
               READ(FILELINE(NPOS:),*)W_TNT
            ENDIF
            LOAD_FLAG=(INDEX(FILELINE,'E N D  L O A D')==0)
         END DO LOAD
         MIXED_FLAG=(INDEX(FILELINE,'M I X E D  D A T A')>0)
         MIXED: DO WHILE(MIXED_FLAG)
            READ(11,'(A)',IOSTAT=IOS)FILELINE
            IF(IOS/=0)EXIT FILE
            NPOS=INDEX(FILELINE,'S_RATE_B=')
            IF(NPOS>0)THEN
               NPOS=NPOS+9
               READ(FILELINE(NPOS:),*)S_RATE_B
            ENDIF
            NPOS=INDEX(FILELINE,'S_RATE_S=')
```

```
            IF(NPOS>0)THEN
               NPOS=NPOS+9
               READ(FILELINE(NPOS:),*)S_RATE_S
            ENDIF
            NPOS=INDEX(FILELINE,'BOUNDARY=')
            IF(NPOS>0)THEN
               NPOS=NPOS+9
               READ(FILELINE(NPOS:),*)BOUNDARY
            ENDIF
            NPOS=INDEX(FILELINE,' T=')
            IF(NPOS>0)THEN
               NPOS=NPOS+3
               READ(FILELINE(NPOS:),*)T
            ENDIF
            NPOS=INDEX(FILELINE,'NO_T=')
            IF(NPOS>0)THEN
               NPOS=NPOS+5
               READ(FILELINE(NPOS:),*)NO_T
            ENDIF
            NPOS=INDEX(FILELINE,'NO_B=')
            IF(NPOS>0)THEN
               NPOS=NPOS+5
               READ(FILELINE(NPOS:),*)NO_B
            ENDIF
            NPOS=INDEX(FILELINE,'SP_H=')
            IF(NPOS>0)THEN
               NPOS=NPOS+5
               READ(FILELINE(NPOS:),*)SP_H
            ENDIF
            MIXED_FLAG=(INDEX(FILELINE,'E N D  M I X E D')==0)
         END DO MIXED
      END DO FILE
      CLOSE(11)
END SUBROUTINE READINPUT
```

Mander's coefficient

```
SUBROUTINE MANDER_COEFFICIENT(L, B, D, COV, FC, D_T, D_B, D_H, SP_T, SP_B, SP_H,
NO_T, NO_B, FY_C, FY_T, FY_H, K)
    IMPLICIT NONE
    REAL(KIND=KIND(0.D0)), INTENT(IN):: L, B, D, COV, FC, D_T, D_B, D_H, SP_T, SP_B,
SP_H, NO_T, NO_B, FY_C, FY_T, FY_H
    REAL(KIND=KIND(0.D0)), INTENT(OUT):: K
    REAL(KIND=KIND(0.D0)), PARAMETER :: PI=4.D0*ATAN(1.D0)
    REAL(KIND=KIND(0.D0)) A_C, RO_L, A_E, K_E, F1

    RO_L= 0.25D0*PI*(D_T**2*NO_T+D_B**2*NO_B)/((B-2.D0*COV)*(D-2.D0*COV))
    A_C=(B-2.D0*COV)*(D-2.D0*COV)*(1.D0-RO_L)
    A_E=((B-2.D0*COV)*(D-2.D0*COV)-&
         ((NO_T-1.D0)*(SP_T-D_T)**2+&
         (NO_B-1.D0)*(SP_B-D_B)**2+&
         2.D0*(D-2.D0*COV-2.D0*D_H)**2)/6.D0)*&
         (1.-SP_H/(2.D0*(B-2.D0*COV)))*&
         (1.D0-SP_H/(2.D0*(D-2.D0*COV)))
    K_E=A_E/A_C
    F1=K_E*RO_L*MIN(FY_C, FY_T, FY_H)
    K=1.D0+3.D0*F1/FC

END SUBROUTINE MANDER_COEFFICIENT
```

Moment curvature relationship

```
SUBROUTINE MOMENT_CURVATURE_BEAM (L,B,D,FC,K,AS_C,AS_T,FY_C,FY_T,EFF_D,EFF_D1)
  IMPLICIT NONE

  REAL(KIND=KIND(0.D0)), INTENT(IN):: L,B,D,FC,K,AS_C,AS_T,FY_C,FY_T,EFF_D,EFF_D1
  REAL(KIND=KIND(0.D0)), PARAMETER ::PI=4.D0*ATAN(1.D0)
  REAL(KIND=KIND(0.D0)), PARAMETER ::ES=2.05D5
  REAL(KIND=KIND(0.D0)) Z,R,EC,EPS_C,EPS_CC,F_RES,ZM,EPS_RES,EPS,EPS_F,C,T,K1,&
       ND,CC,CC1,CC2,EPS_SC,EPS_YC,FS_C,CS,EPS_ST,EPS_YT,FS_T
  REAL(KIND=KIND(0.D0))MTS,MCS,MCC1,MCC2,MCC3,M,PHI,PHI_MAX

  Z=0.018D0*FC+0.55D0
  R=0.28D0-0.0032D0*FC
  EC=9500.D0*FC**0.3D0
  EPS_C=4.26D0*FC**0.75D0/EC
  EPS_CC=(0.24D0*K**3+0.76D0)*EPS_C
  F_RES=R*K*FC
  ZM=0.5D0*Z/((3.D0+0.29D0*FC)/(145D0*FC-1000.D0)-EPS_CC)
  EPS_RES=(1.D0-F_RES/FC)/ZM+EPS_CC
  EPS_F=0.003D0
  M=0.D0;PHI=0.D0; PHI_MAX=0.003D0

  EPS=0.D0

  OPEN (UNIT=1,FILE='M-PHI')
  WRITE (1,40), PHI, M
```

```
40 FORMAT (F16.8,F16.4)

  DO WHILE ((EPS<=EPS_F).AND.(PHI<=PHI_MAX))
     EPS = EPS+1.D-4
     C=1.D0; T=0.D0 ; K1=0.34D0
     DO WHILE (ABS(T-C)>=0.01*MAX(ABS(T),ABS(C)))
        IF (ABS(C)>ABS(T)) THEN
           K1=K1-1.D-5
        ELSE
           K1=K1+1.D-5
        END IF
        ND=K1*EFF_D
        IF (EPS<=EPS_CC) THEN
           CC=K*FC*B*ND*(EPS/EPS_CC)*(1-EPS/(3*EPS_CC))
           CC1=0.D0
           CC2=0.D0
        ELSE IF (EPS<=EPS_RES) THEN
           CC=K*FC*B*ND*EPS_CC/EPS
           CC1=K*FC*B*ND*(EPS-EPS_CC)*(1.D0-0.5D0*ZM*(EPS-EPS_CC))/EPS
           CC2=0.D0
        ELSE
           CC=K*FC*B*ND*EPS_CC/EPS
           CC1=K*FC*B*ND*(EPS_RES-EPS_CC)*(1.D0-0.5D0*ZM)*(EPS_RES-EPS_CC)/EPS
           CC2=K*FC*B*ND*R*(EPS-EPS_RES)/EPS
        END IF

        EPS_SC=EPS*(ND-EFF_D1)/ND
        EPS_YC=FY_C/ES
        IF (ABS(EPS_SC)<=EPS_YC) THEN
           FS_C=ES*EPS_SC
        ELSE
           FS_C=FY_C
        END IF
        CS=AS_C*FS_C
        C=CC+CC1+CC2+CS
        EPS_ST=(EFF_D-ND)*EPS/ND
        EPS_YT=FY_T/ES
        IF (EPS_ST<=EPS_YT) THEN
           FS_T=ES*EPS_ST
        ELSE
           FS_T=FY_T
        END IF
            T=AS_T*FS_T
        END DO
        MTS=T*(EFF_D-ND)
        MCS=CS*(ND-EFF_D1)
        IF (EPS<=EPS_CC) THEN
           MCC1=K*FC*B*((ND)**2)*((2.D0*EPS)/(3.D0*EPS_CC)-
(EPS)**2/(4.D0*(EPS_CC)**2))
           MCC2=0.D0
           MCC3=0.D0
        ELSE IF (EPS<=EPS_RES) THEN
           MCC1=5.D0*K*FC*B*(ND**2)*((EPS_CC/EPS)**2)/12.D0
           MCC2=K*FC*B*((ND/EPS)**2)*(EPS-EPS_CC)*((EPS+EPS_CC)/2-
(ZM/6.D0)*(2.D0*EPS+EPS_CC)*&
                (EPS-EPS_CC))
           MCC3=0.D0
        ELSE
           MCC1=5.D0*K*FC*B*(ND**2)*((EPS_CC/EPS)**2)/12.D0
           MCC2=K*FC*B*((ND/EPS)**2)*(EPS_RES-EPS_CC)*((EPS_RES+EPS_CC)*0.5D0-
(ZM/6.D0)*&
                (2*EPS_RES+EPS_CC)*(EPS_RES-EPS_CC))
           MCC3=K*R*FC*B*((ND/EPS)**2)*((EPS**2)-(EPS_RES)**2)*0.5D0
        END IF

        M=MTS+MCS+MCC1+MCC2+MCC3
        PHI=EPS/ND
        IF (PHI<PHI_MAX) THEN
           WRITE (1,45), PHI, M
45         FORMAT (F16.8,F16.4)
        END IF
     END DO
     CLOSE (1)
   END SUBROUTINE MOMENT_CURVATURE_BEAM
```

Shear stress-strain relationship

```
SUBROUTINE SHEAR_STRESS_STRAIN (FC, RO_LO, RO_TR, FY_LO, FY_TR)
  IMPLICIT NONE

  REAL(KIND=KIND(0.D0)), INTENT(IN) ::FC, RO_LO, RO_TR, FY_LO, FY_TR
  REAL(KIND=KIND(0.D0)), PARAMETER :: PI=4.D0*ATAN(1.D0),ALP2=0.25D0*PI, ES=2.0D5
  REAL(KIND=KIND(0.D0)) EPS1, EPS2, GAMA21, EPSL, EPST, EPS_S, EPS_YS, V12, EPS1_N,&
       EPS2_N,V21, EPSL_N, EPST_N
  REAL(KIND=KIND(0.D0)) NETA, EETA, NETA1, EPS0, K, ZIG_2C, EC, FCR, EPS_CR, ZIG_1C,&
       TOU21, BL, BT, FL, EPSL_N_P, EPS_YL
  REAL(KIND=KIND(0.D0)) FT, EPST_N_P, EPS_YT, ZIG_L, ZIG_T, H1, H2, T1, T2, TOU_LT,&
```

```
      GAMA_LT, TOU_LT_MAX, TEMP1, TEMP2

REAL(KIND=KIND(0.D0)), PARAMETER :: PRECISION=1.D-24
  INTEGER N
  EPS1=0.D0; EPS2 =0.D0; GAMA21 = 0.D0; EPSL = 0.D0; EPST=0.D0; EPS_S=0.D0; EPS1_N =
0.D0
  EPS2_N =0.D0; V12 =0.D0; V21=0.D0; NETA = 0.D0;  EC=0.D0; FCR=0.D0; EPS_CR=0.D0;
ZIG_1C=0.D0
  TOU21=0.D0; FL=0.D0; EPS_YL=0.D0; FT=0.D0; EPS_YT=0.D0; ZIG_L=0.D0; ZIG_T = 0.D0;
H1=0.D0
  H2=0.D0; T1=0.D0; T2=0.D0; TOU_LT=0.D0; GAMA_LT=0.D0; TOU_LT_MAX = 0.D0
  EPS0 = 2.35D-3; TEMP1 =1.D0; TEMP2 =1.D0; EETA = 1.D0

  EC = 3875.D0*SQRT(FC); FCR = 0.31D0*SQRT(FC); EPS_CR = FCR/EC; BL =
(FCR/FY_LO)**1.5D0/RO_LO
  EPS_YL = (FY_LO/ES); EPSL_N_P = EPS_YL*(0.93D0-2.D0*BL); BT =
((FCR/FY_TR)**1.5D0)/RO_TR;
  EPS_YT = (FY_TR/ES); EPST_N_P = EPS_YT*(0.93D0-2.D0*BT)
  OPEN (UNIT=1, FILE ='SHEAR')
  WRITE (1,40) TOU_LT, GAMA_LT
40 FORMAT (F12.8, F12.8)
  N=0
  DO WHILE ((TOU_LT>= (0.75D0*TOU_LT_MAX)))
     N=N+1
     EPS2 = EPS2 -1.D-6
     DO WHILE (TEMP2>=PRECISION)
        GAMA21 = GAMA21 - 1.D-6
        DO WHILE (TEMP1>=PRECISION)
           EPS1 = EPS1+1.D-6
           EPSL = EPS2*(COS(ALP2))**2+EPS1*(SIN(ALP2))**2+GAMA21*SIN(ALP2)*COS(ALP2)
           EPST = EPS2*(SIN(ALP2))**2+EPS1*(COS(ALP2))**2-GAMA21*SIN(ALP2)*COS(ALP2)
           IF (ABS(EPSL) > ABS(EPST)) THEN
              EPS_S=EPSL
              EPS_YS=FY_LO/ES
           ELSE
              EPS_S = EPST
              EPS_YS=FY_TR/ES
           END IF

           IF (EPS_S < EPS_YS) THEN
              V12 = 0.2D0 +850.D0*EPS_S
           ELSE
              V12 = 1.9D0
           END IF
           EPS1_N = (EPS1+V12*EPS2)/(1.D0-V12*V21)
           EPS2_N = (EPS2+V21*EPS1)/(1.D0-V12*V21)
           EPSL_N =
EPS2_N*(COS(ALP2))**2+EPS1_N*(SIN(ALP2))**2+GAMA21*SIN(ALP2)*COS(ALP2)
           EPST_N = EPS2_N*(SIN(ALP2))**2+EPS1_N*(COS(ALP2))**2-
GAMA21*SIN(ALP2)*COS(ALP2)
           NETA = ABS((RO_TR*FY_TR)/(RO_LO*FY_LO))
           IF (NETA<0.2D0) THEN
              NETA1=0.2D0
           ELSE IF (NETA<1.D0) THEN
              NETA1=NETA
           ELSE IF (NETA<5.D0) THEN
              NETA1=1.D0/NETA
           ELSE
              NETA1=0.2D0
           END IF
           EETA = 5.8D0/SQRT(FC)/SQRT(1.D0+400.D0*ABS(EPS1_N/NETA1))
           K = ABS(EPS2_N/(EETA*EPS0))
           IF (K>1.D0) THEN
              ZIG_2C = -(EETA*FC*(1.D0-((K-1.D0)/(4.D0/EETA-1.D0))**2))
           ELSE
              ZIG_2C = -(EETA*FC*(2.D0*(K)-K**2))
           END IF
           IF (ABS(EPS1_N) < EPS_CR) THEN
              ZIG_1C = EC*ABS(EPS1_N)
           ELSE
              ZIG_1C = FCR*(EPS_CR/EPS1_N)**0.4D0
           END IF
           TOU21= (ZIG_1C-ZIG_2C)/(2.D0*(EPS1-EPS2))*GAMA21
           IF (ABS(EPSL_N)<ABS(EPSL_N_P)) THEN
              FL = ES*EPSL_N
           ELSE
              FL = FY_LO*((0.91D0-2.D0*BL)+(0.02D0+0.25D0*BL)*(EPSL_N/EPS_YL))
           END IF
           IF (ABS(EPST_N) < ABS(EPST_N_P)) THEN
              FT = ES*EPST_N
           ELSE
              FT = FY_TR*((0.91D0-2.D0*BT)+(0.02D0+0.25D0*BT)*(EPST_N/EPS_YT))
           END IF
           ZIG_L =
ZIG_2C*(COS(ALP2))**2+ZIG_1C*(SIN(ALP2))**2+TOU21*2*SIN(ALP2)*COS(ALP2)+RO_LO*FL
           ZIG_T = ZIG_2C*(SIN(ALP2))**2+ZIG_1C*(COS(ALP2))**2-
TOU21*2*SIN(ALP2)*COS(ALP2)+RO_TR*FT
           T1 = RO_LO*FL+RO_TR*FT
           T2 = (ZIG_L+ZIG_T) -(ZIG_1C+ZIG_2C)
           TEMP1 = ABS(T1-T2)
```

```
          H1 = RO_LO*FL-RO_TR*FT
          H2 = (ZIG_L-ZIG_T) - (ZIG_2C-ZIG_1C)*COS(2*ALP2)-2*TOU21*SIN(2*ALP2)
          TEMP2 = ABS(H1-H2)
       END DO
       TEMP1 = 1.D0
    END DO
     TEMP2 = 1.D0
     TOU_LT = (-ZIG_2C+ZIG_1C)*SIN(ALP2)*COS(ALP2)+ TOU21*((COS(ALP2))**2-
(SIN(ALP2))**2)
     GAMA_LT = 2.D0*(-EPS2+EPS1)*SIN(ALP2)*COS(ALP2)+GAMA21*((COS(ALP2))**2-
(SIN(ALP2))**2)
     IF (TOU_LT>1.5D0) THEN
        IF (TOU_LT>TOU_LT_MAX) THEN
           TOU_LT_MAX =TOU_LT
        END IF
     ELSE
        TOU_LT_MAX=TOU_LT
     END IF
     WRITE (1,50) GAMA_LT, TOU_LT
50   FORMAT (F12.8, F12.8)
  END DO
  CLOSE (UNIT=1)
END SUBROUTINE SHEAR_STRESS_STRAIN
```

Shear stress-slip relationship

```
SUBROUTINE SHEAR_SLIP (FC, FY_C, FY_T, D_T, D_B, AS_C, AS_T, B, D)

  IMPLICIT NONE
  REAL(KIND=KIND(0.D0)), INTENT(IN)::FC, FY_C, FY_T, D_T, D_B, AS_C, AS_T, B, D
  REAL(KIND=KIND(0.D0)) AS, AC, AS_B, TOU_M, TOU_E, TOU_L, X, D_MAX, D_4
  INTEGER I
  REAL(KIND=KIND(0.D0)), DIMENSION (6):: SHEAR
  REAL(KIND=KIND(0.D0)), DIMENSION (6):: SLIP

  AS=(AS_C+AS_T)/25.4D0**2
  AC=B*D/25.4D0**2
  AS_B=AS_T/25.4D0**2
  TOU_M=8.D0*SQRT(FC*145.D0)+0.8D0*(AS/AC)*MIN(FY_C,FY_T)*145.D0
  TOU_E=165.D0+0.157D0*FC*145.D0

  IF (TOU_E>=(0.5D0*TOU_M)) THEN
     TOU_E=0.5D0*TOU_M
  END IF
  TOU_L=0.85D0*(AS_B/AC)*FY_T*145.D0
  X=(9.D2/2.86D0)/SQRT((FC*145.D0*25.4D0)/(MIN(D_T,D_B)))
  D_MAX=2*(EXP(X)-1)/120.D0
  D_4=(TOU_M-TOU_L)/(2.D3+0.75D0*FC*145.D0)

  SHEAR(1)=0.D0;SLIP(1)=0.D0
  SHEAR(2)=1.4D0*TOU_E/145.D0; SLIP(2)=0.004D0*25.4D0
  SHEAR(3)=1.4D0*TOU_M/145.D0; SLIP(3)=0.012D0*25.4D0
  SHEAR(4)=1.4D0*TOU_M/145.D0; SLIP(4)=0.024D0*25.4D0
  SHEAR(5)=1.4D0*TOU_L/145.D0; SLIP(5)=(0.024D0+D_4)*25.4D0
  SHEAR(6)=1.4D0*TOU_L/145.D0; SLIP(6)=D_MAX*25.4D0

  OPEN (UNIT=1, FILE='SHEAR_SLIP')

  DO I=1,6
     WRITE (1,40), SLIP(I),SHEAR(I)
40   FORMAT (F12.8, F12.8)
  END DO

  CLOSE (1)
END SUBROUTINE SHEAR_SLIP
```

Pressure-time relationship

```
SUBROUTINE PRESSURE_TIME(W_TNT,R, DT, TI_MAX)

         IMPLICIT NONE

         REAL(KIND=KIND(0.D0)), INTENT(IN):: W_TNT, R, DT
         INTEGER, INTENT(IN):: TI_MAX
         INTEGER N, I, TI, X
         REAL(KIND=KIND(0.D0)) Z, TD, PR, J, K
         REAL(KIND=KIND(0.D0)), ALLOCATABLE::PRESSURE(:,:)
         Z=R/(W_TNT**0.33333333)
         K=LOG(Z)
         IF ((Z<0.2) .OR. (Z>40)) THEN
                  PRINT*,'NOT WITHIN THE APPLICABLE RANGE FOR SCALED DISTANCE FOR
THIS PROGRAM CAPABILITIES'
         ELSE IF (Z<1.02D0) THEN
                  PR=EXP(9.006D0-2.6893D0*K-
0.6295D0*K**2+0.1011D0*K**3+0.29255D0*K**4+0.13505D0*K**5+0.019738D0*K**6)
```

```
                TD=Z*EXP(0.5426D0+3.2229D0*K-1.5931D0*K**2-5.9667D0*K**3-
4.0815D0*K**4-0.9149D0*K**5)
        ELSE IF (Z<2.D0) THEN
                PR=EXP(9.006D0-2.6893D0*K-
0.6295D0*K**2+0.1011D0*K**3+0.29255D0*K**4+0.13505D0*K**5+0.019738D0*K**6)
                TD=Z*EXP(0.5440D0+2.7082D0*K-9.7354D0*K**2+14.3425D0*K**3-
9.7791D0*K**4+2.8535D0*K**5)
        ELSE IF (Z<2.8D0) THEN
                PR=EXP(8.8396D0-1.733D0*K-2.64D0*K**2+2.293D0*K**3-
0.8232D0*K**4+0.14247D0*K**5-0.0099D0*K**6)
                TD=Z*EXP(0.5440D0+2.7082D0*K-9.7354D0*K**2+14.3425D0*K**3-
9.7791D0*K**4+2.8535D0*K**5)
        ELSE
                PR=EXP(8.8396D0-1.733D0*K-2.64D0*K**2+2.293D0*K**3-
0.8232D0*K**4+0.14247D0*K**5-0.0099D0*K**6)
                TD=Z*EXP(-2.4608D0+7.1639D0*K-5.6215D0*K**2+2.2711D0*K**3-
0.44994D0*K**4+0.03486D0*K**5)
        END IF
        ALLOCATE (PRESSURE(TI_MAX,2))
        PRESSURE=0.D0; X=TD/DT
        OPEN (UNIT=1, FILE='P-T', STATUS='REPLACE')
        DO TI=1,X+2,1

                PRESSURE (TI,1)=REAL(TI*DT)
                IF (TI<2) THEN
                        PRESSURE(TI,2)=0.D0
                ELSE IF (TI < X+2) THEN
                        J=REAL((TI-2))/REAL(X)
                        PRESSURE(TI,2)=PR*(1.D0-J)*EXP(-J)
                ELSE
                        PRESSURE(TI,2)=0.D0
                END IF
                WRITE (1,45), PRESSURE (TI,1), PRESSURE (TI,2)
       45  FORMAT (F8.4,F12.4)
        END DO

END SUBROUTINE PRESSURE_TIME
```

Finite difference solution

```
SUBROUTINE FINITE_DIFF(NAP,NN,NM,NS,BOUNDARY,DT,DX,RO,MOI,B,D,PHI_MAX,GAMA_MAX,W_MAX,&
     S_RATE_B,S_RATE_S,EFF_D,UDL,M_PHI,TOU_GAMA)
INTEGER, INTENT(IN):: NAP,NN,BOUNDARY
REAL(KIND=KIND(0.D0)),INTENT(IN)::DT,DX,RO,MOI,B,D,PHI_MAX,GAMA_MAX,W_MAX
REAL(KIND=KIND(0.D0))::UDL(NAP,2)
REAL(KIND=KIND(0.D0))::S_RATE_B,S_RATE_S,EFF_D
INTEGER TI,X
REAL(KIND=KIND(0.D0)) DIF_S, DIF_B
REAL(KIND=KIND(0.D0)),ALLOCATABLE::BETA(:,:),W(:,:),GAMA(:,:),PHI(:,:),M(:,:),TOU(:,:)
,& Q(:,:),DEFLECTION(:,:), P(:,:),S_RATE_PHI(:),S_RATE_GAMA(:)
REAL(KIND=KIND(0.D0)),
ALLOCATABLE::BETA_(:),W_(:),GAMA_(:),PHI_(:),M_(:),TOU_(:),Q_(:),DEFLECTION_(:)
  REAL(KIND=KIND(0.D0)), PARAMETER ::PI=4.D0*ATAN(1.D0) !3.141592
LOGICAL FAIL
  ALLOCATE (M(NN,NAP)); ALLOCATE (Q(NN,NAP)); ALLOCATE (BETA(NN,NAP))
  ALLOCATE (P(NN,NAP)); ALLOCATE (GAMA(NN,NAP)); ALLOCATE (PHI(NN,NAP))
  ALLOCATE (W(NN,NAP)); ALLOCATE (TOU(NN,NAP))
  ALLOCATE (S_RATE_PHI(NN));ALLOCATE (S_RATE_GAMA(NN))
  ALLOCATE (DEFLECTION(NN,NAP))
  M=0.D0; Q=0.D0; BETA=0.D0; P=0.D0; GAMA=0.D0; PHI=0.D0; W=0.D0; TOU=0.D0;
DEFLECTION=0.D0
  S_RATE_PHI=0.D0; S_RATE_GAMA=0.D0
ALLOCATE(BETA_(NN),W_(NN),GAMA_(NN),PHI_(NN),M_(NN),TOU_(NN),Q_(NN),DEFLECTION_(NN))
  OPEN (UNIT=66, FILE='BETA', STATUS='REPLACE')
  OPEN (UNIT=67, FILE='W', STATUS='REPLACE')
  OPEN (UNIT=68, FILE='GAMA', STATUS='REPLACE')
  OPEN (UNIT=69, FILE='PHI', STATUS='REPLACE')
  OPEN (UNIT=70, FILE='M', STATUS='REPLACE')
  OPEN (UNIT=71, FILE='TOU', STATUS='REPLACE')
  OPEN (UNIT=72, FILE='Q', STATUS='REPLACE')
  OPEN (UNIT=73, FILE='DEFLECTION', STATUS='REPLACE')
  FAIL=.FALSE.
  DO WHILE (.NOT.FAIL)
     DO TI=3,NAP-2
        PRINT*,TI,' TIME'
        DO X=1,NN
           PRINT*,' POINT ',X
           IF (X==1) THEN
              BETA(X,TI+1)=2.D0*BETA(X,TI)-BETA(X,TI-1.D0)-(DT**2/(RO*(1.D-6)*&
                   MOI))*((-25.D0*M(X,TI)+48.D0*M(X+1,TI)-36.D0*M(X+2,TI)+&
                   16.D0*M(X+3,TI)-3.D0*M(X+4,TI))/(12.D0*DX)-Q(X,TI))
           ELSE IF (X==NN) THEN
              BETA(X,TI+1)=2.D0*BETA(X,TI)-BETA(X,TI-1)-(DT**2/(RO*(1.D-6)*MOI))*&
                   ((25.D0*M(X,TI)-48.D0*M(X-1,TI)+36.D0*M(X-2,TI)-16.D0*M(X-3,TI)+&
                   3.D0*M(X-4,TI))/(12.D0*DX)-Q(X,TI))
           ELSE
              BETA(X,TI+1)=2.D0*BETA(X,TI)-BETA(X,TI-1)-(DT**2/(RO*(1.D-6)*MOI))*&
                   ((M(X+1,TI)-M(X-1,TI))/(2.D0*DX)-Q(X,TI))
           END IF
```

```
          PRINT*,' BETA:',BETA(X,TI+1)
          IF (X==1) THEN
             W(X,TI+1)=2.D0*W(X,TI)-W(X,TI-1)-(DT**2/(RO*(1.D-6)*B*D))*&
                  ((-25.D0*Q(X,TI)+48.D0*Q(X+1,TI)-36.D0*Q(X+2,TI)+16.D0*Q(X+3,TI)-&
                  3.D0*Q(X+4,TI))/(12.D0*DX)&
                  +UDL(TI,2)+P(X,TI)*(-25.D0*BETA(X,TI)+48.D0*BETA(X+1,TI)-&
                  36.D0*BETA(X+2,TI)+16.D0*BETA(X+3,TI)-
3.D0*BETA(X+4,TI))/(12.D0*DX))
          ELSE IF (X==NN) THEN
             W(X,TI+1)=2.D0*W(X,TI)-W(X,TI-1)-(DT**2/(RO*(1.D-6)*B*D))*&
                  ((25.D0*Q(X,TI)-48.D0*Q(X-1,TI)+36.D0*Q(X-2,TI)-16.D0*Q(X-3,TI)+&
                  3.D0*Q(X-4,TI))/(12.D0*DX)+&
                  UDL(TI,2)+P(X,TI)*(25.D0*BETA(X,TI)-48.D0*BETA(X-
1,TI)+36.D0*BETA(X-2,TI)-&
                  16*BETA(X-3,TI)+3*BETA(X-4,TI))/(12.D0*DX))

          ELSE
             W(X,TI+1)=2.D0*W(X,TI)-W(X,TI-1)-(DT**2/(RO*(1.D-6)*B*D))*((Q(X+1,TI)-&
                  Q(X-1,TI))/(2.D0*DX)+UDL(TI,2)+P(X,TI)*((Q(X+1,TI)-Q(X-
1,TI))/(2.D0*DX)))
          END IF
          IF (X==1) THEN
             GAMA(X,TI+1)=(-25.D0*W(X,TI+1)+48.D0*W(X+1,TI+1)-36.D0*W(X+2,TI+1)+&
                  16.D0*W(X+3,TI+1)-3.D0*W(X+4,TI+1))/(12.D0*DX)-BETA(X,TI+1)
             PHI(X,TI+1)=(-25.D0*BETA(X,TI+1)+48.D0*BETA(X+1,TI+1)-
36.D0*BETA(X+2,TI+1)+&
                  16.D0*BETA(X+3,TI+1)-3.D0*BETA(X+4,TI+1))/(12.D0*DX)
          ELSE IF (X==NN) THEN
             GAMA(X,TI+1)=(25.D0*W(X,TI+1)-48.D0*W(X-1,TI+1)+36.D0*W(X-2,TI+1)-&
                  16.D0*W(X-3,TI+1)+3.D0*W(X-4,TI+1))/(12.D0*DX)-BETA(X,TI+1)
             PHI(X,TI+1)=(25.D0*BETA(X,TI+1)-48.D0*BETA(X-1,TI+1)+36.D0*BETA(X-
2,TI+1)-&
                  16.D0*BETA(X-3,TI+1)+3.D0*BETA(X-4,TI+1))/(12.D0*DX)
          ELSE
             GAMA(X,TI+1)=(W(X+1,TI+1)-W(X-1,TI+1))/(2.D0*DX)-BETA(X,TI+1)
             PHI(X,TI+1)=(BETA(X+1,TI+1)-BETA(X-1,TI+1))/(2.D0*DX)
          END IF
       END DO
       DO X=2,NN
          IF (PHI(X,TI+1)>PHI_MAX) THEN
             FAIL=.TRUE.
          END IF
          IF (GAMA(X,TI+1)>GAMA_MAX) THEN
             FAIL=.TRUE.
          END IF
          IF (W(X,TI+1)>W_MAX) THEN
             FAIL=.TRUE.
          END IF
       END DO
       IF (.NOT.FAIL) THEN
          DO X=1,NN
             S_RATE_PHI(X)=(3.D0*PHI(X,TI)-4.D0*PHI(X,TI-1)+PHI(X,TI-2))/(2.D0*DT)
             S_RATE_GAMA(X)=(3.D0*GAMA(X,TI)-4.D0*GAMA(X,TI-1)+GAMA(X,TI-
2))/(2.D0*DT)
          END DO
          DO X=1,NN-1
             IF (ABS(S_RATE_PHI(X))<ABS(S_RATE_PHI(X+1))) THEN
                S_RATE_B=ABS(S_RATE_PHI(X+1))
             ELSE
                S_RATE_B=ABS(S_RATE_PHI(X))
             END IF
             IF (ABS(S_RATE_GAMA(X))<ABS(S_RATE_GAMA(X+1))) THEN
                S_RATE_S=ABS(S_RATE_GAMA(X+1))
             ELSE
                S_RATE_S=ABS(S_RATE_GAMA(X))
             END IF
          END DO
          DIF_S=DIF(FC,S_RATE_S)
          DIF_B=DIF(FC,S_RATE_B)
          DO X=1,NN
             IF (PHI(X,TI+1)<0.D0) THEN
                M(X,TI+1)=-INTERPOLATION(ABS(PHI(X,TI+1)), M_PHI, NM)
             ELSE
                M(X,TI+1)=INTERPOLATION(PHI(X,TI+1), M_PHI, NM)
             END IF
          END DO
         DO X=1,NN

             IF (GAMA(X,TI+1)<0.D0) THEN
                Q(X,TI+1)=-
(PI**2*B*EFF_D/12.D0)*INTERPOLATION(ABS(GAMA(X,TI+1)),TOU_GAMA, NS)
             ELSE
                Q(X,TI+1)=(PI**2*B*EFF_D/12.D0)*INTERPOLATION(GAMA(X,TI+1), TOU_GAMA,
NS)
             END IF
          END DO
          DEFLECTION(1,TI+1)=W(1,TI+1)
          DEFLECTION(NN,TI+1)=W(NN,TI+1)
          DO X=2,NN
             IF (X<NN/2) THEN
```

```
            DEFLECTION(X,TI+1)=DEFLECTION(X-1,TI+1)+W(X,TI+1)+BETA(X-1,TI+1)*DX
         ELSE
            DEFLECTION(X,TI+1)=DEFLECTION(X-1,TI+1)-W(X,TI+1)+BETA(X-1,TI+1)*DX
         END IF
      END DO
      IF(BOUNDARY==1)THEN
         BETA_(:)=BETA(:,TI+1)!-BETA(1,TI+1)
         PRINT*,' BETA_:'
         W_(:)=W(:,TI+1)-W(1,TI+1)
         DO X=1,NN
            IF (PHI(X,TI+1)<0.D0) THEN
               M_(X)=-INTERPOLATION(ABS(PHI(X,TI+1)), M_PHI, NM)
            ELSE
               M_(X)=INTERPOLATION(PHI(X,TI+1), M_PHI, NM)
            END IF
         END DO
         M_=M_+M(:,TI+1)
      ELSE
         BETA_(:)=BETA(:,TI+1)
         W_(:)=W(:,TI+1)
         M_(:)=M(:,TI+1)
      ENDIF
      GAMA_(:)=GAMA(:,TI+1)
      PHI_(:)=PHI(:,TI+1)
      TOU_(:)=TOU(:,TI+1)
      Q_(:)=Q(:,TI+1)
      DEFLECTION_(:)=DEFLECTION(:,TI+1)
      WRITE (66,76)BETA_
      WRITE (67,77)W_
      WRITE (68,78)GAMA_
      WRITE (69,79)PHI_
      WRITE (70,80)M_
      WRITE (71,81)TOU_
      WRITE (73,83)DEFLECTION_
    END IF
  END DO
  FAIL=.TRUE.
END DO
CLOSE (66)
CLOSE (67)
CLOSE (68)
CLOSE (69)
CLOSE (70)
CLOSE (71)
CLOSE (72)
  DEALLOCATE(BETA_,W_,GAMA_,PHI_,M_,TOU_,Q_,DEFLECTION_)
  DEALLOCATE (M,Q,BETA,P,GAMA,PHI,W,TOU,S_RATE_PHI,S_RATE_GAMA,DEFLECTION)
76         FORMAT (25(F16.8, 2X))
77         FORMAT (25(F16.8, 2X))
78         FORMAT (25(F16.8, 2X))
79         FORMAT (25(F16.8, 2X))
80         FORMAT (25(F16.4, 2X))
81         FORMAT (25(F16.8, 2X))
82         FORMAT (25(F16.8, 2X))
83         FORMAT (25(F16.8, 2X))
END SUBROUTINE FINITE_DIFF
```

Strain rate enhancement

```
FUNCTION DIF(FC, S_RATE)
REAL(kind=kind(0.d0)) FC, S_RATE, ALP_S, GAMA_S
ALP_S=1/(5+9*FC/10)
GAMA_S=10**(6.156*ALP_S-2)
         IF (S_RATE<=3E-8) THEN
                  DIF=1
         ELSE IF (S_RATE<=3E-2) THEN
                  DIF=(S_RATE/(3E-8))**(1.026*ALP_S)
         ELSE IF (S_RATE<=3) THEN
                  DIF=GAMA_S*(S_RATE/(3E-8))**(0.33333)
         ELSE
                  DIF=GAMA_S*(3/(3E-8))**(0.33333)
         END IF
RETURN
END
```

1-D analysis main program

```
PROGRAM ONE_D_ANALYSIS
  IMPLICIT NONE
  REAL(KIND=KIND(0.D0)) L, B, D, FC, K, AS_C, AS_T, FY_C, FY_T, EFF_D, EFF_D1,&
       COV, D_C,D_T, D_B, D_H, SP_T, SP_B, SP_H, NO_T, NO_B,FY_H, RO_LO, RO_TR
  REAL(KIND=KIND(0.D0)) FY_LO, FY_TR, EC, FCMI, RO, V, CL, DX, DT, MOI,&
       GAMA_MAX, PHI_MAX, W_MAX, R, W_TNT, S_RATE_B, S_RATE_S, DIF, DIF_S, DIF_B
  REAL(KIND=KIND(0.D0)) INTERPOLATION, K1, K2, K3, K4, K11
  INTEGER NM, NS, NDS, NP, NN, I, NAP, T, TI, TI_MAX, X, BOUNDARY
  REAL(KIND=KIND(0.D0)), PARAMETER ::PI=4.D0*ATAN(1.D0) !3.141592
  REAL(KIND=KIND(0.D0)), ALLOCATABLE:: TOU_GAMA(:,:), M_PHI(:,:), TOU_DELTA(:,:),&
       S_RATE_PHI(:), S_RATE_GAMA(:)
```

```
  REAL(KIND=KIND(0.D0)), ALLOCATABLE::M(:,:), Q(:,:), BETA(:,:), P(:,:), GAMA(:,:),
PHI(:,:),&
       UDL(:,:), W(:,:), TOU(:,:), S_RATE(:,:), DEFLECTION(:,:)
  INTEGER MAXTIME
  REAL(KIND=KIND(0.D0)),
ALLOCATABLE::BETA_(:),W_(:),GAMA_(:),PHI_(:),M_(:),TOU_(:),Q_(:),&
       DEFLECTION_(:)
REAL(KIND=KIND(0.D0))K_B,K_S,K_T,THETA
  LOGICAL FAIL
    CALL READINPUT(L, B,D,FC,K_B,K_S,K_T,AS_C,AS_T,FY_C,FY_T,FY_H,COV,&!D_C
       D_T,D_B,D_H, RO,V,R,W_TNT,S_RATE_B,S_RATE_S,T,BOUNDARY,&
       NO_T,NO_B,SP_H)
  EFF_D=D-COV-D_H-D_B/2; EFF_D1=COV+D_H+D_T/2;
  IF (NO_T<2.D0) THEN
     SP_T=0.D0
  ELSE
     SP_T=(B-2.D0*COV-2.D0*D_H-NO_T*D_T)/(NO_T-1.D0)
  END IF
  IF (NO_B<2.D0) THEN
     SP_B=0.D0
  ELSE
     SP_B=(B-2.D0*COV-2.D0*D_H-NO_B*D_B)/(NO_B-1.D0)
  END IF
  RO_LO=(AS_T+AS_C)/(B*EFF_D)
  RO_TR=2.D0*PI*0.25D0*D_H**2/(SP_H*EFF_D)
  FY_LO=MIN(FY_T, FY_C)
  FY_TR=FY_H
  CALL MANDER_COEFFICIENT(L,B,D,COV,FC,D_T,D_B,D_H,SP_T,SP_B,SP_H,&
       NO_T,NO_B,FY_C,FY_T,FY_H,K)
  CALL MOMENT_CURVATURE_BEAM(L,B,D,FC,K,AS_C,AS_T,FY_C,FY_T,EFF_D,EFF_D1)
  CALL SHEAR_STRESS_STRAIN (FC, RO_LO, RO_TR, FY_LO, FY_TR)
  CALL SHEAR_SLIP (FC, FY_C, FY_T, D_T, D_B, AS_C, AS_T, B, D)
  FCMI=-0.0015D0*(FC**2)+1.1429D0*FC-0.0614D0
  IF (FCMI<40.D0) THEN
     EC=RO**1.5D0*0.043D0*SQRT(FCMI)
  ELSE
     EC=RO**1.5D0*(0.024D0*SQRT(FCMI)+0.12D0)
  END IF
  CL=SQRT((EC*1.D6*(1-V))/((1+V)*(1-2.D0*V)*RO))
  NN=L/D+1.D0
  IF (NN<25.D0) THEN
     NN=25.D0
  END IF
  DX=REAL(L)/REAL(NN)
  DT=DX/CL
  IF (DT<0.005D0) THEN
     DT=0.001D0
  ELSE IF (DT<0.01D0) THEN
     DT=0.005D0
  ELSE IF (DT<0.02D0) THEN
     DT=0.01D0
  ELSE IF (DT<0.05D0) THEN
     DT=0.02D0
  ELSE
     DT=0.05D0
  END IF
  NAP=T/DT+1
  TI_MAX=NAP+2
  CALL PRESSURE_TIME(W_TNT,R, DT, TI_MAX)
  CALL LINE_COUNT(NM, NS, NDS, NP)
  OPEN (UNIT=22, FILE='M-PHI', STATUS='OLD', ACTION='READ')
  ALLOCATE (M_PHI(NM,2))
  DO I=1,NM
     READ(22,34),M_PHI(I,1), M_PHI(I,2)
34   FORMAT (F16.8,F16.4)
     PRINT*,M_PHI(I,1),M_PHI(I,2)
  END DO
  CLOSE (22)
  OPEN (UNIT=23, FILE='SHEAR', STATUS='OLD', ACTION='READ')
  ALLOCATE (TOU_GAMA(NS,2))
  DO I=1,NS,1
     READ(23,36),TOU_GAMA(I,1), TOU_GAMA(I,2)
36   FORMAT (F12.8,F12.8)
     PRINT*,TOU_GAMA(I,1),TOU_GAMA(I,2)
  END DO
  CLOSE (23)
  OPEN (UNIT=24, FILE='SHEAR_SLIP', STATUS='OLD', ACTION='READ')
  ALLOCATE (TOU_DELTA(NDS,2))
165 FORMAT ('SHEAR STRESS', T20, 'SLIP'/12('-'), T20, 4('-'))
166 FORMAT (F12.8,T15,F12.8)
  PRINT 165
  DO I=1,NDS
     READ(24,38),TOU_DELTA(I,1), TOU_DELTA(I,2)
38   FORMAT (F12.8,F12.8)
     PRINT 166,TOU_DELTA(I,2),TOU_DELTA(I,1)
  END DO
  CLOSE (24)
  OPEN (UNIT=25, FILE='P-T', STATUS='OLD', ACTION='READ')
  ALLOCATE (UDL(NAP,2))
  UDL=0
```

```
  DO I=1,NAP
     IF (I<NP+1) THEN
        READ(25,40),UDL(I,1), UDL(I,2)
40      FORMAT (F8.4,F12.4)
     ELSE
        UDL(I,1)=I*DT
        UDL(I,2)=0.D0
     END IF
  END DO
  CLOSE (24)
  OPEN (UNIT=26, FILE='UDL')
  DO I=1,NAP
     UDL(I,2)=UDL(I,2)*B/1000
     WRITE(26,41),UDL(I,1),UDL(I,2)
41   FORMAT (F8.4, F12.4)
  END DO
  CLOSE (26)
  ALLOCATE (M(NN,NAP)); ALLOCATE (Q(NN,NAP)); ALLOCATE (BETA(NN,NAP))
  ALLOCATE (P(NN,NAP)); ALLOCATE (GAMA(NN,NAP)); ALLOCATE (PHI(NN,NAP))
  ALLOCATE (W(NN,NAP)); ALLOCATE (TOU(NN,NAP))
  ALLOCATE (S_RATE_PHI(NN));ALLOCATE (S_RATE_GAMA(NN))
  ALLOCATE (DEFLECTION(NN,NAP))
  ALLOCATE(BETA_(NN),W_(NN),GAMA_(NN),PHI_(NN),M_(NN),TOU_(NN),Q_(NN),&
       DEFLECTION_(NN));
  M=0.D0; Q=0.D0; BETA=0.D0; P=0.D0; GAMA=0.D0; PHI=0.D0; W=0.D0; TOU=0.D0;
  MOI=B*D**3/12.D0; S_RATE_GAMA=0.D0; S_RATE_PHI=0.D0; DEFLECTION=0.D0
  PHI_MAX=M_PHI(NM,1)
  GAMA_MAX=TOU_GAMA(NS,1)
  W_MAX=TOU_DELTA(NDS,1)
  OPEN (UNIT=66, FILE='BETA', STATUS='REPLACE')
  OPEN (UNIT=67, FILE='W', STATUS='REPLACE')
  OPEN (UNIT=68, FILE='GAMA', STATUS='REPLACE')
  OPEN (UNIT=69, FILE='PHI', STATUS='REPLACE')
  OPEN (UNIT=70, FILE='M', STATUS='REPLACE')
  OPEN (UNIT=71, FILE='TOU', STATUS='REPLACE')
  OPEN (UNIT=72, FILE='Q', STATUS='REPLACE')
  OPEN (UNIT=73, FILE='DEFLECTION', STATUS='REPLACE')
  FAIL=.FALSE.
  DO WHILE (.NOT.FAIL)
     DO TI=3,NAP-2
        DO X=1,NN
           IF (X==1) THEN
              BETA(X,TI+1)=2.D0*BETA(X,TI)-BETA(X,TI-1)-(DT**2/(RO*1.D-6*MOI))*&
                   ((-25.D0*M(X,TI)+48.D0*M(X+1,TI)-36.D0*M(X+2,TI)+&
                   16.D0*M(X+3,TI)-3.D0*M(X+4,TI))/(12.D0*DX)-Q(X,TI))
           ELSE IF (X==NN) THEN
              BETA(X,TI+1)=2.D0*BETA(X,TI)-BETA(X,TI-1)-(DT**2/(RO*(1.D-6)*MOI))*&
                   ((25.D0*M(X,TI)-48.D0*M(X-1,TI)+36.D0*M(X-2,TI)-16.D0*M(X-3,TI)+&
                   3.D0*M(X-4,TI))/(12.D0*DX)-Q(X,TI))
           ELSE
              BETA(X,TI+1)=2.D0*BETA(X,TI)-BETA(X,TI-1)-(DT**2/(RO*(1.D-6)*MOI))*&
                   ((M(X+1,TI)-M(X-1,TI))/(2.D0*DX)-Q(X,TI))
           END IF
           IF (X==1) THEN
              W(X,TI+1)=2.D0*W(X,TI)-W(X,TI-1)-(DT**2/(RO*(1.D-6)*B*D))*&
                   ((-25.D0*Q(X,TI)+48.D0*Q(X+1,TI)-36.D0*Q(X+2,TI)+16.D0*Q(X+3,TI)-&
                   3.D0*Q(X+4,TI))/(12.D0*DX)&
                   +UDL(TI,2)+P(X,TI)*(-25.D0*BETA(X,TI)+48.D0*BETA(X+1,TI)-&
                   36.D0*BETA(X+2,TI)+16.D0*BETA(X+3,TI)-
3.D0*BETA(X+4,TI))/(12.D0*DX))
           ELSE IF (X==NN) THEN
              W(X,TI+1)=2.D0*W(X,TI)-W(X,TI-1)-(DT**2/(RO*(1.D-6)*B*D))*&
                   ((25.D0*Q(X,TI)-48.D0*Q(X-1,TI)+36.D0*Q(X-2,TI)-16.D0*Q(X-3,TI)+&
                   3.D0*Q(X-4,TI))/(12.D0*DX)+&
                   UDL(TI,2)+P(X,TI)*(25.D0*BETA(X,TI)-48.D0*BETA(X-
1,TI)+36.D0*BETA(X-2,TI)-&
                   16*BETA(X-3,TI)+3*BETA(X-4,TI))/(12*DX))
           ELSE
              W(X,TI+1)=2.D0*W(X,TI)-W(X,TI-1)-(DT**2/(RO*(1.D-6)*B*D))*((Q(X+1,TI)-&
                   Q(X-1,TI))/(2.D0*DX)+UDL(TI,2)+P(X,TI)*((Q(X+1,TI)-Q(X-
1,TI))/(2.D0*DX)))
           END IF
           IF (X==1) THEN
              GAMA(X,TI+1)=(-25.D0*W(X,TI+1)+48.D0*W(X+1,TI+1)-36.D0*W(X+2,TI+1)+&
                   16.D0*W(X+3,TI+1)-3.D0*W(X+4,TI+1))/(12.D0*DX)-BETA(X,TI+1)
              PHI(X,TI+1)=(-25.D0*BETA(X,TI+1)+48.D0*BETA(X+1,TI+1)-
36.D0*BETA(X+2,TI+1)+&
                   16.D0*BETA(X+3,TI+1)-3.D0*BETA(X+4,TI+1))/(12.D0*DX)
           ELSE IF (X==NN) THEN
              GAMA(X,TI+1)=(25.D0*W(X,TI+1)-48.D0*W(X-1,TI+1)+36.D0*W(X-2,TI+1)-&
                   16.D0*W(X-3,TI+1)+3.D0*W(X-4,TI+1))/(12.D0*DX)-BETA(X,TI+1)
              PHI(X,TI+1)=(25.D0*BETA(X,TI+1)-48.D0*BETA(X-1,TI+1)+36.D0*BETA(X-
2,TI+1)-&
                   16.D0*BETA(X-3,TI+1)+3.D0*BETA(X-4,TI+1))/(12.D0*DX)
           ELSE
              GAMA(X,TI+1)=(W(X+1,TI+1)-W(X-1,TI+1))/(2.D0*DX)-BETA(X,TI+1)
              PHI(X,TI+1)=(BETA(X+1,TI+1)-BETA(X-1,TI+1))/(2.D0*DX)
           END IF
        END DO
        DO X=2,NN
```

```
          IF (PHI(X,TI+1)>PHI_MAX) THEN
             FAIL=.TRUE.
          END IF
          IF (GAMA(X,TI+1)>GAMA_MAX) THEN
             FAIL=.TRUE.
          END IF
          IF (W(X,TI+1)>W_MAX) THEN
             FAIL=.TRUE.
          END IF
       END DO
       IF (.NOT.FAIL) THEN
          DO X=1,NN
             S_RATE_PHI(X)=(3.D0*PHI(X,TI)-4.D0*PHI(X,TI-1)+PHI(X,TI-2))/(2.D0*DT)
             S_RATE_GAMA(X)=(3.D0*GAMA(X,TI)-4.D0*GAMA(X,TI-1)+GAMA(X,TI-
2))/(2.D0*DT)
          END DO
          DO X=1,NN-1
             IF (ABS(S_RATE_PHI(X))<ABS(S_RATE_PHI(X+1))) THEN
S_RATE_B=ABS(S_RATE_PHI(X+1))
             ELSE
                S_RATE_B=ABS(S_RATE_PHI(X))
             END IF
             IF (ABS(S_RATE_GAMA(X))<ABS(S_RATE_GAMA(X+1))) THEN
                S_RATE_S=ABS(S_RATE_GAMA(X+1))
             ELSE
                S_RATE_S=ABS(S_RATE_GAMA(X))
             END IF
          END DO
          DIF_S=DIF(FC,S_RATE_S)
          DIF_B=DIF(FC,S_RATE_B)
          DO X=1,NN
             IF (PHI(X,TI+1)<0.D0) THEN
                M(X,TI+1)=-INTERPOLATION(ABS(PHI(X,TI+1)), M_PHI, NM)
             ELSE
                M(X,TI+1)=INTERPOLATION(PHI(X,TI+1), M_PHI, NM)
             END IF
          END DO
         DO X=1,NN
             IF (GAMA(X,TI+1)<0.D0) THEN
                Q(X,TI+1)=-
(PI**2*B*EFF_D/12.D0)*INTERPOLATION(ABS(GAMA(X,TI+1)),TOU_GAMA, NS)
             ELSE
                Q(X,TI+1)=(PI**2*B*EFF_D/12.D0)*INTERPOLATION(GAMA(X,TI+1), TOU_GAMA,
NS)
             END IF
END DO
DEFLECTION(1,TI+1)=W(1,TI+1)
DEFLECTION(NN,TI+1)=W(NN,TI+1)
DO X=2,NN
   IF (X<NN/2) THEN
      DEFLECTION(X,TI+1)=DEFLECTION(X-1,TI+1)+W(X,TI+1)+BETA(X-1,TI+1)*DX
   ELSE
      DEFLECTION(X,TI+1)=DEFLECTION(X-1,TI+1)-W(X,TI+1)+BETA(X-1,TI+1)*DX
   END IF
END DO
IF(BOUNDARY==1)THEN
   BETA_(:)=BETA(:,TI+1)-BETA(1,TI+1)
   W_(:)=W(:,TI+1)-W(1,TI+1)
   CALL DERIVATIVE(NN,BETA(:,TI+1),DX,PHI_)
   DO X=1,NN
      IF (PHI_(X)<0.D0) THEN
         M_(X)=-INTERPOLATION(ABS(PHI_(X)), M_PHI, NM)
      ELSE
         M_(X)=INTERPOLATION(PHI_(X), M_PHI, NM)
      END IF
   END DO
   M_=M_+M(:,TI+1)
ELSE IF(BOUNDARY==2)THEN
   W_(:)=W(:,TI+1)-W(1,TI+1)
   DO X=1,NN
      THETA=M(X,TI+1)/(K_S+K_B)
      M_(X)=M(X,TI+1)-K_S*THETA
      BETA_(X)=BETA(X,TI+1)-((NN-1.D0)-2.D0*(X-1.D0))*THETA/(NN-1.D0)
   ENDDO
ELSE IF(BOUNDARY==3)THEN
   M_(:)=M(:,TI+1)-M(1,TI+1)
   W_(:)=W(:,TI+1)-W(1,TI+1)
   DO X=1,NN
      THETA=M(X,TI+1)/(K_S+K_B)
      BETA_(X)=BETA(X,TI+1)-((NN-1.D0)-2.D0*(X-1.D0))*THETA/(NN-1.D0)
   ENDDO
ELSE IF(BOUNDARY==4)THEN
   W_(:)=K_T*Q(:,TI+1)
   BETA_(:)=0.D0
   CALL DERIVATIVE(NN,BETA(:,TI+1),DX,PHI_)
   DO X=1,NN
      IF (PHI_(X)<0.D0) THEN
         M_(X)=-INTERPOLATION(ABS(PHI_(X)), M_PHI, NM)
      ELSE
         M_(X)=INTERPOLATION(PHI_(X), M_PHI, NM)
```

```
      END IF
   END DO
   M_=M_+M(:,TI+1)
ELSE IF(BOUNDARY==5)THEN
   W_(:)=K_T*Q(:,TI+1)
   M_(:)=0.D0
   DO X=1,NN
      THETA=M(X,TI+1)/(K_S+K_B)
      BETA_(X)=BETA(X,TI+1)-((NN-1.D0)-2.D0*(X-1.D0))*THETA/(NN-1.D0)
   ENDDO
ELSE IF(BOUNDARY==6)THEN
   W_(:)=K_T*Q(:,TI+1)
   DO X=1,NN
      THETA=M(X,TI+1)/(K_S+K_B)
      M_(X)=M(X,TI+1)-K_S*THETA
      BETA_(X)=BETA(X,TI+1)-((NN-1.D0)-2.D0*(X-1.D0))*THETA/(NN-1.D0)
   ENDDO
ELSE
   BETA_=BETA(:,TI+1)
   W_=W(:,TI+1)
   M_=M(:,TI+1)
ENDIF
GAMA_=GAMA(:,TI)
PHI_ =PHI(:,TI+1)
TOU_=TOU(:,TI+1)
Q_=Q(:,TI+1)
DEFLECTION_=DEFLECTION(:,TI+1)
WRITE (66,76)BETA_
WRITE (67,77)W_
WRITE (68,78)GAMA_
WRITE (69,79)PHI_
WRITE (70,80)M_
WRITE (71,81)TOU_
WRITE (72,82)Q_
WRITE (73,83)DEFLECTION_
      END IF
   END DO
   FAIL=.TRUE.
  END DO
  CLOSE (66)
  CLOSE (67)
  CLOSE (68)
  CLOSE (69)
  CLOSE (70)
  CLOSE (71)
  CLOSE (72)
  CLOSE (73)
76         FORMAT (25(F16.8, 2X))
77         FORMAT (25(F16.8, 2X))
78         FORMAT (25(F16.8, 2X))
79         FORMAT (25(F16.8, 2X))
80         FORMAT (25(F16.4, 2X))
81         FORMAT (25(F16.8, 2X))
82         FORMAT (25(F16.8, 2X))
83         FORMAT (25(F16.8, 2X))
  DEALLOCATE(BETA_,W_,GAMA_,PHI_,M_,TOU_,Q_,DEFLECTION_)
END PROGRAM ONE_D_ANALYSIS
```

APPENDIX D-I

TIME HISTORY PLOTS FOR PANELS WITH FLEXIBLE CONNECTIONS

Maximum mid-panel deflection

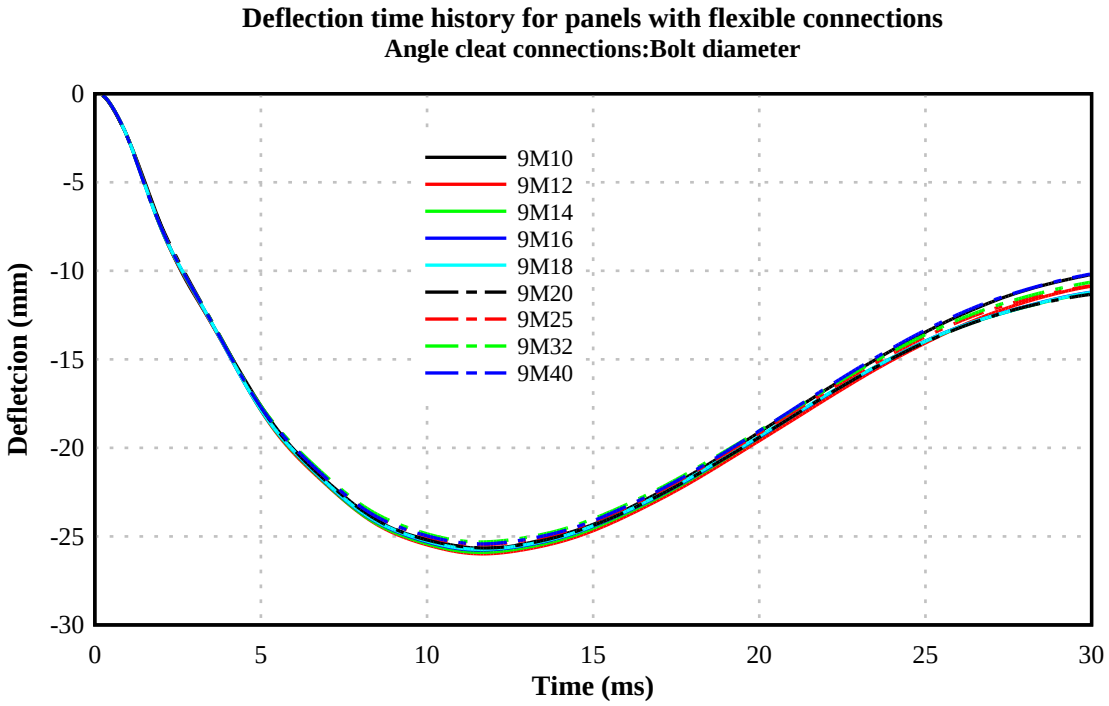

Figure D.1: Maximum mid-panel deflection-Angle cleat connected panels with bolt diameter

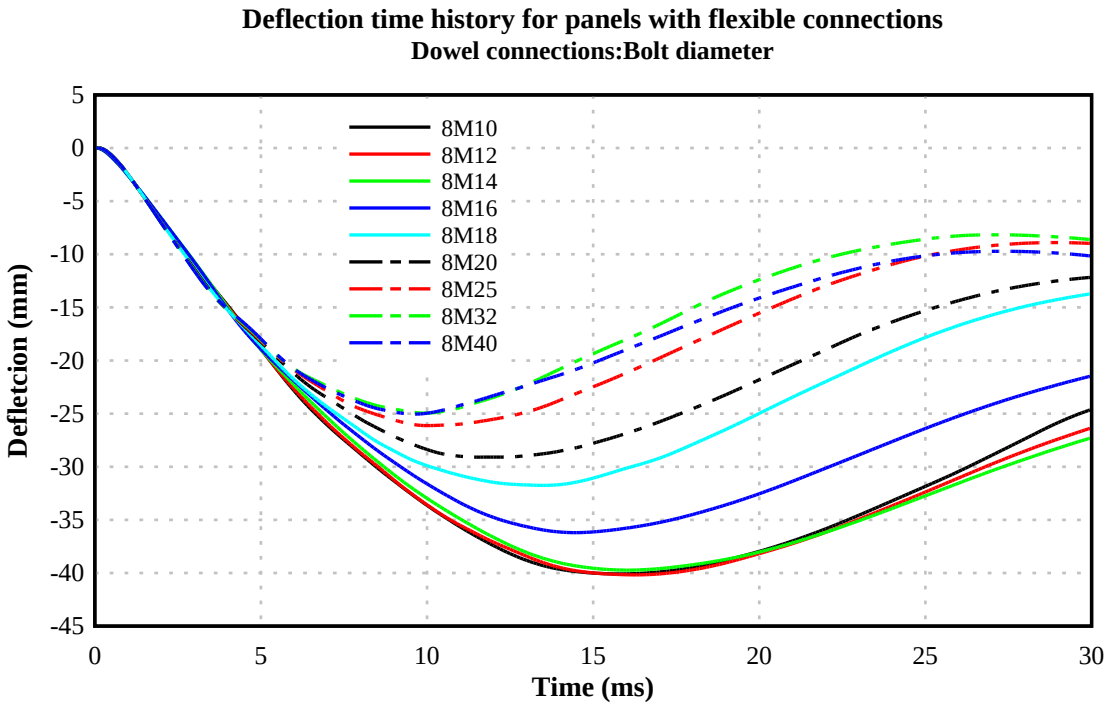

Figure D.2: Maximum mid-panel deflection-Dowel connected panels with bolt diameter

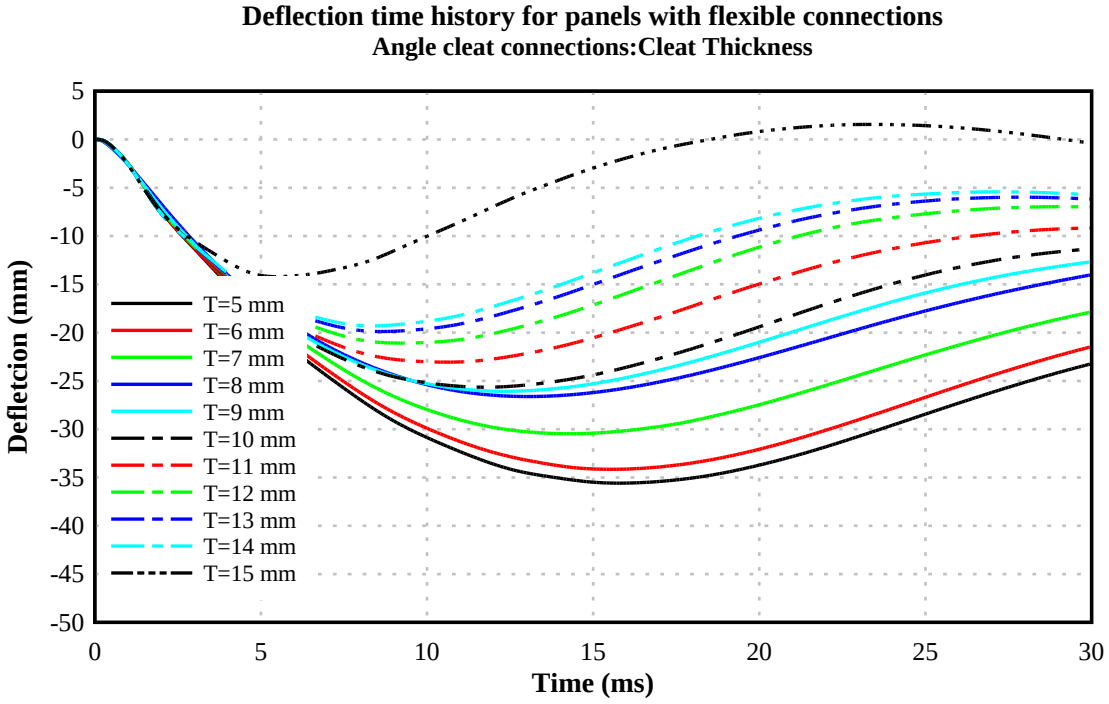

Figure D.3: Maximum mid-panel deflection-Angle cleat connected panels with cleat thickness

APPENDIX D-II

TIME HISTORY PLOTS FOR PANELS WITH OPENINGS

Maximum mid-panel deflection – Dowel connected panels with unstiffened openings

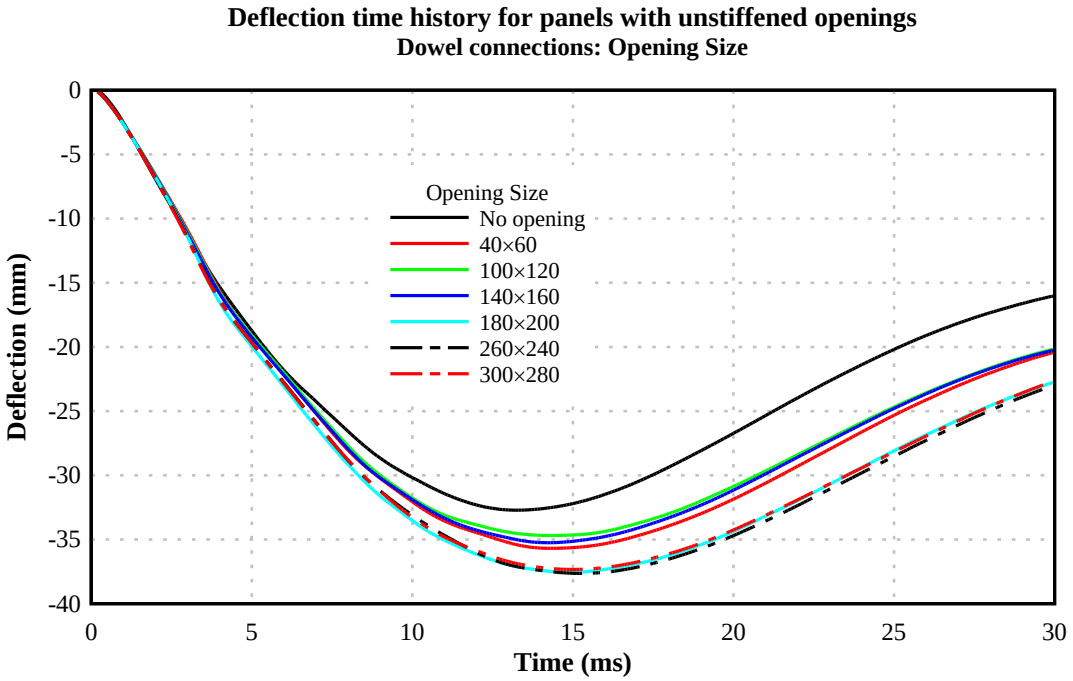

Figure D.4: Maximum mid-panel deflection-Dowel connected panels with unstiffened opening size

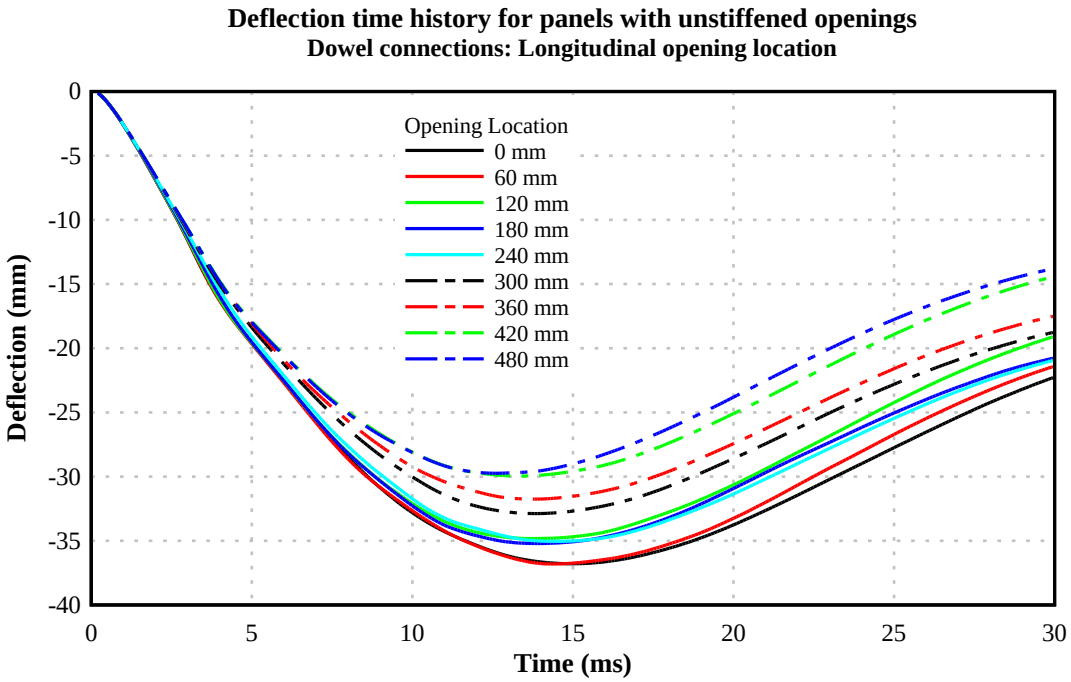

Figure D.5: Maximum mid-panel deflection-Dowel connected panels with unstiffened opening location –Longitudinal

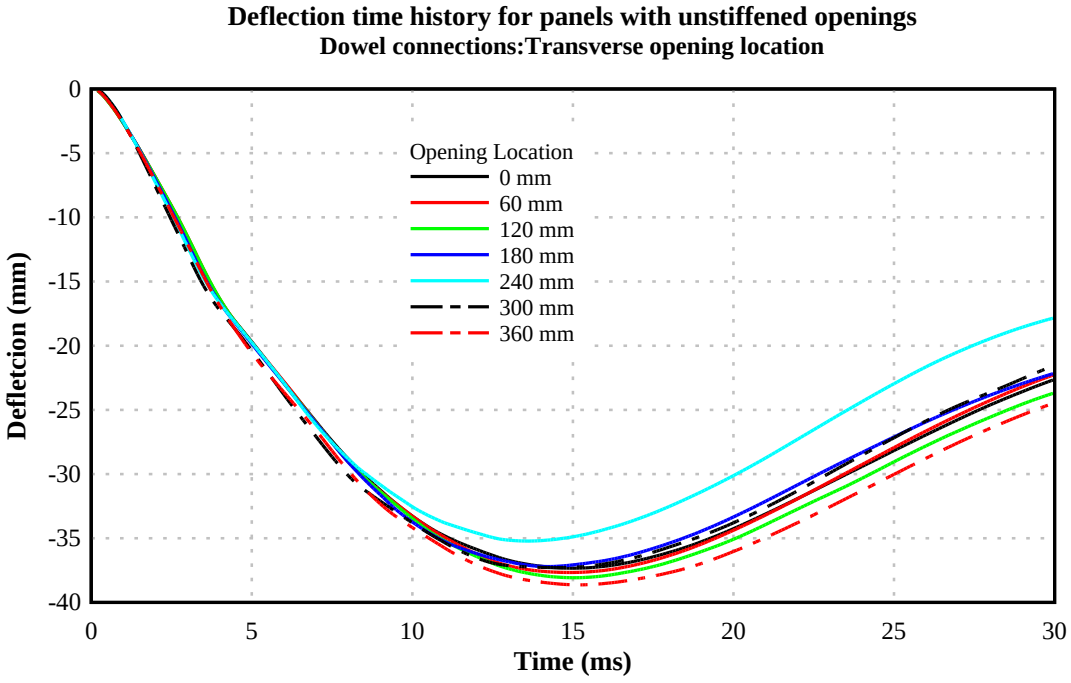

Figure D.6: Maximum mid-panel deflection-Dowel connected panels with unstiffened opening location –Transverse

Maximum mid-panel deflection – Angle cleat connected panels with unstiffened openings

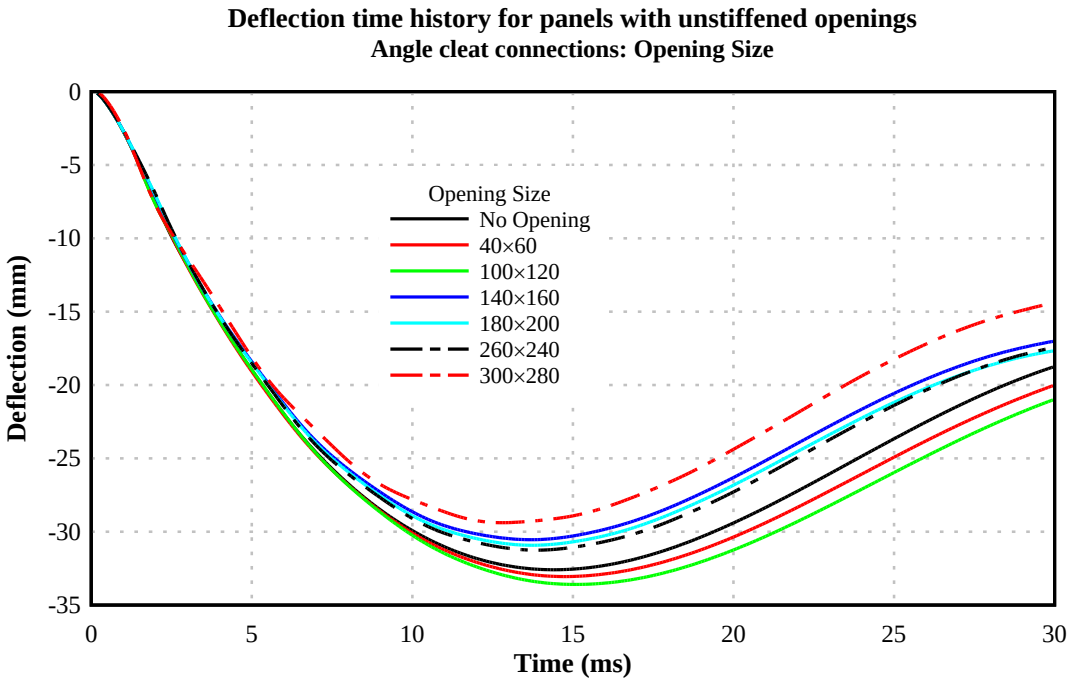

Figure D.7: Maximum mid-panel deflection-Angle cleat connected panels with unstiffened opening size

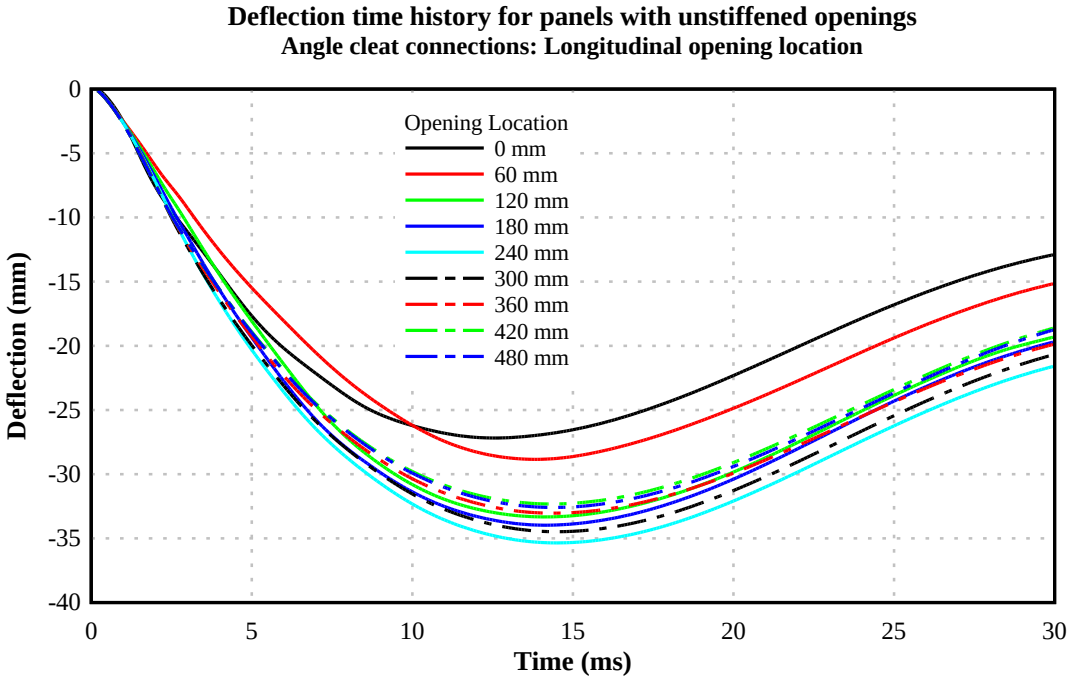

Figure D.8: Maximum mid-panel deflection-Angle cleat connected panels with unstiffened opening location – Longitudinal

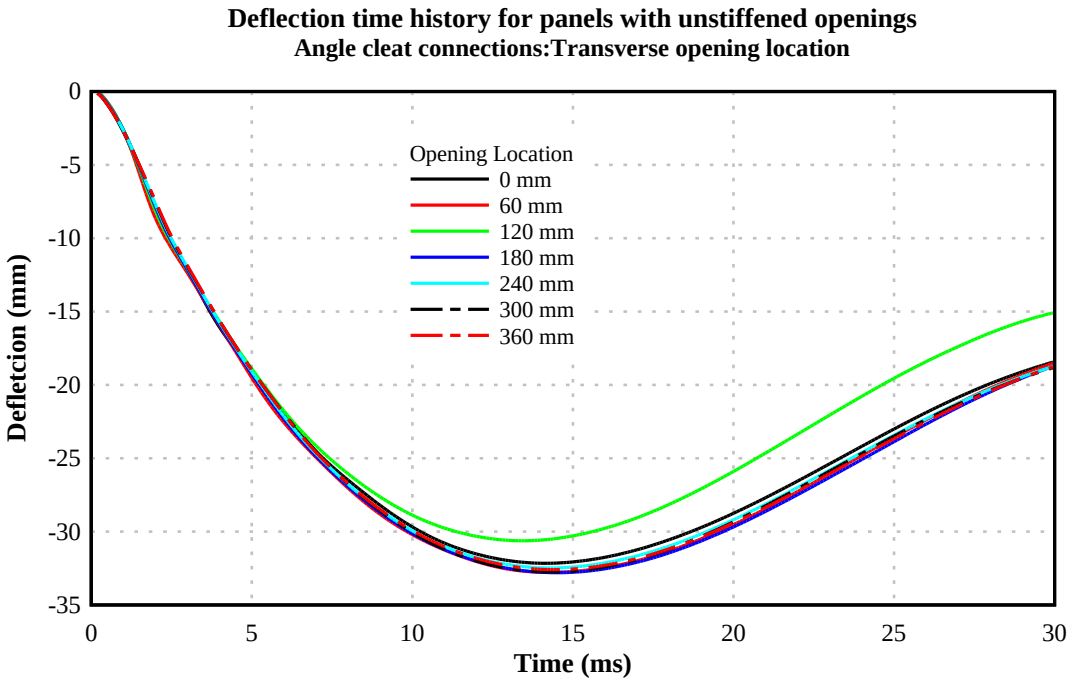

Figure D.9: Maximum mid-panel deflection-Angle cleat connected panels with unstiffened opening location – Transverse

Maximum mid-panel deflection – Dowel connected panels with stiffened openings

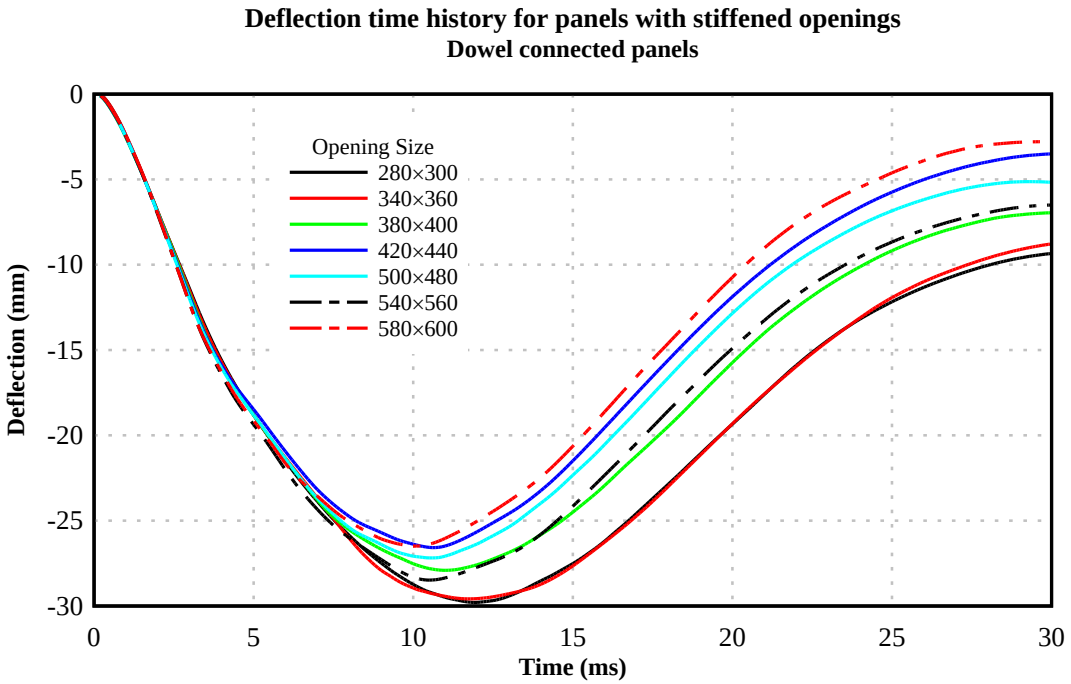

Figure D.10: Maximum mid-panel deflection-Dowel connected panels with stiffened opening size

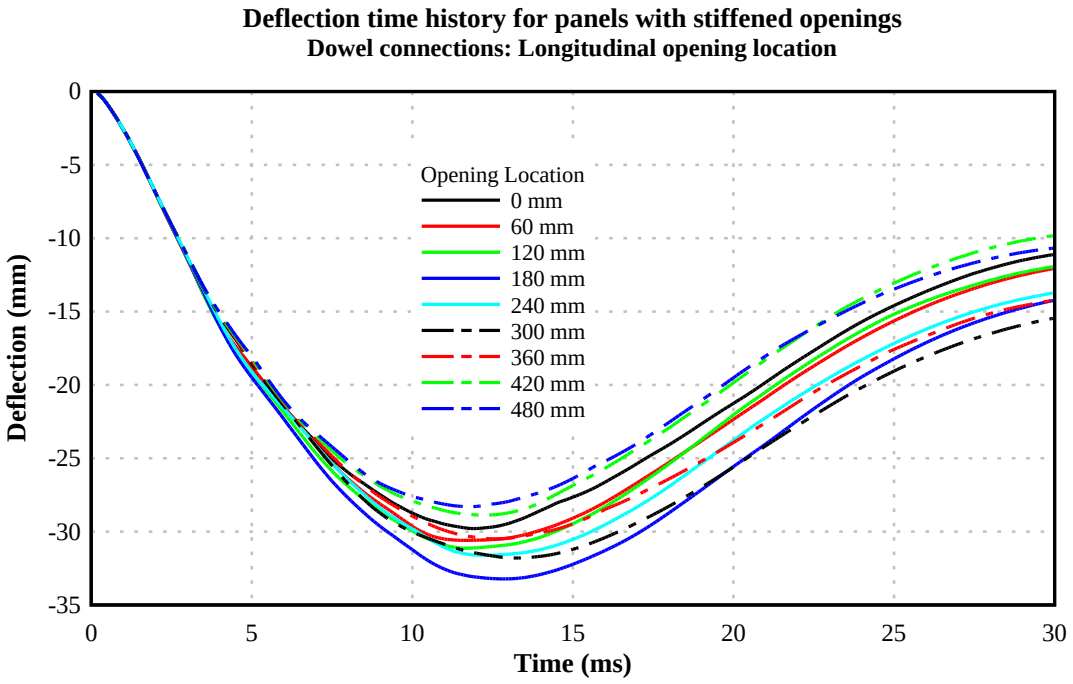

Figure D.11: Maximum mid-panel deflection-Dowel connected panels with stiffened opening location –Longitudinal

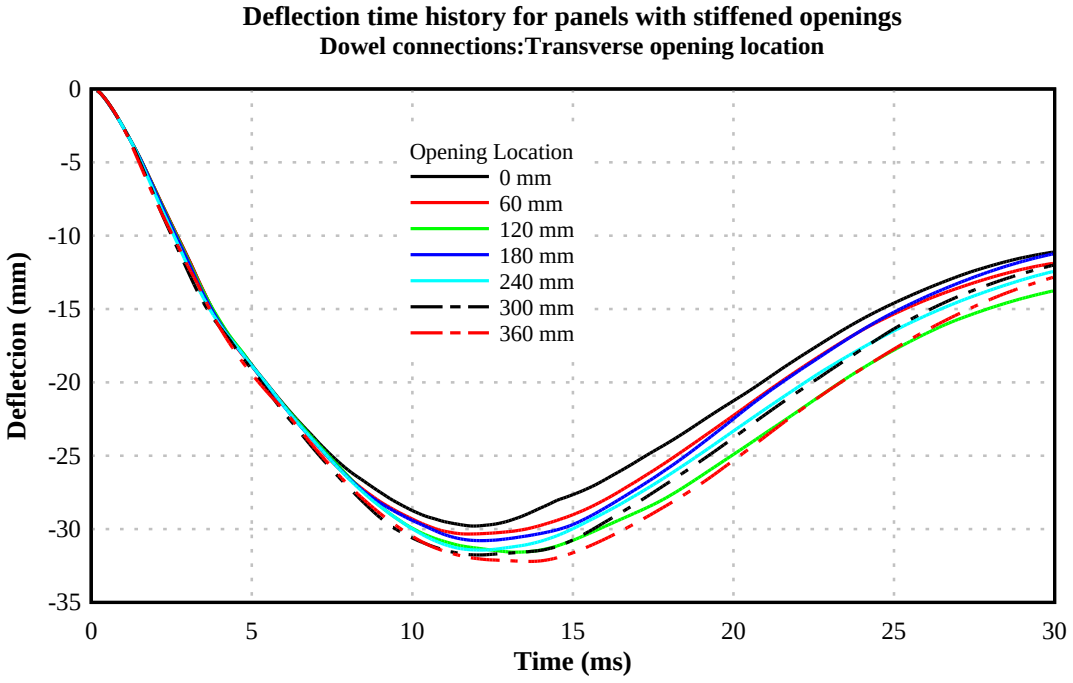

Figure D.12: Maximum mid-panel deflection-Dowel connected panels with stiffened opening location –Transverse

Maximum mid-panel deflection – Angle cleat connected panels with stiffened openings

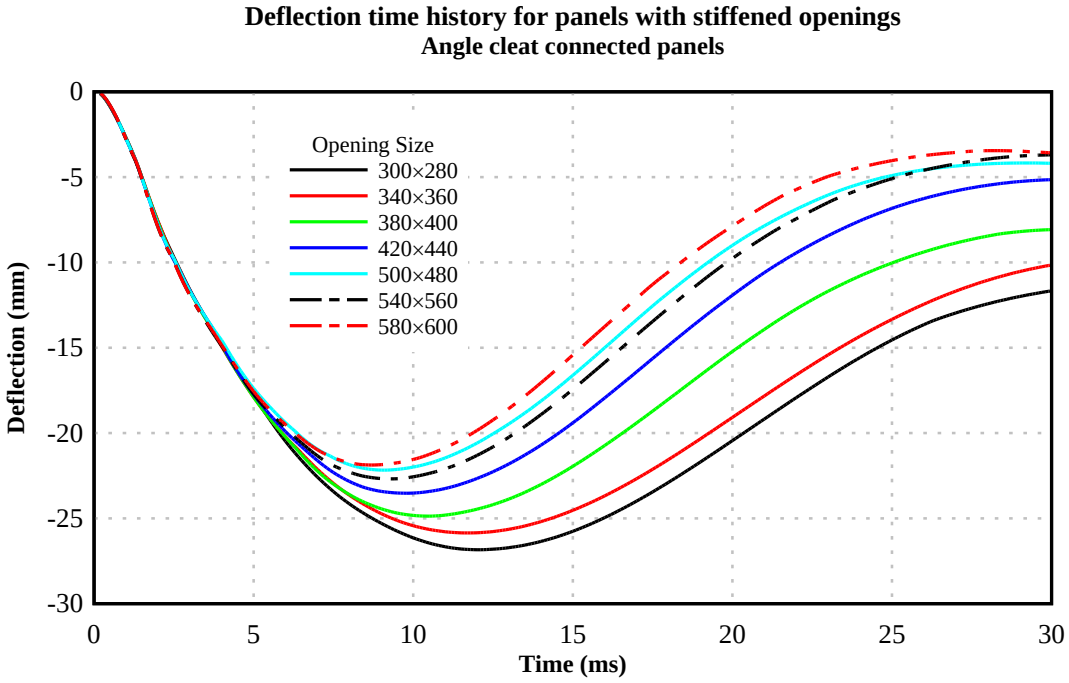

Figure D.13: Maximum mid-panel deflection-Angle cleat connected panels with stiffened opening size

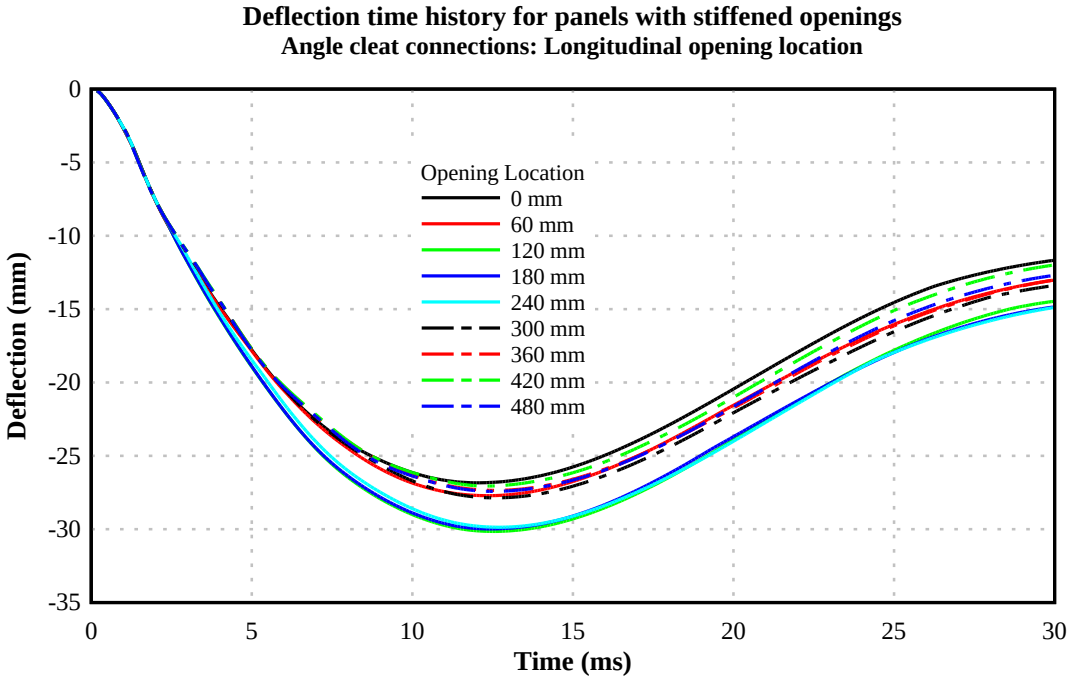

Figure D.14: Maximum mid-panel deflection-Angle cleat connected panels with stiffened opening location – Longitudinal

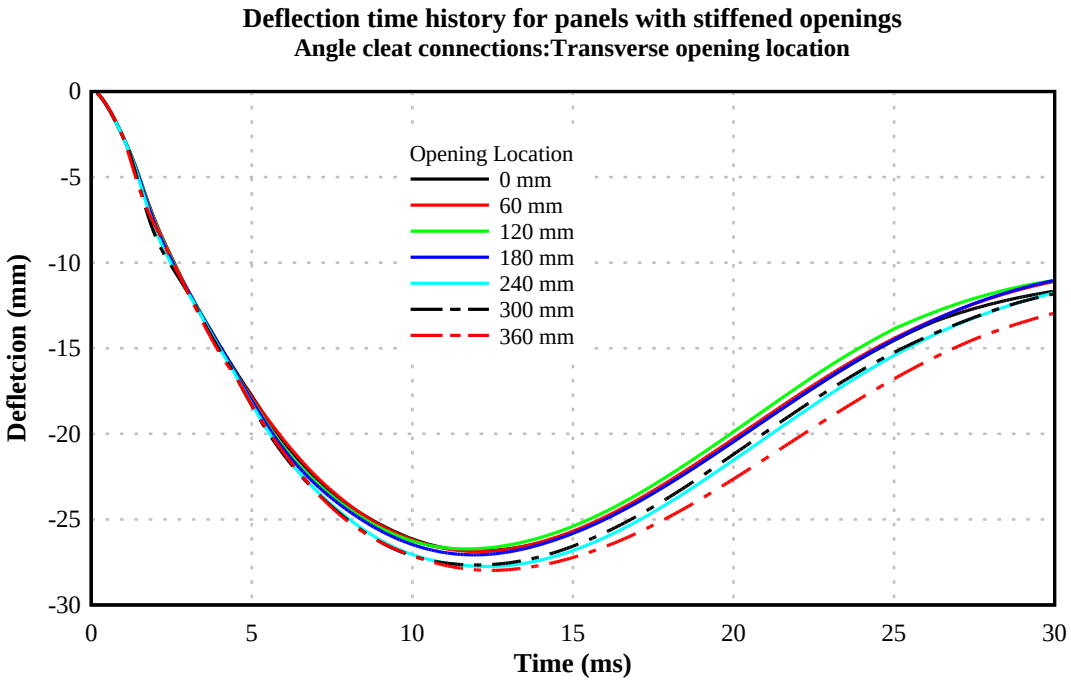

Figure D.15: Maximum mid-panel deflection-Angle cleat connected panels with stiffened opening location – Transverse

APPENDIX D-III

TIME HISTORY PLOTS FOR CURVED PANELS

Maximum mid-panel deflection – Type A

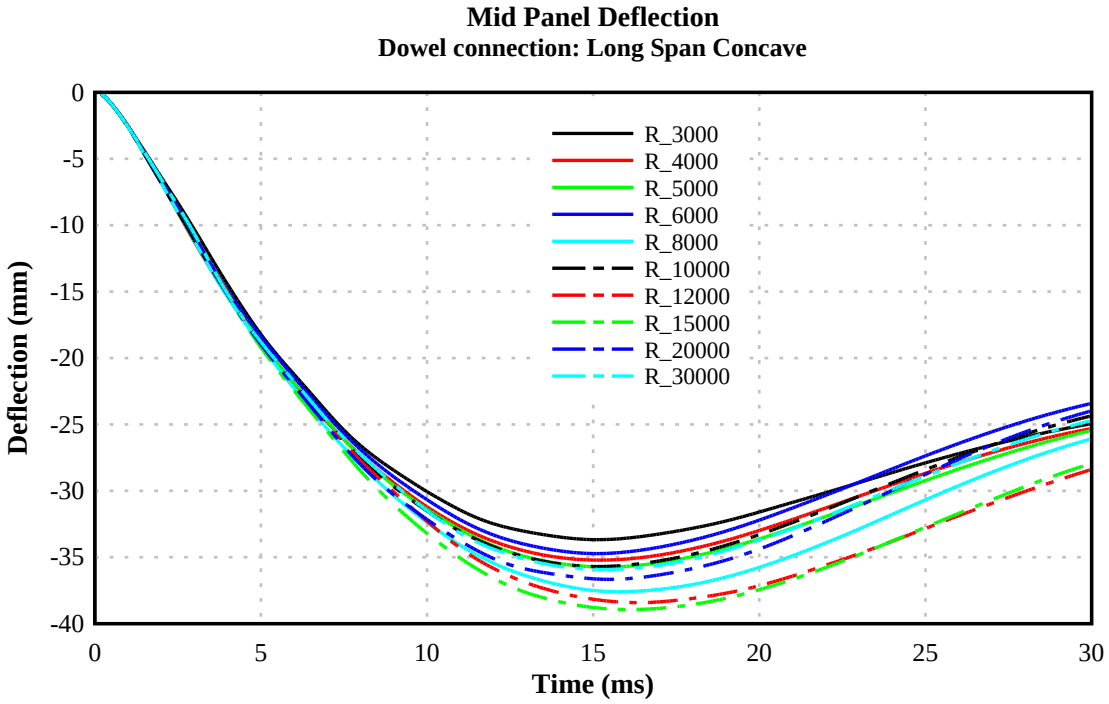

Figure D.16: Maximum mid-panel deflection-Dowel connected, long span, concave panels

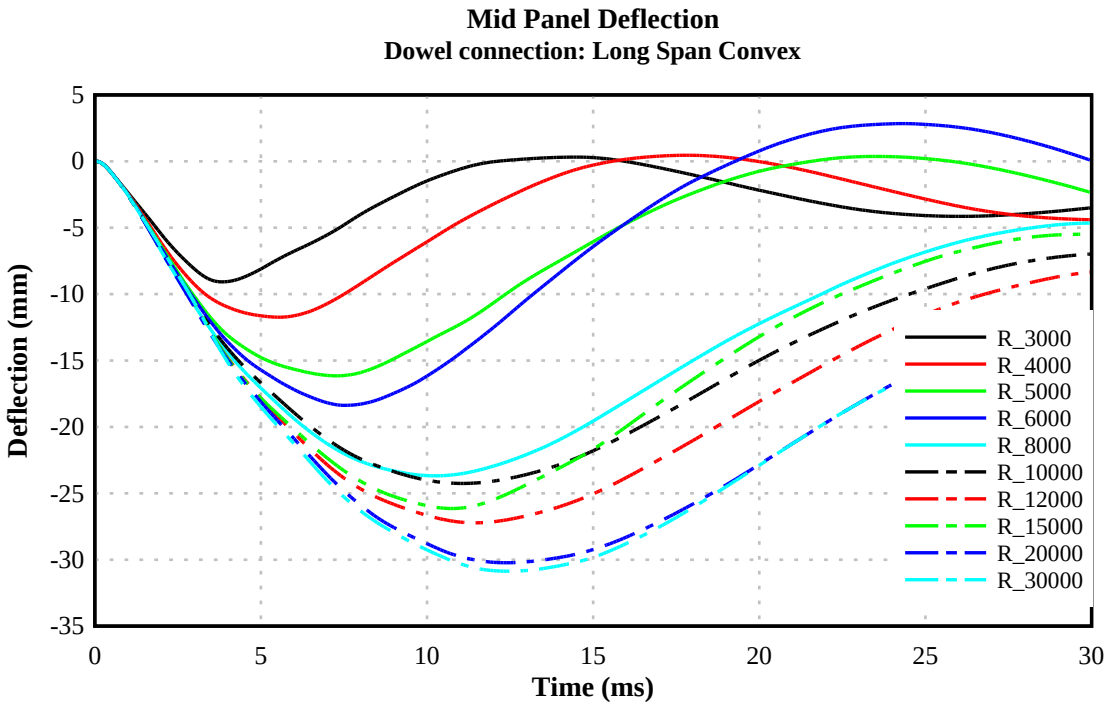

Figure D.17: Maximum mid-panel deflection-Dowel connected, long span, convex panels

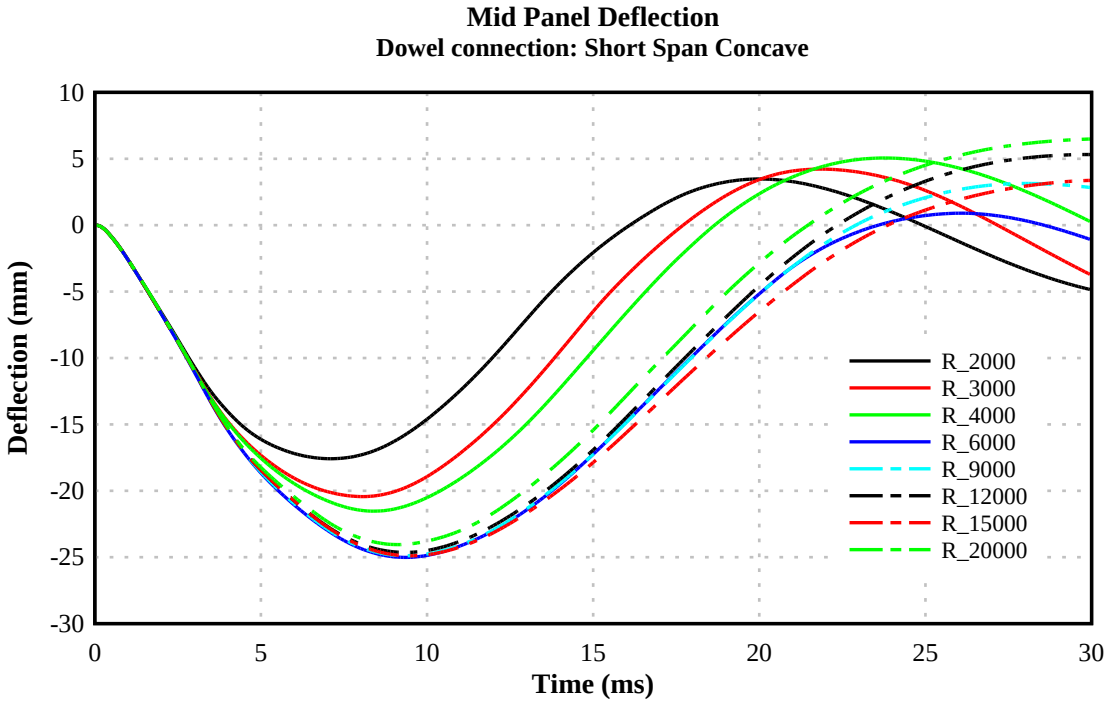

Figure D.18: Maximum mid-panel deflection-Dowel connected, short span, concave panels

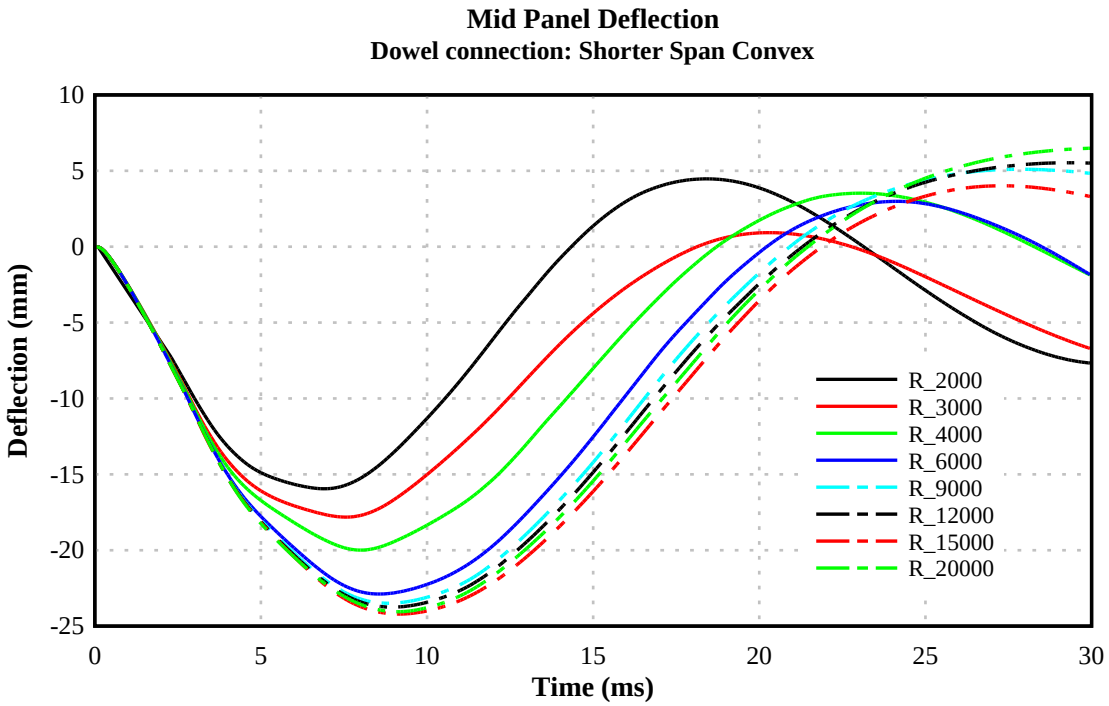

Figure D.19: Maximum mid-panel deflection-Dowel connected, short span, convex panels

Maximum mid-panel deflection – Type B

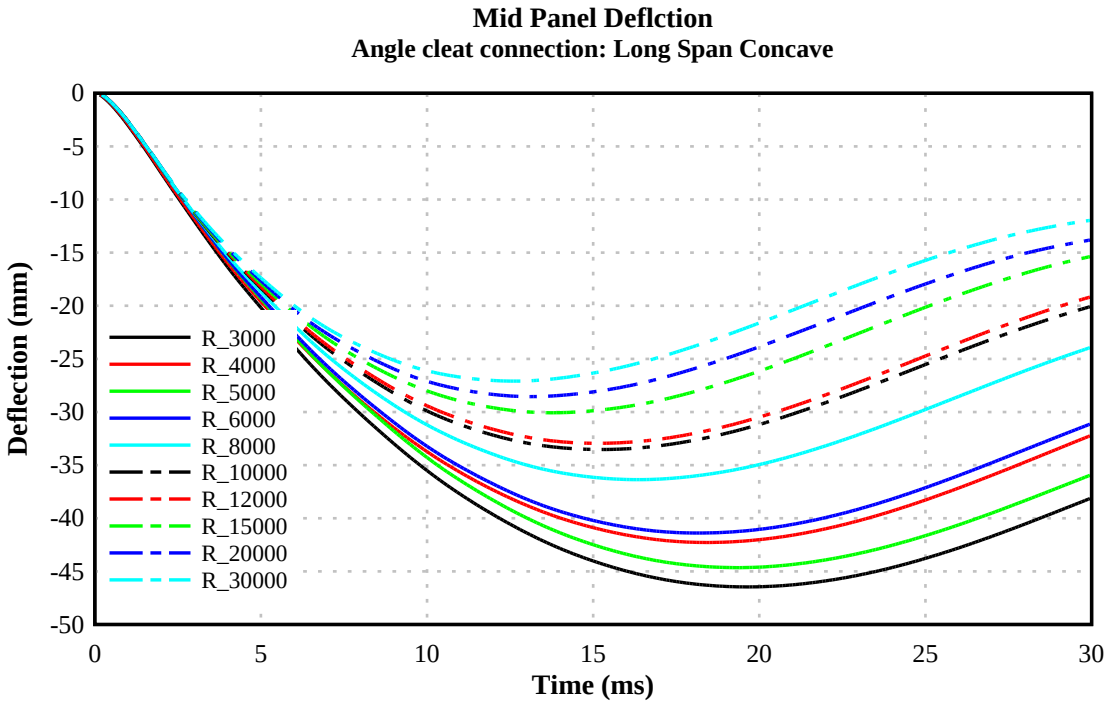

Figure D.20: Maximum mid-panel deflection-Angle cleat connected, long span, concave panels

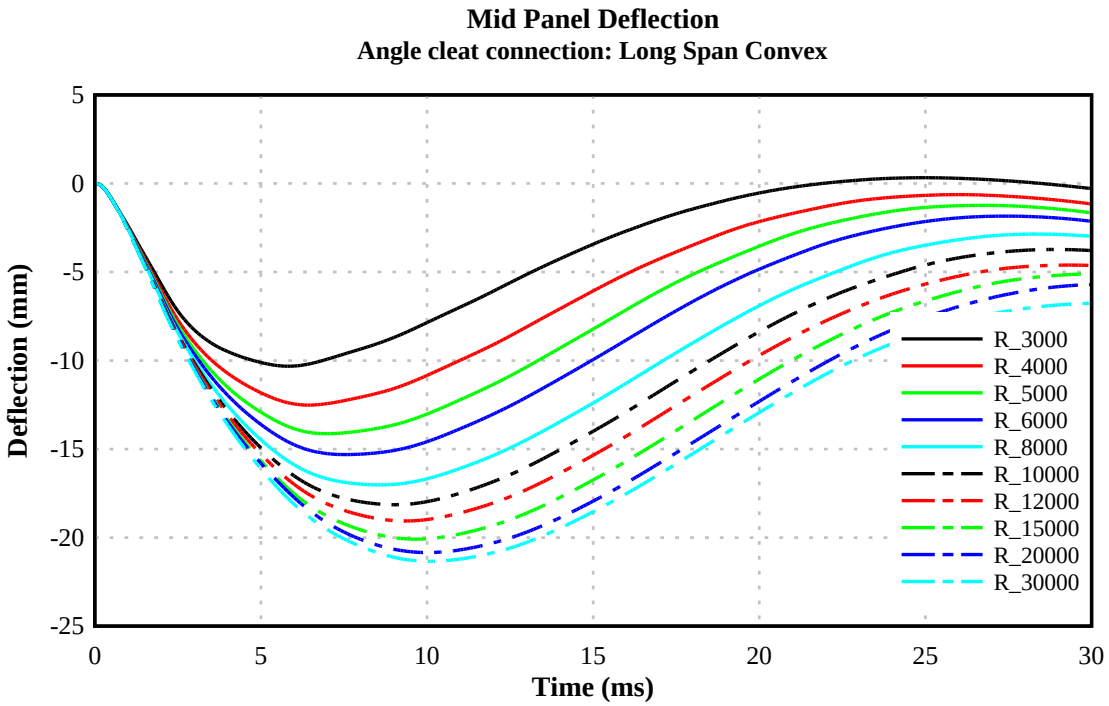

Figure D.21: Maximum mid-panel deflection-Angle cleat connected, long span, convex panels

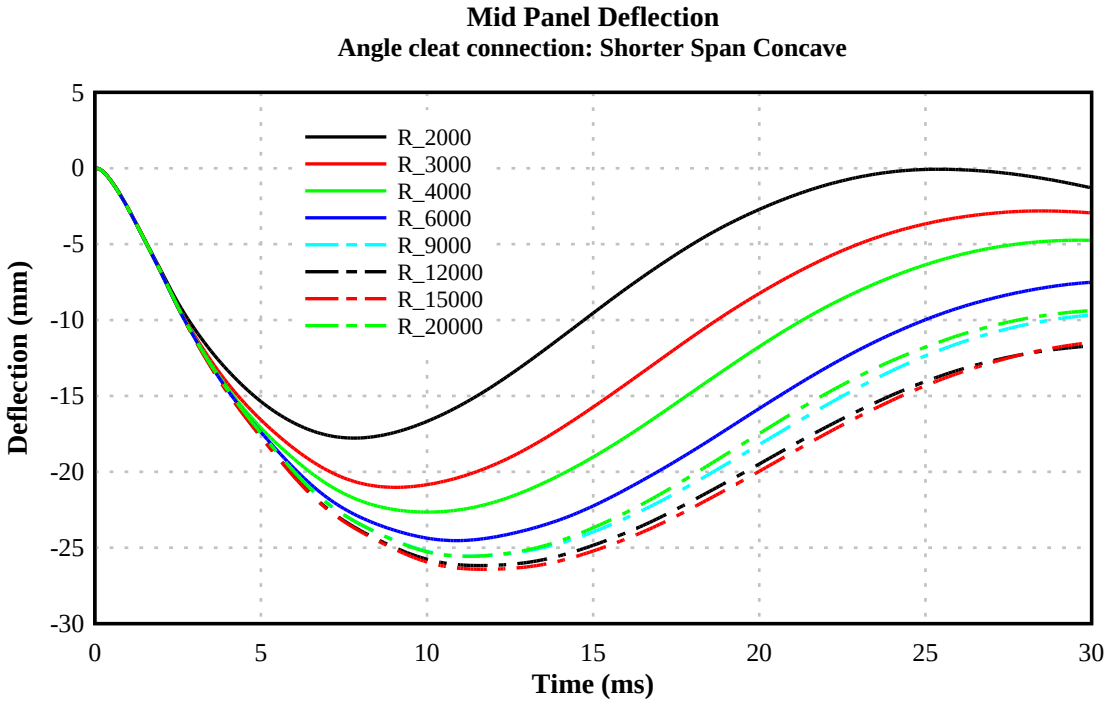

Figure D.22: Maximum mid-panel deflection-Angle cleat connected, short span, concave panels

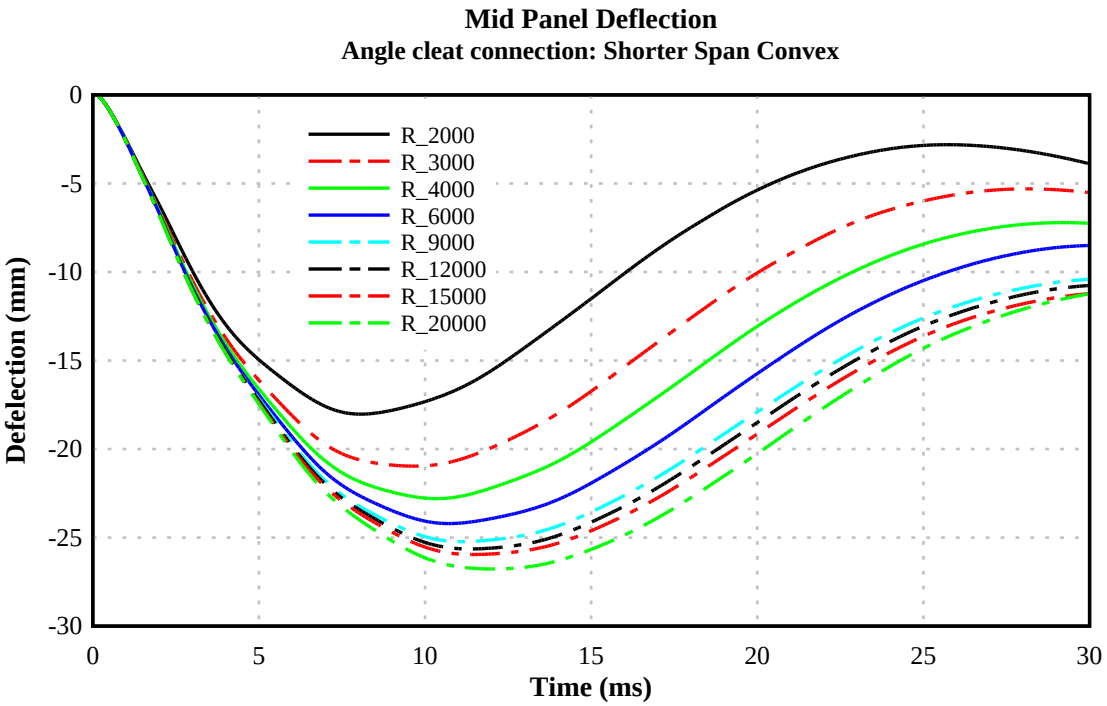

Figure D.23: Maximum mid-panel deflection-Angle cleat connected, short span, convex panels